

THE JOURNAL OF PHYSICAL CHEMISTRY

Volume 74, Number 6 March 19, 1970

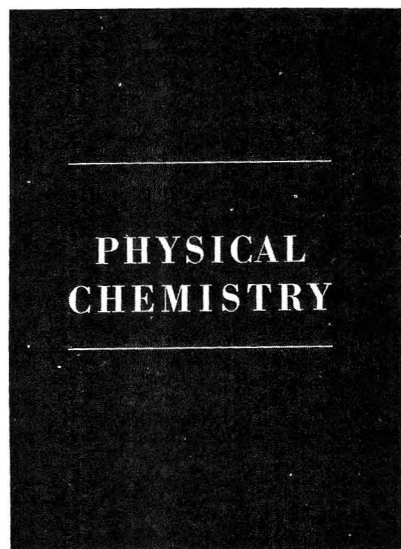
Rotational Barriers in O-(N,N-Dimethylcarbamoyl) Oximes. Experimental Results and Nonempirical Molecular Orbital (NEMO) Calculations C. Hackett Bushweller, Philip E. Stevenson, John Golini, and James W. O'Neil	1155
Ultrasonic Absorption in Aqueous Salts of the Lanthanides. III. Temperature Dependence of LnSO ₄ Complexation Douglas P. Fay and Neil Purdie	1160
Kinetics of Isopropyl Alcohol Radicals by Electron Spin Resonance-Flow Techniques R. E. James and F. Sicilio	1166
The Kinetics of the Reactions of Cobalt(II) and Cobalt(III) Acetates with Benzyl Hydroperoxide in Acetic Acid at 25° E. J. Y. Scott	1174
The Kinetics of Dissociation of Chlorine Pentafluoride J. A. Blauer, H. G. McMath, F. C. Jaye, and V. S. Engleman	1183
A Mass Spectrometric Study of the Dimerization of Nitrosomethane F. A. Thomassy and F. W. Lampe	1188
Chemical Kinetics of Carbonyl Fluoride Decomposition in Shock Waves A. P. Modica	1194
Flash Photolysis of Hydrocarbons in the Far-Ultraviolet. I. Ethane B. C. Roquette	1204
Properties of Trapped H and D Atoms Produced by the Photolysis of HI in 3MP-d ₁₄ Glass Mervyn A. Long and John E. Willard	1207
Pulse Radiolysis of Aliphatic Acids in Aqueous Solution. III. Simple Amino Acids P. Neta, M. Simic, and E. Hayon	1214
High-Intensity Radiolysis of Aqueous Ferrous Sulfate-Cupric Sulfate-Sulfuric Acid Solutions Paul Y. Feng, Ari Brynjolfsson, John W. Halliday, and Robert D. Jarrett	1221
Magnetophotoselection. Effect of Depopulation and Triplet-Triplet Absorption Henry S. Judeikis and Seymour Siegel	1228
Conjugated Radicals. I. Introductory Remarks and Method of Calculation R. Zahradník and P. Čásky	1235
Conjugated Radicals. II. Semiempirical Calculations of Electronic Spectra of Radical Anions Derived from Alternant Hydrocarbons R. Zahradník and P. Čásky	1240
Conjugated Radicals. III. Calculations of Electronic Spectra of Alternant Odd Radicals of the Allyl, Benzyl, and Phenalenyl Type P. Čásky and R. Zahradník	1249
A Spectroscopic Investigation of Intramolecular Interactions in <i>cis</i> and <i>trans</i> Dimers of Acenaphthylene Nori Y. C. Chu and David R. Kearns	1255
Spectroscopy of Sulfur in Ethylenediamine Robert MacColl and Stanley Windwer	1261
The Spin-Lattice Relaxation of Oxygen-17 in Water J. C. Hindman, A. Svirnickas, and M. Wood	1266
Dielectric Studies. XXVII. Relaxation Process of Pyrrole-Pyridine and Chloroform-Pyridine Systems S. W. Tucker and S. Walker	1270
Dielectric and Thermodynamic Behavior of the System 1,1,1-Trichloroethane-Benzene- <i>o</i> -Dichlorobenzene E. M. Turner, D. W. Anderson, L. A. Reich, and W. E. Vaughan	1275
Electrophoresis of a Rod-like Polyelectrolyte in Salt Solution Toru Takahashi, Ichiro Noda, and Mitsuru Nagasawa	1280
Electrical Conductance, Diffusion, Viscosity, and Density of Sodium Nitrate, Sodium Perchlorate, and Sodium Thiocyanate in Concentrated Aqueous Solutions G. J. Janz, B. G. Oliver, G. R. Lakshminarayanan, and G. E. Mayer	1285

Balancing act?

In the field of physical chemistry?

Of course.

*The American Chemical Society's **Journal of Physical Chemistry** does it all the time. It maintains an excellent balance between reporting on classical areas of chemistry and very modern structural quantum mechanical areas.*



Preference is given to papers dealing with fundamental aspects of atomic and molecular phenomena. Emphasis is placed on reportage of work involving new concepts—new techniques—and new interpretations.

Now appearing biweekly, the JOURNAL OF PHYSICAL CHEMISTRY's forty or more articles per issue cover a wide range of subjects that are of interest to ALL physical chemists. You'll profit from the full articles, notes and communications published in the journal . . . since only those which represent distinct contributions to the literature are accepted.

For balanced reading, subscribe to the JOURNAL OF PHYSICAL CHEMISTRY now. Just complete and return the form below.

American Chemical Society / 1155 Sixteenth Street, N.W., Washington, D.C. 20036

Please enter my subscription to **The Journal of Physical Chemistry** at the rates checked below.

ACS Members: U.S. \$20 Canada, PUAS \$24 Other Nations \$25

Nonmembers: U.S. \$40 Canada, PUAS \$44 Other Nations \$45

Bill me Bill employer Payment enclosed (Payable to American Chemical Society)

Name _____ Title _____

Employer _____

Address: Home Business _____

City _____ State/Country _____ Zip _____

Nature of employer's business? Manufacturing or processing Academic Government
 Other _____

(Please indicate)

Note: Subscriptions at ACS Member Rates are for personal use only.

I am an ACS member I am not an ACS member

Payment must be made in U.S. currency, by international money order, UNESCO coupons, U.S. bank draft; or order through your book dealer.

HOA

Ammonium Ion Adsorption in Sintered Porous Glass. An Infrared Determination of Selectivity Constants	Michael L. Hair	1290
Micellar Aggregation Properties of Some Zwitterionic N-Alkyl Betaines	J. Swarbrick and J. Daruwala	1293
Reactive Silica. III. The Formation of Boron Hydrides, and Other Reactions, on the Surface of Boria-Impregnated Aerosil	Claudio Morterra and M. J. D. Low	1297
Thermodynamics of Globular Molecules. XVII. Heat Capacities and Transition Behavior of Bicyclo[2.2.2]octane and Bicyclo[2.2.2]octene	Wen-Kuei Wong and Edgar F. Westrum, Jr.	1303
Dimethyl Sulfoxide and Dimethyl Sulfone. Heat Capacities, Enthalpies of Fusion, and Thermodynamic Properties	H. Lawrence Clever and Edgar F. Westrum, Jr.	1309
Studies of Adsorbed Species. I. Electron Spin Resonance of Nitrogen Heterocyclics Adsorbed on Magnesium Oxide and Silica-Alumina	K. S. Seshadri and L. Petrakis	1317
Membrane Potentials of Fused Silica in Molten Salts. A Reevaluation	Kurt H. Stern	1323
The Effect of Anions on Sodium-Determined Glass Membrane Potentials in Molten Salts	Kurt H. Stern	1329
Determination and Comparison of Hittorf and Cell Transference Numbers for Aqueous Silver Nitrate Solutions at 25°	Michael J. Pikal and Donald G. Miller	1337
A Kinetic Study of the Dehydration and Dehydrobromination of <i>trans</i> -Dibromobis(ethylenediamine)cobalt(III) Diaquohydrogen Bromide, <i>trans</i> -[Co(en) ₂ Br ₂](H ₂ O) ₂ Br ₂	H. Eugene LeMay, Jr.	1345
The Thermal Decomposition of Orthorhombic Ammonium Perchlorate Single Crystals	K. J. Kraeutle	1350
On the Gas-Phase Thermal Reaction between Perfluoroacetone and Propene	Alvin S. Gordon	1357
Paramagnetic Resonance of Sulfur Radicals in Synthetic Sodalites	S. D. McLaughlan and D. J. Marshall	1359
The Molecular Structure of Perfluoroborodisilane, Si ₂ BF ₇ , as Determined by Electron Diffraction	C. H. Chang, R. F. Porter, and S. H. Bauer	1363
Effect of Membranes and Other Porous Networks on the Equilibrium and Rate Constants of Macromolecular Reactions	J. Calvin Giddings	1368
Intercombination Bands in the Spectra of Some Quadrate Chromium(III) Complexes	Robert K. Lowry, Jr., and Jayarama R. Perumareddi	1371
Nuclear Magnetic Resonance Techniques for the Study of Preferential Solvation and the Thermodynamics of Preferential Solvation	Lawrence S. Frankel, Cooper H. Langford, and Thomas R. Stengle	1376
Kinetic Studies of the Reaction of Triphenylmethane Dyes in Acid and Alkaline Media. I. Ethyl Violet in Alkaline Medium	Sudhir K. Sinha and Sarvagya S. Katiyar	1382

NOTES

S-H . . . S Type Hydrogen-Bonding Interaction	Samaresh Mukherjee, Santi R. Palit, and Sadhan K. De	1389
The Circular Dichroism of Some Aliphatic Amino Acid Derivatives. A Reexamination	Claudio Toniolo	1390
The Effect of Visible and Ultraviolet Light on the Palladium-Catalyzed Oxidation of Carbon Monoxide	Raymond F. Baddour and Michael Modell	1392
Gas-Phase Photolysis at 1470 Å of Mixtures of Cyclohexane with Benzene and with Nitrous Oxide at 750 Torr	Robert R. Hentz and D. B. Peterson	1395
Nuclear Magnetic Resonance Study of Solvent Effects on Hydrogen Bonding in Methanol	William B. Dixon	1396

COMMUNICATIONS TO THE EDITOR

Multiple Equilibria in Donor-Acceptor Complexing Studied by Ultracentrifugation	Philip J. Trotter and David A. Yphantis	1399
Holography and Holographic Interferometry for Thermal Diffusion Studies in Solutions	Julius G. Becsey, Gene E. Maddux, Nathaniel R. Jackson, and James A. Bierlein	1401
A Comment on the Infrared Spectrum of Carbon Monoxide Adsorbed on Silica-Supported Platinum	Noel W. Cant and W. Keith Hall	1403

AUTHOR INDEX

- Anderson, D. W., 1275
 Baddour, R. F., 1392
 Bauer, S. H., 1363
 Becsey, J. G., 1401
 Bierlein, J. A., 1401
 Blauer, J. A., 1183
 Brynjolfsson, A., 1221
 Bushweller, C. H., 1155
 Cant, N. W., 1403
 Čársky, P., 1235, 1240, 1249
 Chang, C. H., 1363
 Chu, N. Y. C., 1255
 Clever, H. L., 1309
 Daruwala, J., 1293
 De, S. K., 1389
 Dixon, W. B., 1396
 Engelman, V. S., 1183
 Fay, D. P., 1160
 Feng, P. Y., 1221
 Frankel, L. S., 1376
 Giddings, J. C., 1368
 Golini, J., 1155
 Gordon, A. S., 1357
 Hair, M. L., 1290
 Hall, W. K., 1403
 Halliday, J. W., 1221
 Hayon, E., 1214
 Hentz, R. R., 1395
 Hindman, J. C., 1266
 Jackson, N. R., 1401
 James, R. E., 1166
 Janz, G. J., 1285
 Jarrett, R. D., 1221
 Jaye, F. C., 1183
 Judeikis, H. S., 1228
 Katiyar, S. S., 1382
 Kearns, D. R., 1255
 Kraeutle, K. J., 1350
 Lakshminarayanan, G. R., 1285
 Lampe, F. W., 1188
 Langford, C. H., 1376
 LeMay, H. E., Jr., 1345
 Long, M. A., 1207
 Low, M. J. D., 1297
 Lowry, R. K., Jr., 1371
 MacColl, R., 1261
 Maddux, G. E., 1401
 Marshall, D. J., 1359
 Mayer, G. E., 1285
 McLaughlan, S. D., 1359
 McMath, H. G., 1183
 Miller, D. G., 1337
 Modell, M., 1392
 Modica, A. P., 1194
 Morterra, C., 1297
 Mukherjee, S., 1389
 Nagasawa, M., 1280
 Neta, P., 1214
 Noda, I., 1280
 Oliver, B. G., 1285
 O'Neil, J. W., 1155
 Palit, S. R., 1389
 Perumareddi, J. R., 1371
 Peterson, D. B., 1395
 Petrakis, L., 1317
 Pikal, M. J., 1337
 Porter, R. F., 1363
 Purdie, N., 1160
 Reich, L. A., 1275
 Roquette, B. C., 1204
 Scott, E. J. Y., 1174
 Seshadri, K. S., 1317
 Sicilio, F., 1166
 Siegel, S., 1228
 Simic, M., 1214
 Sinha, S. K., 1382
 Stengle, T. R., 1376
 Stern, K. H., 1323, 1329
 Stevenson, P. E., 1155
 Svirmickas, A., 1266
 Swarbrick, J., 1293
 Takahashi, T., 1280
 Thomassy, F. A., 1188
 Toniolo, C., 1390
 Trotter, P. J., 1399
 Tucker, S. W., 1270
 Turner, E. M., 1275
 Vaughan, W. E., 1275
 Walker, S., 1270
 Westrum, E. F., Jr., 1303, 1309
 Willard, J. E., 1207
 Windwer, S., 1261
 Wong, W.-K., 1303
 Wood, M., 1266
 Yphantis, D. A., 1399
 Zahradník, B., 1235, 1240, 1249

Rotational Barriers in O-(N,N-Dimethylcarbamoyl) Oximes.**Experimental Results and Nonempirical Molecular****Orbital (NEMO) Calculations**by C. Hackett Bushweller, Philip E. Stevenson, John Golini,¹ and James W. O'Neil*Department of Chemistry, Worcester Polytechnic Institute, Worcester, Massachusetts 01609 (Received October 27, 1969)*

A total line shape analysis of the temperature dependence of the proton magnetic resonance spectrum of the $N(CH_3)_2$ group in O-(N,N-dimethylcarbamoyl)-acetone oxime gives $\Delta H^\ddagger = 15.4$ kcal/mol, $\Delta S^\ddagger = +2.7$ eu, $\Delta G^\ddagger = 14.7$ kcal/mol at -10° , and $E_a = 16.0$ kcal/mol for rotation about the carbonyl carbon-nitrogen bond. Similar behavior is observed in O-(N,N-dimethylcarbamoyl)cyclohexanone oxime and O-(N,N-dimethylcarbamoyl)fluorenone oxime. Nonempirical molecular orbital (NEMO) calculations have been performed indicating substantial π bonding involving both oxygen atoms and the nitrogen atom of the carbamoyl group.

Resonance interactions coupled with inductive and steric effects are important in determining the magnitude of barriers about formally single or double bonds. Examples of increased barriers about single bonds due to resonance effects include amides,² formamides,³ enamines,⁴ amidines,⁵ 1-acylpyrroles,⁶ triazenes,⁷ hydrazones,⁴ N-nitrosoamines,⁸ and N,N-dimethylmethanesulfonamides.⁹ Indeed, resonance and steric effects appear to be major factors in the drastic reduction of the barrier to rotation about formal carbon-carbon double bonds in ketene mercaptals,¹⁰ ketene aminals,¹⁰ vinylamines,¹¹ and vinyl ethers.¹²

There have been few reports concerning the detection of a barrier to rotation about the carbonyl carbon-nitrogen bond in carbamates^{13a} or ureas^{13b} and no data concerning O-(N,N-dimethylcarbamoyl) oximes.^{14a}

This paper concerns the measurement using variable temperature nmr spectroscopy of the rotational barrier about the carbonyl carbon-nitrogen bond in O-(N,N-dimethylcarbamoyl)acetone oxime (I), O-(N,N-dimethylcarbamoyl)cyclohexanone oxime (II), and O-(N,N-dimethylcarbamoyl)fluorenone oxime (III). A

complete nmr line shape analysis was performed on the temperature dependence of the $N(CH_3)_2$ resonance

(1) National Science Foundation Undergraduate Research Participant, Summer 1969.

(2) R. C. Neuman, Jr., and V. Jonas, *J. Amer. Chem. Soc.*, **90**, 1970 (1968), and references therein.

(3) M. Rabinovitz and A. Pines, *ibid.*, **91**, 1585 (1969), and references therein.

(4) A. Mannschreck and V. Koelle, *Tetrahedron Lett.*, 863 (1967); A. P. Downing, W. D. Ollis, and J. O. Sutherland, *Chem. Commun.*, 143 (1967).

(5) D. J. Bertelli and J. T. Gerig, *Tetrahedron Lett.*, 2481 (1967).

(6) T. Natsuo and H. Shosenji, *Chem. Commun.*, 501 (1969).

(7) N. P. Marullo, C. B. Mayfield, and E. H. Wagener, *J. Amer. Chem. Soc.*, **90**, 510 (1968).

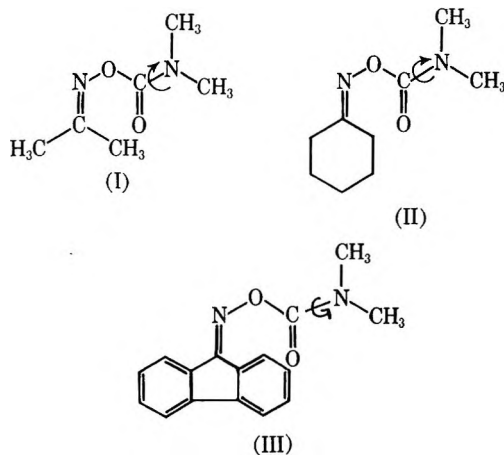
(8) C. E. Looney, W. D. Phillips, and E. L. Reilly, *ibid.*, **79**, 6136 (1957); S. Andreades, *J. Org. Chem.*, **27**, 4163 (1962); A. Mannschreck, H. Munsch, and A. Matteus, *Angew. Chem.*, **5**, 728 (1966); P. K. Korver, P. J. Van Der Haak, and T. J. DeBoer, *Tetrahedron*, **22**, 3157 (1966).

(9) H. J. Jakobsen and A. Senning, *Chem. Commun.*, 617 (1967).

(10) A. Isaksson, J. Sandstrom, and I. Wennerbeck, *Tetrahedron Lett.*, 2233 (1967).

(11) Y. Shvo, E. C. Taylor, and J. Bartulin, *ibid.*, 3259 (1967).

(12) Y. Shvo, *ibid.*, 5923 (1968).



in I. A significantly lower barrier in I as compared to normal amides is qualitatively consistent with nonempirical molecular orbital (NEMO)^{14b} calculations reported here indicating substantial electronic delocalization over the oxime oxygen, the carbonyl group, and the carbamoyl nitrogen.^{14c}

Experimental Section

The nmr spectra were recorded using a Varian HR-60A spectrometer equipped with a custom-built variable temperature probe. Spectral calibrations were performed by the audiomodulation technique using a Hewlett-Packard 651-A audiooscillator and a Hewlett-Packard 5221B electronic counter.

Temperature measurements were performed using a calibrated copper-constantan thermocouple placed about 1 in. below the sample and were taken simultaneously with the recording of the spectrum. In the probe used, the temperature gradient over the sample length is no more than 0.1° and temperature measurements at the sample are accurate to ±0.1°.

O-(N,N-Dimethylcarbamoyl)acetone Oxime. Acetone oxime (5.3 g, 0.079 mol), N,N-dimethylcarbamoyl chloride (8.5 g, 0.079 mol), and 30 ml of anhydrous pyridine were mixed at room temperature and allowed to stand at 0° for 9 days during which time pyridinium chloride precipitated. The reaction mixture was poured into a mixture of 50 ml of concentrated hydrochloric acid, 100 g of sodium chloride, ice, and water totaling 500 ml. This mixture was continuously extracted (ether) for 3 days, the ether solution was dried (Na₂SO₄), and the ether was removed under vacuum. The residue was fractionated to give 8.5 g (75%) of O-(N,N-dimethylcarbamoyl)acetone oxime: bp 86–87° (3 mm); nmr peaks (60 MHz; CS₂) at δ 1.91 (6H) and δ 2.88 (6H). *Anal.* Calcd for C₆H₁₂N₂O₂: C, 49.98; H, 8.39; N, 19.43; O, 22.19. Found: C, 49.92; H, 8.40; N, 19.34; O, 22.14.

O-(N,N-Dimethylcarbamoyl)cyclohexanone Oxime. Cyclohexanone oxime (25.0 g, 0.22 mol), N,N-dimethylcarbamoyl chloride (23.8 g, 0.22 mol), and 50 ml of pyridine were treated identically with the immediately

previous preparation. The ether was removed from the solution resulting from the continuous extraction, and the residue was recrystallized from petroleum ether to give 22.0 g (55%) of O-(N,N-dimethylcarbamoyl)cyclohexanone oxime: mp 56.5–57.5°; nmr peaks (60 MHz, CS₂) at δ 3.03 (6H), δ 2.50 (4H), and δ 1.75 (6H). *Anal.* Calcd for C₉H₁₆N₂O₂: C, 58.67; H, 8.76; N, 15.19; O, 17.38. Found: C, 58.74; H, 8.80; N, 15.19; O, 17.35.

O-(N,N-Dimethylcarbamoyl)fluorenone Oxime. Fluorenone oxime (4.1 g, 0.021 mol), N,N-dimethylcarbamoyl chloride (2.3 g, 0.021 mol), and 30 ml of pyridine were treated as in the two previous preparations. Upon addition of the hydrochloric acid, sodium chloride, ice, and water mixture, a yellow solid formed slowly. The yellow solid was separated by filtration and recrystallized from petroleum ether to give 4.2 g (75%) of O-(N,N-dimethylcarbamoyl)fluorenone oxime: mp 110–111°; nmr peaks at δ 8.1–7.1 (8H) and δ 3.06 (6H).

Results and Discussion

Examination of the nmr spectrum (60 MHz) of the N(CH₃)₂ protons (δ 2.88) of O-(N,N-dimethylcarbamoyl)acetone oxime (I; 0.5 M in CS₂) at 35° revealed a sharp singlet resonance characteristic of rapid exchange on the nmr time scale. Upon lowering the temperature, the N(CH₃)₂ resonance broadens in a manner characteristic of a decreasing rate of conformational exchange and then separates into two resonances of equal intensity in typical fashion. A total line shape analysis of this spectral behavior was performed using computer-generated spectra based on the treatment of Gutowsky and Holm.¹⁵ Equal populations (or intensities) of the two resonances were assumed and the relaxation time (*T*₂) was calculated from the width at half-height of either NCH₃ resonance under conditions of slow exchange.¹⁵

This spectral behavior is entirely consistent with a kinetic effect on the nmr spectrum due to a decreasing rate of rotation about the carbonyl carbon–nitrogen bond and not to a temperature dependence of the chemical shift between the two nonequivalent NCH₃ resonances.³ Indeed, in the sample studied, a negligi-

(13) (a) T. H. Siddall, III, and W. E. Stewart, *J. Org. Chem.*, **34**, 3261 (1967); (b) T. M. Valega, *ibid.*, **31**, 1150 (1966); E. H. White, M. C. Chen, and L. A. Dolak, *ibid.*, **31**, 3038 (1966); M. T. Rodgers and J. C. Woodbrey, *J. Phys. Chem.*, **66**, 540 (1962); S. van der Werf, T. Olijnsma, and J. B. F. N. Engberts, *Tetrahedron Lett.*, 689 (1967); E. Lustig, W. R. Benson, and N. Duy, *J. Org. Chem.*, **32**, 851 (1967).

(14) (a) C. H. Bushweller and M. A. Tobias, *Tetrahedron Lett.*, 595 (1968); (b) M. D. Newton, F. P. Boer, and W. N. Lipscomb, *J. Amer. Chem. Soc.*, **88**, 2353 (1966); (c) For another recent report concerning experimental and theoretical barriers in thioamides, see J. Sandstrom, *J. Phys. Chem.*, **71**, 2318 (1967).

(15) H. S. Gutowsky and C. H. Holm, *J. Chem. Phys.*, **25**, 1228 (1956).

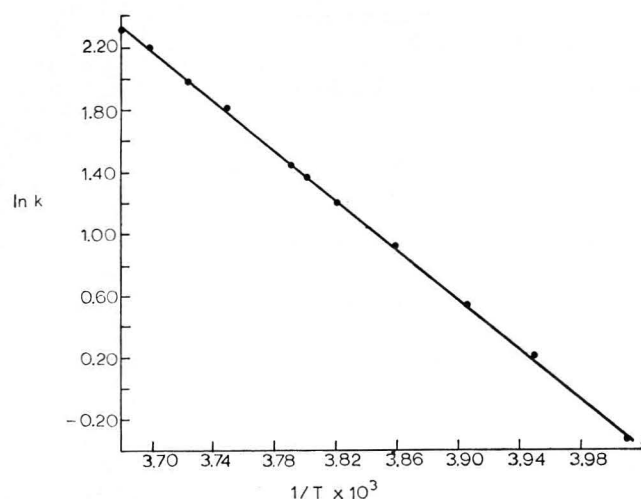


Figure 1. The Arrhenius plot for rotation about the carbonyl carbon-nitrogen bond in O-(N,N-dimethylcarbamoyl)acetone oxime (I). $E_a = 16.0 \pm 0.5$ kcal/mol, $\log \nu_0 = 12.0$, $\Delta H^\ddagger = 15.4 \pm 0.5$ kcal/mol, $\Delta S^\ddagger = 2.7 \pm 1.5$ eu, and $\Delta G^\ddagger_{-10^\circ} = 14.7 \pm 0.1$ kcal/mol.

ble temperature dependence of the chemical shift between NCH_3 resonances was observed from -50 to -20° . Thus, this source of error is apparently not important in our study but has been shown to be important in other compounds.³ For all spectra used in subsequent calculations, it was assured that the internal TMS line shape was Lorentzian in order to avoid the errors associated with asymmetry of line shapes.

A mathematical comparison³ of the experimental and calculated nmr line shapes at various temperatures gave a series of first-order rate constants (k) for rotation about the carbonyl carbon-nitrogen bond in I (Table I). An Arrhenius plot of these data (Figure 1) gave

Table I: The Rate Constants for Rotation about the Carbonyl Carbon-Nitrogen Bond in O-(N,N-Dimethylcarbamoyl)acetone Oxime (I) As a Function of Temperature

T, °C	k, sec ⁻¹
-1.5	10.00
-2.6	9.10
-6.2	6.25
-9.5	4.17
-10.0	3.85
-11.2	3.34
-14.4	2.38
-20.2	1.20
-24.1	0.71

$E_a = 16.0 \pm 0.5$ kcal/mol, $\log \nu_0 = 12.0$, $\Delta H^\ddagger = 15.4 \pm 0.5$ kcal/mol, and $\Delta S^\ddagger = 2.7 \pm 1.5$ eu. The free energy of activation (ΔG^\ddagger) at -10° is 14.7 ± 0.1 kcal/mol as calculated from the Eyring equation assuming a transmission coefficient of 1.

Similar spectral behavior to that found in I was observed in II and III. The free energies of activation (ΔG^\ddagger) for rotation about the central C-N bond in I, II, and III are compiled in Table II. The rate con-

Table II: The Free Energies of Activation (ΔG^\ddagger) for Rotation about the Carbonyl Carbon-Nitrogen Bond of Various O-(N,N-Dimethylcarbamoyl) Oximes at -10°

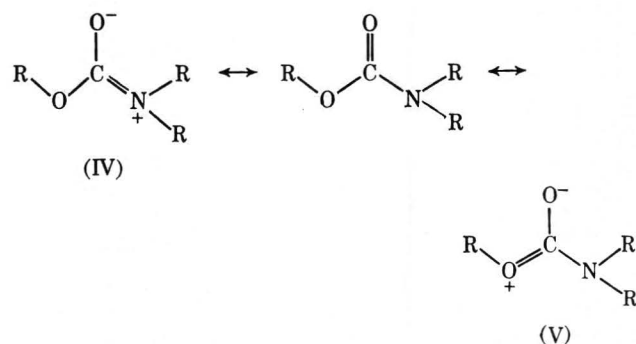
Compound	$\Delta\nu$, Hz ^a	k, sec ⁻¹	ΔG^\ddagger , kcal/mol
I ^b	3.2	3.9	14.7 ± 0.1
II ^c	2.7	4.2	14.6 ± 0.1
III ^d	8.9	12	14.1 ± 0.3

^a Chemical shift between NCH_3 groups. ^b 0.5 M in CS_2 . ^c 0.4 M in CS_2 . ^d 0.1 M in CS_2 .

stants for II and III were derived from a complete nmr line shape analysis at one temperature. Measurements on III were complicated by sparing solubility. The substantially enhanced chemical shift between NCH_3 resonances in III as compared to I and II (Table II) is interesting and suggests a not unexpected diamagnetic anisotropic effect of the aromatic nucleus.

The entropy of activation (ΔS^\ddagger) for C-N bond rotation in I is not atypical of such a kinetic process (Table III). The substantially lower barrier (ΔH^\ddagger) to rotation about the central C-N bond in O-(N,N-dimethylcarbamoyl) oximes and carbamates^{13a} as compared to normal amides² and formamides³ is consistent with the possibility of cross conjugation in these systems. Perusal of Table III illustrates the trends.

In seeking a rationalization for the observed trend, postulation of resonance interactions in ureas^{13a} and carbamates^{13b} with "competition" between canonical forms (e.g., IV and V) seems reasonable to account for the lowered barriers.



Using the NEMO method,^{14b} we have calculated the energy difference between the equilibrium (planar) geometry (VI) and the transition state (twisted) geometry (VII)

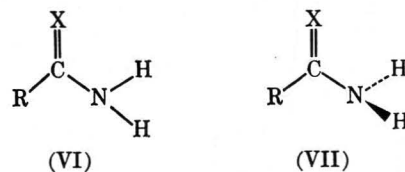


Table III: Pertinent Rotational Barriers about the C-N(CH₃)₂ Bond of Various Compounds

Compound	ΔH^\ddagger , kcal/mol	ΔS^\ddagger , eu	ΔG^\ddagger , kcal/mol	Reference
	19.0	+2.7	18.2 (25°)	2
	20.2	-1.7	21.0 (128°)	3
	11	...	10.7 (-39°)	13a
	~14	...	~14	13b
	15.3	+2.7	14.7 (-10°)	This work

Table IV: Overlap Populations and Computed Barriers to Rotation about the C-N Bond of Various Compounds

Compound	Σ_e , atomic units	π -Overlap populations CO,CS,CSe	CN	Total Overlap populations CO,CS,CSe	CN	Barrier, kcal/mol	
	planar ^a	-53.80202	0.2288	0.2235	0.9499	1.0507	
	twisted ^a	-53.73804	0.3201	0.0721	1.0195	0.9467	40.8
	planar	-152.70024	0.1535	0.2683	0.8066	1.1296	
	twisted	-152.61606	0.3006	0.0794	0.9219	0.9920	52.8
	calculation 1 ^b						
	planar	-750.07300	0.1469	0.2747	0.8488	1.1470	
	twisted	-749.98779	0.2775	0.0811	0.9630	0.9990	53.4
	calculation 2 ^b						
planar	-750.10474	0.1211	0.2933	0.7503	1.1566		
twisted	-750.01343	0.2741	0.0869	0.8805	1.0142	57.2	
	planar	-76.55418	0.1458 ^c	0.1638	0.7943 ^c	0.9382	
	twisted		0.1973 ^d		0.8522 ^d		
			-76.50322	0.1792 ^c	0.0528	0.8249 ^c	0.8378
		0.2327 ^d		0.8705 ^d		31.9	
	planar	-71.19315	0.1901	0.1666	0.8460	0.9641	
	one twist ^e		0.2259	0.0535 ^f	0.8675	0.8740 ^f	
			-71.14532		0.2084 ^g	0.9870 ^g	30.0 ^h
two twists ⁱ	-71.07872	0.3021	0.0650	0.9299	0.8677	41.7 ⁱ	

^a Planar = VI; twisted = VII. ^b These calculations were performed using two different sets of available parameters. ^c To OH oxygen. ^d To C=O oxygen. ^e Only one NH₂ group twisted. ^f To nitrogen on twisted NH₂ group. ^g To nitrogen on planar NH₂ group. ^h Barrier to rotation about one NH₂ group if the other remains planar. ⁱ Both NH₂ groups twisted with respect to NCO plane. ^j Barrier to rotation of one NH₂ group if other NH₂ group is twisted.

(VII) of formamide, thioformamide, selenoformamide, urea, and carbamic acid (H₂N-CO₂H). The calculated energy differences, *i.e.*, barriers to rotation, are based on an approximate formula for total energy proposed by Newton, Boer, and Lipscomb¹⁶ (eq 1). The first term on the right side of eq 1

$$E = \sum_i E_i^A + \sum_j \epsilon_j^B \quad (1)$$

is a summation of one electron energies over occupied orbitals in the *separated atoms*; hence it is independent of

(16) M. D. Newton, F. P. Boer, and W. N. Lipscomb, *J. Amer. Chem. Soc.*, **88**, 2367 (1966).

molecular geometry. The second term is the conventional sum over the eigenvalues of the occupied *molecular orbitals*. Equation 1 allows energy differences between different geometries to be equated to the differences between the eigenvalue sums.

The parameters employed in these calculations have been taken from the literature.^{14b,16,17} For the first row atoms, they differ in one important respect from those originally recommended in that all p- and d-orbital anisotropy in the parameters is averaged out. This was done to preserve a uniform set of parameters for both equilibrium (VI) and transition state (VII) geometries. In addition, not enough is known about the differences among components of p and d orbitals in sulfur and selenium to make any distinctions. Therefore, averaged parameters for 3p, 3d, and 4p orbitals were used for these atoms.

Molecular geometries have been taken from the literature when possible.¹⁸ The C=Se bond length was estimated to be 1.82 Å by comparison of hydrogen sulfide and sulfur dioxide with hydrogen selenide and selenium dioxide.¹⁹ The structure of the yet to be isolated carbamic acid was derived from formamide with a hydroxyl group replacing the aldehydic proton. The NCO bond angle in carbamic acid was assumed to be the same as the NCH bond angle in formamide. The C-O bond length and O-H bond length in carbamic acid were assumed to be 1.31 and 0.95 Å, respectively, being taken from formic acid.¹⁹

In all of these calculations, the equilibrium geometries were planar (VI). The transition state (VII) geometry was constructed from the equilibrium geometry (VI) by rotating the NH₂ group as a unit about the C-N bond until the NH₂ plane was perpendicular to the plane of the remaining atoms.

The computed barriers (ΔH^\ddagger) are compiled in Table IV. Although the calculated barriers are approximately a factor of two higher than the measured values (Table III),²⁰ the sequence of calculated barriers clearly indicates the experimentally observed trend, and the origin of the variation in the rotational barriers for

the various structures. A consideration of the Mulliken overlap populations²¹ (Table IV) for pertinent bonds in the various structures suggests strongly the widely held bonding mechanism for the barrier to C-N bond rotation. This, of course, is consistent with the simple resonance picture presented previously. Indeed, the π -overlap populations (Table IV) for carbamic acid indicate substantial π bonding not only between the carbonyl carbon and nitrogen but also between the carbonyl carbon and hydroxyl oxygen leading to a lowering of the barrier compared to amides. The same considerations apply to urea in the case where one NH₂ group rotates while the other remains planar (Table IV). However, for simultaneous rotation of both NH₂ groups, all π overlap is minimized and the calculated barrier approaches that in normal amides (Table IV). It seems clear that the mechanism for rotation about the C-N bond in urea is rotation of one NH₂ group at a time.

Acknowledgment. We gratefully acknowledge support of this work by Research Corporation (Cottrell Grant) and the National Science Foundation (COSIP Grant) as well as assistance in the syntheses from Dr. M. A. Tobias of Mobil Chemical Company.

(17) W. E. Palke and W. N. Lipscomb, *J. Amer. Chem. Soc.*, **88**, 2384 (1966); F. P. Boer and W. N. Lipscomb, *J. Chem. Phys.*, **50**, 989 (1969).

(18) J. E. Worsham, H. A. Levy, and S. W. Peterson, *Acta Cryst.*, **10**, 319 (1957); R. J. Kurland and E. B. Wilson, Jr., *J. Chem. Phys.*, **27**, 585 (1957); M. R. Truter, *J. Chem. Soc.*, 997 (1960).

(19) "Tables of Interatomic Distances and Configurations in Molecules and Ions," Special Publication No. 11, The Chemical Society, London, 1958.

(20) Similar results were obtained in test calculations of the ethane barrier and of both barriers in propylene. These discrepancies are due partly to the inherent approximations in the theory but also partly to a failure to use the optimum geometry for the transition state. In the case of NH₂CHO, we sought an optimum geometry through variation of the HNH angle and variation of the angle between the HNH plane and CN bond. These variations preserve all bond distances, as well as the mirror plane of the molecule. The results indicate a transition geometry in which the bonds about N are at angles typical of NH₃. The discrepancy between calculated and experimental values is reduced, but only by about one-third.

(21) R. S. Mulliken, *J. Chem. Phys.*, **23**, 1833, 1841, 2238, 2343 (1955).

Ultrasonic Absorption in Aqueous Salts of the Lanthanides. III.

Temperature Dependence of LnSO_4 Complexation

by Douglas P. Fay¹ and Neil Purdie²

Department of Chemistry, Oklahoma State University, Stillwater, Oklahoma 74074 (Received January 29, 1969)

The rates of formation of the trivalent lanthanide monosulfate complexes have been measured as a function of temperature for the ions Ce–Ho. Activation parameters and stepwise enthalpies and entropies in a multistep mechanism are presented and discussed in the light of other available data. Partial molal volume changes are calculated for the slow step of substitution into the cation coordination sphere, and for lanthanum the volume change for the total reaction is calculated and compared with ΔV_T obtained from a study of the pressure dependence of the dissociation constant. There is sufficient contributory evidence to support a multistep mechanism in which the rate-controlling step is dissociative or SN1.

Introduction

In the continuation of previous studies on complex formation of the trivalent lanthanide ions,^{3–6} the rates of complexation of the monosulfates of the ions Ce–Ho have been measured as a function of temperature.

The objectives of this study were to determine the activation parameters from the temperature dependence of the rate constants, which would permit a comparison to be made with the results for the water exchange reaction⁷ and with values for the same cations with other ligands,^{8,9} and to explore the possibility of determining kinetically the thermodynamic parameters for each step in the overall mechanism. A dissociative (SN1) mechanism has been proposed from such observations as similarity in solvent exchange and substitution rates⁴ and from the linear correlation^{5,10,11} between the free energy of activation, ΔG^\ddagger , and the free energy of complexation, ΔG° . Similar activation energies for exchange and substitution would be further confirmation of such a mechanism in which the rate of solvent exchange is paramount. Knowledge of the thermodynamic parameters for the individual steps could contribute to the understanding of the structure of complexes if these results could be correlated somehow with the equivalent parameters for the overall process measured by classical methods.

Experimental Section

The preparation of solutions and sound absorption measurements have been previously described.⁴ Solution temperatures were maintained constant to $\pm 0.05^\circ$.

Results

The effect of temperature on the relaxation frequencies and amplitudes at 5 and 45° are shown in Figure 1 for samarium only; the solid lines are calculated single relaxations. Concentrations and relaxation frequencies are given in Table I. (A complete listing of experi-

mental data has been deposited as Document No. 00719 with the ASIS National Auxiliary Publication Service, c/o CCM Information Corp., Inc., 909 3rd Ave., New York, N. Y. 10022. A copy may be secured by citing the document number and remitting \$1.00 for microfiche or \$3.00 for photocopies. Advance payment is required. Make checks payable to ASIS-NAPS.) Not all members of the series could be studied over the entire temperature range, since, even at 25°, the relaxation frequencies for the slower reactions were close to the lower limit of the available frequency range. Pr and Dy are the real limits in the series for study over the entire 40° range, but the results for Ce and Ho at only two temperatures are included. Although the results for these two cations are subject to some skepticism, they are considered to be equally reliable to those for the remainder. The temperature coefficient of the characteristic relaxation frequency is sufficiently small that additional measurements at intermediate temperatures are unlikely to improve upon the overall accuracy of the calculated values.

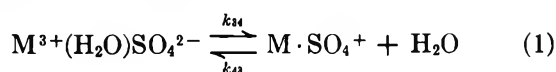
Assignment of the single relaxation to the third step

- (1) Taken in part from the Ph.D. Dissertation of D. P. Fay, Brookhaven National Laboratory, Upton, N. Y. 11973.
- (2) To whom communications should be directed.
- (3) N. Purdie and C. A. Vincent, *Trans. Faraday Soc.*, **63**, 2745 (1967).
- (4) D. P. Fay, D. Litchinsky, and N. Purdie, *J. Phys. Chem.*, **73**, 544 (1969).
- (5) D. P. Fay and N. Purdie, *ibid.*, **73**, 3462 (1969).
- (6) V. L. Garza and N. Purdie, *ibid.*, **74**, 275 (1970).
- (7) R. Marianelli, Ph.D. Dissertation, University of California, Berkeley, 1966.
- (8) A. J. Graffeo and J. L. Bear, *J. Inorg. Nucl. Chem.*, **30**, 1577 (1968).
- (9) H. B. Silber, R. D. Farina, and J. H. Swinehart, *Inorg. Chem.*, **8**, 819 (1969).
- (10) C. H. Langford and T. R. Stengle, *Ann. Rev. Phys. Chem.*, **19**, 193 (1968).
- (11) C. H. Langford, *Inorg. Chem.*, **4**, 265 (1965).

Table I: Relaxation Frequency Data

Ion	$C \times 10^2, F$	$2\pi\nu_{mIII}, \text{MHz}$		
		5°	25°	45°
Ce	1.617	...	114.6	197.8
	1.078	182.7
	0.980	...	105.3	...
	0.539	151.3
Pr	0.490	...	92.5	...
	1.960	74.7
	1.470	71.0	141.9	234.2
	0.980	67.8	130.9	212.9
Nd	0.538	...	120.0	...
	0.490	182.7
	2.034	82.9
	1.526	77.2	160.1	265.6
Sm	1.017	72.8	...	240.5
	0.961	...	147.6	...
	0.508	...	129.4	215.4
	1.460	331.0
Eu	0.976	...	239.3	305.0
	0.949	157.0
	0.488	...	208.5	270.0
	0.474	138.8
Gd	0.244	...	177.7	...
	0.237	118.7
	2.002	147.0
	1.502	139.4	265.6	364.9
Tb	1.001	127.5	...	341.6
	0.980	...	248.4	...
	0.569	304.0
	0.500	...	218.5	...
Dy	1.528	151.3	222.9	348.5
	1.019	140.7	...	314.0
	0.950	...	207.0	...
	0.510	121.2	...	297.0
Ho	0.470	...	171.0	...
	1.551	280.2
	1.500	...	172.7	...
	1.008	105.5	...	248.7
Ho	0.998	...	157.0	...
	0.543	92.3	...	233.0
	0.499	...	133.1	...
	0.310	80.0
Ho	2.023	73.5
	1.517	69.1	116.0	203.5
	1.012	61.5	...	186.5
	0.970	...	104.2	...
Ho	0.650	...	92.9	...
	0.506	166.4
	2.048	138.8
	1.536	...	72.0	128.7
Ho	1.076	...	66.6	...
	1.024	123.1
	0.538	...	55.9	...

in the multistep mechanism of Deibler and Eigen,¹² that of substitution into the coordination sphere of the cation according to the equilibrium



has been made on the basis of previous evidence.^{3,4}

Reference is made later to the preference of a three-

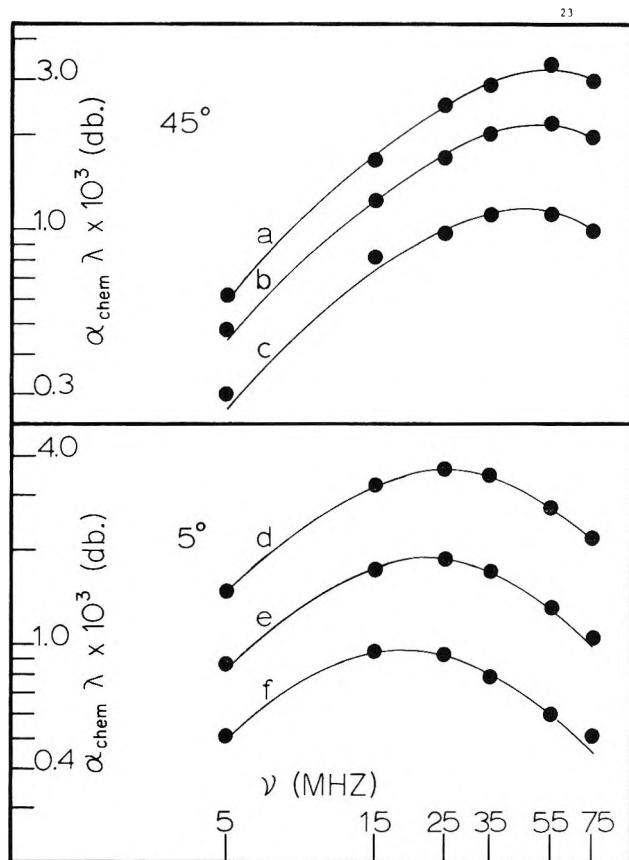


Figure 1. Excess sound absorption vs. frequency for $Sm_2(SO_4)_3$: at 45°, (a) $1.46 \times 10^{-2} F$; (b) $9.7 \times 10^{-3} F$; (c) $4.88 \times 10^{-3} F$; at 5°, (d) $9.49 \times 10^{-3} F$; (e) $4.74 \times 10^{-3} F$; (f) $2.37 \times 10^{-3} F$.

step over a two-step mechanism. The rate constants are determined from a graphical solution of the equation⁴

$$2\pi\nu_{mIII} = k_{43} + \Phi(C)k_{34} \quad (2)$$

where ν_{mIII} is the characteristic relaxation frequency, $\Phi(C)$ is given by the expression $\Phi(C) = \theta(C)/\{K_{12}^{-1} \cdot K_{23}^{-1} + (1 + K_{23}^{-1})\theta(C)\}$ where $\theta(C) = \Pi_t C \{5 - 4\beta + (3 - 2\beta)(\partial \ln \Pi_t / \partial \ln \beta)_C\}$; K_{12} and K_{23} are the association constants for the first and second steps in the consecutive mechanism, and C is the analytical salt concentration. β , the degree of association of the salt, and Π_t , the activity coefficient quotient, were evaluated by a standard reiteration procedure using the Davies equation

$$-\log \gamma_i = Az_i^2 \{ (I^{1/2} / (1 + BdI^{1/2})) - 0.3I \} \quad (3)$$

and the ionic strength expression $I = 3C + 12(1 - \beta)C$. The parameters A and B were corrected for temperature, and the distance of closest approach d was taken as the sum of the Pauling ionic radii plus two water molecule diameters.

(12) H. Deibler and M. Eigen, *Z. Phys. Chem. (Frankfurt am Main)*, **20**, 229 (1959).

Table II: Rate Constants^{a,b} and Stepwise Association Constants

Ion	Temp, °C	$k_{24} \times 10^{-3}$, sec ⁻¹	$k_{44} \times 10^{-4}$, sec ⁻¹	K_{24}	K_{23}	$K_{12} \times 10^{-2}$, l./mol
Ce	25	2.7 (2.0)	0.68	3.9 (2.9)	1.62	4.31 (9.97)
	45	6.3 (5.0)	1.20	5.4 (4.3)	1.67	4.88 (10.8)
Pr	5	1.5 (0.94)	0.58	2.5 (1.6)	1.6	3.92 (9.83)
	25	3.1 (2.5)	1.0	3.0 (2.4)	2.2	4.32 (12.3)
	45	6.7 (5.6)	1.3	5.1 (4.2)	2.0	4.90 (12.1)
Nd	5	2.3 (1.3)	0.57	4.0 (2.3)	1.1	3.93 (8.06)
	25	3.9 (3.1)	1.1	3.7 (2.9)	1.9	4.33 (11.2)
	45	6.7 (5.9)	1.8	3.8 (3.4)	2.6	4.90 (15.5)
Sm	5	4.3 (2.7)	1.0	4.2 (2.6)	1.1	3.96 (7.42)
	25	5.9 (4.7)	1.5	4.0 (3.1)	1.9	4.36 (11.0)
	45	8.2 (7.4)	2.3	3.6 (3.3)	3.0	4.93 (17.0)
Eu	5	4.4 (2.5)	1.0	4.4 (2.5)	1.1	3.96 (7.90)
	25	6.5 (4.9)	1.9	3.5 (2.6)	1.8	4.37 (12.6)
	45	9.4 (8.4)	2.5	3.8 (3.4)	2.8	4.94 (16.1)
Gd	5	4.1 (2.6)	1.1	3.9 (2.4)	1.2	3.97 (8.11)
	25	6.4 (4.9)	1.5	4.3 (3.3)	1.8	4.37 (10.6)
	45	7.8 (7.1)	2.5	3.1 (2.8)	3.2	4.95 (18.4)
Tb	5	4.1 (2.2)	0.74	5.6 (3.0)	0.86	3.98 (6.68)
	25	5.2 (3.8)	1.1	4.9 (3.5)	1.5	4.39 (9.54)
	45	7.1 (6.1)	1.7	4.2 (3.6)	2.4	4.96 (14.4)
Dy	5	3.5 (1.4)	0.39	8.8 (3.6)	0.58	3.99 (5.77)
	25	4.0 (2.9)	0.85	4.8 (3.4)	1.4	4.40 (9.32)
	45	5.0 (4.3)	1.4	3.7 (3.2)	2.4	4.97 (14.2)
Ho	25	2.5 (1.6)	0.38	6.6 (4.2)	1.0	4.41 (7.43)
	45	3.7 (3.0)	0.97	3.8 (3.0)	2.1	4.99 (13.8)

^a Estimated error $\pm 10\%$. ^b Values in parentheses are calculated from the two-step model.

In the solution of eq 2, the unknowns are the overall association constant K_T (required to calculate β), K_{12} , and K_{23} . Values of K_T at 5 and 45° were calculated from the van't Hoff isochore equation

$$d \log K_T / d(1/T) = -\Delta H_T / 2.303R \quad (4)$$

using the known K_T values¹³ at 25° and the enthalpies of complexation, measured calorimetrically under conditions similar to the kinetic experiments.

The results and their interpretation are consequently subject to the assumption that ΔH_T is constant over the entire temperature range, an assumption very often accepted in the determination of heats of complexation from the temperature dependence of the stability constant. Curvature in the plots has been reported for the CrNCS^{2+} ¹⁴ and $\text{Co}(\text{NH}_3)_6\text{Cl}^{2+}$ ¹⁵ complexes. However, both are outer-sphere complexes, and there is good reason to believe that it is a consequence of purely long-range electrostatic interaction.¹⁵ Moreover, it has been shown that ΔH_T is insensitive to K_T , if K_T is sufficiently large,¹⁶ which it is for the present system.^{5,17} This method of extrapolation, therefore, might well make the difference between a calculated K_T and an experimentally measured K_T inconsequential, regardless of the possibility of a nonconstant ΔH_T .

K_{12} was calculated at each temperature using the Bjerrum equation¹⁸ in which the δ value was taken equal to that in the Davies equation. This leaves only K_{23}

as an adjustable parameter which was calculated by iteration around eq 2 and the expression for K_T in terms of the individual association constants

$$K_T = K_{12}(1 + K_{23} + K_{23}K_{34}) \quad (5)$$

where $K_{34} = k_{34}/k_{43}$. Iteration was continued until the difference between successive values of K_{23}^{-1} was less than 0.0001 and required, on the average, five cycles. The procedure involved the calculation of a least-squares line through the data in the solution of eq 2. The relevant rate constants, together with the corresponding equilibrium constants, are given in Table II.

Although there is experimental evidence to support the proposed three-step mechanism¹⁹ for a sulfate system, results are frequently analyzed in terms of a two-step mechanism in which the first two steps are combined and defined by a single association constant, K_{13} . This model permits the direct calculation of K_{13}

(13) F. H. Spedding and S. Jaffe, *J. Amer. Chem. Soc.*, **76**, 882 (1954).

(14) C. Postmus and E. L. King, *J. Phys. Chem.*, **59**, 1208 (1955).

(15) C. H. Langford and W. R. Muir, *ibid.*, **71**, 2602 (1967).

(16) J. J. Christensen, D. P. Wrathall, J. O. Oscarson, and R. M. Izatt, *Anal. Chem.*, **40**, 1713 (1968).

(17) R. M. Izatt, D. Eatough, J. J. Christensen, and C. H. Bartholomew, *J. Chem. Soc., A*, 47 (1969).

(18) R. A. Robinson and R. H. Stokes, "Electrolyte Solutions," 2nd ed, Butterworth and Co., Ltd., London, 1959, p 392.

(19) K. Tamm, 6th International Congress on Acoustics, Tokyo, Japan, 1968, p GP-25.

Table III: Activation Parameters^a at 25° for the Reaction $\text{Ln}^{3+}(\text{H}_2\text{O})\text{SO}_4^{2-} \rightleftharpoons \text{Ln} \cdot \text{SO}_4^+ + \text{H}_2\text{O}$

Ion	$K \mp \times 10^6$ ^b	E_a , kcal/mol ^c	$\Delta H \mp$, kcal/mol	$\Delta G \mp$, kcal/mol ^d	$\Delta S \mp$, eu ^e
Ce forward	4.3 (3.1)	8.1 (8.8)	7.5 (8.2)	6.0 (6.2)	5.2 (7.0)
reverse	1.1	5.0	4.4	6.8	-8.0
Pr forward	5.0 (3.9)	6.7 (7.8)	6.1 (7.2)	5.9 (6.0)	0.77 (4.1)
reverse	1.7	3.7	3.1	6.5	-11.6
Nd forward	6.3 (4.9)	4.8 (6.7)	4.2 (6.1)	5.7 (5.9)	-5.1 (0.8)
reverse	1.7	5.0	4.4	6.5	-7.2
Sm forward	9.6 (7.5)	2.9 (4.5)	2.3 (3.9)	5.5 (5.6)	-10.7 (-5.7)
reverse	2.4	3.6	3.0	6.3	-11.2
Eu forward	10.4 (7.9)	3.4 (4.4)	2.8 (4.8)	5.5 (5.6)	-8.9 (-5.9)
reverse	3.0	4.0	3.4	6.2	-9.2
Gd forward	10.3 (7.8)	2.8 (4.4)	2.2 (3.8)	5.4 (5.6)	-10.9 (-5.9)
reverse	2.4	3.7	3.1	6.3	-10.6
Tb forward	8.4 (6.1)	2.4 (4.5)	1.8 (3.9)	5.6 (5.8)	-12.6 (-6.1)
reverse	1.7	3.7	3.1	6.5	-11.5
Dy forward	6.5 (4.6)	1.6 (4.9)	1.0 (4.3)	5.7 (5.9)	-15.8 (-5.4)
reverse	1.4	5.4	4.8	6.6	-6.1
Ho forward	4.0 (2.5)	3.9 (6.0)	3.3 (5.4)	6.0 (6.3)	-9.2 (-3.0)
reverse	0.6	8.9	8.3	7.1	4.0

^a Values in parentheses are calculated for the two-step model. ^b Error in values $\pm 10\%$. ^c Error estimated to be ± 0.9 kcal/mol. ^d Error estimated to be ± 0.1 kcal/mol. ^e Error estimated to be ± 3.0 eu.

Table IV: Stepwise Thermodynamic Parameters at 25°

Ion	Function ^a	Step 3-4 ^b	Step 2-3 ^b	Step 1-2 ^b	Total (kinetic)	Total (calorimetric)
Ce	ΔH	3.1 (3.8)	0.31	0.97 (0.75)	3.41 (4.21)	3.78
	$-\Delta G$	0.8 (0.6)	0.29	3.6 (4.1)	4.89 (4.89)	4.89
	ΔS	13.2 (15.0)	2.0	15.3 (16.2)	27.9 (30.5)	29.1
Pr	ΔH	3.0 (4.1)	0.96	0.97 (0.92)	3.99 (4.69)	3.92
	$-\Delta G$	0.65 (0.5)	0.46	3.6 (4.2)	4.94 (4.94)	4.94
	ΔS	12.4 (15.7)	4.8	15.3 (17.2)	30.0 (32.3)	29.7
Nd	ΔH	-0.2 (1.7)	3.7	0.97 (2.9)	4.66 (4.46)	4.15
	$-\Delta G$	0.8 (0.6)	0.39	3.6 (4.2)	4.96 (4.96)	4.96
	ΔS	2.1 (8.0)	13.7	15.3 (26.3)	31.7 (31.6)	30.6
Sm	ΔH	-0.7 (0.9)	4.3	0.97 (3.6)	4.79 (4.43)	4.34
	$-\Delta G$	0.8 (0.7)	0.38	3.6 (4.2)	4.99 (4.99)	4.99
	ΔS	0.5 (5.5)	15.7	15.3 (26.1)	32.8 (31.6)	31.3
Eu	ΔH	-0.6 (1.4)	4.0	0.97 (3.1)	4.56 (4.40)	4.13
	$-\Delta G$	0.7 (0.6)	0.36	3.6 (4.2)	4.99 (4.99)	4.99
	ΔS	0.3 (3.3)	14.7	15.3 (24.7)	32.0 (31.5)	30.6
Gd	ΔH	-0.9 (0.7)	4.2	0.97 (3.6)	4.55 (4.24)	4.10
	$-\Delta G$	0.9 (0.7)	0.34	3.6 (4.1)	4.99 (4.99)	4.99
	ΔS	-0.3 (4.7)	15.3	15.3 (25.9)	32.0 (31.0)	30.5
Tb	ΔH	-1.3 (0.8)	4.5	0.97 (3.4)	4.58 (4.12)	4.02
	$-\Delta G$	0.9 (0.7)	0.24	3.6 (4.1)	4.96 (4.96)	4.96
	ΔS	-1.1 (5.4)	15.8	15.3 (24.9)	32.0 (30.5)	30.1
Dy	ΔH	-3.8 (-0.5)	6.2	0.97 (4.0)	4.56 (3.55)	3.58
	$-\Delta G$	0.9 (0.7)	0.21	3.6 (4.1)	4.92 (4.92)	4.92
	ΔS	-9.7 (0.7)	21.4	15.3 (26.9)	31.8 (28.4)	28.5
Ho	ΔH	-5.0 (-2.9)	6.8	0.97 (5.8)	4.33 (3.25)	3.54
	$-\Delta G$	1.1 (0.8)	0.01	3.6 (3.9)	4.89 (4.89)	4.89
	ΔS	-13.2 (-7.0)	22.9	15.3 (32.7)	30.9 (27.3)	28.3

^a ΔH and ΔG are in kcal/mol and ΔS in eu. ^b Errors defined in the footnote to Table III.

from the Bjerrum equation if an appropriately smaller value of d is chosen, and reduces, by K_{23} , the number of parameters needed for the kinetic solution, although it does not change the degrees of freedom in the calcula-

tion. Iteration is still necessary using the $\Phi(C)$ function for a two-step mechanism³ and $K_T = K_{13}(1 + K_{34})$. In this treatment d is the adjustable parameter, and the value is chosen which gives the best comparison

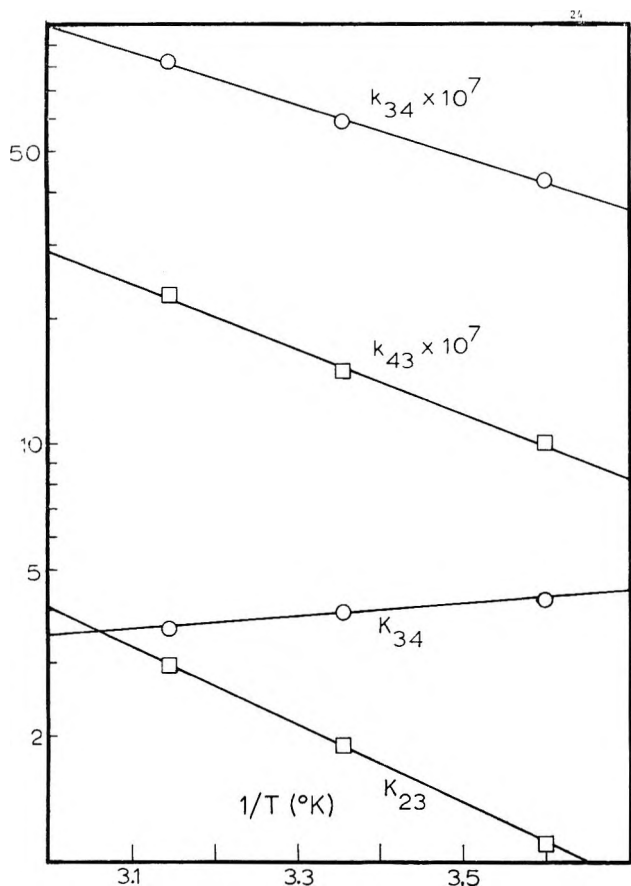


Figure 2. Plot of $\log k_{34}$, $\log k_{43}$, $\log K_{23}$, and $\log K_{34}$ vs. $1/T \times 10^3$.

between K_T calculated and observed. Typically an \bar{a} value of 5.5 Å is obtained at 25°. It will be seen from Table II that the values of k_{34} are lowered slightly from the three-step model while the k_{43} values are unchanged and are not given. Preference for the three-step model is based entirely upon Tamm's experiments¹⁹ at very high frequencies on MnSO_4 and MgSO_4 . The excellent correspondence between the calculated rate constants from both models gives us confidence in the method used to evaluate K_{23} .

Activation parameters, applicable at 25°, are given in Table III. The activation energies and changes in enthalpy accompanying each step were calculated from the slopes of the plots of $\log k_{ij}$, $\log k_{ji}$, and $\log K_{ij}$ vs. $1/T$, respectively. Typical of the results is the plot for samarium, Figure 2. The value of ΔH_{12} is constant throughout the series at 0.97 kcal/mol. In Table IV the individual ΔG_{ij} , ΔH_{ij} , and ΔS_{ij} values are given for a temperature of 25°, and their sums are compared with the results obtained calorimetrically.²⁰ ΔH_{34} and ΔS_{34} as calculated from the two-step model are slightly more positive, but a similar dependence with atomic number is observed.

The excess sound absorption in aqueous systems, which is a result of chemical relaxation, is primarily determined by a finite ΔV_T for the reaction; the pres-

sure change is not accompanied by an appreciable temperature change, owing to the small value of the coefficient of expansion. Relaxation amplitudes can therefore be used to determine the partial molal volume changes²¹ between reactants and products in the individual steps. Because of coupling between the steps in the successive equilibria mechanism, the volume change for the slow step ΔV_{34} is not directly obtained from the amplitude of the observed relaxation unless previous steps relax at a much higher frequency. Instead a weighting factor must be introduced²² according to

$$\Delta V_I = \Delta V_{12} \quad (6)$$

$$\Delta V_{II} = \Delta V_{23} + \frac{k_{21}}{k_{12}' + k_{21}} \Delta V_I \quad (7)$$

$$\Delta V_{III} = \Delta V_{34} + \frac{k_{23}'}{k_{23}' + k_{32}} \Delta V_{II} \quad (8)$$

where k_{12}' and k_{23}' have their usual significance.³ The equation (9) which relates ΔV_{III} to the maximum amplitude is readily derived²²

$$(\Delta V_{III})^2 = \left[\frac{\beta_0 RT}{8.686\pi} \frac{2(\alpha_{\text{chem}}\lambda)_{\text{max}}}{C} \times \frac{1 + K_{34}^{-1}[1 + K_{23}^{-1}]}{1 + K_{12}\theta(C)[1 + K_{23}]} \right] \left[\frac{2\sigma^2 - 4\sigma - 1}{2\sigma(2\sigma^2 - \sigma - 1)} + \frac{1}{\sigma} \frac{\partial \ln \Pi_f}{\partial \ln \sigma} \right] \quad (9)$$

where β_0 is the adiabatic compressibility of the solvent and σ is the degree of dissociation. To a close approximation $\beta_0 = (\rho c^2)^{-1}$ where ρ is the density and c is the velocity of sound. At 25° the value of β_0 is 4.46×10^{-11} ml/erg. The calculated ΔV_{34} values are given in Table V. Compared to divalent metal sulfates the ΔV_{34} values, and consequently the absorption amplitudes, are much greater.

Discussion

The error limits on the activation and thermodynamic parameters are based on a 10% experimental error on the measured rate constants and overall association constants.¹³ It should be reemphasized that the interpretation is subject to constancy in ΔH_T so that a similar error was assumed in the K_T values at 5 and 45°. The same criticism pertains to the method used to determine the stepwise thermodynamic parameters and the

(20) The thermodynamic parameters from calorimetry describe the equilibrium reaction between the free ions and all forms of the ion pairs in solution. In comparing the total kinetic parameters a weighted sum must be calculated in a manner analogous to the determination of ΔV_T . ΔG_T kinetic is always equal to ΔG_T calorimetric, a consequence of the method used to calculate K_{23} in the three-step mechanism or \bar{a} in the two-step mechanism.

(21) Molar concentrations were used in this study, but since the solutions were very dilute the difference has been ignored.

(22) K. Tamm, "Handbuch der Physik," Band XI, Akustik I, Springer-Verlag, Berlin, 1961, p 129.

Table V: Values of ΔV_{III} and ΔV_{34} for $\text{Ln}_2(\text{SO}_4)_3$, at 25°

Ion	$C \times 10^3, F$	σ	$-\frac{\partial \ln \Pi_f}{\partial \ln \sigma}$	$-\Delta V_{\text{III}},$ ml/mol	$-\Delta V_{34},$ ml/mol
La	8.80	0.0987	0.1119	19.1	20.7
Ce	9.80	0.1002	0.1107	19.6	21.6
Pr	9.80	0.0936	0.1062	20.4	22.7
Nd	9.61	0.0912	0.1051	22.1	26.5
Sm	9.76	0.0873	0.1021	22.3	26.7
Eu	9.80	0.0871	0.1020	23.7	28.1
Gd	9.50	0.0886	0.1040	19.5	23.9
Tb	9.98	0.0909	0.1048	20.3	24.8
Dy	9.70	0.0971	0.1104	18.9	23.8
Ho	10.76	0.0963	0.1039	20.2	25.0

activation parameters in that a linear Arrhenius plot was assumed. Error limitations alone, however, do not account for the observed trends in the values of the significant parameters with atomic number which must be considered real, if only relative.

The present results are augmentative to previous convictions that the mechanism is multistep in which the transition state is formed with a reduced coordination number by the elimination of a water molecule. Very good agreement is obtained in E_a and ΔS^\ddagger for complexation with the energy and entropy of activation for water exchange on trivalent gadolinium,⁷ 3.2 ± 0.3 kcal/mol and -7 ± 4 eu, respectively, measured by ¹⁷O nmr line broadening, and the only value yet available. Because of this comparison and the agreement between k_{34} for GdSO_4^+ and the rate of water exchange on Gd,⁷ $k_{\text{ex}} = 9.0 \times 10^8$ or 8.0×10^8 sec⁻¹, for 9 and 8 coordination, respectively, the mechanism may be concluded to be dissociative with little or no steric requirement involved in the substitution. Energies of activation pass through a minimum around the ions in the middle of the series consistent with the trend in rate constants, so that a steric requirement is probably absent for all systems. In a previous test for a dissociative mechanism a linear plot of ΔG^\ddagger vs. ΔG° was described.⁵ Contrary to the suggestion presented in that study, the dependence of ΔS^\ddagger on ΔS° is not linear.

Besides water exchange, a temperature dependence study has been made on two other rare earth systems, anthranilate⁹ and oxalate.⁸ In both of these systems the bimolecular rate constants were measured, and a direct comparison with the sulfates is not totally justified.²³ To complete the comparison for Gd^{3+} ion, the corresponding activation energies and entropies are 8.5 kcal/mol; +9 eu, and 6.5 kcal/mol; -5.2 eu for anthranilate and oxalate, respectively. Some steric requirements may be in operation or else the values are representative of the process in which a further water molecule is lost in ring fusion.⁶ In this regard higher substitution into the metal coordination sphere has been observed to proceed with progressively decreasing rates, at least for ions with inert gas configurations.²⁴

The irregular trend in ΔS^\ddagger with atomic number for the anthranilates, in which only Gd^{3+} and Lu^{3+} have positive values, is not reproduced in the sulfate system.

Nonlinear variations in ΔG_T , ΔH_T , and ΔS_T with atomic number or with inverse cation radius,²⁵ it has frequently been inferred, result from a coordination number change somewhere in the series. The same effect might account for the variation in ΔV_{34} . In the calculation of ΔV_{34} from ΔV_{III} , values for ΔV_{12} and ΔV_{23} were not available for the rare earth sulfates since measurements have not as yet been made in the GHz range. Fisher²⁶ has indicated from a comparison of volume changes obtained from sound absorption measurements and pressure dependence measurements of the dissociation equilibrium constant for lanthanum sulfate that a multistep mechanism exists. Sufficient kinetic evidence is now available to corroborate this conviction. From an entirely pragmatic point of view, we have used the values $\Delta V_{12} = -18.0$ ml/mol and $\Delta V_{23} = +13.2$ ml/mol calculated by Tamm¹⁹ for MgSO_4 . The assumption is made, perhaps with some justification, that ΔV_{12} and ΔV_{23} are independent of the cation. The difference in ΔV_{34} for LaSO_4^+ and MgSO_4 is basically one of the difference in ΔV_{III} observed. Summation of the individual volume changes gives $\Delta V_T = -25.6$ ml/mol for 8.80×10^{-3} M $\text{La}_2(\text{SO}_4)_3$. In view of the necessary assumptions in this calculation the comparison with the value of Fisher, $\Delta V_T = -25.7$ ml/mol for 8.20×10^{-3} M $\text{La}_2(\text{SO}_4)_3$ is remarkably good. The values of ΔV_{12} and ΔV_{23} cannot be too critical and probably are illustrative of little coupling between the third step and previous steps, in that using earlier values²⁷ of $\Delta V_{12} = 0$ ml/mol and $\Delta V_{23} = -14$ ml/mol, a value of $\Delta V_T = -27.7$ ml/mol is obtained, which is still in excellent agreement with the value from pressure studies. To substantiate this proposition recent studies at high frequencies locate the relaxation frequency for sulfate desolvation in the range 300–400 MHz.¹⁹

Probably the most important observations to be made on the variations of ΔH_{1j} and ΔS_{1j} for the second and third steps with atomic number are that the breaks occur where it has been proposed²⁸ that there is a coordination number change and that the trends in these values do not follow the trends in ΔH_T and ΔS_T obtained calorimetrically.⁵ It is possible to divide the series into

(23) The comparison is not strictly correct since the T -jump and P -jump activation parameters include the contribution from faster preequilibrium steps. The results are included only for completeness.

(24) M. Eigen and G. Maass, *Z. Phys. Chem. (Frankfurt am Main)*, **49**, 163 (1966).

(25) The two are comparable because the variation in ionic radius with atomic number is almost linear.

(26) F. H. Fisher and D. F. Davis, *J. Phys. Chem.*, **71**, 819 (1967).

(27) M. Eigen and K. Tamm, *Z. Elektrochem.*, **66**, 93, 107 (1962).

(28) F. H. Spedding, M. J. Pikal, and B. O. Ayers, *J. Phys. Chem.*, **70**, 2440 (1966).

three groups, La-Pr, Nd-Tb, and Dy-Lu, in which ΔH_{34} and ΔS_{34} are reasonably constant. The dependences of ΔH_{23} and ΔS_{23} , the values for anion desolvation, apparently indicate that the ligand contribution is *not* constant across the series as has often been assumed. Reverting to the argument²⁹ that if bonding is electrostatic and if there is no coordination number change in a series of similar cations, *e.g.*, the alkaline earths, a linear plot of ΔH_T of complexation with inverse cation radius would be observed, it seems natural to expect that as the radius decreases across the rare earth series the value of ΔH_T should increase. The increase would not be monotonic because of the change in coordination number. The fact that ΔH_T passes through a maximum and a later minimum might be explained by a nonconstant contribution from the ligand interaction. No implication is being made, nor can it be made on the basis of a single observation, that this is a general phenomenon. An apparent test for this proposition would be a corresponding study of the

temperature dependence of the rates of formation of some alkaline earth or divalent transition metal complexes of both inner- and outer-sphere types.

Although perhaps a little premature, in view of the present remarks, the common practice of using the sign and magnitude of the overall thermodynamic parameters, with the added constraint of a constant contribution from the ligand, to distinguish the structure of a complex species in solution³⁰ would seem to warrant some reconsideration.

Acknowledgment. We wish to acknowledge the financial assistance of the Research Corporation and the Research Foundation, Oklahoma State University. We are also grateful to the National Aeronautics and Space Administration for providing a fellowship to (D. P. F.).

(29) J. F. Duncan, *Aust. J. Chem.*, **12**, 356 (1959).

(30) T. Moeller, E. R. Birnbaum, J. H. Forsberg, and R. B. Gayhart, *Progr. Sci. Tech. Rare Earths*, **3**, 61 (1968).

Kinetics of Isopropyl Alcohol Radicals by Electron Spin

Resonance-Flow Techniques

by R. E. James and F. Sicilio

Department of Chemistry, Texas A & M University, College Station, Texas 77843 (Received September 11, 1969)

Detailed kinetic studies on the Ti(III)-H₂O₂-2-propanol system have supplied evidence for decay modes of radicals from 2-propanol. With $[\text{H}_2\text{O}_2]_0 > 2[\text{TiCl}_3]_0$, the empirical rate law for these radicals is $d[\text{R}]/dt = -k[\text{R}][\text{H}_2\text{O}_2]$. This is supported by dependency studies, invariance of rate constants, values of the Arrhenius parameters, and product analysis. Average second-order rate constants for this case are $4.0 \times 10^2 \text{ M}^{-1} \text{ sec}^{-1}$ for $(\text{CH}_3)_2\dot{\text{C}}\text{OH}$, R₁, and $2.5 \times 10^2 \text{ M}^{-1} \text{ sec}^{-1}$ for $\cdot\text{CH}_2\text{CH}(\text{CH}_3)\text{OH}$, R₂. With $[\text{H}_2\text{O}_2]_0 = [\text{TiCl}_3]_0$, combination of radicals appears to predominate; k (second order) = $1.6 \times 10^7 \text{ M}^{-1} \text{ sec}^{-1}$ for the reaction R₁ + R₁. The ratio of observed concentrations of substrate radicals depends on time after mixing and initial concentrations of TiCl₃ and H₂O₂. The kinetic results and stoichiometry indicate that the "·OH" product from the reactions of R₁ and R₂ with H₂O₂ is relatively unreactive towards this substrate. A reactive "·OH" would not be in accord with the disappearance of R₁ and R₂ at high $[\text{H}_2\text{O}_2]$, since a concurrent increase in $[\text{R}_1]$ and $[\text{R}_2]$ would be developed by abstraction reactions. A cyclic reaction sequence is thus ostensibly not perpetuated by radical-H₂O₂ reactions. Refined values of isotropic hyperfine coupling constants are $a_{\text{H}}(\text{CH}_3) = 20.1 \pm 0.1 \text{ G}$ for $(\text{CH}_3)_2\dot{\text{C}}\text{OH}$; $a_{\text{H}}(\text{CH}_2) = 22.4 \pm 0.2 \text{ G}$, and $a_{\text{H}}(\text{CH}) = 23.8 \pm 0.2 \text{ G}$ for $\cdot\text{CH}_2\text{CH}(\text{CH}_3)\text{OH}$.

Introduction

Rapid flow mixing of aqueous solutions of titanium(III) ion and hydrogen peroxide produces two free-radical species observable by esr spectroscopy.¹⁻⁷ It is now generally agreed that these radicals are forms of ·OH or ·O₂H complexed with Ti(IV).³⁻⁷ In this paper we shall refer to these radicals and their associated

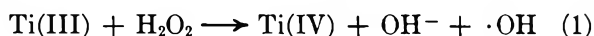
esr signals as S₁ ($g = 2.0132$) and S₂ ($g = 2.0118$). When an alcohol is included as a substrate in one or

(1) F. Sicilio, R. E. Florin, and L. A. Wall, *J. Phys. Chem.*, **70**, 47 (1966).

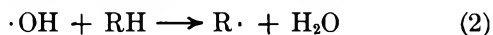
(2) W. T. Dixon and R. O. C. Norman, *J. Chem. Soc.*, 3119 (1963).

(3) Y. S. Chiang, J. Craddock, D. Mickewich, and J. Turkevich, *J. Phys. Chem.*, **70**, 3509 (1966).

both of the reactant solutions, S_1 and S_2 are partially or totally quenched and radicals are formed from abstraction of hydrogen from the substrate molecule.^{2,3,5-9} Thus, $\cdot\text{OH}$ radicals, initially produced by reaction 1

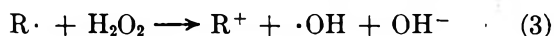


become complexed with forms of Ti(IV) species or abstract a hydrogen atom as in reaction 2.² It is



implicit that complexation and abstraction compete.^{5,7}

In the oxidation of an alcohol with two reactive sites, the relative concentrations of isomeric radicals which are observed depend markedly on the conditions.⁷⁻⁹ The alkoxy radical, $\text{RO}\cdot$, is not observed even though the energetics for its formation are favorable. Shiga⁹ has found that in the $\text{Fe(II)}-\text{H}_2\text{O}_2$ -alcohol system $\cdot\text{CH}_2\text{CH}(\text{CH}_3)\text{OH}$ predominates, whereas $(\text{CH}_3)_2\dot{\text{C}}\text{OH}$ predominates in the analogous Ti(III) system. It is suggested that a different form of abstracting agent, not free $\cdot\text{OH}$, is present in the Fe(II) system.⁹ Norman and West⁷ conclude that the relative reactivities of isomeric radicals toward hydrogen peroxide, reaction 3, are of paramount importance in determining the



relative amounts observed by esr spectroscopy in the Ti(III) system. It will be shown in this paper that time of observation and rates of both production and destruction reactions are the chief factors determining the observed concentrations of radicals from 2-propanol.

From kinetic studies of radicals produced from dimethoxymethane in the Ti(III)- H_2O_2 system, reaction 4 has been proposed to be an important decay mode, in



which an adduct is formed from the substrate radical.¹⁰ Reactions 3 and 4 should have about the same rates. Distinguishing between the two would be difficult, since R^+ and OH^- would be expected to combine very rapidly to form ROH. In this work, additional evidence for reaction of $\text{R}\cdot$ with H_2O_2 was sought.

On the basis of experiments in which substrate is added shortly after the other reactants are mixed, oxidation of alcohol by a chain mechanism involving reactions 2 and 3 has been suggested.⁷ A relatively large consumption of substrate would be expected if this chain were of extensive length. Overall reaction stoichiometry, determined from product analysis, was studied in an effort to resolve this question.

Experimental Section

Reagents. Solutions of TiCl_3 were prepared from W. H. Curtin & Co. technical grade 20% reagent which was determined with standardized KMnO_4 to be 1.43 to 1.49 M . Hydrogen peroxide (H_2O_2) solutions were

made from Baker Analyzed reagent (30% solution), freshly opened bottles of which were 9.2 to 9.7 M . Anionic and metal impurities in this reagent were specified to be less than 0.001%. Potassium nitrosodisulfonate, $\text{NO}(\text{SO}_3\text{K})_2$, Frémy's salt, was prepared according to Harvey and Hollingshead.¹¹

Apparatus. ESR spectra were recorded on a Varian 4502-15 spectrometer system with V-4560 100-kHz field modulation and Fieldial attachment, operated to give a derivative presentation of the resonance absorption. Microwave power was adjusted to about 30 mW for maximum intensity. The field modulation amplitude was adjusted for optimum signal intensity without undue broadening for recording kinetic data and readjusted for maximum resolution for obtaining details of the hyperfine structure. The liquid flow system has been described previously.¹⁰

Procedure. The two aqueous reactant solutions, TiCl_3 (0.1 M in H_2SO_4) and H_2O_2 (containing 2-propanol) were prepared from distilled water which was deaerated by bubbling in nitrogen through a diffusion frit for several minutes. Concentrations of TiCl_3 ranged from 0.005 to 0.1 M , H_2O_2 from 0.1 to 0.2 M , and 2-propanol from 0.2 to 2.0 M . Immediately following preparation, the solutions were transferred to 10-l. glass reservoirs and put under nitrogen pressure. The separate streams flowed by pressure to the mixer and flat cell *via* insulated polyethylene tubing. For runs not at room temperature each solution was passed through coils immersed in a thermostated bath. The temperature of the single stream of mixed solution was measured within 2 ft of the mixer.

Total flow was measured by timing the collection of 100 ml of product solution. Flow rates of each reactant solution were initially measured separately and set equal. During a run the separate flow rates were periodically checked. In all cases the resultant total flow rate was less than the additive flow rates of the individual streams.

For the kinetic measurements, the peak heights of one peak for each of the radicals were recorded as a function of flow rate. Reaction times, t , were calculated from flow rates, r , by the relation $t = V/r$, where V is the dead volume.¹ Immediately after each kinetic run a solution of $1.00 \times 10^{-3} M$ MnSO_4 was introduced into the lines and cell without interrupting the instru-

- (4) K. Takakura and B. Rånby, *J. Phys. Chem.*, **72**, 164 (1968).
- (5) H. Fischer, *Ber. Bunsenges. Phys. Chem.*, **71**, 685 (1967).
- (6) R. E. Florin, F. Sicilio, and L. A. Wall, *J. Phys. Chem.*, **72**, 3154 (1968).
- (7) R. O. C. Norman and P. R. West, *J. Chem. Soc., B*, 389 (1969).
- (8) P. Smith and P. B. Wood, Abstracts, Organic Section, 151st National Meeting of the American Chemical Society, Pittsburgh, Pa., Mar 1966.
- (9) T. Shiga, *J. Phys. Chem.*, **69**, 3805 (1965).
- (10) E. L. Lewis and F. Sicilio, *ibid.*, **73**, 2590 (1969).
- (11) G. Harvey and R. G. Hollingshead, *Chem. Ind. (London)*, 244 (1953).

ment tuning except for adjustment of leakage current. Peak heights were related to concentration by using the area, A_{Mn} , of the six-line spectrum of Mn(II) as an absolute standard. Signal areas for radicals were approximated by I (peak height, cm) $\times \Delta H^2$ (line width², G²). The fraction, A_i , of the total radical signal area represented by the peak being monitored was determined to be relatively constant. Line width measurements were made for each run and area/peak height calculated by $(I\Delta H^2) (A_i)^{-1}/I = \Delta H^2(A_i)^{-1}$. Thus, [radical]/peak height = $[Mn(II)]\Delta H^2(A_i)^{-1}/A_{Mn}$.

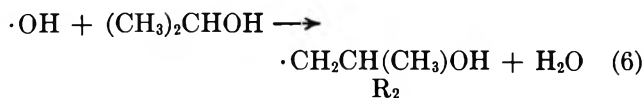
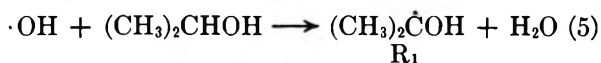
To measure the isotropic g values, an alkaline solution of Frémy's salt ($a = 13.0 \pm 0.1$ G, $g = 2.00550 \pm 0.00005$)¹² was introduced into the lines, and cell and the low-field peak were recorded. Without interrupting the scan, the reactant streams were turned on, and the higher field hyperfine components of the radicals were recorded.

A Hewlett-Packard 5750 gas chromatograph with a flame ionization detector was used for qualitative and quantitative analysis of reaction products. A 6-ft \times $1/8$ -in. column packed with Carbowax 20M on Chromopak support (Curtin Chemical Co. 8-864D) was used for analysis of acetone. Solutions containing glycols were analyzed with 5-ft \times $1/8$ -in. column packed with Porapak.¹³

Treatment of effluent solutions prior to gc analysis generally consisted of neutralization with NaOH, followed by vacuum distillation with mild heating. The distillate was collected in a flask immersed in a Dry Ice-alcohol bath. Distillation at atmospheric pressure was done in the early work but was abandoned due to the possibility of the products undergoing reaction at the higher distillation temperatures.

Results and Discussion

Reaction 1 is the initial reaction occurring when $TiCl_3(aq)$ and $H_2O_2(aq)$ are mixed, in which $\cdot OH$ is considered to be a highly reactive intermediate. When excess 2-propanol is included in the H_2O_2 stream, $\cdot OH$ abstracts hydrogen to produce two radicals, R_1 and R_2



These reactions are so rapid that formation of R_1 and R_2 is not observed even at the lowest times accessible, 10–15 msec after mixing. Formation evidently does not occur through S_1 or S_2 since their formation rates are observable⁶ and therefore must be slower than those for R_1 and R_2 . Furthermore, when titanium is complexed with EDTA, precluding formation of other complexes, substrate radicals may nevertheless be generated, whereas S_1 and S_2 are not observed even in the absence of substrate.^{4,7}

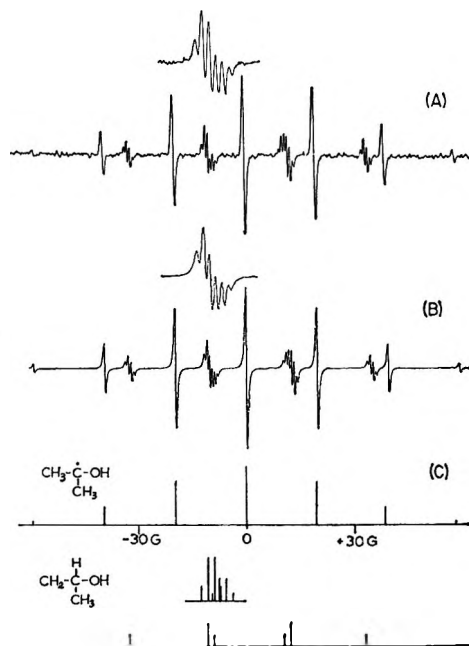


Figure 1. ESR spectrum of 2-propanol radicals in the Ti(III)- H_2O_2 flow system. (A) Experimental spectrum resulting from reaction of 0.01 M $TiCl_3$ (0.1 M H_2SO_4) with 0.10 M H_2O_2 (0.50 M 2-propanol). (B) Computer simulated spectrum, (cf. program using Lorentzian line function for IBM 360/65 by B. D. Faubion, unpublished). (C) Theoretical line spectra for R_1 and R_2 . Insets show γ splitting for R_2 .

Esr Spectra of Radicals. R_1 and R_2 are identified by their characteristic proton hyperfine structure in the esr spectrum, Figure 1. In this paper, α refers to the position of the unpaired electron; β refers to the position once removed. For R_1 , with six equivalent methyl protons ($a_\beta = 20.1 \pm 0.1$ G), seven lines result with intensity ratios approximately 1:6:15:20:15:6:1. The multiplet peaks are due to R_2 and can be understood by comparison of the computed (B) with the experimental (A) spectra in Figure 1. For R_2 , $a_\alpha = 22.4 \pm 0.2$ G and $a_\beta = 23.8 \pm 0.2$ G; the two equivalent α protons give a 1:2:1 triplet, each component of which is split by the single β proton to give six peaks as shown by the lower line plot in Figure 1 (C). Further splitting of each of these lines by the methyl protons in the γ position ($a_\gamma = 0.78$ G) gives six quarters. Overlap in the inner multiplets gives rise to the experimental six-peak signals shown in the insets of Figure 1. Values for the isotropic hyperfine coupling constants for R_2 were previously assigned as $a_\alpha = 23.2$ Oe, $a_\beta = 22.0$ Oe, and $a_\gamma = 0.8$ Oe;⁷ and $a_\alpha = 22.2$ G and $a_\beta = 22.2$ G.⁹ Our computer analyses definitely determine that $a_\beta > a_\alpha$.

Under the conditions for generating the spectrum of Figure 1, no hydroxyl hydrogen hyperfine splitting for

(12) J. Q. Adams, S. W. Nicksic, and J. R. Thomas, *J. Chem. Phys.*, **45**, 654 (1966); J. S. Hyde, personal communication.

(13) O. L. Hollis, *Anal. Chem.*, **38**, 309 (1966).

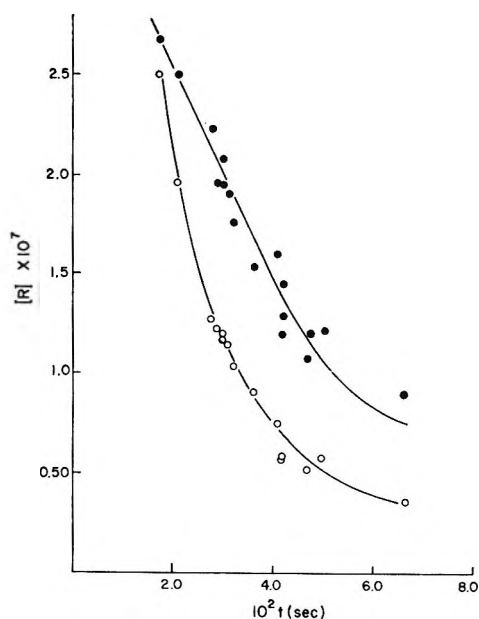


Figure 2. Plots of $[R]$ vs. time after mixing, t , at 27° . Initial concentrations: $0.005 M$ $TiCl_3$, $0.1 M$ H_2SO_4 ; $0.1 M$ H_2O_2 , $0.2 M$ 2-propanol. \circ , R_1 ; \bullet , R_2 .

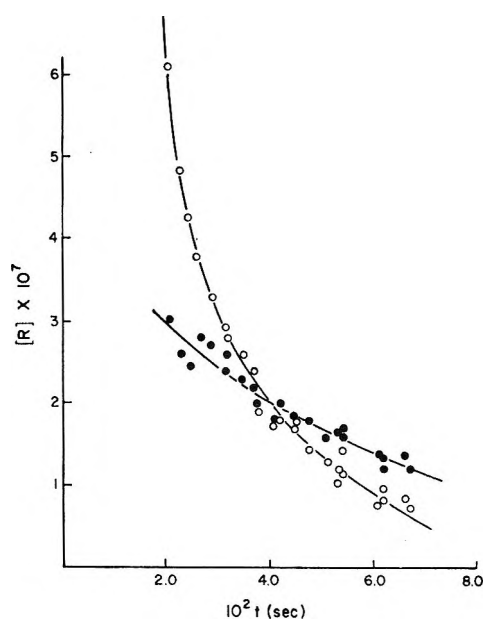


Figure 3. Plots of $[R]$ vs. time after mixing, t , at 27° . Initial concentrations: $0.01 M$ $TiCl_3$, $0.1 M$ H_2SO_4 ; $0.1 M$ H_2O_2 , $0.5 M$ 2-propanol. \circ , R_1 ; \bullet , R_2 .

R_1 was observable. This splitting has been reported for $\cdot CH_2OH$ generated from CH_3OH in the flow-system reaction of $TiCl_3$ and H_2O_2 ¹⁴ and for $(CH_3)_2\dot{C}OH$ in the same system.¹⁵ For $\cdot CH_2OH$, this doublet splitting, maximum value of $0.96 G$, collapses below $pH = 1.11$. For $(CH_3)_2\dot{C}OH$, in this work, a very weak doublet splitting at $pH = 1.80$ (no acid added to either reactant solution) was observed for the central line of the septet of R_1 .

Relative Concentrations of R_1 and R_2 . The observed concentrations of R_1 and R_2 depend on the initial concentrations of starting materials and the time, t , of observation after mixing, as demonstrated by zero-order plots of $[R_1]$ and $[R_2]$, Figures 2-4. In Figure 3, at times below about 40 msec, $[R_1] > [R_2]$ while at longer times, $[R_2] > [R_1]$. Such a crossover of the curves for R_1 and R_2 occurs at longer times as $[TiCl_3]_0$ is increased relative to $[H_2O_2]_0$. Increase in rates of formation for R_1 and R_2 shifts the observed decay curves upward, affecting the crossover point. Thus, the reactivities of R_1 and R_2 toward H_2O_2 are not necessarily the paramount factors in determining their relative concentrations, as suggested by Norman and West.⁷ The differences in ease of formation must also be considered. It is evident that the rate of formation of R_1 is greater than that for R_2 , even though the formation region is inaccessible with this experimental setup.

Kinetic Analysis of Substrate Radical Decay. Kinetic runs in which peak heights for R_1 and R_2 were monitored with reaction time were made at several different sets of initial concentrations of reactants. In an attempt to select a reaction order, plots for first-order (\log peak height, P , vs. t), second-order (P^{-1} vs. t), and three-

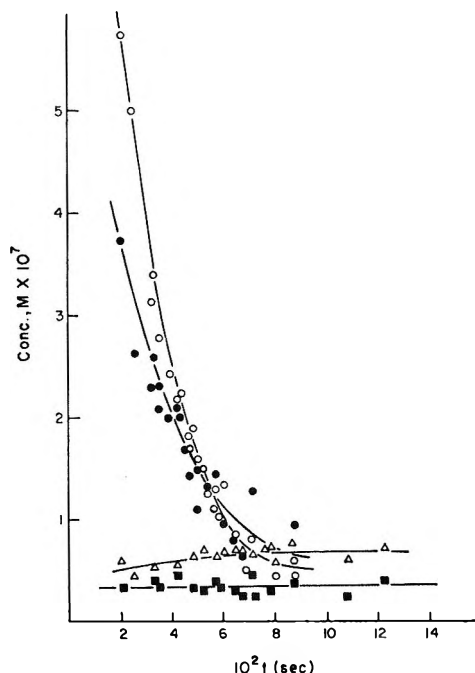


Figure 4. Plots of $[R]$ vs. time after mixing, t , at 27° . Initial concentrations: $0.02 M$ $TiCl_3$, $0.1 M$ H_2SO_4 ; $0.1 M$ H_2O_2 , $0.2 M$ 2-propanol. \circ , R_1 ; \bullet , R_2 ; Δ , S_1 ; \blacksquare , S_2 .

halves-order ($P^{-1/2}$ vs. t) decay were compared for each run. Linear slopes, corresponding to the observed rate constants, were computed by a least-squares calculation using the IBM 360/65 computer. Slopes for three-halves- and second-order plots were converted into molar

(14) H. Fischer, *Mol. Phys.*, **9**, 149 (1965).

(15) R. Poupko and A. Loewenstein, *J. Chem. Soc., A*, 949 (1968).

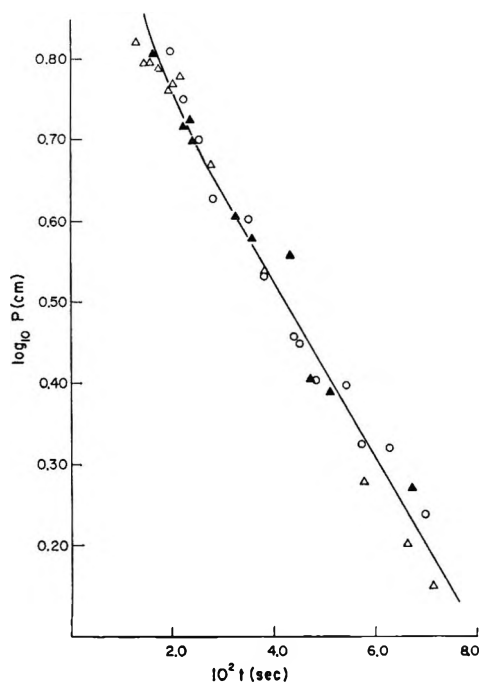
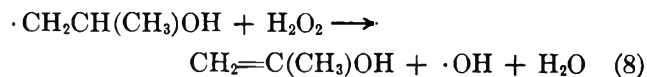
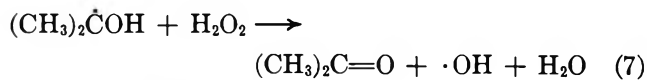


Figure 5. First-order kinetic plot for R_2 . $\log P$ (peak height) vs. time after mixing, t , at 27° . Initial concentrations: $0.01 M$ $TiCl_3$, $0.1 M$ H_2SO_4 ; $0.1 M$ H_2O_2 , $0.5 M$ 2-propanol. Symbols represent different runs.

units using the concentration/ P conversion factor determined from the $Mn(II)$ spectrum taken for each run. First-order and three-halves-order k 's thus determined are tabulated in Table I. By standardizing for each run, problems associated with sensitivity changes in the instrument were minimized. In general, first- and three-halves-order plots, such as Figures 5 and 6 for R_2 , gave the best straight lines. A plausible mechanism for three-halves-order decay is difficult to develop. In view of evidence to be presented, pseudo-first-order decay was chosen as a working hypothesis.

The observed pseudo-first-order decay constants for R_1 and R_2 (Table I) are dependent on $[H_2O_2]_0$ and relatively independent of $[TiCl_3]_0$. Quantitative evaluation shows the order of dependence of these k 's on $[H_2O_2]_0$ to be 1.1 for R_1 and 1.2 for R_2 , from the slopes in Figure 7, for $[H_2O_2]_0 \geq 10^{-2} M$ and $[H_2O_2]_0/[Ti(III)]_0 \geq 2$. These results suggest the following reactions



as principal modes of decay for the substrate radicals. These reactions have exothermicities of approximately 49 and 37 kcal/mol, respectively, and are mechanistically feasible.¹⁶ The product in (8) is the enol form of acetone.

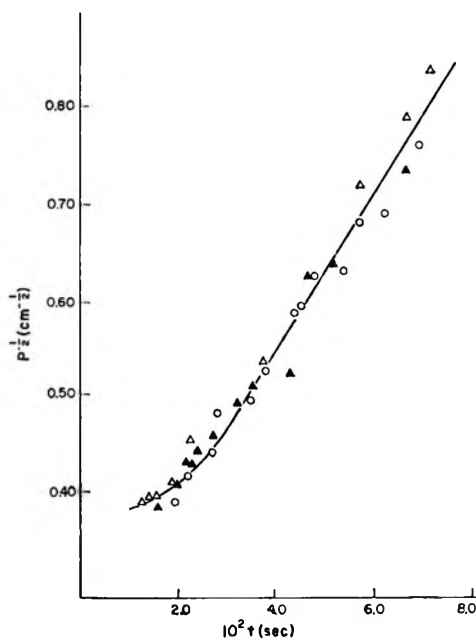


Figure 6. Three-halves-order kinetic plot for R_2 . Reciprocal square root of peak height, $P^{-1/2}$ vs. time after mixing, t , at 27° . Same data as Figure 5.

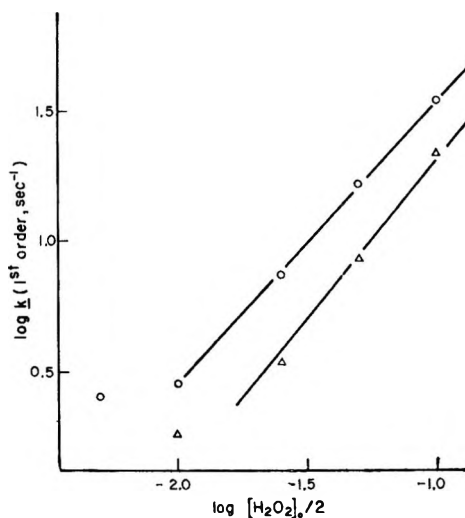


Figure 7. Determination of reaction order with respect to H_2O_2 , $\log k$ (first order) vs. $\log [H_2O_2]_0/2$; $[TiCl_3]_0 = 0.01 M$, $[H_2SO_4]_0 = 0.1 M$, $[2\text{-propanol}]_0 = 0.5 M$, $T = 27^\circ$. \circ , R_1 ; Δ , R_2 .

The deviation from linearity of the R_1 plot in Figure 7 for $[H_2O_2]_0/[Ti(III)]_0 = 1$ is interpreted to be a definite indication of a change in mechanism occurring as $[H_2O_2]_0$ is made smaller. For this ratio of 1, essentially all H_2O_2 is consumed in reaction 1 and the decay of R_1 (Figure 8) fits a second-order plot much better than first- or three-halves-order plots. The signals for R_2 are too low to be meaningful, but the evidence for

(16) We are indebted to a reviewer for pointing out that the exothermicities can be calculated from data presented by S. W. Benson, *J. Chem. Educ.*, **42**, 502 (1965).

Table I: Decay Constants for R_1 and R_2

[TiCl ₃] ₀ ^a	[H ₂ O ₂] ₀ ^a	[i-C ₃ H ₇ OH] ₀ ^a	T, °C	k (first order), sec ^{-1b}		k (second order), M ⁻¹ sec ^{-1c}		k (3/2 order), M ^{-1/2} sec ⁻¹	
				R ₁	R ₂	R ₁	R ₂	R ₁	R ₂
0.0005	0.1	0.2	28	15.8 ± 1.2	10.7 ± 1.0	3.4 ± 0.3 × 10 ²	2.3 ± 0.2 × 10 ²	6.9 ± 0.4 × 10 ⁴	3.3 ± 0.3 × 10 ⁴
0.02	0.1	0.2	28	18.3 ± 1.3	10.3 ± 1.4	4.6 ± 0.3 × 10 ²	2.6 ± 0.4 × 10 ²	6.6 ± 0.6 × 10 ⁴	3.2 ± 0.5 × 10 ⁴
0.05	0.1	0.2	28	9.7 ± 0.8	7.7 ± 0.4	3.9 ± 0.3 × 10 ²	3.1 ± 0.2 × 10 ²	2.1 ± 0.2 × 10 ⁴	2.1 ± 0.1 × 10 ⁴
0.1	0.1	0.2	28	3.5 ± 0.4				8.2 ± 0.9 × 10 ³	
0.01	0.01	0.5	30	2.5 ± 0.1		1.6 ± 0.4 × 10 ^{7*}		4.5 ± 0.1 × 10 ³	
0.01	0.02	0.5	28	2.8 ± 0.1	1.8 ± 0.3	5.6 ± 0.2 × 10 ²	3.7 ± 0.5 × 10 ²	4.6 ± 0.2 × 10 ³	4.7 ± 0.7 × 10 ³
0.01	0.05	0.5	25	6.7 ± 0.3	3.1 ± 0.3	3.4 ± 0.1 × 10 ²	1.6 ± 0.2 × 10 ²	1.8 ± 0.1 × 10 ⁴	8.7 ± 0.8 × 10 ³
0.01	0.1	0.5	27	16.5 ± 0.9	8.5 ± 0.6	3.8 ± 0.2 × 10 ²	1.9 ± 0.1 × 10 ²	4.9 ± 0.2 × 10 ⁴	2.3 ± 0.1 × 10 ⁴
0.01	0.2	0.5	26	33.8 ± 1.3	20.7 ± 1.0	3.6 ± 0.1 × 10 ²	2.2 ± 0.1 × 10 ²	1.1 ± 0.4 × 10 ⁵	5.3 ± 0.3 × 10 ⁴

^a Initial concentrations prior to mixing of streams. Initial concentrations after mixing are these values divided by 2. ^b Standard deviations computed from $\sigma_m^2 = \sum_i (y_i - \epsilon_i)^2 / \{N \sum x_i^2 - (\sum x_i)^2\}$ where $x_i = t$, ϵ_i = least-squares computed $f(P)$, and y_i observed $f(P)$. ^c k (second order) = k (first order) + $([H_2O_2]_0 - [TiCl_3]_0)/2$, with exception of value noted by asterisk.

R_1 indicates that the mechanism has been shifted to the following radical-radical combination reactions



These reactions have been previously rejected as principal decay modes at $[H_2O_2]_0/[Ti(III)]_0 = 10$.¹⁰ Because of the low $[R_2]$, the second-order decay constant for reaction 9, from Figure 8, is $k_9 = 1.6 \times 10^7 M^{-1} sec^{-1}$.

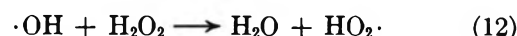
There is additional supporting evidence for reactions 7 and 8. Consider the results outlined in Table II.

Table II: Effects of Varying $[H_2O_2]_0$ and $[i-C_3H_7OH]_0$; Radicals Observed

Experiment no.	$[H_2O_2]_0$ ^a	$[i-C_3H_7OH]_0$	Radicals observed
1	0.2	0.2	S ₁ , S ₂
2	0.2	0.5	S ₁ , S ₂ , R ₁ , R ₂
3	0.2	1.0	S ₁ , S ₂ , R ₁ , R ₂
4	0.2	2.0	S ₁ , S ₂ , R ₁ , R ₂
5	0.6	2.0	S ₁ , S ₂
6	1.0	2.0	S ₁ , S ₂
7	1.0	5.0	S ₁ , S ₂

^a $[TiCl_3]_0 = 0.2$ in all experiments. Actual initial concentrations upon mixing are these tabulated values divided by 2.

All four radicals are observed in experiments 2, 3, and 4; partial spectra are presented in Figure 9. With an increase in $[H_2O_2]_0$ from 0.2 to 0.6 M (experiments 4 and 5), the signals for R_1 and R_2 disappear, indicating a large increase in the rates of reactions 7 and 8. It may seem that a contribution to the disappearance of R_1 and R_2 could be the scavenging of the initial $\cdot OH$ radical by



However, this has been considered previously,⁶ and abstraction reactions such as 5 and 6 predominate over reaction 12. The second-order rate constants for (7) and (8) (Table I) exhibit relatively small variation except for the cases of equal $[TiCl_3]_0$ and $[H_2O_2]_0$. Average values are $k_7 = 4.0 \times 10^2 M^{-1} sec^{-1}$ and $k_8 = 2.5 \times 10^2 M^{-1} sec^{-1}$.

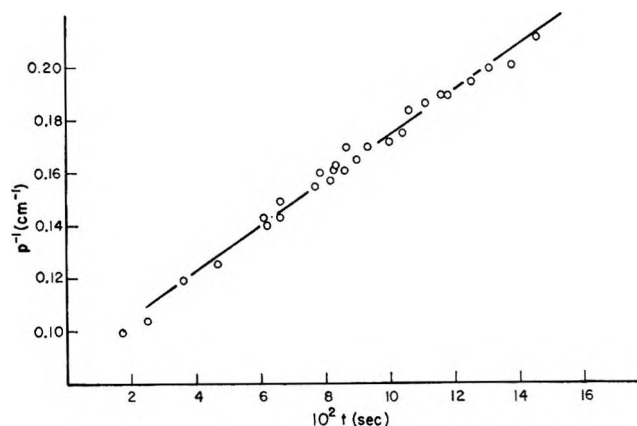


Figure 8. Second-order kinetic plot for R_1 . Reciprocal peak height, P^{-1} , vs. time after mixing, t , at 30°. Initial concentrations: 0.01 M $TiCl_3$, 0.1 M H_2SO_4 ; 0.01 M H_2O_2 , 0.5 M 2-propanol.

Arrhenius plots (Figure 10) of $\log k_7$ and $\log k_8$ vs. T^{-1} gave activation energies of 11.5 and 11.6 kcal/mol for R_1 and R_2 , respectively, and preexponential factor of $10^{11} M^{-1} sec^{-1}$ for both R_1 and R_2 . The E_a values are in the right range for radical-molecule reactions. They are definitely too high for the decay reactions to be diffusion controlled. The A factor is not abnor-

Table III: Results of Product Analyses

Expt no.	[Ti(III)] ₀ / [H ₂ O ₂] ₀ / [i-C ₃ H ₇ OH] ₀	Method of mixing	mmol initial			mmol consumed		Acetone produced, mmol	Consumption ratio Ti(III)/H ₂ O ₂ /i-C ₃ H ₇ OH
			H ₂ O ₂	Ti(III)	i-C ₃ H ₇ OH	Ti(III)	H ₂ O ₂		
1	0.10/0.10/2.0	A ^a	5.0	5.0	100	5.0	5.0	2.3 ± 0.4	2:2:1
		A	5.0	5.0	100	5.0	5.0	2.5 ± 0.2	2:2:1
		A	5.0	5.0	100	5.0	5.0	2.3 ± 0.2	2:2:1
2	0.056/0.092/0.500	B ^b	5.5	3.3	50.0	3.3	...	1.5 ± 0.4	2:-:1
		C ^c	2.3	1.8	12.5	1.8	2.3	0.60 ± 0.03	9:12:3
3	0.047/0.093/0.500	D ^d	1.9	2.3	10.0	2.3	1.9	0.20 ± 0.02	12:10:1
		D	2.0	2.3	10.5	2.3	2.0	0.12 ± 0.02	12:10:0.6
		B	95	55	250	55
4	1.1/1.9/5.0	B	95	55	250	55

^a Four-jet mixer used in flow system. ^b Burets side by side with rapid stirring of reactant solutions. ^c Ti(III)(aq) titrated slowly into H₂O₂-ROH(aq) with rapid stirring. ^d H₂O₂(aq) titrated into Ti(III)(aq).

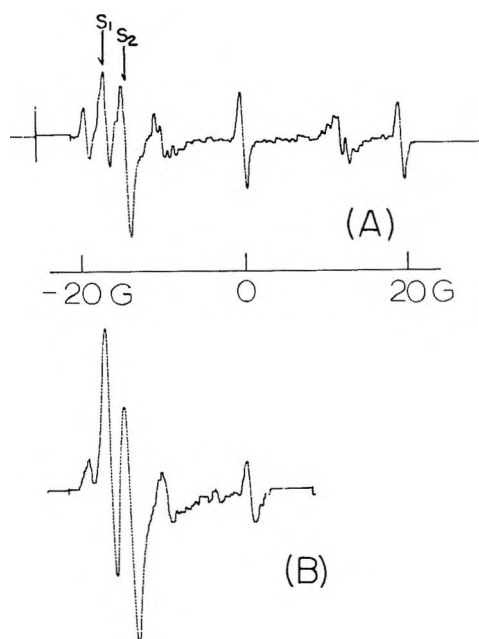


Figure 9. ESR spectra of R₁, R₂, S₁, and S₂ occurring simultaneously. Initial concentrations: 0.1 M TiCl₃, 0.1 M H₂SO₄; 0.2 M H₂O₂, 1.0 M 2-propanol. (A) 40.3 msec after mixing. (B) 79.2 msec after mixing.

mal, in that $10^{11} M^{-1} \text{sec}^{-1}$ is predicted by collision theory for bimolecular reactions in solution.¹⁷

From a reasonable value for the rate constant for reaction 1,⁶ it can be estimated that almost all of the Ti(III) initially present has been converted into Ti(IV) at 20 msec after mixing. Thus in the time region of chief interest, 20–100 msec after mixing, Ti(IV) is available for complexation of ·OH to form S₁ and S₂. With [TiCl₃]₀ = 0.05 M and [H₂O₂]₀ = 0.1 M, maxima of zero-order plots for S₁ and S₂ occur at ~18 and ~10 msec, respectively. Inclusion of 0.2 M 2-propanol in this system shifts the maxima to longer times, ~50 msec, for both S₁ and S₂. Evidently formation of S₁ and S₂ in the latter case takes place by a different, slower pathway than that in the absence of

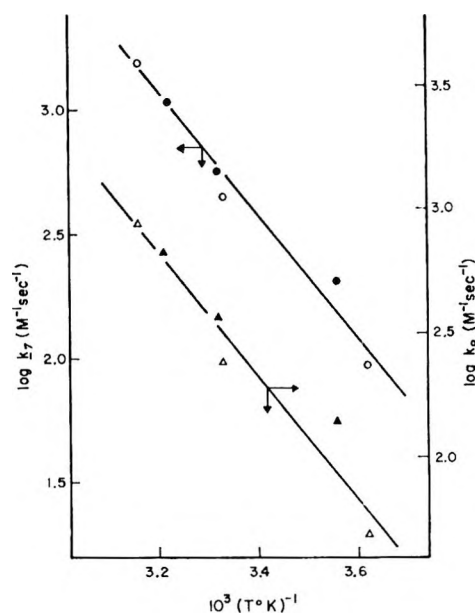


Figure 10. Arrhenius plots, $\log k$ (second order) vs. $(T^\circ\text{K})^{-1}$. Δ , initial concentrations: 0.01 M TiCl₃, 0.1 M H₂SO₄; 0.1 M H₂O₂, 0.5 M 2-propanol. \blacktriangle , initial concentrations: 0.01 M TiCl₃, 0.1 M H₂SO₄; 0.02 M H₂O₂, 0.5 M 2-propanol.

alcohol. This pathway could be *via* (2) and (3) making ·OH available for complexation at a later time after mixing, as suggested by Norman and West.⁷ They presented evidence supporting production of S₁ and S₂ by reaction of R₁ with H₂O₂, with the suggestion that free ·OH is produced by reaction 3. Production by (7) and (8) of a relatively unreactive complexed ·OH species is, however, more compatible with our observed kinetics of R₁ and R₂, $d[R_1]/dt = -k_7[R_1][H_2O_2]$ and $d[R_2]/dt = -k_8[R_2][H_2O_2]$. If ·OH in (7) and (8) were free hydroxyl radical, then the decay of R₁ and R₂ would not have simple first-order dependence on H₂O₂. Also, the overall rate would be slower than that ex-

(17) A. A. Frost and R. G. Pearson, "Kinetics and Mechanism," John Wiley & Sons, Inc., New York, N. Y., 1953, p 130.

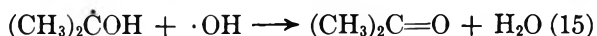
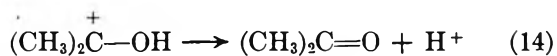
pected for (7) and (8) because of the contributions of (5) and (6). The lifetimes of R_1 and R_2 are not characteristic of ordinary alkyl radicals in that bimolecular rate constants for the latter are usually $\sim 10^{10} M^{-1} \text{sec}^{-1}$. A mean lifetime, $(k[R])^{-1}$, for $[R] = 10^{-7}$ would thus be ~ 1 msec, much shorter than that observed. Complexation of R_1 and R_2 with Ti(IV) could furnish this increased stability and provide complexed $\cdot\text{OH}$ as a product in reactions 7 and 8.

Stoichiometry and Product Analysis. In the absence of a reactive substrate the stoichiometry of the Ti(III)- H_2O_2 reaction is reported to be $2\text{Ti(III)}:1\text{H}_2\text{O}_2$ for titration of peroxide into titanium.^{1,6} Reactions 1 and 13 together account for this observed consumption ratio.



Inclusion of a reactive substrate increases the consumption of H_2O_2 relative to that of Ti(III).⁶ For a $0.1 M \text{TiCl}_3$ - $1.0 M$ 2-propanol solution titrated with $0.1 M \text{H}_2\text{O}_2$, the molar consumption ratio of Ti(III) to H_2O_2 is 1:1. This indicates that reactions 5 and 6 compete with reaction 13 for $\cdot\text{OH}$ and that H_2O_2 is consumed by (7) and (8). Reactions 1, 5-8, and 13 account for the stoichiometry found in experiment 1 (Table III).

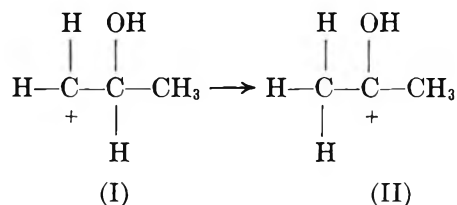
For several different effluent mixtures (Table III), acetone was identified as the predominant organic product. Identity was established by gc elution times and nmr spectra. Acetone could also be formed if R_1 reacted according to (3) followed by (14), or from (15).



1,2-Propanediol, expected from reaction 16, was not



found in any of the product mixtures although millimolar quantities are detectable. This reaction may thus be ruled out. If R_2 decays by a reaction analogous to (3), a carbonium ion (I) is formed, and it would conceivably undergo rearrangement to form a more stable ion (II), ultimately going to acetone as in reaction 14. Intermediate steps between I and II



would be difficult to pinpoint, yet the transformation seems plausible on the basis of stability considerations.

If free $\cdot\text{OH}$ were produced in reactions 7 and 8, it would react with substrate and perpetuate a chain mechanism.⁷ The extent to which this occurs may be judged by the amount of substrate consumed relative to the initial amounts of TiCl_3 and H_2O_2 . In Table III, the results of quantitative gc analyses of reaction products indicate that a maximum of 0.5 mol of alcohol is consumed for 1 mol each of H_2O_2 and Ti(III). On the basis of these results, occurrence of a chain mechanism through extensive cycles does not appear to be plausible. Instead these results, in accord with kinetic results, indicate that the radical produced in (7) and (8) is relatively unreactive towards substrate.

Experiments 2 and 3 of Table III indicate that the method of mixing the reactants affects the amount of product formed. Experiment 2 gives about the same consumption ratio as the value in experiment 1. This is to be expected since method B for mixing should approach closely the conditions in the flow system. In experiment 3, relatively less product is formed by method D than C. This is a reasonable result since, with mixing method C, reactions 5 and 6 would be favored over reaction 13. With method D, more Ti(III) is available at the reaction site to react rapidly with $\cdot\text{OH}$ by reaction 13. Experiment 4 was carried out in an attempt to increase the concentration of possible glycol products, 1,2-propanediol, 2,5-hexanediol ($R_2 + R_2$), 2-methyl-2,4-pentanediol ($R_1 + R_2$), and 2,3-dimethyl-2,3-butanediol ($R_1 + R_1$). None of these were detected in the condensate from 100-ml quantities of effluent solution, indicating that their concentrations are $< 10^{-3} M$.

Acknowledgment. This research was supported by The Robert A. Welch Foundation, Grant A-177. The esr spectrometer was made available by National Science Foundation, Grant GP-3767.

The Kinetics of the Reactions of Cobalt(II) and Cobalt(III)

Acetates with Benzyl Hydroperoxide in Acetic Acid at 25°

by E. J. Y. Scott

Mobil Research and Development Corporation, Central Research Division Laboratory, Princeton, New Jersey 08540
(Received May 8, 1969)

The reaction of Co(II) acetate with benzyl hydroperoxide in acetic acid at 25° at steady-state concentrations of Co(II) and Co(III) acetates obeys the rate law $-d[\text{ROOH}]/dt = 1.15[\text{Co(II)}]_{ss}[\text{Co(III)}]_{ss}^{1/2}[\text{ROOH}]$ where the suffix *ss* indicates steady-state concentration. The half power suggests Co(III) acetate is in monomer-dimer equilibrium. The rate-determining step probably involves monomers of Co(III) acetate and Co(II) acetate, one of which is complexed with a benzyl hydroperoxide ligand. The main product is benzaldehyde which indicates that for primary hydroperoxides, dehydration, not reduction by Co(II), is the main reaction. At high Co(III)/Co(II) ratios the reaction mechanism changes. Reduction of Co(III) acetate dimer by a benzylperoxy anion is probably rate determining.

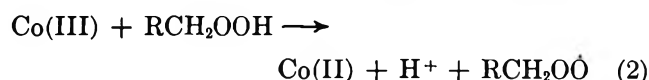
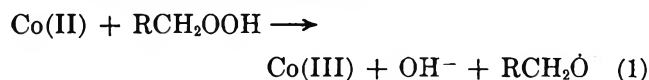
Introduction

The homogeneous catalytic oxidation of hydrocarbons by transition metal salts has considerable theoretical and practical interest. This area of chemistry involves the relatively unexplored reactions of ions with radicals. Moreover, it is also the basis of important industrial processes, for example, the manufacture of terephthalic acid from *p*-xylene.¹

The reactions between aromatic hydroperoxide and metal salts (such as cobalt acetate) have been postulated as initiation reactions in the homogeneous catalytic oxidation of aromatic hydrocarbons.^{2,3} However, much research on this problem does not relate significantly to autoxidation of hydrocarbons for a number of reasons. The kinetics have usually been studied at high ratios of hydroperoxide to metal. When hydroperoxide is in excess over the metal, radical-induced decomposition of hydroperoxide may become a preferred reaction particularly with tertiary hydroperoxides.⁴⁻⁶ These conditions are unrealistic inasmuch as steady-state concentrations of hydroperoxide in many autoxidations are less than catalyst concentrations, *e.g.*, the autoxidation of tetralin² if Co(II) > 0.01 *M*, or of *p*-xylene¹ (Co(II) ~0.1 *M*). Moreover, there is little information on the reactions of metal ions with primary hydroperoxides, and, specifically, with the intermediates formed from toluene and its derivatives (such as *p*-toluic acid and *p*-xylene) in which there is a special interest.^{1,3,7-12} Kinetic data derived using a tertiary hydroperoxide such as *t*-butyl hydroperoxide¹³⁻¹⁶ will not apply inasmuch as a primary hydroperoxide may undergo reactions involving an α -hydrogen atom. In particular, kinetic data are lacking in polar solvents such as acetic acid.

A kinetic and product study of the reaction between cobalt acetate and benzyl hydroperoxide in acetic acid

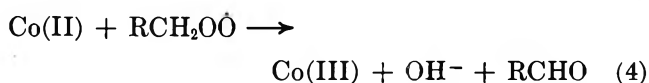
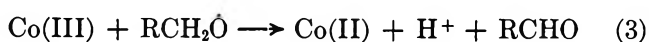
is now reported. It is generally thought that both Co(II) and Co(III) species will react with a hydroperoxide by steps 1 and 2, respectively¹⁷



The ions should not be considered free, but rather as part of the metal-ligand complex. Thus, a study of either Co(II) or Co(III) acetate with benzyl hydroperoxide would be complicated by the hydroperoxide

- (1) W. F. Brill, *Ind. Eng. Chem.*, **52**, 837 (1960).
- (2) A. E. Woodward and R. B. Mesrobian, *J. Amer. Chem. Soc.*, **75**, 6189 (1953).
- (3) E. T. Denisov and N. M. Emanuel, *Russ. Chem. Rev. (English Trans.)*, **29**, 645 (1960).
- (4) Y. Kamiya, S. Beaton, A. Lafortune, and K. U. Ingold, *Can. J. Chem.*, **41**, 2020 (1963).
- (5) R. Hiatt, J. Clipsham, and T. Visser, *ibid.*, **42**, 2754 (1964).
- (6) R. Hiatt, K. C. Irwin, and C. W. Gould, *J. Org. Chem.*, **33**, 1430 (1968).
- (7) D. A. S. Ravens, *Trans. Faraday Soc.*, **55**, 1768 (1959).
- (8) A. S. Hay and H. S. Blanchard, *Can. J. Chem.*, **43**, 1306 (1965).
- (9) Y. Kamiya, T. Nakajima, and K. Sakoda, *Bull. Chem. Soc. Jap.*, **39**, 2211 (1966).
- (10) N. Suzuki and H. Hotta, *ibid.*, **40**, 1361 (1967).
- (11) T. Morimoto and Y. Ogata, *J. Chem. Soc., B*, **62**, 1353 (1967).
- (12) K. Sakoda, Y. Kamiya, and N. Ohta, *Bull. Chem. Soc. Jap.*, **41**, 641 (1968).
- (13) J. A. Sharp, *J. Chem. Soc.*, 2026 (1957).
- (14) M. H. Dean and G. Skirrow, *Trans. Faraday Soc.*, **54**, 849 (1958).
- (15) W. H. Richardson, *J. Amer. Chem. Soc.*, **87**, 1096 (1965).
- (16) M. K. Shchennikova and E. A. Kuzmina, *Tr. Khim. Khim. Tekhnol.*, **29** (1966).
- (17) C. Walling, "Free Radicals in Solution," John Wiley & Sons Inc., New York, N. Y., 1957, p 427.

reacting with the corresponding Co acetate species formed as a product. The extent of the interference had not previously been determined. For example, Takegami, *et al.*,¹⁸ studied the reaction of benzyl hydroperoxide with Co(II) acetate but not with Co(III) acetate. In the present work, reactions starting with both Co(II) and Co(III) acetates have been studied independently. Moreover, some emphasis has been placed on initial reaction rates which would be least affected by back reactions. Also, hydroperoxide has been used in relatively low concentrations and not in large excess over cobalt acetate to minimize radical-induced decomposition of hydroperoxide. Thus, under these conditions, radical-ion steps 3 and 4 might be expected to become more important



Step 4 is particularly relevant to the oxidation of Co(II) acetate to Co(III) acetate during autoxidation.⁷⁻¹²

Experimental Section

Reagents. Benzyl hydroperoxide was prepared by the method of Walling and Buckler.¹⁹ The purity was found to be 80% by iodometric titration. The nmr spectrum contained singlets at $\tau = 5.63$ and $\tau = 6.05$ ascribable to benzylic hydrogens in benzyl hydroperoxide and benzyl alcohol, respectively. Using calibrated samples the amount of benzyl alcohol present was found to be approximately 20%. Less than 1.5% benzaldehyde was detected by infrared analysis. No phenol was detected by analysis on a 10% Carbowax 1000 on Haloport-F column. Neither benzaldehyde nor benzyl alcohol at this concentration level was found to affect reaction rates of the cobalt acetate-hydroperoxide system.

Co(III) acetate was prepared by the peracetic acid method.²⁰ Co(III), determined iodometrically, ranged from 81 to 94% of the total cobalt. This percentage was checked prior to each series of runs. Co(II) acetate tetrahydrate, sodium acetate, and acetic acid were reagent grade and were used as received.

Procedure. Stock solutions of known strength of Co(II) or Co(III) acetate in acetic acid and of benzyl hydroperoxide in acetic acid were prepared prior to each series of runs. Spectroscopic measurements were made on a UNICAM SP800D spectrophotometer. Stock solutions and reactant mixtures were maintained at $25 \pm 0.1^\circ$, and the temperature was checked by an iron-constantan thermocouple. For reactions with Co(II) acetate differential absorption at $23,500 \text{ cm}^{-1}$ was determined with a Co(II) acetate-acetic acid solution as control. For reactions with Co(III) acetate, acetic acid was the control. Co(III) acetate concentrations were computed using a molar absorbance of 465

$M^{-1} \text{ cm}^{-1}$. Zero time was assumed to be the time when half of the benzyl hydroperoxide solution had been added to the cobalt acetate solution. Usually 15 sec elapsed before absorption measurements could be made. At the conclusion of an experiment, the spectrum from $12,500$ to $32,500 \text{ cm}^{-1}$ was recorded. In all instances, the spectrum was found to be a mixture of Co(II) and Co(III) acetates.

Iodometric titration experiments were done separately at 25° . Benzyl hydroperoxide was monitored by adding excess saturated aqueous potassium iodide solution to an aliquot under helium and titrating the iodine with 0.1 N sodium thiosulfate solution. Potassium iodide reacts with hydroperoxide and Co(III) almost instantaneously ($t_{1/2} \sim 10 \text{ sec}$). Appropriate blanks were run simultaneously, and a correction was made for Co(III) present.

Oxygen was measured by gas chromatographic analysis of a gas sample on a 13X molecular sieve column. A correction was made for oxygen dissolved in acetic acid. Prior to reaction, helium was passed through the acetic acid solution to eliminate most of the air from the system. A silica gel column was used to measure carbon monoxide, carbon dioxide, methane, and ethane. None was found.

Organic products were measured after total reaction had occurred (ten half-lives) by gas chromatographic analysis on a 30% silicone gum rubber SE30 60-80S 810 column. Measurement of organic products during a run was difficult because unreacted benzyl hydroperoxide decomposed on the column. Benzaldehyde and benzyl alcohol were isolated and identified by infrared spectroscopy. Benzyl acetate was identified by its retention time.

Electron paramagnetic resonance was measured by a conventional Varian X-band spectrometer operating at a field modulation frequency of 100 kc/sec . A Varian aqueous solution sample cell was used to minimize dielectric loss of acetic acid projecting into the electric field of the cavity. Measurements were made at 25° with reactant concentrations which produced a "peroxide" maximum in the iodometric titration curve.

Results

Reaction of Co(II) Acetate with Benzyl Hydroperoxide. When acetic acid solutions of Co(II) acetate tetrahydrate and benzyl hydroperoxide are mixed, Co(III) acetate concentration rises rapidly to a constant value.²¹ The steady-state value, $[\text{Co(III)}]_{ss}$, is a function of

(18) Y. Takegami, Y. Fujimura, H. Ishii, and T. Iwamoto, *Kogyo Kagaku Zasshi*, **68**, 196 (1965).

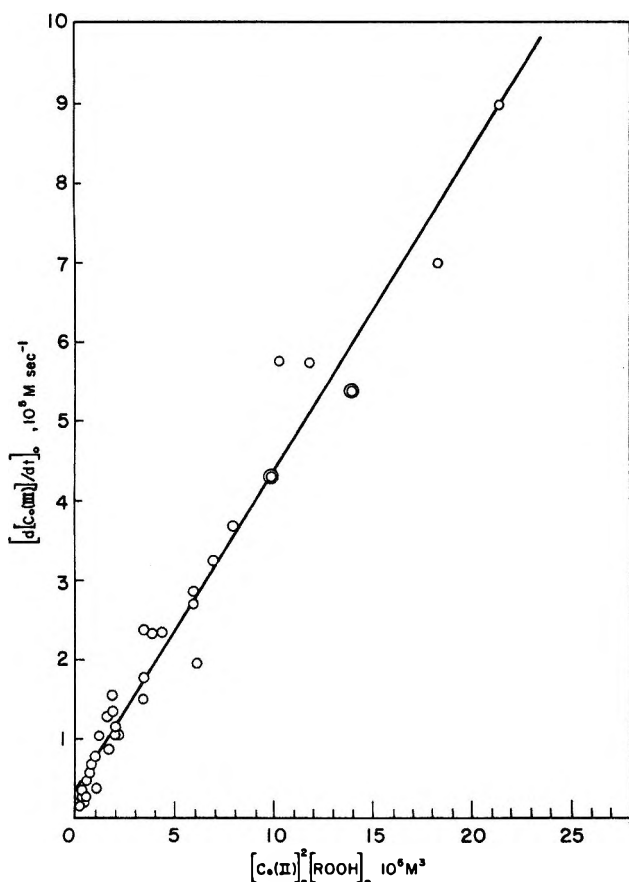
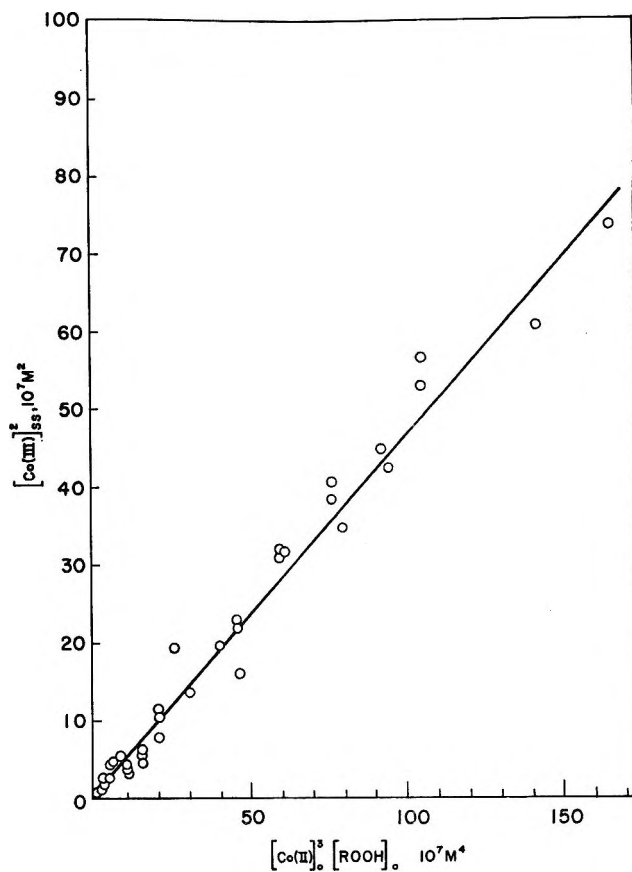
(19) C. Walling and S. A. Buckler, *J. Amer. Chem. Soc.*, **77**, 6032 (1955); U. S. Patent 2,810,766.

(20) E. Koubeck and J. O. Edwards, *J. Inorg. Nucl. Chem.*, **25**, 1401 (1963).

(21) Since Co(III) acetate is a reactant and the system is not in equilibrium, the term "steady-state" will be applied to this condition.

Table I: Kinetic Data for the Reaction of Co(II) Acetate with Benzyl Hydroperoxide in Acetic Acid at 25° at Steady-State Concentrations of Co(II) and Co(III)

[Co(II)] ₀ , 10 ² M	[RO ₂ H] ₀ , 10 ² M	[Co(III)] _{ss} , 10 ³ M	[Co(II)] _{ss} , 10 ² M	t _{1/2} , sec	k _{obsd} , 10 ³ sec ⁻¹	($\frac{10^3 k_{obsd}}{[Co(III)]_{ss}^{1/2}}$)
5	12.0	2.63	4.74	186	3.71	7.22
5	5.9	1.85	4.81	228	3.02	7.02
5	3.2	1.38	4.86	258	2.67	7.20
5	1.4	0.93	4.90	312	2.21	7.26
8	4.5	3.24	7.68	132	5.23	9.10
4	4.5	1.17	3.88	402	1.72	5.03
2	4.5	0.47	1.95	1242	0.56	2.59

**Figure 1.** Test of rate expression $[d[Co(III)]/dt]_0 = k[Co(II)]_0^2 [ROOH]_0$.**Figure 2.** Test of expression $[Co(III)]_{ss}^2 = A[Co(II)]_0^2 \times [ROOH]_0$ where A is constant. Data for 25°.

concentration of reactants. With high concentrations of benzyl hydroperoxide ($\sim 1 M$) the reaction is exothermic and occurs too rapidly for the increase to a steady-state value to be observed easily.

Initial rates and reaction rates under steady-state conditions were studied independently. To determine the initial rate, tangents were drawn to the absorbance curve. The logarithms of the tangential slopes were then plotted *vs.* time and the curve, which was close to linear, was extrapolated to zero time. From the extrapolated value, the value of initial rate, $[d[Co(III)]/dt]_0$, could be computed. Initial rates were determined

for a number of initial concentrations of Co(II) acetate and of benzyl hydroperoxide at 25°.

The orders of reaction with respect to each reactant were determined by plotting $\log [d[Co(III)]/dt]_0$ *vs.* \log initial reactant concentration) while the initial concentration of the other reactant was constant. The orders of reaction were computed to be 0.86 ± 0.06 in hydroperoxide and 2.10 ± 0.18 in Co(II). These values are sufficiently close to 1 and 2, respectively, to warrant comparing the data with a third-order rate expression (Figure 1). The best fit was given by rate eq 5

$$[d[\text{Co(III)}]/dt]_0 = (0.40 \pm 0.01) \times [\text{Co(II)}]_0^2 [\text{ROOH}]_0 + (3.7 \pm 0.9) \times 10^{-6} \quad (5)$$

In a similar way it may be seen from Figure 2 that the steady-state concentration, $[\text{Co(III)}]_{ss}$, is given by the relation

$$[\text{Co(III)}]_{ss}^2 = (0.46 \pm 0.01) [\text{Co(II)}]_0^3 [\text{ROOH}]_0 + (5.6 \pm 5.4) \times 10^{-8} \quad (6)$$

The reaction under steady-state conditions was monitored by measuring the disappearance of benzyl hydroperoxide. Half-lives ($t_{1/2}$) were determined from the approximately linear first-order plots (Figure 3). A plot of $\log t_{1/2}$ vs. \log [initial benzyl hydroperoxide] gave an apparent order of 1.24. Half-lives were then corrected for the steady-state concentration, $[\text{Co(III)}]_{ss}$ (eq 6, Table I). A plot of observed $\log k_{obsd}$ vs. $\log [\text{Co(III)}]_{ss}$ is linear with a slope of 0.49. From Table I it will be seen that for constant $[\text{Co(II)}]_0$, $k_{obsd}/[\text{Co(III)}]_{ss}^{1/2}$ is approximately constant.

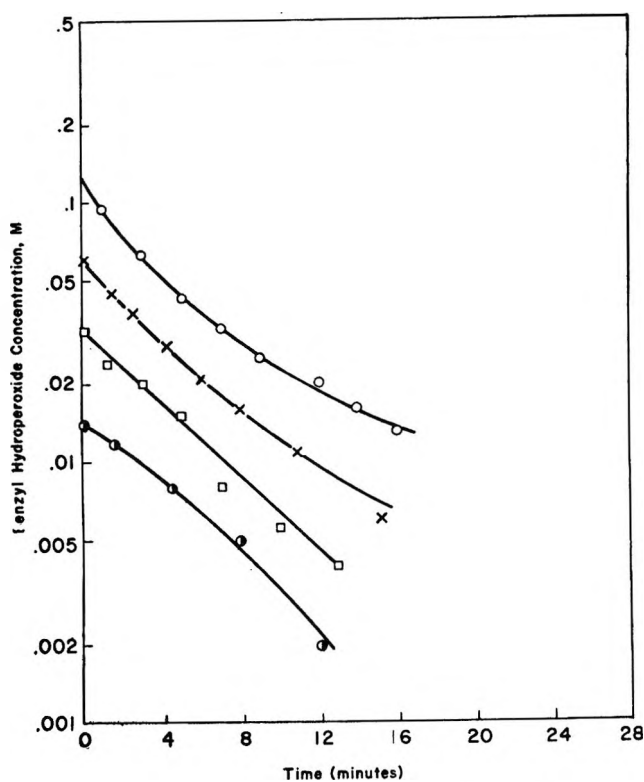
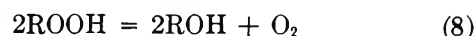


Figure 3. "First-order" plots for the decomposition of benzyl hydroperoxide at 25° in acetic acid (0.05 M Co(II) acetate).

The effect of varying Co(II) concentrations is shown in Table I and Figure 4. First-order k_{obsd} values were compiled and corrected for $[\text{Co(III)}]_{ss}$. A test was made to see whether a first-order reaction in Co(II) predominated. A plot of $k_{obsd}/[\text{Co(III)}]_{ss}^{1/2}$ vs. $[\text{Co(II)}]_{ss}$ is linear with a slope of 1.15 ± 0.19 and an intercept of $(6.9 \pm 9.3) \times 10^{-3}$ (Figure 5). The complete rate expression is therefore

$$-d[\text{ROOH}]/dt = 1.15 [\text{Co(II)}]_{ss} [\text{Co(III)}]_{ss}^{1/2} [\text{ROOH}] \quad (7)$$

The principal final products are benzaldehyde, benzyl alcohol, benzyl acetate, and oxygen. Benzyl acetate is mainly formed by slow reaction of benzyl alcohol with acetic acid and will be included with the benzyl alcohol yield. Allowance was also made for benzyl alcohol originally present as impurity in the benzyl hydroperoxide. For the reaction of 0.05 M Co(II) acetate with 0.06 M benzyl hydroperoxide at 25° in acetic acid, the mole per cent yields are benzaldehyde, 84%; benzyl alcohol, 16%; oxygen, about 10%. The liquid products are the same as those noted by Takegami, *et al.*¹⁸ The oxygen formed corresponds roughly to the stoichiometry



Oxygen was not reported by Takegami.

Reaction of Co(III) Acetate with Benzyl Hydroperoxide. Initial rates were determined for a number of different initial concentrations of Co(III) acetate and of benzyl hydroperoxide. The orders of reaction were found to be 1.92 ± 0.15 and 1.01 ± 0.14 , respectively. In Figure 6 the data are fitted to the third-order eq 9

$$-d[\text{Co(III)}]/dt]_0 = (3.33 \pm 0.1) \times 10^2 [\text{Co(III)}]_0^2 [\text{ROOH}]_0 + (3 \pm 3.4) \times 10^{-8} \quad (9)$$

The observed initial rate constant is therefore $333 \pm 10 \text{ M}^{-2} \text{ sec}^{-1}$. The reaction rate of Co(III) acetate

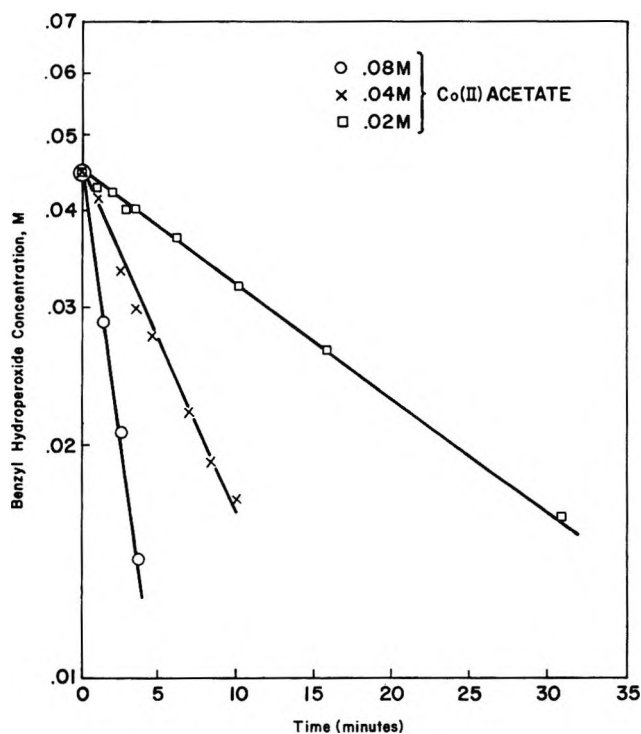


Figure 4. "First-order" plots for the decomposition of 0.045 M benzyl hydroperoxide in Co(II) acetate-acetic acid solutions at 25°.

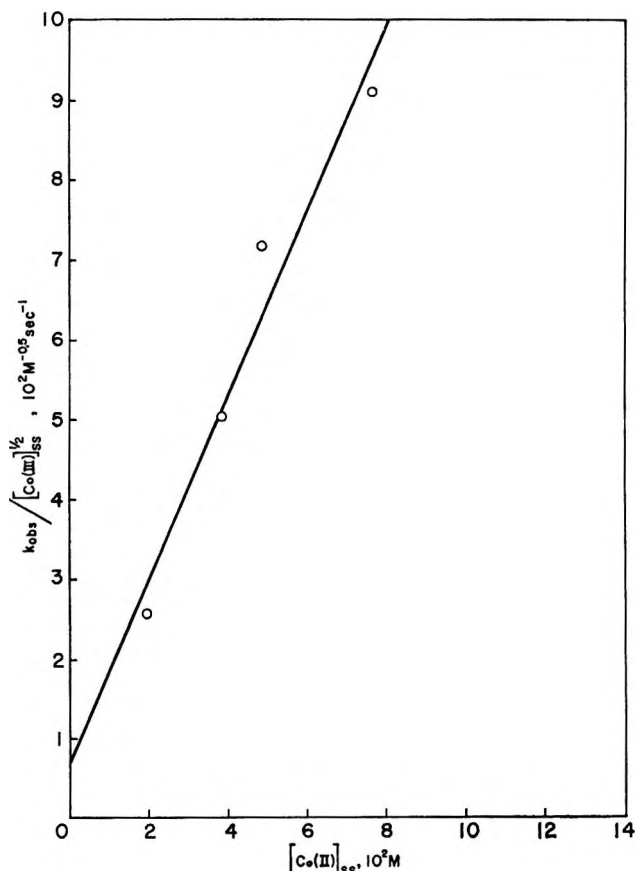


Figure 5. Dependence of $k_{\text{obs}}/[\text{Co(III)}]_{\text{ss}}^{1/2}$ on $[\text{Co(II)}]_{\text{ss}}$. Data for 25°.

with benzyl hydroperoxide was found to be about 300 times as fast as the rate of Co(III) acetate with benzyl alcohol. A correction for the 20% benzyl alcohol impurity is therefore unnecessary since it is within the experimental error.

A crude estimate of the overall expression was made using a differential method described by Benson.²² Benzyl hydroperoxide could not be monitored during the reaction inasmuch as another peroxide species was formed as an intermediate. The conversion of hydroperoxide was therefore estimated from the overall stoichiometry of the reaction and the conversion of Co(III) acetate into Co(II) acetate. Rates of reaction were slightly dependent on the particular sample of Co(III) acetate. This effect could be ascribed in part to the presence of Co(II) acetate. The results of a typical experiment at 35° involving three different initial benzyl hydroperoxide concentrations are shown in Table II. To a crude approximation, the rate expression is

$$-d[\text{Co(III)}]/dt = 2.35[\text{Co(III)}]^{1.71 \pm 0.44}[\text{ROOH}]^{1.17 \pm 0.08} \quad (10)$$

Equation 10 indicates that the order with respect to Co(III) is between 1 and 2, but it should be noted that

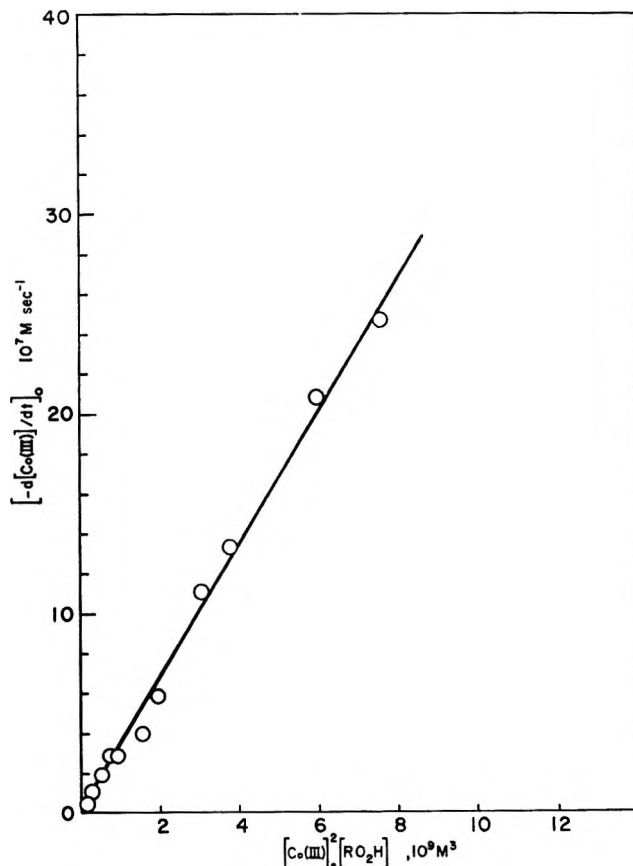


Figure 6. Test of rate expression $[-d[\text{Co(III)}]/dt]_0 = [\text{Co(III)}]_0^2 [\text{RO}_2\text{H}]_0$. Data for 25°.

Table II: Reaction of 0.0395 M Co(III) Acetate with Various Concentrations of Benzyl Hydroperoxide in Acetic Acid at 35.0°

Time, min	[Co(III)], 10 ² M	[RO ₂ H], 10 ³ M	(-d[Co(III)]/dt), 10 ⁶ M sec ⁻¹	
			Obsd	Predicted ^a
0	39.5	20.00		
5	29.8	5.80	11.47	14.05
10	27.2	3.30	6.33	6.18
15	25.7	2.15	3.73	3.41
20	24.9	1.50	1.87	2.12
0	39.5	10.00
5	31.8	3.40	7.85	8.39
10	30.0	1.95	4.67	3.97
15	28.9	1.35	2.72	2.42
20	28.3	1.05	1.59	1.74
0	39.5	5.00
5	33.8	2.25	6.40	5.74
10	32.6	1.60	3.60	3.63
15	31.8	1.22	2.27	2.52
20	31.2	1.00	1.60	1.94

^a Predicted using rate expression

$$-d[\text{Co(III)}]/dt = 2.35[\text{Co(III)}]^{1.71}[\text{RO}_2\text{H}]^{1.17}$$

(22) S. W. Benson, "Foundations of Chemical Kinetics," McGraw-Hill, New York, N. Y., 1960, p 82.

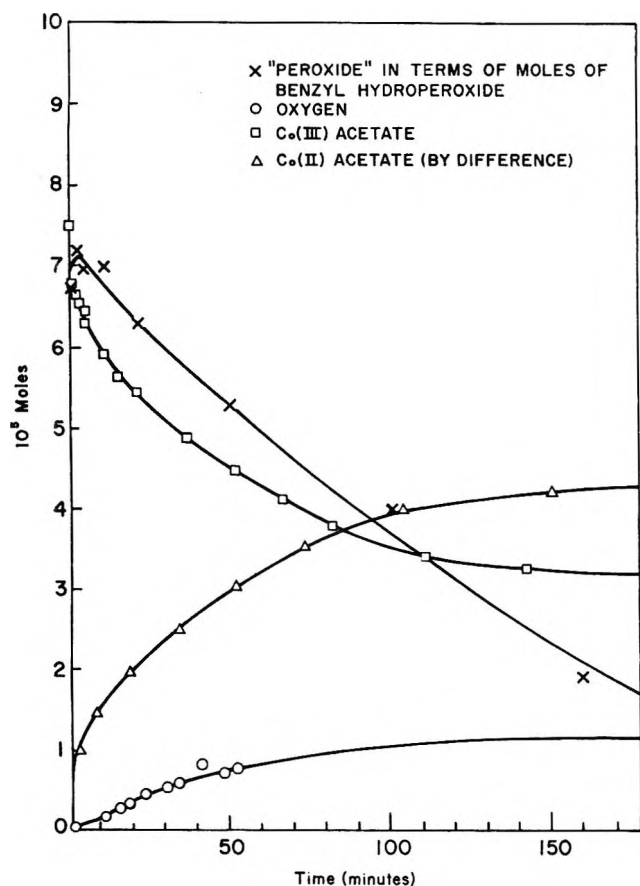


Figure 7. Reaction of 0.0097 *M* benzyl hydroperoxide with 0.0107 *M* Co(III) acetate at 25° (volume of solution, 7 ml).

the dependence of rate on Co(II) acetate concentration has not been included.

Product yields for a typical experiment are shown in Figure 7. The "peroxide" concentration increases initially, reaches a maximum, and then decreases. This fact was confirmed for other reactant concentrations. The Co(II)/O₂ ratio, initially greater than 10, decreases to a final value of approximately 3. The final mole per cent yields are oxygen, 24%; Co(II) acetate, 71%; and benzaldehyde, >90%; based on benzyl hydroperoxide decomposed. A control experiment indicated no benzaldehyde was formed by reacting benzyl alcohol or benzyl acetate with Co(III) acetate in acetic acid for 15 hr at 25°. Oxygen appears to be a secondary product formed from the peroxidic intermediate. No esr signal was observed.

A study of the stoichiometry for 0.04 *M* Co(III) acetate revealed that at 10⁻³ *M* benzyl hydroperoxide concentration at least two and probably three Co(III) atoms are reduced per molecule of hydroperoxide reacted. As benzyl hydroperoxide concentration increases, more benzyl hydroperoxide reacts per unit change in Co(III) acetate. At 0.02 *M* benzyl hydroperoxide, 1.5 molecules react per atom of Co(III) reduced.

The effect of Co(II) acetate concentration was studied for the reaction of 0.041 *M* Co(III) acetate

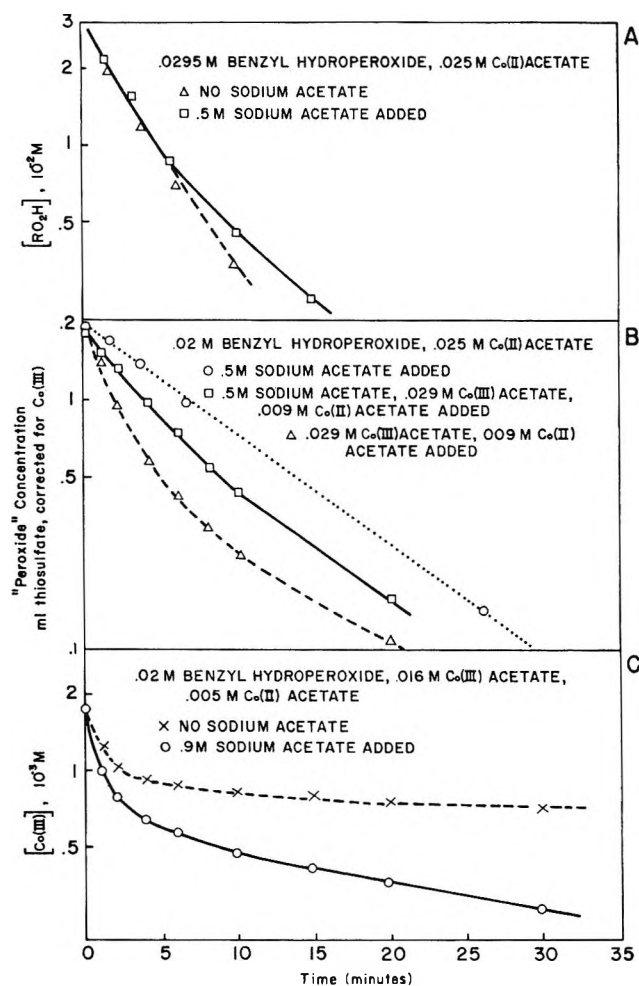


Figure 8. Effect of sodium acetate in acetic acid at 25°.

with 0.02 *M* benzyl hydroperoxide in acetic acid at 35°. The reaction half-life decreases from 36 to 21 sec over a Co(II) acetate concentration range 0.014 to 0.065 *M*. Moreover, the conversion of Co(III) acetate into Co(II) acetate decreased from 56 to 28%. Co(II) acetate also eliminates the maximum in the "peroxide" concentration curve.

The effect of acetate ion concentration was studied by adding sodium acetate. For the reaction of 0.0295 *M* benzyl hydroperoxide with 0.25 *M* Co(II) acetate no effect of 0.5 *M* sodium acetate was noted on the rate of reduction of benzyl hydroperoxide up to at least two half-lives (Figure 8A). Subsequently, there was some inhibition of the reaction. However, when Co(III) acetate was added to the system, sodium acetate inhibits the decomposition of benzyl hydroperoxide (Figure 8B). Figure 8C shows that addition of sodium acetate increases the conversion of Co(III) acetate into Co(II) acetate.

Discussion

Both Co(II) acetate and Co(III) acetate react with benzyl hydroperoxide in acetic acid. In the latter instance, Co(III) acetate concentration gradually de-

creases until all benzyl hydroperoxide is reacted. However, when Co(II) acetate reacts, Co(III) acetate concentration increases to a constant value before appreciable amounts of hydroperoxide have reacted. Is the value of the steady-state concentration determined by competition between simultaneously occurring reactions of hydroperoxide with Co(II) and Co(III) acetates? In Table III the rates of formation of Co-

Table III: Rates of Formation of Co(III) and Co(III) Concentrations at Various Times for 0.0584 M Co(II) Acetate and 0.0608 M Benzyl Hydroperoxide in Acetic Acid at 25°

Time, sec	[Co(III)], 10 ³ M	d[Co(III)]/dt, 10 ⁵ M sec ⁻¹	—Minimum Predicted— d[Co(III)]/dt, based on [Co(III)] formed, 10 ⁵ M sec ⁻¹	
			No back reaction ^a	With back reaction ^b
0	0	8.40	8.66	8.66
30	1.18	2.34	8.44	5.65
45	1.45	1.27	8.25	4.00
60	1.59	0.74	8.12	3.06
75	1.67	0.53	8.09	2.52
90	1.73	0.32	8.07	2.09
120	1.79	0.14	8.05	1.66
480	1.85	0.0	8.03	1.20

^a $d[\text{Co(III)}]/dt = 0.4[\text{Co(II)}]^2[\text{RO}_2\text{H}] + 3.7 \times 10^{-6}$; $\Delta[\text{RO}_2\text{H}]$ assumed = $0.5\Delta[\text{Co(II)}]$. ^b $d[\text{Co(III)}]/dt = 0.4 \times [\text{Co(II)}]^2[\text{RO}_2\text{H}] - 333[\text{Co(III)}]^2[\text{RO}_2\text{H}] + 3.67 \times 10^{-6}$.

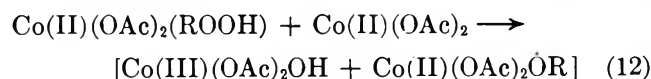
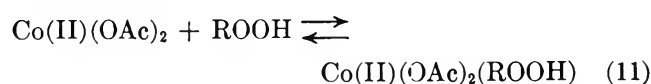
(III) acetate and Co(III) acetate concentrations are shown at various times for the reaction of 0.0584 M Co(II) acetate with 0.0608 M benzyl hydroperoxide in acetic acid at 25°. In the fourth column are shown the rates of formation if no reaction of Co(III) acetate with hydroperoxide occurred, *i.e.*, as predicted by eq 5. Rates of Co(III) acetate formation including the maximum rate of back reaction (eq 9) are shown in column 5. Comparison with the values in column 3 indicates that the rate of Co(III) acetate formation initially decreases much more rapidly than would be predicted by merely adding forward and backward reaction rates. Co(III) acetate appears to promote the reaction of Co(II) acetate with benzyl hydroperoxide but without increasing Co(III) concentration. This is confirmed by rate expression 7 which holds for steady-state conditions.

Also, in view of the maximum in the "peroxide" concentration curve when Co(III) acetate is the reactant, it appears that another peroxidic species is formed in this instance which does not necessarily play a major role when Co(II) acetate is the reactant. The reactions of Co(II) acetate and Co(III) acetate with benzyl hydroperoxide will, therefore, be discussed separately.

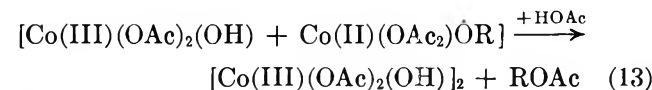
There is some uncertainty about the structures of Co(II) and Co(III) acetates in acetic acid. Richard-

son¹⁵ assumed that Co(II) acetate exists as dimer. This assumption was based on a questionable analogy with cupric acetate. However, there is no evidence that cobaltous ion, unlike the cobaltic ion, has any tendency to form polymeric species. The main species is, therefore, probably octahedral $\text{Co}(\text{OAc})_2(\text{HOAc})_4$. For simplicity, unoccupied sites will be assumed to be filled by acetic acid molecules. Based on spectroscopic evidence, the Co(III) product is Co(III) acetate. Koubeck and Edwards²⁰ and Lande and Kochi²³ have argued that in acetic acid the structure is dimeric, $(\text{AcO})_2\text{Co}(\text{OH})_2\text{Co}(\text{AcO})_2$. The acetate ligands are probably chelated. Benzyl hydroperoxide may be loosely associated with acetic acid; however, perester formation is believed to be small.¹⁶

Reaction of Co(II) Acetate with Benzyl Hydroperoxide. To explain the orders of the initial reaction with respect to Co(II) acetate and benzyl hydroperoxide, it is reasonable to speculate that the two reactants first form a complex, which subsequently reacts with more Co(II) acetate (steps 11 and 12).



There is evidence that *t*-butyl hydroperoxide can readily replace strongly bound chelating ligands like EDTA.^{24,25} Benzyl hydroperoxide should, therefore, readily replace an acetic acid ligand to form the species $\text{Co(II)(OAc)}_2(\text{ROOH})$. Further reaction with Co(II) acetate could produce an unstable complex containing at least one Co(III) ion. It is not necessary to postulate a separate dimer but the separate moieties should be visualized at least as existing within a solvent cage. Subsequently the benzyloxy radical could form a hydroxyl ion by reaction with acetic acid and reduction by Co(II) to yield cobaltic acetate and benzyl acetate (step 13)



The overall mechanism involves a two-electron change and no free-radical formation. This differs from the conventional mechanism which involves the formation of a free aryloxy radical which subsequently participates in a radical chain propagation reaction (step 1). The expression for the initial rate may be simply shown to be

(23) S. S. Lande and J. K. Kochi, *J. Amer. Chem. Soc.*, **90**, 5196 (1968).

(24) W. H. Richardson, *ibid.*, **87**, 247 (1965).

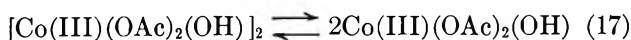
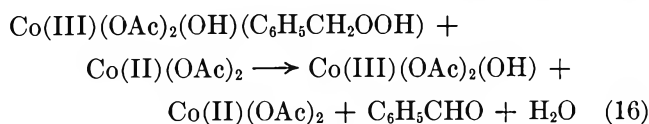
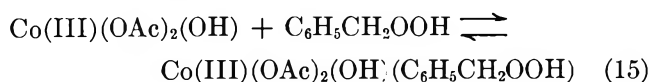
(25) F. A. Long, S. S. Jones, and M. Burke, Brookhaven Conference Report BNL-C-8, Chemical Conference No. 2, 1948, p 106; *Chem. Abstr.*, **45**, 4166h (1951).

$$\left[\frac{d[\text{Co(III)}]}{dt} \right]_0 = 2K_{11}k_{12}[\text{Co(II)(OAc)}_2][\text{ROOH}],$$

if $k_{13} \gg k_{12}$ (14)

Takegami,¹⁸ working at considerably higher hydroperoxide/Co(II) ratios, noticed a similar dependence of reaction rate on Co(II) acetate and benzyl hydroperoxide concentrations. In the present work, this simple rate expression was only found to hold for the initial reaction.

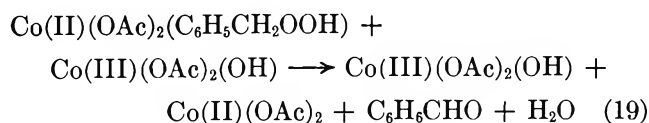
The rate eq 7 is consistent with the following mechanism for the steady-state condition. The mechanism, although speculative, will serve as a starting point for further work



The rate expression predicted by the mechanism is

$$\frac{-d[\text{C}_6\text{H}_5\text{CH}_2\text{OOH}]}{dt} = \frac{1}{\sqrt{2}} k_{16}K_{15}K_{17}^{1/2}[\text{Co(II)}][\text{Co(III)}]^{1/2}[\text{C}_6\text{H}_5\text{CH}_2\text{OOH}] \quad (18)$$

Equilibrium 17 is assumed to be predominantly to the left. An alternative mechanism is possible in which benzaldehyde is formed by the sequence of steps 11 and 19. There is no way to distinguish between alternatives at this juncture.

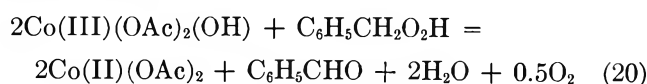


Benzyl alcohol and oxygen may be simultaneously formed by a nonrate-determining step analogous to (16).²⁶⁻²⁸

The reaction of Co(II) acetate with a primary hydroperoxide such as benzyl hydroperoxide is, therefore, mainly a dehydration reaction to form the corresponding aldehyde. It has been proposed in the past that in the catalytic autoxidation of hydrocarbons that Co(III) is regenerated by step 1. This mechanism applies when the hydroperoxide formed from the hydrocarbon contains a tertiary carbon atom, *e.g.*, in the autoxidation of cumene. The present work suggests that in the autoxidation of aromatic hydrocarbons which oxidize to primary hydroperoxides, step 1 is relatively unimportant. In this instance,

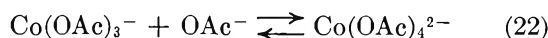
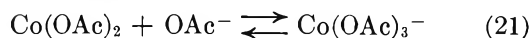
the higher oxidized state of the catalyst is probably regenerated from the lower state by reaction with peroxy radicals derived from the reactant hydrocarbon or from the aldehyde formed by decomposition of hydroperoxide.

Reaction of Co(III) Acetate with Benzyl Hydroperoxide. When benzyl hydroperoxide reacts with Co(II) acetate, the major part of the reaction is dehydration and little oxidation of Co(II) occurs. The reaction with Co(III) acetate differs in that there is considerable reduction of Co(III) to Co(II) and the oxygen yield is higher. At high Co(III) acetate/hydroperoxide ratios, the overall reaction approximates the stoichiometry



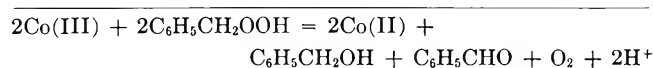
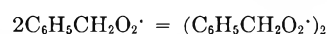
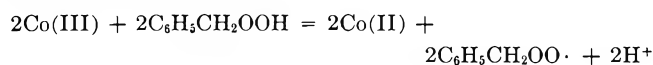
The predicted ratio Co(II)/O₂ = 4 is the value found experimentally when Co(III) acetate reaches a constant concentration (Figure 7). The ratio C₆H₅CHO/Co(II) is dependent on the ratio of initial reactant concentrations and increases as the Co(III) acetate/hydroperoxide ratio decreases. This indicates that the dehydration reaction (steps 15-17) is becoming more important relative to redox reaction 20.

The effects of acetate ion and Co(II) may be rationalized in terms of the competition between redox and dehydration reactions. Based on the results shown in Figure 8, the effect of acetate ion is in the opposite direction to that of Co(II) acetate, that is, the reaction rate is decreased and the conversion of Co(III) acetate into Co(II) acetate is increased. The reactivity of Co(II) acetate in the presence of acetate ion may, therefore, be the critical factor. In the presence of acetate ion, Co(II) acetate forms at least one tetrahedral complex (steps 21 and 22).



The equilibrium constant at 25° for the change from the octahedral to the tetrahedral form is 1.9×10^5 .²⁹ Also, the dissociation constant of sodium acetate in acetic acid at 25°³⁰ is 2.63×10^{-7} . Thus, at 25°

(26) Benzyl alcohol and oxygen cannot be formed *via* dibenzyl tetroxide. Such a mechanism (27, 28) predicts Co(II)/C₆H₅CH₂OH/O₂ = 2:1:1. The ratio found is 0:2:1.

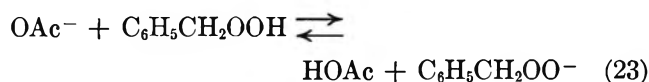


(27) G. A. Russell, *J. Amer. Chem. Soc.*, **79**, 3871 (1957).

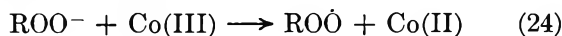
(28) J. A. Howard and K. U. Ingold, *ibid.*, **90**, 1056 (1968).

for 0.5 *M* acetate about 2% of Co(II) acetate should be in the tetrahedral form. Consideration of the electronic configurations of octahedral and tetrahedral forms of Co(II) and Co(III) indicates that tetrahedral Co(II) should be much less readily oxidized than the octahedral form. However, it is unlikely that the relative rates of oxidation of the two forms is a factor since at 25° for 0.5 *M* acetate concentration, the octahedral form still constitutes 98% of the Co(II) acetate. This is supported by the lack of effect of acetate on the reaction of Co(II) acetate with benzyl hydroperoxide (Figure 8A).

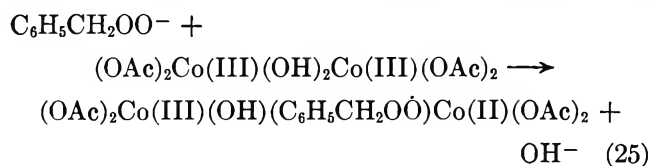
It is reasonable to assume that the effect of acetate ion is on the equilibrium 23



Sharp¹³ has noted that the rate-controlling step in the reaction of *t*-butyl hydroperoxide with Co(III) acetate in acetic acid is



By analogy, the peroxy anion formed in step 23 probably reacts with Co(III) acetate dimer by step 25



The dimer is favored inasmuch as the initial rate is second-order with respect to Co(III) concentration. If we assume that the predominant species in acetic acid is the dimer and that the reaction occurs with the monomer, a first-order dependence would be predicted.

If steps 23 and 25 are the initial steps in the overall reaction represented by the stoichiometric equation 20, then the addition of sodium acetate should increase the peroxy anion concentration and increase the redox reaction rate relative to that of the dehydration re-

action. Consequently, the conversion of Co(III) acetate into Co(II) acetate will be increased. Also, if dehydration is assumed to be faster than the redox reaction, the overall rate will be decreased. On the other hand, addition of Co(II) acetate will promote the dehydration (steps 15 to 17) but not the redox reaction. Thus the overall reaction rate will be increased and the conversion of Co(III) acetate into Co(II) acetate will be decreased.

From a product standpoint the reaction with Co(III) acetate differs from that with Co(II) acetate in that a peroxidic intermediate is formed early in the reaction, which will oxidize 3 equiv of potassium iodide. One possible species is a benzylperoxy radical stabilized by a Co(II) ion (step 25). A *t*-butylperoxy-cobalt species has already been proposed and detected by esr.³¹ In the present work, no esr signal was observed at 25° in acetic acid, but this does not preclude the existence of a stabilized radical since paramagnetic Co(II) could broaden the signals. The fate of the benzylperoxy radical is uncertain. In view of the low yields of benzyl alcohol it seems unlikely that a tetroxide mechanism pertains to this system.²⁶ Note that the low yields of benzyl alcohol cannot be attributed to oxidation by Co(III) acetate to benzaldehyde inasmuch as this reaction rate at 25° is only $1/300$ of the rate of reaction between Co(III) acetate and benzyl hydroperoxide.

Acknowledgments. The author is indebted to Dr. A. W. Chester, Dr. R. F. Bridger, and other colleagues for helpful discussions, to Mr. O. M. Epifanio for making the epr measurements, to Mr. A. T. Marsh for preparing the benzyl hydroperoxide, and to Dr. A. W. Chester for supplying samples of Co(III) acetate.

(29) P. J. Proll, L. H. Sutcliffe, and J. Walkely, *J. Phys. Chem.*, **65**, 455 (1961).

(30) S. Bruckenstein and I. M. Kolthoff, *J. Amer. Chem. Soc.*, **78**, 2974 (1956).

(31) R. W. Brandon and C. S. Elliott, *Tetrahedron Lett.*, **44**, 4375 (1967).

The Kinetics of Dissociation of Chlorine Pentafluoride

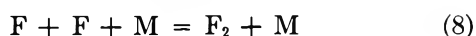
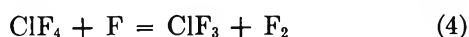
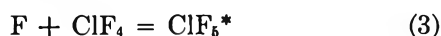
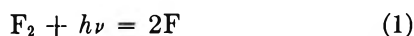
by J. A. Blauer, H. G. McMath, F. C. Jaye, and V. S. Engleman

Air Force Rocket Propulsion Laboratory, Air Force Systems Command, United States Air Force, Edwards, California 93523
(Received September 25, 1969)

The thermal dissociation of ClF_5 was investigated over the temperature range of 520–1120°K. At temperatures above 800°K the course of the reaction occurring behind incident shock waves was followed by monitoring the uv absorption of the reacting system at 2200 Å. At lower temperatures the study was conducted with static reactors which were coupled to a mass spectrometer. The unimolecular decomposition rate constants are compared to the current statistical theory. The theory is found to give a good description of the data taken at elevated temperatures; however, it is at large variance with data taken from the static reactor. The difference is attributed to the presence of the wall in the latter case.

Introduction

The photochemical reaction of ClF_3 with F_2 to form ClF_5 has been subjected to a thorough investigation by Schumacher, *et al.*,¹ who proposed the following mechanism



Here M' is a third body which does not include ClF_3 , and ClF_5^* is an activated form of the product molecule. The maximum temperature achieved in their study was 343°K. Under the conditions considered in the present study, step 1 will be replaced by the reverse of step 8. Similarly, due to the higher temperatures involved here, the reverse of steps 2 and 6 will have increased importance. A further complication arises in the shock tube study due to the thermal degradation of the product molecule, ClF_3 .²

Sullivan and Axworthy³ have made a study of the dissociation of ClF_5 in a flow reactor over the temperature range of 525–581°K. The course of the reaction was monitored by means of infrared spectroscopy. Empirically they found that the reaction is unimolecular, although they did not establish its pressure dependence. They reported the following expression for the rate constant

$$k_1 = 10^{13.0} \exp(-36,800/RT) \text{ sec}^{-1} \quad (9)$$

Our choice of an ultraviolet absorption technique for following the course of the reaction behind incident

shock waves was made possible by the very large extinction coefficient of ClF_5 relative to those for F_2 and ClF at 2200 Å. Although ClF_3 also has a large extinction coefficient at this wavelength, its presence can be accounted for by a consideration of the results of our previous paper.²

Experimental Section

Both experimental techniques and associated apparatus have been adequately described elsewhere.^{2,4,5} The experimental design used at high temperatures was identical in every detail with that used to study the thermal dissociation of ClF_3 . The experimental design used at low temperatures was identical with that used to study the thermal dissociation of OF_2 .⁵ In the present instance the course of the dissociation at low temperatures was followed by monitoring evolved F_2 at m/e 38 and ClF_4^+ at m/e 111.

The chlorine pentafluoride used in this study was provided by the Rocketdyne Division of North American-Rockwell Corporation.⁶ Analyses by gas chromatography and mass spectrometry indicated a minimum purity of 99.5%. The argon carrier gas was Matheson preparative grade; it was used without further purification. Gaseous fluorine having a purity of 98.2% was purchased from Allied Chemical Corporation. A mass analysis revealed the presence of 0.7% O_2 and 0.2% HF as the only significant impurities. After passage through a column of NaF pellets, the gas was used without further purification. Gaseous ClF having

(1) R. L. Krieger, R. Gatti, and H. J. Schumacher, *Z. Phys. Chem.*, **51**, 240 (1966).

(2) J. A. Blauer, H. G. McMath, and F. C. Jaye, *J. Phys. Chem.*, **73**, 2683 (1969).

(3) J. M. Sullivan and A. E. Axworthy, private communications, 1968.

(4) J. A. Blauer and W. C. Solomon, *J. Phys. Chem.*, **72**, 2307 (1968).

(5) W. C. Solomon, J. A. Blauer, and F. C. Jaye, *ibid.*, **72**, 2311 (1968).

(6) Rocketdyne Division of North American-Rockwell Corp., Canoga Park, Calif. Synthesized under Contract AF04(611)-10544.

Table I: Incident Shock Parameters and Initial Reaction Rate Constants

Test no.	ClF ₅ , %	10 ⁴ (ClF ₅), mol/cm ³	10 ⁴ (F ₂), mol/cm ³	P, atm	T, °K	εl × 10 ⁻⁶ , cm ² /mol	k _d × 10 ⁻⁴ , sec ⁻¹
05	0.5	0.673	0.000	10.0	904	0.60	0.09
07	0.5	0.664	0.000	10.0	915	0.67	0.12
01	0.5	0.598	0.000	9.1	924	0.71	0.23
18	2.0	1.004	0.000	3.9	940	0.55	0.22
08	0.2	0.287	0.000	10.2	962	0.75	0.38
10	0.9	0.208	0.000	1.8	991	0.75	0.18
06	0.5	0.683	0.000	11.1	994	0.71	0.75
14	1.8	0.891	0.000	4.1	1004	0.59	0.59
03	0.5	0.426	0.000	7.8	1116	0.71	8.2
17	4.5	1.060	0.000	2.2	1120	0.59	2.3
11	0.17	0.218	0.257	9.4	892	0.67	0.16
12	0.17	0.180	0.212	9.5	1093	0.66	13.3

a purity of 98% was purchased from Ozark-Mahoning Co. and was further purified by trap-to-trap distillation at -140°.

Gaseous mixtures were prepared and stored in stainless steel cylinders. All mixing operations were monitored with Wallace and Tiernan precision manometers or with Heise gauges for higher pressures. All components of the apparatus were initially passivated with F₂ and ClF₅.

Prior to each test conducted in the shock tube, the optical density of the static gas sample was measured at 220 mμ. The results were well described by Beer's law. No change in ClF₅ concentration was noted for gaseous samples which had been stored in the cylinders for as long as 1 week.

Data Analysis

A. Shock Tube. A typical absorption trace is shown in Figure 1. The trace was linearly extrapolated to the shock front to obtain the optical density of the mix under conditions of negligible dissociation. The incident shock parameters were furnished by a solution of the Rankine-Hugoniot equations. The resulting absorption coefficients are tabulated in Table I along with other pertinent information. These coefficients were found to be statistically independent of the temperature in contrast to the results obtained for ClF₃.

Since the absorption coefficients for ClF₃ were found to be of the same magnitude as those for ClF₅, its presence had to be accounted for in the data analysis. Furthermore, the simultaneous degradation of these two species was an additional complicating factor which had to be taken into consideration.

The absorption coefficients for ClF and F₂ were obtained in the manner described in the previous paper.² The dissociation of ClF₅ probably proceeds initially by means of steps -6 and 7 of the mechanism given by Schumacher,¹ *i.e.*

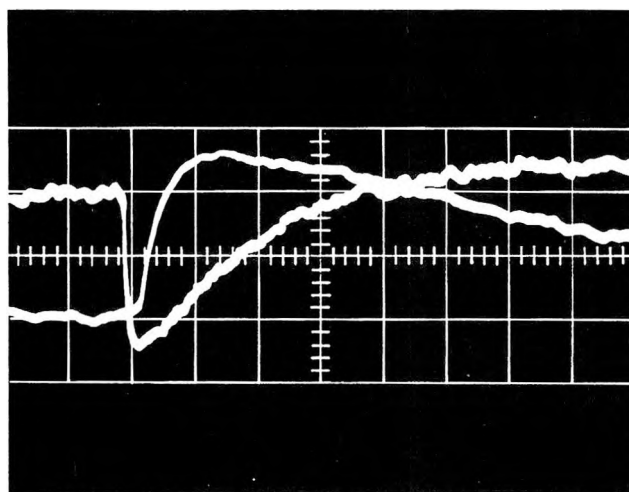
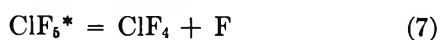
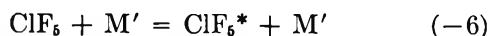
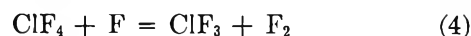
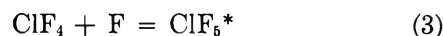


Figure 1. Absorption trace for test no. 6; 0.5% ClF₅ in argon, 994°K, 11.1 atm; 0.1 V/cm, ordinate; 10 and 50 μsec/cm, abscissa.

The ClF₄ will then be further degraded by the other postulated reactions, *i.e.*



The further degradation of the product species, ClF₃, was assumed to follow the mechanism described in the previous paper.²

The rate equations were numerically integrated by means of a computer program⁷ which uses assumed kinetic parameters in conjunction with the computed shock performance parameters to simulate conditions in the chemically reacting, isentropic system.

The optical density, *A*, of the reacting mix was computed according to the form

$$A = P(\text{ClF}_5) + K(\text{ClF}_3) + N(\text{ClF}) + L(\text{F}_2)$$

(7) Furnished by Dr. T. A. Jacobs of Aerospace Corporation, El Segundo, Calif.

The absorption coefficients K , L , and N were taken from the previous study.² Accordingly, the time histories of the various molecular species as given by the computer calculation allowed a calculation of the time dependence of the measured quantity A .

The data analysis proceeded by matching the computed and observed absorption traces. During this process, the rate constants pertinent to the ClF_3 decomposition reactions were not altered and the rate constant for the assumed initial step of the reaction



was altered until the computed profile matched the initial portion of the observed profile. During the course of these calculations, it was found necessary to assign a large value to either k_{-2} or k_4 (ca. k_{-2} greater than 10^8 sec^{-1}) in order to obtain an analytical description of the data. This is tantamount to assuming that ClF_4 is highly unstable or reactive under the conditions encountered in the shock tube. The rate constants obtained by this process for reaction 10 are tabulated in Table I.

B. Static Reactor. The time history of ClF_5 determined directly by monitoring m/e 111 (ClF_4^+) and indirectly by monitoring m/e 38 (F_2^+) is illustrated in Figure 2 for a typical test. In the early tests where only the production of fluorine was followed, it was found that the final fluorine concentration was less than the initial ClF_5 concentration. When mass peak m/e 111 was monitored it exhibited two regions of decay, a region of very rapid change (ca. 60 sec), followed by a region of much slower change which continued through the remainder of the reaction. The rate of fluorine production in the second region was found to correspond with the rate of disappearance of ClF_5 (Figure 2). These results were taken to indicate an absorption of ClF_5 on the walls of the reactor during the first region of the reaction, possibly with compound formation,⁸ which reduced the amount of ClF_5 available for gas phase decomposition. Absorption of chlorine trifluoride on nickel fluoride has been studied by Farrar and Smith.⁹

The rate constants reported here are based on observations made in the second region of the reaction. The resulting data are given in Table II.

Results

A. Shock Tube. The analytical description of the data which resulted from the computer analysis is illustrated in Figure 3 for three tests. It was found that, in most instances, once the value of k_{10} was adjusted to allow a good description of the initial portion of the reaction, a good analytical description of the entire reaction had been obtained. This result, coupled with the results of the previous paper,² lends credence to the overall mechanism assumed for the decomposition; i.e., the ClF_4 formed in step 10 is rapidly decom-

Table II: Rate Data Obtained from the Static Reactor

Test no.	P_{ClF_5} , mm	P_{total} , mm	T , °K	$k_d \times 10^4$, sec^{-1}	Diluent
12	2	2.5	543	3.1	Ar
13	8	10	543	3.3	Ar
14	80	100	543	3.1	Ar
15	240	300	543	2.5	Ar
16	80	800	543	2.4	ClF
17	130	960	543	2.7	NO
18	100	120	534	1.5	Ar
19	100	120	525	0.67	Ar
20	100	120	517	0.35	Ar

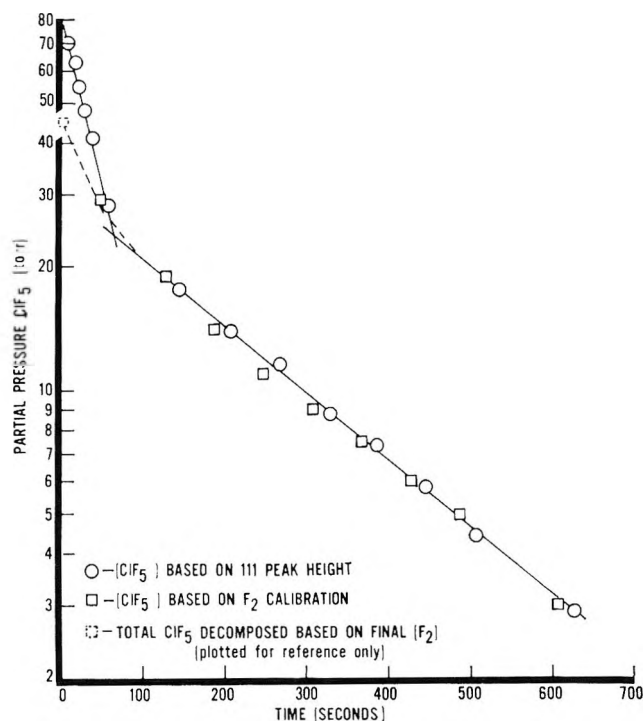


Figure 2. Pressure of ClF_5 vs. time for a typical test in the static reactor.

posed into ClF_3 which is itself further degraded in the manner described previously.

A close examination of the results given in Table I reveals that the rate of step 10 depends strongly upon the total pressure. An analysis of variance of these data which was based upon an assumed function of the form

$$k_{10}/(\text{Ar})^n = A e^{-E/RT} = k_{11} \quad (11)$$

gave the best analytical description of the data when the pressure exponent n had a value of 0.7 ± 0.2 . The resulting 1.7 order rate constant had the following form

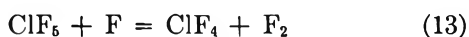
(8) The nature of the absorption was not determined, but possibly $\text{ClF}_5 + \text{W} + \text{WF}_2 \cdot \text{ClF}_3$.

(9) R. L. Farrar, Jr., and H. A. Smith, *J. Amer. Chem. Soc.*, **77**, 4502 (1955).

$$k_{11} = 10^{15.8 \pm 0.5} \exp(-41,500 \pm 2500/RT) \times \\ \text{cc}^{0.7}/\text{mol}^{0.7} \text{ sec} \quad (12)$$

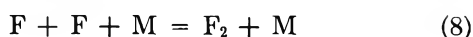
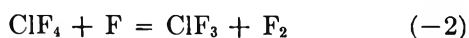
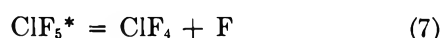
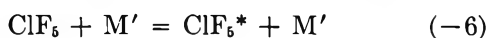
This expression applies only to binary mixes of Ar and ClF_5 . The exponent of (Ar) indicates that step 10 is a unimolecular reaction which is in its intermediate pressure region under the conditions cited. This result is illustrated in Figure 4. The relatively large scatter inherent in these data may be ascribed in part to the uncertainty in the absorption coefficient for ClF_3 coupled to the errors incurred in the evaluation of the rate constants pertinent to its dissociation.

An examination of the results of Figure 4 reveals that if the initial reaction mix contains 2% F_2 , there is a statistically discernible increase in the reaction rate. Since the presence of fluorine was found to inhibit the dissociation of ClF_3 , the effect may be due to an exchange reaction such as



A second possibility is that F_2 is an efficient collision partner in step -6. Since these data are relatively uncertain due to the various cumulative errors involved in their derivation, no attempt was made to establish the nature of this phenomenon. The resulting error in our derived results will be small since the effect is only apparent in mixes containing large excesses of molecular fluorine.

Accordingly, it appears that the initial phase of the dissociation of ClF_5 in the shock tube can be approximately described by the following reaction model



The effect of reaction 5 cannot be estimated from the present data. The further degradation of ClF_3 proceeds as previously discussed.²

B. Static Reactor. These data were collected over wide ranges of pressure (ca. 2.5 to 960 mm) and concentration of ClF_5 (ca. 0.7×10^{-7} to 1×10^{-6} mol/cc). An examination of the resulting rate data, shown in Table II, reveals that changing the total pressure by a factor of 400 does not significantly alter the magnitude of the assumed unimolecular rate constant. Accordingly, at pressures above 2 mm and temperatures below 550°K, the reaction has the characteristics of a unimolecular reaction which is above its high pressure limit.

The temperature dependence of the data is graphically illustrated in Figure 5. The results for binary mixes of argon and ClF_5 can be expressed in the following form

$$k_d = 10^{16 \pm 1} \exp(-46,300 \pm 2300/RT) \text{ sec}^{-1} \quad (14)$$

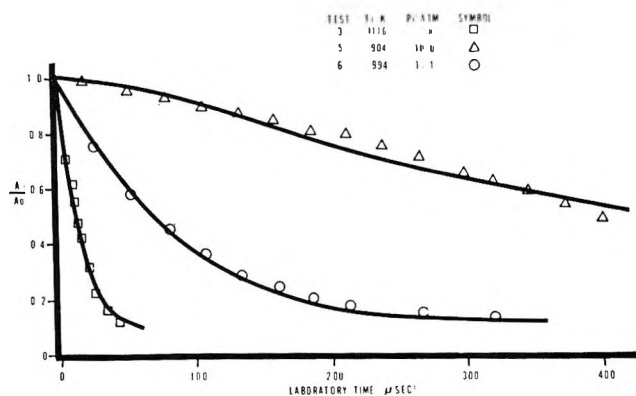


Figure 3. Observed vs. computed reaction profiles for data taken with the shock tube. The assumed rate constant is given by the expression $k_{10} = 0.16 \times 10^{14} \exp(-42,403/RT) \text{ sec}^{-1}$.

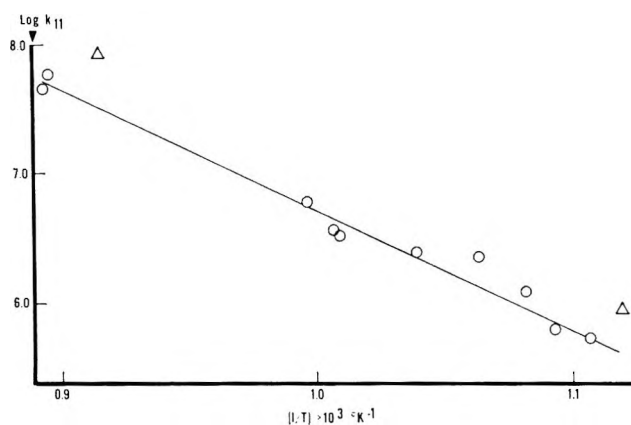


Figure 4. Temperature dependence of 1.7-order decomposition rate constants as measured with a shock tube: ○, binary mixtures of argon and ClF_5 ; Δ, mixes containing initial added fluorine.

The addition of large amounts of NO and ClF to the reacting mixture appeared to have no significant effect on the rate constant. Although these data are somewhat uncertain due to a probable wall effect, the gross kinetic behavior of the system is apparent.

Comparison with Statistical Theory

The statistical theory of unimolecular reactions as developed by Rice and Ramsperger,¹⁰ and Kassel¹¹ has recently been extended by Keck and Kalelkar¹² to the case of a large number of coupled equations which represent the kinetics of a molecule in all the possible vibrational and rotational modes of the ground electronic state. The spontaneous decay rates and vibrational transition probabilities required were derived from the statistical theory.¹³ If the dissociation energy is known, the model will provide an estimate of the dis-

(10) O. K. Rice and H. C. Ramsperger, *J. Amer. Chem. Soc.*, **49**, 1617 (1927).

(11) L. S. Kassel, *J. Phys. Chem.*, **32**, 225, 1065 (1928).

(12) J. C. Keck and A. J. Kalelkar, *J. Chem. Phys.*, **49**, 3211 (1968).

(13) J. C. Keck, *Advan. Chem. Phys.*, **13**, 85 (1966).

Table III: Comparison of Results Obtained at Low Temperatures with Statistical Theory

$T, ^\circ\text{K}$	P_T, mm	$D, \text{kcal/mol}$	m_{obsd}	m_{theo}^a	$k_d, \text{sec}^{-1} \times 10^3$		Method
					Calcd	Obsd	
517	120	47	0	0.2	0.005	0.35	Static reactor
525	120	47	0	0.2	0.010	0.67	Static reactor
543	2.5	49	0	0.5	0.001	3.1	Static reactor
525	760	37	...	0	14	4.8	Flow reactor ^b
580	760	37	...	0	352	135	Flow reactor

^a $m = (\partial \ln k_d / \partial \ln [M])_T$. ^b Sullivan and Axworthy, ref 3.

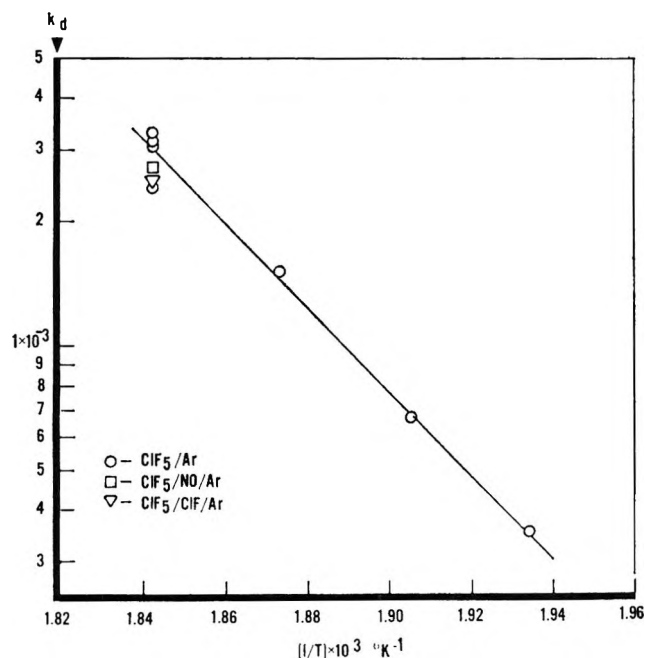


Figure 5. Temperature dependence of decomposition rate constants for static reactor.

sociation rate constant as well as its pressure dependence. If, as in the present instance, the dissociation energy is unknown, the model employs the observed activation energy to compute a dissociation energy which it then uses to estimate the desired quantities. Although the model neglects the conservation of total angular momentum, thus likely leading to an overestimate of the reaction rate, nevertheless, the theory was used with considerable success to correlate experiment with theory for 21 molecules having from 3 to 6 atoms.

Chlorine pentafluoride has been shown to have a square-pyramidal structure in its ground electronic state.¹⁴ All required molecular parameters for this molecule were taken from the "JANAF Thermochemical Tables."¹⁵

In the absence of any data concerning the postulated product, ClF_4 , it was assumed to have a square-planar configuration with a Cl-F bond distance of 1.7 Å. The required vibrational frequencies for this molecule were assumed to be identical in magnitude with those of the corresponding vibrational modes of ClF_5 . Although

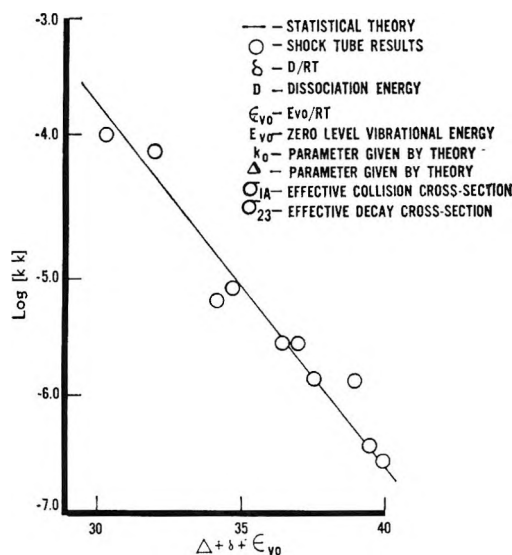


Figure 6. Correlation of experimentally observed first-order dissociation rate constants with statistical theory. (See ref 12.) $D = 47 \pm 2 \text{ kcal/mol}$, $\sigma_{1A} = \sigma_{23} = 1 \times 10^{-16} \text{ cm}^2$.

these assumptions lend uncertainty to the resulting calculation, the errors introduced are probably less than the errors introduced by the assumptions made in the derivation of the mathematical model itself.

The model was first applied to the results obtained from the shock tube. The required activation energy was calculated from eq 12. The model estimated the dissociation energy at $47 \pm 3 \text{ kcal/mol}$ for an average temperature of 1000°K . The pressure dependence of the reaction was estimated to have an exponent of 0.5 ± 0.2 as compared to the observed value of 0.7 ± 0.2 . The analytical description of the data is illustrated in Figure 6. Overall the model gives a good description of all aspects of these experimental results.

The model was also applied to the results obtained from the static reactor. Here again the dissociation energy was estimated by the theory at $47 \pm 3 \text{ kcal/mol}$; however, neither the absolute magnitude of the rate

(14) F. P. Gortsens and R. H. Toeniskoetter, *Inorg. Chem.*, 5, 1925 (1966).

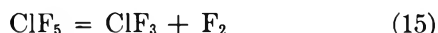
(15) "JANAF Thermochemical Tables," Dow Chemical Co., Midland, Mich., 1968.

constant nor its pressure dependence was reproduced satisfactorily. Typical results are shown in Table III. In every instance, the observed rate constant was at least a factor of 50 larger than the calculated rate. It would appear that this difference is due to the influence of the reactor walls although the actual mechanism is not immediately apparent.

Finally, the results of Sullivan and Axworthy,³ obtained in a flow reactor, were compared with the theory. Although the theory does reproduce the magnitude of their rate constants very well, it gives a dissociation energy of 37 kcal/mol which is at considerable variance with the results obtained from the shock tube.

Although the disagreement between the static reactor data and the shock tube data is probably due to the influence of the wall in the former case, the source of the disagreement between the flow reactor data and the shock tube data is not clear. In the absence of independent thermal data for the ClF_4 molecule, the statistical theory offers no clear choice between these latter two sets of experimental results.

Although the above treatment assumes that ClF_4 and F are initial decomposition products (*ca.* eq 10), it must be admitted that we cannot rule out the following process



Indeed, a statistical treatment based upon this reaction path is in equally good agreement with the data.

Conclusions

In conclusion, the thermal dissociation of ClF_5 at elevated temperatures is well described by the statistical theory of unimolecular reaction rates. This theory points out a large disagreement between these data and the data taken at lower temperatures (*ca.* 550°K) by Sullivan and Axworthy from a flow reactor.³ In the absence of independent thermodynamic data for the ClF_4 molecule, we are unable to clearly define the nature of the decomposition of the ClF_5 molecule (*i.e.*, unimolecular or chain) although by analogy to ClF_3 ,² both mechanisms may be operative. The static reactor data appear to favor the unimolecular decomposition path, although this may be due to the influence of the reactor walls.

Acknowledgments. The authors wish to thank Dr. T. A. Jacobs of Aerospace Corporation and Drs. J. Sullivan and A. Axworthy, both of Rocketdyne Division of North American-Rockwell Corporation, for very useful discussions concerning this and related work. The authors also wish to acknowledge the assistance of Mr. M. A. Abrego in the experimental phases of the work.

A Mass Spectrometric Study of the Dimerization of Nitrosomethane¹

by F. A. Thomassy and F. W. Lampe

Whitmore Laboratory, Department of Chemistry, The Pennsylvania State University, University Park, Pennsylvania 16802
(Received August 25, 1969)

It is shown directly that the disappearance of monomeric nitrosomethane in a second-order reaction is accompanied by the simultaneous formation of dimeric nitrosomethane. The dimerization rate constant has been measured by following the monomer disappearance and has been found to be $0.36 \pm 0.08 \times 10^{-19} \text{ cm}^3 \text{ molecule}^{-1} \text{ sec}^{-1}$. Studies of the initial formation rate of CH_3NO^+ as a function of electron energy lead to an ionization potential of $10.8 \pm 0.3 \text{ eV}$ for monomeric nitrosomethane.

For some time it has been known that the monomeric form of nitrosomethane, CH_3NO , is the primary product of the reaction of methyl radicals with nitric oxide²⁻⁹ and also that this initial product reacts further in a variety of ways.¹⁰ Thus Christie¹⁰ and Johnston and Hecklen¹¹ have shown that monomeric nitrosomethane reacts with nitric oxide, in a reaction second order in nitric oxide, to form nitrogen and nitrate radicals, NO_3 , while simultaneously undergoing a reaction, first order

in nitric oxide, to produce methoxy radicals and nitrous oxide; such reactions are of importance only when the

(1) Based on a thesis submitted by F. A. Thomassy to The Pennsylvania State University in partial fulfillment of the requirements for the M.S. degree.

(2) L. A. K. Staveley and C. N. Hinshelwood, *Proc. Roy. Soc.*, **A159**, 192 (1937).

(3) J. Collin, *Bull. Soc. Roy. Sci. (Liege)*, **23**, 201 (1954).

(4) W. A. Bryce and K. U. Ingold, *J. Chem. Phys.*, **23**, 1968 (1955).

nitric oxide concentration in the system is relatively high. Under the usual radical-scavenging conditions (relatively low nitric oxide concentration) monomeric nitrosomethane reacts with methyl radicals to produce trimethylhydroxylamine;^{8,9,12,13} this reaction path of nitrosomethane is, of course, only of significance when the methyl radical concentration is maintained relatively high. When the concentrations of nitric oxide and methyl radicals are both low as compared with that of the monomeric nitrosomethane, the principal reaction is that of dimerization



a reaction that has been observed and studied by a number of workers.^{3,6b,7,11,14-16} Studies of the various reactions that comprise the fate of the unstable monomeric nitrosomethane were reviewed in a recent article by Heicklen and Cohen.¹⁷

The specific reaction rate for the dimerization (I) has been measured in a number of investigations^{6b,7,11,16} by following the disappearance of the monomer. Good agreement does not exist among the various studies for the value of the dimerization rate constant, the values reported at room temperature ranging from 0.1 to 1.2×10^{-19} cm³ molecule⁻¹ sec⁻¹. In addition, since the reactions were followed by a study of monomer disappearance, it is not known unambiguously that the sole reaction rate being measured was the dimerization. Our attempts to clarify these uncertainties concerning (I) and our results obtained form the subject matter of this paper.

Experimental Section

The nitrosomethane monomer was produced from the photolysis of mixtures of azomethane and nitric oxide at total pressures ranging from 5 to 25 Torr and with nitric oxide concentrations generally of 10 mol % but never higher than 20 mol %. The photolyses were carried out at room temperature (ca. 25°) in a cylindrical cell containing a pinhole leak leading directly into the ionization region of a Bendix Model 14-101 time-of-flight mass spectrometer.^{9,18} Two pinholes were used, the larger one having a first-order leak rate constant of 4.78×10^{-3} sec⁻¹ while the corresponding value for the smaller leak was 2.0×10^{-4} sec⁻¹. The photolysis cell was 8.35 cm in length with a diameter of 2.10 cm and was connected *via* 1/8-in. stainless steel and 6-mm Pyrex tubing to a large reservoir (5-10 l.) containing the reactants. The use of large reactant reservoirs resulted in a negligible decrease in azomethane concentration over the time of a run.

High-pressure mercury arcs were used as light sources in this work. In most of the experiments an Osram HBO-109 lamp was employed. The spectral emission of this lamp and the wavelength dependence of the azomethane absorption coefficient are such that the average effective photolytic wavelength was about

3660 Å. A few experiments were performed using an Illumination Industries Type 110 high-pressure mercury lamp with a similar spectral emission. Both lamps were operated at 5.2 A, but it was noted that the effective intensity from the Osram HBO-109 was 1.8 times greater than for the Illumination Industries lamp. The power supply for both lamps was obtained from George W. Gates Co. (Model P109); with this power supply, the lamp-operating current could be reproduced to $\pm 2\%$.

Azomethane and azomethane-*d*₆ were obtained from Merck Sharp and Dohme, Ltd. Both compounds were purified chemically to greater than 99% purity by repeated freeze-pump-thaw cycles in a cold finger immersed in methanol slush (-97.8°). The isotopic purity of azomethane-*d*₆ was stated by the supplier to be 99% and was verified mass spectrometrically. Technical grade nitric oxide, obtained from the Matheson Company, was treated according to a method described by Hughes¹⁹ until the liquid nitric oxide exhibited its characteristic pale-blue color. Subsequent mass spectrometric examination could detect no impurities.

It was found that *m/e* 30 from azomethane interfered seriously with attempts to measure the formation rate of ethane in photolyses carried out in the absence of nitric oxide. However, ethane-*d*₆ from the photolysis of azomethane-*d*₆ was not subject to such interference (suggesting *m/e* 30 from azomethane contains only a minor contribution from C₂H₆⁺) and the initial formation rate of ethane-*d*₆ was used to compute the effective photolysis rate. Calibration of the mass spectrometer for C₂D₆ was carried out as described previously.⁹

Results and Discussion

As observed previously,^{8,9} when pure azomethane-*d*₆ is photolyzed under our conditions, the only products

- (5) W. Lüttke, *Z. Elektrochem.*, **61**, 302 (1957).
- (6) (a) M. I. Christie, *Proc. Roy. Soc.*, **A249**, 248 (1958); (b) *ibid.*, **A249**, 258 (1958).
- (7) J. G. Calvert, S. S. Thomas, and P. W. Hanst, *J. Amer. Chem. Soc.*, **82**, 1 (1960).
- (8) A. Maschke, B. S. Shapiro, and F. W. Lampe, *ibid.*, **85**, 1876 (1963).
- (9) A. Maschke, B. S. Shapiro, and F. W. Lampe, *ibid.*, **86**, 1929 (1964).
- (10) M. I. Christie, C. Gilbert, and M. A. Voisey, *J. Chem. Soc.*, 3147 (1964).
- (11) T. Johnston and J. Heicklen, *J. Phys. Chem.*, **70**, 3088 (1966).
- (12) B. Bromberger and L. Phillips, *J. Chem. Soc.*, 5302 (1961).
- (13) D. E. Hoare, *Can. J. Chem.*, **40**, 2012 (1962).
- (14) H. W. Thompson and J. W. Linnett, *Trans. Faraday Soc.*, **33**, 874 (1937).
- (15) C. S. Coe and T. F. Doumani, *J. Amer. Chem. Soc.*, **70**, 1516 (1948).
- (16) M. I. Christie, J. S. Frost, and M. A. Voisey, *Trans. Faraday Soc.*, **61**, 674 (1965).
- (17) J. Heicklen and N. Cohen, *Advan. Photochem.*, **5**, 157 (1968).
- (18) F. C. Kohout and F. W. Lampe, *J. Chem. Phys.*, **46**, 4075 (1967).
- (19) E. E. Hughes, *ibid.*, **35**, 1531 (1961).

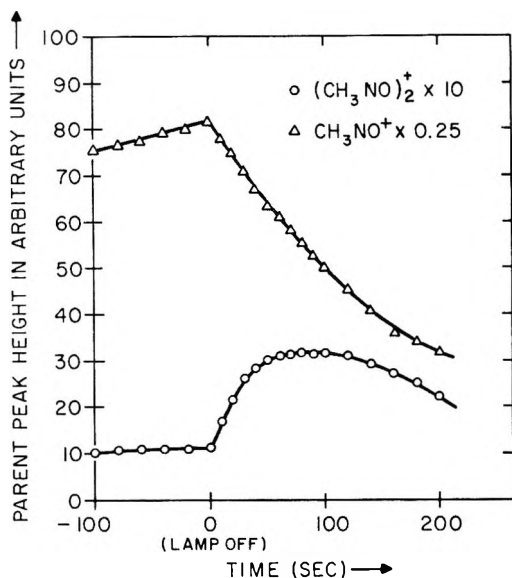
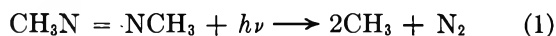


Figure 1. Decay of $[\text{CH}_3\text{NO}]$ and simultaneous formation of $[(\text{CH}_3\text{NO})_2]$.

observed are nitrogen and ethane- d_6 ; in addition, the time dependence of this product formation, as evidenced by the increase in intensity of m/e 36 (C_2D_6^+), is beautifully linear for photolysis times up to about 200 sec.⁹ We may write, therefore, for the photolysis of the pure azomethane (or azomethane- d_6)



Assuming a steady state for methyl radicals it is easily shown that, under conditions for which the rate of light absorption is proportional to $[\text{CH}_3\text{N} = \text{NCH}_3]$, the time dependence of the ethane concentration in the photolysis cell is as given by (3), *viz.*

$$[\text{C}_2\text{H}_6] = \frac{\phi I_0 \alpha [\text{CH}_3\text{N} = \text{NCH}_3]}{\lambda} (1 - e^{-\lambda t}) \quad (3)$$

where ϕ is the primary quantum yield, I_0 is the incident flux of effective radiation, α is the effective absorption coefficient, and λ is the first-order rate constant for leakage into the ion source. For $t < 200$, (3) yields linear plots having slopes identical with the quantity $\phi I_0 \alpha [\text{CH}_3\text{N} = \text{NCH}_3]$. Since the azomethane concentration is known and essentially fixed, studies of the formation rate of ethane- d_6 were used to determine $\phi I_0 \alpha$ for both lamps as $1.08 \pm 0.12 \times 10^{-4} \text{ sec}^{-1}$ and $5.84 \pm 0.35 \times 10^{-5} \text{ sec}^{-1}$, respectively.

When nitric oxide is added to the azomethane at concentration levels of about 10%, no product other than CH_3NO , as evidenced by the sole increase of m/e 45, is observed in the initial stages. This is in agreement with previous results at lower nitric oxide concentration levels.^{8,9} Somewhat later during the photolysis, small but measurable intensities of m/e 90 and

m/e 60 are observed which suggest the presence of nitrosomethane dimer,³ $(\text{CH}_3\text{NO})_2$. We did not observe the formation of trimethylhydroxylamine^{8,9} or ethane under our conditions, but this was expected because we used sufficiently high concentrations of nitric oxide and sufficiently short photolysis time to ensure that all methyl radicals reacted by (4), *viz.*



In addition, it is indicated by the appearance of m/e 60 and m/e 90 that the dimerization of nitrosomethane, (5), is also occurring and, since we observe mass spectro-



metrically both monomer and dimer, we also must have occurring the nonchemical processes of leakage from the cell into the mass spectrometer ion source.

When the light is shut off the methyl radical concentration becomes zero, essentially instantaneously. From this time on, the time dependences of m/e 90 and of m/e 45 will be due solely to (5) and to leakage of monomer and dimer through the pinhole, provided CH_3NO does not react significantly with nitric oxide; since we have not observed, at our low levels of nitric oxide concentration, ions corresponding to the known products^{10,11} of the reactions of CH_3NO with nitric oxide, this provision would seem to be fulfilled.

Typical results are shown in Figure 1, where the parent-ion peak heights of CH_3NO and $(\text{CH}_3\text{NO})_2$ (m/e 45 and m/e 90, respectively) are plotted *vs.* time, time zero corresponding to turn-off of the photolysis lamp. After the photolysis termination one sees the decay of the monomer accompanied by the simultaneous increase and subsequent decay of the dimer. There is, therefore, little cause to doubt that the typical data shown in Figure 1 depict directly the dimerization reaction (5).

At the instant photolysis is stopped we may assume, within our time resolution of ~ 1 sec, that the methyl radical concentration becomes instantly zero and that the only reactions occurring under our conditions are dimerization and negligible^{10,11} amounts of reaction of CH_3NO with NO. Thus, we may write (6) for times after the photolysis is stopped, *viz.*

$$-\frac{d[\text{CH}_3\text{NO}]}{dt} = 2k_5[\text{CH}_3\text{NO}]^2 + \lambda[\text{CH}_3\text{NO}] \quad (6)$$

where k_5 is the specific reaction rate of dimerization, and λ is the leak-rate constant of the pinhole leading to the mass spectrometer. Integration of (6) leads to (7), *viz.*

$$k_5 = -\lambda \frac{\left(1 - \frac{[\text{CH}_3\text{NO}]_t}{[\text{CH}_3\text{NO}]_0} e^{-\lambda t}\right)}{2[\text{CH}_3\text{NO}]_0(1 - e^{-\lambda t})} \quad (7)$$

where $[\text{CH}_3\text{NO}]_0$ is the concentration of the monomer

at the instant that the photolysis is stopped, and $[\text{CH}_3\text{NO}]$ is the monomer concentration at any later time t . Since λ can be measured independently, eq 7, combined with experimental measurements of $[\text{CH}_3\text{NO}]$, permits, in principle, evaluation of k_5 . Our first attempts to so evaluate k_5 from experimental studies using the larger leak were unsuccessful. This was because λ was so large ($4.78 \times 10^{-3} \text{ sec}^{-1}$) that about 90% of even the initial decay of CH_3NO (see eq 6) was due to leakage into the ion source of the mass spectrometer and, therefore, any decay of CH_3NO due to (5) could not be followed with sufficient precision.

However, with the smaller leak ($\lambda 2.0 \times 10^{-4} \text{ sec}^{-1}$) such an evaluation proved feasible for times up to 200 sec after the termination of the photolysis. With the small leak we may, with very little error, expand the exponentials in (7), neglect terms higher than first-order in λt , and rearrange to yield (8), *viz.*

$$\frac{(1 - \lambda t)}{[\text{CH}_3\text{NO}]} = \frac{1}{[\text{CH}_3\text{NO}]_0} + 2k_5 t \quad (8)$$

so that k_5 may be evaluated from the slope of a plot of $(1 - \lambda t)/[\text{CH}_3\text{NO}]$ vs. t . Actually, the quantity measured as a function of time is $h_{45}(t)$, the height of the parent ion peak, CH_3NO^+ . Since at any time $[\text{CH}_3\text{NO}]$ is proportional to $h_{45}(t)$, we may write (8) as

$$\frac{(1 - \lambda t)}{h_{45}(t)} = \frac{1}{h_{45}(0)} + \frac{2k_5}{\beta_{45}} t \quad (9)$$

where β_{45} is the proportionality constant relating $[\text{CH}_3\text{NO}]$ to h_{45} and $h_{45}(0)$ is the height of the m/e 45 peak at the instant of termination of photolysis. The value of β_{45} was calculated from the initial rate of formation of CH_3NO , with the valid assumption^{8,9} that, initially, methyl radicals react only with nitric oxide. Thus, as described earlier, photolysis of pure azomethane- d_6 permitted evaluation of $\phi I_0 \alpha$. Assuming now that α is not changed by substitution of H for D in azomethane, the initial formation rate of CH_3NO must be $2\phi I_0 \alpha$. Hence, we may write

$$\left(\frac{d[\text{CH}_3\text{NO}]}{dt}\right)_0 = \beta_{45} \left(\frac{dh_{45}}{dt}\right)_0 = 2\phi I_0 \alpha \quad (10)$$

The calibration constant so obtained was reproducible to $\pm 17\%$. With β_{45} known we may evaluate k_5 from (9).

Figure 2 shows a plot, according to eq 9, of the intensity function of m/e 45 vs. the time after photolysis termination (for the experiments with the small leak). The linearity of this plot is excellent and permits us to calculate a dimerization rate constant at room temperature (25°) of

$$k_5 = 0.36 \pm 0.08 \times 10^{-19} \text{ cm}^3 \text{ molecule}^{-1} \text{ sec}^{-1}$$

The excellent linearity shown in Figure 2 also permits us to conclude that under our conditions the dimer,

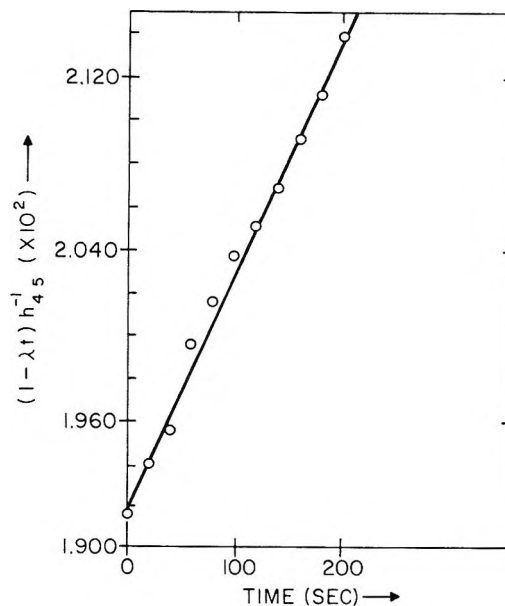


Figure 2. Plot of concentration-time data for CH_3NO , according to eq 9, and for small pinhole leak.

$(\text{CH}_3\text{NO})_2$, makes only negligible contribution to the ion current at m/e 45, and that any reversibility¹⁶ of reaction 5 has no significant effect on the time dependence of the observed CH_3NO concentration.

We have defined the specific reaction rate k_5 by (11), *viz.*

$$\frac{d[(\text{CH}_3\text{NO})_2]}{dt} = k_5 [\text{CH}_3\text{NO}]^2 \quad (11)$$

Converting the value reported by Christie, Frost, and Voisey¹⁶ at 25° to this same definition, we obtain $k_5 = 0.47 \times 10^{-19} \text{ cm}^3 \text{ molecule}^{-1} \text{ sec}^{-1}$. This is in very good agreement with our value, especially considering the diversity of the two methods used to measure monomer concentrations as a function of time. Unfortunately, these authors¹⁶ do not give error limits for their rate constants but it is probably safe to say that the two values agree within the combined experimental errors. Converting the value reported by Calvert, Thomas, and Hanst⁷ to our definition shows that our rate constant value is lower than theirs by a factor of about 2; our value is considerably lower than that reported by Johnston and Heicklen¹¹ who used an indirect method to evaluate k_5 . Since it has been shown conclusively⁷ that k_5 is independent of total pressure and surface effects, these variables were not studied in our work.

We have already mentioned that the curves in Figure 1 (obtained with the large leak) constitute a direct picture of the dimerization, (5), yet the sharp increase in dimer concentration at the instant of termination of photolysis warrants further comment. We have already discussed our conclusion that, under our conditions, the methyl radical concentration

vanishes essentially at the instant of interruption of the photolysis and that from this time on the time dependences of m/e 90 and m/e 45 are due solely to reaction 5 and to leakage of monomer and dimer through the pinhole. Hence, for the rate of change of dimer concentration *after* photolysis termination we may write (12), *viz.*

$$\frac{d[(\text{CH}_3\text{NO})_2]}{dt} = k_5 [\text{CH}_3\text{NO}]^2 - \lambda[(\text{CH}_3\text{NO})_2] \quad (12)$$

It is seen in Figure 1 that for all times after photolysis termination the intensity of m/e 45 and hence, the concentration of CH_3NO , decreases. The sudden increase in slope of the intensity-time curve for m/e 90 in Figure 1 is not compatible with (12) unless during the irradiation the dimer is reacting with something that disappears at the instant of light interruption.

We have already given our reasons for believing that under our conditions methyl radicals do not react with anything except nitric oxide. Therefore, the most likely explanation is that, during the irradiation, photolytic decomposition of the dimer (the rate of which is proportional to the light intensity) results in the observation of a low formation rate (*cf.* Figure 1); then at the instant of light interruption ($I_0 = 0$) the dimer concentration increases suddenly because a dominant destruction channel has been removed.

When the smaller leak was used to obtain decay curves of $[\text{CH}_3\text{NO}]$ that were not so dominated by leakage from the cell and from which we could determine k_5 , we were, unfortunately, not able to detect the dimer with sufficient precision to obtain curves similar to that shown in Figure 1. The dimer curve in Figure 1 cannot be used to evaluate k_5 because we have no independent mass spectrometer calibration for the relationship between m/e 90 and the dimer concentration. However, using the rate constant k_5 , determined from the loss of $[\text{CH}_3\text{NO}]$ (*cf.* Figure 2), we may show that the dimer curve in Figure 1 is of the nature predicted by the kinetics.

The linearity shown in Figure 2 indicates that up to 200 sec after the end of the photolysis, the back reaction of dimer¹⁶ has no significant effect. Considering the thermal rate of the back reaction^{16,20} this absence of any effect is not surprising. Substituting into (12) the expression for $[\text{CH}_3\text{NO}]$, as given by the transposition of (7), and solving the resulting differential equation yields the result shown in (13), where C is the constant of integration. The integral is readily

$$[(\text{CH}_3\text{NO})_2] = \lambda^2 [\text{CH}_3\text{NO}]_0^2 k_5 e^{-\lambda t} \times \int \frac{e^{-\lambda t} dt}{[2k_5 [\text{CH}_3\text{NO}]_0 (1 - e^{-\lambda t}) + \lambda]^2} + C e^{-\lambda t} \quad (13)$$

evaluated by the substitution $x = 1 - e^{-\lambda t}$. Denoting the initial dimer concentration by $[(\text{CH}_3\text{NO})_2]_0$ leads to the expression shown in (14) for the time

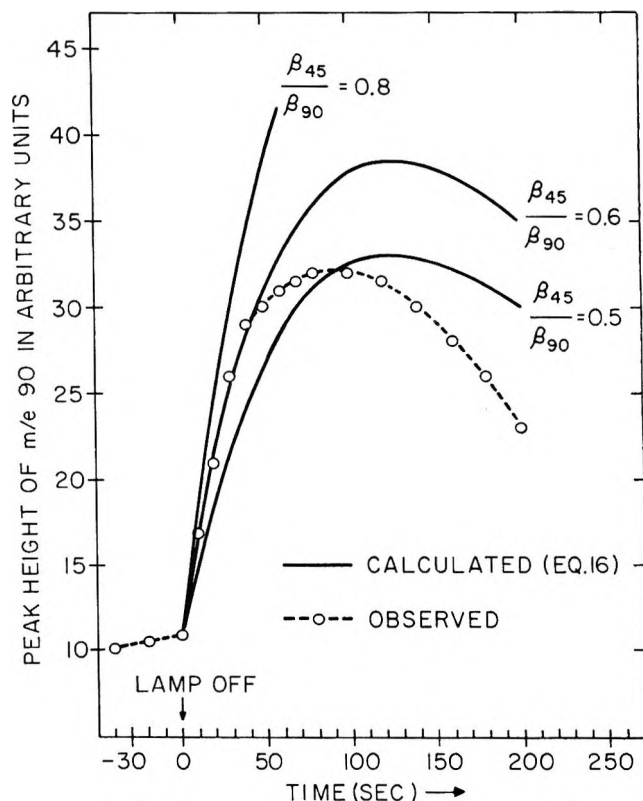


Figure 3. Time dependence of m/e 90 or $[(\text{CH}_3\text{NO})_2]$ after cessation of photolysis.

dependence of dimer concentration after photolysis.

$$[(\text{CH}_3\text{NO})_2] = [(\text{CH}_3\text{NO})_2]_0 e^{-\lambda t} + [\text{CH}_3\text{NO}]_0 e^{-\lambda t} \times \left\{ \frac{k_5 [\text{CH}_3\text{NO}]_0 (1 - e^{-\lambda t})}{\lambda + 2k_5 [\text{CH}_3\text{NO}]_0 (1 - e^{-\lambda t})} \right\} \quad (14)$$

It is easily shown that making the approximation $\lambda \gg 2k_5 [\text{CH}_3\text{NO}]_0 (1 - e^{-\lambda t})$ results in a maximum error of 9% for $t > 50$ sec and a smaller error at $t < 50$ sec. Use of this approximation in (14) gives (15), *viz.*

$$[(\text{CH}_3\text{NO})_2] = [(\text{CH}_3\text{NO})_2]_0 e^{-\lambda t} + \frac{k_5 [\text{CH}_3\text{NO}]_0^2}{\lambda} e^{-\lambda t} (1 - e^{-\lambda t}) \quad (15)$$

In terms of peak heights for the pertinent ion currents, use of the relationship $[M_t] = \beta_t h_t$ in (15) leads to (16) which is the form of presentation of the data in Figure 1. β_{45} is known from our calibration based on the initial rates of formation of ethane in the absence of nitric

$$h_{90}(t) = e^{-\lambda t} h_{90}(0) + \frac{\beta_{45}^2 k_5}{\beta_{90} \lambda} h_{45}^2(0) (1 - e^{-\lambda t}) \quad (16)$$

oxide and nitrosomethane monomer in the presence of nitric oxide, but β_{90} is not known and we have no

(20) B. G. Gowenlock, J. Trotman, and L. Batt, Special Publication No. 10, The Chemical Society, London, 1957, p 75.

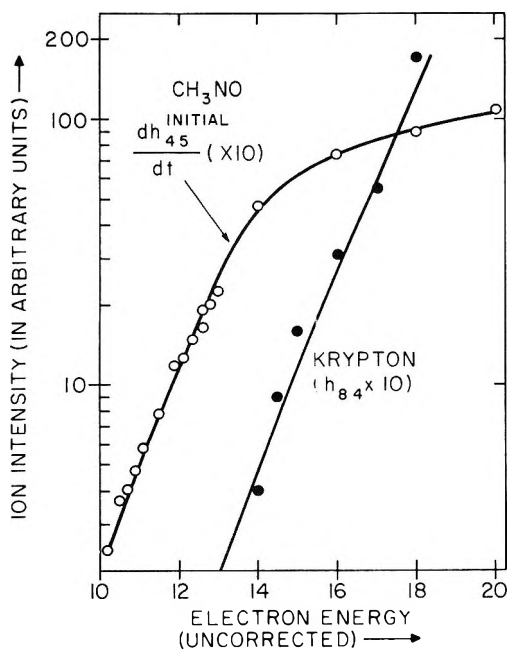


Figure 4. Ionization-efficiency curves of CH_3NO^+ and Kr^+ .

independent way to determine it. We can, however, use the known values of k_5 , λ , and β_{45} and various values of the ratio β_{45}/β_{90} in (16) to calculate the time dependence of the m/e 90 ion intensity after photolysis.

The result is shown in Figure 3, where we see that (16) predicts the same general shape but that the observed intensities go through a maximum at shorter times than calculated and, moreover, exhibit a sharper drop after the maximum. While the thermal decomposition of dimer may make some contribution, the reported rates^{16,20} are too slow at our temperature for the reverse of reaction 5 to be the major cause. It is much more likely that dimer is being removed by condensation on the vessel walls, a phenomenon that is well documented.^{14,15,21-23} If the dimer loss by wall condensation is first order, as is probable, then the mathematical

effect would be to increase the value of λ in (16) and this in turn would lead to a maximum at shorter times and a lower value for the maximum concentration as observed. In the early stages of dimer formation, however, both wall condensation and leakage through the pinhole will have little effect and we may determine β_{90} by finding the "best value" of β_{45}/β_{90} for less than, say, 50 sec. Analysis of all our data similar to that in Figure 3 yields, for the mass spectrometric parent-peak sensitivity ratio for nitrosomethane, the result

$$\frac{\beta_{45}(\text{monomer})}{\beta_{90}(\text{dimer})} = 0.59 + 0.09$$

Ionization Potential of CH_3NO . Since during photolysis the dimer is present in such low concentration relative to monomer (*cf.* Figure 1), we may study the growth curves of m/e 45 as a function of electron energy to obtain the ionization potentials of the nitrosomethane monomer in a manner similar to that reported by Kohout and Lampe¹⁸ for HNO . Thus, for all other conditions held constant, the initial slope of the intensity of m/e 45 in the photolyzed mixtures will depend on electron energy as does the ionization cross-section. Thus, a plot of these initial slopes *vs.* electron energy yields a typical ionization efficiency curve as shown in Figure 4. Using krypton and argon as an internal standards to calibrate the electron energy scale, we find from four such measurements the result: $I_2(\text{CH}_3\text{NO}) = 10.8 \pm 0.3$ eV.

Acknowledgment. This work was supported by the Petroleum Research Fund of the American Chemical Society under Grant 3298-A5. We also wish to thank the National Science Foundation for providing funds to assist in the original purchase of the mass spectrometer.

(21) P. Tarte, *Bull. Soc. Roy. Sci., Liege*, 22, 226 (1953).

(22) H. T. J. Chilton, B. G. Gowenlock, and J. Trotman, *Chem. Ind.*, 538 (1955).

(23) B. G. Gowenlock and J. Trotman, *J. Chem. Soc.*, 4190 (1955).

Chemical Kinetics of Carbonyl Fluoride Decomposition

in Shock Waves¹

by A. P. Modica

Avco Corporation, Wilmington, Massachusetts 01887 (Received February 20, 1969)

An infrared technique has been used to monitor the thermal decomposition of carbonyl fluoride (COF_2) in argon and nitrogen diluent behind incident and reflected shock waves. Data were taken in the temperature range 2200 to 3600°K at total pressures between 0.2 and 26 atm. Direct sampling of reflected shock mixtures with a time-of-flight mass spectrometer provided knowledge of the decomposition products. The pressure and temperature dependence of the COF_2 dissociation rate constants are discussed in terms of the Rice-Ramsperger-Kassel unimolecular theory. Rate constants for the fluorine extraction reactions and COF_2 disproportionation reaction were obtained by curve fitting the complete COF_2 kinetic histories with computed profiles. A chemical nonequilibrium stream-tube program which includes wall boundary layer effects was used for data analysis.

Introduction

Presently, the chemical rates for fluorocarbon decomposition and oxidation kinetics are needed for input to a number of aerospace engineering problems. Mass spectrometer study on the pyrolysis of Teflon plastic (polytetrafluoroethylene) in atmospheres of air and oxygen² shows that carbonyl fluoride (COF_2) is an important low-temperature (800°K) oxidation intermediate, and that at higher temperatures carbon dioxide (CO_2) and perfluoromethane (CF_4) dominate the reaction products. Measurements to identify the infrared and visible spectrum of an air-Teflon boundary layer in a hot subsonic arc jet have shown the presence of the CN violet and red bands and structure in the 2- to 6- μ region characteristic of the COF_2 , CO, and CO_2 molecular bands.^{3a,b} Single-pulse shock-tube experiments of the tetrafluoroethylene oxidation in the range 1200 to 2000°K show product distributions of COF_2 , CO, CF_4 , C_2F_6 , and small amounts of C_3F_8 and CO_2 .⁴ In a shock-tube study of the difluoromethylene-oxygen reaction, infrared measurements have directly identified COF_2 as the initial oxidation product of these reactants. Preliminary results show that at temperatures <2200°K, the COF_2 builds up to a steady concentration behind the shock front and that above 2700°K, a nonequilibrium "overshoot" in COF_2 takes place in the reaction mixture.⁵

From a measurement of the thermal decomposition rates of molecules, the rate constants for their formation can be obtained by the principle of detailed balancing, *i.e.*, taking the ratio of the dissociation rate to the equilibrium constant of the reaction. This approach has previously been used, for example, to determine fluorine-fluorocarbon dissociation and recombination rate constants of CF_4 and CF_3 .⁶ In this report another part of fluorocarbon chemical kinetics has been in-

vestigated and deals with the thermal decomposition of carbonyl fluoride. A shock tube is employed to dissociate COF_2 in dilute mixtures of argon or nitrogen. The rate of COF_2 decomposition is measured by monitoring the COF_2 fundamental band at 5.25 μ with a filtered InSb infrared detector. Rate constants for COF_2 initial dissociation are obtained over a pressure range from about 0.2 to 26 atm between 2400 and 3600°K. The pressure and temperature dependences of these rate constants are expressed in terms of the RRK theory for unimolecular reactions. In addition, the complete COF_2 decomposition records are analyzed with a chemical, nonequilibrium shock-tube program to obtain rate constants for the fluorine extraction and recombination reaction of the COF_2 decomposition mechanism.

Experimental Procedure

Shock Tube. The COF_2 decomposition experiments were conducted behind incident and reflected shock waves in an emission spectroscopy shock tube and behind reflected shock waves in a shock tube coupled to a time-of-flight mass spectrometer.

The optical shock tube is a 1.5 in. i.d. stainless steel tube with a 3.5-ft driver section and a 10-ft driven

(1) The present study was conducted in the Aerophysics Laboratory of the Avco Corporation Space Systems Division and was supported by the Advanced Research Projects Agency under subcontract from the Avco Everett Research Laboratory through Contract F04-701-68-C-0036, part of project DEFENDER.

(2) R. E. Kupel, *et al.*, *Anal. Chem.*, **36**, 386 (1964).

(3) (a) T. Wentink and W. Planet, *J. Opt. Soc. Am.*, **51**, 601 (1961); (b) R. A. Greenberg, N. H. Kemp, and K. L. Wray, Avco Everett Research Laboratory Report 301 (1968).

(4) S. H. Bauer, K. C. Hou, and E. L. Resler, Jr., *Proc. 6th Int. Shock Tube Symp.*, Freiburg, Germany, April 1967, p 504.

(5) A. P. Modica, "A Kinetic Model for Teflon-Air High Temperature Chemistry," Avco/SSD Report AVSSD-046-67-RR (1968).

(6) A. P. Modica and S. J. Sillers, *J. Chem. Phys.*, **48**, 3283 (1968).

section. The shock tube and associated gas handling system are pumped down to less than 3×10^{-3} Torr with a water-cooled oil diffusion pump and have a leak rate of approximately 10^{-3} Torr/min. Cold driving with helium or hydrogen against Mylar diaphragms of 2- to 5-mil thickness was used in the present experiments to generate shock waves into the test chamber. The shock velocity was measured with a series of platinum heat-transfer gauges situated along the driven section. The output of these gauges was displayed on a time-mark folded oscilloscope sweep, operated by a Radionics (Model TWN-2A) triangular wave and marker timing generator. Transit times between stations were measured to within $\pm 1 \mu\text{sec}$. The maximum error in the shock velocity was about $\pm 0.3\%$ and introduced an uncertainty of less than $\pm 15^\circ\text{K}$ in the calculated incident shock temperature or $\pm 40^\circ\text{K}$ for the reflected shock. Infrared emission from the shocked gas was monitored with a filtered InSb detector (Type 1SC-301) and was viewed through calcium fluoride windows, perpendicular to the shock-tube axis.

The mass spectrometer shock-tube apparatus was constructed from 1-in. inside diameter Pyrex glass pipe and has a 5-ft driver section and a 15-ft driven section. A Bendix (Model 14-206) time-of-flight mass spectrometer is attached to the shock tube through the "fast reaction chamber." The reflected shock heated gas was sampled at the shock-tube endwall which is a flat stainless steel plate having in its center a hyperbolic nozzle with a 2-mil inlet and 10-mil exit (Englehard Industries, Englehard, N. J.). Mass spectral recordings were taken at 25- μsec intervals just before and after shock arrival. The time-resolved ion peaks were displayed on a Tektronix 535A oscilloscope in combination with a Type CA preamplifier and multiscan generator.⁷ For initial shock-tube pressures of 3 to 8 Torr, the background pressure in the mass spectrometer before shock arrival ranged between 10^{-6} and 10^{-5} Torr.

A complete description of the optical and mass spectrometer shock-tube facilities may be found in previous reports.⁸

Reagents. Infrared measurements of COF₂ decomposition were made behind incident argon and nitrogen shocks containing COF₂ in a mole ratio of 2:100 with the inert gas. The same measurements were made behind reflected shocks using 0.25:100 and 0.5:100 COF₂-argon mixtures. Mass spectral data on the COF₂ decomposition reaction were taken with a 5:100 COF₂-argon mixture. The COF₂ gas used in this study was obtained from Peninsular Chemresearch (Gainesville, Florida) and had a stated purity of 95%. Infrared analysis of completely decomposed COF₂ in excess argon showed that the commercial gas contained about $4.4 \pm 2.4\%$ CO₂. Mass spectrometer analysis of a COF₂ gas sample did not show any other impurity. The buffer gases were of research grade (argon, 99.999% purity and N₂, 99.997% purity).

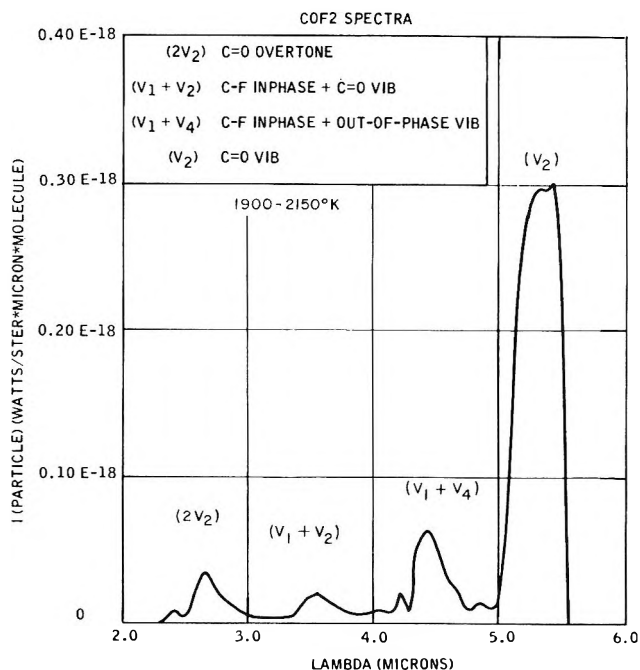


Figure 1. Absolute intensity of COF₂ spectra in the 2 to 6- μ region.

Infrared Measurements

The infrared absorption spectra of the COF₂ molecule is found to consist of a number of vibrational-rotational bands between 2 and 38 μ .⁹ Recently in this laboratory, spectral band intensities in the 2- to 6- μ region of COF₂ (Figure 1) have been determined by employing a "fast scanning" monochromator to record the infrared spectra of reflected shock heated samples of COF₂ in excess argon.¹⁰ For the purpose of studying the thermal decomposition kinetics of COF₂, the fundamental vibrational band at 5.25 μ was monitored with a filtered InSb detector to observe the time rate of change of the COF₂ concentration behind the shock wave. Examples of infrared oscillogram records depicting COF₂ decomposition at several temperatures behind incident and reflected shock waves are shown in Figures 2 and 3, respectively. The COF₂ concentrations of the study were typically less than 2×10^{-7} mol/cm³ for which the infrared emission at 5.25 μ was below 8% blackbody intensity. Under these conditions, the COF₂ gas was considered optically thin and the measured infrared signal was taken to be linearly dependent on concentration. From the infrared emission peak height at the shock front and the initial concentration of COF₂ behind the shock wave, each

(7) G. P. Glass, *et al.*, *J. Chem. Phys.*, **42**, 608 (1965).

(8) J. A. Harrington, A. P. Modica, and D. R. Libby, *J. Chem. Phys.*, **44**, 3380 (1966); A. P. Modica, *J. Phys. Chem.*, **69**, 2111 (1965).

(9) A. H. Nielson, *et al.*, *J. Chem. Phys.*, **20**, 596 (1952).

(10) A. P. Modica and R. R. Brochu, *J. Quant. Spectrosc. Radiat. Transfer*, **9**, 1105 (1969).

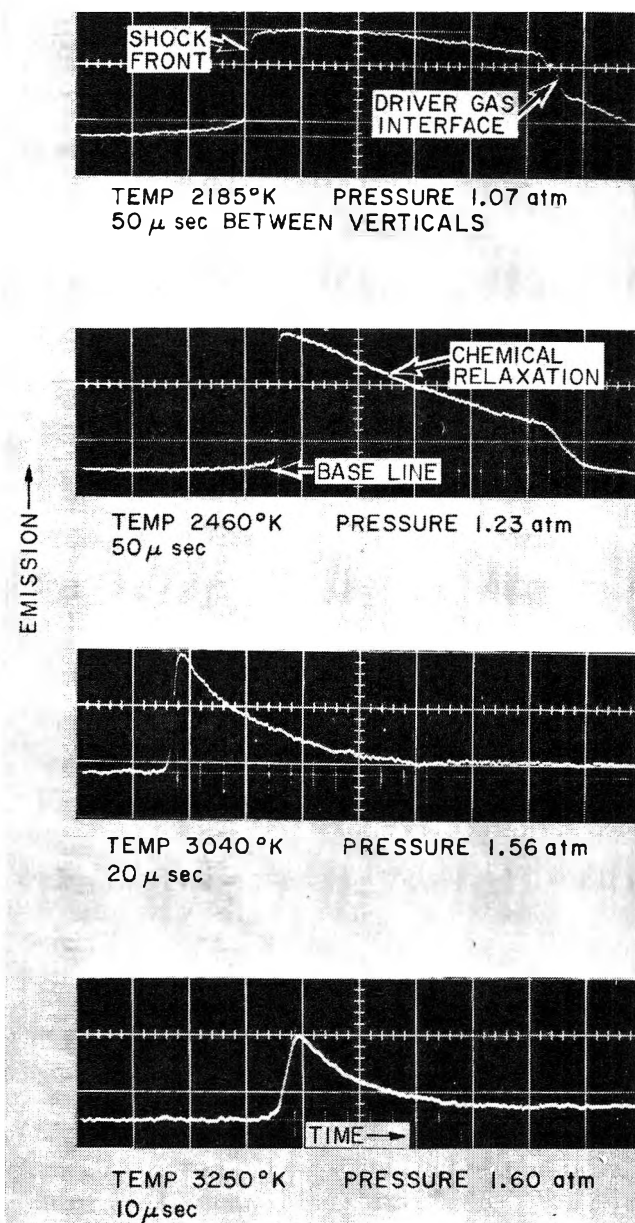


Figure 2. Examples of COF_2 infrared emission at 5.25μ behind incident shock waves into 2:100 COF_2 -argon mixtures.

oscillogram record was self-calibrating. The spectral response characteristics of the $5.25\text{-}\mu$ radiometer used in these experiments is shown in Figure 4. The temperature dependence of the COF_2 $5.25\text{-}\mu$ emission band measured with the present radiometer is plotted in Figure 5. Both the incident and reflected shock data showed that in the temperature range 2200 to 3400°K, the COF_2 emission was slightly increasing with temperature ($\sim 30\%$ change). It was found in the experiments that the CO decomposition product and the trace amount of CO_2 impurity in the COF_2 reaction mixture radiated in the band pass of the $5.25\text{-}\mu$ filter. Corrections to the COF_2 infrared records were made by subtracting out the CO (less than 10%) and CO_2 (less than 5%) spectra. Necessary correction factors were

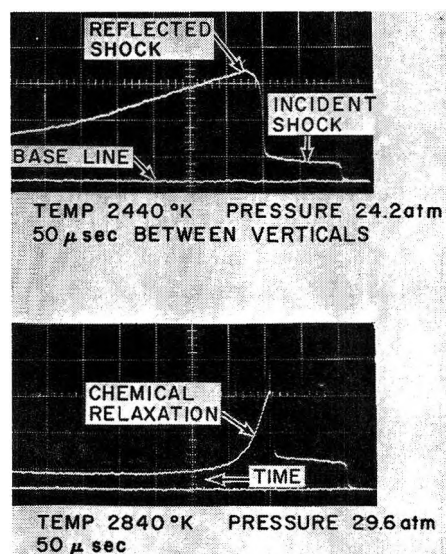


Figure 3. Records of COF_2 infrared emission at 5.25μ behind reflected shock waves into 0.25:100 COF_2 -argon mixtures.

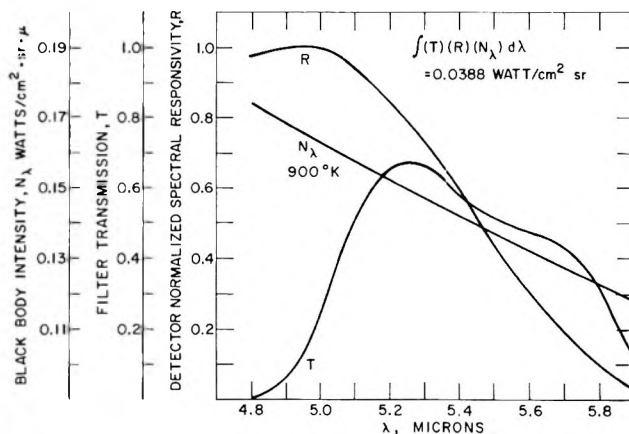


Figure 4. Transmission characteristics of $5.25\text{-}\mu$ radiometer.

obtained from infrared measurements of known quantities of CO and CO_2 in argon shocks.

Mass Spectrometer Measurements

Reaction mixtures of reflected shock heated COF_2 in excess argon were sampled directly through the shock-tube endwall and analyzed in a time-of-flight mass spectrometer. The mass spectral data were used to study the change in COF_2 mass peak with time (25- μ sec intervals after shock compression) and to determine the nature of the decomposition products to gain insight about the COF_2 decomposition mechanism. A typical mass spectrum of a COF_2 decomposition mixture is seen in Figure 6. Ion peaks for COF_2^+ (66), COF (47), CO_2 (44), Ar(40), Ar(36), and CO(28) are clearly identified. Major ion peaks for CF_3 (69), CF_2 (50), and CF (31) are absent in the spectra. The small signals recorded in these regions are believed to result from background ion-molecule reactions in the drift tube of the mass spectrometer. The prominent peak at 39 is actually

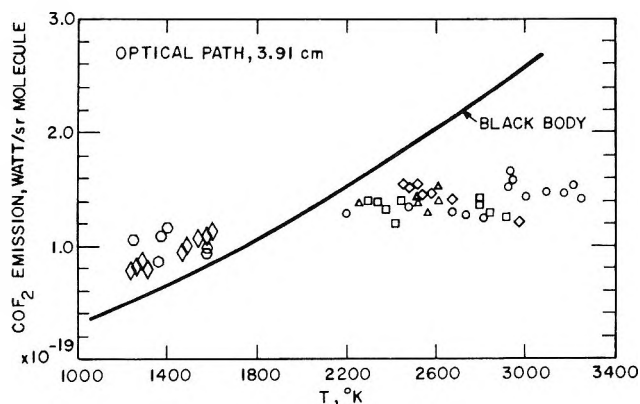


Figure 5. Experimental temperature dependence of COF₂ 5.25 μ band emission. Incident shock data: \circ , 2:100 COF₂-Ar(1.5 atm); Δ , 2:100 COF₂-N₂ (1.5 atm); \square , 0.5:100 COF₂-Ar(2.2 atm); \circ , 0.25:100 COF₂-Ar(6.5 atm). Reflected shock data: \diamond , 0.5:100 COF₂-Ar(10 atm); \square , 0.25:100 COF₂-Ar(26 atm).

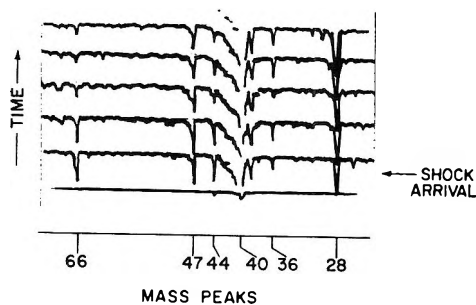


Figure 6. Mass spectrogram of decomposed COF₂ behind reflected shock wave. Shock temperature, 3650°K; pressure, 0.17 atm (5:100 COF₂-argon); mass analysis, 25 μ sec/scan; mass peaks, 66(COF₂), 47(COF), 44(CO₂), 40(Ar), 36(Ar), 28(CO).

not a discrete ion peak but is part of the broadened argon (40) peak. The same peak structure is found when pure argon is shocked. The CO ion peak appearing in the first trace after shock passage is part of the ion cracking pattern of COF₂. The ratios of COF₂, COF, and CO peak heights are similar to the room temperature ion cracking pattern ratios of COF₂ samples. Because the CO ion peak may have several origins, *i.e.*, from ion cracking of COF₂ and COF, from the CO₂ impurity, and from the CO reaction product, it is a poor peak for obtaining kinetic data. However, it may be concluded from the mass spectrometer records that CO is the major molecular end product of COF₂ decomposition. If this were not the case, the CO ion peak would diminish in time following the depletion of COF₂ or COF in the reaction mixture. This latter observation concurs with CO infrared analyses which show that after complete decomposition of COF₂, the residual infrared emission in the 5.25- μ radiometer oscillograms corresponds to a CO concentration equal to the stoichiometric CO content of the COF₂ molecules initially present in the mixture.

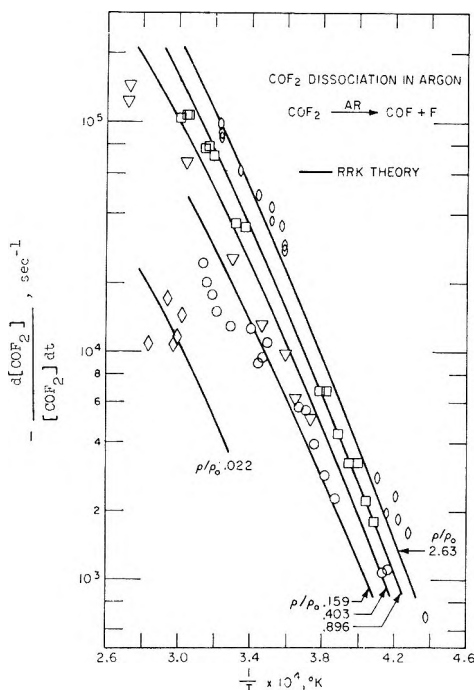
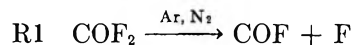


Figure 7. Apparent first-order rate constants of COF₂ thermal dissociation in argon diluent. ρ/ρ_0 is a gas density normalized to density at 1 atm and 273°K. Solid lines are RRK rate integral with $A = 6.14 \times 10^{11} \text{ sec}^{-1}$, $E_0 = 91,912 \text{ cal/mol}$, $m = 6$ and $z = 7.5 \times 10^{10} \text{ cc/mol sec}$. Incident shock data: \circ , $\rho/\rho_0 = 0.159$. Reflected shock data: \diamond , $\rho/\rho_0 = 0.022$; ∇ , $\rho/\rho_0 = 0.403$; \square , $\rho/\rho_0 = 0.896$; \circ , $\rho/\rho_0 = 2.63$; \diamond , mass spectrometer measurements. All other data are from infrared measurements.

Thermal Dissociation Rate Constant of Carbonyl Fluoride

The kinetics of COF₂ thermal dissociation was studied over a pressure range from about 0.2 to 26 atm in argon shocks and from about 0.4 to 1.5 atm in shock-heated nitrogen. The temperature interval of the data extended from 2400 to 3600°K. The rate constant for thermal dissociation of COF₂



was determined from the initial slope of the infrared emission records, corresponding to the first 10% decay in the COF₂ concentration. Some dissociation rate constants were also measured from mass spectrometer oscillogram records for the first 50 μ sec of COF₂ dissociation. The "apparent" dissociation rate constant defined by

$$\frac{d[\text{COF}_2]}{[\text{COF}_2]dt} = k_{\text{obsd}} \quad (1)$$

where [COF₂] is the COF₂ concentration behind the shock wave, is plotted against reciprocal temperature in Figures 7 and 8. The average total concentration associated with each set of dissociation rate constants is denoted by a normalized density equal to the density

of the shocked gas divided by the density of the gas at 1 atm pressure and 273°K. Examples of the shock tube experiments performed in this study are given in Table I.

Table I: COF₂ Dissociation in Argon Shocks and Nitrogen Shocks

Expt no.	Shock temp, °K	Total concn, mol/cc	Apparent rate constant, sec ⁻¹	Total pressure, atm
2:100 COF ₂ -Argon				
1 ^a	2405	6.245 × 10 ⁻⁶	1.11 × 10 ³	1.23
2	2545	6.270 × 10 ⁻⁶	2.42 × 10 ³	1.31
3	2880	6.345 × 10 ⁻⁶	9.45 × 10 ³	1.50
4	3195	6.395 × 10 ⁻⁶	2.42 × 10 ⁴	1.68
0.5:100 COF ₂ -Argon				
5 ^b	2678	1.586 × 10 ⁻⁵	4.95 × 10 ³	3.48
6	2880	2.231 × 10 ⁻⁵	1.29 × 10 ⁴	5.27
7	3304	1.686 × 10 ⁻⁵	6.79 × 10 ⁴	4.57
8	3680	1.300 × 10 ⁻⁵	1.24 × 10 ⁵	3.93
9	2475	3.840 × 10 ⁻⁵	2.23 × 10 ³	7.80
10	2655	3.930 × 10 ⁻⁵	6.70 × 10 ³	8.60
11	3010	4.090 × 10 ⁻⁵	3.62 × 10 ⁴	10.10
12	3270	4.180 × 10 ⁻⁵	1.08 × 10 ⁵	11.20
0.25:100 COF ₂ -Argon				
13	2343	1.19 × 10 ⁻⁴	1.62 × 10 ³	22.9
14	2410	1.20 × 10 ⁻⁴	1.92 × 10 ³	23.8
15	2795	1.18 × 10 ⁻⁴	2.71 × 10 ⁴	27.2
16	2905	1.12 × 10 ⁻⁴	4.91 × 10 ⁴	26.7
17	3100	1.10 × 10 ⁻⁴	9.88 × 10 ⁴	28.0
2:100 COF ₂ -Nitrogen				
1 ^a	2460	1.756 × 10 ⁻⁶	4.88 × 10 ²	0.354
2	2615	1.779 × 10 ⁻⁶	1.45 × 10 ³	0.382
3	2795	1.804 × 10 ⁻⁶	4.42 × 10 ³	0.414
4	2915	1.819 × 10 ⁻⁶	7.39 × 10 ³	0.435
5	2555	3.542 × 10 ⁻⁶	1.38 × 10 ³	0.743
6	2715	3.586 × 10 ⁻⁶	4.27 × 10 ³	0.799
7	2840	3.620 × 10 ⁻⁶	6.23 × 10 ³	0.844
8	2970	3.651 × 10 ⁻⁶	1.50 × 10 ⁴	0.890
9	2478	7.035 × 10 ⁻⁶	1.53 × 10 ³	1.450
10	2590	7.104 × 10 ⁻⁶	2.61 × 10 ³	1.510
11	2796	7.215 × 10 ⁻⁶	8.15 × 10 ³	1.660
12	2863	7.250 × 10 ⁻⁶	1.34 × 10 ⁴	1.700

^a Incident shock data. ^b Reflected shock data.

It is seen from the data of Figures 7 and 8 that the apparent first-order rate constants are neither independent nor increasing linearly with increasing total concentration at a given temperature. This type of behavior for thermal dissociation reactions of polyatomic molecules has been explained by a number of theoretical formulations.¹¹⁻¹³ The COF₂ dissociation rate constants of this work are fitted by the general rate constant equation derived from the Rice-Ramsperger-Kassel (RRK) theory on unimolecular reactions. The

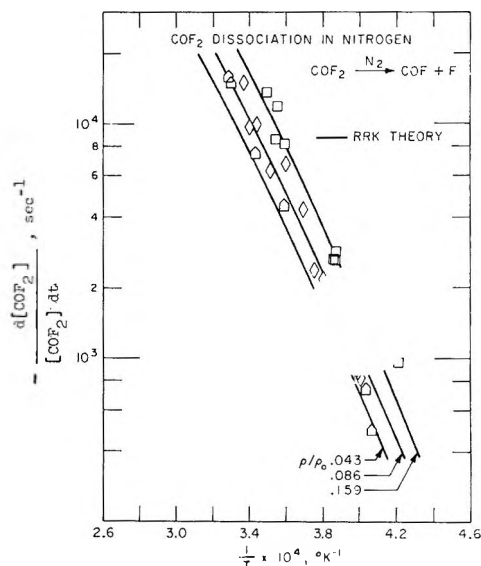


Figure 8. Apparent first-order rate constants of COF₂ thermal dissociation in nitrogen diluent. Solid lines are RRK theory integral with $A = 6.14 \times 10^{11} \text{ sec}^{-1}$, $E_0 = 91912 \text{ cal/mol}$, $m = 6$, and $Z = 1.0 \times 10^{11} \text{ cc/mol sec}$. All data are from infrared measurements behind incident shock waves.

general rate constant formula of the RRK theory is given by

$$k(\text{RRK}) = \frac{Ae^{-E_0/RT}}{m!} \times \int_0^\infty \frac{x^m e^{-x} dx}{1 + (AT^{-0.5}/cZ) \left[x / \left(\frac{E_0}{RT} + x \right) \right]^m} \quad (2)$$

where $k_\infty = Ae^{-E_0/RT}$ is the Arrhenius high-pressure rate constant; E_0 is the minimum energy for dissociation; A is the frequency factor. The quantities m and c are the number of classical oscillators participating in the dissociation process and total concentration. In the expression, $T^{-0.5}/Z$ is the inverse of the collision frequency where Z denotes the effective cross section for reaction. x is the dimensionless variable, $(E - E_0)/RT$. The parameters of eq 2 giving a best fit to the observed COF₂ rate constant were evaluated as follows. The k_∞ were determined by plotting the experimentally observed rate constants at a given temperature against pressure (Figure 9) and to a first approximation least-squares fitting the data with the phenomenological equation, $k_{\text{obsd}} = k_\infty P/P + r$, based on the Lindemann mechanism for a unimolecular reaction.¹⁴ The k_∞ 's were

(11) N. B. Slater, "Theory of Unimolecular Reactions," Cornell University Press, Ithaca, N. Y., 1959.

(12) D. L. Bunker, "Theory of Elementary Gas Reaction Rates," Pergamon Press, New York, N. Y., 1966.

(13) J. Keck and A. Kalekar, "Statistical Theory of Dissociation and Recombination for Moderately Complex Molecules," Avco Everett Research Laboratory, Everett, Mass., Report 289, 1968.

(14) S. W. Benson, "The Foundation of Chemical Kinetics," McGraw-Hill Book Co., Inc., New York, N. Y., 1960, pp 223-224.

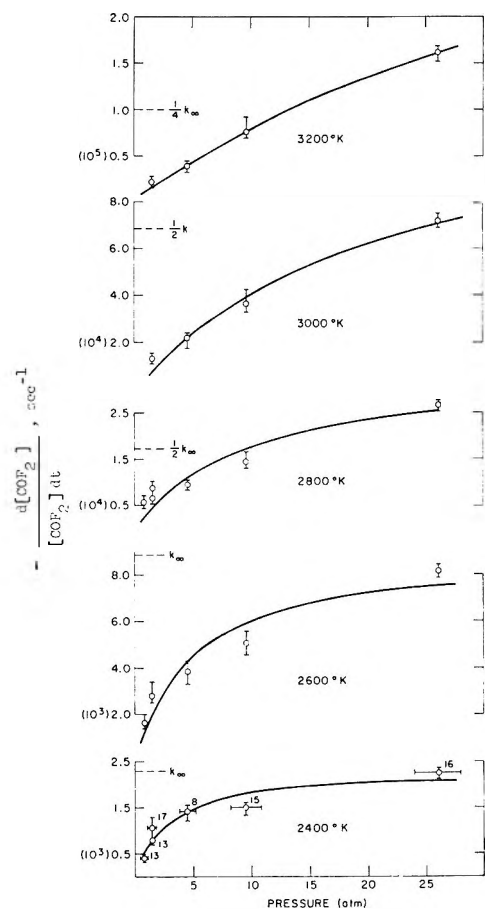


Figure 9. Pressure dependence of COF₂ dissociation rate constant with temperature. Vertical bar indicates experimental scatter of original rate constants adjusted to a common temperature with apparent activation energy. Total number of experiments appears beside vertical bar. Horizontal bar shows mean deviation of original data from the average pressure. Solid lines are nonlinear least squares fit of data

$$\text{with } k_{\text{obad}} = \frac{k_{\text{exp}} P}{P + r}$$

next used to determine A by a least-squares fit of the Arrhenius rate constant, taking $E_0 = 91.912$ kcal/mol¹⁵ (see Figure 10). The RRK rate integral eq 2 was solved on an IBM 360 computer for $A = 6.14 \times 10^{11}$ sec⁻¹ and $E_0 = 91.912$ kcal/mol where m and Z were varied systematically until a satisfactory fit was achieved with one set of the experimental data (Figure 11). The solid curves in Figures 7 and 8 are the theoretical RRK rate constants and show that with the kinetic parameters A , E_0 , m , and Z for argon and nitrogen, respectively, 6.14×10^{11} sec⁻¹, 91.912 kcal/mol, 6, 7.5×10^{10} cm³/mol sec and 6.14×10^{11} sec⁻¹, 91.912 kcal/mol, 6, and 1.0×10^{11} cm³/mol sec, an accurate correlation (within 40%) of both the argon and nitrogen data is obtained over the concentration range of the study. However, it is pointed out here that these values of m and Z are not at all unique in fitting the data. Reasonable curve fits within the scatter of the experimental points are also obtained for $m = 4$ and

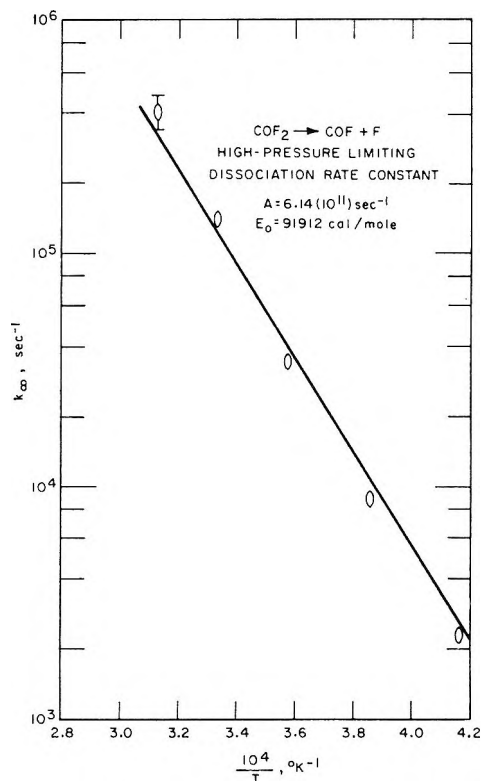


Figure 10. Least-squares fit of extrapolated limiting-high-pressure rate constant with Arrhenius formula for $E_0 = 91,912$ cal/mol. Vertical bar shows statistical spread of k_{∞} values.

$Z = 5.0 \times 10^{11}$ cm³/mol-sec. Calculations with the RRK integral for $m > 6$ equally can show agreement with the experimental data.

Mechanism and Kinetics of Carbonyl Fluoride Decomposition

Mass spectrometer and infrared evidence show that under the experimental conditions of this study COF₂ would mainly decompose to CO and fluorine atoms. A set of reactions which would lead to these results are the thermal dissociation reactions of COF₂ and COF, the fluorine extraction reactions, and the COF disproportionation reaction (Table II). The rate constant of R1 was obtained, as described in the preceding section, from the initial decay in the infrared records of COF₂ behind the shock front. The thermal dissociation rate constant of the COF radical (R2) is based on the difference in the first and second bond dissociation energies, $D(\text{F-COF}) = 91,912$ cal/mol and $D(\text{F-CO}) = 68,570$ cal/mol of the COF₂ molecule. The rate constants for the fluorine extraction reactions and COF disproportionation reaction were derived from an Arrhenius expression by incorporating the energy of

(15) In order to be consistent with current JANAF thermochemical data, the first and second bond dissociation energies of COF₂ were based on the enthalpy change for the reaction $\text{COF}_2 = \text{CO} + 2\text{F}$, $\Delta H_f = 160.5$ kcal/mol, and were taken to be in the same ratio as the first and second bond dissociation energies of CF₄. Analogous to $D(\text{F-CF}_3)/D(\text{F-CF}_2) = 1.34$, the values of $D(\text{F-COF})$ and $D(\text{F-CO})$ are 91.912 and 68.57 kcal/mol, respectively.

Table II: Chemistry and Rate Constants for COF₂ Decomposition

Reaction	Rate constant ^a
R1 COF ₂ $\xrightarrow{\text{Ar}}$ COF + F	$8.52 \times 10^8 e^{-46.257/T} \int_0^\infty \frac{x^6 e^{-x} dx}{1 + \frac{8.19T^{-0.5}}{c} \left[\frac{x}{(46257/T) + x} \right]^6}$
R2 COF $\xrightarrow{\text{Ar}}$ CO + F	$1.02 \times 10^{11} e^{-34610/T} \int_0^\infty \frac{x^2 e^{-x} dx}{1 + \frac{2.05T^{-0.5}}{c} \left[\frac{x}{(34510/T) + x} \right]^3}$
R3 COF ₂ + F \rightarrow COF + F ₂	$1.0 \times 10^{12} T^{0.5} e^{-27.740/T}$
R3' COF + F ₂ \rightarrow COF ₂ + F	$4.72 \times 10^{10} T^{0.5} e^{1037/T}$
R4 COF + F \rightarrow CO + F ₂	$1.0 \times 10^{13} T^{0.5} e^{-16.429/T}$
R5 COF + COF \rightarrow COF ₂ + CO	$1.07 \times 10^8 T^{0.5} e^{695/T}$
R5' COF ₂ + CO \rightarrow COF + COF	$1.0 \times 10^{11} T^{0.5} e^{-11.658/T}$
R6 F ₂ + Ar \rightarrow F + F + Ar	$1.52 \times 10^{12} e^{-12.038/T}$
R6' F + F + Ar \rightarrow F ₂ + Ar	$1.40 \times 10^{11} e^{8097/T}$

^a Units of cubic centimeters, °K, mol, and sec. Energy of reaction in exponential terms is calculated from heat of formation of 0°K for COF₂ ($\Delta H_f = -150.96$ kcal/mol), COF ($\Delta H_f = -77.41$ kcal/mol), CO ($\Delta H_f = -27.2$ kcal/mol), and F ($\Delta H_f = 18.36$ kcal/mol). ^b RRK rate constant obtained by curve-fitting 2:100 COF₂-argon kinetic data for total concentration of 6.2×10^{-6} mol/cm³. *M* is taken to be maximum number of vibrational degree of freedom for a nonlinear COF molecule. Critical frequency is assumed to be same as first (C-F) bond in COF₂. ^c Preexponential factor determined from JANAF entropy of reaction and curve-fit of reverse reaction. ^d Obtained from experimental dissociation rate constant [R. W. Diesen, *J. Chem. Phys.*, **44**, 3663 (1963)] and JANAF equilibrium constant.

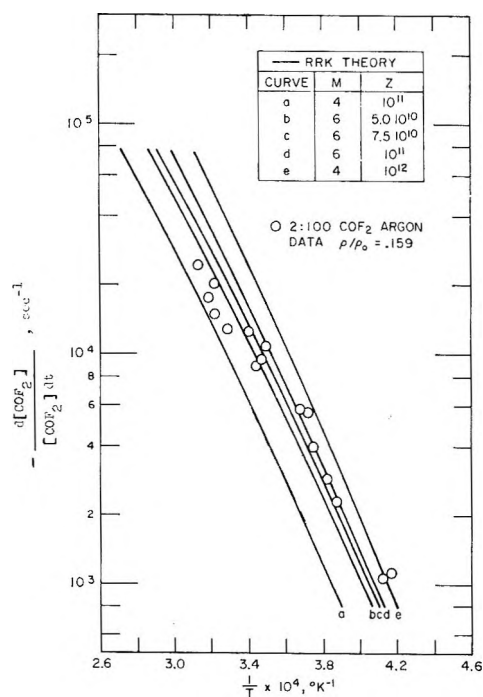


Figure 11. Parametric analysis of COF₂ first-order rate constants with RRK rate integrals.

reaction at 0°K in the exponential term and curve fitting measured COF₂ profiles over the complete chemical relaxation period to establish the magnitude of the preexponential factor. Calculated COF₂ profiles are obtained from a nonequilibrium shock-tube computer program which solves simultaneously the Rankine-Hugoniot differential equations for a normal shock wave

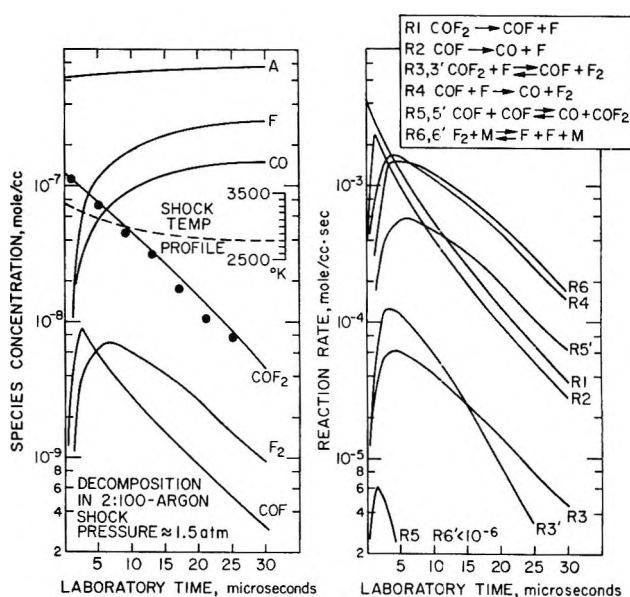


Figure 12. Nonequilibrium stream-tube species profiles behind incident shock wave into a 2:100 COF₂-argon mixture: ●, experimental COF₂ infrared measurements. Solid lines were calculated with chemistry and rate constants of Table II.

and the appropriate chemical kinetic equations. The present shock-tube computer program also includes the effect of wall boundary layer on the temperature and density behind the shock front (see Appendix). Species profiles typical of a chemically relaxing shock wave into a 2:100 COF₂-Ar mixture are displayed in Figure 12. Also depicted in the figure are the chemical rates of the decomposition reactions. It is seen for these particular

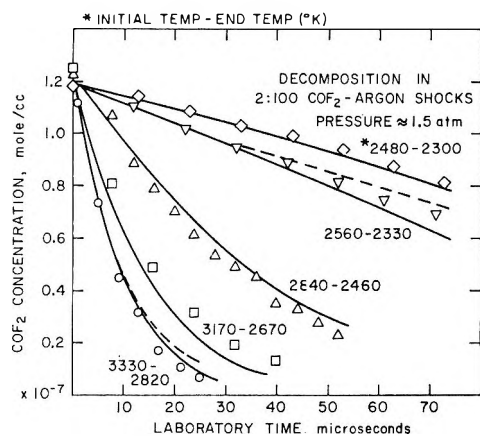


Figure 13. COF₂ history behind incident shock waves. Symbols are experimental infrared data. Solid lines are nonequilibrium stream-tube kinetic profiles including wall boundary layer effects. Broken lines are same calculations with wall boundary-layer effect deleted.

experimental conditions that the COF₂ thermal dissociation rate (R1) dominates the first 20% of COF₂ decomposition and then later R5' becomes the most important path for COF₂ removal.

Similar calculations were carried out for the 5:100 COF₂-argon mass spectrometer experiments in order to check that R1, over the first 50 μsec of reaction time, was the dominant mechanism for COF₂ decomposition. The results of the calculation showed that R5' would have contributed on the average less than 30% to the COF₂ decomposition mechanism.

The reasonableness of the chemistry and rate constants in Table II to predict experimental COF₂ decomposition profiles is demonstrated in Figure 13. The experimental points were corrected for temperature by making use of the calculated shock-temperature profile and the measured temperature dependence of the COF₂ 5.25-μ emission band given in Figure 5. The solid curves in Figure 13 are computed with the nonequilibrium shock-tube program including wall boundary layer corrections to temperature and density behind the shock front. The broken curve is calculated without the boundary layer corrections to temperature and density behind the shock front. For the experimental conditions chosen, the boundary layer effect is negligible near the shock front but does have a noticeable influence on the analysis of the data taken at long times behind the shock wave. In Figure 14, various chemical models for COF₂ decomposition are compared to assess their compatibility with the experimental data. According to the sensitivity of the rate data and the curve fits of Figure 14, the rate constants of Table II should be considered only as probable values and at best to within a factor of 10.

Discussion

Experimental rate constants for COF₂ dissociation were obtained from incident and reflected shock data

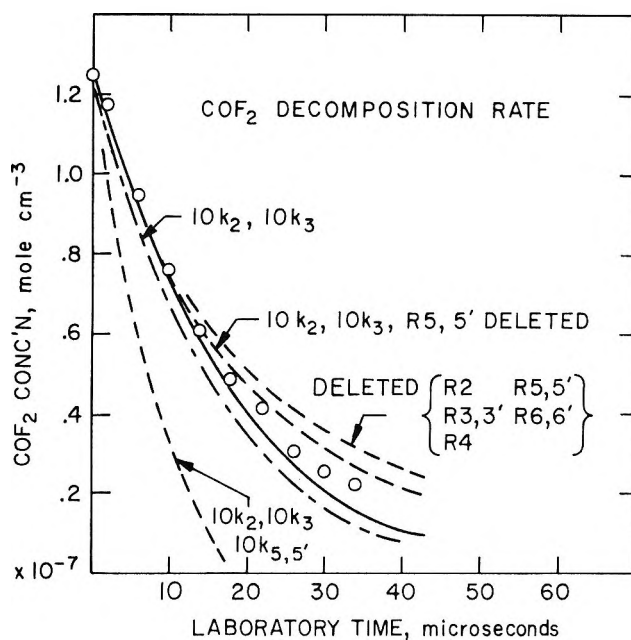


Figure 14. Comparison of several chemical models for COF₂ decomposition behind incident shock wave: O, experimental infrared data of decomposed 2:100 COF₂-argon mixture at 1.5 atm and 3095°K.

covering a 100-fold range in pressure and a temperature interval from 2400 to 3600°K. Gas properties in the reflected shock region were checked for consistency with incident gas properties by comparing the COF₂ emission at the reflected shock front with that at the incident shock front before dissociation and over a common temperature interval (see Figure 5). Oscillogram records of COF₂ emission in reflected shocks (Figure 3) were made to show the COF₂ emission ramp in the incident wave before the arrival of the reflected wave. The steady COF₂ emission in the incident gas shows that the COF₂ molecules were not undergoing dissociation and appear to be in vibrational equilibrium. Hence, under the conditions of the present experiments, the gas properties in the reflected region can be ascertained from ideal-gas reflected shock relationships.¹⁶

The experimental COF₂ rate constants in this study were analyzed according to RRK theory. Theoretical kinetic parameters were determined from a set of rate constants taken near 1.4 atm total pressure and over a temperature range from 2400 to 3200°K. Theoretical rate constants based on these kinetic parameters were checked for consistency against the other experimental data (Figures 7 and 8).

The value of the Arrhenius preexponential factor *A* used in the RRK rate integral was obtained by extrapolating the experimental data to the high-pressure unimolecular limit and is close to values (10¹² to 10¹⁴ sec⁻¹) usually considered "normal" for unimolecular

(16) A. G. Gaydon and I. R. Hurle, "The Shock Tube in High-Temperature Chemical Physics," Reinhold Publishing Corp., New York, N. Y., 1963, pp 24-27.

reactions. The number of "effective" oscillators used in the RRK rate integral to fit the apparent first-order rate constants was chosen to be 6, which is the total number of normal modes in COF_2 and one more than the maximum number indicated by RRK theory for this type of molecule. However, if the theory is expanded to include rotational degrees of freedom, the maximum number would be 6.5. Values of m less than 6 were not considered because they resulted in fits whose temperature dependences are qualitatively steeper than the trend indicated by the data. Use of values greater than 6 would have resulted in unusually low Z numbers. Although the kinetic parameters obtained in this work are somewhat vagarious, nonetheless, it is instructive to use them in examples to compare other theoretical relations with experiment.

Theoretically the transition pressure for a unimolecular reaction is approximately related to the high-pressure frequency factor A by

$$A[\Delta E/(E_0 + \Delta E)]^m RT = pZ \quad (3)$$

where at moderate pressures ΔE on the average has the value $(m + 1)RT$.¹⁷ With $E_0 = 91.912$ kcal/mol and the experimental values of $m = 6$, $A = 6.14 \times 10^{11}$ sec⁻¹, the transition pressure for the unimolecular dissociation of COF_2 in argon at 3000°K is calculated to be 15.4 atm, which appears to be in line with the observed pressure dependence (Figure 9).

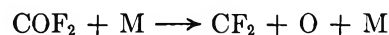
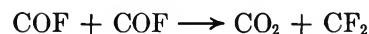
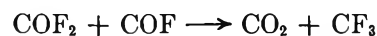
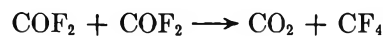
The concept that in a unimolecular reaction the activated complex is in quasi-equilibrium with the normal molecule has led to the formulation of Eyring's transition state theory and a rationale for the Arrhenius preexponential factor. The quantity A is related

$$A = \left(\frac{kT}{h}\right) \frac{Q^\ddagger}{Q} \quad (4)$$

where Q^\ddagger is the partition function of the activated complex and Q is the partition function of the normal molecule. Theoretically to evaluate the preexponential factor for the COF_2 unimolecular dissociation, the electronic contribution to the partition function for both the complex and normal molecule is assumed to be unity. The transition state of the activated COF_2 molecule is next thought of being a COF fragment bounded by a weakly attached fluorine atom. It is also assumed that the COF fragment rotates and vibrates independently of its satellite fluorine atom. On the basis of the model presented, the rotational partition function of the activated complex was calculated with the moments of inertia for a COF radical. The ratio of the rotational partition function of the activated complex to that of the normal molecule was thus calculated to be 0.348. Moments of inertia for COF_2 and COF were obtained from the JANAF thermochemical tables.¹⁸ In its activated state, the deformation modes of the COF_2 molecule are assumed to be drastically

weakened in which case the vibration function of the complex is largely determined by the V_1 , V_2 , V_4 modes of the COF_2 molecule, that is, the in-phase (C-F), the (C=O) vibration and the out-of phase (C-F) vibration. Accordingly, the ratio of the vibrational partition functions was calculated to be 0.316. Substitution of these numbers for the ratio of the partition functions in eq 4 gives a calculated preexponential factor of 6.86×10^{11} sec⁻¹ at 3000°K. Although the result is in remarkable agreement with the experimental value, the coincidence is believed to be more fortuitous than real, since the nature of the complex, though reasonably assumed, must be regarded as only a guess.

It is concluded from mass spectra obtained in the present study that the fluorocarbon species CF_4 , CF_3 , and CF_2 , which are produced by C_2F_4 oxidation, are not products of COF_2 decomposition. Infrared measurements of 4.3- μ radiation did not show kinetic evidence for CO_2 production, nor did ultraviolet measurements at 2660 Å indicate the existence of CF_2 species in the COF_2 decomposition mixtures. In accordance with these observations, the reactions



appear to be unimportant in the decomposition chemistry of COF_2 .

Acknowledgment. The author expresses thanks to S. J. Sillers for programming the chemical nonequilibrium stream-tube computer problem and to R. R. Brochu for assisting in the collection and reduction of the shock-tube data.

Appendix. Formulation of a Generalized Chemical Nonequilibrium Stream-Tube Computer Program with Wall Boundary Layer Effects

Recently, Teare has pointed out that in shock-tube chemical kinetic studies, the accuracy of the results may be significantly impaired, if variations in the flow velocity and state properties due to wall boundary layer growth are neglected in the data analysis.¹⁹ Generally it is understood that the presence of wall boundary layer in the shock tube causes the gas behind the shock wave to behave as if it were passing through a divergent channel where the flow velocity decreases and the gas density and thermodynamic temperature increase with increasing distance. An analytical basis for these effects is provided by the theoretical work of Mirels, who

(17) Reference 14, pp 230-231.

(18) "JANAF Thermochemical Tables," D. R. Stull, Ed., Dow Chemical Co., Midland, Mich.

(19) M. Camac, R. M. Feinberg, and J. D. Teare, Avco Everett Research Laboratory Report 245 (1966).

has made use of Duff's concept of a "limiting separation distance" to obtain a local similarity solution for the boundary layer displacement thickness.²⁰ The constraints placed on the problem require that the mass per unit time integrated over the entire shock tube area be conserved and that the mass of gas entering the shock front be equal to the mass entering the boundary layer at the limiting separation distance.

For the purpose of analyzing shock-tube chemical kinetic data taken at long times behind the shock front, a nonequilibrium stream-tube computer program has been developed to include area variation due to wall boundary layer growth. The quantities describing the flow in wave-stationary coordinates are shown in Figure 15, which is similar to the diagram given in ref 20. The "jump" conditions across the shock wave are obtained from the Hugoniot conservation equations²¹

$$\text{mass: } \rho_1 U_s = \rho_{e0} u_{e0}$$

$$\text{momentum: } P_1 + \rho_1 U_s^2 = P_{e0} + \rho_{e0} u_{e0}^2$$

$$\text{enthalpy: } h_1 + 1/2 U_s^2 = h_{e0} + 1/2 u_{e0}^2$$

The equations governing the chemical relaxation zone behind the shock wave are expressed in time differential form by

$$\text{continuity: } \left. \frac{d(\rho u A)}{dt_p} \right|_{\rho_1 U_s A_0} = 0$$

$$\text{momentum: } \left. \frac{dP}{dt_p} + u \frac{du}{dt_p} \right|_{P_1 \rho_1 U_s} = 0$$

$$\text{enthalpy: } \left. \frac{d(h + 1/2 u^2)}{dt_p} \right|_{h_1 U_s} = 0$$

For a laminar boundary layer (Reynolds number less than 5×10^7) the area variation of the divergent channel from Mirels' results is given by

$$A_0/A = 1 - (x/x_l)^{0.5}$$

The ideal-gas equation

$$P = (\rho \sum c_i / \sum c_i M_i) RT$$

is used to relate the thermodynamic temperature to pressure and density. The molar enthalpy of each species is expressed in terms of temperature by a power series

$$h_i = [L_1 T + 1/2 L_2 T^2 + 1/3 L_3 T^3 + 1/4 L_4 T^4 - L_5 T^{-1} + L_6]_i$$

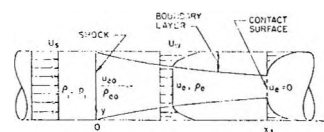
in which the temperature coefficients are determined from curve fits of JANAF thermochemical data. The variation in species concentration resulting from chemical reaction and volumetric change behind the shock wave is given by

$$\frac{dc_i}{dt_p} - \frac{c}{\rho} \frac{d\rho}{dt_p} = \sum_j \nu_{ij} [\pi_k c_k^{\nu_{ki}}] A_{fj} T^{n_i} \exp\left(\frac{E_{fi}}{RT}\right) - \sum_j c_i^{\nu_{ij}} [\pi_m c_m^{\nu_{mj}}] A_{rj} T^{n_i} \exp\left(\frac{E_{rj}}{RT}\right)$$

where the positive term on the right of the equality reflects the sum of the chemical rates leading to species production and the negative term, the rates for removal. Events measured in laboratory time are related to the particle time in the shock tube by

$$t_l = \frac{x}{U_s} = \int \left(\frac{u_e}{U_s}\right) dt_p$$

The above set of differential equations is solved on an IBM 360 computer, using a fourth-order predictor-corrector integration scheme. The predictor-corrector method was devised to vary its own integration interval depending on the estimated truncation error available at each step. A Runge-Kutta method was used to obtain the starting values.²² However, a computa-



SHOCK TUBE FLOW DIAGRAM FOR FIXED SHOCK WAVE COORDINATE SYSTEM INCLUDING WALL BOUNDARY LAYER DEVELOPMENT

SYMBOLS:

A	SUBSONIC FLOW CROSS-SECTIONAL AREA, PRE-EXPONENTIAL FACTOR
c	SPECIES CONCENTRATION
E	ACTIVATION ENERGY
h	STATIC ENTHALPY
M	GRAM MOLECULAR WEIGHT
n	TEMPERATURE EXPONENT
p	STATIC PRESSURE
R	IDEAL-GAS CONSTANT
T	THERMODYNAMIC TEMPERATURE
t	TIME
U	SUBSONIC FLOW VELOCITY
U _s	SHOCK WAVE VELOCITY
x	DISTANCE BEHIND SHOCK WAVE
x _l	LIMITING SEPARATION DISTANCE
ρ	DENSITY
ν	REACTANT STOICHIOMETRIC-COEFFICIENT

SUBSCRIPTS:

1	CONDITION AHEAD OF SHOCK WAVE
0	SHOCK FRONT CONDITION
e	CONDITION BEHIND SHOCK WAVE
f	FORWARD REACTION
i, k	PROPERTY OF I TH SPECIES, ETC.
j	I TH REACTION
l	LABORATORY COORDINATE
p	PARTICLE COORDINATE
r	REVERSE REACTION

Figure 15. Shock tube flow diagram for fixed shock wave coordinate system including wall boundary layer development.

tional difficulty imposes itself on the formulation of this type of problem, since the time derivative of the area goes to infinity when x approaches zero. Teare has overcome this singularity by assuming for small x 's that the area variation is a linear function dependent on the translational-rotational relaxation thickness of the shock wave. In the present program, the computa-

(20) H. Mirels, *Phys. Fluids*, **6**, 1201 (1963).

(21) Reference, 16 p 14.

(22) A. Ralston and H. S. Wilf, "Mathematical Methods for Digital Computers," John Wiley & Sons, New York, N. Y., 1964.

tional difficulty is avoided by simply introducing an arbitrary parameter to start the area change at an infinitesimal distance behind the shock front. Calculations show that the results are virtually unaffected by this parameter for values less than 0.0001 of the chemical relaxation distance.

The computer program is general in that the inputs to the calculation are the shock velocity, state of the gas

ahead of the shock wave, and the chemical species and reactions to be considered. The thermodynamic properties of the species used in the calculation are automatically furnished by a computer tape library containing almost every molecule which may be of interest for shock tube study. The computer program is capable of solving chemistry problems with up to 100 reactions and 200 species.

Flash Photolysis of Hydrocarbons in the Far-Ultraviolet. I. Ethane^{1a}

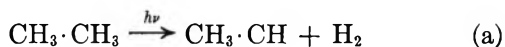
by B. C. Roquette^{1b}

Radiation Research Laboratories, Mellon Institute, Pittsburgh, Pennsylvania 15213 (Received July 14, 1969)

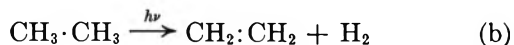
The flash photolysis of ethane in the far-uv has been studied with a newly developed flash lamp of 10^{21} quanta/sec intensity below 1650 Å. The products of decomposition were primarily hydrogen, methane, and ethylene with propane and *n*-butane amounting to 2–5% of the total product. Both ethane-1,1,1-*d*₃ and an equimolar mixture of ethane-*d*₀–ethane-*d*₆ were photolyzed, and the isotopic compositions of hydrogen and methane in the product were measured. The result shows that the molecular detachment of hydrogen is the major primary process in the flash decomposition of ethane: $C_2H_6 \xrightarrow{h\nu} C_2H_4 + H_2$. Also, the methane-forming reactions appear to be one-third as important as the hydrogen-producing processes. The effect of different rare gas continuum as a flash light source on the decomposition of ethane has been investigated.

Introduction

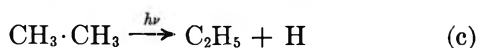
In recent years, attention has been focused on the mechanism of the decomposition of hydrocarbons in the far-uv.² In particular, the decomposition of ethane has been the subject of several investigations.³ In most of these studies a low-intensity rare gas resonance lamp⁴ was used to initiate photodecomposition. It appears that, in the decomposition of ethane, the molecular detachment of hydrogen from one carbon atom



constitutes the major primary step and that the elimination of one hydrogen atom from each carbon atom



is a much less important process. In these studies it appears that the primary formation of ethyl radicals and hydrogen atoms as originally proposed by Wijnen⁵ prove to have little significance. However, in the



mercury ³P₁ sensitized decomposition of ethane,⁶ primary step (c) appears to be the important reaction.

In the continuous irradiation technique which has previously been used in the investigation of the ethane decomposition, it is possible that secondary reaction of the products might obscure the importance of (c). The end product analysis in flash photolysis, where the combination reaction of radicals may become more significant than in the low-intensity photolysis, is performed to reexamine the direct decomposition of ethane.

Experimental Section

The sketch and the detailed construction of the flash lamp used in this investigation have been described elsewhere.⁷ Argon, krypton, or xenon at a pressure of

(1) (a) Supported in part by the U. S. Atomic Energy Commission. Presented at the 153rd National Meeting of the American Chemical Society, Miami Beach, Fla., April 10–14, 1967. (b) Department of Chemistry, University of Minnesota, Morris, Minn. 56267.

(2) "Advances in Photochemistry," W. A. Noyes, Jr., G. S. Hammond, and J. N. Pitts, Jr., Ed., John Wiley & Sons, New York, N. Y., Vol. 3, 1964, p 204.

(3) (a) See ref 2, page 210; (b) J. R. McNesby, *et al.*, *J. Chem. Phys.*, **40**, 1099 (1964); (c) T. Tanaka *et al.*, *ibid.*, **42**, 3864 (1965); (d) D. R. Crosley, *ibid.*, **47**, 1351 (1967).

(4) H. Okabe, *J. Opt. Soc. Amer.*, **54**, 478 (1964).

(5) M. H. J. Wijnen, *J. Chem. Phys.*, **24**, 851 (1956).

(6) S. Bywater and E. S. R. Steacie, *ibid.*, **19**, 326 (1951).

(7) B. C. Roquette, *J. Appl. Opt.*, **6**, 415 (1967).

Table I: Flash Photolysis of Equimolar Mixture of C₂H₆-C₂D₆ Using Different Rare Gases as Flash Discharge Media^a

Pressure, mm	Rare gas in flash tube, 15 mm	Hydrogen, μmol	% Hydrogen			Methane, μmol	% Methane ^c				
			H ₂	HD	D ₂		CH ₄	CH ₃ D	CH ₂ D ₂	CD ₃ H	CD ₄
111.0	Argon	0.94	64.3	7.3	28.4	0.27	38.5	10.8	8.9	15.5	26.3
132.5	Argon	0.90	65.0	7.1	27.9	0.23	39.6	11.4	6.3	15.6	27.1
128.0	Krypton	1.07	63.9	7.8	28.3	0.34	36.6	9.4	11.3	15.2	27.4
111.0	Xenon	0.48	67.9	6.2	25.8	0.15	41.3	8.7	12.3	14.7	24.0
7-9 ^b	1067 Å		43.0	19.0	38.0		42.0	4.0	...	9.0	45.0
15.0 ^b	1236 Å		53.0	12.0	35.0		40.0	4.0	...	5.0	50.0
35.0 ^b	1470 Å		65.0	3.0	32.0		65.0	3.0	...	7.0	25.0

^a All experiments were carried out with 10 flashes of 1215 J per flash. ^b Data taken from J. R. McNesby, *et al.*, *J. Chem. Phys.*, **42**, 3329 (1965). ^c For analysis of methanes, the mass spectrometer was calibrated with standard mixed methanes.

Table II: Flash Photolysis of CH₃CD₃ Using Different Rare Gases as Flash Discharge Media^a

Pressure, mm	Rare gas in flash tube, 15 mm	Hydrogen, μmol	% Hydrogen			Methane, μmol	% Methane				
			H ₂	HD	D ₂		CH ₄	CH ₃ D	CH ₂ D ₂	CD ₃ H	CD ₄
111.0	Argon	1.04	50.2	24.7	25.1	0.99	4.8	4.2	12.8	48.9	29.3
162.5	Argon	1.01	51.2	23.9	24.9	0.68	6.0	4.9	12.0	48.5	28.6
126.0	Krypton	0.79	51.3	24.5	24.2	0.25	11.3	18.6	13.1	44.7	12.2
194.0	Krypton	1.26	51.8	24.0	24.2	0.35	10.6	16.8	14.9	44.5	13.2
128.0	Xenon	0.76	52.3	23.2	24.5	0.62	4.8	4.0	11.0	49.7	30.5
172.0	Xenon	1.00	52.2	23.5	24.3	0.48	7.6	9.9	14.0	46.6	21.9
10.0 ^b	1236 Å		44.6	30.3	25.1		2.0	22.4	5.6	65.8	4.2
25.0 ^b	1470 Å		51.6	19.5	28.9						

^a All experiments were carried out with 10 flashes of 1215 J per flash. ^b Data taken from I. Tanaka, *et al.*, *J. Chem. Phys.*, **42**, 3864 (1965), and J. R. McNesby, *et al.*, *ibid.*, **40**, 1099 (1964).

15 mm has been used in the lamp as a discharge medium. In most of the experiments reported here, a 120- μF capacitor bank charged up to 6.0 kV was discharged through the lamp to produce the photochemically effective light. The absorbed intensity was $\sim 10^{21}$ quanta/sec. The effective light was a rare gas continuum which covers the wavelength region 1600-1040 Å. In the case of argon, krypton, and xenon these continua cover the regions 1680-1040 Å, 1880-1236 Å, and 2250-1470 Å, respectively.⁸

The reaction cell (~ 200 cc), which was separated from the lamp by means of an 8 cm² and 4 mm thick LiF window, was permanently connected through a mercury cutoff to the analytical system. The latter consisted of two LeRoy traps, a solid nitrogen trap, a small mercury diffusion pump, and a toepler pump-gas buret. After the reaction, the noncondensable fraction at -210° was toepled into a sample tube for mass spectrometric analysis. The condensable fraction was analyzed by gas chromatographic equipment provided with a flame ionization detector and temperature programming arrangement. A 2-m silica gel column was used for complete analysis of the condensable products.

Research grade ethane from Phillips Petroleum Co. was purified by cold temperature distillation through a silica gel trap at -78° . Gas chromatographic analysis

of this sample indicated the presence of only one constituent. Ethane-1,1,1-*d*₃ was supplied by Volk Radiochemical Co. with stated purity of 99 atom per cent of deuterium, while the sample of C₂D₆, also from Volk, contained 3.5% of C₂D₅H. These deuterated samples were degassed prior to use.

Results

The main products of the decomposition of ethane were H₂, CH₄, and C₂H₄. Propane and *n*-butane were detected to the extent of 2-5% of the total products. In all experiments conversion was less than 0.01% per flash. The results of the analysis of these products from an equimolar mixture of C₂H₆-C₂D₆ and CH₃D₃ with different rare gas continuum and at different pressures are summarized in Tables I and II. For comparison, the results of the isotopic analysis of hydrogen and methane from continuous photolysis experiments are included in the same table.

The plot of hydrogen yield per ten flashes as a function of the applied voltage squared is shown in Figure 1. Three experiments were carried out with different incident intensities. All the products were analyzed quantitatively in these runs. Since propane and *n*-

(8) Y. Tanaka, A. S. Jursa, and F. J. LeBlanc, *J. Opt. Soc. Amer.*, **48**, 304 (1958).

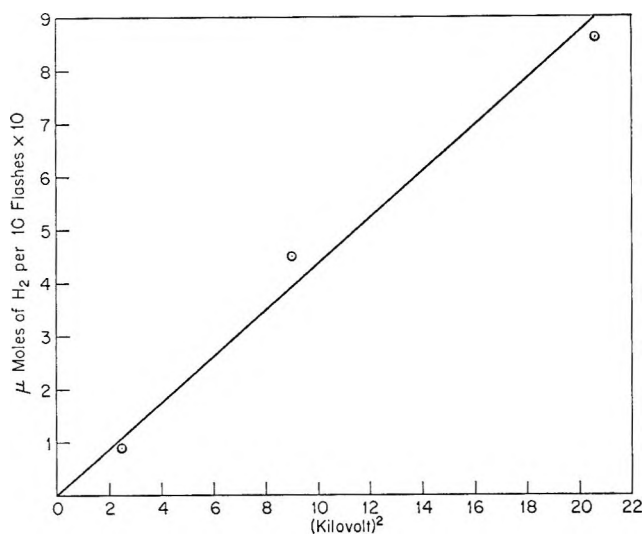


Figure 1. Hydrogen yield as a function of flash intensity (kV^2).

butane were present in the reaction mixture in very small amounts, their analyses were not very reliable. Thus, in the material balance calculation given in Table III, propane and *n*-butane were not taken into

Table III: Material Balance in the Flash Photolysis of C_2H_6^a

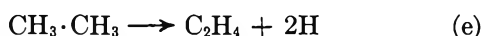
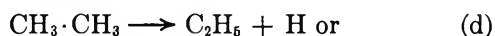
Voltage, kV	Products, μMole			Ratio H/C
	H_2	CH_4	C_2H_4	
1.5	0.09	0.01	0.09 ^b	3.05
3.0	0.45	0.12	0.49	3.03
4.5	0.86	0.29	0.90	3.10

^a Initial pressure 171.0 mm. Products obtained per 10 flashes. Minor products were not taken into account for carbon-hydrogen calculation. ^b Assumed to be equal to hydrogen yield.

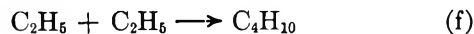
account. The average ratio, $\text{H/C} = 3.06$, is in good agreement with the theoretical ratio $\text{H/C} = 3.00$ considering the difficulties involved in the analysis of ethylene in the presence of the large excess of ethane.

Discussion

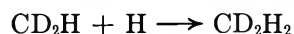
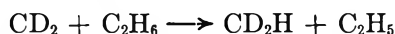
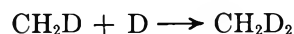
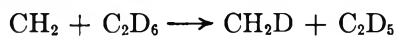
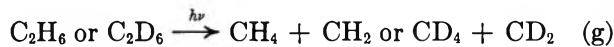
As it has been mentioned previously, the primary processes (a) and (b) in the vacuum-uv photolysis of ethane appear to be well established.^{2,3} Our results on the flash photolysis of ethane indicate that molecular detachment of hydrogen is the major primary step. From the isotopic analysis of hydrogen (Table I), assuming complete random mixing of hydrogen atoms, it may be shown that about 87% of the hydrogen is formed by a molecular process. The remaining 13% appears to form from atomic processes such as



In the present investigation, it is rather difficult to prove which of the two hydrogen atom forming primary steps is more important. Nevertheless, it appears that reaction (d) occurs to a certain extent as *n*-butane is a minor product



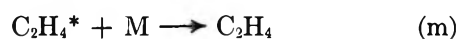
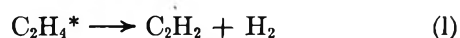
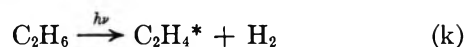
The results given in Table I indicate that a change of rare gas continuum does not change the isotopic hydrogen distributions within the limit of experimental error. However, the distribution of isotopic methane is changed. It is interesting to note that CH_2D_2 is a product of continuous photolysis of CH_3CD_3 but not of C_2H_6 - C_2D_6 mixture. This is in contrast to the flash photolysis results where CH_2D_2 is a product of the decomposition of CH_3CD_3 and C_2H_6 - C_2D_6 mixture as well. The exact source of this difference is not well understood at this time. However, we believe that in our system methylene radical is the precursor of CH_2D_2 and it most probably reacts as follows to produce CH_2D_2 .



The abstraction of a hydrogen by methylene from hydrocarbon to form methyl, which recombine to give ethane, was observed by Frey.⁹ Thus the proposed mechanism for the formation of CH_2D_2 does not appear to be unreasonable. The isotopic analysis of methane also indicates that about 38% of the total methane species is formed by the molecular detachment process compared to 90% in the low intensity system. The mixed methane ($\text{CH}_3\text{D} + \text{CD}_3\text{H}$) in amounts of about 25% appears to have been produced according to the reaction sequence



In their investigation of the continuous photolysis of ethane, McNesby, *et al.*,³ have shown that excited ethylene is produced by reaction (k), which either decomposes to acetylene and hydrogen or deactivates to normal ethylene



(9) H. M. Frey, *J. Amer. Chem. Soc.*, **79**, 1259 (1957); **80**, 5005 (1958); *Proc. Roy. Soc.*, **A250**, 409 (1959); *Proc. Chem. Soc.*, 318 (1959).

In our system, we are unable to detect acetylene.¹⁰ Since the initial pressure of ethane is >100 mm, it is very likely that if excited ethylene is formed, it is quickly deexcited by collision to normal ethylene.

Experimental results on the CH_3CD_3 photolysis (Table II) indicate that the molecular detachment of hydrogen ($\sim 75\%$) takes place from the same carbon atom. The formation of $\sim 25\%$ of HD from CH_3CD_3 may occur by a four-center reaction mechanism involving hydrogen atoms from both the carbon atoms. It is noted from the data of the low intensity photolysis that elimination of molecular hydrogen from the terminal carbon atom was less favorable with a decrease of wave-

length. However, in flash photolysis this appears to be invariant with a change in rare gas continuum.

In brief it may be pointed out that the mechanism of the photodecomposition of ethane, both by continuous and flash irradiation, appears to be generally similar, with, however, a few minor differences. These differences we believe are due to different secondary reactions of products in the continuous and flash photolysis.

(10) In order to be sure that small amounts of acetylene in the reaction products did not get absorbed on the "O" rings, an artificial mixture of small amount of acetylene and large excess of ethane was introduced in the reaction cell; about 1 hr later it was condensed out of the reaction cell and analyzed. It was noted that within the limit of experimental uncertainty, acetylene was quantitatively recovered.

Properties of Trapped H and D Atoms Produced

by the Photolysis of HI in $3\text{MP-}d_{14}$ Glass¹

by Mervyn A. Long and John E. Willard

Department of Chemistry, University of Wisconsin, Madison, Wisconsin 53706 (Received September 12, 1969)

Photolysis of HI dissolved in perdeuterated 3-methylpentane ($3\text{MP-}d_{14}$) glass at any temperature from 4 to 50°K produces trapped H atoms and trapped D atoms observable by esr, as well as C_6D_{13} radicals formed by abstraction of D from the $3\text{MP-}d_{14}$ by hot H. C_6H_{13} radicals, but no trapped H atoms, are produced by photolysis of HI in $3\text{MP-}h_{14}$ under identical conditions, indicating a major effect of isotopic substitution on the trapping capability of the matrix. The initial quantum yield of trapped H in $3\text{MP-}d_{14}$ (ca. 0.03) is independent of temperature over the range of at least $20\text{--}40^\circ\text{K}$ but decreases with time of photolysis until a steady-state concentration is reached, while the concentrations of C_6D_{13} and D continue to grow linearly. The fractional rate of decay of trapped H atoms following short illuminations decreases rapidly with time, but the decay curves for samples with different initial concentrations are superimposable after normalization for dose. The properties of trapped H produced in $3\text{MP-}d_{14}$ in Kel-F tubes are the same as when produced in quartz tubes. Trapped H atoms may be produced by photolysis of empty quartz tubes after certain conditions of aging and γ radiolysis. Trapped D (or H) atoms are not produced by the radiolysis of $3\text{MP-}d_{14}$ (or $3\text{MP-}h_{14}$) with or without dissolved HI present, although photolysis of HI in radiolyzed $3\text{MP-}d_{14}$ produces them. The implications of the data with respect to the mechanism of H atom trapping and decay are discussed.

Introduction

Recent investigations have shown that (a) hydrogen and deuterium atoms produced by photolysis of HI in perdeuterated 3-methylpentane ($3\text{MP-}d_{14}$) at $20\text{--}50^\circ\text{K}$ can be trapped in the matrix and observed by their esr spectra;² (b) photolysis of HI in perprotiated 3-methylpentane ($3\text{MP-}h_{14}$) under identical conditions does not produce trapped H atoms;² (c) radiolysis of $3\text{MP-}d_{14}$ under conditions demonstrated to trap D atoms produced by photolysis of HI does not produce trapped D atoms.³

The present paper reports further investigations of

the photolysis of HI in $3\text{MP-}d_{14}$ and $3\text{MP-}h_{14}$ designed to answer the following questions. (1) What are the kinetics of growth of trapped H and D atoms and of free radicals during photolysis of HI in $3\text{MP-}d_{14}$? (2) What are the kinetics of decay of trapped H and D atoms? (3) What do the kinetics indicate about the mechanisms of trapping and decay? (4) Does D

(1) This work has been supported in part by U. S. Atomic Energy Commission Contract AT(11-1)-1715 and by the W. F. Vilas Trust of the University of Wisconsin.

(2) D. Timm and J. E. Willard, *J. Amer. Chem. Soc.*, **91**, 3406 (1969).

(3) D. Timm and J. E. Willard, *J. Phys. Chem.*, **73**, 2403 (1969).

atom production occur by a displacement by hot H atoms or by photolysis of DI formed by disproportionation ($C_6D_{13} + I \rightarrow C_6D_{12} + DI$)? (5) Are there conditions under which 3MP- h_{14} will trap H atoms as they are trapped in 3MP- d_{14} ? (6) What is the nature of the inhibiting action of isobutene on reactions initiated by photolysis of HI in hydrocarbon matrices? (7) Are H atoms ever photolytically produced in the walls of the quartz sample container?

In addition to investigation of these questions, the fact that radiolysis of 3MP- d_{14} does not produce D atoms has been further confirmed.

Experimental Methods

The methods used for preparing purified degassed samples of HI in hydrocarbons and for examining them with a Varian 4500 X-band esr spectrometer from 10 to 77°K during and after photolysis with a medium pressure mercury lamp have been described.²⁻⁴ In the present work photolysis was also carried out in the 4-10°K range by mounting the esr sample tube in a double-walled quartz tube, 11 mm o.d., 5 mm i.d., and 55 cm long, inserted through the sample opening of the Varian 4531 multipurpose esr cavity. The annulus of the tube was evacuated. The portion of the tube below the cavity passed through a tight-fitting 10-cm thick polyurethane stopper into a 2-l. dewar of liquid helium mounted in a styrofoam box filled with liquid nitrogen. Controlled application of gaseous helium pressure to the surface of the liquid helium, by means of a second tube through the stopper, caused liquid helium to rise in the dewar tube sufficiently to maintain the sample at 4° during photolysis. With less pressure, a flow of evaporating helium such as to provide sample temperatures in the 4-10°K range was maintained.

Measurements of rapid growth and decay of H atoms were made by setting the magnetic field of the esr spectrometer at the value of one of the lines of the hydrogen doublet and allowing the chart recorder to plot the change in concentration as a function of time continuously.

When tubes of liquid 3MP are immersed in liquid nitrogen at 77°K, the 3MP- h_{14} or 3MP- d_{14} changes to a glass with a viscosity⁵ of about $10^{12.5}$ P. Usually this glass is uncracked but cracks when the temperature is subsequently lowered. Such cracking is often accompanied by fracturing of the quartz sample tube. The fracturing can usually be avoided if cracking of the matrix glass is induced at 77°K by repeated partial melting and refreezing, before lowering the temperature further.

Tritiated 3MP [3MP- d_{14} (3H) or 3MP- h_{14} (3H)] was prepared⁶ with specific activities of about 14 Ci g^{-1} by gently agitating 1-ml samples of degassed 3MP with 10 Ci of T_2 gas in the presence of 0.5 g of pre-degassed Raney nickel at 60° for 48 hr. Essentially all of the tritium entered organic combination. Esr sample

tubes containing the high specific activity 3MP were safely handled outside the tritium hood during esr examination by encasing them in 4 mm o.d., 3 mm i.d. Kel-F tubing turned from 0.25-in. o.d. tubing. The Kel-F was sealed at each end by forcing it into the closed end of a glass test tube, while the latter was gently heated in a gas flame. The Kel-F is sufficiently transparent to radiation from the mercury lamp at wavelengths absorbed by the HI so that the rate of growth of the trapped H atom signal from the photolysis of HI-3MP- d_{14} samples in such tubes is 30% or more of the rate without the Kel-F.

The 3MP- d_{14} , obtained from Merck Sharp and Dohme, showed an optical density at 200 nm of ca. 0.2 for a 5-mm thickness of a degassed sample. After passage through a silica gel column, its optical density was less than 0.05. Such treatment did not change the properties with respect to trapping H atoms.

Results

Yields of Trapped H atoms, D Atoms, and Radicals. The quantum yields of trapped H atoms and of 3MP- d_{13} radicals produced during the first few seconds of photolysis of 1×10^{-3} mole fraction (mf) of HI in 3MP- d_{14} at 20, 30, and 40°K are unaffected by temperature (within the experimental error of $\pm 10\%$). This is shown by measurement of esr signal heights, corrected for the inverse proportionality of the esr sensitivity to temperature. This implies that the ratio of prompt geminate recombination of H and I, to abstraction of D by hot H atoms, to thermalization H followed by trapping, is independent of temperature over this range. The areas under the integrated first derivative signals for H and 3MP- d_{13} radicals after a few seconds irradiation indicated a quantum yield for trapped H production of about 0.03, assuming that the quantum yield of the 3MP- d_{13} radicals is 0.2.^{7,8} If the quantum yield of radical production is 0.2, the rate of light absorption in our experiments without filters was about 10^{14} photons sec^{-1} in the volume of the sample which was in the sensitive portion of the esr tube (*i.e.*, ca. 0.1 ml). The rate of consumption of HI was about 0.3%/min of illumination.

The initial rates of trapped H atom production are proportional to the incident light intensity (as varied by varying the position of the lamp and as determined from the rate of radical production), as expected. For illuminations of longer than a few seconds at 20-40°K, the rate of production of trapped H decreases, the rate

(4) D. Timm and J. E. Willard, *Rev. Sci. Instrum.*, **40**, 848 (1969).

(5) A. C. Ling and J. E. Willard, *J. Phys. Chem.*, **72**, 1918, 3349 (1968).

(6) M. A. Long, A. L. Odell, and J. M. Thorp, *Radiochim. Acta*, **1**, 174 (1963).

(7) J. R. Nash, R. R. Williams, and W. H. Hamill, *J. Amer. Chem. Soc.*, **82**, 5974 (1960).

(8) S. Aditya and J. E. Willard, *ibid.*, **88**, 229 (1966).

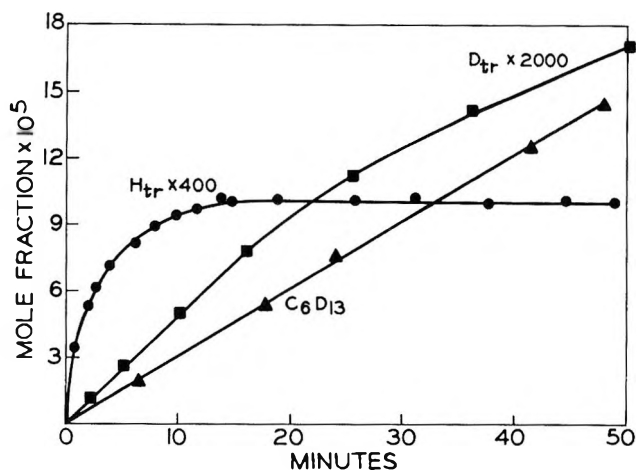


Figure 1. Growth of trapped H atoms, D atoms, and C_6D_{13} radicals during photolysis of 0.1 mol % of HI in 3MP- d_{14} glass at 30°K.

of decrease being greater the higher the temperature. Within about 12 min the concentration reaches a constant value (Figure 1) with the concentration at the plateau being lower at the higher temperatures. Rotation of the esr sample tube in the cavity by 180° after a 15-min photolysis makes $\leq 10\%$ difference in the rates of atom and radical production. The plateaus of H atom concentration have been observed for as long as 2 hr of illumination, during which the concentrations of C_6D_{13} radicals and D atoms continued to rise at nearly constant rates (Figure 1). The growth of D atoms in Figure 1 is plotted on a fivefold more sensitive scale than that of the H atoms; the quantum yield indicated is *ca.* 1×10^{-4} . The steady-state concentration of H atoms increases with increasing light intensity but is proportional to less than the first power, an increase by a factor of 1.8 having been observed after a fourfold increase in intensity.

The temperature of the sample of Figure 1 was raised from 30 to 60°K after 82 min of illumination and allowed to remain there for 15 min during which time all of the H and D atoms decayed, but the radical concentration was unchanged (*i.e.*, at *ca.* 2.5×10^{-4} mf). When the sample was returned to 30° and further illuminated, the D atom concentration grew at about the same rate as before while the H atom concentration grew at about 0.1, its initial rate at the start of the first illumination. When the sample was melted, refrozen, and again illuminated, the growth rates of all three species were equivalent to those at the start of the initial illumination.

In another experiment a concentration of about 6×10^{-6} mf of radicals was produced by a 2-min photolysis at 65°K of 3MP- d_{14} glass containing 1×10^{-3} mf of HI. No trapped H atoms were produced at this temperature. When the sample was then photolyzed at 30°K, trapped H atoms were produced at a rate indistinguishable from that in equivalent samples

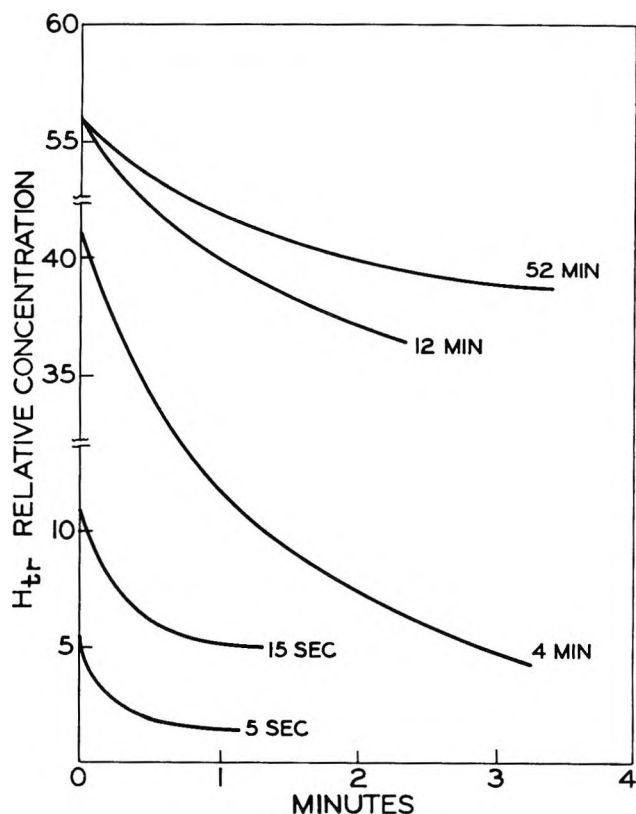


Figure 2. Decay of trapped H atoms produced by different times of equal intensity illumination of 0.1 mol % of HI in 3MP- d_{14} glass at 30°K.

which did not contain an initial concentration of radicals.

Decay Characteristics of the Atoms and Radicals. Figure 2 illustrates the initial rates of decay of H atoms following each of several durations of illumination. The initial decay rates are similar within experimental error following photolysis times of up to 4 min. Determinations following 12 and 52 min indicate decreased initial rates (atoms per second) following these longer photolysis times. Both the initial decay rate and the time required for 50% decay after a given dose indicated a positive temperature coefficient of decay rate (Table I).

Table I: Decay Rates of Trapped H Atoms in 3MP- d_{14} Glass

T, °K	Approx initial decay rates after 5-sec photolysis, % sec ⁻¹	Time for 50% decay, min		
		After 5-sec photolysis	After 15-sec photolysis	After 4-min photolysis
20	5	0.45	0.66	6.4
30	8	0.27	0.52	4.4
40	12	0.15	0.32	2.5

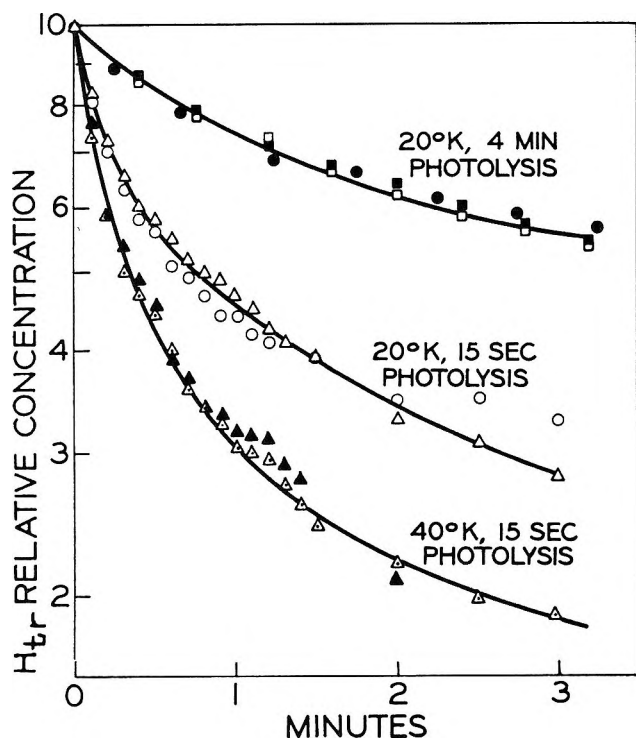


Figure 3. Decay of trapped H and D atoms formed by photolysis of 0.1 mol % of HI in 3MP- d_{14} : ●, D atoms; all other points H atoms. Data obtained following photolysis at different intensities have been normalized for initial concentration; relative light intensities: ■, 1; ○ and ▲, 2.5; □, ●, △, and △, 5.

In all cases the fractional decay rate of trapped H atoms decreases with increasing time of decay (Figure 3). When a sample in which the decay has become very slow is raised to a higher temperature, there is a rapid initial decrease in H_{tr} followed by a new slowly decaying "plateau" concentration. In a typical experiment the ratio of "plateau" values at 30, 35, and 45°K was about 1:0.6:0.1. Essentially all H_{tr} disappear within a few minutes at 50°K.

For illuminations of equal duration carried out at different light intensities, to produce different initial concentrations of H_{tr} , the decay curves are superimposable when normalized for $[H_{tr}]$ at the end of illumination, *i.e.*, the decay is "composite first order."⁹ This has been demonstrated for three illumination times from 5 sec to 4 min, including initial H_{tr} concentrations varying by a factor of 5 for the 4-min illuminations (Figure 3). In no case did the decay data give linearity on a second-order plot ($1/[H_{tr}]$ vs. t) even for the latter portions of decay followed to 85% completion at 40°K.

Fractional decay rates determined following 15-sec illumination at 30°K of samples containing 0.03, 0.1, and 0.3 mf of HI were identical, indicating that the mechanism of decay does not involve reaction with HI.

In contrast to the decay of H_{tr} , the decay of the 3MP- d_{13} radicals is slow, being less than 1.5% hr^{-1} at 40°K after a 12-min photolysis and *ca.* 60% in 10 min at 77°K

after a 2-min photolysis. At the latter temperature it has been shown to be composite first order.⁹

No systematic study has been made of the decay rates of D atoms, but they appear to vary in a manner qualitatively similar to those of H atoms.

Effect of Isobutene on Yields of Trapped H Atoms and 3MP- d_{13} Radicals. In the original investigation² of the trapping of H atoms in 3MP- d_{14} at temperatures below 77°K, it was found that in the presence of 3×10^{-3} mf of isobutene, *t*-butyl radicals are formed at temperatures down to 50°K, but not below, and that trapped H atoms are not produced at any temperature from 77 to 20°K in the presence of isobutene. In brief further tests of these unexpected phenomena we have photolyzed HI in 3MP- d_{14} glass containing 4×10^{-4} , 8×10^{-4} , and 1.8×10^{-3} mf of isobutene. Again, *t*-butyl radicals were produced above 50°K but not below. At 30°K, 4×10^{-4} mf of isobutene reduced the rates of production of both trapped 3MP- d_{13} radicals and trapped H atoms by a factor of 50%, while 1.8×10^{-3} mf of isobutene reduced the radical and H production by 80%. These reductions are unexpected and suggest that the HI may be complexed by the isobutene in a manner to preclude its normal photodissociation. These phenomena require further investigation. To test whether the samples photolyzed at 30°K might contain *t*-butyl radicals in a configuration not observable by esr, such samples were reexamined after warming to 77°K. No *t*-butyl radical signal appeared.

Search for H_{tr} from Photolysis of HI in C_6H_{14} . It has been reported² that, in contrast to the photolysis of HI in 3MP- d_{14} , the photolysis of HI in 3MP- h_{14} in the temperature range from 20 to 50°K does not produce trapped H atoms. We have now extended the temperature range to 4°K. Photolysis of HI in 3MP- d_{14} at 4°K produces both free radicals (by abstraction of D from the matrix) and trapped H atoms. The quantum yields, obtained after correction for the effect of temperature on esr sensitivity, appear to be much lower than at 20° and above, but power saturation effects at 4°K were not investigated. Identical experiments using 3MP- h_{14} produce C_6H_{13} radicals at about the same rate but show no evidence of H_{tr} under the same conditions of esr measurement which gave positive results with the C_6D_{14} .

Because of the unexpectedness of the observation that 3MP- d_{14} is able to trap H and D atoms whereas 3MP- h_{14} is not, we have made particular efforts to determine whether spurious factors, as for example an olefinic impurity in the 3MP- h_{14} , might be the cause. For this purpose samples of Phillips pure grade 3MP- h_{14} which had been purified by passing through activated silica were further treated by each of two methods. In the first, the sample was subjected to catalytic hydrogenation to ensure removal of unsaturates. In the

(9) W. G. French and J. E. Willard, *J. Phys. Chem.*, **72**, 4604 (1968).

second, it was allowed to stand on the vacuum line with molecular bromine to remove unsaturates, following which it was distilled onto precipitated silver to remove excess Br₂ and then distilled three times from 236 to 77°K to remove organic bromides. Samples of 3MP-*h*₁₄ prepared by these methods did not trap H atoms from the photolysis of HI at 30°K. Samples of 3MP-*d*₁₄ treated by the same methods did trap H atoms. Similarly, the ability of 3MP-*d*₁₄ to trap H was not altered by passing it through a column of activated silica gel.

Radiolysis Experiments. Samples of 1 × 10⁻³ mf of HI in 3MP-*d*₁₄ (³H) and 3MP-*h*₁₄ (³H) were observed while undergoing self-radiolysis at 4°K and at higher temperature, in the esr cavity. In no case was there any evidence of an H_{tr} or D_{tr} signal, although in every case the signal of the matrix radical grew in. When the 3MP-*d*₁₄ (³H) sample containing HI was photolyzed at 30°K, H_{tr} and D_{tr} were produced, even after the sample had undergone several days of self-radiolysis.

It was demonstrated that, although self-radiolysis of the 3MP-*h*₁₄ sample did not produce trapped H atoms, it did produce trapped electrons, observable at 77°K by their typical¹⁰ esr singlet.

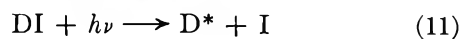
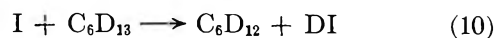
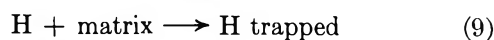
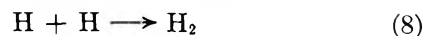
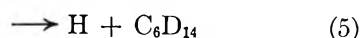
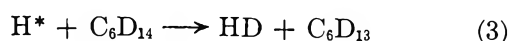
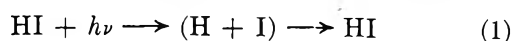
Trapped H in Walls of Quartz Sample Tubes. During the course of this work evidence accumulated that quartz esr sample tubes with certain histories of pre-treatment produce trapped H atoms when photolyzed with the AH4 medium pressure mercury arc. These are readily distinguished from the H atoms trapped in a 3MP-*d*₁₄ matrix because they are stable at temperatures even as high as 77°K (their decay rate is *ca.* 15% hr⁻¹ at 77°K) and because they show strong esr power saturation at powers as low as a few milliwatts at 30°K and below. Photolysis of new evacuated quartz tubes at any temperatures from 4 to 77°K does not produce significant concentrations of trapped H atoms. γ radiolysis of the same tubes at 77°K produces strong H atoms esr signals. These disappear when the sample is warmed to room temperature and recooled to 77°K, but subsequent exposure of the γ -irradiated tube to illumination from the low-pressure mercury arc regenerates an H signal which reaches an equilibrium value after a few minutes of photolysis. There is some evidence that aging of quartz for several months in contact with 0.1 mol % of HI in 3MP at room temperature may condition it to produce H_{tr} during photolysis following removal of the HI-3MP. The heating to 200° of a tube, which before heating produced H on photolysis, removes the ability of the tube to trap H atoms.

Photolysis of 3MP-*d*₁₄ degassed and sealed off with 1 × 10⁻³ mf of HI in Kel-F tubes (used to avoid any possible contribution from signals induced in quartz) for 15 sec or 4 min at 30°K gave growth curves of H_{tr} similar to those observed in quartz tubes. The times required for 50% decay following these illuminations were 0.5 and 4.5 min, respectively, equivalent to the

times observed for samples in quartz tubes. Exposure of empty Kel-F tubes to the medium pressure arc under the standard conditions of illumination at 30°K produces no esr signal.

Discussion

Quantum Yields of Elementary Reactions. Reactions induced by the photolysis of HI in 3MP-*d*₁₄ may include the following, where H* is an H atom born with excess kinetic energy as a result of the photodecomposition



Reaction 1, geminate recombination, is negligible in the liquid at 298°K but increases in importance with decreasing temperature.⁷ The quantum yield for abstraction of D from the matrix by hot H atoms, reaction 3, is 0.2 independent of temperature over the range of 298–120°K,⁷ is about the same at 77°K,⁸ and is *ca.* 0.12 at 4°K.³ The quantum yield of thermalized H atoms, reaction 2 followed by (5), is 0.8 at 298°K⁷ and *ca.* 0.1 at 77°K. The present work indicates an initial quantum yield for trapping of H atoms in 3MP-*d*₁₄ at 50°K and below (reaction 9) of *ca.* one-sixth the yield of radical formation by reaction 3, *i.e.*, *ca.* 0.03. If an equivalent number of thermal atoms are produced in 3MP-*h*₁₄, where trapping does not occur, they must be used up by one or more of the reactions 6, 7, or 8, since abstraction of H from the matrix molecules at these temperatures is precluded by activation energy considerations, assuming activation energies in the solid state are similar to those in the gas and liquid. If reaction 6 has an activation energy as high as 3 kcal mol⁻¹, it cannot be significant at 40°K and below; if *E_A* is as high as 1 kcal mol⁻¹, the reaction cannot occur 4°K.

Origin of D Atoms. Trapped D atoms are produced with a quantum yield of *ca.* 1 × 10⁻⁴ when HI is photolyzed in 3MP-*d*₁₄. Two mechanisms must be considered: (1) displacement of D from C₆D₁₄ (reaction 4)

(10) (a) K. Tsuji and F. Williams, *J. Amer. Chem. Soc.*, **89**, 1526 (1967); (b) M. Shirom, R. F. C. Claridge, and J. E. Willard, *J. Chem. Phys.*, **47**, 286 (1967).

by hot H atoms from reaction 2; (2) photolysis of DI (reaction 11) produced by disproportionation in the reaction of I with C_6D_{13} (reaction 10). There is good evidence that radicals produced by reaction 3 disappear by reaction with the geminate iodine atom produced by reaction 2,⁹ and it is plausible that this reaction may lead, in part at least, to disproportionation. In the absence of complicating factors, the concentration of D atoms produced by the disproportionation route, reactions 10 and 11, would increase as the square of the illumination time at constant intensity absorbed by HI, the rate of production at any time being proportional to the first power of the prior dose. The linear growth of trapped D, illustrated in Figure 1, is contrary to this expectation. If, however, the D atom population has the same properties which lead to the rapidly decreasing quantum yield for production of trapped H atoms (Figure 1), the possibility cannot be excluded that this factor compensates for the second power production rate to give the D atom growth observed. The fact that the available evidence (*i.e.*, for samples photolyzed 4 min or more) indicates that the decay kinetics of trapped D atoms are the same as for trapped H atoms supports the conclusion that there is a single population with respect to the factors which affect decay. Estimates of the conceivable concentrations of DI which might be produced by disproportionation are not low enough to eliminate D_{tr} production by this route.

If D_{tr} results from displacement (reaction 4), its production rate would be expected to be constant with time of illumination (since the rate of radical growth by (3) is constant and (3) and (4) should have a constant branching ratio). Thus the linear growth of the concentration of D_{tr} (Figure 1) seems to support the displacement mechanism. The experiment in which the sample of Figure 1 was raised to 60°K after 82 min of illumination, to remove H_{tr} and D_{tr} by thermal decay, and was then further illuminated at 30°K seems significant. At the start of the second illumination the initial quantum yield of H_{tr} was 0.1 of its value for the first illumination, whereas the values for D and C_6D_{13} were unchanged. This supports the conclusion that D atoms are formed by displacement rather than by photolysis of DI (which would have accumulated during the first period of illumination) and that the freshly formed D atoms, in contrast to H atoms, are not subject to scavenging reactions by trapped atoms and radicals.

Growth of Trapped H Atoms. The fact that the initial quantum yields of production of H_{tr} , D_{tr} , and C_6D_{13} are independent of temperature in the range tested (20–40°K) indicates that the properties of the matrix with respect to favoring geminate recombination are not changing significantly in this temperature range, a fact which is not surprising.

Several hypotheses have been considered and tested to explain why the initial quantum yield of H_{tr} falls off

so rapidly, leading to a plateau in the H_{tr} concentration, which remains constant with prolonged illumination (Figure 1). The plateau is not the result of complete filling of a limited number of trapping sites, since the height of the plateau increases when the intensity of the incident radiation is increased. Likewise, the plateau is not caused by an exact balance between a rate of production equivalent to the initial rate of production and thermal decay. For the conditions of Figure 1 the initial rate of thermal decay of H_{tr} when illumination is turned off is 20% min^{-1} after 12 min of illumination and 11% min^{-1} after 50 min of illumination, whereas the rate of production, as indicated by the initial quantum yield, is 200% of the steady-state level per minute. The possibility that the temperature of the sample is raised sufficiently by continuing illumination to increase the rate of thermal decay has been eliminated by tests with filters which absorb infrared and visible radiation. The linear growth of C_6D_{13} radicals by reaction 3 indicates that the rate of light absorption is constant.

If decay of H_{tr} during radiation of the sample were faster than thermal decay (*e.g.*, as a result of energy deposited in the sample "shaking-up" potential decay pairs), the plateau concentration should be independent of the incident intensity, but it increases with intensity.

It seems clear that there is not one simple process, such as combination with trapped species, which reduces the quantum yield of H_{tr} to zero as irradiation continues. Reduction of the quantum yield with increasing dose would be expected if H atoms react with trapped C_6D_{13} , H, D, and I in competition with trapping. However, if the plateau concentration was determined only by the concentration of trapped intermediates, its height would be independent of light intensity, in contrast to the observations. Also, the concentration would be expected to decrease with increasing radiation dose, after passing through a maximum, because the concentration of trapped radicals and I atoms increases linearly, while at the same time there is continual thermal decay of H_{tr} . In spite of these considerations, there is strong evidence for reaction of thermal H atoms with trapped radicals and I atoms in the fact that the initial quantum yield of H_{tr} in the sample of Figure 1 was much smaller for a second illumination, after thermal decay of the H atoms (but not radicals) produced in a first 82-min illumination, than it was initially. The seemingly contrary evidence might be reconciled in principle if trapped free radicals and atoms are most effective in capturing those H atoms which have the particular energy required to enter the traps which allow most rapid decay. If this were the case, the average decay rate of the H_{tr} would decrease as the trapped radical population increased. Such a decrease in decay rate with increasing time of illumination is actually observed. However, this concept is also inadequate to correlate all the observations since the data of Figure 3 indicate that the initial fractional decay rates of H_{tr} are indepen-

dent of dose when varied doses are given within equal times.

Nature of Trapping Sites; Matrix Isotope Effect. Decay Mechanism. The only theoretical consideration of H atom trapping of which we are aware is that of Adrian,¹¹ stimulated by the esr observation of Foner, Cochran, Bowers, and Jen¹² that H atoms can be trapped in three different types of site in argon at 4°K. The evidence indicates that the ability of an H atom to enter each type of site depends on its energy. Energetic atoms produced by photolysis of HI in the matrix are able to enter all types of sites, whereas thermal atoms, from a microwave discharge, can enter only one. The crystal form of inert gases is face centered cubic. The three types of trapping sites are thought to be (a) matrix atom substitutional sites, (b) octahedral sites, and (c) tetrahedral sites. These involve 12, 6, and 4 nearest-neighbor Ar atoms, respectively. H atoms trapped at one type of site decay rapidly on warming to 12°K, a second type are stable up to 23°K, and the third can be observed as high as 39°K. The energetics of trapping in each type of site are considered by Adrian¹¹ in terms of the opposing forces of repulsion and van der Waals attraction. Experimentally Ne, Ar, Kr, and Xe show different trapping capabilities, three types of trapping site being observed in Ar, two in Kr and Xe, and only one in Ne.

On the basis of this evidence, it is plausible to speculate that in glassy 3MP-*d*₁₄ there may be a wide variety of trapping sites which H atoms from the photolysis of HI populate with a relative probability dependent on the concentration of each type of site and on the steady-state spectrum of H atom energies available as a result of their stepwise thermalization after birth. With such a model it is possible to correlate qualitatively a number of the observed phenomena.

The absence of H trapping in 3MP-*h*₁₄, as contrasted to 3MP-*d*₁₄, may be ascribed to small differences in the matrix structure due to the slightly larger size of 3MP-*h*₁₄ molecules than 3MP-*d*₁₄ molecules, caused by the higher vibration frequency of C-H than C-D bonds. This may shift the close balance between the repulsive forces and the attractive forces in favor of the repulsive forces.

The fact that D_{tr} grow with different kinetics than H_{tr} may be due to the fact that they are produced by a different mechanism (*i.e.*, by displacement (reaction 4)) which produces them in a molecular environment and with an energy favorable for immediate trapping without sufficient diffusion to allow trapped radicals and atoms to compete for them.

The fact that the decay curves for samples which have received the same duration of illumination but at different intensities are superimposable after normalization for the initial concentration (Figure 3), *i.e.*, are composite first order, requires either that each H_{tr} combines with its geminate I atom (or some other predestined partner with which it has been paired in the trapping act) or that the rate-determining step in decay is the act of detrapping, with retrapping being highly improbable relative to removal of the H by reaction with a trapped radical or atom. (If retrapping is probable, decay times must decrease as increasing concentration of scavengers competes with the retrapping.)

In view of the nature of H atoms, their substantial kinetic energy at birth from HI (22–43 kcal mol⁻¹), and the fact that they are not trapped at all in 3MP-*h*₁₄, it is improbable that geminate trapping occurs. If the act of trapping requires energy in excess of thermal energies, as suggested by the results of Foner, Cochran, Bowers, and Jen,¹² it is to be expected that once an atom has been detrapped it will not be trapped again. With this mechanism it would be expected, as observed, that the fractional decay rate of H_{tr} following a given time of illumination should be independent of the intensity of illumination (*i.e.*, of initial concentration) and that it should be time dependent (*i.e.*, "composite first order" rather than "pure first order"). The time dependency of the fractional decay rate arises from the fact that there is a variety of trapping sites. The more weakly trapped H detrapp the fastest. This variety of trapping sites must also account for the step function character of the decay as a sample containing H_{tr} is raised to successively higher temperatures.

(11) F. J. Adrian, *J. Phys. Chem.*, **32**, 972 (1960).

(12) S. N. Foner, E. L. Cochran, V. A. Bowers, and C. K. Jen, *ibid.*, **32**, 963 (1960).

Pulse Radiolysis of Aliphatic Acids in Aqueous Solution.

III. Simple Amino Acids

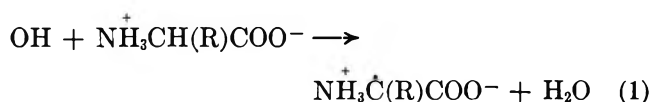
by P. Neta,¹ M. Simic,¹ and E. Hayon

Pioneering Research Laboratory, U. S. Army Natick Laboratories, Natick, Massachusetts 01760
(Received October 15, 1969)

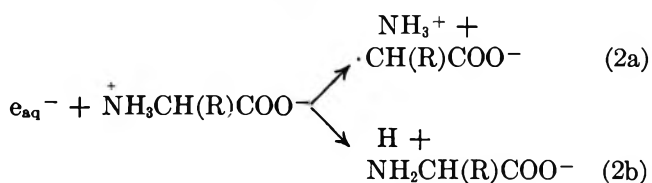
The pulse radiolysis of aqueous solutions of some amino acids—glycine, alanine, α -amino-butyric acids, valine and some of their derivatives (including imino diacetic and nitrolotri-acetic acids)—has been studied. Transient optical absorption spectra of amino carboxyalkyl radicals were produced as a result of dehydrogenation by H atoms and OH radicals, e.g., $\overset{+}{\text{N}}\text{H}_3\text{CH}_2\text{COOH} + \text{OH} \rightarrow \overset{+}{\text{N}}\text{H}_3\dot{\text{C}}\text{HCOOH} + \text{H}_2\text{O}$. The observed changes in the absorption of the transient with variation in pH is attributed to proton dissociation of the carboxyl and amino groups of the radical, which occurs at a pH different from that of the parent compound: $\overset{+}{\text{N}}\text{H}_3\dot{\text{C}}\text{HCOOH} \xrightleftharpoons{-\text{H}^+} \overset{+}{\text{N}}\text{H}_3\dot{\text{C}}\text{HCOO}^- \xrightleftharpoons{-\text{H}^+} \overset{+}{\text{N}}\text{H}_2\dot{\text{C}}\text{HCOO}^-$. In alkaline solutions, a change in the site of attack by OH radicals is suggested, from the C-H to the N-H bond, with the formation of $\overset{+}{\text{N}}\text{HCH}_2\text{COO}^-$ radicals from glycine. The α -amino- α -carboxyalkyl radicals have absorption maxima in the region 250–260 nm, while the β and γ radicals have maxima well below 240 nm. The previously postulated deamination of amino acids by hydrated electrons was confirmed by direct observation of carboxyalkyl radicals, which in the case of glycine and alanine have absorption maxima at 350 and 340 nm, respectively: $\overset{+}{\text{N}}\text{H}_3\text{CRH}\dot{\text{C}}\text{OO}^- + e_{\text{aq}}^- \rightarrow \dot{\text{C}}\text{RHCOO}^- + \text{NH}_3$.

The γ radiolysis of a number of amino acids in aqueous solutions has been studied extensively. The observed radiolytic products and the postulated reaction mechanisms have recently been reviewed by Garrison.² For instance, the major radiolytic products of 1.0 M glycine solutions were ammonia ($G = 4.3$), hydrogen ($G = 2.0$), acetic acid ($G = 1.2$), glyoxylic acid ($G = 2.1$), with smaller yields of formaldehyde ($G = 0.5$) and carbon dioxide ($G = 0.6$). Equivalent products were observed from the higher homologs of aliphatic amino acids.

The OH radicals produced in the radiolysis of water are assumed to attack aliphatic amino acids predominantly at the α position, by abstraction of a hydrogen atom from the C-H bonds.



The reaction of the hydrated electron, e_{aq}^- , with amino acids was envisaged² as a reaction with the protonated amino form leading to deamination as well as to partial formation of H atoms and/or H_2



Direct spectroscopic observation of the transients originating from the reactions of OH and e_{aq}^- have been

reported for a limited number of amino acids. For instance, transient absorption with λ_{max} 260 nm was reported in the pulse radiolysis of 10^{-3} M aqueous solutions of glycine³ at pH 6.5 and was attributed to dehydrogenation of the solute by OH radicals. Transient spectra were also observed in the pulse radiolysis of aqueous solutions of cysteine and cystine⁴ and of phenylalanine and tyrosine.⁵ However, these solutes involve reactions qualitatively different from reactions 1 and 2 due to the comparatively much higher reactivity of the -SH group and the benzene ring toward OH radicals, and of the -S-S- and -SH group toward hydrated electrons.

Some of the amino carboxyalkyl radicals formed by reaction 1 have also been produced from amino acids by the rapid mixing technique using $\text{TiCl}_3 + \text{H}_2\text{O}_2$ and were identified by their esr spectra.⁶

(1) National Academy of Sciences-National Research Council Research Associates at Natick.

(2) W. M. Garrison in "Current Topics in Radiation Research," M. Ebert and A. Howard, Ed., North-Holland Publishing Co., Amsterdam, 1968, p 43.

(3) J. V. Davies, M. Ebert, and A. J. Swallow in "Pulse Radiolysis," M. Ebert, J. P. Keene, A. J. Swallow, and J. H. Baxendale, Ed., Academic Press, New York, N. Y., 1965, p 165.

(4) G. E. Adams, G. S. McNaughton, and B. D. Michael in "Chemistry of Ionization and Excitation," G. R. A. Johnson and G. Scholes, Ed., Taylor and Francis, London, 1967, p 281; E. Hayon and M. Simic, to be published.

(5) J. Chrysochoos, *Radiat. Res.*, **33**, 465 (1968).

(6) H. Taniguchi, K. Fukui, S. Ohnishi, H. Hatano, H. Hasegawa, and T. Maruyama, *J. Phys. Chem.*, **72**, 1926 (1968); R. Poupko, B. L. Silver, and A. Lowenstein, *Chem. Commun.*, 453 (1968); W. A. Armstrong and W. G. Humphreys, *Can. J. Chem.*, **45**, 2589 (1967).

Experimental Section

This work was carried out using a Febetron 705 pulsed radiation source, and the details of the experimental conditions have been described elsewhere.⁷ Briefly, this source produces an electron beam of 2.3 MeV energy and single pulses of ≈ 30 nsec duration. The monitoring light source was an Osram XBO 450-W xenon lamp, and the light output from the lamp was increased by a factor of 25–30 times by increasing the current to the lamp with pulses of ~ 1.2 msec duration. A double monochromator, consisting of two high-intensity Bausch and Lomb monochromators in series, was used to reduce scattered light and improve wavelength resolution.

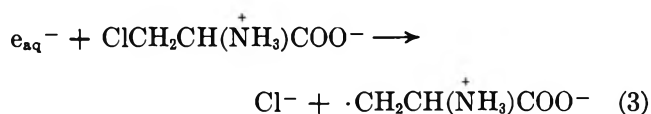
The amino acids and derivatives used were either Calbiochem A Grade or Cyclochemical Grade I reagents. *t*-Butyl alcohol was Mallinckrodt AR, nitriiotriacetic and iminodiacetic acids were supplied by Eastman, and the inorganic chemicals were Baker and Adamson reagents. Nitrous oxide and argon were supplied by Matheson. Solutions were prepared using water purified by triple distillation, radiolysis, and photolysis. The solutions were buffered using perchloric acid, potassium hydroxide, sodium tetraborate (1–3 mM), and potassium phosphates (1–3 mM).

Dosimetry was carried out using a 0.1 M KCNS solution and the $(\text{CNS})_2^-$ radical formed was observed at 500 nm (ϵ 7600 $M^{-1} \text{ cm}^{-1}$). Doses of 2.4 to 36 krad/pulse were used and were derived on the basis of $G_{e_{aq}^-} = G_{OH} = 2.8$. The choice of solute concentration was made on the basis of known radical–radical and radical–solute rate constants,⁸ and complete scavenging of radicals was also experimentally established by comparing yields of transient species at different solute concentrations.

The optical densities were usually read at 1 to 2 μsec after the pulse and were extrapolated to zero time. The reproducibility of readings was better than $\pm 5\%$.

Results and Discussion

As in our previous pulse-radiolysis studies of carboxylic acids,^{9,10} the amino acid transients were produced in aqueous solutions through the reaction of OH radicals with the dissolved amino acids. The hydrated electrons were in general converted ($\sim 98\%$) into OH radicals by saturating the solutions with nitrous oxide. At pH < 3 the hydrated electrons react with H_3O^+ to form H atoms which are expected to react with amino acids in a similar way as the OH radicals. Whenever possible, specific transient species were produced by the reaction of e_{aq}^- with chlorinated compounds, in the presence of a high concentration of *t*-butyl alcohol acting here as a scavenger of OH radicals



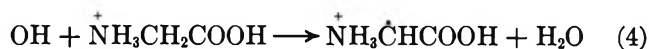
The *t*-butyl alcohol radicals were found not to react with the chlorinated compounds under our experimental conditions.

Glycine and Alanine

A relatively high concentration of glycine, 1.0 M, is needed at pH < 10 for complete scavenging of OH radicals, due to the low reactivity of the protonated forms $\text{NH}_3^+\text{CH}_2\text{COOH}$ and $\text{NH}_3^+\text{CH}_2\text{COO}^-$ with OH radicals and H atoms, $\text{NH}_3^+\text{CHRCOOH} \xrightleftharpoons[\text{pK } 2.3]{-\text{H}^+} \text{NH}_3^+\text{CHRCOO}^- \xrightleftharpoons[\text{pK } 9.6]{-\text{H}^+} \text{NH}_2\text{CHRCOO}^-$. Further increase in the concentration of glycine yielded the same amount of transient. The transient optical absorption spectra produced on pulse radiolysis of aqueous solutions of glycine in the presence of N_2O were recorded at various pH values, in the range 1–13.3, and some of them are presented in Figure 1. All the spectra showed an absorption maximum at ≈ 250 nm, the only apparent variation being in the extinction coefficients of the transients at different pH values. This transient is considered to be the same as that reported by Davies, *et al.*,³ at pH 6.5, with $\lambda_{\text{max}} \sim 260$ nm. The large observed variation in absorption of the transient species with pH was monitored at 250 nm, and is shown in Figure 1.

The transient absorption spectra resulting from the pulse radiolysis of N_2O -saturated solutions of alanine at various pH values are shown in Figure 2. The extinction coefficients of the transient species show a similar pattern with pH dependence, as observed for glycine. In the case of alanine, this variation was monitored at 260 nm.

On the basis of the presently accepted mechanism, the OH radicals dehydrogenate the C–H bond in glycine yielding an aminocarboxymethyl radical. At pH 1.0 this radical is believed to be $\text{NH}_3^+\dot{\text{C}}\text{HCOOH}$ produced according to reaction 4



As the pH is increased this radical is expected to undergo deprotonation of both the carboxyl and the amino group, similar to the parent compound



The increase in absorption between pH 1 and pH 5 is attributed to deprotonation of the carboxyl group, as was observed^{9,10} in the case of a number of other carboxyalkyl radicals. The pK values cannot be determined from Figures 1 and 2 due to the absence of a

(7) M. Simic, P. Neta, and E. Hayon, *J. Phys. Chem.*, **73**, 3794 (1969).

(8) M. Anbar and P. Neta, *Int. J. Appl. Radiat. Isotopes*, **98**, 493 (1967).

(9) P. Neta, M. Simic, and E. Hayon, *J. Phys. Chem.*, **73**, 4207 (1969).

(10) M. Simic, P. Neta, and E. Hayon, *ibid.*, **73**, 4214 (1969).

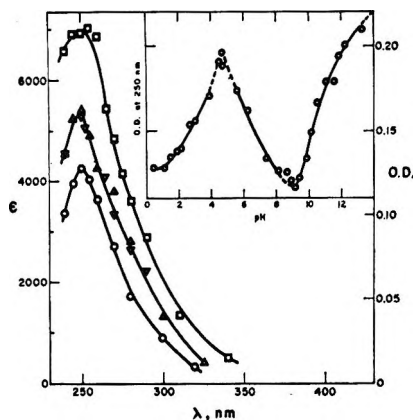


Figure 1. Absorption spectra and OD vs. pH curve of transient species produced from glycine, $\text{NH}_2\text{CH}_2\text{COOH}$, 2.4 krad/pulse, N_2O (1 atm): \circ , 1 M and 2 M glycine, pH 1; ∇ , 1 M, pH 3; Δ , 1 M, pH 6; \square , 0.1 M and 0.5 M, pH 13.3.

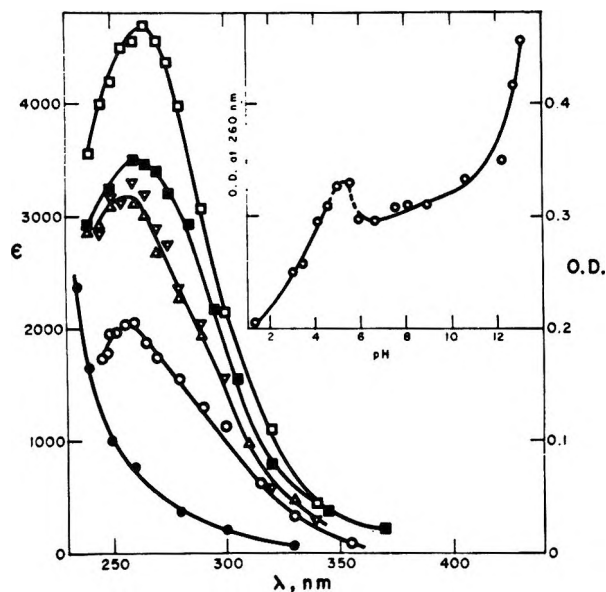


Figure 2. Absorption spectra and OD vs. pH curve of transient species produced from alanine, $\text{CH}_3\text{CH}(\text{NH}_2)\text{COOH}$, 8 krad/pulse, N_2O (1 atm): \circ , 1 M and 2 M alanine, pH 1.4; ∇ , 0.5 M, pH 5.6; Δ , 0.5 M, pH 8.0; \blacksquare , 0.2 M, pH 12.3; \square , 0.1 M and 0.2 M, pH 13.1; \bullet , 2.5×10^{-2} M β -chloroalanine, 1 M *t*-BuOH, pH 6.5, Ar, corrected for the transient absorption of *t*-BuOH radical (only the ϵ scale applies).

plateau region. However, the pK values for deprotonation of the carboxyl groups seem to be between pH 3 and 4, *i.e.*, slightly higher than the pK of the parent molecules ($pK \sim 2.3$).

The decrease in absorption above pH 5 is attributed to the deprotonation of the NH_3^+ group of the radical. Here again the pK cannot be determined for the same reason, although a value between 5 and 7 could be estimated. This value is considerably lower than the pK of the parent molecule (9.6), in general agreement with the similar effect observed¹¹ for the acid-base

properties of other amino radicals, *e.g.*, aminomethyl radicals, and the role of the unpaired electron on the dissociation constant of these radicals.

The change in absorption observed above pH 9, Figure 1, could be explained either by a change of the site of attack by OH radicals or by the dissociation of the NH_2 group of the radical. Deprotonation of the NH_3^+ group of the parent molecule takes place at higher pH ($pK = 9.6$) and dehydrogenation of the N-H bond becomes energetically feasible. Dehydrogenation of N-H bonds in aliphatic amines has already been considered as one of the major reactions in the γ radiolysis of alkaline solutions.¹² Assuming dehydrogenation by OH radicals of the N-H bond in glycine to take place at pH >10, the $\cdot\text{NHCH}_2\text{COO}^-$ radical would appear to have an absorption spectrum very similar to those of the other glycine transients where the unpaired electron is on the carbon atom, but with a higher extinction coefficient.

The assumption that the NH_2 group is involved in the change of absorption at high pH values is also supported by the results for nitrilotriacetic acid (see below), where no N-H bonds are present at high pH and no change in absorption was observed. The effect of pH on the transients produced in the pulse radiolysis of aqueous solutions of methylamine and other amines¹¹ further supports the change in the position for dehydrogenation by OH radicals, from the C-H to the N-H bond, in going to alkaline solutions. Recent¹³ results on the esr spectra of these intermediates seem to support this interpretation of the results.

The decay rates of the radicals over the whole pH region are second order and are too close to provide any additional information (Table I).

The results obtained in the pulse radiolysis of solutions of alanine, Figure 2, can also be interpreted on the basis of the deprotonation of the amino and carboxyl groups of the transient species and the parent molecule. To establish whether the spectra belonged to an α - or β -radical, the pulse radiolysis of β -chloroalanine solutions was carried out in the presence of excess *t*-butyl alcohol. The spectrum belonging to the $\cdot\text{CH}_2\text{CH}(\text{NH}_3^+)\text{COO}^-$ radical, reaction 3, was found to be strikingly different from the α radicals, Figure 2. On the basis of these results it may be concluded that the OH radicals attack preferentially the α -C-H bonds, in agreement with the mechanisms already proposed in the γ radiolysis of aqueous alanine solutions.²

In alkaline solutions, at pH >8, the increase in absorption of the transient species at 260 nm is explained as due to the dehydrogenation of the NH_2 group by OH radicals, *i.e.*, a similar interpretation as given above for glycine.

(11) M. Simic, P. Neta, and E. Hayon, in preparation.

(12) G. G. Jayson, G. Scholes, and J. J. Weiss, *J. Chem. Soc.*, 2594 (1955).

(13) P. Neta and R. W. Fessenden, private communication.

Table I: Absorption Maxima, Extinction Coefficients, and Decay Rate Constants for the Transients Produced on Pulse Radiolysis of Aqueous Solutions of Amino Acids

Acid	pH	λ_{max} , nm	ϵ , $M^{-1} \text{ cm}^{-1}$	$2k \times 10^{-9} M^{-1} \text{ sec}^{-1}$
Glycine	1.0	250	4300	1.2
$\text{NH}_2\text{CH}_2\text{COOH}$	3.0	250	5400	1.3
	6.0	250	5400	1.1
	13.2	250	7000	0.5
Alanine CH_3CHCOOH NH_2	1.4	260	2000	0.8
	5.6	260	3200	0.9
	12.3	260	3500	0.5
	13.1	260	4700	0.3
α -Amino- <i>n</i> -butyric acid $\text{CH}_3\text{CH}_2\text{CHCOOH}$ NH_2	6.5	<235 ^a	>2400	...
	6.0	<235	>2000	~1
	11.9	260	3200	0.5
	13.3	250	3600	0.5
α -Aminoisobutyric acid $(\text{CH}_3)_2\text{CCOOH}$ NH_2	6.4	<240
	9.5	<240	...	1.8
Valine $(\text{CH}_3)_2\text{CHCHCOOH}$ NH_2	13.3	<240	...	0.7
	5.7	<235	...	1
Iminodiacetic Acid $\text{NH}(\text{CH}_2\text{COOH})_2$	11	250	>3200	0.5
Nitrilotriacetic Acid $\text{N}(\text{CH}_2\text{COOH})_3$	4.5	265	5800	0.7
	11.0	265	8300	0.07
	13.0	265	10800	0.12
	3.6	280	5600	...
	11.3	280	9700	0.0005

^a β radical of alanine, $\cdot\text{CH}_2\text{CH}(\text{NH}_2)\text{COO}^-$.

α -Aminobutyric Acids and Valine

The three characteristic spectra produced by the reaction of OH radicals with α -amino-*n*-butyric acid are presented in Figure 3. The spectrum obtained at pH 6.0 is qualitatively different from those at pH 11.9 and 13.3; it resembles the spectrum of the β -radical produced from β -chloroalanine. Assignment of that spectrum to a mixture of the β and γ radicals, $\text{CH}_3\text{-}\dot{\text{C}}\text{HCH}(\text{NH}_3^+)\text{COO}^-$ and $\dot{\text{C}}\text{H}_2\text{CH}_2\text{CH}(\text{NH}_3^+)\text{COO}^-$, is strongly supported not only by spectral differentiation, but also by the analysis of products produced in the γ radiolysis of solutions of α -amino-*n*-butyric acid. The main dimer products at pH 5.5 were found¹⁴ to be diaminosuberic acid ($G \sim 1.2$) and diaminomethyl-pimelic acid ($G \sim 0.2$), indicating almost exclusive formation of the γ radical.

When the parent molecule exists in the deprotonated amino group form, dehydrogenation of the α -C-H bond now becomes more favorable and the characteristic spectrum of the α -amino- α -carboxyalkyl radical appears. The OD vs. pH curve (Figure 3) thus represents the change of the site of attack of the OH radicals from the β and γ positions to the α position. The derived $pK \sim 8.5$ (Figure 3) is somewhat lower than the pK value for the deprotonation of the amino group of the parent acid ($pK \sim 9.6$). This can be explained on

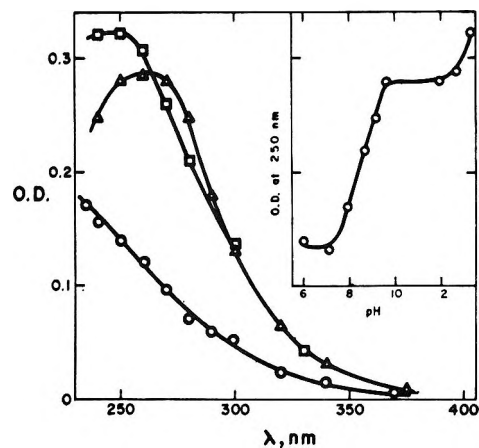


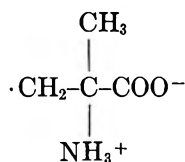
Figure 3. Absorption spectra and o.d. vs. pH curve of transient species produced from α -amino-*n*-butyric acid, $\text{CH}_3\text{CH}_2\text{CH}(\text{NH}_2)\text{COOH}$, 8 krads/pulse, N_2O (1 atm), 0.2 M and 0.5 M ; \circ , pH 6.0; Δ , pH 11.9; \square , pH 13.3.

the basis of the higher value of the rate constant $k(\text{OH} + \text{CH}_3\text{CH}_2\text{CH}(\text{NH}_2)\text{COO}^-)$ as compared to $k(\text{OH} + \text{CH}_3\text{CH}_2\text{CH}(\text{NH}_3^+)\text{COO}^-)$. The spectrum at pH 11.9 is attributed to the $\text{CH}_3\text{CH}_2\dot{\text{C}}(\text{NH}_2)\text{COO}^-$ radical.

(14) J. Kopoldova, J. Liebster, and A. Babicky, *Int. J. Appl. Radiat. Isotopes*, 13, 617 (1962).

Although the formation of the α radical seems to be predominant at pH 10–12, the ratio of the α , β , and γ transients could not be derived. In very alkaline solutions, at pH >12, the α -aminobutyric acid is expected to behave similarly to glycine and alanine although the attack by OH on the NH_2 group should be relatively smaller because the increase in the number of C–H bonds in this molecule provides other sites of attack.

The reaction of OH radicals with α -aminoisobutyric acid, a molecule with no α -C–H bond, results in the formation of the α -amino- β -carboxyalkyl radical



The absorption spectrum of this radical (Figure 4) was very similar to the spectrum of the β radical of alanine (Figure 2). The maximum of the absorption could not be established due to the high absorption of the solutions below 240 nm.

From the shift of the spectrum as a function of pH the following conclusions could be reached. The first change, with $pK \sim 4$, is probably due to the deprotonation of the carboxyl group, while the second one with $pK \sim 9$ is due to deprotonation of the NH_3^+ group of the radical. The unpaired electron, being in the β position to the functional groups, is expected to exert a much smaller influence on these dissociations than when it is in an α position. Hence the pK value for deprotonation of the amino group of this radical lies close to the value of the parent molecule.

In very alkaline solutions at pH >11 these acids are expected to behave similarly to glycine and alanine, although the effect should be different because of the different number and reactivity of the C–H bonds. The observed decrease at 270 nm in the absorption of the transient at pH >11 could be due to either incomplete scavenging of the OH and O^- radicals present at these pH values, or to a lower extinction coefficient of the $(\text{CH}_3)_2\text{C}(\dot{\text{N}}\text{H})\text{COO}^-$ radical presumed to be produced under these conditions. Due to the already high (0.5 M) concentration of α -aminoisobutyric acid used and the relatively low extinction coefficient of the transient, it was not possible to establish the reason for the decrease in OD at pH >11.0.

The change of the site of attack of the OH radicals from predominantly β and γ positions to predominantly α position in the course of deprotonation of the amino group of an α -amino acid is clearly demonstrated by a qualitative spectral change of the absorption of the valine transients, Figure 5. The features of this change are similar to those of the α -amino-*n*-butyric acid which have already been discussed.

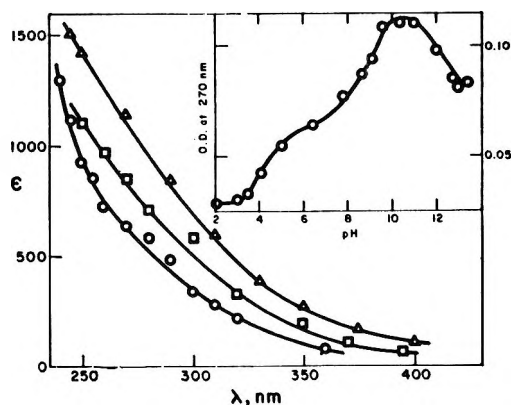


Figure 4. Absorption spectra and OD vs. pH curve of transient species produced from α -aminoisobutyric acid, $(\text{CH}_3)_2\text{C}(\text{NH}_2)\text{COOH}$, 8 krad/pulse, N_2O (1 atm), 0.2 and 0.5 M; \circ , pH 6.4; \triangle , pH 11.1; \square , pH 12.8.

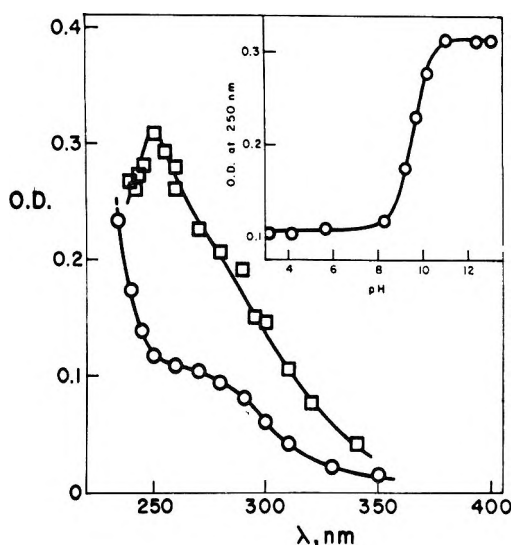


Figure 5. Absorption spectra and OD vs. pH curve of the transient species produced on pulse radiolysis of aqueous solutions of 0.2 and 0.5 M valine, $(\text{CH}_3)_2\text{CHCH}(\text{NH}_2)\text{COOH}$, 8 krad/pulse, N_2O (1 atm), at pH 5.7 \circ , and pH 11.0, \square .

The absence of any pH effect in the pH region 3–8 is believed to be due to the considerably different pK values for dissociation of the β and γ radicals which, contrary to the α radicals, have pK values closer to those of the parent compounds. The extinction coefficient of the α transient at 250 nm at pH 11 cannot be given, since the fraction of the OH radicals attacking the α position is not known. Nevertheless, a lower limit can be assessed, $\epsilon_{250} \geq 3200 \text{ M}^{-1} \text{ cm}^{-1}$.

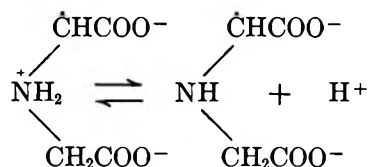
Iminodiacetic and Nitrilotriacetic Acids

The OH radicals are expected to dehydrogenate the C–H bond in iminodiacetic acid, $\text{HN}(\text{CH}_2\text{COOH})_2$. The resulting transient spectra have absorption maxima at 265 nm which are independent of pH, Figure 6a. The pH dependence of the absorption of the various species is substantially different from the other amino

acids. Dissociation of the carboxyl groups takes place below pH 4 but has not been investigated. The absence of any change between pH 4 and 7 and the substantial increase in absorption found between pH 7 and 10 is interpreted to represent the deprotonation of the imino group of the radical. In contrast to the amino acid radicals, this radical has a pK similar to that of the parent acid.

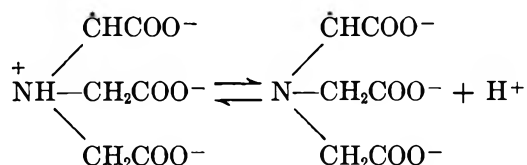
The decay rates (Table I) substantiate this assumption. The decay rate of the transient at pH 11 is 10 times slower than that at pH 4.5, as expected for an increased net charge on the transient.

Hence the pK value for the equilibrium



is believed to be the one derived from the pK curve, *i.e.*, = 8.3. The increase in absorption above pH 10 is probably here as well a consequence of dehydrogenation of the N-H bond.

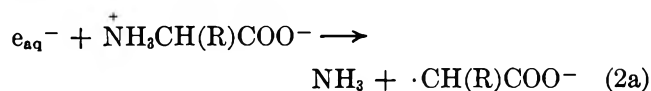
The reaction of OH radicals with nitrilotriacetic acid $\text{N}(\text{CH}_2\text{COOH})_3$ is also assumed to lead to dehydrogenation of C-H bonds. The resulting transient absorption spectrum, Figure 6b, has a maximum at 280 nm. The observed change in absorption with pH ($pK = 8.8$) is attributed to the equilibrium



on the basis of the same arguments presented above for the iminodiacetic acid transient. However, unlike glycine and iminodiacetic acid, nitrilotriacetic acid molecule has no N-H bonds and in fact the absorption of the nitrilotriacetic acid transient is independent of pH above pH 10. This observation substantiates our assumption that the increase in transient absorption in very alkaline solutions of amino acids involves dehydrogenation of the N-H bond by OH radicals.

Deamination of Amino Acids by Hydrated Electrons

The reaction of hydrated electrons with amino acids in their zwitterionic form was suggested by Garrison² to lead partially to reductive deamination. A possible intermediate in this reaction would be the carboxyalkyl radical



These radicals have been investigated⁹ in the pulse radi-

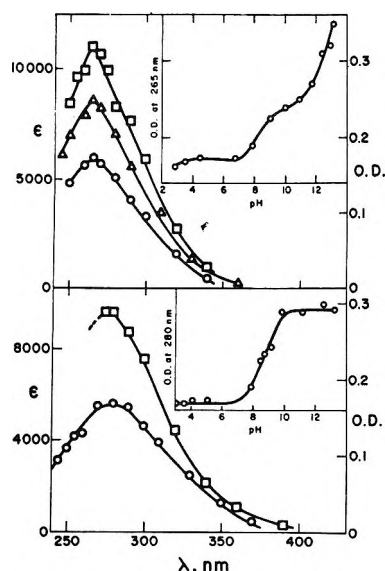


Figure 6. Absorption spectra and OD vs. pH curve of transient species produced from (a) top curve, iminodiacetic acid, $\text{NH}(\text{CH}_2\text{COOH})_2$, at \circ , pH 4.5; Δ , pH 11.0; \square , pH 13.0; and (b) bottom curve, nitrilotriacetic acid, $\text{N}(\text{CH}_2\text{COOH})_3$, at \circ , pH 3.6; \square , pH 11.3. 2.4 krad/pulse, N_2O (1 atm), 0.1 M and 0.2 M.

olysis of aqueous solutions of carboxylic acids and their chloro derivatives, and the transient spectra have been identified. An attempt was made to observe these radicals in the pulse radiolysis of solutions of glycine and alanine. In order to eliminate the reaction of OH radicals with the amino acids, which results in strongly absorbing transients, *t*-butyl alcohol has been used as an OH radical scavenger. Nevertheless, because of the relative reactivities of these compounds and the lower extinction coefficients of the carboxyalkyl radicals compared to the aminocarboxyalkyl radicals, the contribution of the latter could not be entirely suppressed.

Solutions of glycine and alanine with added *t*-butyl alcohol have been irradiated in the absence and presence of N_2O , and correction for the OH radical reactions has been made. A correction was also made for the *t*-butyl alcohol transient below 280 nm.

The results are presented in Figure 7 and clearly show peaks at 350 nm in glycine and at 340 nm in alanine solutions. These corrected spectra with maxima at 350 and 340 nm are identical with those obtained⁹ for $\cdot\text{CH}_2\text{COO}^-$ and $\text{CH}_3\dot{\text{C}}\text{HCOO}^-$ radicals. Both of these radicals have also been identified by their esr spectra under similar conditions.¹³ The peak at 260 nm is probably due to the contribution of H atoms reacting with glycine. The rate constant for the reaction of e_{aq}^- with glycine and alanine zwitterion forms is about $10^7 \text{ M}^{-1} \text{ sec}^{-1}$ and very high concentrations had to be used to approach complete scavenging. Unfortunately, the concentration of the amino acids could not be further increased without increasing the contribution of the OH radical reaction with these acids, hence in-

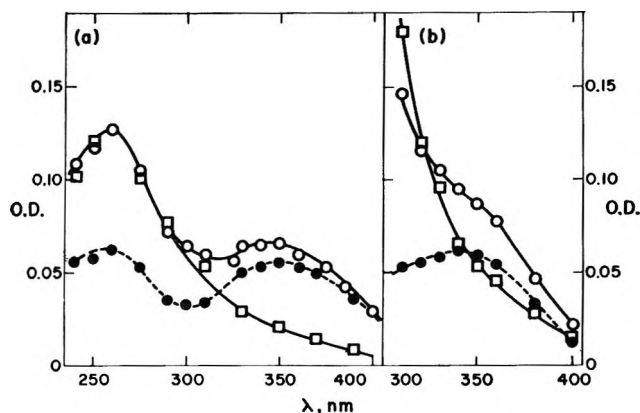


Figure 7. Absorption spectra of transient species produced by the reaction of hydrated electrons with glycine and alanine, 36 krad/pulse; (a) 0.5 *M* glycine + 1 *M* *t*-BuOH, pH 7.8; (b) 0.5 *M* alanine + 2 *M* *t*-BuOH, pH 7.8; ○, Ar saturated; □, N₂O saturated; ●, OD_{Ar} - 1/2 OD_{N₂O}.

creasing the error in determination of the *G* value of the carboxyalkyl radicals. Nevertheless, from the derived absorption and the known extinction coefficient for the $\cdot\text{CH}_2\text{COO}^-$ radical it appears that only $\sim 40\%$ of the e_{aq}^- react with glycine to give rise to this radical. Other reaction paths such as formation of H atoms (reaction 2b) have been already mentioned.

From the decay of the $\cdot\text{CH}_2\text{COO}^-$ radicals ($\sim 10^9 \text{ M}^{-1} \text{ sec}^{-1}$) it seems that under the pulse radiolytic conditions (relatively high radical concentration) this radical disappears by a bimolecular reaction, in contrast to the proposed² mechanism for γ radiolysis where the radical has been suggested to abstract H atoms from the glycine molecule.

General Conclusions

The predominant mode of reaction of the OH radicals with glycine and alanine, as concluded² from the product analysis of the γ -irradiated solutions, is the abstraction of hydrogen from the α -C-H bonds. Hence the observed transient spectra with λ_{max} in the region of 250 to 260 nm were assigned to the α -amino- α -carboxyalkyl radicals. It was shown subsequently that the β -amino- β -carboxyalkyl radicals $\cdot\text{CH}_2\text{CH}(\text{NH}_3^+)\text{-}$

COOH and $\begin{array}{c} \text{CH}_3 \\ \diagdown \\ \text{C}(\text{NH}_3^+)\text{COOH} \\ \diagup \\ \cdot\text{CH}_2 \end{array}$ have distinguish-

able spectra from those of the α, α radicals, *i.e.*, the λ_{max} of the β, β radicals lie below 240 nm. This characteristic shift of the spectrum has already been observed⁹ for

various β -carboxyalkyl radicals. For amino acids with a longer chain, dehydrogenation takes place at various positions along the chain. The fractions are governed by the inductive effects of the amino and carboxyl groups, being different for the protonated and deprotonated forms. The NH_3^+ group has a strong deactivating effect and directs the OH radical attack farther away from it. When the amino group is deprotonated, formation of an α radical takes place to a greater extent. This was clearly demonstrated in the α -amino-*n*-butyric acid and the valine systems. Due to the instability of the α -chloro- α -amino acids and the inaccessible region of the absorption of β and γ radicals, the fraction of α , β , and γ radicals could not be estimated, as it was with the various radicals produced from carboxylic acids.⁹ Thus, the extinction coefficients of the α -amino acid transients (except that of glycine) have to be taken as lower limits.

The absorption spectra of aminocarboxyalkyl radicals are strongly dependent on pH and, in comparison to the other carboxyalkyl radicals, this dependence is considerably more complex.

The change in absorption of the α radicals in the pH region 1-9 is suggested to be due to the overlapping acid-base equilibria of the carboxyl and amino groups of the radical. From the estimates of the *pK* values it seems that the *pK* for deprotonation of the carboxyl group of the radical is slightly higher (1-2 units); while deprotonation of the NH_3^+ in the radicals takes place at a considerably lower pH (2-4 units) than that of the parent molecule.

The change in absorption in strongly alkaline solutions is considered to be due to a change in site of attack by OH radicals from the C-H to the N-H group. The absence of any change in the case of nitrilotriacetic acid transient and the considerably smaller effect observed for the amino acids with longer chains and higher C-H reactivity indicates that this change involves the N-H bonds reacting in competition with the C-H bonds.

The reaction of the hydrated electron e_{aq}^- with the zwitterion form of the amino acids has been conclusively shown to lead, in part, to deamination with the formation of the corresponding α -carboxyalkyl radicals. The remaining fraction of e_{aq}^- is considered to form H atoms and/or H₂. If an electron adduct of the amino acids is initially produced, its lifetime must be considerably less than 1 μsec .

High-Intensity Radiolysis of Aqueous Ferrous Sulfate-Cupric Sulfate-Sulfuric Acid Solutions¹

by Paul Y. Feng,

Marquette University, Milwaukee, Wisconsin 55233, and U. S. Army Natick Laboratories, Natick, Massachusetts 01760

Ari Brynjolfsson, John W. Halliday, and Robert D. Jarrett

U. S. Army Natick Laboratories, Natick, Massachusetts 01760 (Received September 2, 1969)

The radiolysis of aqueous FeSO₄-CuSO₄-H₂SO₄ solutions has been studied at dose rates up to $\sim 3 \times 10^{27}$ eV l.⁻¹ sec⁻¹ ($\sim 5 \times 10^{10}$ rads sec⁻¹). $G(\text{Fe}^{3+})$, which equals ~ 0.7 at low irradiation intensities, increased to ~ 4 with increasing dose rate, acidity, and the extent of oxygenation. This increase is significantly reduced for systems containing higher concentrations of Cu²⁺. Kinetic analysis of the results showed that the increase in $G(\text{Fe}^{3+})$ values at the higher radiation intensities is due to the reactions $\text{H} + \text{H} \xrightarrow{k_{12}} \text{H}_2$, $\text{H} + \text{HO}_2 \xrightarrow{k_{15}} \text{H}_2\text{O}_2$, and $\text{OH} + \text{HO}_2 \xrightarrow{k_{16}} \text{H}_2\text{O}_3$, and good agreement between calculated and experimental values is obtained using the following rate constant values (in l. mol⁻¹ sec⁻¹): $k_{12} = 1.4 \times 10^{10}$, $k_{15} = 2.0 \times 10^{10}$, $k_{16} = 1.1 \times 10^{10}$, and k_{14} (for $\text{H} + \text{OH} \rightarrow \text{H}_2\text{O}$) = 2.0×10^{10} . Our studies show also that (1) some of the hydrogen atoms are produced in primary radiolytic processes together with solvated electrons, (2) hydrogen sesquioxide, produced by the recombination of OH and HO₂ radicals, is capable of oxidizing four equivalents of Fe²⁺ even in the presence of excess Cu²⁺ ions and therefore the oxidation of Fe²⁺ by H₂O₃ does not proceed *via* processes which regenerates the HO₂ radical, and (3) radiation-produced hydrogen peroxide is partially decomposed during the pulse, particularly at the higher intensities.

Introduction

The radiation chemistry of FeSO₄-CuSO₄-H₂SO₄ solutions has been examined by a number of investigators.²⁻⁵ In most cases, these studies have been carried out either to elucidate the reactions which take place at relatively low radiation intensities or to evaluate the application of such systems as dosimeters.

In this paper, we report on a study of the radiolysis of the FeSO₄-CuSO₄-H₂SO₄ system in the dose rate range up to $\sim 3 \times 10^{27}$ eV l.⁻¹ sec⁻¹ ($\sim 5 \times 10^{10}$ rads sec⁻¹). At such high radiation intensities, radical recombination reactions compete efficiently with radical-solute reactions,⁶⁻¹¹ and as a result, $G(\text{Fe}^{3+})$ increases with increasing dose rate. Because of the rather low G value (~ 0.7) of this system at low dose rates, the relative increase in ferric yield is large, and is consequently convenient for studying the reaction kinetics in the high-intensity radiolysis of aqueous systems.

Experimental Section

Materials. ACS reagent grade ferrous sulfate, cupric sulfate, and sulfuric acid were used without further purification. Singly distilled water was used for preparing the experimental samples since our previous experience showed no detectable difference between the response of samples prepared with the singly distilled water and samples prepared with water which had been triply distilled from a chromic-alkaline permanganate mixture using an all-quartz system.

Irradiation. Irradiation was carried out using a 10-MeV linear accelerator. The high-energy electron beam was focused through a collimator, a 3 × 6 mm hole in an aluminum block. The FeSO₄-CuSO₄-H₂SO₄ samples were placed in a long tube (~ 500 mm long and 4 mm i.d.) which was moved lengthwise in front of the electron beam in a reciprocating manner at a rate so that no overlap of successive radiation pulses at the rate of 15 pulses/sec would occur. In addition, the average total dose for any given sample was also kept within the linear response region for FeSO₄-CuSO₄-H₂SO₄ systems irradiated at low dose rates, and ranged between 3×10^{21} and 1×10^{22} eV l.⁻¹.

Dosimetry. Radiation dosimetry was based principally on coulometric measurement of the collimated electron beam using a modified Keithley 610B elec-

(1) Partially reported as a postdeadline paper at the International Conference on Radiation Chemistry, Argonne, Illinois, August 14, 1968.

(2) E. J. Hart and P. D. Walsh, *Radiat. Res.*, **1**, 342 (1954).

(3) E. J. Hart, *ibid.*, **2**, 33 (1955).

(4) E. Bjerbakke and K. Sehested, *Advances in Chemistry Series*, No. 81, American Chemical Society, Washington, D. C., 1968, p 579.

(5) J. W. Halliday and R. D. Jarrett, ref 4, p 604.

(6) A. Brasch and W. Huber, *Science*, **105**, 112 (1947).

(7) F. Hutchinson, *Radiat. Res.*, **9**, 13 (1957).

(8) J. Rotblat and H. C. Sutton, *Proc. Roy. Soc.*, **A255**, 490 (1960).

(9) P. Ya. Glazunov and A. K. Pikayev, *Dokl. Akad. Nauk SSSR*, **130**, 1061 (1960).

(10) A. R. Anderson and E. J. Hart, *J. Phys. Chem.*, **66**, 70 (1962).

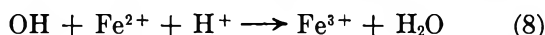
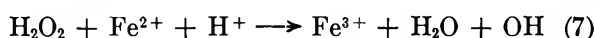
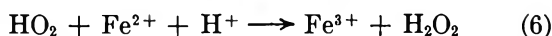
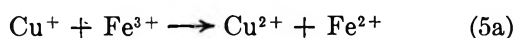
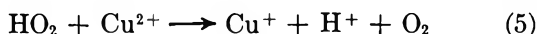
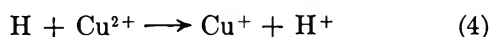
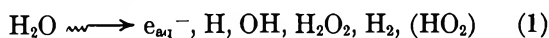
(11) J. K. Thomas and E. J. Hart, *ibid.*, **66**, 70 (1962); **68**, 2414 (1964).

trometer and the $-dE/dx$ values of high energy electrons reported in the literature,¹² supplemented by comparative measurements of the response of standard Fricke dosimeters with the results reported by Thomas and Hart¹¹ and by Rotblat and Sutton.⁸ The extent of ferric ion concentration was determined spectrophotometrically using a Cary Model 15 spectrophotometer at 25° and 302.5 nm (ϵ 2170).

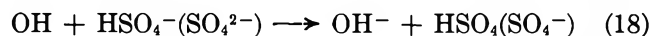
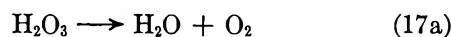
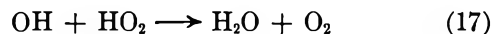
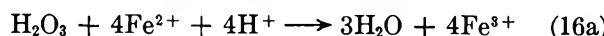
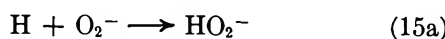
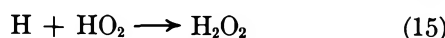
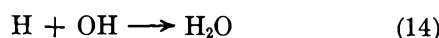
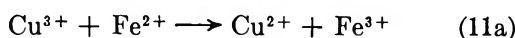
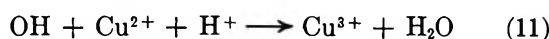
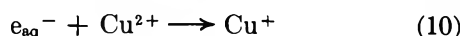
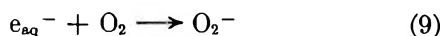
Results and Discussion

A large number of experiments have been carried out to examine the behavior of aqueous $\text{FeSO}_4\text{-CuSO}_4\text{-H}_2\text{SO}_4$ systems at different dose rates as a function of sample composition. The results show that although $G(\text{Fe}^{3+})$ is usually higher at the higher dose rates, its magnitude is a function of the concentration of the cupric and hydrogen ions as well as the extent of oxygenation. These are summarized in Figures 1-3.

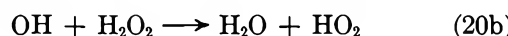
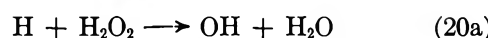
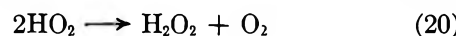
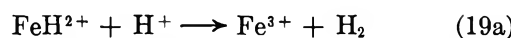
Reaction Mechanisms. Examination of our experimental data led to the conclusion that in addition to the reactions normally used in the description of the ferrous sulfate-cupric sulfate dosimeters, *i.e.*



it was necessary to include also the following reactions which influence either directly or indirectly the reaction kinetics at the high dose rates.



In an acidic medium, O_2^- is rapidly converted to HO_2 according to (9a), and consequently, (15a) is not an important process under the conditions of our experiment. Several other processes, though well established in the radiolysis of aqueous systems, have also been neglected. These include



Specifically, although reaction 19 represents one of the key processes in the radiolysis of deaerated acidic ferrous sulfate solutions,¹³ it is relatively unimportant under our experimental conditions because of the higher concentrations of the cupric ion. Similarly, reaction 20 is neglected because its rate constant is some four orders of magnitude lower than any other combination process listed in the preceding reaction mechanism. Reactions 20a and 20b are not explicitly included inasmuch as they are reflected in the empirical relationship between $G(-\text{H}_2\text{O}_2)$ and $[\text{H}_2\text{O}_2]$ in eq 28.

To a large extent, the probable values of the rate constants for these processes are known and have been summarized in the literature.¹⁴

Analysis of the Reaction Kinetics. Reactions 12, 15, and 16 represent the conversion of the reducing species H and HO_2 into either inert H_2 or the oxidizing species H_2O_2 and H_2O_3 , and are all favored by increasing radical concentration. Consequently, $G(\text{Fe}^{3+})$ should increase with increasing dose rate as is indeed observed in our experiments.

Quantitatively, we have

$$G(\text{Fe}^{3+}) = G_{\text{obs}}(\text{Fe}^{3+}) - G_0(\text{Fe}^{3+}) =$$

$$\frac{100N_0}{IT} \int_0^\infty \{2k_{12}[\text{H}]^2 + 4k_{15}[\text{H}][\text{HO}_2] + 4k_{16}[\text{OH}][\text{HO}_2]\} dt - 2\Gamma(-\text{H}_2\text{O}_2) \quad (21)$$

where G_{obs} is the experimentally observed yield of ferric ions in the high intensity experiment, G_0 is the yield when a similar sample is exposed to low intensity radiations such as the γ rays from a cobalt-60 source, N_0 is Avogadro's number, I is the dose rate in eV/

(12) M. J. Berger and S. M. Seltzer, NASA SP-3012, 89 (1964).

(13) G. Czapski, J. Jortner, and G. Stein, *J. Phys. Chem.*, **65**, 960 (1961).

(14) M. Anbar and P. Neta, *Int. J. Appl. Radiat. Isotop.*, **18**, 493 (1967).

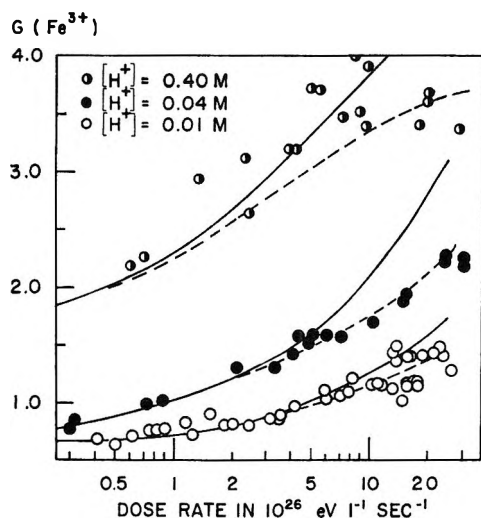


Figure 1. Effect of hydrogen ions on $G(\text{Fe}^{3+})$; $[\text{Cu}^{2+}] = 0.01 M$, $[\text{Fe}^{2+}] = 0.001 M$, $[\text{O}_2] = 0.00024 M$: —, calcd omitting H_2O_2 decomposition; - - -, calcd including H_2O_2 decomposition.

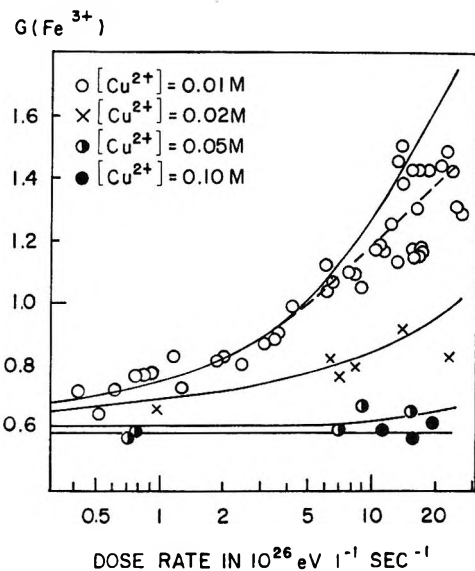


Figure 2. Effect of cupric ions on $G(\text{Fe}^{3+})$; $[\text{Fe}^{2+}] = 0.001 M$, $[\text{H}^+] = 0.01 M$, $[\text{O}_2] = 0.00024 M$: —, calcd omitting H_2O_2 decomposition; - - -, calcd including H_2O_2 decomposition.

l. sec, T is the pulse length in seconds, and $\Gamma(-\text{H}_2\text{O}_2)$ is a measure of the extent of radiation-induced decomposition of the hydrogen peroxide molecules formed during the high-intensity radiolysis.

The terms in eq 21 are obtained by solving the simultaneous differential eq 22, 23, and 24 or 22a, 23a, and 24 together with eq 29 using reiterative numerical programs developed during the course of this research.

$$\frac{d[\text{H}]}{dt} = k_2[e_{\text{aq}}^-][\text{H}^+] + \frac{g_{\text{H}}^0 I}{100N_0} - \{k_3[\text{O}_2] + k_4[\text{Cu}^{2+}] + k_{14}[\text{OH}] + k_{15}[\text{HO}_2]\} [\text{H}] - 2k_{12}[\text{H}]^2 \quad (0 \leq t \leq T) \quad (22)$$

$$\frac{d[\text{H}]}{dt} = -\{k_3[\text{O}_2] + k_4[\text{Cu}^{2+}] + k_{14}[\text{OH}] + k_{15}[\text{HO}_2]\} [\text{H}] - 2k_{12}[\text{H}]^2 \quad (t > T) \quad (22a)$$

$$\frac{d[\text{OH}]}{dt} = \frac{g_{\text{OH}} I}{100N_0} - \{k_8[\text{Fe}^{2+}] + k_{11}[\text{Cu}^{2+}] + k_{14}[\text{H}] + (k_{16} + k_{17})[\text{HO}_2] + k_{18}[\text{SO}_4^{2-}]\} [\text{OH}] - 2k_{13}[\text{OH}]^2 \quad (0 \leq t \leq T) \quad (23)$$

$$\frac{d[\text{OH}]}{dt} = -\{k_8[\text{Fe}^{2+}] + k_{11}[\text{Cu}^{2+}] + k_{14}[\text{H}] + (k_{16} + k_{17})[\text{HO}_2] + k_{18}[\text{SO}_4^{2-}]\} [\text{OH}] - 2k_{13}[\text{OH}]^2 \quad (t > T) \quad (23a)$$

and

$$\frac{d[\text{HO}_2]}{dt} = \{k_9[e_{\text{aq}}^-] + k_3[\text{H}]\} [\text{O}_2] - \{k_5[\text{Cu}^{2+}] + k_{15}[\text{H}] + (k_{16} + k_{17})[\text{OH}]\} [\text{HO}_2] \quad (24)$$

in which g_{H}^0 and g_{OH} designate respectively the primary 100-eV yield of the "residual" hydrogen atoms¹⁵ and the hydroxyl radicals, and $[e_{\text{aq}}^-]$, the concentration of the solvated electrons, is given by

$$\frac{d[e_{\text{aq}}^-]}{dt} = \frac{g_e^0 I}{100N_0} - \{k_2[\text{H}^+] + k_9[\text{O}_2] + k_{10}[\text{Cu}^{2+}]\} [e_{\text{aq}}^-] \quad (25)$$

where g_e^0 is the primary 100-eV yield of the electrons which have escaped from the spurs in the irradiated aqueous system. Under the conditions of our experiment, however, the steady-state concentration of the solvated electrons is reached in less than 10^{-8} sec. Consequently, we have

$$[e_{\text{aq}}^-] = \frac{g_e^0 I}{100N_0 \{k_2[\text{H}^+] + k_9[\text{O}_2] + k_{10}[\text{Cu}^{2+}]\}} \quad (26)$$

The extent of radiation-induced decomposition of hydrogen peroxide, $\Gamma(-\text{H}_2\text{O}_2)$ in eq 21 is calculated from eq 29 as follows. By disregarding the negligible contribution from eq 7 during the pulse, we have

$$\Gamma(-\text{H}_2\text{O}_2) = \int_0^T \left\{ k_{13}[\text{OH}]^2 + k_{15}[\text{H}][\text{H}_2\text{O}] + \frac{I}{100N_0} g_{\text{H}_2\text{O}_2}^0 \right\} dt - \int_0^T \left\{ k_{13}[\text{OH}]^2 + k_{15}[\text{H}][\text{HO}_2] + \frac{I}{100N_0} (g_{\text{H}_2\text{O}_2}^0 - G(-\text{H}_2\text{O}_2)) \right\} dt \quad (27)$$

Rigorous calculation of $G(-\text{H}_2\text{O}_2)$ on the basis of the interaction of the various radiation-produced intermediates with H_2O_2 and subsequent reactions cannot be

(15) J. T. Allan and G. Scholes, *Nature*, **187**, 218 (1960).

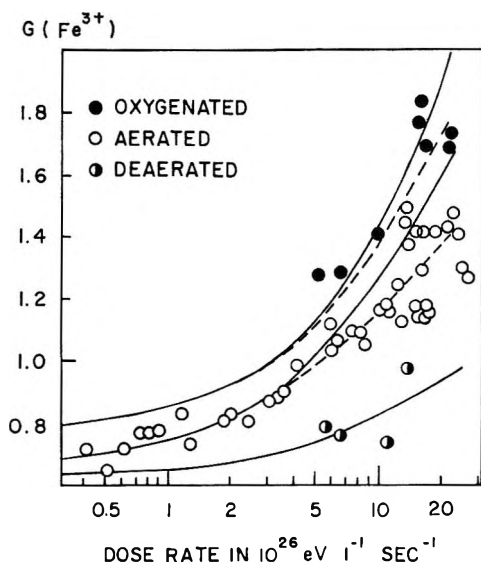


Figure 3. Effect of oxygen on $G(\text{Fe}^{3+})$: $[\text{Cu}^{2+}] = 0.01 M$, $[\text{Fe}^{2+}] = 0.001 M$, $[\text{H}^+] = 0.01 M$: —, calculated omitting H_2O_2 decomposition; ---, calcd including H_2O_2 decomposition.

made at the present time, however, on account of the unavailability of established values of the rate constants for a number of possibly important processes such as the reactions between either Cu^{3+} or Cu^+ ions and H_2O_2 molecules. Consequently, the relationship

$$G(-\text{H}_2\text{O}_2) \sim 2 \times 10^2 [\text{H}_2\text{O}_2]^{1/2} \quad (28)$$

which describes quite well the experimental data of Balkwell and Oldham¹⁶ on the radiolysis of hydrogen peroxide in aqueous solutions (for $[\text{H}_2\text{O}_2] \lesssim 10^{-3} M$) was assumed to be also a reasonable approximation under the conditions of our experiment ($[\text{H}_2\text{O}_2] \lesssim 10^{-4} M$), and eq 27 thus becomes

$$\Gamma(-\text{H}_2\text{O}_2) = \int_0^T \left\{ k_{13}[\text{OH}]^2 + k_{15}[\text{H}][\text{HO}_2] + \frac{I}{100N_0} g_{\text{H}_2\text{O}_2^0} \right\} dt - \int_0^T \left\{ k_{13}[\text{OH}]^2 + k_{15}[\text{H}][\text{HO}_2] + \frac{I}{100N_0} (g_{\text{H}_2\text{O}_2^0} - 2 \times 10^2 [\text{H}_2\text{O}_2]^{1/2}) \right\} dt \quad (29)$$

Because of the lack of good agreement among the literature values of some of the second-order radical reaction rate constants, a series of calculations was made using different rate constants. The results are illustrated in Figure 4, which shows that $\Delta G(\text{Fe}^{3+})$ is not significantly affected by variations in k_{12} and k_{13} , but is noticeably affected by k_{14} and $k_{16} + k_{17}$. The best agreement between our calculated and experimental values are obtained using $g_{\text{H}^0} = 0.6$, $g_e = 3.1$, and the rate constant values listed in Table I.

Discussions of some of the reactions and the effects of selected experimental parameters are now in order. These are given below.

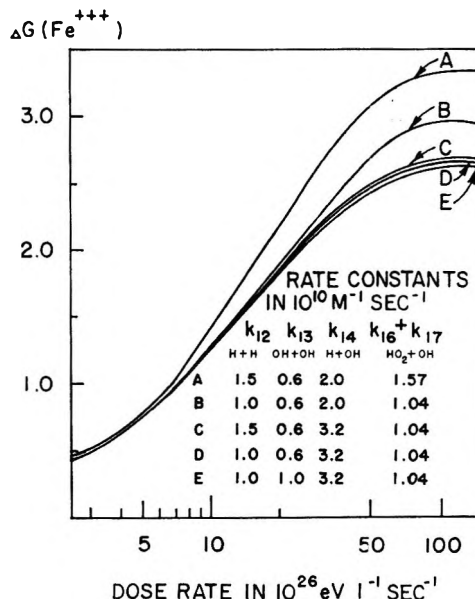


Figure 4. Effect of rate constants on calcd ΔG values; $[\text{Cu}^{2+}] = 0.01 M$, $[\text{Fe}^{2+}] = 0.001 M$, $[\text{H}^+] = 0.04 M$, $[\text{O}_2] = 0.00024 M$.

Table I: Pertinent Rate Constants in High-Intensity Irradiated FeSO_4 - CuSO_4 - H_2SO_4 Solutions^a

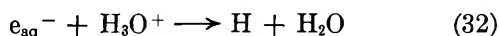
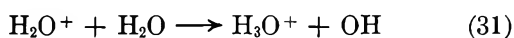
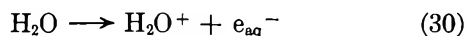
Rate constant	Reaction	Value (in $\text{l. mol}^{-1} \text{ sec}^{-1}$)
k_2	$e^- + \text{H}^+$	2.0×10^{10}
k_3	$\text{H} + \text{O}_2$	1.9×10^{10}
k_4	$\text{H} + \text{Cu}^{2+}$	1.5×10^8
k_5	$\text{HO}_2 + \text{Cu}^{2+}$	1.5×10^7
k_6	$\text{HO}_2 + \text{Fe}^{2+}$	$3.0 \times 10^7 \times [\text{H}^+]$
k_8	$\text{OH} + \text{Fe}^{2+}$	3.2×10^8
k_9	$e^- + \text{O}_2$	1.9×10^{10}
k_{10}	$e^- + \text{Cu}^{2+}$	3.0×10^{10}
k_{11}	$\text{OH} + \text{Cu}^{2+}$	3.5×10^8
k_{12}	$\text{H} + \text{H}$	1.4×10^{10}
k_{13}	$\text{OH} + \text{OH}$	0.6×10^{10}
k_{14}	$\text{H} + \text{OH}$	2.0×10^{10}
k_{15}	$\text{H} + \text{HO}_2$	2.0×10^{10}
k_{16}	$\text{OH} + \text{HO}_2 \rightarrow \text{H}_2\text{O}_2$	1.1×10^{10}
k_{17}	$\text{OH} + \text{HO}_2 \rightarrow \text{H}_2\text{O} + \text{O}_2$	4.7×10^9
k_{18}	$\text{OH} + \text{HSO}_4^- (\text{SO}_4^{2-}) \rightarrow \text{OH}^- + \text{HSO}_4 (\text{SO}_4^-)$	4×10^6

^a Except for k_5 and k_6 , literature references for other rate constants may be found in the rate constant compilations of Anbar and Neta.¹⁴ The value of k_5 is that reported by S. H. Baxendale, *Radiat. Res.*, **17**, 312 (1962); k_6 was evaluated experimentally and from the known k_5/k_6 ratio³ at $[\text{H}^+] = 0.01 M$. The values of k_{12} and k_{18} are averages of two or more literature values.

The Role of the Solvated Electron and the Effect of Hydrogen Ion Concentration. Although water and aqueous solutions are the most investigated systems in modern radiation chemical research, some of the specific primary processes which occur during the radiolysis of

(16) W. R. Balkwell and S. B. Oldham, USNRDL-TR-903 (1966).

water are not yet fully understood. Specifically, a degree of uncertainty still exists concerning the mechanism of formation of the radiolytically produced hydrogen atoms, *i.e.*, whether some of the hydrogen atoms observed in the radiolysis of aqueous systems are produced from the direct dissociation of water molecules,^{15,17,18} or whether all hydrogen atoms result from the reaction between solvated electrons and hydrogen ions as indicated in reaction 2. Allan and Scholes,¹⁵ for example, believed on the basis of experiments involving organic solutes that hydrogen atoms are formed directly from single excited molecules with $G(H) \sim 0.6$. Lifschitz,¹⁹ on the other hand, concluded on the basis of isotope effect experiments that even the so-called "residual" hydrogen atoms could not possibly result from the dissociation of one single water molecule, but must require a reaction involving separate water "molecules," supporting thereby the hypothesis that all hydrogen atoms are produced by sequences such as



i.e., the initial ionization of the water molecule to form the H₂O⁺ and e⁻ ion pairs, followed by the reaction of the electron with a hydrated hydrogen ion to form the free hydrogen atom. This latter possibility has not been supported by our experimental results, and consequently the 100 eV yield of the primary hydrogen atoms in acid solutions²⁰ is a reflection of the primary yields of both hydrogen atoms and solvated electrons with $g_{\text{H}}^0 = 0.6$, $g_e = g_{\text{H}} - g^0 = 3.1$.

The concept that both electrons and hydrogen atoms are produced in a highly acidic medium is not inconsistent with the experimental fact that only hydrogen atoms and not solvated electrons are observed in pulse radiolysis experiments involving acidic aqueous systems. Observations in pulse radiolysis experiments, for practical reasons, are made only after the completion of the pulse, *i.e.*, after a time period which is usually on the order of a microsecond. Since the pseudo-first-order rate constant for the conversion of electrons into hydrogen atoms is on the order of $2 \times 10^9 \text{ sec}^{-1}$ at pH 1, the residual electron concentration will be well below the detection capability of available methods, and solvated electrons have therefore been detected only in alkaline or nearly neutral media. The events of interest to high-intensity radiation chemistry, on the other hand, occur during the pulse period when both reactions 9 and 10 can effectively compete with reaction 2. Consequently, depending on the relative concentrations of the hydrogen and cupric ions in the system, the cuprous ions can be formed directly from electrons without requiring hydrogen atoms as the intermediate species.

At the higher acidities, reaction 6 is enhanced at the expense of reaction 5. Consequently, some of the perhydroxyl radicals will eventually oxidize three equivalents of ferrous ions according to reactions 6 and 7 instead of reducing one equivalent of ferric ions according to reactions 5 and 5a. $G(\text{Fe}^{3+})$ thus increases with increasing hydrogen ion concentration even at low dose rates as shown in Table II. More importantly, in-

Table II: Low Dose Rate $G(\text{Fe}^{3+})$ Values (G_0)^a

[Cu ²⁺], <i>M</i>	[H] ⁺ , <i>M</i>	[O ₂], <i>M</i>	G_0	Reference
0.01	0.01	0.0012	0.76	4
0.01	0.01	0.00024	0.66	3
0.01	0.04	0.00024	0.80	This work
0.01	0.40	0.00024	1.4	This work
0.01	0.01	0	0.63	4
0.02	0.01	0.00024	0.63	This work
0.05	0.01	0.00024	0.58	This work
0.20	0.01	0.00024	0.57	This work

^a [Fe²⁺] = 0.001 *M*.

creased acidity of the irradiated sample will also favor the formation of hydrogen atoms at the expense of the direct formation of the cuprous ions according to eq 2 and 10. As a result, the concentration of both the H and HO₂ radicals will increase with increasing acidity, enhancing the extent of the three radical combination processes responsible for increased $G(\text{Fe}^{3+})$, *i.e.*, reactions 12, 15, and 16. As Figure 1 shows, this expectation is indeed borne out by our experiments.

The Role of the Cu³⁺ Ions and the Effect of Cu²⁺ Ion Concentration. The absorption peak at 265 nm observed in the pulse radiolysis of acidic aqueous solutions of cupric salts has been interpreted²¹ on the basis of kinetic evidence to be due to the transient Cu³⁺ ion. Reactions 11 and 11a are, however, not always included in the reaction network describing the radiation chemistry of aqueous FeSO₄-CuSO₄-H₂SO₄ systems. Inasmuch as the overall results of these two reactions are identical with that of reaction 8, such an approach is well justified in the case of low-intensity irradiation experiments where radical combination reactions are negligible. At the high intensities which prevail in our experiments, however, combination of the radiation-produced radicals affects $G(\text{Fe}^{3+})$ as indicated in eq 22, and consequently, reactions 11 and 11a have been included in our kinetic analysis.

(17) J. Rabani, *J. Amer. Chem. Soc.*, **84**, 868 (1962).

(18) E. Hayon, *Trans. Faraday Soc.*, **60**, 1059 (1964).

(19) C. Lifschitz, *Can. J. Chem.*, **40**, 1903 (1962).

(20) F. S. Dainton and W. S. Watt, *Nature*, **195**, 1294 (1962).

(21) J. H. Baxendale, E. M. Fielden, and J. P. Keene, "Pulse Radiolysis," (Proc. 1st Int. Symp. on Pulse Radiolysis, Manchester, England, 1965) Academic Press, New York, N. Y., 1965 p 218.

The role of cupric ions in the high-intensity radiolysis of the $\text{FeSO}_4\text{-CuSO}_4\text{-H}_2\text{SO}_4$ is severalfold. Increased cupric ion concentration reduces the extent of hydrogen atom formation as the result of the very large rate constant of reaction 10. In addition, it also will reduce the extent of the various radical combination reactions by the competing processes 4, 5, and 11. Consequently, $G(\text{Fe}^{3+})$ for systems containing higher concentrations of cupric ions may be expected to show little, if any, dependence on the radiation dose rate. As Figure 2 shows, this conclusion is well supported by our experimental findings.

It is to be noted that even a low dose rate, $G(\text{Fe}^{3+})$ in the $\text{FeSO}_4\text{-CuSO}_4\text{-H}_2\text{SO}_4$ system decreases with increasing Cu^{2+} concentration.^{3,22} Consequently, the low dose rate Fe^{3+} yields, *i.e.*, G_0 , have been obtained and are summarized in Table II.

The Role of Oxygen and Radiation-Induced Decomposition of Hydrogen Peroxide. Hydrogen peroxide, which can be formed by both eq 13 and 15 through the combination of two OH or the H and HO_2 radicals, is an important factor responsible for the higher $G(\text{Fe}^{3+})$ values only in the case of aerated systems. No net change in $G(\text{Fe}^{3+})$ is expected from reaction 13. Reaction 15 is inherently impossible in deaerated systems, and in addition, as Figure 5 shows, is also not a major process in oxygenated systems inasmuch as most of the radiation-produced hydrogen atoms would actually be converted into the HO_2 species. In all cases, however, the radiation-produced hydrogen peroxide molecules are expected to be decomposed by further irradiation. Consequently, $\Delta G(\text{Fe}^{3+})$ values calculated omitting this decomposition would be increasingly too high at the higher dose rates as illustrated in Figures 1-3. Calculations including this decomposition reaction, on the other hand, are seen to agree well with the experimental data. Equation 28, obtained on the basis of the experimental results for hydrogen peroxide solutions in the absence of Cu^{2+} and Fe^{2+} ions thus appears to be also a reasonable approximation under the conditions of our experiment. It is to be pointed out, however, that the importance of the hydrogen peroxide decomposition process increases with increasing dose rate, and the application of eq 28 to experiments at still higher radiation intensities may well result in appreciable discrepancies between the observed and calculated G values.

Among other factors, the extent of decomposition of H_2O_2 is also a function of the pulse rate. Specifically, low repetition rates should lead to $G(\text{Fe}^{3+})$ values which are higher as it may be evidenced by a comparison of the data reported by Bjerbakke and Sehested⁴ with those observed in our experiments.

The Role of Hydrogen Sesquioxide (H_2O_3). Hydrogen sesquioxide, discovered in 1963 by Czapski and Bielski,²³ is formed by the combination of OH and HO_2 radicals when aerated or oxygenated water is exposed to high-

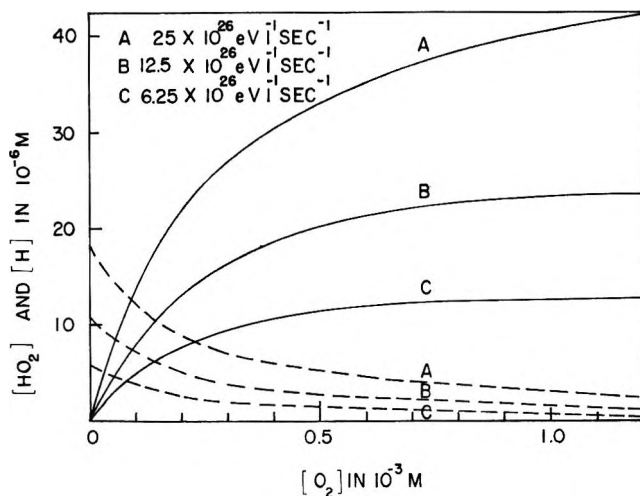
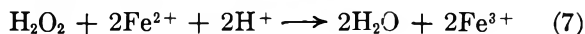
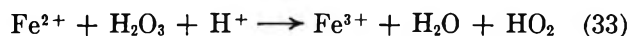


Figure 5. Effect of oxygen on the concn of HO_2 and H. Radicals (at 1 μsec after initiation of pulse). —, $[\text{HO}_2]$; ---, $[\text{H}]$.

intensity radiation. According to these investigators, $k_{16} = 1.1 \times 10^{10} \text{ l. mol}^{-1} \text{ sec}^{-1}$ whereas $k_{17} = k_{16}/2.3 = 4.7 \times 10^9 \text{ l. mol}^{-1} \text{ sec}^{-1}$. More recently, Sehested, Rasmussen, and Fricke,²⁴ using a somewhat different procedure, reported that $k_{16} + k_{17}$, which is a function of the pH of the sample, equals $1.27 \times 10^{10} \text{ l. mol}^{-1} \text{ sec}^{-1}$ in an acidic medium. In either case, radiation-induced decomposition of H_2O_3 has not been explicitly considered, and consequently, the values of k_{16} represent descriptions of the net rate of formation of H_2O_3 under high intensity irradiation conditions.

H_2O_3 decomposes to form water and molecular oxygen with a pH-dependent first order rate constant on the order of 1 sec^{-1} . It therefore mainly reacts with the reducing species in the irradiated medium. In an acidic solution of ferrous sulfate, for example, there is considerable evidence that each molecule of H_2O_3 will lead to the oxidation of four ferrous ions, a phenomenon which has been explained on the basis of the following mechanisms²⁴



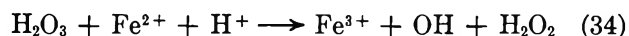
This mechanism is, however, probably of only limited importance in the oxidation of ferrous ions by H_2O_3 . If reaction 33 were indeed the principal path for such oxidation processes, the formation of H_2O_3 from OH and HO_2 radicals should not have any effect on $G(\text{Fe}^{3+})$ inasmuch as the HO_2 radicals formed in reaction 28 will act mainly as a reducing agent in accordance to reaction 5. Our calculations, on the other hand, show that

(22) D. Katakis and A. O. Allen, *J. Phys. Chem.*, **68**, 657 (1964).

(23) G. Czapski and B. H. J. Bielski, *ibid.*, **67**, 2180 (1963).

(24) K. Sehested, O. L. Rasmussen, and H. Fricke, *ibid.*, **72**, 626 (1968).

H₂O₃ is the principal species responsible for the very high $G(\text{Fe}^{3+})$ values in oxygenated aqueous FeSO₄-CuSO₄-H₂SO₄ systems. Indeed, good agreements between calculation and experiment are obtained if each molecule of H₂O₃ is assumed to oxidize in full four ferrous ions. An alternate path must therefore be considered. We believe this to be



followed by the oxidation of three additional Fe²⁺ ions by OH and H₂O₂ according to reactions 7 and 8.

At least in principle, determination of the validity of reaction 34 may be afforded by performing H₂O₃ under high intensity irradiation conditions followed by direct observation of the radical species formed when the H₂O₃ so produced is allowed to react with a solution of FeSO₄. Alternatively, the preformed H₂O₃ may be allowed to react with an acidic aqueous solution containing both CuSO₄ and FeSO₄ in which $[\text{Cu}^{2+}]/[\text{Fe}^{2+}] \geq 10$. The extent of Fe³⁺ formation would then provide a direct measure of the relative importance of the two alternative paths indicated by reactions 33 and 34.

The Effect of Pulse Length. The time required for the reactions of the H atoms in deaerated samples and that of the HO₂ radicals in the oxygen-containing solutions are all on the order of a few microseconds. The $G(\text{Fe}^{3+})$ values should, therefore, increase initially with increasing pulse length, reaching a maximum value, and then possibly decrease at even longer pulse lengths as the result of the decomposition of hydrogen peroxide by prolonged irradiation.

Comparative experiments have been carried out at a number of selected pulse lengths. These results are summarized in Table III.

Table III: Effect of Pulse Length on $G(\text{Fe}^{3+})^a$

[Cu ²⁺], M	[O ₂], M	Dose rate, 10 ²⁷ eV l. ⁻¹ sec ⁻¹	Pulse length, 10 ⁻⁸ sec	$G(\text{Fe}^{3+})$
0.01	0.0012	1.63	5	1.84
		1.60	2	1.77
0.01	0.00024	2.44	2	1.41
		2.50	1.5	1.17
0.01	0	1.54	5	1.22
		1.41	2	0.98
0.02	0.00024	1.37	2	0.92
		1.31	1	0.84
0.05	0.00024	1.56	2	0.66
		1.44	1	0.62
0.10	0.00024	2.00	2	0.65
		2.00	1	0.65

^a [Fe²⁺] = 0.001 M.

G(Fe³⁺) at Very High Dose Rates. According to our calculations, the maximum $G(\text{Fe}^{3+})$ value which can be reached is approximately 4. At the very highest dose rates, recombination of the H and OH radicals to form water, hydrogen peroxide, and molecular hydrogen assumes increasing importance, and may indeed even lead to decreases from the maximum value. It would be interesting to examine the validity of this conclusion in experiments using the very intense pulses from machines such as the field-emission sources.

Acknowledgment. The authors are indebted to Dr. E. J. Hart of the Argonne National Laboratory for his valuable advice, Dr. Raymond D. Cooper, Mr. Christopher W. Rees, Mr. James M. Caspersen, Mr. George Dewey, Mr. Christopher Hursh, and Mr. Leon Gricus at the Linear Accelerator Branch of the U. S. Army Natick Laboratories for experimental support.

Magnetophotoselection. Effect of Depopulation and Triplet-Triplet Absorption¹

by Henry S. Judeikis and Seymour Siegel

The Aerospace Corporation, El Segundo, California 90045 (Received September 18, 1969)

The combined use of electron spin resonance (esr) spectroscopy and polarized exciting optical radiation to study the spectra of excited triplet electronic states of molecules dissolved in rigid glasses has been named magnetophotoselection (mps). This paper discusses the quantification of this technique and describes the equations for obtaining quantitative results. The emphasis is on determining the polarization of exciting singlet-singlet transitions; however, the model described is general and can be extended to other studies. Effects due to depopulation of the ground-state molecules and to triplet-triplet absorption are explicitly considered. The results of computer-simulated mps experiments are given for several representative cases. Finally, rules are given for maximizing the accuracy of an mps experiment.

I. Introduction

A. Background. Much information on the nature of optical electronic transitions in molecules can be obtained by the determination of the polarization of the electronic absorption spectra with respect to the molecular axes.² The most detailed data in this area have been obtained with dilute solutions of the molecule to be examined in single crystal host matrices. Unfortunately, many practical restrictions exist that severely limit the number of solute-solvent single-crystal systems that can be examined. The development of photoselection techniques expanded the number of molecules that could be examined for polarization data.³ This latter technique uses a rigid optical glass as the host medium and photoselects a weighted distribution of excited states from a random distribution of ground-state molecules by the use of polarized exciting optical radiation; the details of the weighting are a function of the polarization of the electronic transition. The emission from an excited state, not necessarily the same one originally excited, is also observed with the use of a polarizer. Information on the polarization of the absorption process can be obtained if the polarization of the emitting transition is known; the converse is equally true.

A new type of photoselection technique, described in several recent papers, uses the electron paramagnetic resonance (epr) spectrum of the excited triplet state of the molecule to sample the weighting function resulting from the polarization of the exciting transition.⁴⁻¹⁰ This technique is based on the anisotropy characteristics of the $\Delta m = \pm 1$ Zeeman transitions observed in the epr spectra of triplet-state molecules.^{11,12} The relationships between the spectral transition intensities, the direction of the applied magnetic field, and the directions of the principal magnetic axes in the molecule are such that, operationally, the only transitions observed in the epr spectra of triplet-state molecules dissolved in rigid glasses are those due to the molecules whose principal magnetic axes are aligned essentially parallel

(to within $\pm 5^\circ$) to the applied magnetic field (\vec{H}).¹³ The remaining molecules contribute to a broad, unresolved base line. For molecules of sufficient symmetry that the magnetic axes of the triplet state are coincident with the symmetry axes of the electron distribution, we have molecules with known spatial orientations to examine. The combination of the use of polarized light to prepare a nonrandom distribution of excited molecules and epr observation has been designated magnetophotoselection (mps).⁵

The most common use of mps has been to determine the polarization of singlet-singlet absorption bands for a variety of molecules.⁵⁻⁷ Since this technique observes only triplet-state molecules, the latter use requires that the lowest excited triplet state of the solute molecule, which is excited by intersystem crossing from the excited singlet state, retain the same symmetry axes as the singlet states involved. Changes in the symmetry group of the molecules in the different electronic states involved introduce complications into

(1) This work was supported by the United States Air Force under Contract No. F04701-69-C-0066.

(2) See, for example, S. P. McGlynn, T. Azumi, and M. Kinoshita, "Molecular Spectroscopy of the Triplet State." Prentice-Hall, Inc., Englewood Cliffs, N. J., 1969.

(3) A. C. Albrecht, *J. Mol. Spectra.*, **6**, 84 (1961), and references therein.

(4) P. Kottis and R. Lefebvre, *J. Chem. Phys.*, **41**, 3660 (1964).

(5) M. A. El-Sayed and S. Siegel, *ibid.*, **44**, 1416 (1966).

(6) S. Siegel and H. S. Judeikis, *J. Phys. Chem.*, **70**, 2205 (1966).

(7) G. P. Rabold and L. H. Piette, *Photochem. Photobiol.*, **5**, 733 (1966).

(8) S. Siegel and L. Goldstein, *J. Chem. Phys.*, **43**, 4185 (1965).

(9) S. Siegel and L. Goldstein, *ibid.*, **44**, 2780 (1966); **45**, 1860 (1966).

(10) J. M. Lhosti, A. Haug, and M. Ptak, *ibid.*, **44**, 648, 654 (1966).

(11) P. Kottis and R. Lefebvre, *ibid.*, **41**, 379 (1964).

(12) E. Wasserman, L. C. Snyder, and W. A. Yager, *ibid.*, **41**, 1763 (1964).

(13) Contributions to the epr signal intensities rapidly diminish for angles much greater than $\pm 5^\circ$. Theory does, however, predict a small contribution for specific angles $\gg 5^\circ$. Using the computed spectrum for naphthalene, kindly furnished to us by Dr. L. C. Snyder, we estimate these contributions to be of the order of 10% or less.

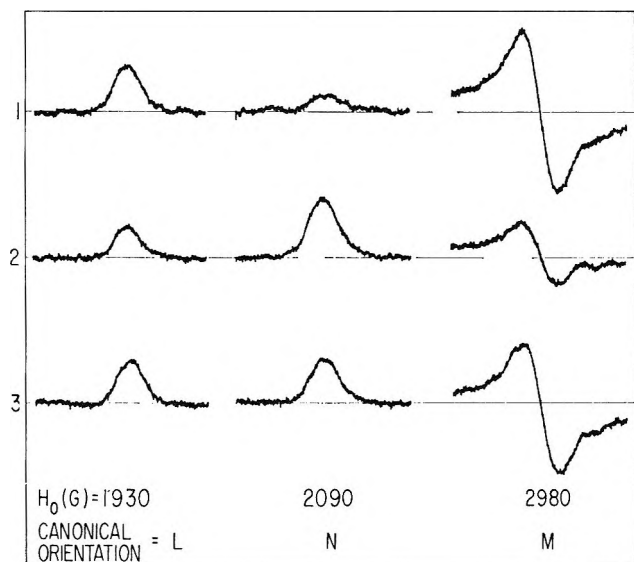


Figure 1. The low-field half of the $\Delta m = \pm 1$ epr spectrum of the triplet state of phenanthrene- d_{10} . The spectra are due to excitation of a 0.02 M solution of phenanthrene- d_{10} in ethanol at 77°K with polarized light at different angles with respect to H: (1) $\vec{E} \parallel \vec{H}$; (2) $\vec{E} \perp \vec{H}$; and (3) the angle between E and H equals 45°. The approximate resonant fields correspond to spectra taken with an x -band spectrometer.

the data analysis to the extent that we do not know the relative orientations of the symmetry axes. For this discussion we ignore any complications due to symmetry changes. Additional uses of mps have been in the determination of the mutual molecular orientation dependence of triplet-triplet transfer between unlike molecules,⁸ the efficiency of energy transfer between like molecules,⁹ polarized photochemistry, and assignment of epr spectra.¹⁰

The mps technique is especially well suited for use with planar aromatic molecules, and in this discussion we concentrate on this type of molecule. In accordance with common practice, we label the molecular symmetry axes L , M , and N , where L and M are the long and short axes, respectively, in the plane of the molecule and N is the axis perpendicular to the molecular plane. The spectra shown in Figure 1 are obtained when the system of an aromatic molecule dissolved in a rigid optically transparent glass is excited with optical radiation polarized at various angles with respect to the magnetic field. The three lines shown in Figure 1 correspond to each of the three canonical orientations; there are three similar lines on the high-field side of $g = 2.0$.^{11,12}

B. Idealized Case. The experimental data⁵⁻¹⁰ have been analyzed either implicitly or explicitly with idealized solutions, which are based on the assumption that negligible depopulation or depletion of the ground state exists. Under this assumption the components (r_i) of the polarization of the exciting singlet-singlet transition along the molecular axes can be written⁶

$$r_i = \frac{1 + [1 + (4/3)k']P_i}{3 - P_i} \quad (1)$$

where $i = L, M, N$, and

$$P_i = \frac{N_{T,i}(\parallel) - N_{T,i}(\perp)}{N_{T,i}(\parallel) + N_{T,i}(\perp)} = \frac{h_i(\parallel) - h_i(\perp)}{h_i(\parallel) + h_i(\perp)} \quad (2)$$

In these equations $N_{T,i}(\parallel)$ and $N_{T,i}(\perp)$ are the concentrations of molecules in the triplet state and with the i th canonical orientation when $\vec{E} \parallel \vec{H}$ and $\vec{E} \perp \vec{H}$, respectively; $h_i(\parallel)$ and $h_i(\perp)$ represent the corresponding relevant epr signals; and k' is equal to the ratio of nonpolarized to polarized exciting light. Equation 1 assumes that any nonpolarized component in the exciting light, as measured by k' , is equally divided into three mutually orthogonal components. If the nonpolarized light has no component in the direction of propagation

$$r_i = \frac{P_i(1 + k) + (1 - k)}{3(1 - k) - P_i(1 + k)} \quad (3)$$

In eq 3, k is defined as the ratio of the minor to the major component of exciting light. [Note that this definition of k is slightly different from that of k' in eq 1.] Thus, for $\vec{E} \parallel \vec{H}$, $k = I(\perp)/I(\parallel)$. Several uncertainties are experimentally introduced with these equations that result from changes in the value of k (or k') and the incident light intensity when the polarizer used in the excitation process is rotated.

Another method to determine the values of r_i involves using just the results from the $\vec{E} \parallel \vec{H}$ spectrum. Under these conditions

$$r_i = \frac{2H_i(1 + k) - k}{2 - k} \quad (4)$$

where

$$H_i = \frac{h_i^s}{\sum_i h_i^s} \quad (i = L, M, N) \quad (5)$$

In eq 5, h_i^s represents the normalized intensity of the epr signal corresponding to the i th canonical orientation. This normalization can be effected by use of the results of triplet-triplet energy transfer experiments.^{8,9} Considering that triplet-triplet energy transfer for at least some donor-acceptor pairs is essentially nonpolarized, excitation of the molecule being examined by such a transfer reaction will give $r_i = 1/3$. Using these results, we can normalize the experimental h_i values to give intensities that are now independent of line shape (h_i^s). Alternatively, computer programs can be used to compute the epr line shapes corresponding to equal excitation of the three canonical orientations.^{11,12} The computed line shapes can then be used to normalize h_i .

The use of eq 4 yields three equations in four unknowns; the relationship $\sum r_i = 1$ was already used to

obtain these equations. It is conceivable that a direct measurement of k can be made; however, the experimental arrangement in the epr spectrometer makes a meaningful measurement difficult. In practice, k has been determined with the assumption that $r_N = 0$ for at least one molecule. [It should be remembered that the derivation of eq 4 assumes that there is no component of exciting light polarization along the direction of propagation. If this assumption is incorrect, then eq 4 must be modified. However, the modification is trivial, and the results of the determination of r_i will not be affected if the $r_N = 0$ assumption is used to calculate k .]

C. The Problem. Since in the mps method we are looking at only a small fraction of the total number of triplet-state molecules excited, there are serious problems with the ratio of signal to noise. Usually, intense light sources are employed and depopulation of the ground state occurs. With the advent of depopulation, several complications are introduced, and the equations discussed must be modified; the relative absorption of light by the canonically oriented molecules will no longer be related to the values of r_i in the simple manner of eq 4. For optically thick samples (*i.e.*, samples in which a significant fraction of the incident light is absorbed) it is also necessary to consider variations in the molecular distributions across the sample thickness, as well as the competition between the absorption of the exciting light by the ground-state molecules and by the molecules in their triplet states (the triplet-triplet absorption process is not spin-forbidden).

The purpose of this paper is to consider how we can use the mps technique to determine transition polarizations in depopulated and optically thick systems in the presence and absence of triplet-triplet absorption. We are also interested in discovering what additional information about molecular absorption processes can be derived from the effects of these complications on the mps epr spectra; in other words, how can we capitalize on these complications?

II. Extension of the Model

A. Depopulation Of Optically Thin Systems. If the rate of excitation of the triplet state is sufficiently high compared to the rate of decay, an appreciable fraction of the molecules can exist in the triplet state. Under these conditions, the equations in the preceding sections are no longer applicable and must be modified. If we assume that $E \parallel H$, with a small component of light with $E \perp H$ due to incomplete polarization or to depolarization effects in the optics, the rate of excitation (R_{ex}) of molecules representing the i th canonical orientation is

$$R_{ex} = 3\alpha_0\varphi_{ISC}I(\parallel)[r_i + k(r_j \sin^2 \theta + r_i \cos^2 \theta)]N_{0,i} \quad (6)$$

where φ_{ISC} is the quantum yield for intersystem crossing and α_0 is equal to $2.303 \times \epsilon_0 \times (10^3/A)$, ϵ_0 being

the molar extinction coefficient of the ground-state molecules, and A being Avogadro's number. With this definition of α_0 , the light intensities are in units of photons/cm² sec. In addition, θ is the angle between the exciting light component with $\vec{E} \perp \vec{H}$ and the j and l molecular axes in the plane normal to $\vec{E} \parallel \vec{H}$, $N_{0,i}$ is the concentration of molecules in the ground or unexcited state and, as before, $k = I(\perp)/I(\parallel)$. Making use of the relation

$$R_{decay} = k_p N_{T,i} \quad (7)$$

where k_p is the phosphorescent decay constant and $N_{T,i}$ is the concentration of triplet molecules, the steady-state ($R_{ex} = R_{decay}$) equation is given by

$$3\alpha_0\varphi_{ISC}I(\parallel)[r_i + k(r_j \sin^2 \theta + r_i \cos^2 \theta)]N_{0,i} = k_p N_{T,i} \quad (8)$$

But $N_{0,i}$ and $N_{T,i}$ are related by

$$N_i \simeq N_{0,i} + N_{T,i} \quad (9)$$

where N_i is the total of all molecules possessing the i th canonical orientation. Substitution of eq 9 into eq 8 and rearrangement gives

$$f_i = \frac{3\alpha_0\varphi_{ISC}I(\parallel)[r_i + k(r_j \sin^2 \theta + r_i \cos^2 \theta)]}{k_p + 3\alpha_0\varphi_{ISC}I(\parallel)[r_i + k(r_j \sin^2 \theta + r_i \cos^2 \theta)]} \quad (10)$$

In eq 10, $f_i = N_{T,i}/N_i$ is the fraction of all molecules in the triplet state with a particular orientation with regard to the directions of \vec{H} and \vec{E} . Except in oriented systems (*e.g.*, single crystals), θ can take on all values between 0 and $\pi/2$. Therefore, experimentally observable quantities will be proportional to the average value of f_i

$$\langle f_i \rangle = \frac{\int_0^{\pi/2} f_i d\theta}{\int_0^{\pi/2} d\theta} \quad (11)$$

Substitution of eq 10 into eq 11 and integration gives

$$\langle f_i \rangle = 1 - 1/(a_i^2 - b_i^2)^{1/2} \quad (12)$$

where

$$a_i = 1 + \frac{3\alpha_0\varphi_{ISC}}{k_p} I(\parallel)[r_i + \frac{1}{2}k(r_i + r_j)] \quad (13)$$

$$b_i = \frac{3\alpha_0\varphi_{ISC}}{k_p} I(\parallel)[\frac{1}{2}k(r_i - r_j)] \quad (14)$$

Since eq 12 represents the fraction of molecules in the i th canonical orientation that are in the triplet state, the relevant epr line intensity is given by

$$h_i^s = \beta_i^s \langle f_i \rangle N_i \quad (15)$$

where β_i^s is a factor relating the triplet molecular concentration to the epr spectral intensity, and the S superscript indicates that β_i has been normalized by use

of the results of an energy transfer experiment or a computer calculation (see above). Equations 12 and 15 represent solutions for the case of nonnegligible depopulation of the ground state. For very weak light intensities, eq 15 reduces to eq 4.

B. Optically Thick Systems. High concentrations are generally used to increase experimental sensitivities. So long as the exciting light is sufficiently weak to prevent significant depopulation of the ground state, eq 3 and 4 are still applicable for optically thick samples. When higher light intensities are used, the problem becomes more complex. For optically thick samples, both $I(\parallel)$ and k will vary with path length. This variation will depend not only on the absorption coefficient of the ground-state molecules and the polarization of the absorption, but also on the absorption, if any, by the triplet-state molecules. If $I(\parallel)$ and k are known as a function of path length, eq 12 and 15 can be used to calculate, at each point along the path, the average triplet concentration corresponding to the i th canonical orientation and its contribution to the total epr intensity. These quantities can then be averaged over the entire path length for the purpose of comparison with experiment. Thus, the problem reduces to the calculation of the light intensities as a function of path length. In the latter calculation, since there is a competition for the available light, we must consider all solute molecules, not just those representing the canonical orientations.

First we assume that the system of interest consists of randomly oriented solute molecules in which both the ground-state concentration (C_0) and excited triplet-state concentration (C_T) absorb light. The total solute concentration (C) is

$$C \simeq C_0 + C_T \quad (16)$$

With this assumption, the change in transmitted light intensity on passing through the system will be

$$dI = -I(\alpha_0 C_0 + \alpha_T C_T) dx \quad (17)$$

where α_0 and α_T are proportional to ϵ_0 and ϵ_T , respectively, the singlet-singlet and triplet-triplet molar extinction coefficients. In addition

$$C_T = C \left(\frac{k_{EX}}{k_{EX} + k_p} \right) \quad (18)$$

where k_{EX} is the rate constant for triplet excitation (equal to $\alpha_0 \varphi_{ISC} I$) and k_p is the phosphorescent decay constant. We have recently reported the solution of eq 17 for cases in which polarization effects were neglected.¹⁴ In this paper we include these effects, particularly in reference to the utilization of polarized exciting light and the magnetophotoselection technique.

Two modifications of eq 17 are required to account for the effects of exciting with polarized light. The first consists of separating the light intensity into two or-

thogonal components,¹⁵ designated $I(\parallel)$ and $I(\perp)$. Both components are normal to the direction of propagation. The second modification consists of introducing the polarization of the S-S and T-T transitions. In the following, the r 's will refer to the S-S polarization and the ρ 's to the T-T polarization. This problem is best handled in Euler space and has previously been discussed by Albrecht, *et al.*^{16,17} We shall use Albrecht's notations throughout, except that we shall use L, M, N , respectively, in place of the Z, Y, X axial designation. The major difference between the present treatment and that of Albrecht, *et al.*, is that depopulation effects are not neglected here. Application of these modifications to eq 17 and 18 leads to the following expressions for C_T and $dI(\parallel)$

$$C_T = C \frac{(k_{\parallel} + k_{\perp})_{EX}}{k_p + (k_{\parallel} + k_{\perp})_{EX}} \quad (19)$$

$$dI(\parallel) = - \frac{2.303[3CI(\parallel)]}{8\pi^2} \left\{ \int_0^{2\pi} \int_0^{2\pi} \int_0^{\pi} \times \right. \\ \left[\epsilon_0 \left(1 - \frac{C_T}{C} \right) (\lambda_{L\parallel}^2 r_L + \lambda_{M\parallel}^2 r_M + \lambda_{N\parallel}^2 r_N) + \right. \\ \left. \epsilon_T \left(\frac{C_T}{C} \right) (\lambda_{L\parallel}^2 \rho_L + \lambda_{M\parallel}^2 \rho_M + \lambda_{N\parallel}^2 \rho_N) \right] \times \\ \left. \sin \theta d\theta d\varphi d\psi \right\} dx \quad (20)$$

The expression for $dI(\perp)$ is identical with eq 20 if the \perp subscript is inserted in place of the \parallel subscript. Additional definitions are

$$k_{\parallel,EX} = 2.303(3\epsilon_0 I_{\parallel}) (\lambda_{L\parallel}^2 r_L + \lambda_{M\parallel}^2 r_M + \lambda_{N\parallel}^2 r_N) \quad (21)$$

$$k_{\perp,EX} = 2.303(3\epsilon_0 I_{\perp}) (\lambda_{L\perp}^2 r_L + \lambda_{M\perp}^2 r_M + \lambda_{N\perp}^2 r_N) \quad (22)$$

and

$$\lambda_{L\parallel} = \cos \theta \quad (23)$$

$$\lambda_{M\parallel} = \sin \theta \sin \psi \quad (24)$$

(14) H. S. Judeikis and S. Siegel, *J. Phys. Chem.*, **73**, 2036 (1969).

(15) Again we assume there is no component in the direction of propagation. For magnetophotoselection experiments conducted in cylindrical sample tubes, this assumption is obviously incorrect. However, taking into account refractions at various interfaces in the usual experimental geometry, we estimate the component in the direction of propagation to be $\sim 5\%$ or less. Of course, different geometries could reduce this contribution considerably. Another possibility we neglect is internal randomization of the exciting light (*e.g.*, scattering) which could give a component in the direction of propagation. Albrecht and Simpson have introduced this concept in their treatment of polarization in negligibly depopulated systems.¹⁶ When depopulated systems are considered the problem becomes more complex, since the randomized light must now be calculated as a function of path length.

(16) A. C. Albrecht and W. T. Simpson, *J. Amer. Chem. Soc.*, **77**, 4454 (1955).

(17) J. R. Lombardi, J. W. Raymond, and A. C. Albrecht, *J. Chem. Phys.*, **40**, 1148 (1964).

Table I: Parameters used in Sample Calculations^{a,b}

Table ^c	τ_M	τ_L	τ_N	ϵ_T/ϵ_S	ρ_M	ρ_L	ρ_N	k^d	OD ^e
II	0.8	0.2	0.0	0	0.05	vary
III	0.8	0.2	0.0	2	0.5	0.5	0.0	0.05	vary
IV	vary	vary	0.0	0	0.05	1.0
V	0.8	vary	vary	0	0.05	1.0
VI	0.8	0.2	0.0	2	vary	vary	vary	0.05	1.0
VII	0.8	0.2	0.0	0	vary	1.0

^a Calculations are for a round sample tube with a 0.25-cm diameter. ^b For all cases $\varphi_{TSC} = 1.0$, $k_p = 1.0 \text{ sec}^{-1}$, $\epsilon_a = 5000 \text{ l. mol}^{-1} \text{ cm}^{-1}$. ^c In Tables II–VII, % DP is defined as the average per cent depopulation of all molecules at the incident face of the sample tube and OD is defined as the maximum optical density in the circular sample tube assuming no depopulation (*e.g.*, $OD = \epsilon_a C_0 l$ where $l = 0.25 \text{ cm}$, the diameter of the sample tube). ^d $k = I(\perp)/I(\parallel)$.

$$\lambda_{N\parallel} = \sin \theta \cos \psi \quad (25)$$

$$\lambda_{L\perp} = -\sin \theta \cos \varphi \quad (26)$$

$$\lambda_{M\perp} = \sin \varphi \cos \psi + \cos \theta \cos \varphi \sin \psi \quad (27)$$

$$\lambda_{N\perp} = \cos \theta \cos \varphi \cos \psi - \sin \varphi \sin \psi \quad (28)$$

The factors of 3 and $8\pi^2$ in eq 20–22 arise from application of boundary conditions [*e.g.*, in the limit of zero light intensity, $dI(\parallel) + dI(\perp)$ must reduce to eq 17], and the factor of $2.303 = \ln(10)$ arises because the ϵ 's refer to the decadic extinction coefficients.

The complexity of these equations does not suggest a useful general analytical solution. Consequently, a computer program has been written to obtain numerical solutions for C_T , $I(\parallel)$, and $I(\perp)$ as a function of path length. By use of the latter quantities and eq 12–15, the contributions to the $\Delta m = \pm 1$ epr intensities were also determined at each path length increment. The incremental contributions were then summed to give quantities related to experiment.

III. Results and Discussion

In lieu of presenting large quantities of computer results to quantitatively indicate the magnitude of these effects on the epr spectra for all possible varieties of conditions, we present results for representative systems and concentrate on establishing experimental guidelines for conducting magnetophotoselection experiments. Toward this end we use the computed epr intensities, in conjunction with eq 4 and 5 and the assumption $\tau_N = 0$, to calculate apparent values for τ_i and k . We then attempt to define the conditions under which the apparent values of τ_i and k are in agreement with the true (input) values with minimal uncertainties.¹⁸ The various parameters used in the sample calculations are given in Table I.

Table II illustrates the effects of concentration (optical density) and light intensity on apparent polarization values when no triplet–triplet absorption occurs; Table III gives similar results for a strong triplet–triplet absorption. To assess the significance of the results in terms of experimental applications we should

Table II: Effects of Concentration (Optical Density) and Light Intensity on Apparent Polarizations ($\epsilon_T = 0$)^a

A. Apparent Values of τ_M (true value = 0.8)				
% DP	OD =	2.0	0.30	0.01
10^{-4}		0.800	0.800	0.800
1		0.798	0.798	0.797
3		0.795	0.792	0.791
10		0.785	0.777	0.772
25		0.757	0.736	0.728
49		0.697	0.661	0.654
B. Apparent Values of τ_L (true value = 0.2)				
% DP	OD =	2.0	0.30	0.01
10^{-4}		0.200	0.200	0.200
1		0.202	0.202	0.203
3		0.205	0.208	0.209
10		0.215	0.223	0.228
25		0.243	0.264	0.272
49		0.303	0.339	0.346
C. Apparent Values of k (true value = 0.05)				
% DP	OD =	2.0	0.30	0.01
10^{-4}		0.0502	0.0501	0.0500
1		0.0508	0.0509	0.0511
3		0.0517	0.0527	0.0534
10		0.0546	0.0582	0.0605
25		0.0634	0.0756	0.0816
49		0.0910	0.1280	0.1398

^a See Table I.

note that the experimental uncertainties in the values of τ_i are usually ~ 0.01 to 0.03 unit. Several trends appear in the results of Tables II and III that we have found to be fairly general trends. These are (1) with increasing depopulation (especially for front face depopulation > 10 to 20%), the apparent polarizations (and k) show increasing deviations from the true values; (2) the apparent value of k is most sensitive to devia-

(18) In this discussion, we ignore two trivial cases that always give the correct polarizations. These cases are τ_L (or τ_M) = 1, and $\tau_L = \tau_M = 0.5$. However, even in these cases, the correct value of k is obtained only for ideal conditions.

Table III: Effects of Concentration (Optical Density) and Light Intensity on Apparent Polarizations ($\epsilon_T = 10,000$)^a

A. Apparent Values of r_M (true value = 0.8)				
% DP	OD =	2.0	0.3	0.01
10 ⁻⁴		0.800	0.800	0.800
1		0.798	0.798	0.797
3		0.794	0.792	0.791
10		0.785	0.778	0.773
25		0.762	0.742	0.729
49		0.720	0.678	0.655
B. Apparent Values of r_L (true value = 0.2)				
% DP	OD =	2.0	0.3	0.01
10 ⁻⁴		0.200	0.200	0.200
1		0.202	0.202	0.203
3		0.206	0.208	0.209
10		0.215	0.222	0.227
25		0.238	0.258	0.271
49		0.280	0.322	0.345
C. Apparent Values of k (true value = 0.05)				
% DP	OD =	2.0	0.3	0.01
10 ⁻⁴		0.0502	0.0501	0.0500
1		0.0509	0.0510	0.0511
3		0.0524	0.0529	0.0534
10		0.0561	0.0585	0.0605
25		0.0661	0.0749	0.0816
49		0.0916	0.1184	0.1393

^a See Table I.**Table IV:** Apparent Polarizations for Various Values of r_M and r_L ^{a,b,c}

A. Apparent Values of r_M					
% DP	true $r_M =$	0.900	0.800	0.700	0.600
10 ⁻⁴		0.900	0.800	0.700	0.600
1		0.899	0.798	0.698	0.599
3		0.896	0.794	0.695	0.597
10		0.886	0.782	0.685	0.591
25 ^d		0.859	0.750	0.659	0.577
49 ^d		0.788	0.679	0.607	0.550
B. Apparent Values of r_L					
% DP	true $r_L =$	0.100	0.200	0.300	0.400
10 ⁻⁴		0.100	0.200	0.300	0.400
1		0.101	0.202	0.302	0.401
3		0.104	0.206	0.305	0.403
10		0.114	0.218	0.315	0.409
25 ^d		0.141	0.250	0.341	0.423
49 ^d		0.212	0.321	0.393	0.450
C. Apparent Values of k (true value = 0.05)					
% DP	true $r_M =$	0.900	0.800	0.700	0.600
10 ⁻⁴		0.0502	0.0502	0.0502	0.0502
1		0.0509	0.0508	0.0508	0.0507
3		0.0522	0.0520	0.0518	0.0517
10		0.0563	0.0556	0.0551	0.0548
25 ^d		0.0696	0.0672	0.0658	0.0650
49 ^d		0.1136	0.1063	0.1028	0.1011

^a See Table I. ^b For all cases in this table, $r_M + r_L = 1$, and $r_N = 0$. ^c For r_M (or r_L) = 1, or for $r_M = r_L = 0.5$, the true polarizations will always be obtained. However, k will vary in a manner similar to that indicated in the table. ^d $\pm 1-2\%$.

tions from ideal conditions, with depopulation $>$ optical density $>$ ϵ_T in their effect on k ; and (3) the values of r_i are less sensitive to optical density and ϵ_T than are the values of k , but, other things being equal, the higher the values of optical density and ϵ_T , the closer the agreement between the apparent and true values of r_i .

To some extent, deviations from ideality depend on the absolute values of r_L and r_M , as shown in Table IV. In the latter case, the trends are similar for different values of r_L and r_M , but they differ in magnitude.

When computations were made for small, but non-zero, values of r_N , quite different results were obtained. In this case, we have still used the assumption that $r_N = 0$ in conjunction with eq 4 and 5 for calculating apparent values of r_L and k . Table V shows that results computed with the assumption $r_N = 0$ tend to substantially change the resulting values of r_L and r_M , but by far the biggest effect is on the value of k . Thus, even for an r_N as small as 0.01 (compared to the usual limits of experimental error of 0.01 to 0.03) the observed value of k can be in error by as much as a factor of two or more. Indeed, it is found that, even as the depopulation approaches zero, the apparent values of k (for $r_N \neq 0$) differ significantly from the true values. An interesting application of this result is discussed below.

Variations in the values of ρ_i , the triplet-triplet polarization, had little effect on the computed results, except at the highest depopulations and optical densities. Even under these conditions, the apparent values of r_i were essentially independent of ρ_i . (However, the values of r_i did not agree with the true values.) Only the value of k showed any significant dependence on ρ_i . Some examples are indicated in Table VI.

Table VII gives results for variations in the value of k . Here, as in the preceding case where variations in ρ_i were considered, the apparent values of r_i are essentially independent of k . While the apparent values of k naturally differ because of different input values, the relative effects of depopulation are essentially independent of the absolute value of k . Thus, for example, at 49% depopulation, the apparent values of k in Table VII are all in error by a factor of 2.

IV. Conclusion

The interdependence of the various parameters does not allow us the luxury of constructing universal curves with which the reader can correct his experimental data, even assuming that he knows the values of the pertinent parameters. However, the tables given

Table V: Effects of Nonzero Values of r_N on Apparent Values of r_M , r_L , and k^a

A. Apparent Values of r_M (true value = 0.8)					
% DP	true r_N =	0.00	0.01	0.02	0.05
10^{-4}		0.800	0.814	0.830	0.882
1		0.798	0.813	0.828	0.881
3		0.794	0.809	0.824	0.878
10		0.782	0.797	0.814	0.870
25		0.750	0.766	0.783	0.845
49		0.679	0.696	0.715	0.786
B. Apparent Values of r_L (True Value = 0.200 - r_N)					
% DP	true r_N =	0.00	0.01	0.02	0.05
10^{-4}		0.200	0.186	0.170	0.118
1		0.202	0.187	0.172	0.119
3		0.206	0.191	0.176	0.122
10		0.218	0.203	0.186	0.130
25		0.250	0.234	0.217	0.155
49		0.321	0.304	0.285	0.214
C. Apparent Values of k (true value = 0.05)					
% DP	true r_N =	0.00	0.01	0.02	0.05
10^{-4}		0.0502	0.0711	0.0928	0.1636
1		0.0508	0.0720	0.0940	0.1658
3		0.0520	0.0737	0.0964	0.1702
10		0.0556	0.0792	0.1038	0.1840
25		0.0672	0.0968	0.1274	0.2271
49		0.1063	0.1542	0.2033	0.3596

^a See Table I.**Table VI:** Effects of the Triplet-Triplet Polarization on the Apparent Values of r_i and k^a

A. Apparent Values of r_M (true value = 0.8)					
% DP	ρ_M^b =	1.0	0.5	0.0	0.33 ^c
10^{-4}		0.800	0.800	0.800	0.800
1		0.798	0.798	0.798	0.798
3		0.794	0.794	0.794	0.794
10		0.782	0.783	0.783	0.783
25		0.755	0.757	0.755	0.756
49		0.710	0.709	0.706	0.706
B. Apparent Values of r_L (true value = 0.2)					
% DP	ρ_M^b =	1.0	0.5	0.0	0.33 ^c
10^{-4}		0.200	0.200	0.200	0.200
1		0.202	0.202	0.202	0.202
3		0.206	0.206	0.206	0.206
10		0.218	0.217	0.217	0.217
25		0.245	0.243	0.245	0.244
49		0.290	0.291	0.294	0.294
C. Apparent Values of k (true value = 0.05)					
% DP	ρ_M^b	1.0	0.5	0.0	0.33 ^c
10^{-4}		0.0502	0.0502	0.0502	0.0502
1		0.0511	0.0509	0.0507	0.0508
3		0.0531	0.0525	0.0516	0.0520
10		0.0589	0.0566	0.0545	0.0554
25		0.0739	0.0684	0.0634	0.0652
49		0.1075	0.0982	0.0896	0.0919

^a See Table I. ^b Also, $\rho_M + \rho_L = 1$ and $\rho_N = 0$. ^c Here only, $\rho_M = \rho_L = \rho_N = 1/3$.**Table VII:** Effects of Variations in k on the Apparent Values of r_i and k^a

A. Apparent Values of r_M (true value = 0.8)				
% DP	k^b =	0.02	0.05	0.10
10^{-4}		0.800	0.800	0.800
1		0.798	0.798	0.798
3		0.794	0.794	0.795
10		0.782	0.782	0.784
25		0.748	0.750	0.754
49		0.673	0.679	0.688
B. Apparent Values of r_L (true value = 0.2)				
% DP	k^b =	0.02	0.05	0.10
10^{-4}		0.200	0.200	0.200
1		0.202	0.202	0.202
3		0.206	0.206	0.205
10		0.218	0.218	0.216
25		0.252	0.250	0.246
49		0.327	0.321	0.312
C. Apparent Values of k				
% DP	true k^b =	0.02	0.05	0.10
10^{-4}		0.0201	0.0502	0.100
1		0.0203	0.0508	0.102
3		0.0208	0.0520	0.104
10		0.0223	0.0556	0.110
25		0.0272	0.0672	0.132
49		0.0437	0.1063	0.204

^a Table I. ^b These are actual values of k at incident face.

in this paper can be used to determine qualitative trends and to make first-order corrections in many experiments. For more exact analysis of experimental data in an mps experiment, the computer code must be used.

The results of the computer simulation exercises can be used to formulate a set of empirical rules to be used in mps experiments designed to determine the polarization of the exciting molecular transition. These rules result in accurate analytical results using idealized models, even though experiments are not performed under truly ideal conditions. The key points to be considered in these experiments follow. (1) Conduct experiments with minimal light intensities (*e.g.*, avoid depopulation as much as possible, especially depopulation >10%). (2) For best results (and also most intense epr signals) use optically thick samples. (3) Make spectral measurements at several different (low) light intensities. For best results, apparent values of k should be independent of light intensity. (4) Check for out-of-plane polarization ($r_N \neq 0$) by comparing the apparent value of k to that obtained from an experiment using the same solvent, geometry, etc., and a molecule whose polarization is known.

If the above four conditions are satisfied, polarizations calculated from the equations for the ideal case

[eq 4 and 5] should be accurate to well within experimental errors; computer calculations will not be necessary. The use of eq 4 and 5 in the prescribed manner (*e.g.*, assuming that $r_N \neq 0$ is known for at least one molecule) causes the computed value of k to be most sensitive to deviations from ideality, as shown above. Thus, if k is found to be independent of the experimental light intensity below a certain level, the resulting values of r_i will represent the true singlet-singlet polarization. One exception to this conclusion is the case of $r_N \neq 0$, as indicated above; even at very weak light intensities, the computed values of r_i and k can be quite different from the true values. Under these conditions, a molecule where it is known that $r_N = 0$ should be used for calibration purposes, *e.g.*, to determine the true value of k .

The sensitivity of the magnetophotoselection method to any out-of-plane polarization can be put to good use in the appropriate experiment. The magnetophotoselection method, as outlined here, can easily detect a change in r_N as small as 1%, *e.g.*, 1% of the total polarization being out of plane. For example, for $r_N = 0.01$, the apparent value of k will differ from the true value by $\geq 40\%$ (see Table V). This sensitivity can be used to examine the influence of matrix chemical

character and microscopic viscosity on the polarization of the excitation process. In turn, conclusions about bonding or molecular geometry changes can be deduced from this information, especially if temperature studies are made.

With regard to obtaining information about ϵ_T or ρ_i from magnetophotoselection experiments, it appears that changes in apparent values of r_i and k are of little use. The observed changes are too small or too nonspecific to be of much use for this purpose (Table VI). However, as discussed in a prior publication,¹⁴ changes in h_i (or, alternatively, the intensity of the more intense $\Delta M = \pm 2$ signal) as a function of light intensity or concentration can be used as the basis for a method to determine ϵ_T . Of course, other methods are also available for obtaining the latter quantity.

Finally, from the data in Table VII, which illustrate the independence of the apparent values of r_i and the relative deviations in the apparent values of k on the absolute value of k , we can conclude that, within reason, the degree of polarization in an experiment has little effect on the accuracy of the results. Of course, this statement has obvious limits, since the experimental uncertainties dominate the data when the degree of polarization of the exciting light becomes too small.

Conjugated Radicals. I.

Introductory Remarks and Method of Calculation

by R. Zahradník and P. Čářský

Institute of Physical Chemistry, Czechoslovak Academy of Sciences, Prague, Czechoslovakia (Received February 6, 1969)

This is an introductory communication of a series of papers on conjugated open-shell systems (radicals and radical ions) with emphasis on their electronic spectra and chemical reactivity. Description of the semiempirical methods of calculation (self-consistent field and limited configuration interaction) together with data of parameters is given in a form suitable for writing a computer program.

Quite considerable knowledge on the relationship between structure and numerous physical and chemical characteristics of many various classes of organic compounds has resulted from the development and systematic application of semiempirical quantum chemical methods, particularly the MO-LCAO method. Not even the fact that the most important theory in chemistry, the theory of chemical reactivity, is at present very imperfect destroys this encouraging picture. Although much is left to be done, there is little doubt

that, *e.g.*, the Pariser-Parr-Pople method provides reasonable interpretations of electronic spectra of conjugated compounds with such a regularity that it becomes nearly more interesting to find a discrepancy than an agreement. Nowadays these disagreements could even be used to solve constitutional problems. Thus, the question could be asked about the next goal for semiempirical theories of conjugated systems.

Among numerous open problems, there are two groups which according to our opinion are of rather general

importance: a theoretical interpretation of the properties (i) of systems with open shells in the ground state (radicals and polyradicals) and (ii) of systems in electronically excited states (singlets and triplets, doublets and quartets). Semiempirical quantum chemical methods cannot be applied to these systems automatically, because the experience available so far is very limited. This is why both areas offer a possibility for further investigation of how reasonable the present quantum chemical tools are. Of course, from the chemical point of view one may hope that present or future quantum chemical methods will contribute significantly to the understanding of the relations between structure and properties in these two attractive and important fields.

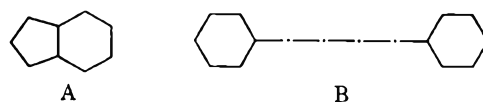
Communications in this series will be devoted to the first of these two groups of problems, with emphasis on comparison of calculated and experimental properties, both in the ground state (heats of formation and electron distribution) and in the excited doublet and quartet states (electronic spectra, electron distribution). As unpaired electron distribution has been already extensively studied by measuring esr spectra, the esr technique will serve in these papers only as the means for identification of the experimentally studied radicals.

Present State of the Literature

We restricted our attention to the conjugated radicals of all types. Most of the theoretical studies were concerned with the electronic spectra and only a few of them were devoted to the calculation of the delocalization energy¹ or other properties of radicals.² Rather intensively were studied the allyl³⁻⁸ and benzyl^{4,6,9-14} radicals; in this group belong also various triarylmethyl radicals.⁴ Particularly important is the pioneering work of Hoijtink and coworkers (*cf.* ref 15, 16, and papers cited therein), who studied theoretically and experimentally a representative set of radical anions derived from benzenoid hydrocarbons. They employed a simple version of the configuration interaction (CI) method by using Hückel molecular orbitals and energies. A somewhat more sophisticated method was used in the study of the naphthalene, anthracene, and tetracene radical anions¹⁷ and of the tetracene radical cation.¹⁸ Further methodical progress was reached by Ishitani and Nagakura,¹⁹ who used rather extensive CI and constructed determinantal functions from SCF MO's. Besides naphthalene and anthracene, they studied (also experimentally) radical anions derived from nitroso- and nitrobenzene, benzonitrile, and four polycyanobenzenes. A recent study dealt with benzene and paracyclophane radical anions.²⁰ Tetramethylparaphenyldiamine radical cation was studied by the Roothaan SCF method²¹ and tetracyanoparaquinodimethane by the same method but combined with configuration interaction (the extent of CI was very limited, only five configurations were considered).²²

Classification of the Systems Studied

For an easier orientation we introduce here an outline of the parent systems that will be treated in this series of papers. The classification is based on the same principles that we used for a classification of closed shell systems.²³ We divide hydrocarbons into two great groups: alternant and nonalternant. Further classification depends on a number of cycles in the parent skeleton; for assignment of number of cycles in this skeleton we do not take into account cata-condensed benzene rings or phenyl (and other aryl) substituents. For this reason we treat indenyl (A) as a nonalternant monocycle and 1,4-diphenylbutadiene (B) as an alternant system without a cycle. Table I presents our classification (only a few representatives of the individual groups are given).

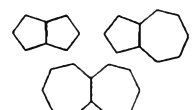
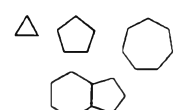
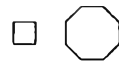
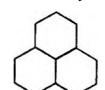
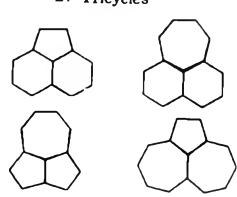
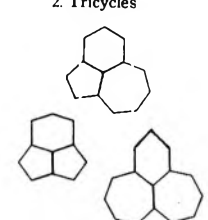
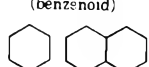


Methods of Calculation

In this series of papers we are concerned with conjugated, *i.e.*, relatively extensive, systems. In view of the experience which has been acquired with closed shell systems in ground state as well as in the study of their electronic spectra, we are interested in methods

- (1) G. W. Wheland, "Resonance in Organic Chemistry," John Wiley & Sons, Inc., New York, N. Y., 1955.
- (2) M. J. S. Dewar, J. A. Hashmall, and C. G. Venier, *J. Amer. Chem. Soc.*, **90**, 1953 (1968).
- (3) W. Moffitt, *Proc. Roy. Soc.*, **A218**, 486 (1953).
- (4) H. C. Longuet-Higgins and J. A. Pople, *Proc. Phys. Soc.*, **A68**, 591 (1955).
- (5) G. Berthier, *J. Chim. Phys.*, **52**, 141 (1955).
- (6) H. Brion, R. Lefebvre, and C. Moser, *ibid.*, **54**, 363 (1957).
- (7) D. M. Hirst and J. W. Linnett, *J. Chem. Soc.*, 1035 (1962).
- (8) J. W. Linnett and O. Sovers, *Discussions Faraday Soc.*, **35**, 58 (1963).
- (9) W. Bingel, *Z. Naturforsch.*, **10a**, 462 (1955).
- (10) V. Mori, *Bull. Chem. Soc. Jap.*, **34**, 1031, 1035 (1961).
- (11) C. Bertheuil, *Compt. Rend.*, **256**, 5097 (1963).
- (12) J. Baudet and G. Berthier, *J. Chim. Phys.*, **60**, 1161 (1963).
- (13) G. Berthier, "Molecular Orbitals in Chemistry, Physics, and Biology," P. O. Löwdin and B. Pullman, Ed., Academic Press, New York, N. Y., 1964.
- (14) A. Hinchliffe, R. E. Stainbank, and M. A. Ali, *Theoret. Chim. Acta*, **5**, 95 (1966).
- (15) G. J. Hoijtink and P. J. Zandstra, *Mol. Phys.*, **3**, 371 (1960).
- (16) G. J. Hoijtink, N. H. Velhorst, and P. J. Zandstra, *ibid.*, **3**, 533 (1960).
- (17) A. Hinchliffe, J. N. Murrell, and N. Trinajstić, *Trans. Faraday Soc.*, **62**, 1362 (1966).
- (18) N. Trinajstić, *Croat. Chem. Acta*, **38**, 283 (1966).
- (19) A. Ishitani and S. Nagakura, *Theoret. Chim. Acta*, **4**, 236 (1966).
- (20) A. Ishitani and S. Nagakura, *Mol. Phys.*, **12**, 1 (1967).
- (21) H. J. Monkhorst and J. Kommandeur, *J. Chem. Phys.*, **47**, 391 (1967).
- (22) D. A. Lowitz, *ibid.*, **46**, 4698 (1967); **47**, 3692 (1967).
- (23) R. Zahradník and J. Michl, *Collect. Czech. Chem. Commun.*, **30**, 515 (1965).

Table I: Hydrocarbon Radicals

I. Alternant		II. Nonalternant	
Even	Odd	Even	Odd
1. Without a cycle $C-C-(C-C)_n$ $H_3C_6-(C-C)_n-C_6H_5$	1. Without a cycle $(C-C)_nC$ $H_3C_6-(C-C)_n-C_6H_5$	1. Bicycles 	1. Monocycles 
2. With a cycle (except benzenoid) 	2. With a cycle 	2. Tricycles 	2. Tricycles 
3. With a cycle (benzenoid) 			

that are closely related to the Pople version of the SCF method²⁴ and the Pariser and Parr version of the CI method.²⁵ Such methods do exist and will be mentioned further on. These semiempirical methods will be used most frequently, but we shall also try to investigate the limits of applicability of the HMO method, on the one hand, and to investigate the usefulness of *ab initio* calculations on small systems, on the other hand.

With regard to our interest in electronic spectra (and with regard to the limited possibilities of annihilation of the higher multiplets in unrestricted methods),²⁶⁻²⁸ we shall be concerned merely with restricted methods. Similarly as for closed-shell systems, one requires that the first variation of the total energy of the ground state be zero. For open-shell systems (as opposed to closed-shell systems) the variation method leads to two systems of equations; combining these and forming one common pseudoeigenvalue problem is not a simple matter and was done by Longuet-Higgins and Pople,⁴ Lefebvre,²⁹ and Roothaan³⁰ in different ways. In the following part we write down only the expressions that are necessary for reproducing our calculations; detailed information about the employed methods is given in the cited papers.^{4,9,13,21,22,29,30}

Most frequently we shall use the SCF method of Longuet-Higgins and Pople,⁴ which is applicable to all systems having in the ground state one unpaired electron in a nondegenerate level. In the approximation used by Pople for closed-shell systems,²⁴ matrix elements have the form

$$F_{\mu\mu} = -I_{\mu\mu} + 1/2 P_{\mu\mu} \gamma_{\mu\mu} + \sum_{\sigma(\neq\mu)} (P_{\sigma\sigma} - Z_{\sigma}) \gamma_{\mu\sigma} \quad (1)$$

$$F_{\mu\nu} = \beta_{\mu\nu}^{\text{core}} - 1/2 P_{\mu\nu} \gamma_{\mu\nu} \quad (2)$$

where

$$P_{\mu\nu} = 2 \sum_{i=1}^{m-1} c_{i\mu} c_{i\nu} + c_{m\mu} c_{m\nu} \quad (3)$$

$$\gamma_{\mu\nu} = \iint \chi_{\mu}(1) \chi_{\nu}(2) e^2 / r_{12} \chi_{\mu}(1) \chi_{\nu}(2) d\tau \quad (4)$$

$$\beta_{\mu\nu}^{\text{core}} = \int \chi_{\mu} H^{\text{core}} \chi_{\nu} d\tau \quad (5)$$

$I_{\mu\mu}$ is the valence state ionization potential; $c_{i\mu}$ and χ_{μ} are expansion coefficients and atomic orbitals appearing in the LCAO form of molecular orbitals

$$\varphi_i = \sum_{\mu} c_{i\mu} \chi_{\mu} Z_{\sigma} \quad (6)$$

Total π -electron energy (not including nuclear repulsion) may be expressed as

$$E = \sum_{\mu} \sum_{\nu} 1/2 P_{\mu\nu} (F_{\mu\nu} + H_{\mu\nu}^{\text{core}}) - 1/4 \sum_{\mu} \sum_{\nu} c_{m\mu}^2 c_{m\nu}^2 \gamma_{\mu\nu} \quad (7)$$

For the semiempirical parameters we chose the same quantities that have been used in the closed-shell calculations in this laboratory:³¹ carbon ionization potential 11.22 eV and electron affinity 0.69 eV, resonance integral $\beta_{CC}^{\text{core}} - 2.318$ eV. Repulsion integrals were evaluated according to Mataga and Nishimoto.³² Calculations were carried out in an iterative way starting from the Hückel MO's. The approximations made in this method lead to nonvanishing matrix elements of the Hamiltonian between the ground state and some excited states. The more advanced Lefebvre method²⁹ is free of this deficiency but its complexity prevents a more general employment.

(24) J. A. Pople, *Trans. Faraday Soc.*, **49**, 1375 (1953).

(25) R. Pariser and R. G. Parr, *J. Chem. Phys.*, **21**, 466, 767 (1953).

(26) J. A. Pople and R. K. Nesbet, *ibid.*, **22**, 571 (1954).

(27) T. Amos and L. C. Snyder, *ibid.*, **41**, 1773 (1964).

(28) L. C. Snyder and T. Amos, *ibid.*, **42**, 3670 (1965).

(29) R. Lefebvre, *J. Chim. Phys.*, **54**, 168 (1957).

(30) C. C. J. Roothaan, *Rev. Mod. Phys.*, **32**, 179 (1960).

(31) R. Zahradnik, *Fort. Chem. Forsch.*, **10**, 1 (1968).

(32) N. Mataga and K. Nishimoto, *Z. Phys. Chem. (Frankfurt am Main)*, **13**, 140 (1957).

Roothaan's method³⁰ offers a significant advantage since it can be used for systems with more than one open shell. Pople's approximations lead to the following expressions for the matrix elements in the LCAO form³³

$$F_{\mu\nu} = H_{\mu\nu}^{\text{core}} + 2J_{C,\mu\nu} - K_{C,\mu\nu} + 2J_{0,\mu\nu} - K_{0,\mu\nu} + (D_T B)_{\mu\nu} + (B D_T)_{\mu\nu} - B_{\mu\nu} \quad (8)$$

where

$$J_{C,\mu\mu} = \sum_k \sum_{\sigma} c_{k\sigma}^2 \gamma_{\mu\sigma} \quad (9)$$

$$K_{C,\mu\nu} = \sum_k c_{k\mu} c_{k\nu} \gamma_{\mu\nu} \quad (10)$$

$$J_{0,\mu\mu} = f \sum_m \sum_{\sigma} c_{m\sigma}^2 \gamma_{\mu\sigma} \quad (11)$$

$$K_{0,\mu\nu} = f \sum_m c_{m\mu} c_{m\nu} \gamma_{\mu\nu} \quad (12)$$

$$J_{C,\mu\nu} = J_{0,\mu\nu} = 0 \quad (\mu \neq \nu) \quad (13)$$

$$D_{T,\mu\nu} = D_{C,\mu\nu} + D_{0,\mu\nu} = \sum_k c_{k\mu} c_{k\nu} + f \sum_m c_{m\mu} c_{m\nu} \quad (14)$$

$$B_{\mu\nu} = 2\alpha J_{0,\mu\nu} - \beta K_{0,\mu\nu} \quad (15)$$

$$\alpha = (1 - a)/(1 - f); \quad \beta = (1 - b)/(1 - f) \quad (16)$$

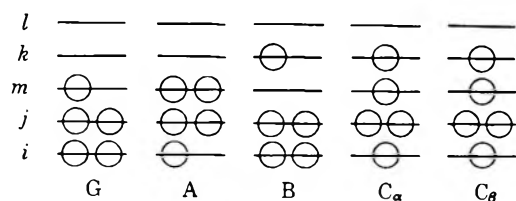
k is a numbering index for closed shells; m is a numbering index for open shells. Numerical constants f , a , and b depend on the specific case. For systems with one unpaired electron in a nondegenerate level $f = 1/2$, $a = 1$, $b = 2$. The expression for the total π -electron energy in the LCAO approximation is^{21,30}

$$E = \sum_{\mu\nu} (H_{\mu\nu}^{\text{core}} + F_{\mu\nu}) D_{T,\mu\nu} - Q_{\mu\nu} (D_{C,\mu\nu} + f D_{0,\mu\nu}) \quad (17)$$

where

$$Q_{\mu\nu} = \delta_{\mu\nu} 2\alpha \sum_{\sigma} D_{0,\sigma\sigma} \gamma_{\mu\sigma} - \beta \gamma_{\mu\nu} D_{0,\mu\nu} \quad (18)$$

Configuration Interaction. For systems with one unpaired electron in a nondegenerate level in the ground state, there are four types of configurations corresponding formally to one-electron transitions. These configurations are denoted in the literature^{19,34} as A, B, C_{α} , C_{β} , and the ground state as G.



The corresponding wave functions are

$$\left. \begin{aligned} {}^2\psi_G &= |\varphi_1 \bar{\varphi}_1 \dots \dots \dots \varphi_{m-1} \bar{\varphi}_{m-1} \varphi_m| \\ {}^2\psi_A &= |\varphi_1 \bar{\varphi}_1 \dots \dots \dots \varphi_i \bar{\varphi}_m \dots \dots \dots \varphi_{m-1} \bar{\varphi}_{m-1} \varphi_m| \\ {}^2\psi_B &= |\varphi_1 \bar{\varphi}_1 \dots \dots \dots \varphi_{m-1} \bar{\varphi}_{m-1} \varphi_k| \\ {}^2\psi_{C_{\alpha}} &= 1/\sqrt{2} (|\varphi_1 \bar{\varphi}_1 \dots \dots \dots \varphi_i \bar{\varphi}_k \dots \dots \dots \varphi_{m-1} \bar{\varphi}_{m-1} \varphi_m| \\ &\quad + |\varphi_1 \bar{\varphi}_1 C_{\beta} \dots \dots \dots \varphi_k \bar{\varphi}_i \dots \dots \dots \varphi_{m-1} \bar{\varphi}_{m-1} \varphi_m|) \\ {}^2\psi_{C_{\beta}} &= 1/\sqrt{6} (|\varphi_1 \bar{\varphi}_1 \dots \dots \dots \varphi_i \bar{\varphi}_k \dots \dots \dots \varphi_{m-1} \bar{\varphi}_{m-1} \varphi_m| \\ &\quad - |\varphi_1 \bar{\varphi}_1 \dots \dots \dots \varphi_k \bar{\varphi}_i \dots \dots \dots \varphi_{m-1} \bar{\varphi}_{m-1} \varphi_m| \\ &\quad + 2|\varphi_1 \bar{\varphi}_1 \dots \dots \dots \varphi_i \bar{\varphi}_m \dots \dots \dots \varphi_{m-1} \bar{\varphi}_{m-1} \varphi_k|) \end{aligned} \right\} \quad (19)$$

The wave function for quartets is

$${}^4\psi = 1/\sqrt{3} (|\varphi_1 \bar{\varphi}_1 \dots \dots \dots \varphi_i \varphi_k \dots \dots \dots \bar{\varphi}_m| \\ + |\varphi_1 \bar{\varphi}_1 \dots \dots \dots \varphi_i \bar{\varphi}_k \dots \dots \dots \varphi_m| \\ + |\varphi_1 \bar{\varphi}_1 \dots \dots \dots \bar{\varphi}_i \varphi_k \dots \dots \dots \varphi_m|) \quad (20)$$

Matrix elements for doublets constructed from the Longuet-Higgins and Pople SCF MO's were derived by Ishitani and Nagakura.¹⁹ Upon rederivation we found one minor mistake. The correct expression for the matrix element $\langle {}^2\psi_{C_{\alpha}}(i \rightarrow k) | H | {}^2\psi_{C_{\beta}}(i \rightarrow l) \rangle$ is ${}^{3/2} (ml | G | km)$ (plus sign).

Matrix elements for quartets are

$$\langle {}^4\psi(i \rightarrow k) | H | {}^4\psi(i \rightarrow k) \rangle - \langle {}^2\psi_G | H | {}^2\psi_G \rangle = \\ F_{kk} - F_{ii} - (ik | G | ik) - 1/2 (mk | G | km) - \\ 1/2 (mi | G | im) \quad (21)$$

$$\langle {}^4\psi(i \rightarrow k) | H | {}^4\psi(i \rightarrow l) \rangle = -(ik | G | il) - \\ 1/2 (km | G | ml) \quad (22)$$

$$\langle {}^4\psi(i \rightarrow k) | H | {}^4\psi(h \rightarrow k) \rangle = -(hk | G | ik) - \\ 1/2 (mh | G | im) \quad (23)$$

$$\langle {}^4\psi(i \rightarrow k) | H | {}^4\psi(h \rightarrow l) \rangle = -(hk | G | il) \quad (24)$$

where

$$(hk | G | il) = \iint \phi_h(1) \phi_k(2) \frac{e^2}{r_{12}} \phi_i(1) \phi_l(2) d\tau$$

On the basis of the Roothaan SCF theory we obtained the following expressions for matrix elements between doublets

$$\langle {}^2\psi_A(i \rightarrow m) | H | {}^2\psi_A(i \rightarrow m) \rangle - \langle {}^2\psi_G | H | {}^2\psi_G \rangle = \\ F_{mm} - F_{ii} + 1/2 (mm | G | mm) + \\ 3/2 (im | G | mi) - (im | G | im) \quad (25)$$

$$\langle {}^2\psi_B(m \rightarrow k) | H | {}^2\psi_B(m \rightarrow k) \rangle - \langle {}^2\psi_G | H | {}^2\psi_G \rangle = \\ F_{kk} - F_{mm} + 1/2 (mm | G | mm) + 3/2 (mk | G | km) - \\ (mk | G | mk) \quad (26)$$

(33) O. W. Adams and P. G. Lykos, *J. Chem. Phys.*, **34**, 1444 (1961).

(34) P. Balk, S. De Bruin, and G. J. Hoijtink, *Rec. Trav. Chim.*, **76**, 907 (1957).

$$\langle {}^2\psi_{C_\alpha}(i \rightarrow k) | H | {}^2\psi_{C_\alpha}(i \rightarrow k) \rangle - \langle {}^2\psi_G | H | {}^2\psi_G \rangle = F_{kk} - F_{ii} - (ik|G|ik) + 2(ik|G|ki) + (im|G|mi) + (km|G|mk) \quad (27)$$

$$\langle {}^2\psi_{C_\beta}(i \rightarrow k) | H | {}^2\psi_{C_\beta}(i \rightarrow k) \rangle - \langle {}^2\psi_G | H | {}^2\psi_G \rangle = F_{kk} - F_{ii} - (ik|G|ik) + 2(im|G|mi) + 2(mk|G|km) \quad (28)$$

$$\langle {}^2\psi_G | H | {}^2\psi_A(i \rightarrow m) \rangle = 0 \quad (29)$$

$$\langle {}^2\psi_G | H | {}^2\psi_B(m \rightarrow k) \rangle = 0 \quad (30)$$

$$\langle {}^2\psi_G | H | {}^2\psi_{C_\alpha}(i \rightarrow k) \rangle = 0 \quad (31)$$

$$\langle {}^2\psi_G | H | {}^2\psi_{C_\beta}(i \rightarrow k) \rangle = \sqrt{6}/2(im|G|mk) \quad (32)$$

$$\langle {}^2\psi_A(i \rightarrow m) | H | {}^2\psi_A(h \rightarrow m) \rangle = {}^{3/2}(hm|G|mi) - (hm|G|im) \quad (h \neq i) \quad (33)$$

$$\langle {}^2\psi_A(i \rightarrow m) | H | {}^2\psi_B(m \rightarrow k) \rangle = (mm|G|ik) \quad (34)$$

$$\langle {}^2\psi_A(h \rightarrow m) | H | {}^2\psi_{C_\alpha}(i \rightarrow k) \rangle = \sqrt{2}/2[2(im|G|kh) - (im|G|hk) + \delta_{hi}(mm|G|mk)] \quad (35)$$

$$\langle {}^2\psi_A(h \rightarrow m) | H | {}^2\psi_{C_\beta}(i \rightarrow k) \rangle = \sqrt{6}/2[\delta_{hi}(mm|G|mk) - (im|G|hk)] \quad (36)$$

$$\langle {}^2\psi_B(m \rightarrow k) | H | {}^2\psi_B(m \rightarrow l) \rangle = {}^{3/2}(mk|G|lm) - (mk|G|ml) \quad (k \neq l) \quad (37)$$

$$\langle {}^2\psi_B(m \rightarrow l) | H | {}^2\psi_{C_\alpha}(i \rightarrow k) \rangle = \sqrt{2}/2[2(il|G|km) + \delta_{ki}(im|G|mk) - (il|G|mk)] \quad (38)$$

$$\langle {}^2\psi_B(m \rightarrow l) | H | {}^2\psi_{C_\beta}(i \rightarrow k) \rangle = \sqrt{6}/2[(il|G|mk) - \delta_{ki}(im|G|mm)] \quad (39)$$

$$\langle {}^2\psi_{C_\alpha}(i \rightarrow k) | H | {}^2\psi_{C_\alpha}(h \rightarrow l) \rangle = 2(hk|G|li) - (hk|G|il) + \delta_{hi}(mk|G|lm) \quad (40)$$

(k ≠ l) or (i ≠ h)

$$\langle {}^2\psi_{C_\alpha}(i \rightarrow k) | H | {}^2\psi_{C_\beta}(h \rightarrow l) \rangle = \sqrt{3}/2[\delta_{hi}(km|G|ml) - \delta_{ki}(hm|G|mi)] \quad (41)$$

$$\langle {}^2\psi_{C_\beta}(i \rightarrow k) | H | {}^2\psi_{C_\beta}(h \rightarrow l) \rangle = 2[\delta_{hi}(mk|G|lm) + \delta_{ki}(hm|G|mi)] - (hk|G|il) \quad (42)$$

(h ≠ i) or (k ≠ l)

In CI calculations we use a standard procedure in which a configuration of the ground state, 4 configura-

tions of type A, 4 configurations of type B, 16 configurations of type C_α, and 16 configurations of type C_β are taken into account. The total number of 41 configurations represents all configurations arising formally from one-electron transitions between the four highest doubly occupied orbitals, the singly occupied orbital, and the four lowest vacant orbitals. Whenever a different number of configurations was used, it is stated explicitly. If the geometry is not mentioned, the calculation was carried out assuming an idealized structure (r_{CC} = 1.4 Å; ∠ CCC = 120°).

Matrix elements for configurations of the A, B, and C_α type were recently published by Lowitz.²² Expressions for ⟨²ψ₁⁺⁺ | r̄⁺ | ²ψ₂⟩, which are necessary for calculations of oscillator strengths, are given in Ishitani and Nagakura's paper.¹⁹ In their general form they are identical for both methods. Analogous expressions for quartets are

$$\langle {}^4\psi(i \rightarrow k) | \vec{r} | {}^4\psi(i \rightarrow l) \rangle = r_{ki} \quad (43)$$

$$\langle {}^4\psi(i \rightarrow k) | \vec{r} | {}^4\psi(h \rightarrow k) \rangle = -r_{hi} \quad (44)$$

$$\langle {}^4\psi(i \rightarrow k) | \vec{r} | {}^4\psi(h \rightarrow l) \rangle = 0 \quad (45)$$

where

$$r_{ij} = \int \varphi_i \vec{r} \varphi_j d\tau \quad (46)$$

LCI SCF calculations were carried out on an EL X8 (Electrologica) computer using programs written in ALGOL.³⁵

Acknowledgment. Our thanks are due to Professor Dr. S. Hünig (University of Würzburg) not only for the friendly and stimulating atmosphere he created during our stay in his Institute but also for drawing our attention and interest to radical chemistry. We are also indebted to him for the possibility of performing numerical calculations on the EL X8 computer at the University of Würzburg.

(35) NOTE ADDED IN PROOF. Recently several papers appeared which are closely related to the problems studied. J. C. Schug and D. H. Phillips (*J. Chem. Phys.*, **49**, 3734 (1968)) and Yu. A. Kruglyak (*Theoret. Chim. Acta*, **15**, 374 (1969)) interpreted the electronic spectrum of benzyl radical with the aid of the Roothaan open-shell SCF method combined with the configuration interaction. The same procedure was used by J. Fajer, B. H. J. Bielski, and R. H. Felton (*J. Phys. Chem.*, **72**, 1281 (1968)) to interpret the electronic spectra of the perfluoro-2,1,3-benzoselenadiazole anion radical. Excitation energies calculated by the CNDO method were published by O. Kikuchi (*Bull. Chem. Soc. Japan*, **42**, 1187 (1969)) for the nitric oxide radical and by G. W. King, D. P. Santry, and C. H. Warren (*J. Chem. Phys.*, **50**, 4565 (1969)) for the fluorosulfate radical.

Conjugated Radicals. II.¹ Semiempirical Calculations of Electronic Spectra of Radical Anions Derived from Alternant Hydrocarbons

by R. Zahradník and P. Čárský

Institute of Physical Chemistry, Czechoslovak Academy of Sciences, Prague, Czechoslovakia (Received February 6, 1969)

In this paper we present the results of semiempirical self-consistent field calculations combined with a limited configuration interaction (LCI-SCF) for seventeen radical anions derived from polyenes, α,ω -diphenylpolyenes, and benzenoid hydrocarbons. Molecular orbitals (MO's) were obtained by the Longuet-Higgins and Pople method and by the Roothaan method; both procedures lead practically to the same results. Agreement of calculated excitation energies with experimental data (taken from literature) is satisfactory. It appears that calculations by the Hückel method (HMO) can be used to interpret the electronic spectra of these radicals in a qualitative way. We mention structural features of the parent hydrocarbons, for which we expect a significant (or negligible on the contrary) bathochromic shift when passing from hydrocarbons to their radical anions. On the basis of a first-order perturbation treatment and in contrast to the parent hydrocarbons, we expect that the radical ions will exhibit a similarly significant effect of alkyl substitution as has been found with nonalternant hydrocarbons.

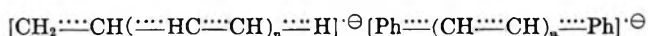
The subject of this paper is a theoretical study of electronic spectra of radical anions derived from even alternant hydrocarbons: polyenes (1-5),² biphenyl and α,ω -diphenylpolyenes (6-9),² and benzenoid hydrocarbons (10-17) (Table I); group I-1 and I-3 of the suggested classification¹.

position of the LCI wave functions are given in Appendix I. Details of the calculations are given in part I of this series.¹

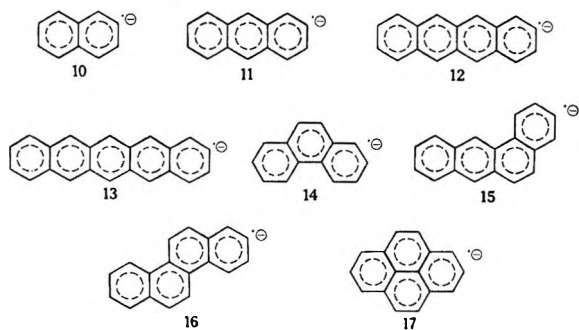
Discussion

Let us start the discussion with a note about the "striking" color of rather small conjugated radicals (8-12 π electrons); this fact is well known in chemistry. Such radicals frequently have one and sometimes several electronic bands in the near-infrared region. This is not usual in the case of small or medium-sized conjugated systems with closed-shell ground states. Closed-shell systems which exhibit a first electronic band in the near-infrared region have been found only recently; these are first, unnatural ions⁹ (e.g., the fluorenylium cation and benzo-derivatives thereof¹⁰) and second, some nonalternant systems (e.g., cyclopentaheptalen¹¹). In the first group this phenomenon arises from the $N \rightarrow V_1$ excitations that occur either between two bond-

Table I



1, $n = 1$	6, $n = 0$
2, $n = 2$	7, $n = 1$
3, $n = 3$	8, $n = 2$
4, $n = 4$	9, $n = 3$
5, $n = 5$	



Absorption curves of ten of these radicals were recorded by Hoijsink, *et al.*;³⁻⁷ the absorption curve of 1 was published in ref 8. The results of the LCI-SCF calculations were entered in the figures showing these curves. For the remaining seven radicals we predict the positions and intensities of bands in the electronic spectra (Figures 1-4). Data on the com-

(1) Part I: R. Zahradník and P. Čárský, *J. Phys. Chem.*, **74**, 1235 (1970).

(2) We consider all-*trans* configuration in the polyenic part of molecules. For systems having less than ten MO's all possible A, B, C α , and C β configurations were taken into CI.

(3) P. Balk, G. J. Hoijsink, and J. W. H. Schreurs, *Rec. Trav. Chim. Pays-Bas*, **76**, 813 (1957).

(4) P. Balk, S. De Bruijn, and G. J. Hoijsink, *ibid.*, **76**, 907 (1957).

(5) G. J. Hoijsink and P. H. van der Meij, *Z. Phys. Chem.*, (Frankfurt am Main), **20**, 1 (1959).

(6) G. J. Hoijsink, N. H. Velthorst, and P. J. Zandstra, *Mol. Phys.*, **3**, 533 (1960).

(7) K. H. J. Buschow, J. Dieleman, and G. J. Hoijsink, *J. Chem. Phys.*, **42**, 1993 (1965).

(8) T. Shida and W. H. Hamill, *J. Amer. Chem. Soc.*, **88**, 5371 (1966).

(9) R. Zahradník, *Fort. Chem. Forsch.*, **10**, 1 (1968).

(10) J. Michl, R. Zahradník, and P. Hochman, *J. Phys. Chem.*, **70**, 1732 (1966).

(11) K. Hafner and G. Schneider, *Ann.*, **672**, 194 (1964).

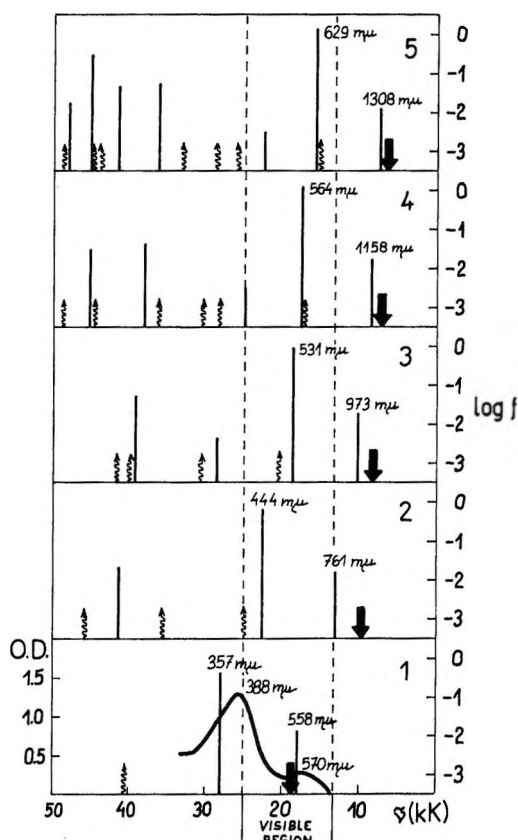


Figure 1. Prediction of electronic spectra of polyene radical anions 1-5 and the experimental absorption curve of 1 (ref 8). LCI data are indicated by vertical lines (forbidden transitions by the wavy lines with arrows); f stands for the oscillator strengths. Predicted positions of the first quartet-quartet transitions are indicated by thick arrows.

ing or between two antibonding MO's, *i.e.*, in the region of the "unnatural" $N \rightarrow V_1$ gaps (Figure 5). In small and medium-sized conjugated systems the "unnatural" $N \rightarrow V_1$ gaps are always smaller than "natural" $N \rightarrow V_1$ gap and that is why radical ions are colored, or in more precise language why we observe a great bathochromic shift when passing from the closed-shell hydrocarbon to its radical ion. In the second group of hydrocarbons, $N \rightarrow V_1$ excitation occurs in a "natural" gap; however, this happens to be relatively small due to the specific arrangement of atoms in the molecule (pericondensed nonalternant systems); this case does not occur for the radicals studied in this paper.

For radicals of odd alternant systems (*e.g.*, allyl, benzyl) Dewar and Longuet-Higgins¹² demonstrated that the reason for a bathochromic shift of the first band (with respect to the band of a corresponding cation or anion) was configuration interaction between the first monoexcited configurations of type A and B. On the other hand, in radical ions the position of the first band is usually only slightly influenced by CI. This is not true for polyenes and their derivatives (*e.g.*, 1,6-diphenylhexatriene radical anion) and sometimes for large conjugated systems, where the natural $N \rightarrow V_1$

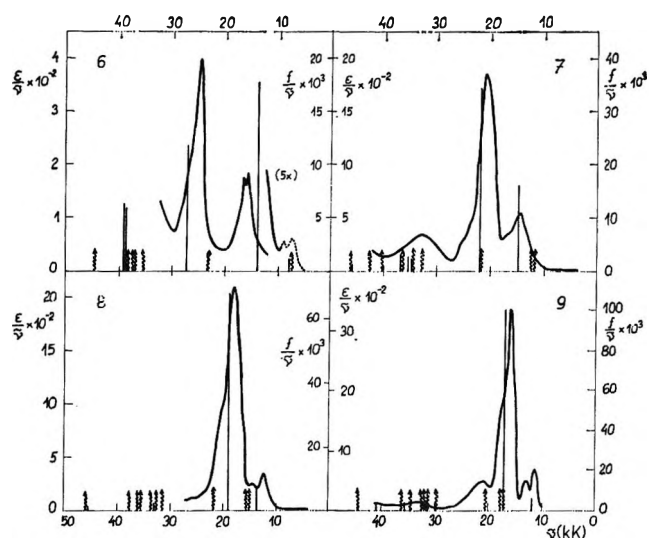


Figure 2. Experimental absorption curves of α,ω -diphenylpolyene radical anions 4-7 (ref 3-5) and results of LCI-SCF calculations, the latter being indicated by vertical lines or by the wavy lines with arrows (for forbidden transitions). The left side scales give experimental intensities and the right side scales the calculated ones, where f stands for the theoretical oscillator strengths.

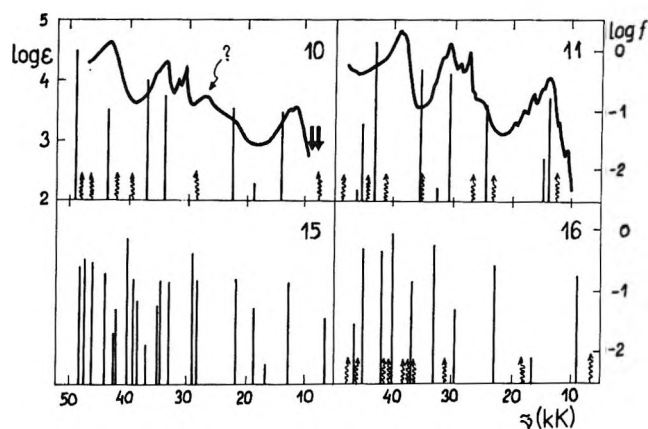


Figure 3. Comparison of experimental (K. K. Brandes and R. J. Gerdes, *J. Phys. Chem.*, **71**, 508 (1967)) and calculated electronic spectra of naphthalene (10) and anthracene (11) radical anions. Two arrows indicate positions of the experimentally found³ weak long-wave maxima of 10. The band at 27.3 kK designated by a question mark was attributed to an impurity or to the protonated anion.⁶ In case of benz[*a*]anthracene (15) and chrysene (16) radical anions, predictions of spectra are presented. For the meaning of the scales *cf.* Figure 2.

gap approaches an unnatural gap. If in such a case the corresponding configurations are of the same symmetry, then interaction between them can be strong.

Radical ions derived from even polyenes are definitely less stable than radical ions derived from benzenoid hydrocarbons; however, π -bond orders indicate a superior delocalization in comparison with the parent

(12) M. J. S. Dewar and H. C. Longuet-Higgins, *Proc. Phys. Soc.*, **A67**, 795 (1954).

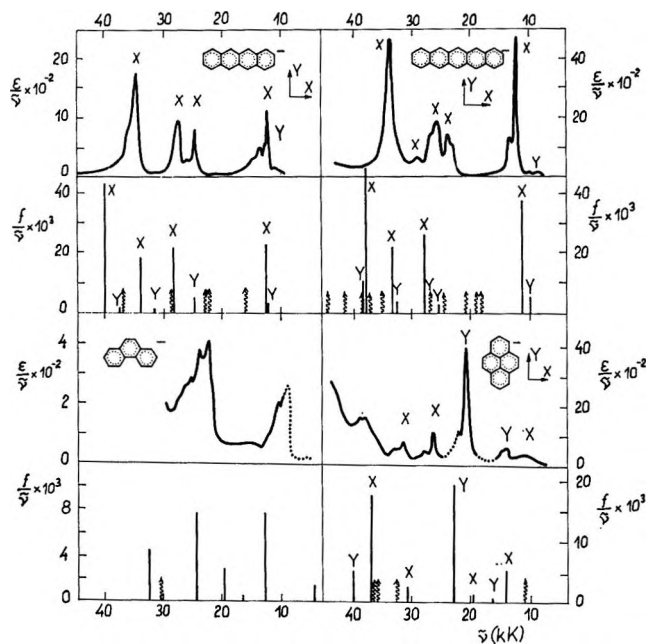


Figure 4. Experimental absorption curves of tetracene (12), pentacene (13), phenanthrene (14), and pyrene (17) radical anions together with the polarization data (ref 3, 6, and 7). Results of LCI-SCF calculations (below the curves) are indicated as in Figure 2.

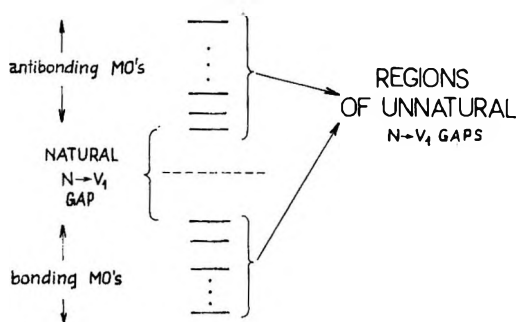


Figure 5. Typical scheme of MO energy levels of a hydrocarbon.

polyenes (Table II). This change of bond orders is understandable if pairing properties of MO's of alternant hydrocarbons are considered together with the fact that nodal planes in HOMO lie in even π bonds while they lie in odd bonds in LFMO. Thus, when passing from a polyene to the corresponding radical anion or cation we get the same changes in bond orders. The predicted positions of the absorption bands of polyenic systems (2-5) seem to be reasonably reliable in view of the satisfactory agreement which was obtained for the butadiene radical anion and several other hydrocarbon radical ions and radicals. Therefore, we expect the radical 2 to be green-blue, while the radical 3 could be merely red, because the first band is expected in the near-infrared region and the color-determining band should be the second one.

Table II: Comparison of SCF π -Bond Orders for Polyenes

System	Bond	Hydrocarbon	Radical anion
1	1-2	0.928	0.675
	2-3	0.374	0.578
2	1-2	0.915	0.757
	2-3	0.400	0.569
3	3-4	0.848	0.618
	1-2	0.911	0.801
	2-3	0.407	0.540
	3-4	0.832	0.644
	4-5	0.433	0.613

According to the calculations, the first two allowed bands of systems 1-5 are mutually shifted by about 8-10 kK and correspond to the states formed by a strong interaction between the first monoexcited A- and B-type configurations (cf. Appendix I). The first absorption band of radical anions derived from α,ω -diphenylpolyenes exhibits a hypsochromic shift as the polyenic chain becomes longer (transition from the system 6 to 7 means a shift of about 5 kK!) and only for higher members of this series the usual bathochromic shift is observed. This trend agrees well not only with the calculated first LCI excitation energies but also with the HMO excitation energies of the first $N \rightarrow V$ transitions (Figure 6). In general the agreement between results of the LCI-SCF calculations and the experimental absorption curves is fair. In the case of the first three members of this series, B-type configurations dominate in the three or four lowest excited doublet states, e.g., for biphenyl radical anion (6) these configurations are $7 \rightarrow 8$, $7 \rightarrow 9$, $7 \rightarrow 10$, and $7 \rightarrow 11$. This is also true for 1,6-diphenylhexatriene (9) but with the difference that energies of the configurations B ($10 \rightarrow 11$) and A ($9 \rightarrow 10$) are near to each other and thus a considerable interaction between them takes place.

Radical anions of benzenoid hydrocarbons have been studied experimentally rather intensely. This is of great importance for testing the applicability of theoretical methods. The spectrum of the naphthalene radical anion was recorded by other authors^{13,14} besides Hoi-jtink and coworkers;^{3,6} data are in good agreement. By means of polarization measurements⁶ the band at 27.3 kK was deduced not to belong to radical ion 10 but probably to the protonated anion or some impurity. The calculations support this suggestion (Figure 3). In Figure 7 spectral characteristics (designated as 1-9)

(13) D. E. Paul, D. Lipkin, and S. I. Weissman, *J. Amer. Chem. Soc.*, **78**, 116 (1956).

(14) K. K. Brandes and R. J. Gerdes, *J. Phys. Chem.*, **71**, 508 (1967).

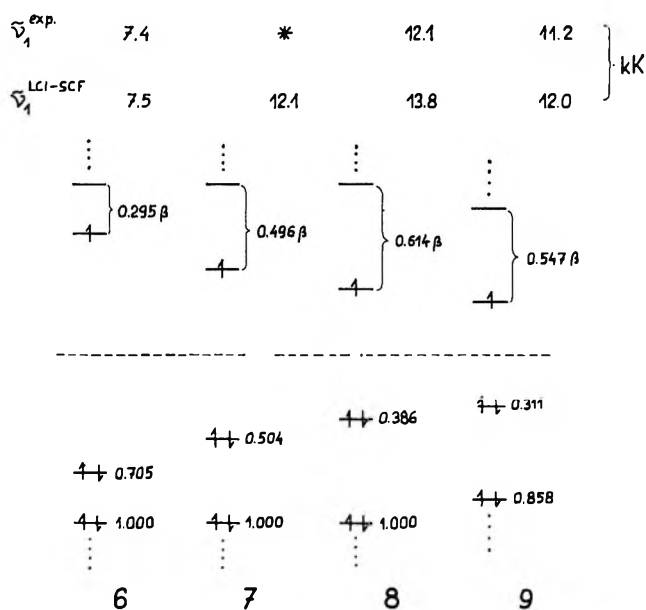


Figure 6. Values of the HMO $N \rightarrow V_1$ transitions of α,ω -diphenylpolyene radical anions 6–9 together with the experimental and LCI–SCF excitation energies. Explanation of *: according to the theory that band is forbidden and moreover it lies in the region of another strong band (cf. Figure 2), therefore its presence is difficult to prove experimentally.

calculated by different methods are compared. It is possible to state that all versions of the LCI method give a correct picture of two characteristic bands of the radical **10**, the forbidden band at 7.8 kK and the first strong band at 12.3 kK. To estimate correctly how theory agrees with experiment in general (Figure 7), there are two circumstances that must be taken into account: (i) the way in which the experimental curve is presented does not enable us to include the band at 23 kK (cf. Figure 3) and (ii) the authors of calculation 3 listed only the allowed transitions. Calculations 6–9 follow experiment in the whole range studied and predict four important strong bands to be polarized along the longer molecular axis in agreement with the experimental data. From a quantitative point of view the agreement for the short-wavelength strong band is not satisfactory (exptl, 43.5 kK; calcd, about 49 kK). Results of other methods are even worse: calculation 2 predicts 63 kK and calculations 3 about 51 kK. Ishitani and Nagakura¹⁵ mentioned the fact that the discrepancy of the theoretical and experimental excitation energy for system **10** becomes larger for higher energy transitions. In order to decrease this discrepancy, these authors suggested taking into the configuration interaction calculation for open-shell systems also of higher energy configurations such as doubly excited ones. By extending the basis set for CI we obtained only a slight improvement (cf. calculations 6–8 in Figure 7), the effect of biexcited configurations remains to be investigated. Calculations 3 and 8 are based on the same method with very similar

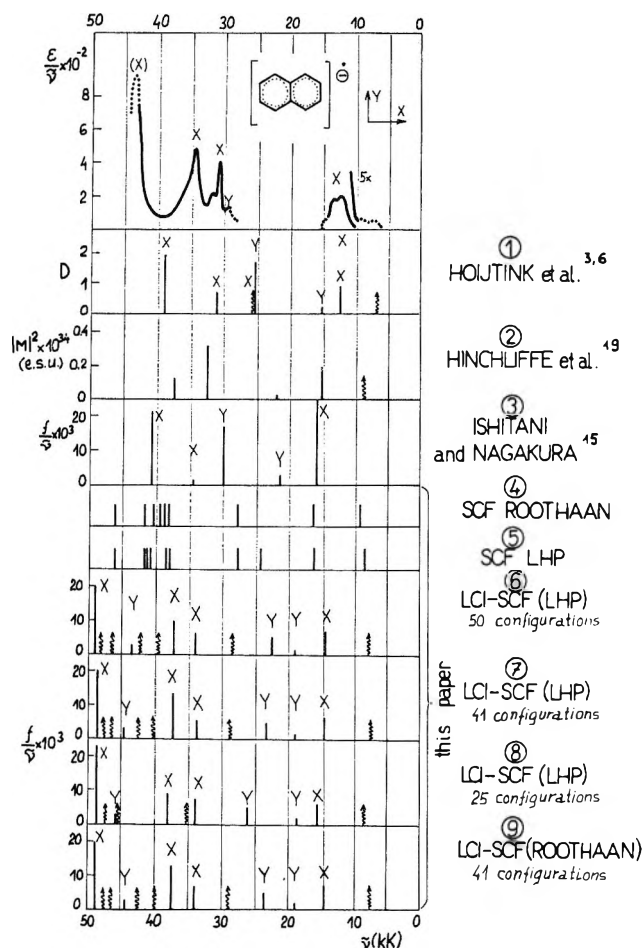


Figure 7. Comparison of various calculated electronic spectral data for the naphthalene radical anion with the experimental absorption curve (ref 3 and 6). LHP stands for the SCF–MO's obtained by the Longuet-Higgins and Pople method.

semiempirical parameters but a different approximation used for the electronic repulsion integrals, the latter being probably the reason of rather great difference in results. In calculation 3 the approximation according to Pariser and Parr¹⁶ was used, while in this paper we use the approximation by Mataga and Nishimoto,¹⁷ which seems to be more successful in the interpretation of spectra.¹⁸ Difference in the number of configurations included in CI is probably not important because in calculation 3, 29 configurations were used (the authors did not specify them) and in calculation 8, 25 configurations were used (ground state and 24 mono-excited configurations, cf. ref 1). Results 4 and 5 indicate that interpretation without CI would hardly be possible.

(15) A. Ishitani and S. Nagakura, *Theoret. Chim. Acta*, **4**, 236 (1966).

(16) R. Pariser and R. G. Parr, *J. Chem. Phys.*, **21**, 466 (1953).

(17) N. Mataga and K. Nishimoto, *Z. Phys. Chem. (Frankfurt am Main)*, **13**, 140 (1957).

(18) J. Koutecký, P. Hochman, and J. Michl, *J. Chem. Phys.*, **40**, 2439 (1964).

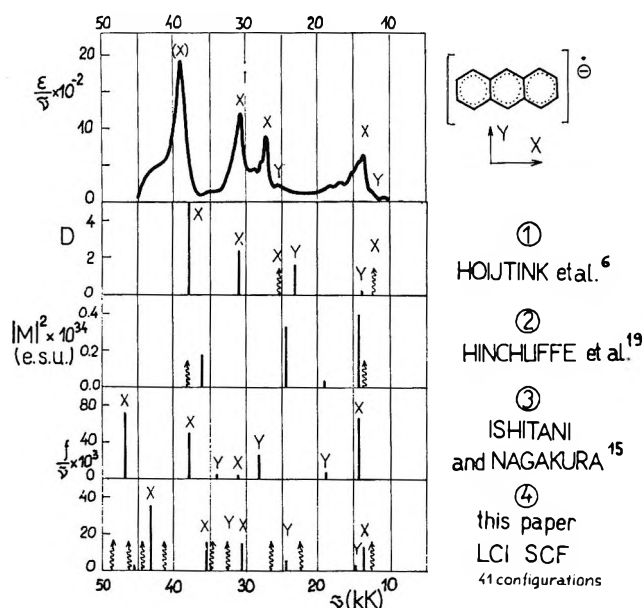


Figure 8. Comparison of various calculated electronic spectral data for the anthracene radical anion with the experimental absorption curve (ref 6).

Great attention has been paid to the anthracene anion radical, both from the experimental^{6,14} and theoretical^{15,19} points of view. Figure 8 presents a comparison of the theoretical and experimental data similar to that for system 10 in Figure 7. Agreement of the theory with experiment can be regarded as reasonable. The whole character of the spectra is represented well; the same is true about the polarization directions. It is noteworthy that according to our calculation (4 in Figure 8) the long-wavelength band (10–15 kK) corresponds to three transitions, two of them being allowed; this agrees well with the shape of the experimental curve.

A similar situation is found with further radical anions (12–14 and 17); Figure 3 also contains a prediction for systems 15 and 16 which have not yet been prepared.

Both versions of the SCF procedure (Longuet-Higgins and Pople, or Roothaan) lead to the very similar MO's; differences in bond orders, excitation energies, and other spectral characteristics are, from the practical point of view, unimportant. We carried out a comparison of LCI excitation energies calculated by both methods for systems 2–5 and 10–17. For excitation energies up to 40 kK we found that differences were mostly less than 0.5 kK; only in few cases was this differences about 1 kK. Absolutely the greatest difference (about 2 kK) was found in system 12 for the forbidden transition 10 → 12. We shall return to the question about the comparison of both methods in more detail in one of the following papers; for the present, data for system 10 are to serve as a short illustration (*cf.* Table III).

It is surprising how much information about the electronic spectra of radical ions could be gained from the HMO orbital energies, MO's, and their symmetries.

Table III: Comparison of Data Based on Longuet-Higgins and Pople (L-H, P) or Roothaan (R) MO's for 10

Bond order	HMO	SCF (L-H, P)	SCF (R)
1-1	1.181	1.174	1.169
2-2	1.069	1.087	1.091
9-9	1.000	0.979	0.979
1-2	0.613	0.613	0.608
1-9	0.555	0.553	0.554
2-3	0.672	0.674	0.681
9-10	0.518	0.519	0.518

Transition	Excitation energy in eV (log <i>f</i>)	
	LCI-SCF (L-H, P)	LCI-SCF (R)
1	0.928 (<i>f</i>)	0.922 (<i>f</i>)
2	1.801 (−1.037) ^a	1.806 (−1.037) ^a
3	2.367 (−1.828)	2.359 (−1.791)
4	2.915 (−0.957)	2.903 (−0.970)

^a In Roothaan's model the MO's 7 and 8 are nearly degenerate and that is why the first excitation corresponds to the 6 → 8 transition and the second one to the 6 → 7 transition. If Longuet-Higgins and Pople MO's are used, the sequence of the transitions is reversed.

Exploitation of data based on the simple theory could be best demonstrated at the systems just discussed; for an illustration we chose five of them: 3, 6, 10, 11, and 14. Their HMO characteristics are apparent from Figure 9.

Let us start with naphthalene. Table IV presents possible transitions with increasing excitation energy up to the value of the HMO $N \rightarrow V_1$ energy in the parent

Table IV: HMO Characteristics of the Lowest Excited States of System 10

No. of transition	Type of configuration	Configuration	Representation of configuration	Energy (β)
1	B	6,7	B _{3g}	0.4
2	B	6,8	B _{1u}	0.7
3	B	6,9	B _{2u}	1.0
4	A	5,6	B _{2u}	1.2

closed-shell system. According to these data, the spectral characteristics expected could be: first band (arising from the symmetry forbidden transition 6 → 7) of low intensity in the near infrared region, second band corresponding to the transition 6 → 8, and third band arising from the weak interaction between the configurations 5 → 6 and 6 → 9, both with the symmetry B_{2u} (but with a considerable energy differences). This

(19) A. Hinchliffe, J. N. Murrell, and N. Trinajstić, *Trans. Faraday Soc.*, **62**, 1362 (1966).

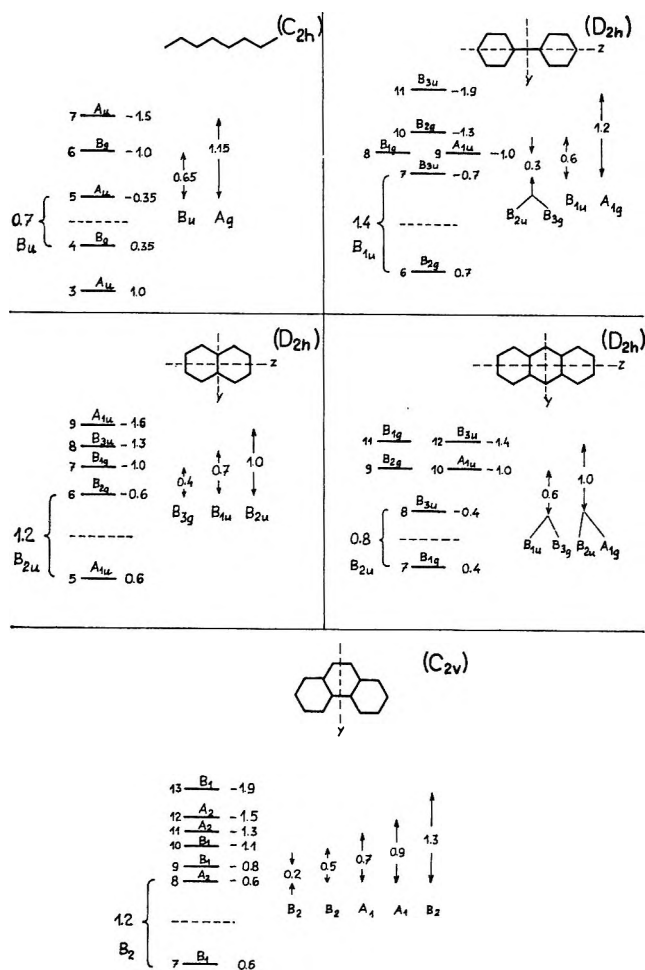


Figure 9. HMO spectral characteristics of systems 3, 6, 10, 11, and 14.

estimate is in good agreement both with experimental and CI data.

For octatetraene radical anion the first two bands could be expected to arise from an interaction between configurations $4 \rightarrow 5$ and $5 \rightarrow 6$ (both with symmetry B_u). It is also possible that a band corresponding to the $5 \rightarrow 7$ transition and influenced perhaps by an interaction with the $3 \rightarrow 5$ configuration will lie between the two above-mentioned bands.

Biphenyl radical anion will exhibit a band in the near-infrared region, arising from the transition to the degenerate or nearly degenerate states $7 \rightarrow 8$ and $7 \rightarrow 9$. The next band will be in the visible region (transition $7 \rightarrow 10$), followed by a symmetry forbidden band ($7 \rightarrow 11$) and by a band arising from the transition into a state in which configuration $6 \rightarrow 7$ dominates.

For anthracene radical anion we expect that its first band with a hypsochromic shift with respect to the system 10 will arise from the transitions $8 \rightarrow 9$ and $8 \rightarrow 10$ (corresponding configurations of different symmetry) which will be degenerate or slightly split owing to an interaction with other configurations of the same symmetry. The next two states ($8 \rightarrow 11$ and $8 \rightarrow 12$) are

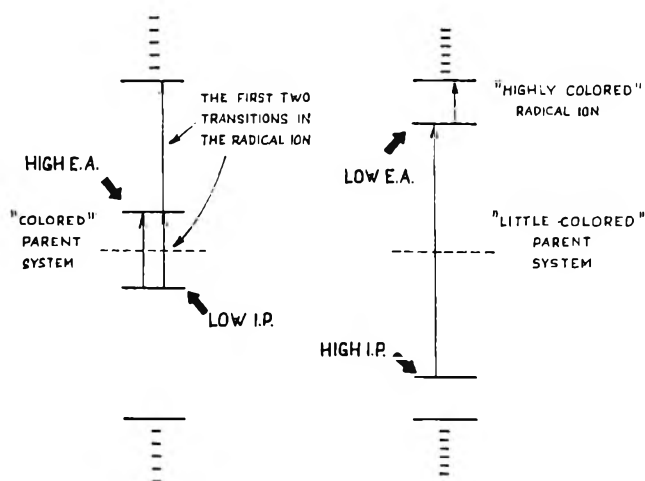


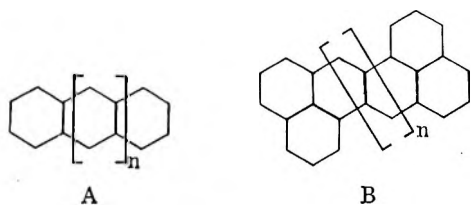
Figure 10. MO energy scheme of the "colored" and the "little colored" parent systems.

again degenerate (B_{2u} , A_{1g}), one of them (B_{2u}) having the same symmetry as the configuration $7 \rightarrow 8$ and not too much different energy. Thus, the third band will probably be a transition to the state described by the wave function $\psi(7 \rightarrow 8) + \psi(8 \rightarrow 12)$.

In the last example (phenanthrene radical anion) we expect four bands arising from nearly pure transitions $8 \rightarrow 9$, $8 \rightarrow 10$, $8 \rightarrow 11$, and $8 \rightarrow 12$. At the same time we suppose that the first band will be rather far in the near-infrared region (excitation energy of only 0.2β !) and that the state due to the transition $8 \rightarrow 12$ will not be influenced strongly by CI, because the state $7 \rightarrow 8$, which has similar energy, does not have correct symmetry. In disagreement with the result of the LCI calculation, the next band, according to this simple consideration, should be ascribed to excitation into the state described by the wave function $\psi(7 \rightarrow 8) + \psi(8 \rightarrow 13)$.

In general, it is possible to state that an analysis based on the HMO data is in qualitative (or sometimes even semiquantitative) agreement with the results of LCI calculations.

These results enable us to draw a conclusion concerning a more general relation between structure and color. It was found empirically that systems with a rather small natural $N \rightarrow V_1$ gap have "a similarly colored" radical. However, in the case of systems with relatively large natural $N \rightarrow V_1$ gap the respective radical ion is "highly colored." Schematically this situation is visualized in Figure 10. The first group ("colored" parent system) comprises polyacenes A ($n \geq 3$) and polyacene dibenzoderivatives of type B ($n = 0$, perylene; $n \geq 1$, zethrenoid hydrocarbons). For systems of this group we expect only a little change in the first band when passing from hydrocarbon to its radical ion, because this band arises from the same transition (A-type configuration) in both. Systems of the second group consist of two relatively weak-inter-



acting subsystems. In general, it is possible to form such systems, *e.g.*, from two benzenoid hydrocarbons by a bond connecting the positions of the class zero²⁰ (benzene-like position, *e.g.*, 2,2'-binaphthyl, polyphenyls) or by joining two pairs of positions of the class zero by two bonds (*e.g.*, dibenzo[*b,h*]biphenylene) or by a bond and an ethylene bridge (*e.g.*, picene). The effect of the position type on magnitude of the $N \rightarrow V_1$ gap (transition energy from the highest occupied into the lowest free molecular orbital) in radical anions is demonstrated in Figure 11 by using a system of two naphthalenes. In Table V formulas of representatives of both groups together with their $N \rightarrow V_1$ energies (HMO) are given. An experimental check of these would be an attractive task. In this connection it seems to be interesting to follow the dependence of the $N \rightarrow V_1$ energy on the size of system in various homologous series of hydrocarbons and their radical ions (Figure 12). At least three aspects of these dependences are worth mentioning. (i) An extension of the conjugated system in certain radical ions is connected with a hypsochromic shift of the first absorption band (for α,ω -diphenylpolyenes this is in agreement with experimental data; experimental evidence in the series of *p*-polyphenyls remains to be obtained); (ii) in some series very near $N \rightarrow V_1$ energies of the parent systems and their corresponding radical ions indicate the importance of CI (*e.g.*, this interaction is nearly of the first order for α,ω -diphenylpolyenes); and (iii) extremely low excitation energies are to be expected for radical anions derived from *m*-polyphenyls, whose first electronic bands should lie in the infrared region (the

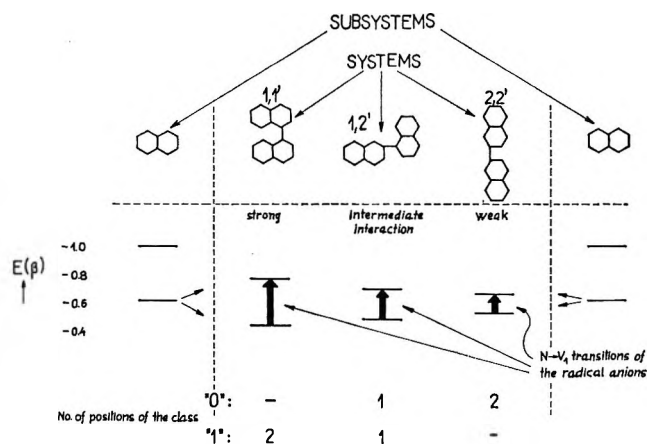


Figure 11. Dependence of the $N \rightarrow V_1$ transition energy in the composite system on the nature of the positions.

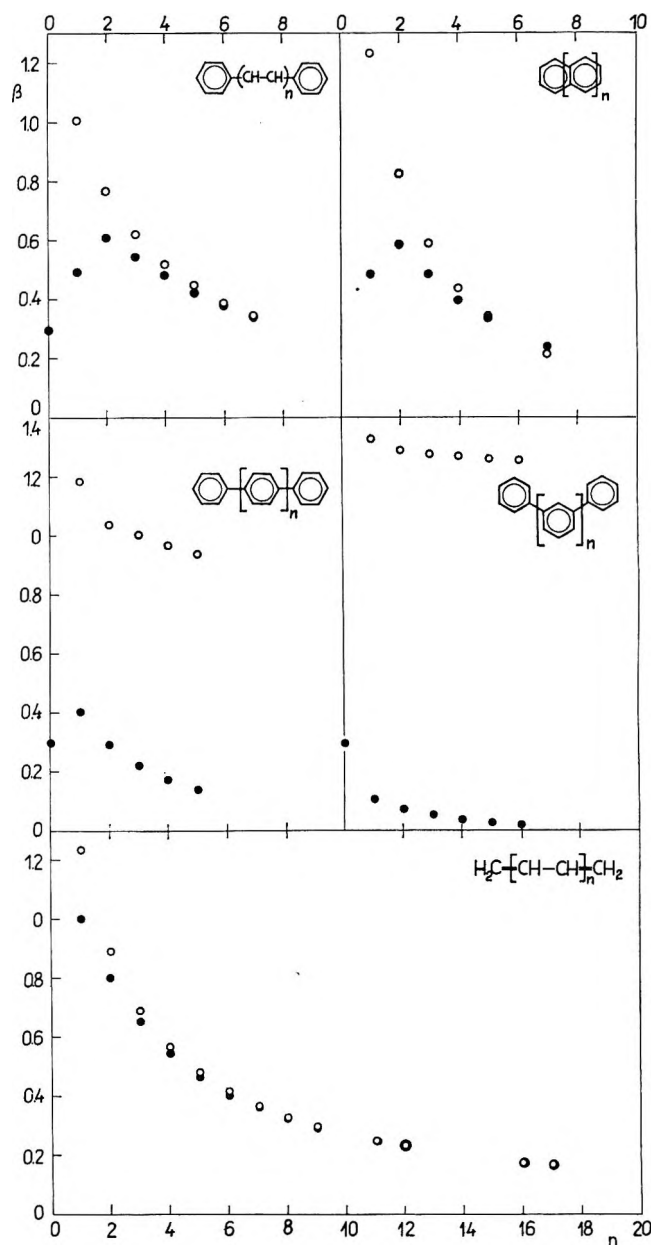
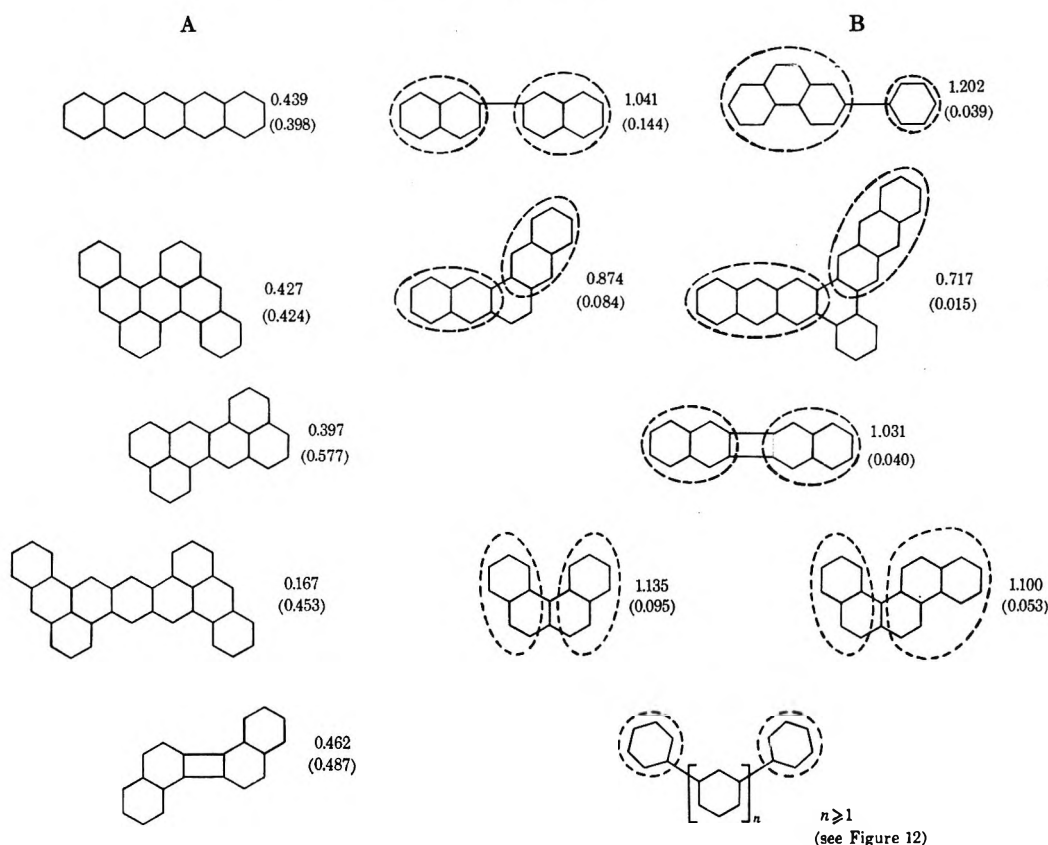


Figure 12. Dependence of the $N \rightarrow V_1$ gap on the size of molecules: O, parent systems; ●, radical anions.

Born–Oppenheimer approximation might be invalid here). For systems of this type we can expect that it would be possible to prepare radical triions and perhaps even tetraions.

Groups with a predominantly inductive effect such as the alkyls should affect the position of the first band considerably in direct contrast to their very small effect on the spectra of neutral parent hydrocarbons; Table VI lists the values for methyl derivatives of naphthalene and tetracene obtained using a first-order perturbation treatment. It is seen that alkyl groups cause a bathochromic or hypsochromic shift depending on the nature

(20) J. Kouřecký, R. Zahradník, and J. Čížek, *Trans. Faraday Soc.*, **57**, 169 (1961).

Table V: Systems with the Extreme Values of the HMO $N \rightarrow V_1$ Energies^a


^a A, low value in the parent hydrocarbon; B, low value in the radical anion. (Both values are given for each hydrocarbon, that for the radical anion being in brackets; in group B the subsystems are indicated by dashed circles; for simplicity double bonds are omitted.)

Table VI: Effect of Methyl Substitution on the Position of the First Absorption Band of Naphthalene and Tetracene Radical Anions, Estimated by Perturbation Treatment^a

System	Position	$\Delta c_{\mu}^2 \delta \alpha_{\mu}$, kK	Expected position of the 1st band in the CH_3 subst. radical anions, kK
10	1	-0.78	6.71
	2	0.42	7.91
12	1	0.30	12.57
	2	0.03	12.30
	5	-0.43	11.84

^a $\Delta E(N \rightarrow V_1) = (c_{m+1,\mu}^2 - c_{m,\mu}^2) 4.29$ kK where $c_{m,\mu}$ is HMO expansion coefficient of the in ground state singly occupied MO in position μ , into which a substituent was introduced.

of the frontier orbitals, similarly as in nonalternant systems.

Finally, it is noteworthy that there is a parallelism between the first LCI excitation energies and the first HMO excitation energies (Figure 13). We want to stress that this relation is entirely empirical and that we do not analyze it. The reason why do we mention

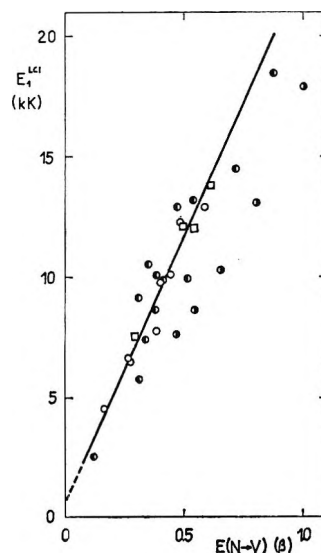


Figure 13. Plot of the lowest LCI excitation energies against the HMO energies of the first transitions: \bullet , polyene radical anions; \square , α,ω -diphenylpolyene radical anions; \circ , radical anions of benzenoid hydrocarbons; \bullet , nonalternant radical cations and anions. Regression line (data for polyene radical anions not included) $E_1^{\text{LCI}} = 22.232E(N \rightarrow V) + 0.4922$; $r = 0.95$, $n = 25$.

it is its possible use for rough predictions of the position of the first band of radical ions using the HMO data that are available in literature for many hundreds of systems. Among the systems studied, significant CI takes place in polyenes (data for them lie on a separate line) and in polyacenes; for other systems, the configuration of the monoexcited state, corresponding to the

lowest excited state in the HMO scheme, dominates in the LCI wave function of the first excited doublet state.²¹

(21) NOTE ADDED IN PROOF. Calculations of the PPP-type performed recently for butadiene anion and cation radicals were reported by T. Amos and M. Woodward, *J. Chem. Phys.*, **50**, 119 (1969).

Appendix I: Calculated Spectral Characteristics of Systems 2, 6, and 10^a

	Transi- tion	$\bar{\nu}$, kK	$m\mu$	f	$\log f$	Weights					
Hexatrien anion radical ²	1	13.13	761.6	0.016	-1.791	A (3 → 4)	50.0;	B (4 → 5)	42.7;	C _β (2 → 5)	3.8
	2	22.52	444.0	0.690	-0.161	B (4 → 5)	47.4;	A (3 → 4)	37.4;	C _β (1 → 6)	5.2
	3	24.96	400.6	0.000	...	B (4 → 6)	55.2;	A (2 → 4)	25.5;	C _β (3 → 5)	17.3
	4	35.47	281.9	0.000	...	A (2 → 4)	40.5;	B (4 → 6)	31.3;	C _β (1 → 5)	8.8
	5	41.20	242.8	0.024	-1.633	A (1 → 4)	61.9;	C _β (2 → 5)	17.2;	C _β (3 → 6)	14.7
	6	46.63	214.5	0.000	...	C _α (3 → 5)	86.8;	B (4 → 6)	3.8;	C _β (3 → 5)	3.3
Biphenyl anion radical	1	7.54	1326	0.000	...	B (7 → 8)	95.8;	C _β (6 → 9)	3.1;	C _β (4 → 11)	0.6
	2	7.71	1296	0.002	-2.724	B (7 → 9)	95.5;	C _β (6 → 8)	3.2;	A (5 → 7)	0.4
	3	14.06	711.0	0.250	-0.600	B (7 → 10)	91.0;	A (6 → 7)	6.2;	C _β (6 → 11)	1.5
	4	23.31	429.0	0.000	...	B (7 → 11)	70.2;	C _β (5 → 9)	9.4;	C _β (4 → 8)	8.8
	5	27.23	367.2	0.320	-0.498	A (6 → 7)	63.9;	C _β (4 → 9)	13.3;	C _β (5 → 8)	12.8
	6	35.46	282.0	0.000	...	A (3 → 7)	30.2;	C _β (4 → 8)	25.7;	C _β (5 → 9)	23.4
	7	37.06	269.8	0.000	...	A (5 → 7)	60.1;	C _α (6 → 8)	25.8;	C _β (4 → 10)	6.5
	8	37.34	267.8	0.000	...	A (4 → 7)	64.1;	C _α (6 → 9)	14.4;	C _β (5 → 10)	7.8
	9	38.60	259.1	0.000	...	C _α (6 → 9)	45.3;	C _β (6 → 9)	38.2;	C _β (3 → 8)	7.4
	10	39.04	256.2	0.235	-0.629	C _β (6 → 8)	51.8;	C _α (6 → 8)	26.0;	C _β (3 → 9)	9.8
	11	39.18	255.3	0.250	-0.602	C _β (5 → 8)	36.8;	C _β (4 → 9)	36.2;	A (6 → 7)	22.0
Naphthalene anion radical (50 configura- tions)	1	7.75	1291	0.000	...	B (6 → 7)	93.8;	C _β (4 → 9)	2.9;	C _β (2 → 7)	1.6
	2	14.42	693.4	0.091	-1.042	B (6 → 8)	91.0;	C _α (5 → 7)	2.6;	C _β (5 → 10)	2.5
	3	19.24	519.7	0.006	-2.223	B (6 → 9)	59.5;	A (5 → 6)	32.3;	C _β (3 → 8)	4.6
	4	22.69	440.7	0.114	-0.943	A (5 → 6)	44.2;	B (6 → 9)	20.6;	C _β (4 → 7)	20.2
	5	28.54	350.4	0.000	...	A (3 → 6)	37.6;	B (6 → 10)	35.2;	C _β (5 → 8)	23.7
	6	34.40	290.7	0.196	-0.708	C _α (5 → 7)	51.3;	A (4 → 6)	31.8;	C _β (5 → 7)	13.2
	7	37.33	267.9	0.363	-0.441	C _β (5 → 7)	46.2;	A (4 → 6)	40.0;	C _β (3 → 9)	4.1
	8	39.71	251.8	0.000	...	B (6 → 10)	43.0;	A (3 → 6)	23.3;	C _β (4 → 9)	10.1
	9	42.26	236.7	0.000	...	A (2 → 6)	47.0;	C _β (5 → 9)	24.8	C _β (3 → 7)	14.8
	10	43.87	228.0	0.101	-0.997	C _β (4 → 7)	66.2;	B (6 → 9)	12.9;	A (5 → 6)	10.9
	11	46.35	215.8	0.000	...	C _α (3 → 7)	38.5;	C _α (4 → 8)	28.8;	C _β (3 → 7)	14.1
	12	48.05	208.1	0.000	...	C _α (5 → 8)	94.9;	C _β (2 → 7)	1.9;	C _β (4 → 9)	1.0
	13	49.25	203.0	0.975	-0.011	C _α (5 → 7)	41.8;	C _β (5 → 7)	31.7;	A (4 → 6)	21.8

^a Data for other systems studied in this paper are obtainable from the authors on request.

Conjugated Radicals. III.¹ Calculations of Electronic Spectra of Alternant

Odd Radicals of the Allyl, Benzyl, and Phenalenyl Types

by P. Čársky and R. Zahradník

Institute of Physical Chemistry, Czechoslovak Academy of Sciences, Prague, Czechoslovakia (Received February 6, 1969)

The results of the LCI-SCF study of odd polyene radicals, odd α,ω -diphenylpolyene radicals, benzyl radical, and benzo derivatives, and phenalenyl radical and benzo and naphtho derivatives are presented. Experimental data on the electronic spectra are still rather poor and in some cases even not very reliable. These radicals are "little colored" in comparison with the radical ions of a similar size and having the same number of π -electrons (e.g., the pair 1-naphthylmethyl radical and naphthalene radical anion) due to the fact that the position of the first band of radical anions is connected with an unnatural $N \rightarrow V$ gap in the HMO scheme, whereas that of neutral radicals is connected with a natural gap (which is considerably greater than an unnatural gap for systems of similar size). First-order CI does not change this situation substantially.

Natural radicals studied in this paper belong to the odd alternant systems without a cycle or with a cycle (I odd 1 or I odd 2 according to our classification^{2,3}).

Methods, Compounds, and Results

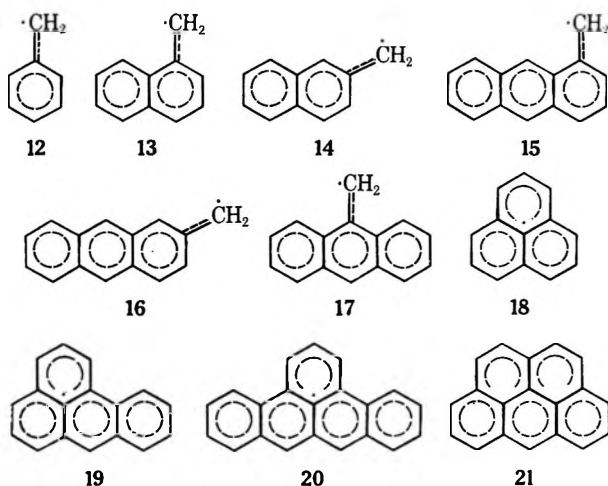
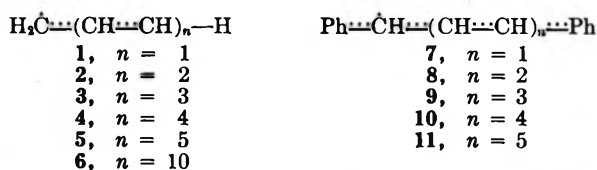
Methods and procedures were exactly the same as described in part I.³ We considered an interaction of the ground state (G) with 40 singly excited configurations (of types A, B, C_α , and C_β), or, for smaller systems (e.g., pentadienyl, benzyl), with all singly excited configurations. Calculations were carried out by the LCI-SCF (Longuet-Higgins and Pople) method. Systems 2 and 18 were also calculated by the LCI-SCF (Roothaan) method. The following systems were studied: odd polyenes (1-6),⁴ odd α,ω -diphenylpolyenes (7-11),⁴ benzyl (12), 1-naphthylmethyl (13), 2-naphthylmethyl (14), 1-anthrylmethyl (15), 2-an-

thrylmethyl (16), 9-anthrylmethyl (17), phenalenyl (18), benzophenalenyl (19), dibenzophenalenyl (20), and benzo[cd]pyrenyl (21).

In order to obtain as complete a knowledge of the properties of the studied systems as possible, calculations were also carried out for systems for which no experimental data are available at present. Great reactivity of these radicals is a reason why the experimental studies proceed rather slowly. Data on electronic spectra are available in the literature for six of the systems studied: 1, 12, 13, 14, 17, and 18. Theoretical electronic spectra of systems 1-11 are drawn schematically in Figure 1. Experimental and theoretical (LCI-SCF) data for arylmethyl radicals 12-14 are given in Figures 2 and 3. Finally, results of calculations for the phenalenyls together with the experimental data for 18 are presented schematically in Figure 4.

Discussion

Comparison of Theoretical and Experimental Data. Experimental data for allyl given by several authors are available in literature.⁵⁻¹⁰ These data differ from each other rather considerably: Ohnishi, Sugimoto, and Nitta⁵ reported absorption maximum at 236 m μ ;



(1) Part II: R. Zahradník and P. Čársky, *J. Phys. Chem.*, **74**, 1240 (1970).

(2) R. Zahradník and J. Michl, *Collect. Czech. Chem. Commun.*, **30**, 515 (1965).

(3) R. Zahradník and P. Čársky, *J. Phys. Chem.*, **74**, 1235 (1970).

(4) In the polyenic part of molecule, all-trans configuration was considered.

(5) S. Ohnishi, *et al.*, *J. Chem. Phys.*, **39**, 2647 (1963).

(6) T. Shida and W. H. Hamill, *J. Amer. Chem. Soc.*, **88**, 5371 (1966).

(7) C. L. Currie and D. A. Ramsay, *J. Chem. Phys.*, **45**, 488 (1966).

(8) D. M. Bodily and M. Dole, *ibid.*, **44**, 2821 (1966).

(9) E. J. Burrell, Jr., and P. K. Bhattacharyya, *J. Phys. Chem.*, **71**, 774 (1967).

(10) A. B. Callear and H. K. Lee, *Trans. Faraday Soc.*, **64**, 308 (1968).

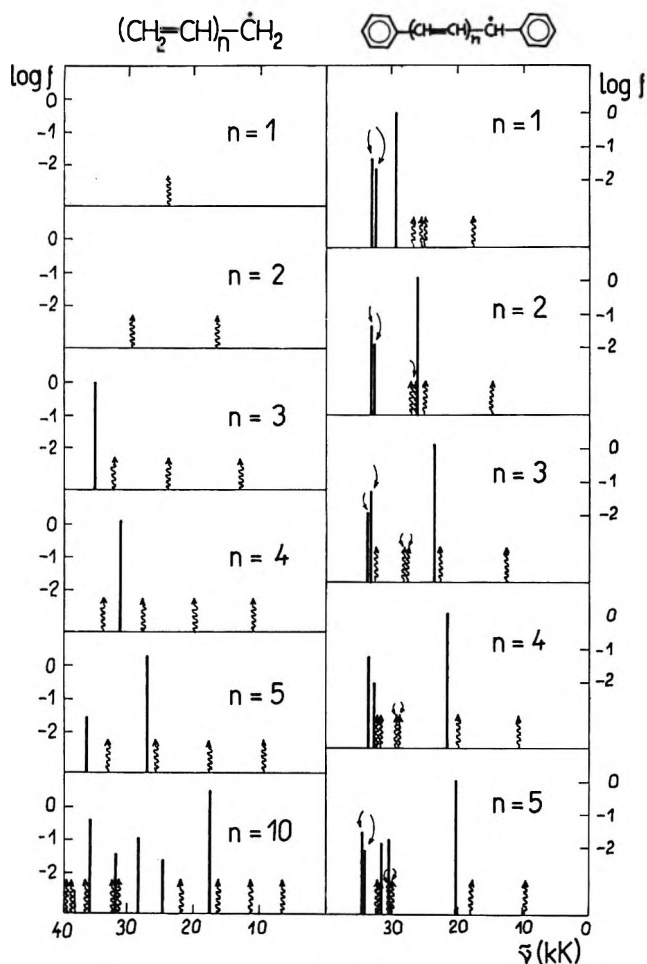


Figure 1. LCI-SCF prediction of electronic spectra of odd polyenes 1-6 and odd α,ω -diphenylpolyenes 7-11. Allowed transitions are indicated by vertical lines, forbidden ones by wavy lines with arrows; f stands for the oscillator strengths.

Shida and Hamill⁶ recorded absorption band of α -methylallyl with a maximum at $500\text{ m}\mu$; Currie and Ramsay⁷ recorded absorption maximum of allyl at $408\text{ m}\mu$; Bodily and Dole⁸ measured the absorption spectrum of allyl in the region $230\text{--}270\text{ m}\mu$ with a maximum at $258\text{ m}\mu$, and Burrell and Bhattacharyya⁹ found in the region $290\text{--}380\text{ m}\mu$ a maximum at $310\text{ m}\mu$. According to the recent measurement by Callear and Lee,¹⁰ allyl exhibits an absorption in the region of $222\text{--}249\text{ m}\mu$ with maxima at $224, 225, 227,$ and $229\text{ m}\mu$. For theoretical data, cf. ref 11-16. Our LCI-SCF calculation (configurations G, A(1 \rightarrow 2), B(2 \rightarrow 3), C_α (1 \rightarrow 3), and C_β (1 \rightarrow 3) were taken into account) results in a first strongly forbidden electronic transition at $423\text{ m}\mu$ (this differs by only about 0.8 kK from the band position reported by Currie and Ramsay), and a second (allowed) transition at $197\text{ m}\mu$, the value of which is different by approximately 6.5 kK from the maximum given by Callear and Lee. Evidently, it is questionable how reasonable the π -electron approximation is in so small a molecule as allyl. Without any doubt, σ -levels lie between the

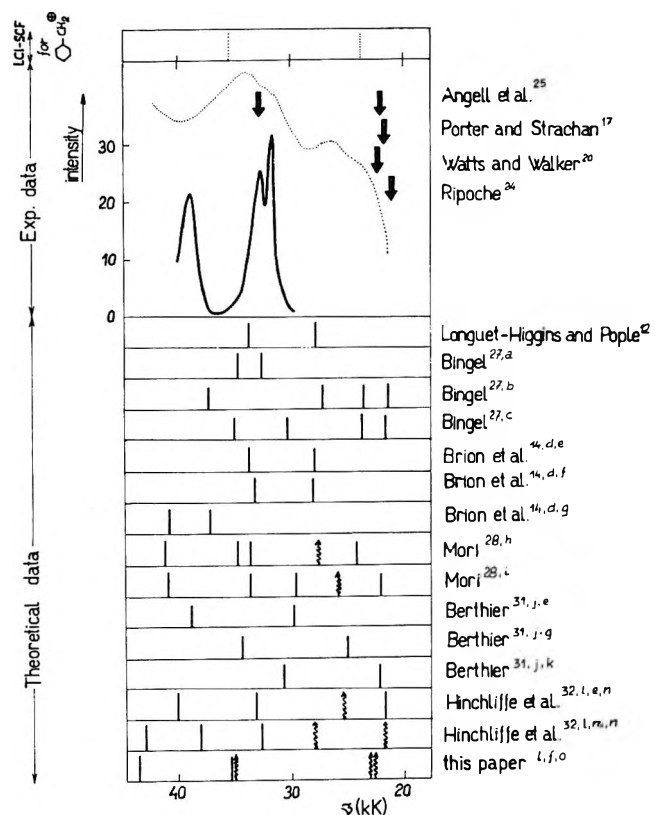


Figure 2. Experimental and theoretical spectral data for 12 (for details see text). Arrows and solid curve indicate the positions of experimentally found maxima. Calculated electronic transitions are indicated by vertical lines (forbidden transitions by wavy lines with arrows). Dotted lines and curve represent LCI results for the benzyl cation³⁵ and electronic spectrum of the dimethylbenzyl cation,³⁶ respectively. Explanation: ^aVB calculation, ^bHMO with first-order CI treatment, ^cFE-MO; ^dfirst-order CI, oscillator strengths are not given, ^eHückel MO's, ^fLonguet-Higgins and Pople MO's, ^gSCF-MO, ^{h,i} method of composite system (benzene and methylene group), ^jLCI, ^k different MO's for each configuration, ^lLCI, ground state, 3 A-type, 3 B-type, 9 C_α -type, and 9 C_β -type configurations, ^mRoothaan MO's, ⁿbicentric repulsion integrals calculated according to Pariser and Parr, and ^obicentric repulsion integrals calculated according to Mataga and Nishimoto.

π -levels; nevertheless we believe that owing to the interaction between degenerate configurations A and B (first order CI, cf. Figure 5), the calculated excitation energy of the first transition is reasonable and lower than the energies of the $\pi \rightarrow \sigma^*$ and $\sigma \rightarrow \pi^*$ transitions, which, moreover, should be weak.

Benzyl has been studied intensively both experimentally¹⁷⁻²⁶ and theoretically.^{12,14,27-32} The LCI-

(11) W. Moffitt, *Proc. Roy. Soc.*, **A218**, 486 (1953).

(12) H. C. Longuet-Higgins and J. A. Pople, *Proc. Phys. Soc.*, **A68**, 591 (1955).

(13) G. Berthier, *J. Chim. Phys.*, **52**, 141 (1955).

(14) H. Brion, R. Lefebvre, and C. Moser, *ibid.*, **54**, 363 (1957).

(15) D. M. Hirst and J. W. Linnett, *J. Chem. Soc.*, 1035 (1962).

(16) J. W. Linnett and O. Sovers, *Discussions Faraday Soc.*, **35**, 58 (1963).

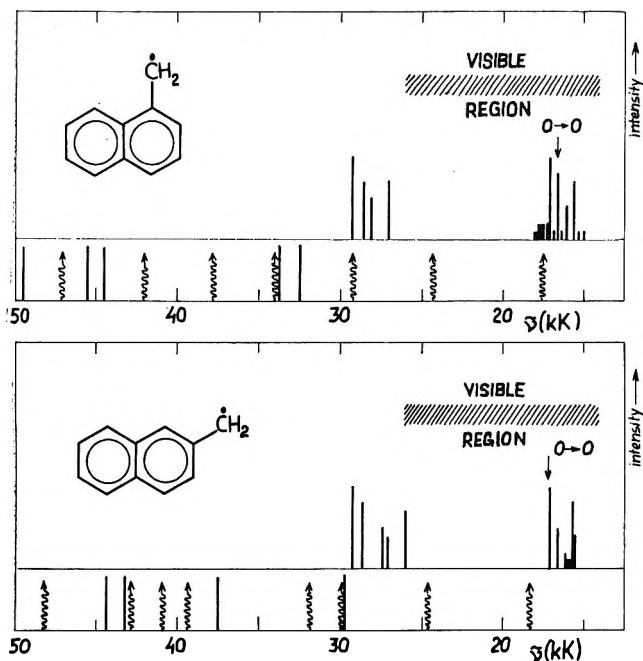


Figure 3. Comparison of experimental and theoretical spectral data of 13 and 14. Intensities of the experimentally found maxima in the visible²³ and ultraviolet²⁴ regions are drawn in independent arbitrary units. LCI data are indicated below by vertical lines (forbidden transitions by wavy lines with arrows).

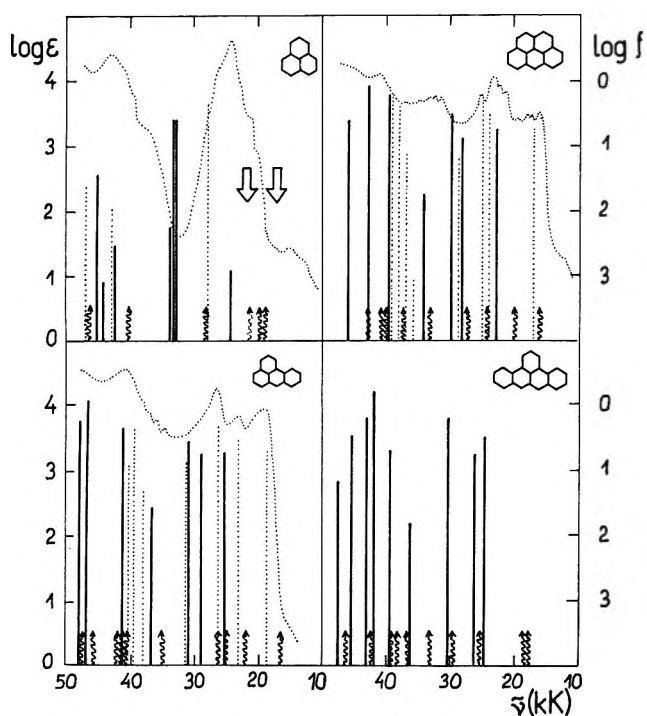


Figure 4. LCI-SCF prediction of electronic spectra of 18-21 (—). Arrows indicate the experimental data of 18 (for details see text). Allowed calculated transitions are indicated by vertical lines (forbidden by wavy lines with arrows); f stands for the calculated oscillator strengths. For comparison, experimental and theoretical data for the cations corresponding to 18, 19, and 22 are added (.....), cf. R. Zahradník, M. Tichý, P. Hochmann, and D. H. Reid, *J. Phys. Chem.*, 71, 3040 (1967).

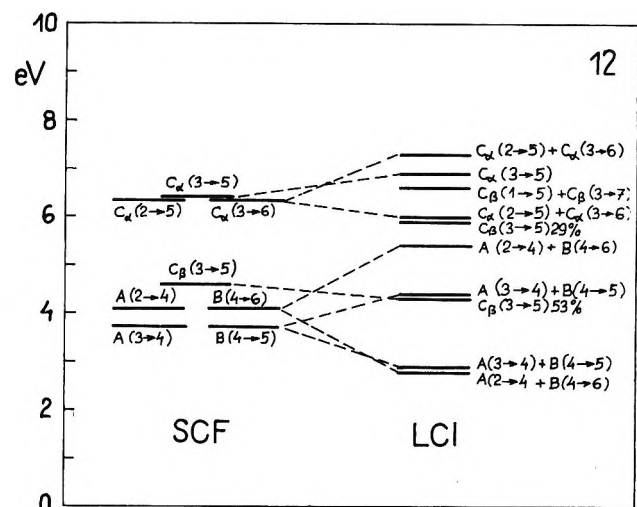
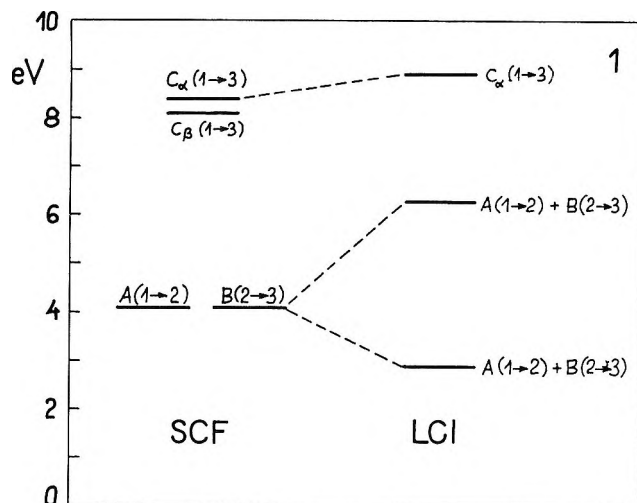


Figure 5. SCF and LCI excitation energies in allyl (1) and benzyl (12) radicals.

(17) G. Porter and E. Strachan, *Spectrochim. Acta*, 12, 299 (1958).
 (18) G. Grajcar and S. Leach, *Compt. Rend.*, 252, 1014 (1961).
 (19) H. Schtler and J. Kusjakow, *Spectrochim. Acta*, 17, 356 (1961).
 (20) A. T. Watts and S. Walker, *J. Chem. Soc.*, 4323 (1962).
 (21) B. Brocklehurst and M. I. Savadatti, *Nature*, 212, 1231 (1963).
 (22) G. Porter and M. I. Savadatti, *Spectrochim. Acta*, 22, 803 (1966).
 (23) J. Ripoché, *Compt. Rend.*, 262, 30 (1966).
 (24) J. Ripoché, *Spectrochim. Acta*, 23A, 1003 (1967).
 (25) C. L. Angell, E. Hedaya, and D. McLeod, Jr., *J. Amer. Chem. Soc.*, 89, 4214 (1967).
 (26) P. M. Johnson and A. C. Albrecht, *J. Chem. Phys.*, 48, 851 (1968).
 (27) W. Bingel, *Z. Naturforsch.*, 10a, 462 (1955).
 (28) Y. Mori, *Bull. Chem. Soc. Japan*, 34, 1031, 1035 (1961).
 (29) C. Bertheuil, *Compt. Rend.*, 256, 5097 (1963).
 (30) J. Baudet and G. Berthier, *J. Chim. Phys.*, 60, 1161 (1963).
 (31) G. Berthier, "Molecular Orbitals in Chemistry, Physics, and Biology," P. O. Löwdin and B. Pullman, Ed., Academic Press, New York, N. Y., 1964.
 (32) A. Hinchliffe, R. E. Stainbank, and M. A. Ali, *Theoret. Chim. Acta*, 5, 95 (1966).

Table I: LCI-SCF Spectral Characteristics (Doublet-Doublet Transitions)

	Transi- tion	$\bar{\nu}$, kK	λ , m μ	f	log f	Weights				
Allyl	1	23.65	422.9	0	...	A (1 \rightarrow 2)	50;	B (2 \rightarrow 3)	50	
	2	50.81	196.8	0.382	-0.418	A (1 \rightarrow 2)	50;	B (2 \rightarrow 3)	50	
Pentadienyl	1	16.48	606.9	0	...	A (2 \rightarrow 3)	45.5;	B (3 \rightarrow 4)	45.5	
	2	29.28	341.5	0	...	A (1 \rightarrow 3)	41.8;	B (3 \rightarrow 5)	41.8;	C_β (2 \rightarrow 4) 14.8
	3	40.91	244.4	0.711	-0.144	A (2 \rightarrow 3)	49.1;	B (3 \rightarrow 4)	49.1	
1,3-Diphenyl- allyl	1	17.89	559.0	0	...	A (7 \rightarrow 8)	44.3;	B (8 \rightarrow 9)	44.3	
	2	25.44	393.2	0	...	A (6 \rightarrow 8)	37.3;	B (8 \rightarrow 10)	37.3	
	3	25.44	393.2	0	...	A (5 \rightarrow 8)	37.3;	B (8 \rightarrow 11)	37.3	
	4	26.83	372.7	0	...	A (4 \rightarrow 8)	33.9;	B (8 \rightarrow 12)	33.9;	C_β (7 \rightarrow 9) 22.0
	5	29.40	340.1	1.177	0.071	A (7 \rightarrow 8)	48.2;	B (8 \rightarrow 9)	48.2	
Benzyl	1	22.75	439.5	0	...	A (2 \rightarrow 4)	40.4;	B (4 \rightarrow 6)	40.4;	C_β (3 \rightarrow 5) 6.6
	2	23.21	430.8	0	...	A (3 \rightarrow 4)	43.1;	B (4 \rightarrow 5)	43.1	
	3	34.90	286.5	0	...	C_β (3 \rightarrow 5)	53.5;	A (1 \rightarrow 4)	16.0;	B (4 \rightarrow 7) 16.0
	4	35.41	282.4	0.056	-1.253	A (3 \rightarrow 4)	44.8;	B (4 \rightarrow 5)	44.8	
	5	43.63	229.2	0.309	-0.510	A (2 \rightarrow 4)	44.1;	B (4 \rightarrow 6)	44.1;	C_α (3 \rightarrow 5) 6.2
	6	47.52	210.4	0	...	C_β (3 \rightarrow 5)	28.8;	A (1 \rightarrow 4)	18.7;	B (4 \rightarrow 7) 18.7
	7	48.00	208.4	0	...	C_α (3 \rightarrow 6)	34.3;	C_α (2 \rightarrow 5)	34.3	
α -Naphthyl- methyl	1	17.50	571.5	0	...	A (5 \rightarrow 6)	39.1;	B (6 \rightarrow 7)	39.1	
	2	24.30	411.6	0	...	A (4 \rightarrow 6)	37.6;	B (6 \rightarrow 8)	37.6;	C_β (5 \rightarrow 7) 4.5
	3	29.29	341.4	0	...	A (3 \rightarrow 6)	24.6;	B (6 \rightarrow 9)	24.6;	C_β (5 \rightarrow 7) 18.9
	4	32.52	307.5	0.154	-0.812	A (5 \rightarrow 6)	34.6;	B (6 \rightarrow 7)	34.6	
	5	33.79	296.0	0.159	-0.798	A (4 \rightarrow 6)	34.5;	B (6 \rightarrow 8)	34.5	
	6	33.85	295.4	0	...	A (2 \rightarrow 6)	19.5;	B (6 \rightarrow 10)	19.5;	C_β (5 \rightarrow 7) 15.8
	7	37.83	264.3	0	...	C_β (4 \rightarrow 8)	33.7;	C_β (5 \rightarrow 8)	10.0;	C_β (4 \rightarrow 7) 10.0
	8	42.00	238.2	0	...	C_α (4 \rightarrow 7)	39.9;	C_α (5 \rightarrow 8)	39.9;	C_β (4 \rightarrow 8) 8.0
	9	44.56	224.4	0.148	-0.831	A (3 \rightarrow 6)	39.6;	B (6 \rightarrow 9)	39.6;	C_α (5 \rightarrow 7) 3.6
	10	45.57	219.4	0.136	-0.868	C_α (5 \rightarrow 7)	79.9;	A (3 \rightarrow 6)	2.5;	B (6 \rightarrow 9) 2.5
Phenalenyl	1	19.21	520.6	0	-3.892	B (7 \rightarrow 9)	42.9;	A (5 \rightarrow 7)	42.6;	A (6 \rightarrow 7) 3.1
	2	19.89	502.7	0	...	B (7 \rightarrow 8)	45.0;	A (6 \rightarrow 7)	44.9;	A (5 \rightarrow 7) 3.4
	3	24.67	405.3	0.001	-2.893	B (7 \rightarrow 10)	45.9;	A (4 \rightarrow 7)	45.8;	A (5 \rightarrow 7) 2.0
	4	28.16	355.1	0	-3.692	A (4 \rightarrow 7)	48.5;	B (7 \rightarrow 10)	48.5;	C_β (6 \rightarrow 9) 1.0
	5	32.13	311.2	0.297	-0.528	B (7 \rightarrow 9)	42.8;	A (5 \rightarrow 7)	41.7;	A (6 \rightarrow 7) 3.5
	6	32.28	309.8	0.278	-0.556	B (7 \rightarrow 8)	41.1;	A (6 \rightarrow 7)	40.9;	A (5 \rightarrow 7) 3.2
	7	32.31	309.5	0.010	-1.987	A (3 \rightarrow 7)	31.9;	B (7 \rightarrow 11)	31.8;	C_β (5 \rightarrow 9) 8.7
	8	40.18	248.9	0	...	C_β (4 \rightarrow 10)	82.9;	C_β (6 \rightarrow 8)	5.8;	C_β (5 \rightarrow 9) 2.3
	9	42.67	234.4	0.003	-2.512	C_β (4 \rightarrow 8)	22.1;	C_β (6 \rightarrow 10)	20.4;	C_α (4 \rightarrow 8) 14.0
	10	44.52	224.6	0	-3.173	C_α (4 \rightarrow 9)	27.5;	C_α (5 \rightarrow 10)	25.7;	C_β (4 \rightarrow 9) 14.7
	11	45.49	219.8	0	-1.427	A (3 \rightarrow 7)	28.1;	B (7 \rightarrow 11)	28.1	
	12	46.97	212.9	0	...	C_α (5 \rightarrow 8)	35.5;	C_α (6 \rightarrow 9)	35.4;	C_α (6 \rightarrow 8) 13.2

SCF theory accounts for both the band at 22 kK and the intense band at 32 kK. The absorption curve presented in Figure 2 was recorded by Porter and Savadatti,²² who produced benzyl by photolysis of toluene at 77°K. This result agrees well with the one reported recently by Johnson and Albrecht.²⁶ Results of other experimental and theoretical studies are given in Figure 2 in which also the experimental and theoretical data for the benzyl cation are presented for comparison. Arrows mean the positions of the 0 \rightarrow 0 transitions in the first (and in one case also the second) band of the benzyl radical which was generated under various conditions (by photolysis⁶ of toluene in glass at 77°K,¹⁷ by a discharge in toluene vapor (emission),²⁰ by photolysis of toluene in different glasses at 88°K (fluorescence),²⁴ and by flash pyrolysis of benzylbromide *in vacuo*.²⁵) Experimental data agree fairly well with each other and also the

agreement of theory with experiment for the first two bands is reasonable. Evident discrepancy occurs at the third band; at present it is difficult to decide whether the reason is a trouble of a general nature which manifests itself in the short-wavelength region by a rather poor agreement (effect of neglect of doubly excited configurations?), or if $\sigma \rightarrow \pi^*$ and $\pi \rightarrow \sigma^*$ transitions are "wedged" in between the $\pi \rightarrow \pi^*$ transitions similarly as in allyl.

Results of calculations reproduce well the positions of the 0 \rightarrow 0 transitions in the first bands of naphthylmethyl radicals reported by Watts and Walker,³³ who measured emission in the visible region after discharge in 1- and 2-methylnaphthalene vapor (Figure 3). Absorption spectra in the ultraviolet region were mea-

(33) A. T. Watts and S. Walker, *Trans. Faraday Soc.*, **60**, 484 (1964).(34) G. Porter and E. Strachan, *ibid.*, **54**, 1595 (1958).

Table II: LCI-SCF Spectral Characteristics (Quartet-Quartet Transitions)^a

	Transi- tion	$\bar{\nu}$, kK	λ , m μ	f	$\log f$	Weights			
Allyl (Energy of Q ₁ is 3.051 eV)	Q (1 → 3)	100		
Pentadienyl (Energy of Q ₁ is 2.122 eV)	Q (2 → 4)	88.5;	Q (1 → 5) 11.5	
	1	10.97	912	0	...	Q (1 → 4)	50,	Q (2 → 5) 50	
	2	36.64	273	0.525	-0.280	Q (1 → 4)	50,	Q (2 → 5) 50	
	3	40.26	248	0	...	Q (1 → 5)	88.5;	Q (2 → 4) 11.5	
1,3-Diphenylallyl (Energy of Q ₁ is 2.925 eV)	Q (7 → 9)	52.4;	Q (5 → 11) 20.2;	Q (6 → 10) 20.2
	1	2.64	3786	0	...	Q (5 → 10)	46.0;	Q (6 → 11) 46.0	
	2	5.32	1879	0	...	Q (7 → 9)	38.1;	Q (5 → 11) 29.7;	Q (6 → 10) 29.7
	3	9.30	1075	0	...	Q (6 → 9)	36.6;	Q (7 → 10) 36.6	
	4	9.31	1074	0	...	Q (5 → 9)	36.5;	Q (7 → 11) 36.5	
	5	10.27	974	0	...	Q (4 → 9)	46.2;	Q (7 → 12) 46.2	
	6	13.97	716	0	...	Q (5 → 9)	39.0;	Q (7 → 11) 39.0	
	7	14.01	714	0	...	Q (6 → 9)	39.0;	Q (7 → 10) 39.0	
	8	26.46	378	0.80	-0.097	Q (4 → 9)	50.0;	Q (7 → 12) 50.0	
Benzyl (Energy of Q ₁ is 2.552 eV)	Q (3 → 5)	78.2;	Q (2 → 6) 16.0;	Q (1 → 7) 5.1
	1	11.41	877	0	...	Q (2 → 5)	44.3;	Q (3 → 6) 44.3	
	2	11.90	840	0	...	Q (2 → 6)	76.5;	Q (3 → 5) 16.8	
	3	18.82	531	0.001	-3.08	Q (2 → 5)	49.9;	Q (3 → 6) 49.9	
	4	24.74	404	0	...	Q (1 → 5)	44.3;	Q (3 → 7) 44.3	
	5	26.56	376	0	...	Q (1 → 6)	46.6;	Q (2 → 7) 46.6	
	6	43.41	230	0.338	-0.472	Q (1 → 5)	49.9;	Q (3 → 7) 49.9	
α -Naphthylmethyl (Energy of Q ₁ is 2.225 eV)	Q (5 → 7)	79.8;	Q (4 → 8) 9.3;	Q (3 → 9) 6.5
	1	9.62	1040	0	...	Q (4 → 7)	28.0;	Q (5 → 8) 28.0	
	2	11.51	869	0	...	Q (4 → 8)	69.6;	Q (5 → 7) 9.1	
	3	12.86	778	0	...	Q (3 → 7)	32.2;	Q (5 → 9) 32.2	
	4	15.57	642	0	...	Q (4 → 7)	48.4;	Q (5 → 8) 48.4	
	5	17.27	579	0	...	Q (3 → 8)	25.0;	Q (4 → 9) 25.0	
	6	24.90	401	0	...	Q (2 → 8)	40.4;	Q (4 → 10) 40.4	
	7	27.41	365	0.080	-1.096	Q (3 → 8)	31.4;	Q (4 → 9) 31.4	
	8	29.78	336	0.318	-0.498	Q (3 → 7)	35.9;	Q (5 → 9) 35.9	
Phenalenyl (Energy of Q ₁ is 3.155 eV)	Q (4 → 10)	29.9;	Q (5 → 9) 26.3;	Q (6 → 8) 23.2
	1	6.06	1649	0	...	Q (5 → 10)	35.2;	Q (4 → 9) 29.6;	Q (6 → 8) 17.0
	2	6.34	1578	0	...	Q (6 → 10)	38.4;	Q (4 → 8) 32.8;	Q (6 → 9) 7.9
	3	7.20	1389	0	...	Q (6 → 9)	38.8;	Q (5 → 8) 36.8;	Q (6 → 10) 5.7
	4	9.11	1098	0.001	-3.054	Q (5 → 9)	42.8;	Q (6 → 8) 36.3;	Q (4 → 9) 8.2
	5	11.83	845	0	...	Q (6 → 9)	24.2;	Q (5 → 8) 23.6;	Q (5 → 9) 21.6
	6	12.17	821	0.003	-2.592	Q (4 → 10)	47.8;	Q (5 → 8) 18.0;	Q (6 → 9) 16.7
	7	15.14	660	0	...	Q (4 → 8)	43.9;	Q (6 → 10) 41.0;	Q (5 → 10) 7.1
	8	15.50	645	0	...	Q (4 → 9)	48.4;	Q (5 → 10) 43.1;	Q (6 → 10) 3.3
	9	21.31	469	0.010	-2.022	Q (5 → 11)	34.3;	Q (3 → 9) 31.9;	Q (4 → 11) 8.0
	10	24.31	411	0.051	-1.293	Q (3 → 8)	40.2;	Q (6 → 11) 39.8;	Q (4 → 10) 9.2
	11	30.33	330	0.131	-0.884	Q (4 → 11)	26.6;	Q (3 → 10) 26.2;	Q (3 → 9) 13.9
	12	32.37	309	0.049	-1.309	Q (5 → 11)	37.6;	Q (3 → 9) 34.4;	Q (4 → 11) 10.4
	13	34.53	290	0.023	-1.646	Q (3 → 8)	38.6;	Q (6 → 11) 36.5;	Q (3 → 10) 12.6
	14	35.84	279	0.248	-0.605	Q (4 → 11)	39.6;	Q (3 → 10) 35.0;	Q (3 → 9) 11.1

^a In contrast to the ground (doublet) state the lowest quartet cannot be described by one dominating configuration. The composition of the latter is given at each system in the first line above the first quartet-quartet transition.

sured by Porter and Strachan³⁴ by photolysis of 1- and 2-methylnaphthalenes at 77°K. A more thorough comparison of theory with experiment requires further experimental information about the short-wavelength region.

It was found recently³⁵ that probably 9-anthrylmethyl radical was formed besides or instead of the expected 9-anthrylmethyl cation when 9-chloromethylanthracene was treated with aluminum chloride in

methylene chloride. This possibility was supported both by esr and electronic spectra (first and second bands: exptl, 15.0 and 22.5 kK; LCI-SCF, 14.5 and 22.5 kK). For isomers **15** and **16**, theory predicts two weak or forbidden bands in the visible region and a strong band in the ultraviolet region as the

(35) R. Zahradník, A. Kröhn, J. Pančíř, and D. Šnobl, *Collect. Czech. Chem. Commun.*, to be published.

third band (predicted positions of maxima of **15**: 14.6, 23.8, and 26.6 kK; and those of **16**: 14.6, 23.0, and 25.6 kK).

Results of the LCI-SCF calculations for systems **18-21** are given in Figure 4. Very few experimental data are available in the literature: according to ref 36 and 37, the solution containing **18** is yellow and blue, respectively, and Reid³⁸ reported the first band at 613 m μ . These results are indicated by arrows in Figure 4. The first allowed theoretical transition (LCI) lies at 25 kK and that corresponds to a yellow color of solution. Clearly, a thorough experimental study becomes very topical.

When Roothaan MO's were used, practically the same SCF and LCI-SCF results were obtained. This was demonstrated with systems **2** and **18**.

Similarity and differences in the electronic spectra of radicals and corresponding ions (formed by an abstraction or addition of one electron) were analyzed by Longuet-Higgins and Pople:¹² first band of radicals is always shifted bathochromically with respect to the first band of ions owing to first-order CI. It is worth mentioning (Figures 2 and 4) that this difference is rather small (about 3 kK) and that two or three first transitions in the radicals are forbidden. In contrast to radicals, mixing of configurations is unimportant for the long-wave transitions in the corresponding ions (*cf. e.g.*, data on arylmethyl cations³⁵).

First-order perturbation treatment (in the HMO framework) indicates a negligible effect of inductively acting substituents on the first band of radicals (a

band arising from the transition from the ground into the state described by the configurations $A(m - 1 \rightarrow m)$ and $B(m \rightarrow m + 1)$, where m denotes the singly occupied MO in the ground state). In contrast to it we expect a considerable effect in radical ions of benzenoid hydrocarbons.¹ A parallelism appears in the behavior of the pairs odd alternant radical-alternant even hydrocarbon and odd alternant ion-radical ion of the alternant even hydrocarbon.

Composition of the LCI Wave Functions. In Tables I and II we present the weights of configurations in the LCI wave functions of several systems, particularly of those studied experimentally. Most of the transitions in the visible and ultraviolet regions arise from excitation into states that are formed by an interaction between degenerate configurations. Position of the longest wave-length band is nearly always connected with the transitions $m - 1 \rightarrow m$ and $m \rightarrow m + 1$; however, in benzyl, this band is connected with the transitions $2 \rightarrow 4$ and $4 \rightarrow 6$ (Figure 5).³⁹

(36) P. B. Sogo, M. Nakazaki, and M. Calvin, *J. Chem. Phys.*, **26**, 1343 (1957).

(37) D. H. Reid, *Chem. Ind. (London)*, 1504 (1956).

(38) D. H. Reid, *Quart. Rev.*, **19**, 274 (1965).

(39) NOTE ADDED IN PROOF. Recently three papers were published which are closely related to the problems studied. PPP-type calculations on allyl and pentadienyl were carried out by T. Amos and M. Woodward, *J. Chem. Phys.*, **50**, 119 (1969). Doublet electronic states of the benzyl radical were studied by means of the Roothaan SCF procedure combined with configuration interaction by J. C. Schug and D. H. Phillips, *J. Chem. Phys.*, **49**, 3734 (1968), and by Yu. A. Kruglyak, *Theoret. Chim. Acta*, **15**, 374 (1969).

A Spectroscopic Investigation of Intramolecular Interactions in

cis and *trans* Dimers of Acenaphthylene

by Nori Y. C. Chu and David R. Kearns

Department of Chemistry, University of California, Riverside, California 92502 (Received September 17, 1969)

The absorption and emission spectra of acenaphthene and the *cis* and *trans* dimers of acenaphthylene have been measured and the lower-lying excited states have been assigned. Intramolecular exciton effects on the spectra of the *cis* and *trans* dimers are found to be small, although the *cis* dimer displays intramolecular excimer formation at the singlet state level. Triplet excimer formation could not be observed. The temperature dependence of the quantum yields for fluorescence and for photodissociation of the *cis* and *trans* isomers were measured in order to determine the interrelation between these two modes for dissipation of electronic excitation.

Introduction

Irradiation of solutions of acenaphthylene is known to result in the formation of dimers which exist in either a *cis* or *trans* conformation.¹ With the formation of a cyclobutane ring, the π -electron system of the dimers consists essentially of two weakly coupled naphthalene systems, which are held in either a *cis* or *trans* conformation. Because of these structural features the dimers offer an interesting opportunity to examine the effect of trans-annular interactions on various spectral properties and to compare these with the properties of their monomeric counterpart, acenaphthene.

In the work reported here we have examined the spectroscopic properties of acenaphthene and naphthalene and the *cis* and *trans* dimers of acenaphthylene in order to (i) assign the lower-lying excited states of the dimers, (ii) determine the magnitude of intermolecular exciton effects on the dimer spectra, (iii) look for intramolecular excimer formation at both the singlet and triplet state levels of the *cis* dimer, and finally, (iv) to examine the interrelation between the photochemical and spectroscopic properties of the dimers.

Experimental Section

Acenaphthylene (technical grade), obtained from Aldrich, was crystallized from reagent grade methanol once before it was used in the preparation of the *cis* and *trans* dimers. Acenaphthene, purchased from Matheson Coleman and Bell Company, was vacuum sublimed before being passed through a 40-stage zone refiner. Naphthalene was also purified by zone refining.

The photodimerization of acenaphthylene was carried out in a water-cooled Pyrex cell using a tungsten-halogen lamp as irradiation source with 1 *M* solutions in methanol. The relative amounts of the *cis* or *trans* dimer obtained depend on temperature. From 20 to about 40° the *trans-cis* ratio increased with increasing

temperature. The dimers precipitated upon photodimerization and unreacted acenaphthylene which precipitated during photodimerization was subsequently removed by washing with methanol. Following this, the dimers were dissolved in chloroform, treated with activated carbon, and then recrystallized from the chloroform solution three or four times. The *trans* dimer crystallized in a long needle form, whereas the *cis* dimer crystallized in a wide flat form, and it was therefore possible to separate the two dimers from each other manually.

Absorption spectra were measured at room temperature and at 77°K by using a Cary 14 spectrophotometer. Emission spectra were measured by using either a Bausch & Lomb or a McPherson monochromator for excitation and either a Jarrel-Ash or a McPherson monochromator (together with an RCA 7265 (S-20) photomultiplier) for detection. A 450-W xenon lamp or a SP-200 mercury lamp was used as a light source. For polarization measurements, a Glan prism was used in the excitation side, and a Polacoat GS-10 polaroid sheet was used in the detection side.^{2a} A correction for the polarizing effects introduced by the grating of the monochromator was made by the method described by Azumi and McGlynn.^{2b} The Raman spectra were measured by using a Perkin-Elmer LR-1 Raman spectrometer with an He-Ne laser source.

The excitation spectra of the *cis* and *trans* dimers given in Figure 1 were obtained in the following manner. After correction for the wavelength dependence of the photon intensity of the lamp, the excitation spectrum of the *cis* dimer was adjusted so that the peak height at 296.0 nm had the same value as the absorption

(1) K. Dziewonski and G. Rapalski, *Chem. Ber.*, **45**, 2491 (1912); **46**, 1986 (1913); **47**, 1679 (1914).

(2) (a) A. C. Albrecht, *J. Chem. Phys.*, **27**, 1413 (1957); *J. Mol. Spectrosc.*, **6**, 84 (1961). (b) T. Azumi and S. P. McGlynn, *J. Chem. Phys.*, **37**, 2413 (1962).

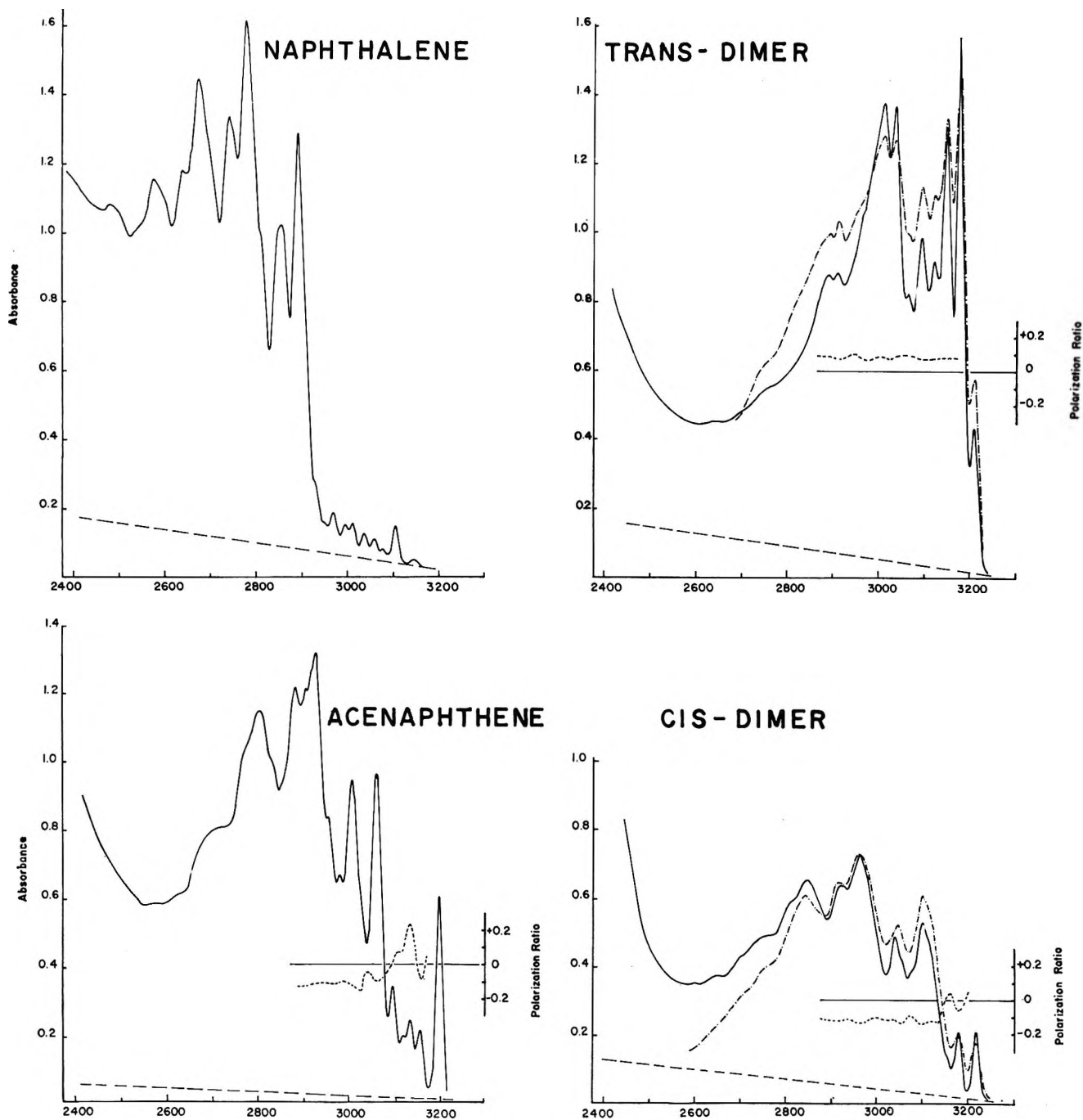


Figure 1. The absorption (—), fluorescence excitation (· · · · ·), and polarized excitation (----) spectra of naphthalene, acenaphthene, and the *cis* and *trans* dimers of acenaphthylene. All spectra were obtained at 77°K in EPA solutions. The broken line at the bottom of each spectrum represents base line due to light scattering by the cells. The polarization ratios are accurate to ± 0.02 .

spectrum. Similarly, the *trans* dimer excitation was adjusted to match the absorption spectrum at 314.7 nm. The wavelength variation in the photon intensity of the exciting beam was measured using an Eppley thermopile.

Measurements of the temperature dependence of the fluorescence of the *trans* and *cis* dimers were carried out using a Beckman quartz cell surrounded by a square brass block which was in direct thermal contact with

the container of the coolant (Dry Ice and acetone bath, pentane or isopentane slush, or liquid nitrogen). The temperature variation during a measurement of the fluorescence spectrum was about 5°K. The temperature dependence of the photodissociation of the dimers was studied using a SP-200 mercury lamp as light source. An exciting wavelength of 290 nm was used for the *cis* dimer and 300 nm was used for the *trans* dimer. The samples were precooled before transfer to

the irradiation dewar, and relative rates of the photodissociation were measured by comparing the heights of the absorption peaks of acenaphthylene at about 340 nm.

Quantum yields of fluorescence of the *cis* and *trans* dimers at 300°K, 145°K, and 77°K and the phosphorescence quantum yield of the *cis* dimer at 77°K were obtained by comparison with emission of naphthalene in the same solvent, EPA. The quantum yield of fluorescence of naphthalene in ethanol reported by Dawson and Windsor³ as 0.205 ± 0.014 at 300°K was used as reference. For the quantum yield measurements the concentrations of the dimer solution and the naphthalene solution were adjusted to give the same optical density at the excitation wavelength, 252.5 nm, and concentration changes due to the volume change of the solution upon cooling were taken into consideration in calculating the yields at low temperatures. Due to the similarity of the emission spectra of the dimers and naphthalene, no corrections for the spectral response of the instrument were made in the quantum yield measurements.

The phosphorescence quantum yield of the *cis* dimer was found by comparison with naphthalene to be 0.006.

Results and Discussion

1. *Interpretation of the Absorption Spectra.* The absorption spectra of the *cis* and *trans* dimers of acenaphthylene, acenaphthene, and naphthalene at 77°K are shown for comparison in Figure 1. Since the absorption spectrum of naphthalene has already been assigned,^{4,5} this information can be utilized in assigning the transitions of acenaphthene and the acenaphthylene dimers. The relatively weak absorption band at 314.7 nm in the naphthalene spectrum is the origin of the long-axis polarized ${}^1L_b \leftarrow {}^1A$ transition, and the much stronger absorption starting at 289.1 nm is the origin of the short-axis polarized ${}^1L_a \leftarrow {}^1A$ transition. The prominent 500-cm⁻¹ and 1400-cm⁻¹ progressions have been attributed to an in-plane skeletal distortion and to an in-plane C-C stretching vibration, respectively.⁵

The assignment of the acenaphthene spectrum appears to be fairly straightforward. The 77°K polarized fluorescence excitation spectrum of acenaphthene shown in Figure 1 behaves similarly to that of naphthalene, indicating that the band observed at 320.2 nm is the origin of a ${}^1L_b \leftarrow {}^1A$ transition. The bands at 313.8 nm, 312.2 nm, and 310.0 nm are polarized parallel to the O-O band of fluorescence, indicating that they too are associated with the transition to the 1L_b state. The band at 316.0 nm ($0 + 448$ cm⁻¹) is polarized opposite to the O-O band of fluorescence and is attributed to a vibrationally induced transition associated with the ${}^1L_b \leftarrow {}^1A$ transition since it is too weak to be the origin of the ${}^1L_a \leftarrow {}^1A$ and since there is a prominent ir band at 444 cm⁻¹. The somewhat stronger band located at 306.6 nm is polarized opposite to the O-O band of the

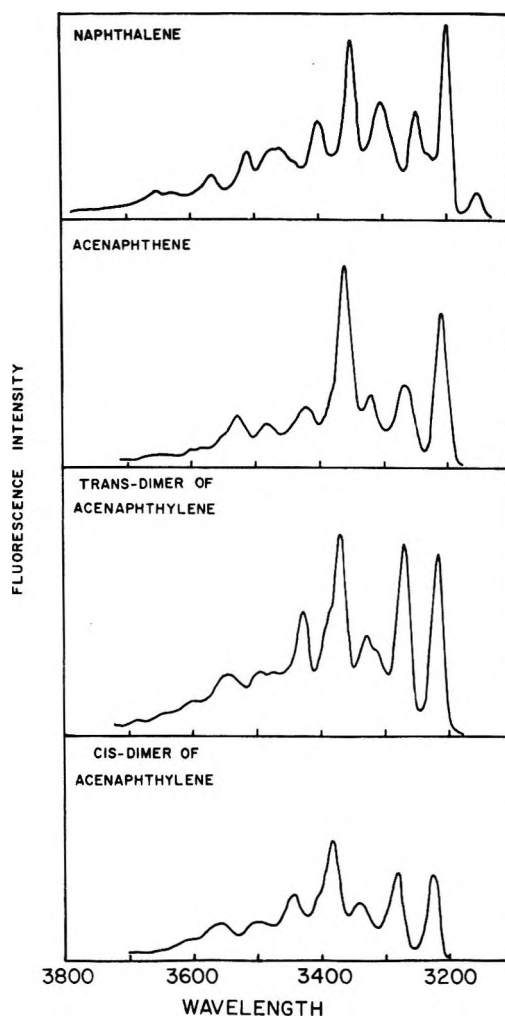


Figure 2. The 77°K fluorescence spectra of naphthalene, acenaphthene, and the *cis* and *trans* dimers of acenaphthylene in EPA.

fluorescence, indicating that this is the origin of the ${}^1L_a \leftarrow {}^1A$ transition.

The low-temperature fluorescence spectrum of the *cis* dimer of acenaphthylene is so similar to that of acenaphthene that we initially suspected that it might be due to acenaphthene impurity emission. The fluorescence excitation spectrum shown in Figure 1 proves, however, that the emission is authentic *cis* dimer fluorescence, and that the lowest excited singlet state in this molecule can also be assigned as a 1L_b state. The polarized fluorescence excitation spectrum further demonstrates that the shoulder located at 315.3 nm is part of the 1L_b system. The negatively polarized band at 317.9 nm is probably vibronically induced.

The negative polarization and the abrupt change in intensity indicate that the band at 310.2 nm in the *cis* dimer is the origin of the ${}^1L_a \leftarrow {}^1A$ transition. Just

(3) W. R. Dawson and M. W. Windsor, *J. Phys. Chem.*, **72**, 3251 (1968).

(4) J. R. Platt, *J. Chem. Phys.*, **17**, 484 (1949).

(5) D. S. McClure, *ibid.*, **22**, 1668 (1954); **24**, 1 (1956).

as in naphthalene and acenaphthene, the ${}^1L_a \leftarrow {}^1A$ shows two prominent vibrational progressions based on $1400\text{--}1500\text{ cm}^{-1}$ and $\sim 500\text{--}600\text{ cm}^{-1}$ frequencies. The greater diffuseness in the spectrum of the *cis* dimer in the 1L_a region, as compared with the acenaphthene and *trans* dimer spectra, is probably due to the fact that the plus and minus exciton components are not resolved at 77°K .

The low temperature fluorescence emission spectrum of the *trans* dimer shown in Figure 2 conclusively demonstrates that the emission is from a 1L_b state, and the fluorescence excitation spectrum presented in Figure 1 proves that the emission is from the *trans* dimer. The weak first band at 320.9 nm is accordingly assigned as the origin of the ${}^1L_b \leftarrow {}^1A$ transition. The second band observed at 317.5 nm is much too intense to be part of the 1L_b system and we therefore assign this as the origin of the ${}^1L_a \leftarrow {}^1A$ transition. This assignment does appear to present problems since the polarized excitation spectrum shows that the entire absorption spectrum from 317 to 290 nm is polarized *parallel* to the O–O band of the ${}^1L_b \leftarrow {}^1A$ emission. There are the additional, unexpected features that the ${}^1L_a \leftarrow {}^1A$ transition in the *trans* dimer is approximately twice as intense as the ${}^1L_a \leftarrow {}^1A$ transition in either acenaphthene⁶ or in the *cis* dimer and the O–O band of the ${}^1L_b \leftarrow {}^1A$ transition is about two times more intense in the *trans* than in the *cis* dimer. We believe that both the polarizations and intensities can be accounted for in the following manner. According to the X-ray measurements of Dunitz and Schomaker⁷ in the crystal the *trans* dimer is centrosymmetric with a planar cyclobutane ring. It is well known, however, that with the other simple substituted cyclobutanes such as the octafluoro- and octachloro-derivatives the cyclobutane ring is puckered.⁸ We suggest, therefore, that while intermolecular interactions force the *trans* dimer into a centro-symmetric configuration in the crystal, in solution the cyclobutane ring is slightly puckered. As a result of the puckering the symmetry of the molecule is reduced from C_{2h} to C_1 and in this lowered symmetry, the 1L_b , 1L_a and 1B_b ring states all have the same symmetry and can therefore mix with one another *via* inter-ring interactions.

Mixing of the 1L_b state with the nearly degenerate 1L_a state would then account for the intensification of the ${}^1L_b \leftarrow {}^1A$ transition and for the fact that the transitions to the 1L_a and 1L_b states in this molecule are polarized more or less parallel to one another. Because of the near degeneracy of these two states an interaction less than $\sim 100\text{ cm}^{-1}$ would be adequate to account for the observation. Similarly, mixing of the 1L_a state with the higher energy 1B_b state would account for the intensification of the ${}^1L_a \leftarrow {}^1A$ transition. In this case an interaction energy of $\sim 4000\text{ cm}^{-1}$ would be required.

The ${}^1L_a \leftarrow {}^1A$ transition of the *trans* dimer also differs from the corresponding transition in acenaphthene in

that in addition to the two prominent vibrational progressions which appeared in naphthalene and acenaphthene based on 1453 cm^{-1} and 545 cm^{-1} , there is a new distinct progression built on $0 + 280\text{ cm}^{-1}$. The absence of this band in naphthalene and in acenaphthene suggests that the 280 cm^{-1} vibration might be unique to the dimer structure. Accordingly, we find a fairly prominent band at 269 cm^{-1} in the Raman spectrum of the *trans* dimer of acenaphthylene, but not in either naphthalene or acenaphthene. A Raman band at 285 cm^{-1} was reported by Lippincott and O'Reilly⁹ for naphthalene, but we have been unable to observe this band. In a more recent study of the Raman spectrum of crystalline naphthalene, Ito did not report this band either.¹⁰

2. Emission Spectra. A. Fluorescence. The fluorescence properties of the *cis* and *trans* dimer are similar in that the fluorescence yields for both compounds increase with decreasing temperature, as indicated by the data presented in Table I. We shall sub-

Table I: The Absolute Fluorescence and the Relative Photodissociation Quantum Yields for the *cis* and *trans* Dimers of Acenaphthalene at Various Temperatures

Isomer	Relative photo-dissociation yield			Fluorescence yield		
	T, °K			T, °K		
	300	145	77	300	145	77
<i>cis</i> dimer	(1) ^a	0.58	0	~ 0.01	0.16	0.53
<i>trans</i> dimer	(1) ^b	0.78	0.20	~ 0.01	0.04	0.44

^a Absolute value 0.91 (ref 14). ^b Absolute value 0.85 (ref 14).

sequently provide data which indicate that photodissociation is the principal cause of this temperature dependence.

The fluorescence spectrum of the *trans* dimer appears to be similar to that of acenaphthene at all temperatures. The fluorescence spectrum of the *cis* dimer is somewhat unusual, however, in that at low temperatures it is structured and acenaphthene-like, but at higher temperatures it becomes diffuse and the maximum in intensity shifts from 338 nm to 344 nm (see Figure 3). The fluorescence excitation spectrum dem-

(6) J. A. Petruska in "Systematics of the Electronic Spectra of Conjugated Molecules," J. R. Platt, Ed., John Wiley & Sons, New York, N. Y., 1964.

(7) J. D. Dunitz and V. Schomaker, *J. Chem. Phys.*, **20**, 1703 (1952).

(8) (a) H. P. Lemaire and R. L. Livingston, *ibid.*, **18**, 569 (1950);

(b) T. B. Owen and J. L. Hoard, *Acta Cryst.*, **4**, 172 (1951).

(9) E. R. Lippincott and E. J. O'Reilly, *J. Chem. Phys.*, **23**, 238 (1955).

(10) M. Ito, M. Susuki, and T. Yokoyama, "Excitons, Magnons and Photons in Molecular Crystal," A. B. Zahlan, Ed., Cambridge University Press, 1968.

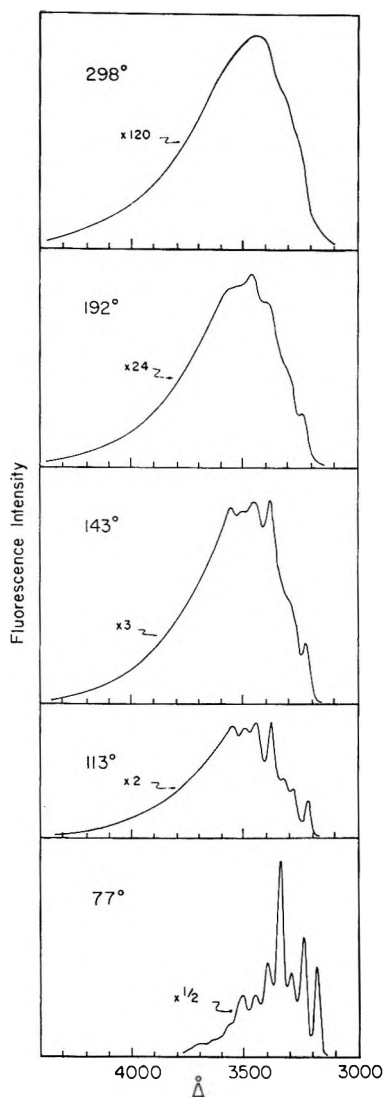


Figure 3. The temperature dependence of the fluorescence spectrum of the *cis* dimer of acenaphthylene in EPA. The gains indicated on the spectra are only approximate.

onstrates that this weaker broad emission is actually due to excitation of the *cis* dimer, and it is important to note that this change in the emission spectrum occurs at a temperature of 195°K at which the solvent is still fluid. In view of these differences in the fluorescence behavior of the two dimers, and their obvious structural differences, we suggest that the broad emission observed from the *cis* dimer at the higher temperatures is due to formation of an intramolecular excimer. At room temperature both the diphenylalkanes and polyvinyl-naphthalenes exhibit a similar fluorescence behavior which is also attributed to intramolecular excimer formation.¹¹ In rigid glass solutions at 77°K the polyvinyl-naphthalene excimer fluorescence disappears and is replaced by monomer fluorescence, but the low-temperature behavior in fluid solutions was not reported.¹² Although the shift of the *cis* dimer excimer relative to the normal emission is small, molecular models indicate

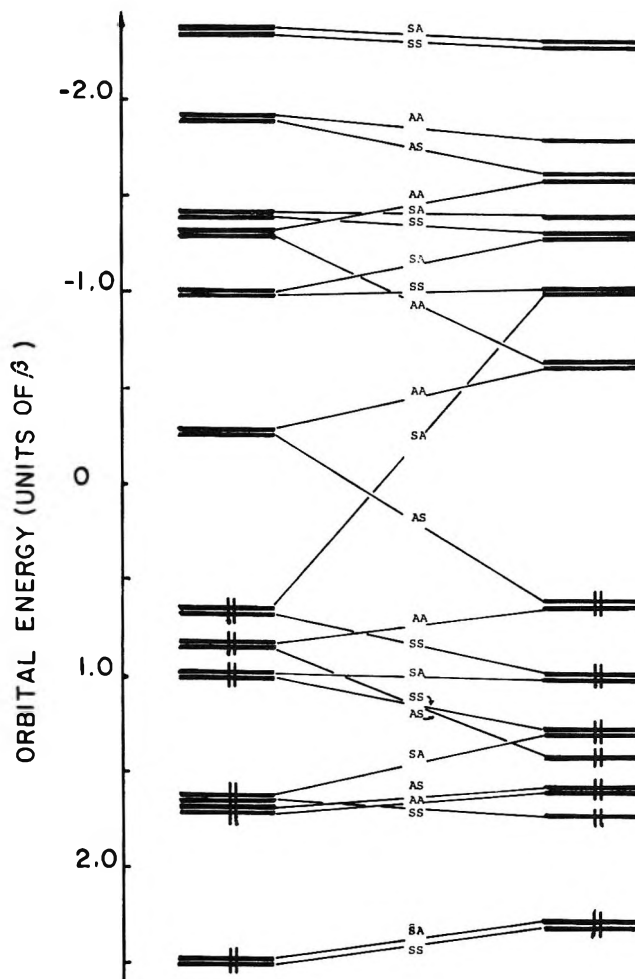


Figure 4. A molecular orbital correlation diagram depicting the interconversion of the *cis* dimer of acenaphthylene and acenaphthylene. Orbital energies were taken from C. A. Coulson and A. Streitwieser, "Dictionary of π Electron Calculations," Pergamon Press, Oxford, 1965. The symmetry of the molecular orbitals with respect to a symmetry plane that is perpendicular to both naphthalene rings is indicated first, followed by the symmetry with respect to a symmetry plane that passes between the two naphthalene rings. The orbitals of the *cis* dimer are depicted on the right-hand side and those of two acenaphthylene molecules on the left side of the diagram.

that in the *cis* dimer, the naphthalene chromophores are probably oriented about 60° to each other and prevented from attaining the coplanar sandwich structure required for a fully effective excimer interaction.¹³ The fact that the excimer-like emission disappears in fluid solutions below 100°K indicates that there is a barrier to excimer formation of about 0.2 kcal/mol.

B. Phosphorescence. The 77°K phosphorescence spectra of acenaphthene and the acenaphthylene dimers were virtually identical. In particular, there was no evidence for triplet excimer formation in the case of the

(11) F. Hirayama, *J. Chem. Phys.*, **42**, 3163 (1965).

(12) M. T. Vala, J. Haebig, and S. A. Rice, *ibid.*, **43**, 886 (1965).

(13) B. Stevens, *Spectrochim. Acta*, **18**, 439 (1962).

cis dimer, but this was not surprising in view of the lack of singlet excimer formations at 77°K. The phosphorescence from the *trans* dimer was much weaker (factor of at least 20) than from the *cis* dimer, which had a quantum yield of 0.006. At the present time we have no explanation for the differences in phosphorescence quantum yields.

With this discussion of the spectroscopic properties of the *cis* and *trans* dimers of acenaphthylene we now turn to an examination of their relation to the photochemical properties of the dimers.

3. Photodissociation and Radiationless Transitions.

In an earlier study, Livingston and Wei reported that the quantum yield for the photodissociation of the *cis* dimer was on the order of 0.91 and 0.85 for the *trans* dimer for temperatures ranging from 0 to 75°.¹⁴ We have extended this range to lower temperatures and our results are summarized in Table I. The photodissociation of the *cis* dimer decreases with decreasing temperature, until it is entirely stopped at 77°K. The *trans* dimer exhibits a similar behavior but even at 77°K the photodissociation quantum yield is still 20% of the room temperature value.

The inverse relation between the quantum yields for photodissociation and for fluorescence which we observe, taken together with the high room temperature dissociation yields, clearly indicate that photodissociation (from the singlet state) is the major pathway for deactivation of the excited dimers and that the temperature dependence of the dissociation rate constant is largely responsible for the very significant temperature dependence of the fluorescence quantum yields.

The temperature dependence of the photodissociation quantum yields suggests that there is a small activation energy for the photodissociation process. The origin of this barrier is suggested by consideration of the molecular orbital correlation diagram for the acenaphthalene ⇌ dimer interconversion which is shown in Figure 4. With a few differences this diagram is generally similar

to those which Hoffmann and Woodward have suggested are a characteristic of thermally forbidden but photochemically allowed transformations.¹⁵ Since the lowest energy antibonding orbital of acenaphthalene is stabilized by dimer formation to about the same extent that the highest energy bonding orbital is destabilized, we expect that the photodimerization of acenaphthalene will proceed with little or no activation energy. This is not true, however, for the photodissociation process. As the diagram indicates, dissociation of the dimer does not significantly stabilize the *lowest energy* antibonding molecular orbital (an orbital of AA symmetry which correlates with an antibonding orbital of the monomers). Rather it is a higher energy antibonding orbital of SA symmetry which is stabilized by the dissociation. Accepting this diagram literally, it appears that the lowest excited state of the dimer would not be stabilized until the point is reached on the diagram where the SA orbital crosses the AA antibonding orbital, and that some activation energy would be required to reach this point. This could be the origin of the temperature dependence of the photodissociation quantum yield. It is perhaps worth noting that extensive configuration interaction is needed in order to account for the spectroscopic properties of the aromatic hydrocarbons and this could significantly alter conclusions based solely on orbital considerations.¹⁶

Acknowledgments. We gratefully acknowledge the assistance of Dr. William Fenical with the photochemical studies. The support of the U. S. Army Research Office, Durham (Grant ARO-D-31-124-G804), is also gratefully acknowledged.

(14) R. Livingston and K. S. Wei, *J. Phys. Chem.*, **71**, 541 (1967).

(15) R. Hoffmann and R. B. Woodward, *J. Amer. Chem. Soc.*, **87**, 2046, 4388 (1965).

(16) M. J. S. Dewar and H. C. Longuet-Higgins, *Proc. Phys. Soc.*, **A67**, 795 (1954).

Spectroscopy of Sulfur in Ethylenediamine

by Robert MacColl and Stanley Windwer^{1a}

Department of Chemistry, Adelphi University, Garden City, New York 11530 (Received September 9, 1969)

The ultraviolet-visible spectra of green solutions of sulfur in ethylenediamine exhibit bands at 616, 400, 316, and 239 $m\mu$. The concentration and temperature dependence of these bands and their decomposition show the 616- $m\mu$ band represents a different species from the others. In the lower concentration range, a shoulder appears at 266 $m\mu$. The spectra of solutions of sulfur in 1,3-diaminopropane were studied and compared to the ethylenediamine results. The 616- $m\mu$ band again showed behavior that was different from the other bands. The 616- $m\mu$ band was shown to represent a negative species by moving-boundary electrophoresis experiments. The results are interpreted in that the 616- $m\mu$ band is due to sulfur radical ions ($^-\text{S}-\text{S}_2-\text{S}^{\cdot-}$). A scheme is presented to account for these results. Past reports of sulfur radical ions are discussed, and comparisons are made to similar systems.

Introduction

Solutions of sulfur in many organic solvents contain sulfur dissolved in the form of cyclooctasulfur molecules. These solvents include benzene, alcohols, and hexane. Friedman and Kerker^{1b} found an almost linear relationship between the refractive indices (n) of these solvents and the extinction coefficients at a particular wavelength in the ultraviolet absorption region. The relation between extinction coefficient and refractive index was derived by Davis² using quantum theory. He found that the extinction coefficient was actually proportional to $n^3 + 4n + 4/n$. Davis and Nakshbendi³ found this relationship was accurate for sulfur in many solvents, but amines did not obey this cubic equation. It is concluded that amines do not dissolve sulfur as cyclooctasulfur molecules. That sulfur-amine solutions contained ions was demonstrated by conductance measurements.^{3,4} Hodgson, Buckler and Peters⁵ showed the presence of free radicals in these amine-sulfur solutions by measuring their electron spin resonance spectra.

The purpose of this investigation was to study solutions of sulfur in ethylenediamine in an attempt to better understand the nature of these solutions. The principal method used was ultraviolet-visible spectroscopy under a variety of conditions.

Experimental Section

Sulfur (Baker, NF grade) was purified by the method of Bacon and Fanelli.⁶ Ultrapure grade sulfur from the Research Chemical Company was used without additional purification. Both types of sulfur gave identical spectroscopic results.

Ethylenediamine (Baker reagent grade) and 1,3-diaminopropane (Eastman Yellow Label) were treated as follows. The amine was refluxed from reagent grade potassium hydroxide and anhydrous barium oxide under nitrogen and a pressure of about 20 Torr and then distilled over a packed 900-mm column. The

middle cut was collected. The distillation process was repeated. The flask containing the doubly distilled amine was attached to a high-vacuum system by means of a ground-glass joint. The remainder of the vacuum system was evacuated using a mechanical pump and an oil diffusion pump. Pressures obtained were usually near 5×10^{-6} Torr, but pressures as high as 5×10^{-5} Torr were also considered adequate. Apiezon N or T greases were used on stopcocks and joints on the high-vacuum system.

The amine was then allowed into the vacuum system and distilled under vacuum over lithium. The distillation proceeded as follows. A dark blue solution of lithium in amine was heated in a warm water bath, while the collection flask was placed in an acetone-Dry Ice bath. This collection flask contained additional pieces of lithium. After completion of the first distillation, the frozen material was immediately melted with a warm water bath and a dark blue solution formed as the lithium dissolved. Lithium was less soluble in 1,3-diaminopropane than it was in ethylenediamine. The amine was distilled into a solvent reservoir flask. Nitrogen from a nitrogen reservoir flask was used to push amine through an inlet tube into a buret as needed. The buret emptied into a reaction flask that contained a weighed amount of sulfur. The reaction flask was evacuated using the oil diffusion pump prior to the addition of the amine.

(1) (a) To whom requests for reprints should be addressed; (b) H. L. Friedman and M. Kerker, *J. Colloid Sci.*, **8**, 80 (1953).

(2) R. E. Davis, *Proc. Indiana Acad. Sci.*, **71**, paper II (1962).

(3) R. E. Davis and H. F. Nakshbendi, *J. Amer. Chem. Soc.*, **84**, 2085 (1962).

(4) G. L. Putnam and K. A. Kobe, *Trans. Electrochem. Soc.*, **74**, 609 (1938).

(5) W. G. Hodgson, S. A. Buckler, and G. Peters, *J. Amer. Chem. Soc.*, **85**, 543 (1963).

(6) R. F. Bacon and R. Fanelli, *Ind. Eng. Chem.*, **34**, 1043 (1942); *J. Amer. Chem. Soc.*, **65**, 639 (1943); T. J. Murphy, W. S. Clabough and R. Gilchrist, *J. Res. Natl. Bur. Std.*, **69A**, 355 (1960).

Two reaction flasks, both specially designed to fit into the normal cell compartment of the Cary 14 spectrophotometer, were used. The first had a 2.003-mm quartz optical cell (Americal Instrument Co.) attached through a quartz-Pyrex graded seal. The second reaction flask had two quartz cells (0.105 and 0.504 mm) at about ninety degrees apart. This allowed a change in path length by simply rotating the flask in the cell compartment of the Cary 14. Neutral density filters were used when required.

When the amine had been added to the sulfur, a stopcock was closed and the reaction flask was removed from the vacuum system. A glass-coated stirring bar was used to stir the solution. All the absorption bands increased for a period of time until the absorbances were constant. The solutions in this condition exhibited no spectral changes for several hours. Some showed no change for 24 hr and more. After a period of time the solutions decomposed. This stability was considerably better than that found by earlier workers, who did not use ultra high-vacuum techniques.

When sulfur and ethylenediamine are initially mixed, the sulfur dissolves to give a red color in the vicinity of the solid sulfur. The red quickly changed to green. In the concentration range studied, the color of the sulfur-ethylenediamine solutions varied from light green to very dark green at 25°.

The temperature in the cell compartment of the Cary 14 was regulated by a Haake constant-temperature circulator. Most experiments were performed at 25°, and the temperature control was ± 0.08 or better. When temperature changes were made, the absorbances of the various bands were frequently measured. When all the bands exhibited constant absorbances for a long period of time, equilibrium was assumed to have been reestablished.

All the glassware used on the high-vacuum system was cleaned with an HF-HNO₃ cleaning solution, rinsed five times with distilled water, treated with freshly prepared aqua regia, rinsed ten times with distilled water, and dried at 140° in an oven. The optical cells were cleaned with dilute HCl and distilled water.

The amine used in the reference cells was purified in the same manner as the amine used in the reaction flask.

Apparent molar concentrations were calculated using 32.064 for the molecular weight of the various species. All absorbances reported here have been scaled, so that they represent absorbances for a 1-mm cell.

The moving-boundary electrophoresis experiments were based on those of Burton.⁷ This procedure involved the careful addition of sulfur-ethylenediamine solution to a U-tube containing purified ethylenediamine. The addition was accomplished through a stopcock on the bottom of the U-tube. Thus a sharp

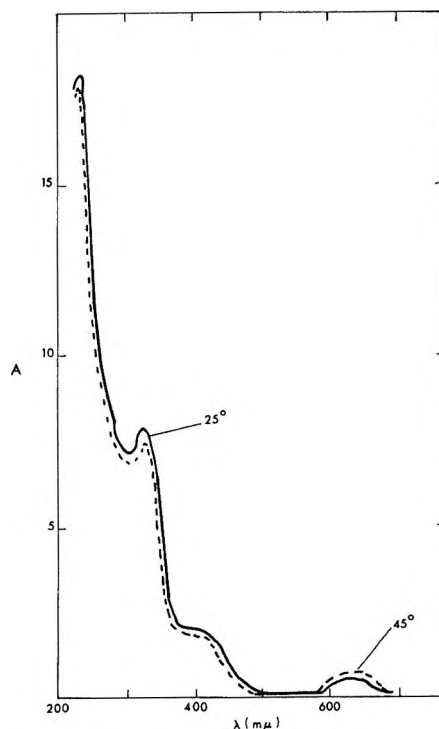


Figure 1. Visible-ultraviolet absorption spectrum of a sulfur-ethylenediamine solution (0.086 *M* at 25 and 45°).

boundary was established between the green solution and colorless solvent. When voltage was applied, this sharp boundary was not maintained. Either sodium chloride or potassium nitrate was present to act as an inert electrolyte, and the electrodes were platinum disks. The voltage was maintained at 150 V, and the current was less than 1 mA.

Results

The ultraviolet-visible spectra exhibited four absorbance bands (Figure 1). As the temperature was increased, the 616- $m\mu$ band increased in absorbance and the bands at 400, 316, and 239 $m\mu$ decreased. Thus, the broad 616- $m\mu$ band is probably caused by a different chemical species. The temperature dependence of the 400- and 316- $m\mu$ bands was slight, about a 0.2 to 0.4% change in absorbance for each degree, while the absorbance of the 616- $m\mu$ band changed about 20% per degree. Little quantitative data was obtained on the 239- $m\mu$ band, since its peak was very near the solvent cut-off wavelength.⁸

The concentration dependence of the electronic spectra was studied from 0.00164 to 0.151 *M* (Figure 2). The absorbance at 400 and 316- $m\mu$ increased linearly with concentration, but the 616- $m\mu$ band had a non-linear dependence (Figure 3). At the lower concentrations, the 616- $m\mu$ band had greater absorbance than the

(7) E. F. Burton, *Phil. Mag.*, **11**, 425 (1906).

(8) Measurements of the 239- $m\mu$ band were limited to the 0.105-mm cell and concentrations between 0.0680 and 0.0870 *M*.

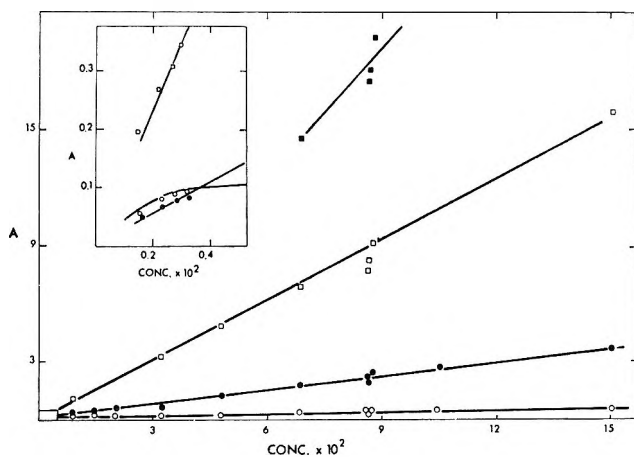


Figure 2. Concentration dependence of the absorption maxima of sulfur-ethylenediamine solutions at 25°C: O, 616 mμ; ●, 400 mμ; □, 316 mμ; ■, 239 mμ.

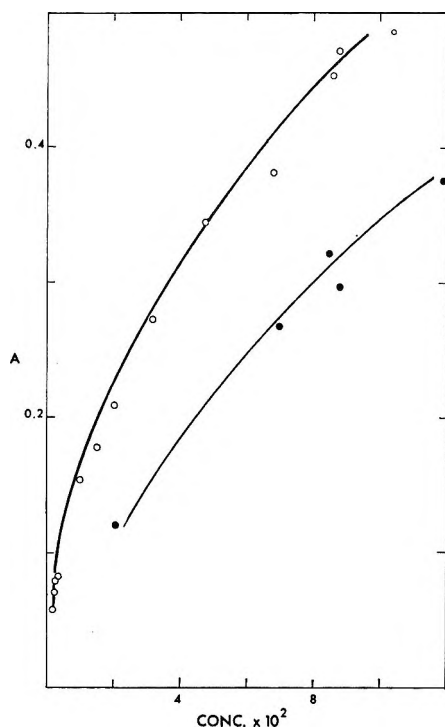


Figure 3. Concentration dependence of the 616-mμ absorption maximum of sulfur dissolved in ethylenediamine, O, and 1,3-diaminopropane, ●, at 25°C.

400-mμ band, but at concentrations above about 0.004 *M* the 400-mμ band had the greater absorbance. The concentration dependence and also the effect of temperature suggests that the species absorbing at 616 mμ is involved in an equilibrium relationship.

The decomposition proceeded with the green color diminishing and the solution becoming yellow and finally colorless. Exposure to the atmosphere caused rapid decay. The yellow color was observed since the 616-mμ band decreased in intensity faster than the others (Figure 4). The 239-mμ band did not show any

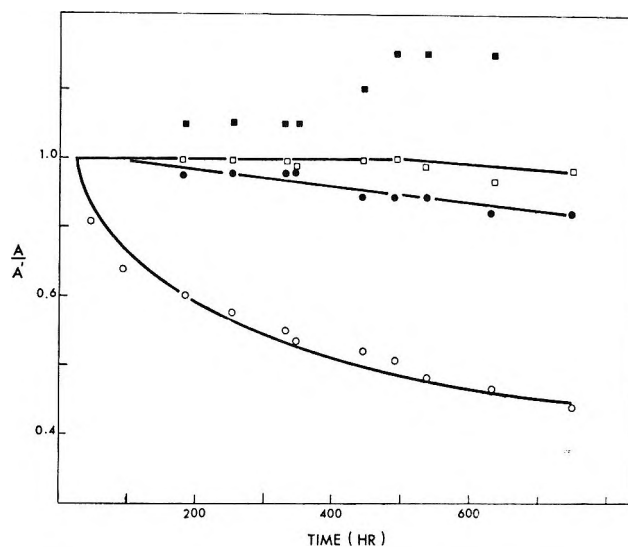


Figure 4. A typical decomposition for a spectrum of a sulfur-ethylenediamine solution at 25°C: O, 616 mμ; ●, 400 mμ; □, 316 mμ; ■, 239 mμ. For this particular example no change in absorbance was observed after 90 hr for ●, ■, and □. The A' are the absorption maxima for the various bands before any decay has occurred.

decay in the 800 hr plotted in Figure 4. All the bands eventually decayed. No attempt was made to control decomposition, but the 616-mμ band always decayed at the fastest rate.

At the lowest concentrations studied a shoulder appeared, suggesting a band was present that was completely submerged at higher concentrations. The absorbance of this shoulder increased as the temperature was increased and became quite distinct (Figure 5). The wavelength of the maximum absorbance was 266 mμ. These dilute solutions also showed a striking thermochromism when heated above 25°C. The solutions, due to the change in absorbance of the 400- and 616-mμ bands, changed gradually from green to blue as the temperature was raised.

Solutions of sulfur in 1,3-diaminopropane were also studied. The ultraviolet-visible spectra were very similar to those obtained with ethylenediamine. An exception was the 616-mμ band which showed lower absorbances in 1,3-diaminopropane than in ethylenediamine (Figures 3 and 6).

A significant difference between 1,3-diaminopropane and ethylenediamine is their dielectric constants. Ethylenediamine at 25°C has a dielectric constant of 12.5, while 1,3-diaminopropane has a dielectric constant of 9.6. Having a higher polarity, ethylenediamine would favor the existence of an ionic species more than 1,3-diaminopropane. Thus, it is possible that the 616-mμ band is due to an ionic species. To validate this interpretation, a moving boundary electrophoresis experiment was performed on sulfur-ethylenediamine solutions. The concentration of the solutions for this study were always near 0.085 *M*. A separation of the

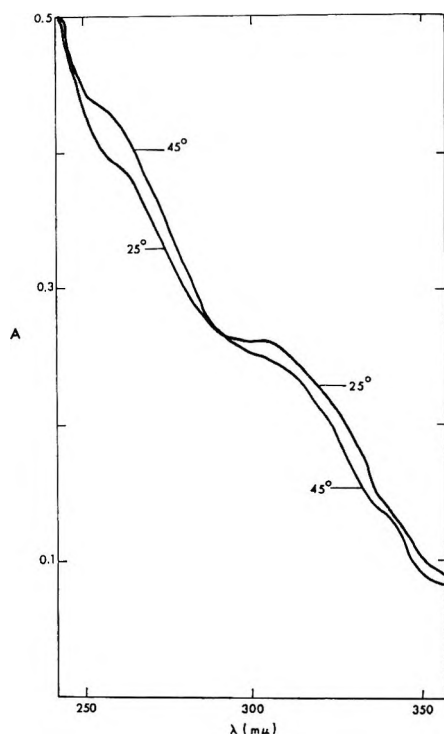


Figure 5. Spectrum of the 266- $m\mu$ band in a 0.00236 M sulfur-ethylenediamine solution at 25 and 45°.

616- $m\mu$ and 400- $m\mu$ species was not effected by this experiment. The green color migrated toward the positive electrode. Thus, it is concluded that the species responsible for both the 616- and 400- $m\mu$ bands are negatively charged.

Discussion

The 616- $m\mu$ absorption band has characteristics which indicate that it may represent a free-radical species. Electron spin resonance spectroscopy showed an increase in the concentration of the free radicals when the temperature was raised.⁵ The absorbance of the 616- $m\mu$ band, likewise, increased when the temperature was increased. This band showed instability by decaying faster than the others. The wavelength of its absorption maximum is typical for sulfur radicals. Green, purple,⁹ and most commonly blue (absorption maxima between 580 and 620 $m\mu$) radicals have been reported. Free radicals with unpaired spins on sulfur atoms have been postulated as the source for the blue color of sulfur dissolved in LiCl-KCl melts,¹⁰ sulfur-oleum solutions¹¹ and in several other paramagnetic, sulfur-containing systems.¹² Thus, the 616- $m\mu$ band seems to represent an anion radical.

Evidence that the unpaired electrons are located on sulfur atoms comes from the esr experiments of Hodgson, Buckler, and Peters.⁵ Ethylenediamine was one of the amines studied. Most primary and secondary amines produced paramagnetic solutions, and tertiary amines did not. Some esr measurements made during this present study confirmed that sulfur-ethylenedia-

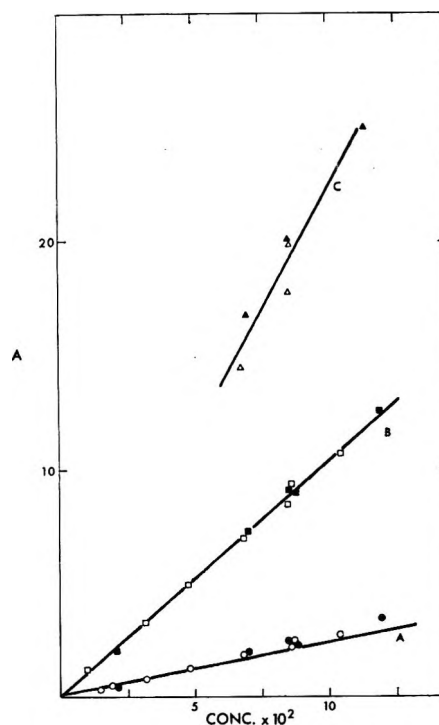


Figure 6. Concentration dependence of the absorption spectrum of sulfur-1,3-diaminopropane solutions compared to sulfur-ethylenediamine solutions at 25°: A, 400 $m\mu$; B, 316 $m\mu$; and C, 239 $m\mu$. The solid data symbols (\bullet , \blacksquare , and \blacktriangle) represent 1,3-diaminopropane solutions and the open symbols (\circ , \square , and \triangle) represent ethylenediamine solutions.

mine solutions are paramagnetic. They found a g value of 2.030 for paramagnetic sulfur-amine solutions. Due to spin-orbit coupling, sulfur radicals exhibit characteristically higher g values (in liquid sulfur, $g = 2.024$) than the free electron spin g factor of 2.002.¹³ This high g value is considered excellent proof that the unpaired spin is on a sulfur atom. This anion radical present in sulfur-ethylenediamine solutions is probably a sulfur radical ion



The high concentrations (0.3 to 3 M) needed for the esr experiments compared to those for the ultraviolet-visible work indicates a low concentration of these radicals.

Davis³ has proposed a scheme for the initial steps in the reaction of sulfur and amines. For ethylenediamine this scheme would be

(9) For example, H. E. Raford, and F. O. Rice, *J. Chem. Phys.*, **33**, 774 (1960).

(10) J. Greenberg, B. R. Sundheim, and D. M. Gruen, *ibid.*, **29**, 461 (1958).

(11) For example, M. C. R. Symons, *J. Chem. Soc.*, 2440 (1957).

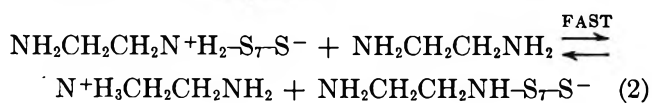
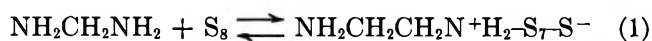
(12) Giggenbach¹⁶ related the blue color of several sulfur-containing materials to the presence of sulfur radicals.

(13) D. M. Gardner and G. K. Fraenkel, *J. Amer. Chem. Soc.*, **78**, 3279 (1956).

Table I: Absorption Spectra of Cyclooctasulfur Solutions

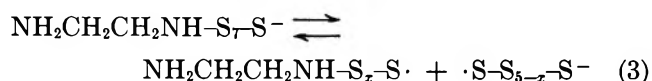
Solvent	T, °C	λ_{\max} , m μ	Color ^a	References
Inert (n-hexane, etc.)	Room temp.	260–280, 225	Canary yellow	3
Ethylenediamine ^b	25	616, 400, 316, 239 ^c	Green	This research
Liquid ammonia	–35 and –40 ^d	580, 430, 295–97	Green to blue-red ^e	28, 29
DMF ^f with Na ₂ S	20	617, 435, 347	Blue	18
Alkali halide melts	400	588, 417, 278	Blue	16
Oleum (65%)	20	588, 400, 333	Blue	g
Oleum (65%)	...	590, 355	Blue	11

^a Davis and Nakshbendi³ found sulfur-amine solutions with colors ranging from orange-yellow and red-orange to green. ^b At 60°, for solutions around 0.002 M the color is blue. ^c For solutions around 0.002 M a shoulder emerges at 266 m μ . ^d At –77°, Nelson and Lagowski²⁹ found the peak at 580 m μ had disappeared. ^e Solutions 0.01 M and greater are dichroic and show a blue-red color. Solutions less concentrated are green. ^f DMF = dimethylformamide. ^g H. Lux and E. Böhm, *Chem. Ber.*, **98**, 3210 (1965).

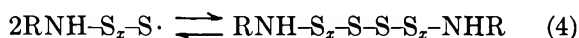


Equation 1 shows a nucleophilic attack on the sulfur ring causing heterolytic cleavage of the ring. Many substances react with sulfur in this manner.¹⁴

We suggest that sulfur radical ions could then arise from homolytic scission of an S–S bond.



Levi¹⁵ has found that amines and sulfur can react to yield N,N'-polythio-bisamines. These N,N'-polythio-bisamines could be formed by the dimerization of the thioamine from eq 3. In general, this would occur as follows.



Since sulfur radical ions are postulated for sulfur-ethylenediamine solutions, the existence of these species in other systems is of great interest. The scarcity of data on these ionic radicals and the controversial nature of some of these reports makes the following brief discussion on sulfur radical ions pertinent and necessary. Giggenbach¹⁶ found the S₂^{·-} ion, having an absorbance maximum at 617 m μ , in the blue solutions of alkali metal tetrasulfide in dimethylformamide. He also postulated that sulfur radical ions were present in solutions of sulfur and alkali metal sulfide in dimethylformamide, where a small amount of water was also present. In addition to the S₂^{·-} ion, he postulated the existence of S₄^{·-} and S₃^{·-} (*g* = 2.027). The S₂^{·-} ion shows extreme *g* anisotropy, and Morton reported that its resonance spectrum is undetected except at liquid helium temperature.¹⁷ Lux, Benninger, and Böhm¹⁸ studied very dilute solutions of sulfur and alkali metal sulfide in anhydrous dimethylformamide and found no sulfur ions present other than the sulfide ion.

Sulfur radical ions have been suggested for ultramarine^{16,19–21} and sulfur-doped alkali metal halides.^{17,22,23} Gardner and Fraenkel¹⁹ reported a *g* value of 2.028 for the blue ultramarine. In selenium-doped alkali metal halides,^{23,24} Se₂^{·-} and Se₃^{·-} have been observed. In alkali metal halides doped with both selenium and sulfur, SSe^{·-} was discovered.²⁴ Hashimoto, Sunamoto, and Aoki²⁵ found an esr signal in solutions of alkali metal tetrasulfide in water that were kept under nitrogen for 30 days. They also postulated the presence of sulfur radical ions. However, they found a *g* value of 2.002, which is lower than the other reported values for sulfur radicals.

Solutions of sulfur in liquid ammonia give results similar to those in ethylenediamine. The sulfur-liquid ammonia solutions have been studied since 1873,²⁶ and the species present are still unknown. Both liquid ammonia²⁷ and ethylenediamine^{3,4} dissolve sulfur to produce ionic solutions. The absorption

(14) M. Schmidt in "Elemental Sulfur," B. Meyer, Ed., Interscience Publishers, New York, N. Y., 1965, Chapter 15.

(15) T. G. Levi, *Gazz. Chim. Ital.*, **60**, 975 (1930); *ibid.*, **61**, 286 (1931).

(16) W. Giggenbach, *J. Inorg. Nucl. Chem.*, **30**, 3189 (1968).

(17) J. R. Morton, *J. Chem. Phys.*, **43**, 3418 (1965); *J. Phys. Chem.*, **71**, 89 (1967); J. R. Morton and L. E. Vannotti, *Phys. Rev.*, **161**, 282 (1967).

(18) H. Lux, S. Benninger, and E. Böhm, *Chem. Ber.*, **101**, 2485 (1968).

(19) D. M. Gardner and C. K. Fraenkel, *J. Amer. Chem. Soc.*, **77**, 6399 (1955).

(20) W. G. Hodgson, J. S. Brinen, and E. F. Williams, *J. Chem. Phys.*, **47**, 3719 (1967).

(21) R. Böttcher, S. Wartewig, W. Windsch, and A. Zschunke, *Z. Naturforsch.*, **23a**, 1766 (1968).

(22) J. H. Schulman and R. D. Kirk, *Solid State Commun.*, **2**, 105 (1964).

(23) J. Schneider, B. Dischler, and A. Räuber, *Phys. Status Solidi*, **13**, 141 (1966); J. Sulwalski and H. Seidel, *ibid.*, **13**, 159 (1966).

(24) L. E. Vannotti and J. R. Morton, *Phys. Lett.*, **24A**, 520 (1967); J. Rolfe, *J. Chem. Phys.*, **49**, 4193 (1968).

(25) S. Hashimoto, J. Sunamoto, and A. Aoki, *Bull. Chem. Soc. Jap.*, **40**, 2867 (1967).

(26) G. Gore, *Proc. Roy. Soc.*, **21**, 140 (1873).

(27) E. C. Franklin and C. A. Kraus, *Am. Chem. J.*, **24**, 89 (1900).

spectra were studied by Zipp²⁸ and Nelson and Lagowski.²⁹ They found bands with maxima at 580, 430, and 295–297 $m\mu$. The temperature dependence and the manner of decomposition were similar in both solvents. Zipp studied the concentration dependence of the visible spectrum and found that at lower concentrations the 430- $m\mu$ band had higher absorbances than the 580- $m\mu$ band, but at higher concentrations the 580- $m\mu$ band had the higher absorbances. We found the reverse relationship between the 616- $m\mu$ band and the 400- $m\mu$ band in ethylenediamine. Table I shows a comparison of the absorption spectra of some sulfur solutions. In both amines and liquid ammonia sulfur dissolves reversibly.^{3,26} From liquid ammonia, sulfur is recovered by evaporation and from amines by dilution with aqueous hydrochloric acid. The sulfur-ammonia solutions, if they are truly analogous to the amine solutions, will be paramagnetic. Therefore, esr spec-

trosopy may prove valuable in the study of these liquid ammonia solutions. The conductance behavior of these sulfur-liquid ammonia solutions was recently reported by Zipp and Evers.³⁰

The concentration and temperature dependence of the visible absorption spectra of sulfur-ethylenediamine solutions indicate that the 616- $m\mu$ species is involved in an equilibrium relationship. If this equilibrium was either a dimerization or a disproportionation, the sulfur radicals would form polysulfide ions.

Acknowledgments. R. M. gratefully acknowledges the receipt of a NASA Predoctoral Fellowship during the tenure of this work.

(28) A. P. Zipp, Ph.D. Thesis, University of Pennsylvania, 1964.

(29) J. T. Nelson and J. J. Lagowski, *Inorg. Chem.*, **7**, 1292 (1967).

(30) A. P. Zipp and E. C. Evers, *ibid.*, **8**, 1746 (1969).

The Spin-Lattice Relaxation of Oxygen-17 in Water¹

by J. C. Hindman, A. Svirmickas, and M. Wood

Chemistry Division, Argonne National Laboratory, Argonne, Illinois 60439 (Received September 3, 1969)

The quadrupole relaxation time, T_1 , has been measured in liquid water over the temperature range from -17 to 95° . $\ln T_1$ is found to be a smoothly varying function of $1/T$ down into the supercooled region. The temperature behavior is non-Arrhenius. The data can be fit by the empirical equation, $\ln T_1 = 75.13 \pm 3.53 - 10.76 \pm 0.53 \ln T - 5608 \pm 161/T$. Similar equations can be used to express the temperature dependence of dielectric and deuteron quadrupole relaxation data in water. The question of the temperature variation of the oxygen-17 and deuteron quadrupole coupling constants in liquid water is discussed. The physical interpretation of the equation used to represent the relaxation data is also discussed briefly.

Two recent experimental studies have been made of the oxygen-17 quadrupole relaxation in water.^{2,3} Glasel² concluded, from his measurements and a comparison of the deuteron and oxygen-17 spin-lattice relaxation times with dielectric relaxation data, that there was a temperature coefficient for both the ^2H and ^{17}O quadrupole coupling constants, with a well defined minimum in the ^{17}O coupling constant in the region of 40° . On the other hand, Garrett, Denison, and Rabideau³ concluded from their data that the ^{17}O quadrupole coupling constant was essentially independent of temperature in the interval between 5 and 95° . Since in both cases the calculations of the quadrupole coupling constants were based on the assumption of a classical rotational diffusion model for the relaxation process, the data appear to be discordant. In view of the importance of the conclusions with respect to the nature of the relaxing

species, a reinvestigation of the ^{17}O relaxation appeared in order. The present communication summarizes the results.

Experimental Section

The H_2^{17}O water samples were prepared from Yeda Research and Development Company water enriched to 26.94% in oxygen-17. The samples were prepared by multiple distillation on a vacuum line and sealed after gas removal by the usual freeze, pump, thaw technique. To ensure reproducibility of the results it was found necessary to boil all the glassware for several hours in

(1) Based on work performed under the auspices of the U. S. Atomic Energy Commission.

(2) J. A. Glasel, *Proc. Nat'l. Acad. Science*, **58**, 27 (1967).

(3) B. B. Garrett, A. B. Denison, and S. W. Rabideau, *J. Phys. Chem.*, **71**, 2606 (1967).

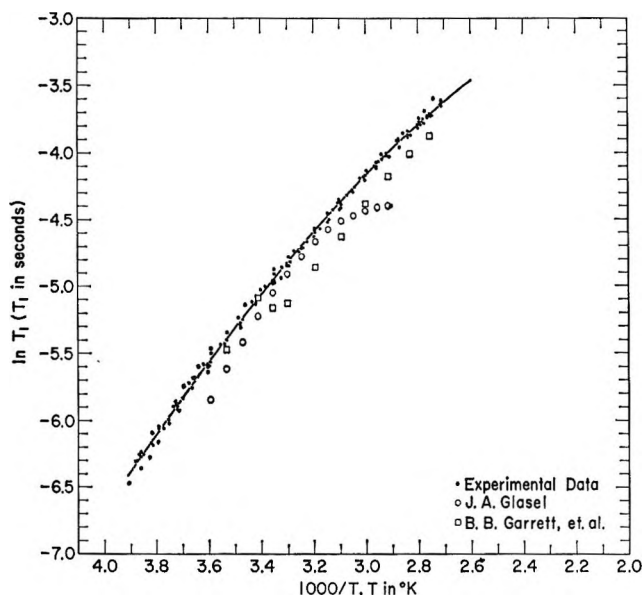


Figure 1. Experimental values for $\ln T_1$ as a function of $1000/T$. Solid line, eq 3.

hydrochloric acid before rinsing with conductivity grade water and drying. The fact that the hydrochloric acid treatment was necessary indicates the presence of difficultly removable traces of paramagnetic ions on the glass surfaces.

The spin-lattice relaxation times, T_1 , were measured using an NMR Specialties Company spin-echo spectrometer with a crossed coil probe operating at 8.134 MHz. The pulse sequence used was $180-90^\circ$. The probe was specially constructed to allow sample temperature control with a flowing liquid coolant. Temperature control to approximately $\pm 0.1^\circ$ was obtained. Although tests indicated excellent thermal equilibrium between the sample and the coolant, check measurements of the sample temperature for all temperatures were made by substitution of a sample tube containing a thermocouple.

Results and Discussion

The experimental results are shown in Figure 1. Each black dot represents the mean observed T_1 at the measured temperature. The experimental uncertainty in the determination of T_1 was found to be $\pm 3-4\%$, independent of temperature. Included in the figure are T_1 values derived from the data reported by Glasel² and by Garrett, *et al.*³ We note that $\ln T_1$ is a smoothly varying function of $1/T$ down into the supercooled region. We find that our T_1 values are in general appreciably longer than those reported by either Glasel² or Garrett, *et al.*,³ suggesting the possibility that these authors may not have effected complete removal of paramagnetic impurities from their sample containers.

The solid line in Figure 1 is the computer-calculated least-squares fit to the equation

$$\ln T_1 = a + b \ln T + \frac{c}{T} \quad (1)$$

An equation of this form results where a non-Arrhenius temperature behavior is observed, *e.g.*, in a number of first-order reactions in solution, and where the rate behavior can be expressed by the empirical equation⁴

$$k = BT^{c/R} e^{-E/RT} \quad (2)$$

The possible applicability of this form of the rate equation in the present case was indicated by Conway's⁵ treatment of dielectric relaxation in water. According to Conway, the constant c in eq 1 is identified with $-\Delta H_0^\ddagger/R$, where ΔH_0^\ddagger is the heat of activation at absolute zero (if water remained liquid down to this temperature). The constant b in eq 1 is then equal to $(\Delta c_p^\ddagger + R)/R$, where Δc_p^\ddagger is defined as the difference in heat capacity between molecules in the activated state and those in the initial state of the relaxation process.

The numerical equation for the oxygen-17 relaxation data obtained from a computer least-squares fit to the experimental results is

$$\ln T_1, (^{17}\text{O}) = 75.13 \pm 3.53 - (10.76 \pm 0.53) \ln T - (5608 \pm 161)/T \quad (3)$$

To facilitate comparison with Glasel's² results we have also computed numerical equations for the dielectric⁶ and deuteron⁷ relaxation data. The equations are

$$\ln (1/\tau_c), (\text{H}_2\text{O}) = 134.8 \pm 9.6 - (15.15 \pm 1.43) \ln T - (6850 \pm 432)/T \quad (4)$$

where τ_c is the dielectric correlation time

$$\ln T_1, (\text{D}_2\text{O}) = 127.5 \pm 14.8 - (17.79 \pm 2.19) \ln T - (8030 \pm 702)/T \quad (5)$$

and

$$\ln (1/\tau_c), (\text{D}_2\text{O}) = 152.2 \pm 20.0 - (17.71 \pm 2.98) \ln T - (7765 \pm 906)/T \quad (6)$$

Glasel assumed relaxation by a classical isotropic rotational diffusion process,^{2,3,7} where

$$\tau_Q = \frac{\tau_c}{3} f(\epsilon, \epsilon_\infty) = \frac{\tau_c}{3} \left(\frac{2\epsilon + \epsilon_\infty}{3\epsilon} \right) \quad (7)$$

with $f(\epsilon, \epsilon_\infty)$ the internal field correction,⁸ nearly independent of temperature.

(4) *cf.* E. A. Moelwyn-Hughes, "Physical Chemistry," Pergamon Press, London, 1961, p 1246.

(5) B. E. Conway, *Can. J. Chem.*, **37**, 613 (1959).

(6) Numerical data for dielectric calculations from combined results: H_2O , (a) J. B. Hasted and S. M. H. El Sabah, *Trans. Faraday Soc.*, **49**, 1003 (1953); (b) C. H. Collie, J. B. Hasted, and D. M. Ritson, *Proc. Phys. Soc. (London)*, **60**, 145 (1948); (c) E. H. Grant, T. J. Buchanan, and H. F. Cook, *J. Chem. Phys.*, **26**, 156 (1957); D_2O , (b).

(7) D. E. Woessner, *J. Chem. Phys.*, **40**, 2341 (1964).

(8) J. G. Powles, *ibid.*, **21**, 633 (1953).

The quadrupole coupling constants can be calculated from the equation⁹ for the quadrupole relaxation time, T_1 , in the reduced forms

$$(1/T_1)_Q, {}^{17}\text{O} = 3/125(1 + \eta^2/3)(e^2qQ/\hbar)^2\tau_Q, {}^{17}\text{O} \quad (8)$$

and

$$(1/T_1)_Q, {}^2\text{H} = 3/8(1 + \eta^2/3)(e^2qQ/\hbar)^2\tau_Q, {}^2\text{H} \quad (9)$$

where the η 's are the respective asymmetry parameters. For the deuteron, η is small for water molecules in both the gas¹⁰ ($\eta = 0.14$) and solid¹¹ (ice, $\eta = 0.1$) states and its effect on the calculation of the quadrupole coupling constant can be neglected. For oxygen-17 in the gas¹² ($\eta = 0.75$) and solid¹³ (ice, $\eta = 0.94$) water molecules, η is relatively large and must be taken into account in the calculation of the quadrupole coupling constant.

It is obvious from an inspection of eq 4 and 5 that there will be an apparent temperature coefficient for the oxygen-17 quadrupole coupling constant if the quadrupole correlation time is derived from the dielectric data. With an internal field factor of 0.69, the numerical value of the quadrupole coupling constant varies from $(e^2qQ/h) = 7.9\text{--}8.2$ MHz (± 0.2 MHz) at 0° to $7.6\text{--}7.9$ MHz (± 0.2 MHz) at 60° the numbers depending on whether the asymmetry parameter for the molecule in the solid or gas state is used in the calculation. These values can be compared with the values of 10.17 ± 0.07 MHz and 6.66 ± 0.1 MHz for the quadrupole coupling constant of the H_2^{17}O molecule in the gas¹² and solid,¹³ respectively. The apparent quadrupole coupling constant decreases in a regular manner with increasing temperature. There is no evidence for the minimum near 40° reported by Glasel,² an observation that can be directly related to the difference in the two sets of experimental data. The trend toward a lower quadrupole coupling constant with increasing temperature is unexpected. We have no immediate explanation for this result (but see later text).

A similar inspection of eq 5 and 6 reveals that there will be no apparent temperature coefficient for the deuteron quadrupole coupling constant if the quadrupole correlation time is derived from the dielectric data for D_2O . Powles, Rhodes, and Strange¹⁴ came to a similar conclusion with respect to the temperature invariance of the deuteron quadrupole coupling constant from calculations based on the use of correlation times obtained from proton spin-lattice relaxation measurements. In fact, from the observation that the deuteron quadrupole coupling constant was calculated to be closer to the value in ice than in the gas, they concluded that the molecules in the liquid are strongly hydrogen bonded even at high temperatures. A different interpretation of the deuteron⁷ T_1 and oxygen-17³ T_2 experimental data for D_2^{17}O has been suggested by Spiess, *et al.*¹³ They start from the Debye equation^{15,16}

$$\tau_Q = \tau_c/3 = 4\pi\eta a^3/3kT \quad (10)$$

where η is the viscosity and a the molecular radius. They make the further assumption that a^3 is proportional to the molecular volume.¹⁷ They then plot $1/T_2$ vs. $\eta/\rho T$, where ρ is the density. They find a nonzero intercept for their oxygen-17 data in D_2^{17}O and indicate that this is also the case for Woessner's⁷ deuteron data in D_2O . They then suggest that these data can be fit by a curve calculated on the basis that the quadrupole coupling constants are strongly temperature dependent with ice and gas like values at the extremes. That a similar behavior is not found for the oxygen-17 in H_2^{17}O is attributed to a lower structural temperature for D_2O . Our data confirm the fact that such a plot is linear for the $0\text{--}90^\circ$ interval and gives a zero intercept for oxygen-17 in H_2^{17}O . We have replotted Woessner's⁷ data together with some deuteron relaxation data from experiments presently being carried out in this laboratory. We note (a) that the curvature in the plot of Woessner's data is opposite to that which would be expected if the interpretation of Spiess, *et al.*,¹³ were correct and (b) that within experimental error our data as well as those of Woessner⁷ yield zero intercept in the $1/T_1$ vs. $\eta/\rho T$ plot. We therefore do not consider that there is any real evidence from the presently available data for a marked temperature dependence of the deuteron quadrupole coupling constant in D_2O . On the other hand, it is obvious that different comparisons lead to conflicting views with respect to the temperature dependencies of the quadrupole coupling constants of both oxygen-17 and deuterium in water. For the oxygen-17, the linearity of the $1/T_1$ vs. $\eta/\rho T$ plot indicates that the quadrupole coupling constant is independent of temperature while the calculations based on dielectric data indicate a small temperature coefficient. Precisely the opposite conclusions would be reached from the same comparisons for the deuteron relaxation data. It is obvious that further work will be required before the situation can be clarified.

Finally, we consider the question of the physical interpretation of the equation used in the present paper for representation of the relaxation time data. We note that an explanation of the C/R term in eq 2 can be given

(9) A. Abragam, "The Principles of Nuclear Magnetism," Oxford University Press, London, 1961, p 314.

(10) H. Bluysen, J. Verhoeven, and A. Dymanus, *Phys. Lett.*, **25A**, 214 (1967).

(11) P. Waldstein, S. W. Rabideau, and J. A. Jackson, *J. Chem. Phys.*, **41**, 3407 (1964).

(12) J. Verhoeven, A. Dymanus, and H. Bluysen, *ibid.*, **50**, 3330 (1969).

(13) H. W. Spiess, B. B. Garrett, R. K. Sheline, and S. W. Rabideau *ibid.*, **51**, 1201 (1969).

(14) J. G. Powles, M. Rhodes, and J. H. Strange, *Mol. Phys.*, **11**, 515 (1966).

(15) P. Debye, "Polar Molecules," Dover Publications, New York, N. Y., 1945, Chapter V.

(16) N. Bloembergen, E. M. Purcell, and R. V. Pound, *Phys. Rev.*, **73**, 679 (1943).

(17) L. Onsager, *J. Amer. Chem. Soc.*, **58**, 1486 (1936).

in terms of a distribution of activation energies among many harmonic oscillators.⁴ The picture of liquid water behaving as a continuum of oscillators of different frequencies is in accord with the interpretation of the ir and Raman spectrum of the liquid given by Schiffer and Hornig.¹⁸ The number of oscillators is approximately⁴

$$s = (C/R + 3/2) \quad (11)$$

A consideration of the numerical results indicates that the explanation in terms of numbers of oscillators in the present case is questionable. For example, it is noted that the Δc_p^\ddagger term, which is presumed to be related to the number of oscillators, is considerably larger for processes involving relaxation in D_2O than in H_2O . This is contrary to what we expect from the observation that the half-width of the coupled or uncoupled OH stretching band, which represents the range of frequencies available to an OH group subject to the interactions present in the liquid, is considerably greater than the half-width of the coupled or uncoupled OD stretching band.¹⁹

There is an additional observation that suggests eq 1 may be simply an empirical equation suitable for representing the experimental data over a limited temperature range. For example, application of eq 5 to calculate deuteron T_1 values at higher temperatures ($> 100^\circ$) reveals an increasingly non-Arrhenius temperature behavior. This is contrary to the experimental observations.¹⁴ In order to reproduce the experimental

behavior in this case it would be necessary to add additional terms to eq 1, *i.e.*, to allow Δc_p^\ddagger to vary with temperature.

The preceding discussion indicates that we should consider the representation of the data by equations based on other physically plausible relaxation mechanisms. One possibility, suggested by the fact that the calculated values for the deuteron quadrupole coupling constant in liquid water indicate that the relaxing water molecules are hydrogen-bonded^{4,7} rather than unbonded monomeric species²⁰ and by the general shape of relaxation time *vs.* $1/T$ plots, is that we have two relaxation processes, a rotational diffusion process dominant at high temperatures and a hydrogen-bond breaking process important at low temperatures. We find, however, that even in this simple case the resulting equation for the temperature dependence of the relaxation time involves the sum of two exponentials. With an extra adjustable parameter, the data can, of course, be fitted. It is obvious, however, that if we are to make an adequate test of this or other possible relaxation processes it will be necessary to have more precise experimental data than are presently available over a wide temperature range. We are at present engaged in making such measurements for the deuteron relaxation in D_2O .

(18) J. Schiffer and D. F. Hornig, *J. Chem. Phys.*, **49**, 4150 (1968).

(19) T. T. Wall and D. F. Hornig, *ibid.*, **43**, 2079 (1965).

(20) J. C. Hindman, A. Svirnickas, and M. Wood, *J. Phys. Chem.*, **72**, 4188 (1968).

Dielectric Studies. XXVII. Relaxation Processes of

Pyrrrole-Pyridine and Chloroform-Pyridine Systems

by S. W. Tucker

University of Aston, Birmingham, England

and S. Walker

Chemistry Department, Lakehead University, Port Arthur, Ontario, Canada (Received October 2, 1969)

Dielectric absorption measurements have been made on ternary solutions of pyrrole, pyridine, and cyclohexane and the relaxation time of the hydrogen-bonded complex deduced. A similar study has been made of a pyridine, chloroform, and cyclohexane system. By comparison of the relaxation time of the complex with that of a molecule of similar size and shape, it is shown that the pyrrole-pyridine and chloroform-pyridine systems each form 1:1 complexes where the hydrogen bonding is of the type $\text{NH}\cdots\text{H}$ and $\text{CH}\cdots\text{N}$, respectively. This dielectric approach yields information as to both size and shape of small complexed species in solution.

Introduction

The formation of hydrogen bonds between two polar solute molecules in a nonpolar solvent has been studied by a number of techniques.¹ Perhaps the most fruitful measurements have been made using nmr and ir approaches. These methods detect hydrogen bond formation and, in some cases, yield the association constant. They do not, however, yield direct information as to the size and shape of the complex. It was our aim to examine the feasibility of determining the relaxation time of a polar complex in equilibrium with its two polar components in a nonpolar solvent and from that to deduce information as to the size and shape of the complex by comparison of its value with that of a rigid molecule of similar size and shape.

Two approaches will be taken to determine the relaxation time of the complex: (i) that for the pyrrole-pyridine system where a literature association constant for 1:1 complex formation will be assumed and (ii) that for the pyridine-chloroform system where the relaxation time will be deduced solely from dielectric data. Thus procedure (ii) is an independent evaluation of the complex size and shape, whereas that of (i) is dependent on that of another method in that the type of complex formed (*e.g.*, a 1:1) is assumed. However, method (i) (and also ii) not only yields a check on the type of complex formed but may give specific information regarding its shape. For example, the relaxation time of a 1:1 complex of pyridine and pyrrole would be very dependent as to whether the hydrogen of the NH group of the pyrrole hydrogen bonded to the π -electrons of the pyridine along the six-fold axis or whether it formed a linear hydrogen bond of the type $\text{NH}\cdots\text{N}$. Thus the relaxation time approach differs from that of nmr and ir techniques in that it can sometimes yield direct information on both size and shape of small complexed species.

Experimental Section

The apparatus and procedure for determining the dielectric constant and loss have been previously described.²

Materials. Pyridine was purified by drying initially with potassium hydroxide and then phosphorus pentoxide. The pyridine was then distilled from a spinning band column of about thirty theoretical plates and then stored over phosphorus pentoxide.

Chloroform was purified by washing with sulfuric acid and distilled water. This was followed by washing with sodium hydroxide solution. It was then shaken six times with distilled water and dried over calcium chloride before being distilled from phosphorus pentoxide.

Pyrrole was dried over potassium hydroxide pellets before distillation. Samples of each were analyzed by infrared and gas chromatography techniques to check purity and dryness.

Results

The dielectric absorption of dilute solutions of pyrrole and pyridine in cyclohexane at 15, 25, 35, and 50° were measured at 9.313, 16.20, 23.98, 34.86, and 70.0 GHz. In addition, the static dielectric constant at 2 MHz for each solution was determined. The data for these solutions were treated in the usual manner³ and the results are given in Tables I and II.

Ternary solutions of pyrrole and pyridine in different mole fraction ratios in cyclohexane at 25° and in a 1:1 mole fraction ratio at 15, 35, and 50° were also measured.

(1) G. C. Pimentel and A. L. McClellan, "The Hydrogen Bond," W. H. Freeman and Co., San Francisco, Calif., 1960.

(2) W. F. Hassell, M. D. Magee, S. W. Tucker, and S. Walker, *Tetrahedron*, **20**, 2137 (1964).

(3) M. D. Magee and S. Walker, *Trans. Faraday Soc.*, **62**, 3093 (1966).

Table I: Dielectric Constant and Loss Data for Solutions of Pyrrole and Pyridine in Cyclohexane at Specified Weight Fractions w_2

Frequency, GHz	ϵ'	ϵ''
Pyrrole at 15° ($w_2 = 0.05738$)		
9.313	2.216	0.0443
16.20	2.204	0.0563
23.98	2.175	0.0663
34.86	2.161	0.0693
70.0	2.118	0.0651
Pyrrole at 25° ($w_2 = 0.06959$)		
9.313	2.251	0.0471
16.20	2.229	0.0668
23.98	2.197	0.0771
34.86	2.179	0.0805
70.0	2.130	0.0905
Pyrrole at 35° ($w_2 = 0.05387$)		
9.313	2.179	0.0309
16.20	2.168	0.0413
23.98	2.154	0.0584
34.86	2.143	0.0651
70.0	2.096	0.0678
Pyrrole at 50° ($w_2 = 0.06083$)		
9.313	2.170	0.0255
16.20	2.160	0.0358
23.98	2.145	0.0476
34.86	2.133	0.0547
70.0	2.095	0.0682
Pyridine at 15° ($w_2 = 0.03355$)		
9.313	2.221	0.0365
16.20	2.209	0.0554
23.98	2.194	0.0738
34.86	2.170	0.0815
70.0	2.092	0.0853
Pyridine at 35° ($w_2 = 0.03355$)		
9.313	2.173	0.0263
16.20	2.163	0.0435
23.98	2.148	0.0597
34.86	2.125	0.0675
70.0	2.071	0.0748
Pyridine at 50° ($w_2 = 0.03355$)		
9.313	2.139	0.0226
34.86	2.106	0.0587
70.0	2.055	0.0750

The experimental data did not give a Cole-Cole⁴ semicircle, but a flattened plot for which ϵ_∞ , the high-frequency dielectric constant, could not be determined by the usual procedure.

Budó⁵ has considered the complex dielectric constant to be the sum of Debye terms arising from discrete relaxation processes. For the pyrrole-pyridine system, three relaxation processes would be expected corresponding to the free pyrrole (τ_2), free pyridine (τ_3), and the pyrrole-pyridine complex (τ_1), each process having the weight factors C_1 , C_2 , C_3 , respectively, where

$$C_1 + C_2 + C_3 = 1$$

Then

$$\frac{\epsilon' - \epsilon_\infty}{\epsilon_0 - \epsilon_\infty} = \frac{C_1}{1 + \omega^2\tau_1^2} + \frac{C_2}{1 + \omega^2\tau_2^2} + \frac{C_3}{1 + \omega^2\tau_3^2} = \eta'$$

and

$$\frac{\epsilon''}{\epsilon_0 - \epsilon_\infty} = \frac{C_1\omega\tau_1}{1 + \omega^2\tau_1^2} + \frac{C_2\omega\tau_2}{1 + \omega^2\tau_2^2} + \frac{C_3\omega\tau_3}{1 + \omega^2\tau_3^2} = \eta''$$

where the symbols have their usual meaning. Providing that τ_1 , τ_2 , and τ_3 are of similar magnitude, a plot of η' against η'' will approximate to a semicircle, but when the ratio of any two relaxation times is large, and their weight factors significant, the beginning of the separation into two distinct dispersion regions becomes apparent. In the pyrrole-pyridine system at 25°, $\tau_2 \sim \tau_3 \sim 2.5 \times 10^{-12}$ sec for the noncomplexed molecules in cyclohexane solution.

Discussion

Previous polarization studies of the system by Gomel and Lumbroso⁶ have determined the dipole moment of the pyrrole-pyridine complex to be 4.05 D, which is slightly larger than the sum of the parent molecules, 3.93 D. Happe⁷ has calculated the association constant of the system in cyclohexane at different temperatures from nmr measurements, and his results have been used to interpolate the association constants at the temperatures used in the present work.

If a and b are the initial mole fractions of pyrrole and pyridine, respectively, in the ternary solutions, and the mole fraction of this 1:1 complex⁷ formed is m , the association constant K will be given by

$$K = \frac{m}{(a - m)(b - m)}$$

Thus, by using Happe's association constant, m may be calculated for each solution.

By using the literature value for the dipole moment of the complex (μ_c), the dispersion of the complex (D_c) may be deduced from the Debye equation

$$\mu^2 = \frac{9kTM}{4\pi Nd} \left(\frac{\epsilon_0 - 1}{\epsilon_0 + 2} - \frac{\epsilon_\infty - 1}{\epsilon_\infty + 2} \right)$$

to be

$$D_c = \frac{\mu_c^2 4\pi N(\epsilon_1 + 2)^2 m d_1}{27kTM_1}$$

where M_1 , ϵ_1 , and d_1 are the molecular weight, static dielectric constant, and density of the solvent, respec-

(4) K. S. Cole and R. H. Cole, *J. Chem. Phys.*, **9**, 341 (1941).

(5) A. Budó, *Phys. Z.*, **39**, 706 (1948).

(6) M. Gomel and H. Lumbroso, *Compt. Rend.*, **252**, 3039 (1961).

(7) J. Happe, *J. Phys. Chem.*, **65**, 72 (1961).

Table II: Dipole Moments (μ), Dielectric Constant at Infinite Frequency (ϵ_∞), Static Dielectric Constant (ϵ_0), Distribution Parameter (α), and Mean Relaxation Time (τ_0) for Specified Weight Fractions (w_2) of Pyrrole and Pyridine in Cyclohexane

Solute	w_2	$T, ^\circ\text{C}$	$\tau_0 \times 10^{11}$	μ	α	ϵ_0	ϵ_∞
Pyrrole	0.05738	15	2.6	1.70	0.25	2.239	2.007
	0.06959	25	2.5	1.70	0.22	2.269	2.012
	0.05387	35	2.4	1.70	0.18	2.195	1.999
	0.06083	50	1.9	1.70	0.16	2.178	1.984
Pyridine	0.03355	15	3.0	2.23	0.06	2.231	2.032
	0.03355	35	2.5	2.23	0.05	2.180	2.001
	0.03355	50	2.2	2.23	0.03	2.141	1.973

Table III: Interpolated Equilibrium Constant (K), Calculated Dispersions, and Relaxation Time (τ_1) of Complex for the Pyrrole-Pyridine System in Cyclohexane

Solution	Initial mole fraction pyrrole a	Initial mole fraction pyridine b	$T, ^\circ\text{C}$	K	Mole fraction complex m	Dispersion complex D_c	Dispersion pyrrole D_P	Dispersion pyridine D_{PY}	$\tau_1 \times 10^{11}$
A	0.02352	0.02333	25	27.5	0.00724	0.120	0.048	0.081	~25
B	0.01764	0.02582	25	27.5	0.00609	0.101	0.034	0.099	~21
C	0.01532	0.03119	25	27.5	0.00635	0.106	0.026	0.125	~22
D	0.03468	0.01711	25	27.5	0.00735	0.122	0.080	0.049	~23
E	0.02320	0.02297	15	35.3	0.00800	0.140	0.047	0.080	~35
F	0.02329	0.02375	25	21.7	0.00647	0.102	0.048	0.080	~20
G	0.02308	0.02315	50	15.9	0.00513	0.075	0.046	0.079	~14

tively, since for dilute solutions $\epsilon_0 \sim \epsilon_\infty \sim \epsilon_1$ and $\epsilon_0 - \epsilon_\infty$ is the dispersion of the complex.

The dispersion of the free pyrrole D_P and free pyridine D_{PY} may be calculated using the same equation with the appropriate values for the dipole moments and mole fractions. The total dispersion D_T will then be given by

$$D_T = D_c + D_P + D_{PY}$$

and ϵ_∞ for the solution may be calculated from

$$\epsilon_\infty = \epsilon_0 - D_T$$

where ϵ_0 is the measured static dielectric constant for the solution. The dispersions of the pyrrole-pyridine system are given in Table III.

The ϵ'' vs. ϵ' plot is given in Figure 1 for one of the pyrrole-pyridine systems; the outer envelope embodies the experimental curve. The dispersions for the pyrrole, pyridine, and the complex are PQ, QR, and RS, respectively, and the distribution coefficients of the pyridine and pyrrole are taken into account in the corresponding Cole-Cole semicircles. The complex is assumed to have a zero distribution coefficient which would normally be the case for a species of such a size. The data for these ternary solutions are given in Table IV and those for the pyridine-chloroform-cyclohexane systems in Table V.

For dilute solutions of polar molecules, dielectric loss at each wavelength is proportional to the mole fraction. Thus, from measurements at one or more

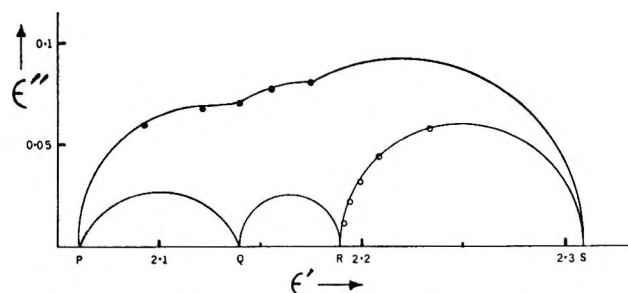


Figure 1. The ϵ'' vs. ϵ' plot for a pyrrole ($m = 0.03468$)-pyridine ($m = 0.01711$) mixture in the solvent cyclohexane at 25° where m is the initial mole fraction of the polar component. The dispersions for the pyrrole, pyridine, and the complex are PQ, QR, and RS, respectively.

concentrations, the loss at each waveband of the free pyrrole ϵ_P'' and free pyridine ϵ_{PY}'' may be estimated. The loss of the complex ϵ_c'' is given by

$$\epsilon_c'' = \epsilon_{\text{meas}}'' - (\epsilon_P'' + \epsilon_{PY}'')$$

These calculated ϵ_c'' values have been inserted on the absorption curve for the complex in Figure 1 taking into account that the higher the frequency the closer the point will lie to the ϵ_∞ value. The relaxation time (τ_1) of the complex has then been deduced from this curve by employing the equation

$$v/u = \omega\tau_1$$

where v is the chord on this curve between the estimated loss point and ϵ_0 , and u is the distance from the calcu-

Table IV: Measured Dielectric Constant and Loss Data, ϵ_{meas}' and ϵ_{meas}'' and the Calculated Loss of the Free Pyrrole and Pyridine $\epsilon_p'' + \epsilon_{\text{py}}''$ and Complex ϵ_c'' for the Pyrrole-Pyridine System in Cyclohexane^a

Solu- tion	Frequency, GHz	ϵ_{meas}'	ϵ_{meas}''	$\epsilon_p'' + \epsilon_{\text{py}}''$	ϵ_c''
A	9.313	2.179	0.0782	0.020	0.058
	16.20	2.161	0.0749	0.034	0.041
	23.98	2.147	0.0708	0.041	0.030
	34.86	2.129	0.0686	0.049	0.020
	70.0	2.081	0.0618	0.052	0.010
	(2KHz)	2.3132			
B	9.313	2.179	0.0698	0.021	0.050
	16.20	2.162	0.0691	0.034	0.035
	23.98	2.139	0.0674	0.042	0.025
	34.86	2.128	0.0672	0.052	0.015
	70.0	2.095	0.0620	0.054	0.008
	(2KHz)	2.2891			
C	9.313	2.202	0.0772	0.023	0.054
	16.20	2.180	0.0769	0.039	0.038
	23.98	2.153	0.0755	0.049	0.027
	34.86	2.134	0.0682	0.060	0.010
	70.01	2.095	0.065	0.063	0.002
	(2KHz)	2.2994			
D	9.313	2.179	0.0779	0.020	0.058
	16.20	2.160	0.0750	0.041	0.034
	23.98	2.141	0.0685	0.044	0.025
	34.86	2.124	0.0657	0.046	0.020
	70.0	2.100	0.060	0.050	0.010
	(2KHz)	2.3114			
E	9.313	2.179	0.079	0.024	0.055
	16.20	2.161	0.0759	0.034	0.042
	23.98	2.147	0.070	0.043	0.027
	34.86	2.129	0.065	0.047	0.018
	70.0	2.081	0.0566	0.049	0.008
	(2KHz)	2.3509			
F	9.313	2.170	0.0746	0.021	0.053
	16.20	2.152	0.0737	0.034	0.040
	23.98	2.123	0.0689	0.043	0.026
	34.86	2.116	0.0679	0.050	0.018
	70.0	2.064	0.0586	0.054	0.005
	(2KHz)	2.2749			
G	9.313	2.149	0.0641	0.026	0.038
	16.20	2.123	0.0673	0.032	0.035
	23.98	2.109	0.0644	0.035	0.029
	34.86	2.082	0.0605	0.043	0.017
	70.0	2.054	0.0627	0.052	0.011
	(2KHz)	2.2187			

^a The lettering characterizing the solution is that employed in Table III.

lated high-frequency dielectric constant for the complex and the same loss point.

The τ_1 values for the complex for the four solutions at 25° (see Table III) are in good agreement and the trend of decreasing relaxation time with increase in temperature can be seen.

The relaxation time of the complex of $\sim 23 \times 10^{-12}$ sec $\pm 20\%$ (Table III) may be compared with that of the molecular relaxation time of *p*-phenylphenol in benzene⁸ which has a value of 23×10^{-12} sec at 25°

Table V: Dielectric Constant and Loss Data for Ternary Solutions of Pyridine and Chloroform at 25° at Specified Mole Fractions *a* and *b*, Respectively, in Cyclohexane

Frequency, GHz	ϵ_{meas}'	ϵ_{meas}''	ϵ_{calcd}'	$\epsilon_{\text{calcd}}''$
$a = 0.01751, b = 0.02779$				
9.313	2.141	0.0352	2.13	0.035
16.20	2.134	0.0438	2.12	0.041
23.98	2.118	0.0476	2.11	0.048
34.86	2.105	0.0535	2.10	0.055
70.0	2.062	0.0519	2.06	0.055
$a = 0.02687, b = 0.01203$				
9.313	2.167	0.0360	2.16	0.036
16.20	2.161	0.0469	2.15	0.046
23.98	2.147	0.0548	2.14	0.056
34.86	2.130	0.0634	2.12	0.066
70.0	2.072	0.0655	2.07	0.070
$a = 0.01294, b = 0.01740$				
9.313	2.107	0.0238	2.10	0.022
16.20	2.101	0.0287	2.09	0.028
23.98	2.092	0.0322	2.09	0.034
34.86	2.081	0.0360	2.08	0.039
70.0	2.061	0.0384	2.05	0.040
$a = 0.01268, b = 0.03365$				
9.313	2.125	0.0288	2.12	0.030
16.20	2.120	0.0375	2.11	0.036
23.98	2.110	0.0421	2.10	0.042
34.86	2.100	0.0471	2.09	0.049
70.0	2.072	0.0490	2.06	0.050

which is a molecule fairly similar in size to a 1:1 complex of pyrrole and pyridine where the $\text{NH} \cdots \text{N}$ is linear. Thus these relaxation time values establish both the size and shape of the complexed species and are in agreement with the 1:1 type of complex favored by Gomel and Lumbroso⁶ and also by Happe.⁷

Four solutions each having a different mole fraction ratio of pyridine to chloroform were studied in cyclohexane at 25°. The Cole-Cole plots approximated to semicircles, and so the high-frequency dielectric constant ϵ_{∞} could be determined by computer analysis. Pyridine in various solvents has been previously examined by Hassell.⁹

For Debye behavior the plot of ϵ' vs. $\epsilon''\omega^{10}$ is a straight line of slope $-\tau$, but for two relaxation times, sufficiently distinct in magnitude, a curve results. The extremes of slope then give an estimate of τ_1 and τ_2 , but the steeper slope gives a value less than the true τ_1 and the lesser slope is greater than τ_2 . The present results showed two slopes, yielding relaxation times

(8) F. K. Fong and C. P. Smyth, *J. Amer. Chem. Soc.*, **85**, 1565 (1963).

(9) W. F. Hassell, Ph.D. Thesis, University of Aston in Birmingham, 1966.

(10) W. P. Purcell, K. Fish, and C. P. Smyth, *J. Amer. Chem. Soc.*, **82**, 6299 (1960).

Table VI: Static Dielectric Constant, High-Frequency Dielectric Constant, Relaxation Times,^a Distribution Coefficient, and Weight Factor Data for Various Mole Fractions of the Pyridine–Chloroform System in Cyclohexane at 25°

Solution	Initial mole fraction pyridine	Initial mole fraction chloroform	τ_0	τ_{init}	τ_{sec}	τ_1	τ_2	C_1	α	ϵ_0	ϵ_∞
A	0.01751	0.02779	3.8	12	3.4	29	2.9	0.27	0.18	2.1650	2.018
B	0.02687	0.01203	3.2	10	3.4	30	2.8	0.19	0.17	2.1890	2.018
C	0.01294	0.01740	3.3	8.5	2.6	27	2.9	0.20	0.18	2.1176	2.018
D	0.01268	0.03365	3.6	9.5	3.3	30	2.9	0.25	0.19	2.1487	2.020

^a The relaxation time values have been multiplied by 10^{12} .

which are referred to as τ_{init} and τ_{sec} and the results are given in Table VI, where τ_{init} provides a lower limit for the relaxation time of the complex (τ_1). Pyridine has a τ_0 (mean relaxation time) of 2.7×10^{-12} sec in cyclohexane at 25°, and for chloroform in cyclohexane the value is $\sim 3.5 \times 10^{-12}$ sec (literature values ranging from 3.2 to 4.1×10^{-12} sec) and the distribution coefficient, zero. Thus, it was thought feasible to analyze the results in Table V into two relaxation times,³ the shorter one (τ_2) being taken as a composite relaxation time of uncomplexed chloroform and pyridine. The τ_{sec} value would thus be an upper limit for the τ_2 value. The τ_2 value obtained from the analysis of 2.9×10^{-12} sec may be compared with $\tau_{\text{sec}} \sim 3.3 \times 10^{-12}$ sec and lies between that for the molecular relaxation of chloroform and pyridine. The mean relaxation time (τ_0) values are not appreciably longer

than the τ_2 values, indicating that the weight factor for the τ_2 process is much larger than that for the complex itself. These relaxation time values are given in Table VI.

The relaxation time of benzotrichloride in cyclohexane at 25° is 23.5×10^{-12} sec.¹¹ A 1:1 complex of chloroform–pyridine complex with the $\text{N} \cdots \text{H}-\text{C}$ linear would be slightly longer and would be expected to have a longer relaxation time. The τ_1 value of $\sim 30 \times 10^{-12}$ sec obtained from the analysis would seem reasonable for reorientation of such a complex and may be compared with the molecular relaxation times of 33×10^{-12} sec for phenyltrimethylsilane in cyclohexane at 25°.¹¹ Thus, this approach indicates the formation of a 1:1 complex and also identifies its shape.

(11) J. Crossley and S. Walker, *Can. J. Chem.*, **46**, 841 (1968).

Dielectric and Thermodynamic Behavior of the System

1,1,1-Trichloroethane-Benzene-*o*-Dichlorobenzene^{1,2}

by E. M. Turner, D. W. Anderson, L. A. Reich, and W. E. Vaughan

Department of Chemistry, University of Wisconsin, Madison, Wisconsin 53706 (Received September 6, 1969)

Measurements of the dielectric permittivity and loss at 20° at various wavelengths in the microwave region are reported for mixtures containing 1,1,1-trichloroethane, benzene, and *o*-dichlorobenzene. These data are fitted to a microscopic molecular model which assumes that the dielectric behavior is a superposition of Debye processes. The model parameters are interpreted in terms of molecular and liquid structure. The effect of long range dipole-dipole forces on the static and dynamic dielectric behavior is considered in light of existing theories of the internal field. Boiling point diagrams and heats of mixing are reported for this system in order to check for the existence of strong specific short range forces.

Introduction

Measurements of the dielectric permittivity and loss at a few wavelengths in the microwave region have been reported for an assortment of normal polar binary liquid mixtures.³ These data are consistent with dielectric relaxation by a superposition of two exponential decay processes. Such behavior would be expected for these systems if the Onsager model applies to the dynamic dielectric properties. Model calculations using the Onsager model have been carried out^{4,5} and the data of Kilp, Garg, and Smyth have provided support for the validity of the calculations.⁶ The mixtures were chosen to have widely separated decay times for the individual components. This work reports an investigation of a single binary polar mixture (with nonpolar diluent) at 20° using a large number of wavelengths and concentrations to see if the Onsager model calculations remain valid as the decay times for the individual components approach each other. Boiling point diagrams and heats of mixing were determined to check for the existence of strong intermolecular association, which would invalidate the use of the Onsager model.

Experimental Section

Purification of Materials. 1,1,1-Trichloroethane (TCE) was obtained from the Aldrich Chemical Company and was purified by fractional distillation. *o*-Dichlorobenzene (DCB) was obtained from Eastman Organic Chemicals and was purified by fractional distillation. Benzene was taken from laboratory stock, and was dried over anhydrous calcium sulfate. Boiling points and refractive indices agreed with values found in the literature.

Dielectric Measurements. Static dielectric permittivities were determined by the heterodyne beat technique at a frequency of 2 MHz.⁷ Measurements of dielectric permittivity and loss at wavelengths of 7.5 and 15 cm were made by the "breadth-

of-the-minimum" techniques, using a coaxial transmission line.⁷ Centimeter wavelength determinations of the dielectric permittivity and loss were made with apparatus described previously.^{7,8} Measurements of dielectric permittivity and loss at a wavelength of 2 mm were made by a free-space oblique incidence interferometric technique.^{7,9} Values of the permittivity and loss, solution compositions, and exact wavelengths used are shown in Table I.

Thermodynamic Measurements. Boiling point diagrams at atmospheric pressure (740 mm) for the binary mixtures benzene-1,1,1-trichloroethane, *o*-dichlorobenzene-benzene, and *o*-dichlorobenzene-1,1,1-trichloroethane were determined using apparatus described in the literature.¹⁰ Liquid and vapor (distillate) compositions were found from refractive index measurements using working curves generated from measurements on solutions of known composition. Enthalpies of mixing at room temperature were determined for the three binary mixtures above using a calorimeter

(1) This work was supported by the National Science Foundation and by the Wisconsin Alumni Research Foundation through the University Research Committee.

(2) This work was presented at the Symposium on Dielectric Properties honoring Professor Charles P. Smyth at the 158th National Meeting of the American Chemical Society, New York, N. Y., Sept 8, 1969.

(3) H. Kilp, S. K. Garg, and C. P. Smyth, *J. Chem. Phys.*, **45**, 2799 (1966).

(4) R. H. Cole, *ibid.*, **42**, 637 (1965).

(5) D. D. Klug, D. E. Kranbuehl, and W. E. Vaughan, *ibid.*, **50**, 3904 (1969).

(6) D. E. Kranbuehl, D. D. Klug, and W. E. Vaughan, *ibid.*, **50**, 5266 (1969).

(7) N. Hill, W. E. Vaughan, A. H. Price, and M. Davies, "Dielectric Properties and Molecular Behaviour," Van Nostrand Reinhold Company, London, 1969.

(8) J. D. Cutnell, D. E. Kranbuehl, E. M. Turner, and W. E. Vaughan, *Rev. Sci. Instrum.*, **40**, 908 (1969).

(9) W. E. Vaughan, W. S. Lovell, and C. P. Smyth, *J. Chem. Phys.*, **36**, 535 (1962).

(10) F. Daniels, J. W. Williams, P. Bender, R. A. Alberty, and C. D. Cornwell, "Experimental Physical Chemistry," 6th ed, McGraw-Hill, New York, N. Y., 1962.

Table I: Dielectric Permittivities, Losses, Wavelengths, Mixture Compositions^a

TCE	Mole fraction		Wavelengths, cm												
	Benzene	DCB	5893 (Å)	0.2174	1.2602	1.4010	1.7000	1.9440	2.4385	2.6187	2.9058	7.50	15.00	14990	
1.00	0	0	2.067	2.525	5.183	5.329	5.820	6.154	6.391	6.480	6.581	7.228	
			...	0.884	2.378	2.355	2.412	2.129	2.048	1.719	1.766	
0.75	0.25	0	2.100	2.396	4.459	4.532	4.769	5.137	5.159	5.219	5.296	5.670	
			...	0.578	1.612	1.534	1.494	1.352	1.321	1.117	1.051	
0.50	0.50	0	2.145	2.346	3.648	3.760	3.958	4.000	4.125	4.200	4.205	4.37	...	4.391	
			...	0.414	0.957	0.943	0.896	0.797	0.803	0.679	0.626	0.33	
0.25	0.75	0	2.192	2.339	2.968	3.028	3.106	3.129	3.231	3.288	
			...	0.247	0.453	0.425	0.387	0.366	0.256	
0	0	1.000	2.408	2.576	3.264	3.537	3.735	3.953	4.532	4.413	5.066	10.573	
			...	0.435	1.910	2.056	2.495	2.708	3.176	3.448	3.428	
0	0.25	0.75	2.367	2.533	3.262	3.334	3.698	3.800	4.560	4.581	4.673	7.20	...	8.205	
			...	0.359	1.674	1.806	2.073	2.204	2.418	2.704	2.574	1.15	
0	0.50	0.50	2.332	2.425	3.078	3.178	3.472	3.590	4.186	4.125	4.240	5.88	...	6.364	
			...	0.294	1.285	1.345	1.522	1.630	1.793	1.785	1.742	0.93	
0	0.75	0.25	2.290	2.274	2.777	2.852	2.985	3.097	3.343	3.327	3.451	4.27	...	4.245	
			...	0.191	0.727	0.770	0.808	0.882	0.978	0.900	0.884	0.66	
0.25	0	0.75	2.329	2.529	3.692	3.755	4.203	4.356	5.066	5.049	5.375	...	9.01	9.619	
			...	0.519	2.040	2.226	2.609	2.718	3.083	3.069	3.163	...	0.98	...	
0.50	0	0.50	2.246	2.519	4.044	4.170	4.717	4.939	5.549	5.848	6.208	8.29	8.90	8.888	
			...	0.531	2.212	2.335	2.641	2.705	3.031	3.059	2.992	1.32	1.08	...	
0.75	0	0.25	2.166	2.510	4.594	4.677	5.263	5.488	6.046	6.417	6.727	7.83	8.16	8.185	
			...	0.765	2.292	2.351	2.620	2.463	2.677	2.546	2.382	1.14	0.80	...	
0.33	0.33	0.33	2.245	2.424	3.606	3.725	4.188	4.279	4.861	4.834	4.948	6.15	6.52	6.415	
			...	0.462	1.525	1.588	1.729	1.747	1.867	1.745	1.698	0.87	0.71	...	
0.25	0.25	0.50	2.286	2.488	3.548	3.410	4.147	4.260	4.892	4.999	5.191	7.366	
			...	0.462	1.708	1.755	2.036	2.109	2.358	2.305	2.247	
0.50	0.25	0.25	2.204	2.447	3.942	4.020	4.574	4.658	5.304	5.390	5.468	6.46	6.68	6.620	
			...	0.534	1.663	1.796	1.873	1.815	1.956	1.818	1.701	0.89	0.65	...	
0.25	0.50	0.25	2.245	2.369	3.277	3.398	3.756	3.731	4.055	4.243	4.242	5.06	5.26	5.308	
			...	0.364	1.101	1.124	1.176	1.206	1.392	1.220	1.203	0.73	0.50	...	

^a The upper numbers are the dielectric permittivities and the lower numbers the losses. Reported permittivities are accurate to $\pm 1\%$ except at 2 mm, 7.5 cm, and 15 cm wavelengths where the accuracy is $\pm 3\%$. Losses are accurate to $\pm 1\%$ except at 2 mm ($\pm 5\%$) and at 7.5 cm and 15 cm where the accuracy is $\pm 5\%$ and deteriorates further as the loss exceeds unity. All measurements at 20°.

described in the literature.¹⁰ The temperature changes following stepwise addition of one component were measured. The heat capacity of the calorimeter was determined by measuring the temperature change produced by known amounts of electrical work.

Discussion

Low Frequency Dielectric Permittivities. Dipole moments were computed from the measurements at 2 MHz for each of the binary mixtures with benzene using the Onsager equation for mixtures.¹¹ θ_i is the volume fraction, μ_i is the dipole moment, N_i is the

$$\sum_i \theta_i \frac{(\epsilon_0 - \epsilon_{\infty i})}{(2\epsilon_0 + \epsilon_{\infty i})} = \sum_i \frac{\epsilon_0(\epsilon_{\infty i} + 2)^2}{3(2\epsilon_0 + \epsilon_{\infty i})^2} \frac{4\pi N_i \mu_i^2}{3kT} \quad (1)$$

number of molecules per unit volume, and $\epsilon_{\infty i}$ is the high frequency dielectric permittivity for each species. This last quantity may be obtained from fitting the pure polar liquid dispersion measurements to the Debye equation, or n_D^2 may be used as an estimate. The calculated dipole moments are shown in Table II.

Table II: Calculated Dipole Moments

TCE	Mole fraction		μ, D	
	Benzene	DCB	Using ϵ_{∞}	Using n_D^2
1.00	0	0	1.73	1.86
0.75	0.25	0	1.66	1.78
0.50	0.50	0	1.62	1.74
0.25	0.75	0	1.63	1.73
0	0	1.00	2.05	2.25
0	0.25	0.75	1.98	2.17
0	0.50	0.50	2.01	2.19
0	0.75	0.25	2.01	2.18

The calculated dipole moments do not vary appreciably with concentration, which supports the use of the Onsager model for describing the static dielectric behavior. The values obtained for the dipole moments depend on the estimates of distortion polarization. Use of n_D^2 for $\epsilon_{\infty i}$ instead of the limiting microwave permittivity at high frequency (ϵ_{∞}) corresponds to a partial neglect of atomic polarization and a larger

(11) L. Onsager, *J. Amer. Chem. Soc.*, **58**, 1486 (1936).

Table III: Calculated Static Permittivities

Mole fraction			ϵ_0		
TCE	Benzene	DCB	Using n_D^2	Using ϵ_∞	Exptl
0.25	0	0.75	9.15	9.27	9.62
0.50	0	0.50	8.38	8.42	8.89
0.75	0	0.25	7.46	7.54	8.19
0.33	0.33	0.33	6.38	6.42	6.41
0.25	0.25	0.50	7.33	7.38	7.37
0.50	0.25	0.25	6.42	6.46	6.62
0.25	0.50	0.25	5.36	5.35	5.31

value for the dipole moment. Dipole moment values reported in the literature vary according to estimates of distortion polarization. Values in debyes for 1,1,1-trichloroethane in benzene solution are 1.5, 1.58, and 1.66 and values for *o*-dichlorobenzene range from 2.0 to 2.35.¹² The quantity of interest in this work is the ratio of dipole moments, a quantity which is less sensitive to the method of estimation of distortion polarization than the dipole moment values themselves, provided a consistent procedure is used.

The calculated dipole moments may be used in the Onsager equation for mixtures to predict the static dielectric permittivities of the mixtures with two polar components. The results are shown in Table III. The agreement with experiment is reasonable and use of ϵ_∞ for ϵ_∞ ; instead of n_D^2 (and using the corresponding dipole moment values) gives a slightly better fit.

Dynamic Dielectric Behavior. Since the polar molecules considered here approximate rigid ellipsoids with the dipole moment along a symmetry axis it is reasonable to assume that the dielectric behavior, in the absence of internal field effects, would be a superposition of Debye processes, that is^{3,6,13}

$$\mathcal{L}_{i\omega}(-\dot{\gamma}) = C_1/(1 + i\omega\tau_1) + (1 - C_1)/(1 + i\omega\tau_2) \quad (2)$$

where the left-hand side represents the Laplace transform of the negative time derivative of the microscopic correlation function. The relative magnitude of the two dispersion regions depends on the number of moles and the dipole moment of each species according to

$$C_1/(1 - C_1) = n_1\mu_1^2/n_2\mu_2^2 \quad (3)$$

Two calculations, using the Onsager model which treats the liquid outside of a spherical molecular cavity as a continuum, were used to account for the effect of the internal field and to relate the microscopic model parameters to the dielectric permittivities and losses. The equations are due to Cole⁴ (eq 4) and a revision discussed by Klug, Kranbuehl, and Vaughan^{5,14} (eq 5).

$$\mathcal{L}_{i\omega}(-\dot{\gamma}) = 3\epsilon_0(\epsilon^* - \epsilon_\infty)/(\epsilon_0 - \epsilon_\infty)(\epsilon^* + 2\epsilon_0) \quad (4)$$

$$\mathcal{L}_{i\omega}(-\dot{\gamma}) = \epsilon_0(\epsilon^* - \epsilon_\infty)(2\epsilon^* + \epsilon_\infty)/\epsilon^*(\epsilon_0 - \epsilon_\infty)(2\epsilon_0 + \epsilon_\infty) \quad (5)$$

Equations 4 and 2 imply that

$$\frac{\epsilon^* - \epsilon_\infty}{\epsilon_0 - \epsilon_\infty} = \frac{X_1}{1 + i\omega T_1} + \frac{1 - X_1}{1 + i\omega T_2} \quad (6)$$

The dielectric measurements were fitted to eq 5 and 6 using a least squares criterion and treating C_1 , τ_1 , τ_2 (or equivalently X_1 , T_1 , T_2) and ϵ_∞ as variable parameters. The results are shown in Table IV. C_1 equals unity if only one polar species is present in the mixture. With the Cole equation, C_1 (τ_1 and τ_2) may be calculated from X_1 , T_1 , and T_2 using equations derived by Vaughan and Provder.¹⁵ The agreement between the dielectric measurements and the back calculated curve for a typical system is shown in Figure 1.

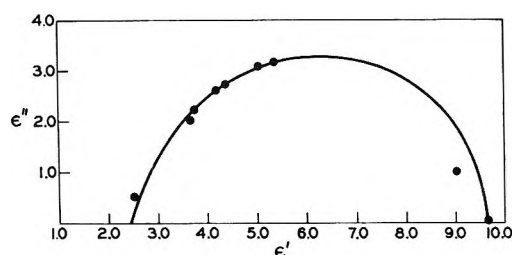


Figure 1. Cole-Cole locus of experimental measurements of the dielectric permittivity and loss at 20°. For a mixture containing 3 mol of *o*-dichlorobenzene per mole of 1,1,1-trichloroethane. The solid curve is back calculated from eq 6 using the parameters in Table IV. The dielectric loss of the coaxial point is very low compared to the back calculated value.

The decay times (T_1) found for the mixtures with a single polar component are of reasonable magnitude considering the molecular size and shape and they show realistic trends with concentration. The 1,1,1-trichloroethane molecule is very symmetrical since the methyl group approximates the chlorine in size. The relatively short decay time found is in accord with the notion that the molecule could undergo rotational diffusion without significant rearrangement of the surrounding liquid. The larger and less symmetrical *o*-dichlorobenzene molecule diffuses less easily and has a considerably longer decay time. As benzene is added to either mixture, the decay time decreases, paralleling decreases in the solution viscosity and the internal field. The difference in decay times of the two species is such that in the mixtures with two polar components the dispersion region with the shorter decay time may be assigned with confidence to the 1,1,1-trichloroethane molecule. The dielectric data for the mixtures with a single polar component were fitted to the empirical

(12) A. L. McClellan, "Tables of Experimental Dipole Moments," W. H. Freeman and Company, San Francisco, Calif., 1963.

(13) F. Perrin, *J. Phys. Radium*, **5**, 497 (1934).

(14) H. C. Bolton, *J. Chem. Phys.*, **16**, 486 (1948).

(15) W. E. Vaughan and T. Provder, *ibid.*, **44**, 1306 (1966).

Table IV: Dielectric Dispersion Parameters^a

Mole fraction			Eq 5				$\frac{n_1\mu_1^2}{n_2\mu_2^2}$	Eq 6				
TCE	Benzene	DCB	τ_1	τ_2	C_1	$C_1/(1 - C_1)$		$C_1/(1 - C_1)$	$X_1/(1 - X_1)$	X_1	T_1	T_2
0.25	0	0.75	20.0	2.6	0.84	5.3	4.4	7.1	10.4	0.91	20.5	2.6
0.50	0	0.50	14.1	2.2	0.84	5.4	1.5	7.8	11.5	0.92	14.6	2.4
0.75	0	0.25	11.1	2.3	0.74	2.6	0.5	2.9	4.5	0.82	11.3	2.6
0.33	0.33	0.33	12.8	2.7	0.74	2.9	1.5	3.1	4.6	0.82	13.2	3.0
0.25	0.25	0.50	14.4	2.2	0.85	5.8	2.9	8.9	12.1	0.93	15.1	2.1
0.50	0.25	0.25	10.6	2.5	0.75	3.0	0.7	3.3	5.0	0.83	10.9	2.8
0.25	0.50	0.25	14.1	3.0	0.66	2.0	1.5	1.9	2.7	0.73	14.6	3.4
1.00	0	0									5.85	
0.75	0.25	0									5.28	
0.50	0.50	0									4.92	
0.25	0.75	0									3.87	
0	0	1.00									24.8	
0	0.25	0.75									20.2	
0	0.50	0.50									16.6	
0	0.75	0.25									13.1	

^a Relaxation and decay times in units of 10^{-12} sec (psec).

Cole-Cole¹⁶ equation to see how well the assumption of a single dispersion region was met. For the TCE mixtures the distribution parameter (α) was found in each case to be 0.000 indicating no distribution of decay times. The DCB mixtures showed a very slight distribution, the average value of α being 0.03. Such values for the distribution parameter are commonly found and are not accounted for in terms of molecular model calculations although the concepts of Anderson and Ullman concerning a distribution of environments could be relevant.¹⁷

The decay time found for pure 1,1,1-trichloroethane at 20° is close to values reported by Holland, Roberts, and Smyth¹⁸ (5.5 psec) and by Poley¹⁹ (5.4 psec).

For the mixtures with two polar components, the longer decay time or the corresponding relaxation time (the relaxation time is typically about 5% smaller than the decay time¹⁵) has the magnitude expected. The thermodynamic measurements indicate that the intermolecular forces in 1,1,1-trichloroethane are similar in strength to those in benzene. It is not surprising then that the decay time for the *o*-dichlorobenzene molecule depends principally on its concentration in the mixture. One may compare decay times of 20.5 psec and 20.2 psec for the mixtures with mole fraction 0.75 DCB, decay times of 14.6 psec, 15.1 psec, and 16.6 psec for mole fraction 0.50 DCB, and decay times 11.3 psec, 10.9 psec, 14.6 psec, and 13.1 psec for mole fraction 0.25 DCB. On the other hand the shorter decay times are all anomalously short (by about a factor of two) when compared to the decay times found for the TCE-benzene mixtures. In addition the C_1 values found, from either eq 4, 5, or 6 lead to values of $C_1/(1 - C_1)$ which are larger than $n_1\mu_1^2/n_2\mu_2^2$ in every case. The fit using eq 5 is fractionally better, but neither equation gives a satisfactory result. The computer output shows that the parameters X_1 and T_2 (and consequently C_1 and τ_2) are cor-

related in such a way that if X_1 were decreased T_2 would increase, a result which seems intuitively reasonable. Thus if T_2 had a physically reasonable magnitude one could expect the C_1 values to fall into line. The least squares error surfaces found here are such that a satisfactory fit to the data is possible for a considerable range of C_1 values (provided the other parameters are allowed to adjust themselves). This inherent insensitivity is largely a consequence of the choice of a system with similar decay times (if T_1 and T_2 were identical it would be impossible to obtain X_1 (or C_1) from the dynamic dielectric behavior). Kilp, Garg, and Smyth's³ systems had more resolved dispersion regions which enabled X_1 to be determined with higher accuracy despite the use of fewer experimental data than reported here. It seems likely that the failure of the data to follow eq 3 results from experimental uncertainties. However, the possibility that eq 4 and/or 5 breaks down for overlapping dispersion regions cannot be ruled out.

Thermodynamic Behavior. The experimental and calculated boiling point diagrams are shown in Figures 2, 3, and 4. In all cases the boiling temperature-liquid composition curves agree with the ideal solution prediction within the experimental error. One would expect, therefore, the boiling temperature-vapor composition curves to agree as well to the extent that the vapor may be treated as ideal. The benzene-1,1,1-trichloroethane vapor curve agrees closely with the ideal solution-ideal gas prediction while the other two systems show some disagreement. This disagreement probably reflects shortcomings in the apparatus design.¹⁰ Even if the

(16) K. S. Cole and R. H. Cole, *J. Chem. Phys.*, **9**, 341 (1941).

(17) J. E. Anderson and R. Ullman, *ibid.*, **47**, 2178 (1967).

(18) R. S. Holland, G. N. Roberts, and C. P. Smyth, *J. Amer. Chem. Soc.*, **78**, 20 (1956).

(19) J. P. Poley, *Appl. Sci. Research*, **B4**, 337 (1955).

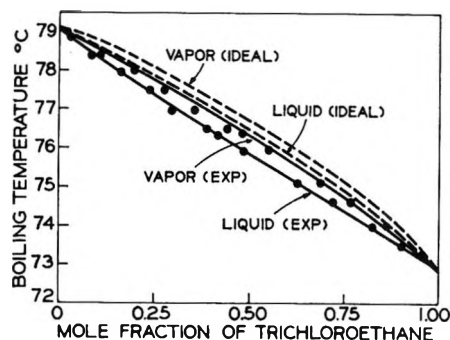


Figure 2. Boiling point diagram (740 mm), benzene-1,1,1-trichloroethane.

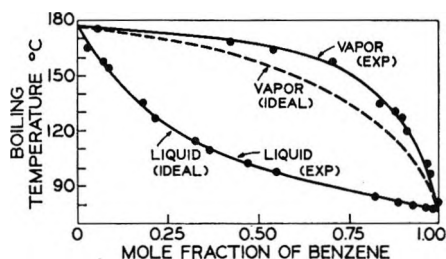


Figure 3. Boiling point diagram (740 mm), *o*-dichlorobenzene-benzene.

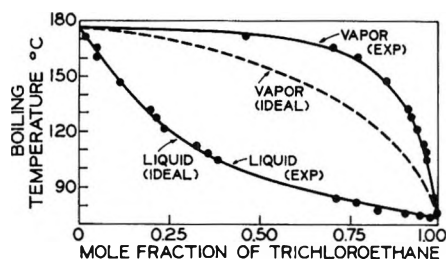


Figure 4. Boiling point diagram (740 mm), *o*-dichlorobenzene-1,1,1-trichloroethane.

apparatus were subject to systematic error in the vapor curve determination, the benzene-TCE vapor curve would agree since the closeness of the boiling points of the two components and the quasi-ideality of the solutions ensures that the vapor curves will lie close to the liquid curves which agree. It appears that the mixtures behave as nearly ideal solutions over the temperature ranges between the normal boiling points of the pure components. Nonidealities should become more pronounced as the temperature approaches that of the dielectric determinations.

For ideal solutions the enthalpy of mixing is zero. The enthalpy of mixing is a measure of deviations from ideal behavior and reflects the relative strengths of intermolecular forces between like and unlike components of the mixture. For most mixtures the pure liquids are stable with respect to the mixture and the enthalpy of mixing is positive. The observed enthalpies of mixing for the three binary mixtures along with some data from the literature are shown in Table V. The method of

Table V: Enthalpies of Mixing

Benzene(1)-1,1,1-Trichloroethane(2)		Benzene(1)-Toluene(2) ^a	
X_1	Q_P	X_1	Q_P
		0.324	61.9
0.752	10	0.490	75.3
0.694	10	0.500	71.9
0.460	50	0.600	70.3
0.415	50	0.750	56.1
0.362	40	0.857	36.0
0.299	30		
0.221	20	Benzene(1)-Carbon tetrachloride(2) ^a	
0.124	20	X_1	Q_P
		0.133	54
		0.236	72
		0.269	89
		0.364	98
		0.382	104
		0.462	106
		0.493	111
		0.499	107
		0.557	110
		0.649	106
		0.700	91
		0.744	86
		0.967	13
		Benzene(1)-Cyclohexane(2) ^a	
		X_1	Q_P
		0.097	301.3
		0.670	714.0
		0.752	606.8
		0.859	402.8
		0.924	232.3
		Carbontetrachloride(1)-Aniline(2) ^a	
		X_1	Q_P
		0.094	405
		0.185	707
		0.300	991
		0.415	1181
		0.482	1218
		0.550	1245
		0.622	1209
		0.718	1129
		0.789	1030
		0.863	787
		0.909	623

^a "International Critical Tables," McGraw-Hill Book Co., Inc., New York N. Y., 1929, Vol. V, p 154. Q_P is the heat absorbed in joules per mole of solution formed.

calculation requires that Q_P approach zero when the mole fraction of either component approaches zero. The magnitudes of Q_P are a measure of deviations from ideal solution behavior. On this basis the benzene-TCE mixture compares to the very ideal mixture benzene-toluene; the other two mixtures studied here lie

between benzene-carbon tetrachloride and benzene-cyclohexane and they are considerably more ideal than carbon tetrachloride-aniline. Even this last mixture has been considered normal as far as dielectric measurements are concerned. The principal concern is the avoidance of complex formation. This would result in a large *negative* enthalpy of mixing. The system chloroform-acetone, which shows large negative deviations from Raoult's law, has a maximum Q_P of -2000

J/mol. The small positive values for Q_P found here indicate a slight tendency for like species to cluster, a circumstance which might lead to small deviations from Debye behavior for the dispersion of the individual species in the mixture provided the clusters persisted over a time comparable to the time required for dielectric relaxation.¹⁷ This would seem unlikely, however, since the dielectric behavior of the two mixtures with benzene is Debye-like at all concentrations.

Electrophoresis of a Rod-like Polyelectrolyte in Salt Solution

by Toru Takahashi, Ichiro Noda, and Mitsuru Nagasawa

Department of Synthetic Chemistry, Faculty of Engineering, Nagoya University, Chikusa-ku, Nagoya, Japan
(Received September 2, 1969)

The electrophoretic mobilities of α -helical poly(sodium glutamate) at a degree of neutralization of 0.25 are measured in NaCl solutions of various ionic strengths. The mobilities obtained compare favorably with the theory of Henry for rigid cylinders at high ionic strengths. However, a disagreement between experimental mobilities and calculated ones is observed at low ionic strengths if the Debye-Hückel approximation is assumed in calculating the electrostatic potential at the surface of the cylinder. The agreement is improved if numerical solutions of the Poisson-Boltzmann equation are used for the comparison.

Introduction

Moving boundary electrophoresis in the Tiselius apparatus has long been employed for the characterization of biological molecules, for example, in the determination of the composition of protein mixtures, the electric charge density of a protein molecule, and the number of ions bound on a protein molecule.^{1,2} In practice, much useful information of a somewhat qualitative nature has been obtained from electrophoretic patterns. However, concerning the quantitative determination of the electric charge densities of various proteins, agreement between the theory of electrophoresis and experimental data is not very satisfactory. The charge densities calculated from electrophoretic mobilities are often lower than the values determined by other analytical methods. The disagreement is usually attributed to ion binding, but this explanation appears to be too arbitrary.²

One of the reasons for the lack of definite conclusions on the validity of electrophoresis in obtaining the charge density of biological molecules may surely be the complexity of biological systems. However, another reason may be that the assumptions involved in the theories of electrophoretic mobility of a rigid sphere or a rigid cylinder have not yet been fully examined by experiments in well defined systems.

The purpose of the present paper is to determine the electrophoretic mobility of helical poly(sodium glutamate) in sodium chloride solutions of various concentration and to compare the observed mobilities with the values calculated from the theories of Henry³ and Gorin¹ for rod-like molecules. The molecular conformation of poly(glutamic acid) (PGA) at various degrees of neutralization and ionic strengths has been well clarified by the potentiometric titration and other methods.⁴⁻⁷ There exists a pH range (corresponding to a range of degree of neutralization) in which the molecule has the conformation of an α -helix and is molecularly dispersed. Moreover, it is unnecessary to take into account specific ion binding if we use a simple salt such as sodium chloride as the added salt, since the

(1) H. A. Abramson, L. S. Moyer, and M. H. Gorin, "Electrophoresis of Protein," Reinhold Publishing Corp., New York, N. Y., 1942.

(2) M. Bier, "Electrophoresis," Academic Press Inc., London, 1959.

(3) D. C. Henry, *Proc. Roy. Soc.*, **A123**, 216 (1929).

(4) A. Wada, *J. Mol. Phys.*, **3**, 409 (1960).

(5) M. Nagasawa and A. Holtzer, *J. Amer. Chem. Soc.*, **86**, 538 (1964).

(6) J. Hermans, Jr., *ibid.*, **88**, 248 (1966); J. Hermans, Jr., *J. Phys. Chem.*, **70**, 510 (1966); A. Ciferri, D. Puett, L. Rajagh, and J. Hermans, Jr., *Biopolymers*, **6**, 1019 (1968).

(7) D. Olander and A. Holtzer, *J. Amer. Chem. Soc.*, **90**, 4549 (1968).

ionizable groups on PGA are exclusively carboxylic acid groups. Therefore, helical PGA appears to be an appropriate sample to test the theory of Henry and Gorin for rod-like molecules quantitatively.

Experimental Section

Sample. Poly(D-sodium glutamate) used in this study was kindly supplied by Ajinomoto Co., Ltd. The molecular weight of the sample was determined from the intrinsic viscosity in 0.1 M sodium chloride solution using an intrinsic viscosity-molecular weight relationship⁸ and found to be 75,000. The sodium form of the sample was purified by repeated precipitation from aqueous solutions with a 1:3 mixture of methyl alcohol and acetone, and then freeze-dried from an aqueous solution. The sodium form of the sample thus purified was converted into the acidic form by passing its aqueous solution through a mixed-bed ion-exchange resin column of Amberlite IRA 400 and IR 120. The polymer concentration was determined by the potentiometric titration in the presence of 0.02 M NaCl.

For the measurement of electrophoretic mobility, aqueous solutions of the acidic form were brought to desired degrees of neutralization and desired concentrations of sodium chloride by adding calculated amounts of 0.1 M sodium hydroxide and concentrated sodium chloride solutions successively. The sample solutions used for electrophoresis were dialyzed against NaCl solutions used as solvent until Donnan equilibrium was reached. The polymer concentrations (C_p) used in this work were between 0.15 and 0.02 g/dl, while the concentrations of NaCl solution used as solvent (C_s) were between 0.2 and 0.0035 M. It was reported that partially neutralized PGA molecules associate with each other at high ionic strengths even if the pH is as high as 5.0.⁹ In all measurements of electrophoresis reported here, however, only a single peak was observed on the schlieren patterns even at the highest polymer concentration, *i.e.*, $C_p = 0.15$ g/dl, and moreover, the sedimentation pattern of a sample of 0.25 degree of neutralization taken with a Beckman Spinco Model E ultracentrifuge did not show double peaks in 0.2 M and 0.0035 M NaCl solutions.

Determination of Helix Region. To determine the helix region of PGA, the potentiometric titration of the acidic sample was carried out in sodium chloride solutions of 0.0035, 0.02, and 0.2 M. Plots of $\text{pH} + \log(1 - \alpha)/\alpha$ vs. α are shown in Figure 1, where α is the degree of neutralization. The concentration of hydrogen ion was calculated from pH values by assuming that the activity coefficient of hydrogen ion is not affected by the presence of PGA.¹⁰ The titration curves of poly(D-glutamic acid) are entirely the same as those of poly(L-glutamic acid) as reported previously.⁵ Thus, the helix of PGA is stable throughout all ionic strengths used here, if $\alpha = 0.25$ is selected. To confirm it, measurement of the optical rotatory dispersion of the par-

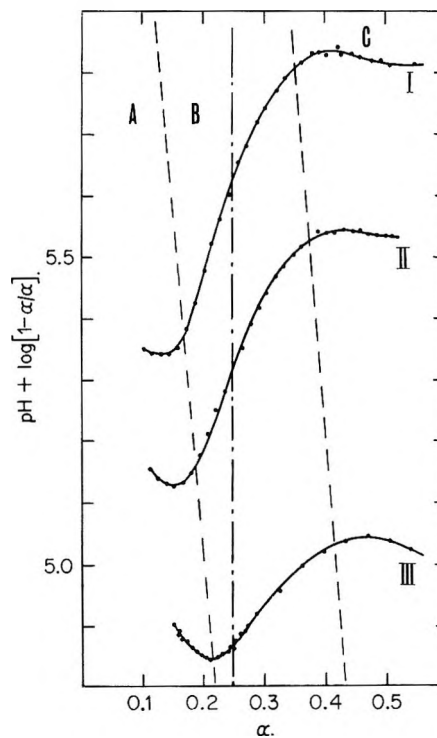


Figure 1. Examples of potentiometric titration curves: (I) 0.0035 M NaCl; 0.0216 N PGA; (II) 0.02 M NaCl, 0.0226 N PGA; (III) 0.2 M NaCl, 0.0086 N PGA. A, B, and C regions denote aggregated, helix, and transition regions of PGA, respectively.⁵

tially neutralized PGA at $\alpha = 0.25$ was carried out in 0.0035 M and 0.2 M NaCl by using a spectropolarimeter manufactured by Japan Spectroscopic Co., Ltd., Model ORD/UV-5. The slopes obtained from the Moffitt plot¹¹ were found to be -635 at 0.0035 M and -612 at 0.2 M of NaCl solutions. Thus, it is certain that the helix content is 100% at $\alpha = 0.25$ within the limit of experimental error.

Electrophoresis. Electrophoresis was carried out by using a Beckman Spinco Model H electrophoresis apparatus with a schlieren optical system at $25 \pm 0.01^\circ$ and displacements of schlieren peaks on photographic plates were measured by a Shimadzu microcomparator. The limiting electrophoretic mobility was obtained by extrapolating the apparent mobilities to zero polymer concentration in the same way as reported previously.^{12,13}

Results

A typical example of a plot of the apparent electrophoretic mobilities of helical PGA ($\alpha = 0.25$) vs. poly-

- (8) R. B. Hawkins, Jr., Dissertation, Washington University, 1967.
- (9) T. M. Schuster, *Biopolymers*, **3**, 681 (1965).
- (10) C. Tanford, "Electrochemistry in Biology and Medicine," T. Shedlovsky, Ed., John Wiley & Sons, Inc., New York, N. Y., 1955.
- (11) W. Moffitt, *J. Chem. Phys.*, **25**, 467 (1956).
- (12) M. Nagasawa, A. Soda, and I. Kagawa, *J. Polym. Sci.*, **31**, 439 (1958).
- (13) I. Noda, M. Nagasawa, and M. Ota, *J. Amer. Chem. Soc.*, **86**, 5075 (1964).

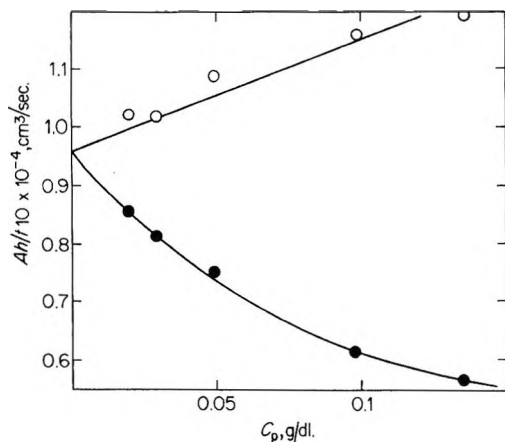


Figure 2. An example of the concentration dependence of observed migrating velocities. Upper, ascending boundary; lower, descending boundary. NaCl concentration, 0.0035 *M*; temperature, 25°.

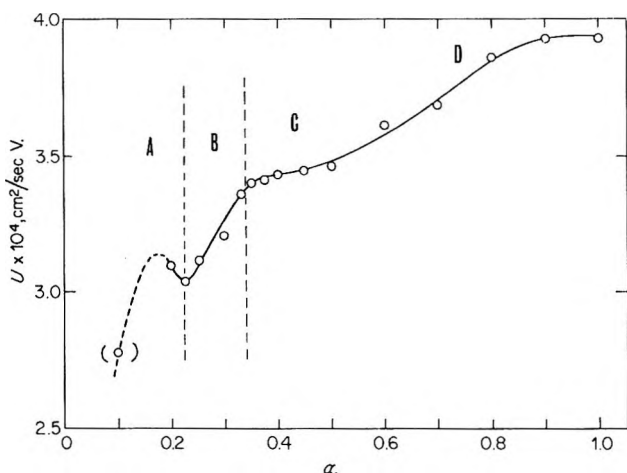


Figure 3. Dependence of electrophoretic mobility *U* on the degree of neutralization α . PGA concentration, 0.05 g/dl; NaCl concentration, 0.02 *M*; temperature, 25°. A, B, C, and D regions denote aggregated, helix, transition, and coil regions of PGA, respectively.

mer concentration is shown in Figure 2. The polymer concentration dependence of the apparent electrophoretic mobility is qualitatively similar to that reported for linear flexible polyelectrolytes.^{12,13} It is clear that both graphs of descending and ascending boundaries give the same intercept at $C_p = 0$, which is the limiting electrophoretic mobility *U*. Moreover, it may be concluded^{12,13} that the value of *U* may be approximately determined by taking the average value between the ascending and descending velocities at a polymer concentration if the ionic strength is high enough. The relationship between the mobility of PGA, *U*, and the degree of neutralization, α , was determined by this approximate method, as shown in Figure 3. The concentrations of polymer and sodium chloride used were 0.05 g/dl and 0.02 *M*, respectively. The curve of *U* vs. α is similar to the potentiometric titration curves.

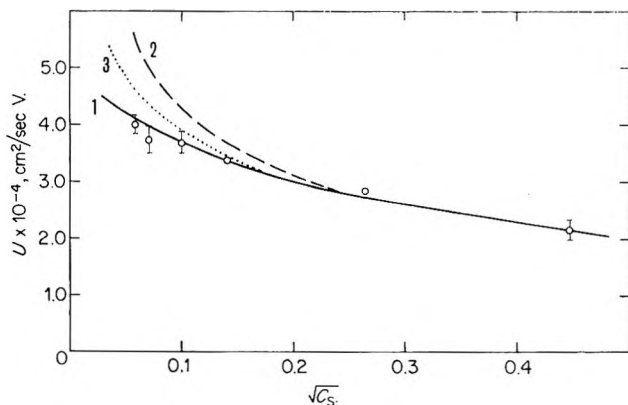


Figure 4. Comparison between the observed and the calculated mobilities: 1, observed; 2, calculated with use of the Debye-Hückel approximation, $b = 7.5 \text{ \AA}$, $a - b = 1.88 \text{ \AA}$ assumed; 3, calculated from numerical solutions of the Poisson-Boltzmann equation without use of the Debye-Hückel approximation, $b = 7.5 \text{ \AA}$, $a - b = 1.28 \text{ \AA}$, assumed.

From this figure it is clear that the helix region of PGA (region B) can be distinguished from its transition and coil regions (C and D). The deviation observed in the region A of lower degree of neutralization ($\alpha < 0.2$) is probably due to the aggregation preceding precipitation of the sample. In fact, the peak of the electrophoretic schlieren pattern was split into double peaks at $\alpha = 0.1$.

The limiting electrophoretic mobilities of the helical PGA with $\alpha = 0.25$ at various ionic strengths were determined by the extrapolation method shown in Figure 2. The plot of these limiting mobilities, *U*, thus determined vs. square root of added NaCl concentration, $\sqrt{C_s}$, is shown in Figure 4, where the limits of error in observed values are also indicated. From the figure it is clear that the mobility increases with decreasing ionic strength.

Discussion

Although the helix content of partially neutralized PGA ($\alpha = 0.25$) is almost 100% as calculated from the measurement of optical rotatory dispersion as described in the experimental part, we cannot expect the helical molecule of PGA to be a perfectly rigid rod-like molecule in solution. However, since the broken rod of PGA molecule is undoubtedly free draining for solvent, it may be reasonable to assume that its electrophoretic mobility must be determined by the electrostatic potential around the rod-like helix. Furthermore, we may assume that the rod-like molecules are randomly oriented in the solution so that the observed mobility may be given by the simple average over all possible orientation. That is

$$U = \frac{2}{3}U_{\perp} + \frac{1}{3}U_{\parallel} \quad (1)$$

where U_{\perp} and U_{\parallel} are the mobilities of the infinite cylinder oriented perpendicular and parallel to the applied electric field. This assumption is justified by the fact

that the observed mobility is independent of the electric field strength under the present experimental conditions.

The electrophoretic mobility of an infinite cylinder oriented perpendicularly to the applied electric field was calculated by Henry³ to be

$$U_{\perp} = \frac{D\psi_b}{8\pi\eta} + \left[8a^4 \int_{\infty}^a \frac{\psi(r)}{r^5} dr - 2a^2 \int_{\infty}^a \frac{\psi(r)}{r^3} dr \right] \quad (2)$$

if the helix is an insulating cylinder. Here, $\psi(r)$ and ψ_b are the electrostatic potential around the cylinder given as a function of the distance from the center of cylinder, r , and the value of $\psi(r)$ at the surface of the cylinder ($r = b$) relative to the electrostatic potential at infinity, respectively, a is the radius within which salt ions are excluded, D , is the dielectric constant, and η is the viscosity of solvent.

The mobility parallel to the applied field, U_{\parallel} , has also been given by Henry³ and Gorin,¹ namely

$$U_{\parallel} = \frac{D\psi_b}{4\pi\eta} \quad (3)$$

The electrostatic potential around a cylinder, $\psi(r)$, can be calculated from the following Poisson-Boltzmann equation

$$\nabla^2\psi = -\frac{4\pi N_A e}{10^3 D} C_s [e^{-e\psi/kT} - e^{e\psi/kT}] \quad (4)$$

where C_s is the molar concentration of added 1:1 electrolyte and N_A is Avogadro's number. If the well known Debye-Hückel approximation, $e\psi/kT \ll 1$, is applied, we have^{1,14}

$$\psi = \frac{2Ze}{DL} \left[\frac{K_0(\kappa r)}{\kappa a K_1(\kappa a)} \right] \quad (5)$$

neglecting the effects of the rod ends and assuming a uniform charge distribution. Z/L is the linear charge density of the cylinder and κ is the reciprocal thickness of the ionic atmosphere defined by Debye and Hückel;

$$\kappa^2 = \frac{8\pi N_A e^2 C_s}{DkT \times 10^3}$$

K_0 and K_1 are the modified Hankel functions of the 0th and 1st orders. At $r = a$, eq 5 becomes

$$\psi_a = \frac{2Ze}{DL} \left[\frac{K_0(\kappa a)}{\kappa a K_1(\kappa a)} \right] \quad (6)$$

The potential at the surface of the cylinder, ψ_b , is related to ψ_a by

$$\psi_b = \psi_a + \frac{2Ze}{DL} \ln \left(\frac{a}{b} \right) \quad (7)$$

If we assume values of b and $a - b$, we can therefore calculate U from eq 1-7, for comparison with the observed values. As is clear from the definitions of the radii a and b , $a - b$ is the effective radius of the ion, e.g.,

about 2.5 Å for sodium ion, and $b = 7.5$ Å. The calculated values of U are not so sensitive to the value of b but very sensitive to the assumed value of $a - b$. Considering the roughness of the model, however, the only practical way of proceeding is to treat $a - b$ as an adjustable parameter which is expected to be roughly of the dimension of a salt ion.¹⁵

The mobilities U thus calculated assuming $a - b = 1.88$ Å are plotted against $\sqrt{C_s}$ as a broken line, which is compared with the experimental data in Figure 4. The integration of the second term on the right side of eq 2 was carried out graphically. We can see good agreement between calculated mobilities and observed ones at high ionic strengths, but as the ionic strength decreases we find clear disagreement between them. The deviation may be caused by two factors: (1) failure of the Debye-Hückel approximation used in the theory and (2) the nature of the solution of the Poisson-Boltzmann equation for cylinders. In practice, $e\psi_a/kT$ calculated from eq 4 is as large as 3 in a 0.0035 M solution of NaCl so that the Debye-Hückel approximation cannot be valid.

As was discussed for potentiometric titration, better agreement can be expected if the values of ψ_a and $\psi(r)$ calculated numerically without use of the approximation are used instead of eq 5-6. The dotted line in Figure 4 shows the values of U calculated by using the numerical solution of eq 4 carried out with a high speed electronic computer.¹⁶ The agreement between the calculated values and the observed ones is clearly improved. Here, however, it is to be pointed out that the calculated values tend to infinity as the ionic strength decreases to zero, since ψ_b relative to the potential at $r = \infty$ becomes infinite at zero ionic strength where no ionic atmosphere exists. On the other hand, the experimental results must tend to a constant value. Therefore, it is meaningless to compare the electrophoretic mobility of a rod-like molecule with theories based on the Poisson-Boltzmann equation at very low ionic strengths. Thus, we may conclude that, if the ionic strength is not too low, the electrophoretic mobility of helical PGA can be quantitatively accounted for by the theory of Henry and Gorin for infinite cylinders, even though the helix is not a perfect cylinder but, rather, an interrupted cylinder.

Finally, it seems meaningful to point out the following. It is assumed in the theory of Henry that the electrophoretic mobility of a rod-like molecule is independent of the molecular weight. That is, at the limit of zero polymer concentration and zero ionic strength, there should be no effects of ionic atmosphere and hydrodynamic interaction between polymers, so that

(14) T. L. Hill, *Arch. Biochem. Biophys.*, **57**, 229 (1955).

(15) M. Nagasawa and A. Holtzer, *J. Amer. Chem. Soc.*, **86**, 531 (1964).

(16) L. Kotin and M. Nagasawa, *J. Chem. Phys.*, **36**, 873 (1962).

the electrophoretic mobility U^0 there may be determined by

$$U^0 = Ze/F^0 \quad (8)$$

where F^0 is the frictional coefficient of the polymer rod. Even at finite ionic strength, the effect of ionic atmosphere around a rod-like molecule is proportional to Ze as is clear from eq 5 and others. In the theory of Henry, therefore, the frictional coefficient of a rod-like molecule, F^0 , is assumed to be proportional to its molecular weight. This assumption stems from the assumption of the symmetrical flow lines around the cylinder. (The present experimental results were obtained for one sample of PGA without changing the molecular weight.) On the other hand, the frictional coefficient of a rod-like molecule is generally considered to be a function of molecular weight. According to the theory of Kirkwood,¹⁷ the mean translational diffusion coefficient \bar{D} of a macromolecule is given by

$$\bar{D} = kT \left[\frac{1}{N\zeta} + \frac{1}{6\pi\eta N^2} \sum_i \sum_j (1 - \delta_{ij}) \left\langle \frac{1}{R_{ij}} \right\rangle \right] \quad (9)$$

where N is the number of the structural element in the molecule, ζ is the frictional coefficient of the element, δ_{ij} is the Kronecker function, and R_{ij} is the distance between elements i and j . If the summation term is calculated for a rod-like molecule, eq 9 becomes

$$\bar{D} = \frac{kT}{N\zeta} \left[1 + \frac{\zeta}{3\pi\eta b} (\ln N - 1) \right] \quad (10)$$

The corresponding equation for the mobility of the cylinder \bar{L} is

$$\bar{L} (= U^0/e) = \frac{1}{\zeta} \left[1 + \frac{\zeta}{3\pi\eta b} (\ln N - 1) \right] \quad (11)$$

That is, the mobility increases to infinity as the molecular weight increases. The linear relationship between sedimentation coefficient and logarithmic molecular weight, which can also be derived from eq 9, was favorably compared with experimental results of poly(γ -benzyl-L-glutamate) in dimethyl formamide.¹⁸ This molecular weight dependence of the mobility of a cylinder stems from the use of the equation of Oseen for hydrodynamic perturbation in eq 9. It is also to be noted that the hydrodynamic equations for the translation of a cylinder fail to give the frictional coefficient if Stoke's approximation is employed.¹⁹ Therefore, it may be important for an examination of theories of the frictional coefficients of rod-like molecules to clarify the molecular weight dependence of electrophoretic mobility. Unfortunately, however, the solubility of partially neutralized PGA is so limited that it is difficult to change the molecular weight of the sample widely enough to solve this problem, and, moreover, it may be useless to study the molecular weight dependence of electrophoretic mobility until a really rigid rod-like polyelectrolyte becomes available.

Acknowledgment. We wish to thank Ajinomoto Co., Ltd., for supplying us with the samples.

(17) J. Riseman and J. G. Kirkwood, "Rheology," Vol. 1, F. R. Eirch, Ed., Academic Press Inc., New York, N. Y., 1956.

(18) H. Fujita, A. Teramoto, T. Yamashita, K. Okita, and S. Ikeda, *Biopolymers*, **4**, 781 (1966); A. Teramoto, T. Yamashita, and H. Fujita, *J. Chem. Phys.*, **46**, 1919 (1967).

(19) H. Lamb, "Hydrodynamics," Cambridge University Press, 1932, p 614.

Electrical Conductance, Diffusion, Viscosity, and Density of Sodium Nitrate, Sodium Perchlorate, and Sodium Thiocyanate in Concentrated Aqueous Solutions

by G. J. Janz, B. G. Oliver, G. R. Lakshminarayanan, and G. E. Mayer

Rensselaer Polytechnic Institute, Department of Chemistry, Troy, New York 12181 (Received October 14, 1969)

The properties of NaNO_3 , NaClO_4 , and NaCNS in concentrated aqueous solutions have been investigated at 25° by the techniques of electrical conductance, diffusion (Stokes' diaphragm technique), viscosity, and density, and the comparison of these with those of NaCl (as model electrolyte) is reported. In addition to the analytical characterization, the data are examined as an indication of ion-ion and solvation type interactions, and structural transitions in very concentrated salt solutions.

Introduction

While the use of electrical conductance, diffusion, and viscosity measurements to study the nature of the kinetic species in salt solutions has long been recognized, relatively little work on the conductance and viscosity of concentrated electrolytes has been done, and precise diffusion coefficients of electrolytes in such concentrated solutions are virtually nonexistent. The present communication reports the accurate and precise characterization of these properties, and, as well, the densities, for a series of 1:1 salts, NaNO_3 , NaClO_4 , and NaCNS , and the comparison of these data with those of NaCl (as model electrolyte). Application of the Wishaw-Stokes conductance and the Hartley-Crank diffusion equations is examined; in addition, empirical equations for the analytical characterization of these salt solutions are developed. The use of electrical conductance and diffusion as criteria for structural changes in very concentrated solutions is examined.

Experimental Results

Doubly-distilled water was obtained from a two stage still composed of a Stokes forestill (Model 171-E, F. J. Stokes Co.) and a Corning all-glass final still (Model AG-2, Fisher Scientific Co.). The specific conductance of water prepared in this way was $1-3 \times 10^{-6}$ mho.

Sodium nitrate (analytical grade) was recrystallized twice from double-distilled water, sodium perchlorate (analytical grade) was recrystallized twice from *n*-butyl alcohol, and sodium thiocyanate (analytical grade) was recrystallized twice from double-distilled water and twice from ethanol. All the salts were dried in a vacuum oven at 110° and stored over $\text{Mg}(\text{ClO}_4)_2$.

The conductance measurements were made with a Jones bridge (L & N) with accessories. Correction for polarization effects at the bright platinum electrodes was made by extrapolation to infinite frequency, and all measurements were corrected for the conductance of the solvent.

Densities were determined to an accuracy of $\pm 0.02\%$ using a 25-ml pycnometer (Fisher Scientific Company, Weld Type). Viscosity measurements were made with Ostwald viscometers (Cannon Fenske design, Fisher Scientific Co.) which were calibrated with conductivity water and benzene.

The stirred diaphragm diffusion cell has been described elsewhere¹⁻³ so it is sufficient to remark on a few salient features. Each half-cell capacity was about 50 ml, while the diaphragm (Gallenkamp, 76×14 ; average pore size 15μ) had a volume of about 0.5 ml. The stirrers were made of soft iron wire sealed in glass. The changes of density and viscosity of the solutions were sufficiently great to require several changes of the stirrers.

The diaphragm was flushed with several liters of degassed water prior to cell filling. The initial concentrations for the solutions in upper and lower compartments of the cell were selected so that differential diffusion coefficients could be obtained directly from the relation

$$\bar{D} = \frac{1}{kt} \ln \frac{c_1 - c_2}{c_3 - c_4} \quad (1)$$

Here c_1 and c_3 are the concentrations in the lower compartment at time $t = 0$ and $t = t$, respectively, c_2 and c_4 are the corresponding concentrations in the upper compartment, and k is the cell constant. To establish the tolerance limits for c_1 and c_2 in this differential technique, a series of exploratory measurements was required. It was found empirically that concentration differences between the two solutions up to 0.2 mol/l. gave identical diffusion coefficients (within the limits of error) for the

(1) R. H. Stokes, *J. Amer. Chem. Soc.*, **72**, 763 (1950).

(2) G. J. Janz and G. E. Mayer, "Diffusion of Electrolytes: Principles and Practice of the Diaphragm Diffusion Technique," Research and Development Progress Report No. 196, United States Department of the Interior (1966).

(3) R. Mills and L. A. Woolf, "The Diaphragm Cell." Diffusion Research Unit 67-1, The Australian National University, Canberra (1967).

Table I: Equations for the Equivalent Conductances, Diffusion Coefficients, Relative Viscosities, and Densities of Aqueous NaNO₃, NaClO₄, and NaCNS Solutions at 25°

	Best equation	Standard ^a deviation	Concentration range and number of data points
NaNO ₃	$\Lambda = 83.921 - 8.4679c + 0.39726c^2 - 18.663 \log(c + 0.001)$	0.171	0.1–7.3 M (18)
	$D = 1.4320 - 8.0034 \times 10^{-2}c + \frac{1.3761 \times 10^{-4}}{(c^2 + 0.001)}$	0.007	0.05–7.2 M (10)
	$\eta/\eta_0 = 0.9998 + 4.0273 \times 10^{-2}c + 2.2289 \times 10^{-2}c^2$	0.002	0.1–4.0 M (11)
	$\eta/\eta_0 = 1.3143 + 3.5343 \times 10^{-3}c^3$	0.019	4.0–7.8 M (8)
NaClO ₄	$\rho = 0.99844 + 5.3742 \times 10^{-2}c - 4.2901 \times 10^{-4}c^2$	0.0005	0.1–7.8 M (18)
	$\Lambda = 85.455 - 8.3959c + 2.1777 \times 10^{-2}c^3 - 5.7838 \ln(c + 0.001)$	0.105	0.1–9.1 M (16)
	$D = 1.4040 + 5.3804 \times 10^{-2}c - 6.1248 \times 10^{-3}c^2 + \frac{1.7635 \times 10^{-4}c^3 - \frac{7.3565 \times 10^{-5}}{(c + 0.001)}}{2.8739 \times 10^{-2} \ln(c + 0.001)}$	0.007	0.05–12.0 M (10)
	$\eta/\eta_0 = 1.0148 + 3.2564 \times 10^{-2}c^2$	0.004	0.5–4.0 M (8)
NaCNS	$\eta/\eta_0 = 1.1540 + 6.0861 \times 10^{-3}c^3 + 1.9846 \times 10^{-4}c^6$	0.017	4.0–9.1 M (5)
	$\rho = 0.99834 + 7.6913 \times 10^{-2}c - 3.9159 \times 10^{-4}c^2$	0.0007	0.1–9.1 M (16)
	$\Lambda = 86.952 - 7.4086c - 4.9473 \ln(c + 0.001) + 5.9554 \times 10^{-4}c^6$	0.253	0.1–9.2 M (19)
	$D = 1.3171 + 0.20081c - 3.4266 \times 10^{-2}c^2 + \frac{1.6157 \times 10^{-3}c^3 - \frac{2.8700 \times 10^{-4}}{(c^2 + 0.001)}}{0.16349 \log(c + 0.001)}$	0.010	0.05–9.8 M (13)
	$\eta/\eta_0 = 1.0354 + 3.0071 \times 10^{-2}c^2 + 1.7947 \times 10^{-2} \ln(c + 0.001)$	0.003	0.1–4.0 M (8)
	$\eta/\eta_0 = 1.2151 + 5.2020 \times 10^{-3}c^3 + 1.2599 \times 10^{-4}c^6$	0.028	4.0–10.6 M (6)
	$\rho = 0.99784 + 3.9762 \times 10^{-2}c - 3.5933 \times 10^{-4}c^2$	0.0004	0.1–10.6 M (20)

^a Standard deviation is defined as $\sqrt{\sum^n (X_e - X_c)^2 / n - p}$, where X_e is the experimental value at a particular concentration, X_c the calculated value from the least squares equation at the same concentration, n the number of experimental data points, p the number of coefficients in the least-squares equation.

same average concentration. In all subsequent work the maximum concentration difference (0.2 M) was used in order to aid the accuracy in the ultimate analyses. Initial concentrations for the lower compartment, c_1 , were calculated by the characteristic cell equation

$$c_1 = c_3 + (c_4 - c_2)f \quad (2)$$

where f is the cell factor. This is defined as $(V'' + V)/(V' + V)$ and can be calculated from the volumes of the diaphragm cell compartments (corrected for stirrer volumes) V' and V'' , and the pore volume of the diaphragm, V . The compartment and diaphragm volumes could be determined by direct weight calibrations with water to an accuracy of ± 0.001 ml because of the use of 10/20 teflon-lined capillary bore plugs on the cell.

The diaphragm cell constant, k , is defined by the expression

$$k = \frac{A}{l} \left(\frac{1}{V'} + \frac{1}{V''} \right) \quad (3)$$

where A is the total effective cross-sectional area for the

pores, and l , an average length. With prolonged use, the wear of the diaphragm leads to an increase in k over a period of time. In the present study, this effect was investigated, and the variation was found to be related to the cell lifetime, L , (hr) by

$$\frac{A}{l} = 2.9694 \times 10^{-5}L + 6.60605 \quad (4)$$

A/l rather than k is used since the former is characteristic of the diaphragm only. For these periodic calibration experiments, aqueous KCl data^{4–6} were used in the conventional manner.

The compositions of all the solutions used in the diffusion measurements were analyzed conductometrically.

The thermostats for the above measurements were controlled at $25.00 \pm 0.003^\circ$.

In Table I are the concentration-dependent equations for the electrical conductance Λ , viscosity η/η_0 , diffusion D , and density ρ ; these were calculated from the

(4) R. H. Stokes, *J. Amer. Chem. Soc.*, **73**, 3527 (1951).

(5) L. S. Gosting, *ibid.*, **72**, 4418 (1950).

(6) H. S. Harned and R. L. Nuttall, *ibid.*, **71**, 1460 (1949).

Table II: Equivalent Conductance, Diffusion Coefficients, and Relative Viscosities of Aqueous NaCl, NaNO₃, NaClO₄, and NaCNS Solutions at 25°

c, mol/l.	Λ, mhos				D, cm ² sec ⁻¹				η/η ₀			
	NaCl	NaNO ₃	NaClO ₄	NaCNS	NaCl	NaNO ₃	NaClO ₄	NaCNS	NaCl	NaNO ₃	NaClO ₄	NaCNS
0.1	106.74	101.66	97.88	97.55	1.484	1.437	1.475	1.474	1.010	1.004
0.5	93.62	85.39	85.26	86.67	1.474	1.393	1.449	1.457	1.046	1.026	1.023	1.031
1.0	85.76	75.84	77.07	79.54	1.483	1.352	1.452	1.485	1.096	1.062	1.047	1.065
2.0	74.71	62.95	64.83	68.71	1.514	1.272	1.469	1.545	1.219	1.169	1.145	1.168
3.0	65.57	53.19	54.50	59.30	1.544	1.192	1.483	1.577	1.379	1.321	1.308	1.326
4.0	57.23	45.17	45.25	50.49	1.584	1.112	1.493	1.577	1.580	1.518	1.554	1.555
5.0	49.46	38.47	36.89	42.03	...	1.032	1.496	1.552	1.858	1.756	1.944	1.884
6.0	...	32.89	29.42	33.88	...	0.952	1.493	1.519	...	2.078	2.549	2.390
7.0	...	28.34	22.90	26.12	...	0.872	1.485	1.460	...	2.527	3.459	3.138
8.0	17.41	19.17	1.473	1.410	4.862	4.254
9.0	13.06	14.23	1.458	1.371	7.199	6.028

preceding experimental observations⁷ and with the computer facility at Rensselaer, using double precision Fortran IV programming. The number of experimental data points and the precisions of the least-squares data analysis are also given for reference. A comparison of these properties as $\log \Lambda\eta/\eta_0$ vs. concentration (on a log scale), and D vs. the square root of concentration, is shown in Figures 1 and 2, respectively, and numerical values at rounded concentrations are shown in Table II.

Discussion

From the experimental densities and those from reference 8, the apparent molal volumes were calculated. The concentration dependence of ϕ_v for the electrolytes can be represented with a precision of 0.3% by equations

$$\text{NaCl} \quad \phi_v = 16.364 + 2.172\sqrt{c} \quad (5)$$

$$\text{NaNO}_3 \quad \phi_v = 27.710 + 2.495\sqrt{c} \quad (6)$$

$$\text{NaClO}_4 \quad \phi_v = 42.737 + 2.104\sqrt{c} \quad (7)$$

$$\text{NaCNS} \quad \phi_v = 38.962 + 1.870\sqrt{c} \quad (8)$$

Thus the order of apparent molal volumes is ClO₄⁻ > CNS⁻ > NO₃⁻ > Cl⁻. This trend is the same as that reported by Padova⁹ for limiting partial molar volumes.

The above equations have the same form as those used by Masson¹⁰ to represent the apparent molal volumes of various aqueous electrolytes. While this equation is theoretically significant as a limiting law,¹¹ it is empirical when used at higher concentrations.

An aim in the present work was to investigate the changes in the transport properties of sodium salts for which the anions varied from Cl⁻ to CNS⁻. From Table II it is evident that the conductance of NaCl at a fixed concentration is higher than the conductance of the other electrolytes in the series. This correlates with a trend in the apparent molal volumes, although it does not necessarily follow that the higher conductance is solely due to the smaller volume requirements for the Cl⁻ ion in this series. The results for NaNO₃, NaClO₄,

and NaCNS fall more closely together. This proximity may be accounted for, in part, by cancellation of a number of effects such as ionic volume, viscosity, and ion-pair formation, *e.g.*, NaClO₄ has a larger apparent molal volume than NaCNS but a smaller relative viscosity. An examination of Figure 1 ($\log \Lambda\eta/\eta_0$ vs. $\log c$) gives some indication of the magnitude of the above effects.

Figure 2 shows that changing the anion has a noticeable effect on the diffusion coefficient of sodium salts. The diffusion data for the sodium salts of the monatomic anions are uniformly above those of the sodium salts with polyatomic anions. Intuitively this seems to correlate with lower mobilities expected of the polyatomic anions because of lowered symmetry, and larger spatial requirements. However, the driving force for diffusion is the gradient of chemical potential in the solutions, and a more correct representation of the mobility of the ions is gained if the diffusion coefficient is divided by $d(\ln f^\pm)/d(\ln m)$, the thermodynamic driving force. When such a procedure is carried out the "corrected" diffusion data give a series of curves of similar forms, and clustered more closely than the corresponding "uncorrected" diffusion data. There is, then, little doubt that the observed disparity between diffusion coefficient curves can be ascribed, in large part, to activity coefficient differences.

Samoilov¹² has stated that the structure of concentrated solutions resembles the crystal hydrates, if

(7) For detailed tables (III-IX) supplementary to this article order Document 00750 from National Auxiliary Publication Service, c/o CCM Information Sciences, Inc., 909 3rd Ave., New York, N. Y., 10022. A copy may be secured by citing the document number and by remitting \$1.00 for microfiche or \$3.00 for photocopies. Advance payment is required. Make checks or money orders payable to: ASIS-NAPS.

(8) International Critical Tables, Vol. III, p 79, 1926.

(9) J. Padova, *J. Chem. Phys.*, **39**, 1552 (1963).

(10) H. S. Harned and B. B. Owen, "The Physical Chemistry of Electrolyte Solutions," Reinhold Publishing Corp., New York, N. Y., 1958.

(11) B. B. Owen and S. R. Brinkley, Jr., *Ann. N. Y. Acad. Sci.*, **51**, 753 (1949).

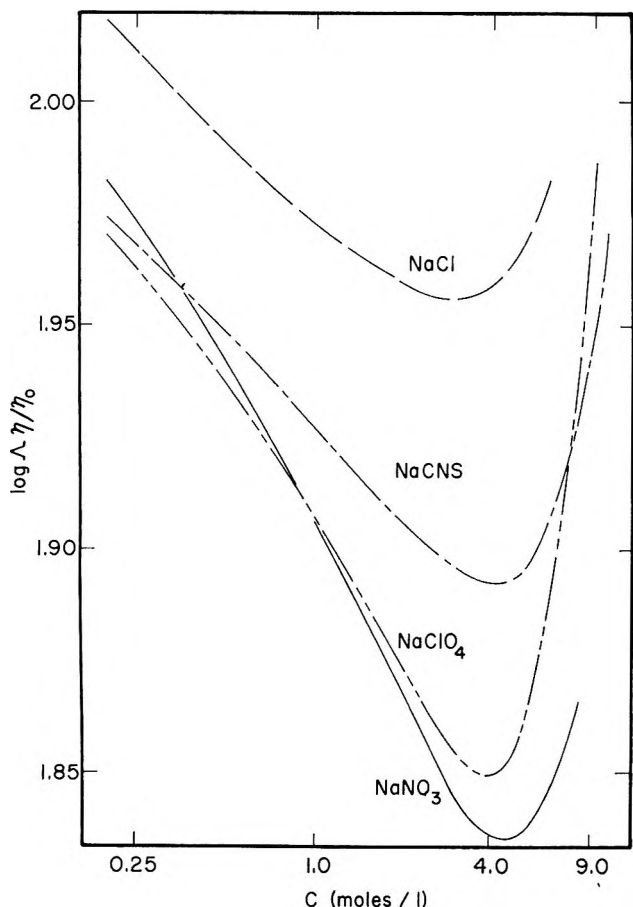


Figure 1. $\log \Delta\eta/\eta_0$ vs. c (log scale) for aqueous NaCl, NaNO₃, NaClO₄, and NaCNS solutions at 25°.

such are formed by the solute-solvent pair. Some support for this has been advanced by Mathieu and Lounsbury¹³ in the studies of the vibrational spectroscopy of aqueous metallic nitrates; the results could be interpreted qualitatively if it was assumed that the ions approached a distribution characteristic of crystal hydrate at high concentrations (*i.e.*, near saturation). Similarly, Klotschko¹⁴ has interpreted the maxima exhibited by specific conductance curves in salt-water systems as due to a probable transition of solution structure. The current investigation shows that, in addition to specific conductance maxima, the systems studied show a sharp minimum in $\log \Delta\eta/\eta_0$ vs. $\log c$ curves (Figure 1) and a definite break at high concentration in the mobility ratio, D_{corr}/Λ , vs. c curves. The preceding two observations may be additional indicators for transition of solution structure from that of water to that of crystal hydrate.

To gain information on the hydration interactions in these solutions, the Hartley-Crank diffusion equation¹⁵ (as extended to electrolytes by Wishaw and Stokes¹⁶) has been applied to the diffusion data. The two equations, respectively, may be written

$$F(D) = 1 + 0.036m \left(\frac{D_{\text{H}_2\text{O}}^*}{D^0} - h \right) \quad (9)$$

and

$$\left(\frac{\eta}{\eta_0} \right) F(D) = 1 + 0.036m \left[\frac{D_{\text{H}_2\text{O}}^*}{D^0} - h' \right] \quad (10)$$

where $F(D)$ is defined by

$$F(D) = D_{\text{obsd}} / \left[(D^0 + \Delta_1 + \Delta_2) \left(1 + \frac{m \, d \ln \gamma}{d \, m} \right) \right] \quad (11)$$

The two parameters, h and h' , are the hydration numbers introduced by Hartley and Crank, and Wishaw and Stokes, and may be gained from a graphical analysis of $F(D)$ and $F(D)\eta/\eta_0$ vs. m , respectively. The other parameters have their conventional significance,¹⁷

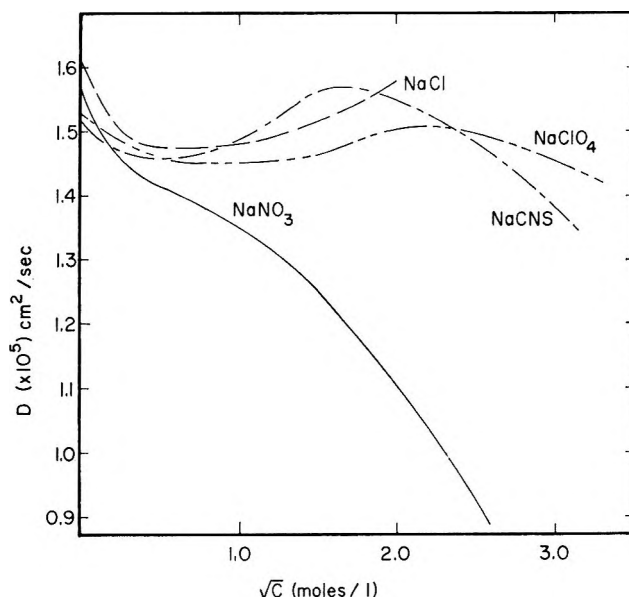


Figure 2. Diffusion coefficient vs. the square root of concentration for aqueous NaCl, NaNO₃, NaClO₄, and NaCNS solutions at 25°.

and need not be defined here. The values of h and h' gained in this manner, and which represent the experimental results with an average deviation of about 1% below 1.0 M, are: NaCl,¹⁷ $h = 3.5$, $h' = 1.1$; NaNO₃, $h = 1.4$, $h' = -0.3$; NaClO₄, $h = 2.8$, $h' = 1.3$; NaCNS, $h = 4.3$, $h' = 2.6$. The values of the hydration numbers calculated from the viscosity-corrected and

(12) O. Y. Samoilov, "Structure of Aqueous Electrolyte Solutions and the Hydration of Ions," Translated from Russian by D. J. G. Ives, London, 1965; Consultants Bureau Publishers, New York, N. Y.

(13) J. P. Mathieu and M. Lounsbury, *Discussions Faraday Soc.*, **9**, 196 (1950).

(14) M. A. Klotschko, *Dokl. Akad. Nauk SSSR*, **82**, 261 (1952).

(15) G. S. Hartley and J. Crank, *Trans. Faraday Soc.*, **45**, 801 (1949).

(16) B. F. Wishaw and R. H. Stokes, *J. Amer. Chem. Soc.*, **76**, 2065 (1954).

(17) R. A. Robinson and R. H. Stokes, "Electrolyte Solutions," 2nd ed, rev, Butterworths and Co. Ltd., London, 1968.

the uncorrected Wishaw-Stokes equations (eq 10 and 9, respectively) differ considerably. Because the change of the bulk viscosity resulting from the addition of ions is not necessarily a fair measure of the change in the frictional resistance experienced by the ions, the true hydration number probably lies in between these two values.¹⁷ Hydration numbers calculated from activity data¹⁸ (NaCl, 3.5; NaNO₃, 0.5; NaClO₄, 2.1; NaCNS, 2.6) reinforce this viewpoint.

The large change in the hydration number with changing anion is somewhat surprising, but can be rationalized on the basis of structure making and breaking effects of the anions. The larger the hydrophobic structure breaking effect of the anion the smaller will be the hydration number of the salt. On this basis, keeping in mind that these hydration numbers were calculated by fitting the observed diffusion data to a semiempirical expression, it is possible to arrange the anions according to their structure-breaking effect: NO₃⁻ > ClO₄⁻ > Cl⁻ > CNS⁻. This is to be compared with the sequence advanced from infrared studies by Choppin and Buijs,¹⁹ *i.e.*, ClO₄⁻ > NO₃⁻ > Cl⁻ > CNS⁻. The two are basically in agreement, the sequence being the same with the exception of ClO₄⁻ and NO₃⁻.

An evaluation of the semiempirical Wishaw-Stokes conductance equation¹⁶

$$\Lambda = \left[\Lambda^\circ - \frac{B_2\sqrt{c}}{1 + Ba\sqrt{c}} \right] \left[1 - \frac{B_1F\sqrt{c}}{1 + Ba\sqrt{c}} \right] \frac{\eta^\circ}{\eta} \quad (12)$$

is of interest in view of its moderate success in other concentrated aqueous systems.^{16,20,21} The equation represents the conductance of NaCl, NaNO₃, NaClO₄, and NaCNS with average deviations of about 0.5% up to concentrations of 3 M using the *a* parameter values 5.5, 3.3, 4.1, and 5.7 Å, respectively. If the Wishaw-Stokes equation for associated electrolytes is used together with values for *a* the predicted²²⁻²⁴ from ion-cavity considerations and crystallographic radii, it is found that NaNO₃ and NaClO₄ are partially

associated while NaCl and NaCNS are essentially unassociated for the concentration range investigated.

The free volume-entropy interpretation^{25,26} for concentrated electrolytes leads to an expression for the conductance and fluidity

$$\Lambda, \phi = A \exp [-k/(N_0 - N)] \quad (13)$$

It is found that the present data may be expressed by this equation ($\pm 1\%$) over the entire concentration range; *N*₀ is not constant for Λ and ϕ but the values found are, respectively: NaNO₃, *N*₀^Λ = 46, *N*₀^φ = 29; NaClO₄, *N*₀^Λ = 32, *N*₀^φ = 19; NaCNS, *N*₀^Λ = 23, *N*₀^φ = 20. The aqueous quasi-lattice model^{27,28} is essentially one of competing association and hydration equilibria and is similar to the B.E.T. adsorption model²⁹ first advanced by Stokes and Robinson¹⁸ in the extension of the Debye-Hückel theory to concentrated solutions. Recent successes in applying such models to activity³⁰ and diffusion³¹ would seem to indicate this area warrants further attention.

Acknowledgments. This research was supported by the Office of Saline Water, U. S. Department of the Interior, Washington, D. C.

(18) R. H. Stokes and R. A. Robinson, *J. Amer. Chem. Soc.*, **70**, 1870 (1948).

(19) G. R. Choppin and K. Buijs, *J. Chem. Phys.*, **39**, 2042 (1963).

(20) A. N. Campbell and W. G. Paterson, *Can. J. Chem.*, **36**, 1004 (1958).

(21) A. N. Campbell and E. M. Kartzmark, *ibid.*, **33**, 887 (1955).

(22) G. J. Janz and M. J. Tait, *ibid.*, **45**, 1101 (1967).

(23) E. Andalaft, R. P. T. Tomkins, and G. J. Janz, *Can. J. Chem.*, **46**, 2959 (1968).

(24) W. M. Latimer, *J. Chem. Phys.*, **23**, 90 (1955).

(25) C. A. Angell, *J. Phys. Chem.*, **70**, 3988 (1966).

(26) C. A. Angell, *J. Chem. Phys.*, **46**, 4673 (1967).

(27) J. Braunstein, *J. Phys. Chem.*, **71**, 3402 (1967).

(28) J. Braunstein in "Ionic Interactions: Dilute Solutions to Molten Salts," S. Petrucci, Ed., Academic Press, New York, N. Y., 1969, Chapter 4.

(29) S. Brunauer, P. H. Emmett, and E. Teller, *J. Amer. Chem. Soc.*, **60**, 309 (1938).

(30) A. N. Campbell and B. G. Oliver, *Can. J. Chem.*, **47**, 2671 (1969).

(31) G. J. Janz, G. R. Lakshminarayanan, and M. P. Klotzkin, *J. Phys. Chem.*, **70**, 2562 (1966).

Ammonium Ion Adsorption in Sintered Porous Glass.

An Infrared Determination of Selectivity Constants

by Michael L. Hair^{1a}

Research and Development Laboratories, Corning Glass Works, Corning, New York 14830
(Received July 23, 1969)

Infrared data are presented showing the adsorption of NH_4^+ into a sintered porous glass from aqueous solution. Effects due to the anions are discussed and the equilibrium constants K_{NaK} , $K_{\text{NH}_4\text{K}}$, and $K_{\text{NH}_4\text{Na}}$ are determined to be 2.06, 2.95, and 1.43, respectively. The "pores" in the glass are estimated to be between 2.8 and 4.5 Å in diameter.

Introduction

Previous work has shown that when porous glass is slowly sintered, its behavior as an ionic membrane changes drastically.^{1b} Thus, though the original porous glass shows only slight selectivity for K^+ relative to Na^+ , as the membrane is slowly sintered, the pore size decreases, water is eliminated from the pores, and a point is eventually reached where the potassium-over-sodium selectivity, $K_{\text{NaK}}^{\text{pot}}$, reaches a value of 10. On further heating, the glass completely sinters and has such a high resistance that its electrochemical properties become unmeasurable. The initial selectivity to Ca^{2+} in the presence of Na^+ and K^+ is virtually eliminated during sintering. Infrared spectra taken after varying degrees of sintering show that molecular water is eliminated from the pores of the glass. At the point where $K_{\text{NaK}}^{\text{pot}} = 10$, the infrared spectrum of the porous membrane appears to be identical with that of a completely fired, nonporous, 96% SiO_2 glass. However, as has been pointed out, the unusually high K^+/Na^+ selectivity is associated with a state just prior to complete sintering. This material is of some interest, as its composition is essentially 97% SiO_2 and 3% B_2O_3 and bears no relationship in chemical composition to glasses used in specific-ion electrodes. In view of its unique properties, the almost-sintered porous glass has been examined further in an attempt to define its porosity. Infrared spectra have been obtained for NH_4^+ ions adsorbed in the glass from aqueous solutions and these have been used to determine selectivity constants.

Experimental Section

The sample examined in this work was prepared from a disk of porous glass, Corning Code 7930, which was sintered at 1006° for 21 hr. Its potential selectivity constant $K_{\text{NaK}}^{\text{pot}}$ was 10.0 and its membrane response between 0.1 and 0.01 *N* KCl solution was 55 mV at 25°.

Infrared spectra were recorded at room temperature on a Perkin-Elmer 421 grating spectrophotometer. All experiments were performed at room temperature.

Results and Discussion

A unique difference between the sample and a completely sintered porous glass is shown in Figure 1. After recording the infrared spectrum of the sample, it was immersed in 3 *N* NH_4Cl . Equilibrium was established within 15 min, after which time the sample was removed, dried with tissue paper, and its spectrum rerecorded.

The results show that NH_4^+ ions have entered the glass from the aqueous solution, and a remarkably clear spectrum is obtained. This spectrum can be compared with that of crystal NH_4Cl as reported by Wagner and Hornig.² According to those authors, NH_4Cl is characterized by the vibrations shown in Table I. Of particular interest are the bands 2005 and 1800 cm^{-1} . These are attributed to combination bands associated with the ν_2 and ν_4 vibrations interacting with the crystal lattice. These bands are completely absent from the spectrum of NH_4^+ in the glass, and bands attributable only to a free NH_4^+ ion are observed. It should also be noted that no molecular water accompanies the NH_4^+ ion during adsorption into the glass. In particular, changes in the OH stretching region have been sought but not observed, indicating that the observable OH groups associated with the glass do not enter into the interaction that causes the electrochemical potential.

It is normally assumed³ that the potential arises from an ion exchange of the type



On immersing the sample in the NH_4Cl solution, a decrease in pH was observed, but was insufficient to give quantitative results. The absence of observable changes in the infrared spectrum suggests that this ion exchange, if it does occur, must involve groups which do not give observable infrared vibrations. Completely

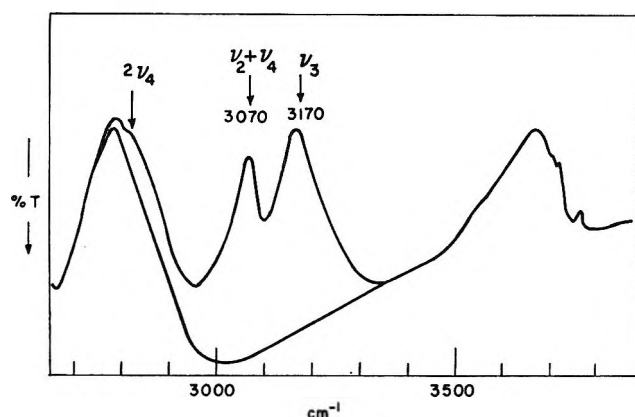
(1) (a) Research Laboratories, Xerox Corporation, Webster, N. Y. 14580; (b) I. Altug and M. L. Hair, *J. Phys. Chem.*, **72**, 2976 (1968).

(2) E. L. Wagner and D. F. Hornig, *J. Chem. Phys.*, **18**, 296 (1950).

(3) G. Eisenman, *Biophys. J.*, **2**, 286 (1962).

Table I: Vibration Frequencies of NH_4Cl (Crystal) (from Reference 2)

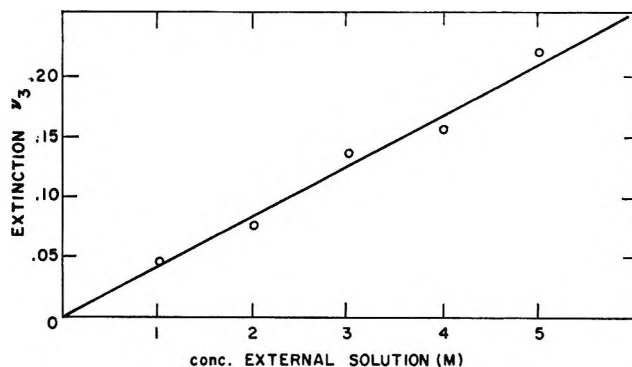
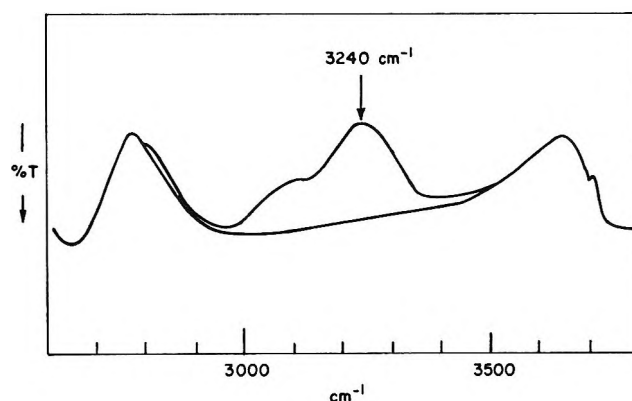
Band, cm^{-1}	Assignment	Relative intensity
3223	$\nu_1 + \nu_6$	6
3126	ν_3	41
3050	$\nu_2 + \nu_4$	42
(3048)	(ν_1)	...
2828	$2\nu_4$	8
2005-2100	$\nu_2 + \nu_6$	2
1794-1817	$\nu_4 + \nu_6$	4
1403	ν_4	10

Figure 1. Infrared spectrum of NH_4^+ in sintered porous glass after adsorption from 3 *N* NH_4Cl solution. Lower line is background due to sample.

ionized protons would not cause an observable infrared vibration. Similarly, a strongly acidic OH group, expected at low frequencies, could well be broadened beyond recognition.

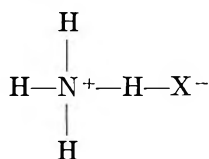
The amount of NH_4^+ which enters the glass depends on the concentration of the external NH_4Cl solution. Figure 2 plots the extinction of the 3160-cm^{-1} ν_3 vibration as a function of the external solution concentration up to 5 *N*. The amount adsorbed can be represented as either a linear function of the external solution concentration or as a slightly S-shaped curve, reminiscent of many adsorption isotherms. Further speculation seems unwarranted in view of possible deviations of the extinction coefficient in this system.

The NH_4^+ which is adsorbed into the glass from NH_4NO_3 solutions differs considerably from that adsorbed from NH_4Cl solutions. The spectrum of this species is shown in Figure 3. The ν_3 vibration now occurs at 3230 cm^{-1} rather than 3170 cm^{-1} . Relative to the $\nu_2 + \nu_4$ vibration, it is also more intense and broader than when adsorbed from NH_4Cl . This suggests that anions accompany the NH_4^+ into the membrane and affect the cationic species. Immersing the membrane in NH_4SCN solutions seems to prove this because the NH_4^+ spectrum then resembles that obtained with NH_4Cl , but another band can be distinctly

Figure 2. Extinction of ν_3 band of adsorbed NH_4^+ as a function of concentration of external NH_4Cl solution.Figure 3. Infrared spectrum of NH_4^+ in sintered porous glass after adsorption from 3 *N* NH_4NO_3 solution. Lower line is background due to sample.

observed at 2070 cm^{-1} . By analogy to the spectra of inorganic thiocyanides, this can be attributed to the presence of SCN^- in the membrane. Unfortunately, the intensity of this band cannot be determined since it lies on the transmission cut-off. NH_4^+ is not adsorbed from pure NH_4OH solutions, probably because of the low dissociation constant of NH_4OH (1.77×10^{-5}). However, if NH_4OH is added to, say, 3 *N* NH_4Cl solutions, the amount of NH_4^+ adsorbed is greater than observed with 3 *N* NH_4Cl alone. This again points out the importance, perhaps even the necessity, of the anion to the process.

The relative intensities of the bands at 3170 cm^{-1} and 3070 cm^{-1} require comment. By analogy to the NH_4Cl crystal spectrum, the band at 3070 cm^{-1} was assigned to a combination $\nu_2 + \nu_4$ vibration. However, examination of Figure 1 shows that ν_3 and $\nu_2 + \nu_4$ have comparable extinctions. The intensity of the 3070-cm^{-1} band seems to be surprisingly high for a combination band, even though it is comparable to that reported for the crystal spectrum. It is possible that this band is due to the normally inactive ν_1 vibration. If the NH_4^+ entered the glass as an "ion pair" together with its co-ion, the structure



can be envisioned. The hydrogen bond between N and X reduces the symmetry of the NH_4^+ from T_d to C_{3v} , and the ν_1 vibration is thus activated. Surface effects are known to cause activation of normally inactive modes.⁴ In this case, the presence of a counterion explains the dependence of the intensity of this band on the nature of the NH_4^+ salt used for the experiment.

In previous work,¹ it was suggested that the surface properties of the porous glass were unchanged during sintering, and the observed increase in K^+/Na^+ selectivity was, therefore, attributable to a change in the relative mobilities of the K^+ and Na^+ ions in the sintered glass. The ability to spectroscopically observe the adsorbed NH_4^+ offers a means of measuring the equilibrium constant $K_{\text{NaK}}^{\text{eq}}$. Thus, if ϵ_1 is the extinction of the 3170-cm^{-1} band in the glass after adsorption from 1 *N* NH_4Cl , and ϵ_2 and ϵ_3 are the extinctions after adsorption from solutions which are normal with respect to NH_4Cl but contain equal amounts of NaCl or KCl , then the relative selectivities can be calculated.

$$K_{\text{NaK}} = \frac{\epsilon_1 - \epsilon_3}{\epsilon_1 - \epsilon_2}$$

These experiments show that the order of selectivity is $\text{K}^+ > \text{Na}^+ > \text{NH}_4^+$. The equilibrium selectivity constants are given in Table II. These values can be com-

Table II: Equilibrium Selectivity Constants

K_{NaK}	2.06
$K_{\text{NH}_4-\text{K}}$	2.95
$K_{\text{NH}_4-\text{Na}}$	1.43

pared with those derived from Eisenman's glass isotherms for sodium aluminosilicate glass electrodes.⁵ The equilibrium selectivity constants are almost identical with the potential selectivity constants observed by Eisenman for his group VIIa selectivity sequence and correspond to the equilibrium selectivities projected from free-energy considerations for widely separated

ion-exchange sites with a pK_a value of about 3. It has been shown⁶ that the surface of the unsintered porous glass has a slight preference for K^+ over Na^+ . It must thus be concluded that the potential selectivity constant of 10 is due to changes in the mobility of the ions. It should be noted that Eisenman⁷ has shown that both $U_{\text{K}}/U_{\text{Na}}$ and $K_{\text{NaK}}^{\text{pot}}$ can vary over a wide range while still giving rise to similar $K_{\text{NaK}}^{\text{pot}}$ values.

Attempts to further define the pore size of the partially sintered glasses were made by trying to adsorb the quaternary amines $(\text{CH}_3)_4\text{N}^+\text{Cl}^-$ and $(\text{C}_2\text{H}_5)_4\text{N}^+\text{Cl}^-$ into the glass in the same manner as NH_4Cl . These cations have diameters of 4.5 and 7.0 Å, respectively,⁸ as compared to the diameter of the NH_4^+ which is 2.82 Å. Only slight traces of these materials could be detected in the glass; thus, a pore diameter of between 2.8 and 4.5 Å can be tentatively assigned.

The origin of the selectivity in these sintered porous glasses can be reconciled with the Eisenman ion-exchange theory for glass electrodes. If the glass is considered to consist of charged pores, then, as the glass is sintered, the pore size is reduced and the pores approach ionic sizes. At this stage, the pore is little different from a "site" in a crystal lattice and if the main contribution to the ion selectivity is the free energy of hydration, then patterns of selectivity remain the same as those predicted by Eisenman. One important difference, however, is the fact that the sintered porous glasses used in this work do have "pores" which are of such a size that they admit NH_4^+ , but exclude H_2O . The "pores" were therefore estimated to be between 2.8 and 4.5 Å. A completely sintered glass will not adsorb either NH_4^+ or H_2O . The actual mechanism of ion selectivity in this case thus appears to be a molecular sieve effect and it is interesting to note that the lower value of 2.8 Å corresponds to the diameter of the nonhydrated K^+ ion.

(4) M. L. Hair, "Infrared Spectroscopy in Surface Chemistry," Marcel Dekker, Inc., New York, N. Y., 1967, pp 117-118.

(5) G. Eisenman, "The Glass Electrode," Interscience Publishers, Inc., New York, N. Y., 1965, pp 257, 287.

(6) I. Altug and M. L. Hair, *J. Phys. Chem.*, **71**, 4260 (1967).

(7) Reference 5, p 307.

(8) F. Helfferich, "Ion Exchange," McGraw-Hill Book Co., Inc., New York, N. Y., 1962, p 161.

Micellar Aggregation Properties of Some Zwitterionic N-Alkyl Betaines¹

by J. Swarbrick² and J. Daruwala

Division of Pharmaceutics, School of Pharmacy, The University of Connecticut, Storrs, Connecticut 06268
(Received June 24, 1969)

The weight-average aggregation numbers, A_w , and micellar molecular weights, M_w , of four homologous zwitterionic N-alkyl betaines (N-alkyl-N,N-dimethylglycines) have been determined by light scattering. A linear relationship was found between the logarithm of A_w and the alkyl chain length for the C₁₀, C₁₁, C₁₃, and C₁₅ homologs. The effect of temperature on A_w and M_w was studied using the C₁₀ and C₁₁ homologs. As the temperature was raised, a trend was observed, in that A_w and M_w for both homologs increased, reached a maximum, and then decreased. This trend was not significant at the 95% level of confidence for the C₁₀ homolog. However, the behavior exhibited by these compounds is related to changes in the critical micelle concentration with temperature reported previously.³

Introduction

Little information is available on the aggregation properties of zwitterionic surfactants.^{4,5} This is in contrast to the many reports for ionic⁶⁻⁹ and nonionic¹⁰⁻¹⁴ surfactants which have considered the effects of such variables as temperature, added electrolyte, head group, and length of alkyl chain on the weight-average micellar molecular weight, M_w , viscosity, and the size and shape of micelles. This information has come mainly from light scattering studies.

In their study of the zwitterionic C-alkyl betaines, Tori and Nakagawa⁵ observed a linear relationship between the logarithm of the weight-average aggregation number, A_w , and the alkyl chain length. The effects of chain length, electrolyte, and type of head group on the micellar aggregation properties of a number of other zwitterionic surfactants have been investigated by Herrmann.⁴ This worker concluded that there were no repulsive interactions between the zwitterionic head groups and that M_w was less influenced by electrolytes than with ionic surfactants. It was further shown that, while the type of zwitterionic head group influenced the micellar properties, these surfactants as a whole were intermediate between ionic and nonionic surfactants.

In neither of these reports was the effect of temperature on the aggregation numbers studied. As pointed out previously,³ such data are necessary to establish the applicability of the phase separation model of micellization to a particular surfactant system.

In the present paper we report the effect of alkyl chain length and temperature on the aggregation number of several N-alkyl betaines, as determined from light scattering measurements.

Experimental Section

Materials. All materials were as described previously.³

Method. The light scattering photometer, temperature control, clarification procedure, and cell have been

described elsewhere.^{3,15} Nanograde benzene (Mallinckrodt Chemicals) was used without further purification as a primary standard for calibration. A value of $46.5 \times 10^{-6} \text{ cm}^{-1}$ at a wavelength of 4358 Å and 20° was used as the standard value of the Rayleigh ratio, R_{90} , for pure, dust-free benzene.¹⁶ The calibration was confirmed by scattering measurements on fresh, multiple-distilled, dust-free toluene, for which R_{90} was found to be $54.7 \times 10^{-6} \text{ cm}^{-1}$, in good agreement with literature values of $53.5 \times 10^{-6} \text{ cm}^{-1}$ and $55.2 \times 10^{-6} \text{ cm}^{-1}$.⁴

The concentrations of all betaine solutions were determined refractometrically from standard plots for each homolog of Δn vs. C (g ml⁻¹). A Brice-Phoenix differential refractometer, with facilities for temperature control of the sample, was used at a wavelength

(1) This work was supported by a grant from the University of Connecticut Research Foundation.

(2) Author to whom inquiries should be directed.

(3) J. Swarbrick and J. Daruwala, *J. Phys. Chem.*, **73**, 2627 (1969).

(4) K. W. Herrmann, *J. Colloid Interface Sci.*, **22**, 352 (1966).

(5) K. Tori and T. Nakagawa, *Kolloid-Z.Z. Polymere*, **191**, Heft 1, 48 (1963).

(6) H. F. Huisman, *Koninkl. Ned. Akad. Wetenschap., Proc. Ser.*, **B67** (4), 367 (1964).

(7) P. Debye, *J. Phys. Colloid Chem.*, **53**, 1 (1949).

(8) K. J. Mysels and J. N. Phillips, *ibid.*, **59**, 325 (1955).

(9) K. Shinoda, T. Nakagawa, B. Tamamushi, and T. Isemura, "Colloidal Surfactants" Academic Press Inc., New York, N. Y., 1963, Chapter 1.

(10) J. M. Corkill, J. F. Goodman, and R. H. Ottewill, *Trans. Faraday Soc.*, **57**, 1627 (1961).

(11) R. R. Balmbra, J. S. Cluine, J. M. Corkill, and J. F. Goodman, *ibid.*, **60**, 979 (1964).

(12) P. H. Elworthy and C. McDonald, *Kolloid-Z.Z. Polymere*, **195**, Heft 1, 16 (1964).

(13) J. M. Corkill, J. F. Goodman, and T. Walker, *Trans. Faraday Soc.*, **63**, 759 (1967).

(14) R. R. Balmbra, J. S. Cluine, J. M. Corkill, and J. F. Goodman, *ibid.*, **58**, 1661 (1962).

(15) J. Daruwala, Ph.D. Thesis, University of Connecticut, 1968.

(16) J. P. Kratochvil, G. J. Dezelic, M. Kerker, and E. Matijevic, *J. Polymer Sci.*, **57**, 59 (1962).

Table I: Aggregation Properties of N-Alkyl Betaines

N-Alkyl betaine	$T, ^\circ\text{C}$	c_{mc} ($M \times 10^3$)	dn/dC , ml g^{-1}	$M_w \times 10^{-3}$ ^a	A_w ^a	B , $\text{ml g}^{-1} \times 10^4$
C_8^b	21	250	...	5.10	23.7	...
C_{10}	20	22.83	0.163	8.18 (7.54–8.95)	33.7 (31.0–36.8)	7.5
	25	23.27	0.160	8.25 (7.68–8.91)	34.0 (31.6–36.7)	7.3
	31	22.69	0.158	8.47 (7.22–10.2)	34.9 (29.7–42.0)	8.2
	37	21.83	0.155	8.60 (7.94–9.38)	35.4 (32.7–38.6)	6.3
	43	21.86	0.152	8.07 (7.57–8.64)	33.2 (31.2–35.6)	5.3
	50	22.06	0.149	7.82 (6.77–9.26)	32.2 (27.9–38.1)	4.0
	58	22.44	0.145	7.76 (6.82–8.99)	31.9 (28.1–37.0)	4.8
	65	23.36	0.142	7.66 (7.00–8.45)	31.5 (28.8–34.8)	4.3
C_{11}	25	7.23	0.156	14.9 (13.4–16.5)	58.0 (52.1–64.2)	0.7
	35	6.82	0.149	17.5 (16.5–18.5)	68.1 (64.2–72.0)	9.3
	45	7.15	0.142	17.6 (16.3–19.0)	68.5 (63.4–73.9)	4.3
	55	7.36	0.136	17.7 (16.7–18.9)	68.9 (65.0–73.5)	3.7
	65	7.63	0.129	16.2 (15.2–17.2)	63.0 (59.1–66.9)	–2.8
C_{13}	25	0.795	0.159	26.5 (25.9–27.1)	87.3 (85.3–89.4)	2.6
C_{15}	25	0.056	0.159	43.1 (42.3–43.9)	130 (128–133)	–1.1

^a 95% confidence limits shown in parentheses. ^b See reference 17.

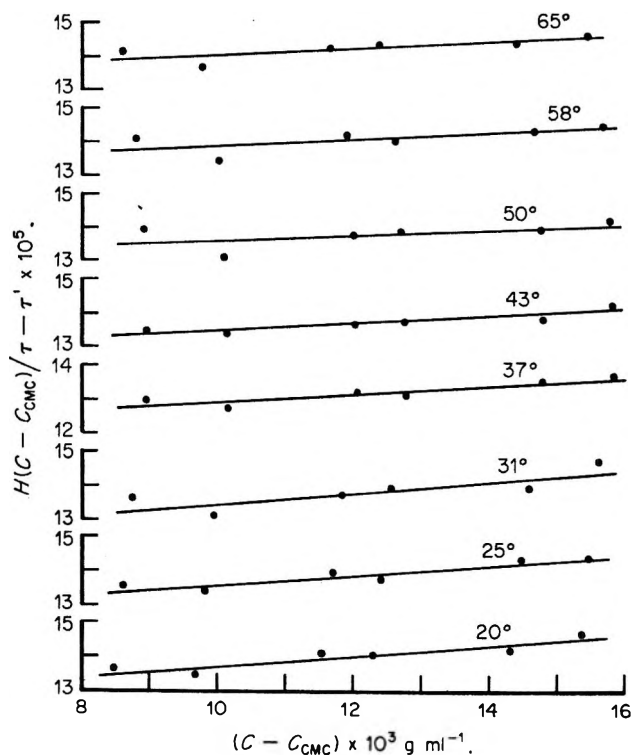


Figure 1. Debye plots for the C_{10} N-alkyl betaine in water at a wavelength of 4358 Å.

of 4358 Å. Care was taken to ensure that no evaporation took place from the samples at elevated temperatures. Sodium chloride solutions¹⁸ were used to calibrate the instrument.

Results

The refractive index increments, dn/dC (ml g^{-1}), corrected for the change in concentration due to expansion of the solvent with temperature, are shown in

Table I. In all instances, the concentrations used to determine dn/dC were above the critical micelle concentration of each homolog.

Weight-average micellar molecular weights were calculated from the Debye equation applicable to micellar systems,⁷ namely

$$\frac{H(C - C_{cmc})}{(\tau - \tau')} = \frac{1}{M_w} + 2B(C - C_{cmc}) \quad (1)$$

where H is the usual optical constant, C is the total concentration (g ml^{-1}) of surfactant. C_{cmc} is the concentration at the critical micelle concentration (g ml^{-1}), M_w is the weight-average micellar molecular weight, B is the second virial coefficient, and τ and τ' are the excess turbidities of the solute above and at the critical micelle concentration, respectively. The values of C_{cmc} , which have been reported elsewhere,^{3,15} are also included in Table I.

A typical series of plots of $H(C - C_{cmc})/(\tau - \tau')$ vs. $(C - C_{cmc})$ is shown in Figure 1. The statistically computed values of M_w , A_w , and B for the four N-alkyl betaines studied are given in Table I. The change in the logarithm of A_w with alkyl chain length for these surfactants is compared with similar data for other types of surfactants in Figure 2. The variation of M_w with temperature is illustrated in Figure 3.

Discussion

The logarithm of A_w at 25° increases linearly with the length of the alkyl chain, as seen in Figure 2 where the data are compared with that for other surfactants. It is apparent that the slopes of the zwitter-

(17) K. Tori and T. Nakagawa, *Kolloid-Z.Z. Polymere*, **188**, Heft 1, 47 (1963).

(18) Operation Manual, Brice-Phoenix Differential Refractometer.

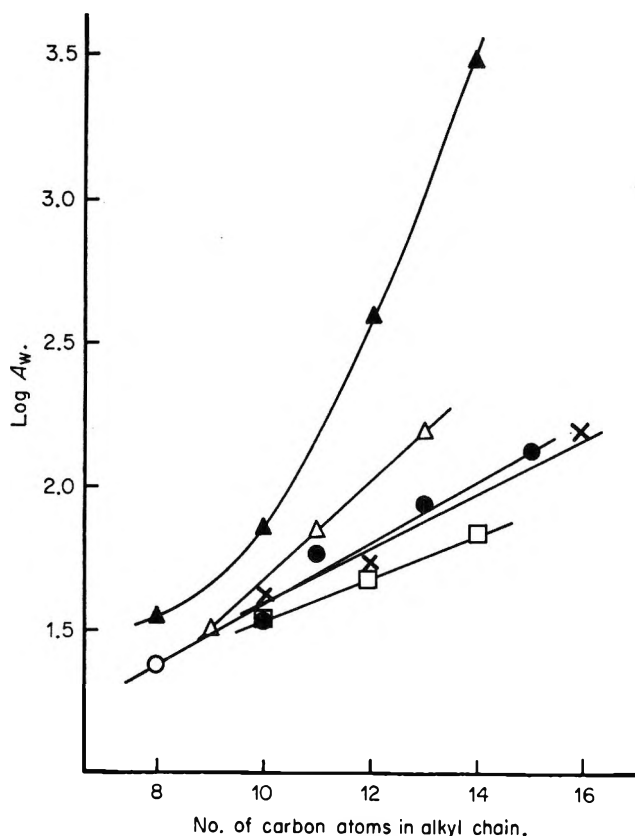


Figure 2. Variation of the logarithm of the weight-average aggregation number, A_w , with alkyl chain length: ▲, *n*-alkyl hexaoxyethylene glycol monoethers at 25°;^{10,11,14} △, C-alkyl betaines at 21°;⁵ ●, N-alkyl betaines at 25°, this work; ○, N-octyl betaine at 21°;¹⁷ ×, dimethylalkylammonio propane sulfonates at 37°;⁴ □, alkyltrimethylammonium bromides at 25°.⁷

ionic surfactants are intermediate between those for nonionic and ionic surfactants. A similar situation has been shown to exist in terms of the thermodynamics of micellization of these various types of surfactant.³

At the present time it is difficult to quantitatively rationalize aggregation numbers and the manner in which they change with alkyl chain length and/or temperature. However, the relative changes in A_w with chain length will be a function, primarily, of the polar head group. The smaller slope observed with the ionic surfactant implies that aggregation is less sensitive than the other two types of surfactant to an increase in the lipophilicity of the molecule. This is due, presumably, to the presence of the ionic heads which make it more difficult to introduce monomers into the micelle. A further constraint on the size of the micelle may be the inability of the ionic heads to cover adequately the micelle-bulk phase interface when a certain micelle size is exceeded. The aggregation properties of the nonionic surfactants are, on the other hand, considerably more sensitive to changes in alkyl chain length. Such behavior is obviously related to the absence of a formal charge on the polyoxyethylene

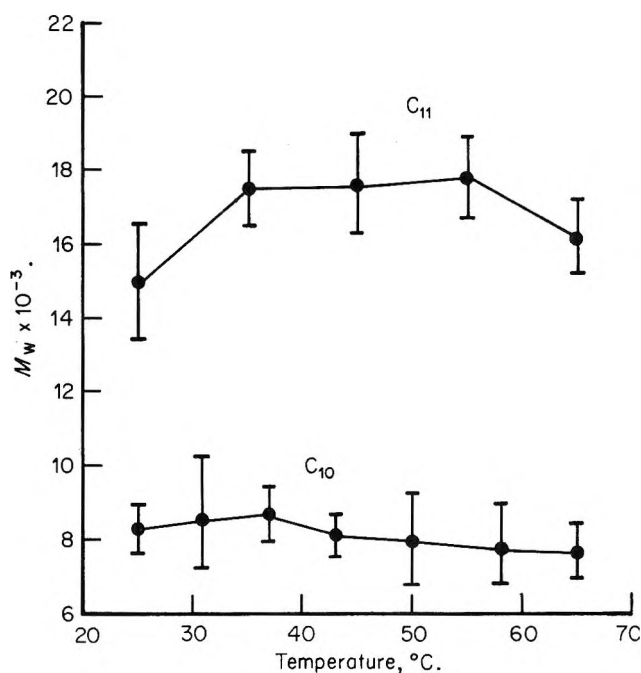


Figure 3. Variation of weight-average micellar molecular weight, M_w , of the C₁₀ and C₁₁ N-alkyl betaines with temperature. See Table I for the corresponding values of A_w .

head group. At the same time, it is conceivable that the flexible polyoxyethylene chain would be able to cover more effectively an expanded micelle-bulk phase interface.

Although the slope for the N-alkyl betaines in Figure 2 is close to that for the zwitterionic dimethylalkylammonio propane sulfonates (DAS),⁴ it does differ from that of the C-alkyl betaines,⁵ suggesting that the type of zwitterionic head can affect the aggregation number at a particular chain length and temperature. In this regard, it is significant that the critical micelle concentration for the C₁₀ DAS surfactant at 30° is 39 mM,⁴ whereas that for the C₁₀ N-alkyl betaine at the same temperature is 22.7 mM.³ However, while the critical micelle concentration for DAS is approximately 75% greater than that of the C₁₀ betaine, the values of A_w , determined from the statistically fitted curves in Figure 2, are within 8% of each other. This suggests that, while the critical micelle concentration depends primarily on the balance between the hydrophilic and lipophilic moieties of the surfactant monomer, the electrostatic and steric properties of the particular polar head group involved play a decisive role in determining the extent of aggregation once the critical micelle concentration is exceeded.

The dissymmetries of scattering, $z_{45/135}$, for the C₁₀, C₁₁, C₁₃, and C₁₅ homologs at all temperatures and concentrations were less than 1.04. This absence of measurable dissymmetry is to be expected, the micellar diameters being less than 218 Å, $1/20$ of the wavelength of light used. This observation is consistent with simi-

lar data for zwitterionic⁴ and ionic⁶ surfactants of comparable chain lengths.

Equation 1 is the original Debye light scattering equation modified by Debye⁷ so as to represent the post-critical micelle concentration region of a plot of excess turbidity *vs.* concentration. In view of the approximations involved in this modification, the interpretation of the slopes, *B*, in terms of solvent-solute and solute-solute interactions in micellar systems is not simple.¹⁹ However, the slopes obtained for the *N*-alkyl betaines (Table I) are closer to zero than those for ionic surfactants of comparable chain length, indicating that the betaine micelles do not interact appreciably and behave ideally as suggested by Herrmann⁴ from his studies on other zwitterionic surfactants. For example, the Debye plot for sodium undecyl sulfate yields a value for *B* of 74×10^{-4} ,⁶ in contrast to a value of 0.7×10^{-4} for the *C*₁₁ *N*-alkyl betaine. This is taken to indicate that the forces of repulsion which exist between ionic heads are absent in the betaine micelles, and is further evidence of their zwitterionic nature.

The temperature dependence of *M*_w, and hence *A*_w, for the *C*₁₀ and *C*₁₁ *N*-alkyl betaines is shown in Figure 3, where it is apparent that both these parameters increase with temperature initially, reach a maximum, and then decrease. Unfortunately, the changes observed with the *C*₁₀ homolog are not significant at the 95% confidence limits. Nevertheless, this trend is the reverse of that reported previously³ for the effect of temperature on the cmc of these same compounds, where a minimum value, rather than a maximum value, was observed. This situation is reasonable, since the factors responsible for lowering the critical micelle concentration and enhancing micellization should also increase the aggregation number. In a similar study on a series of nonionic *n*-alkyl polyoxyethylene glycol monoethers, Balmbra, *et al.*,¹¹ found that the critical micelle concentrations decreased while the micellar molecular weights increased with increasing temperature. A similar inverse relationship has also been reported by Debye²⁰ for *n*-dodecyl trimethylammonium bromide. However, with this cationic surfactant the critical micelle concentration increased while *M*_w decreased with increasing temperature.

With nonionic surfactants, it is likely that the extent

of hydration, especially of the ether oxygens in the polyoxyethylene chain, will decrease with increasing temperature. This effectively renders the amphiphile more lipophilic, a condition whereby, in a homologous series, the critical micelle concentration decreases and *M*_w increases. With ionic surfactants, desolvation effects are minimal, except at relatively low temperatures. The observed reduction in *M*_w is due to thermal agitation which progressively decreases the adhesion between monomers.²¹ Bearing in mind the intermediate character of zwitterionic surfactants, it would seem that, with the *C*₁₀ and *C*₁₁ betaines, desolvation of the polar head predominates at the lower temperatures studied where *M*_w increases with temperature. At higher temperatures, thermal agitation becomes more significant, resulting in the observed decrease in *M*_w.

Over the entire concentration and temperature ranges examined, the change in turbidity with betaine concentration, *dτ/dC*, remained constant once the critical micelle concentration had been exceeded. Under these conditions, Balmbra, *et al.*,¹⁴ have shown that

$$d\tau/dC = HM_w \quad (2)$$

implying that *M*_w also remains constant. Accordingly, the addition of surfactant, at least over the concentration ranges used in the present study, results in the addition of more micelles of size *M*_w rather than an increase in the size of those already present. The micelle size distribution may be taken, therefore, to be fairly narrow. These findings are confirmed by the linearity of the Debye plots in Figure 1. Similar results have been obtained by Herrmann⁴ for zwitterionic surfactants. Tori and Nakagawa,¹⁷ however, found turbidity to be a curvilinear function of concentration with the *C*₈ *N*-alkyl betaine, the slope decreasing with concentration. No explanation was offered for this observation. These workers did find the Debye plot to be linear and concluded that *M*_w remained constant over the concentration range studied.

(19) D. G. Hall and B. A. Pethica in "Nonionic Surfactants," Vol. I, M. J. Schick, Ed., Marcel Dekker, Inc., New York, N. Y., 1967, Chapter 16.

(20) P. Debye, *Ann. N. Y. Acad. Sci.*, **51**, 575 (1949).

(21) K. Shinoda, T. Nakagawa, B. Tamamushi, and T. Isemura, "Colloidal Surfactants," Academic Press, Inc., New York, N. Y., 1963, p 55.

Reactive Silica. III. The Formation of Boron Hydrides, and Other Reactions, on the Surface of Boria-Impregnated Aerosil¹

by Claudio Morterra and M. J. D. Low²

Department of Chemistry, New York University, New York, New York 10453 (Received July 14, 1969)

The activation of boria-impregnated Aerosil by a methylation-pyrolysis-degassing procedure was studied by infrared techniques. The spectra showed that the surface structures related to the silica portion of the composite adsorbent, and their reactions, were entirely like those previously described for reactive silica prepared from pure Aerosil (*J. Phys. Chem.*, **73**, 327 (1969)); a second set of structures and reactions was related to the boria portion of the surface. The pyrolysis of B—OCH₃ groups leads to the formation of three surface =B—H structures absorbing at 2621, 2601, and 2580 cm⁻¹. Removal of these boranes by high-temperature degassing then leads to the formation of "reactive boria" dispersed on the surface of the reactive silica. The nature of the surface, and its reaction with H₂, H₂O, and O₂, are discussed.

The reaction of methanol with siliceous adsorbents produces surface Si—OCH₃ groups.³ The high-temperature pyrolysis of the methoxy groups of methylated Aerosil and subsequent degassing⁴ then lead to the formation of an adsorbent, previously termed reactive silica,⁵ which exhibits unusually high reactivity toward molecular hydrogen,⁶ ammonia,⁷ methane,⁷ and other adsorbates.⁷ However, surface B—OCH₃ as well as Si—OCH₃ groups are formed on porous glass,⁸ and the boria impurity responsible for the formation of the B—OCH₃ groups also appears to exert a modifying effect on the overall reactivity of the porous glass surface.^{8,9} It was therefore of interest to determine if the thermal collapse of surface B—OCH₃ groups and the presence of boron would lead to a change of the nature or properties of reactive silica. An infrared study of the nature and properties of the surface species formed on a reactive adsorbent prepared from boria-impregnated Aerosil was consequently carried out and is the topic of the present paper.

Experimental Section

Aerosil¹⁰ was impregnated with aqueous H₃BO₃ solution using the incipient wetness method. The dry powder, containing 0.5-1 wt % of boron, was pressed at 10 tons/in.² to form self-supporting sample disks of about 40 mg/cm². The general methylation, pyrolysis, and degassing procedures used to activate such a boria-impregnated silica (BIS) sample, as well as other experimental techniques and details, were like those described previously.^{5,6}

Results and Discussion

Formation of the Reactive Adsorbent. The spectrum of methylated BIS showed the usual absorptions¹¹ due to surface Si—OCH₃ groups^{5,8,11,12} and to B—OCH₃

groups.⁸ The latter, as in the case with porous glass,⁸ absorbed at 2973 and 2886 cm⁻¹. The positions and assignments of these and other bands pertinent to the present work are summarized in Table I.

Degassing of the methylated specimen at temperatures higher than room temperature, but lower than 500°, led to the slow elimination of the broad absorptions in the 3700–3200-cm⁻¹ range (spectrum A, Figure 1). One broad band centering near 3650–3620 cm⁻¹ is attributed to hydrogen-bonded hydroxyl and methoxy groups.¹² The elimination of these groups occurs quite slowly with pure silica and requires temperatures above 350°. The second broad band, centered near 3500 cm⁻¹, is usually attributed to strong physically adsorbed species.^{12,13} These are almost impossible to desorb from pure silica at room temperature, but car-

- (1) For part I, see ref 5; for part II, see ref 6.
- (2) To whom inquiries should be directed.
- (3) For prior work, see the literature cited in ref 8.
- (4) C. Morterra and M. J. D. Low, *Chem. Commun.*, 1968, 203.
- (5) C. Morterra and M. J. D. Low, *J. Phys. Chem.*, **73**, 321 (1969).
- (6) C. Morterra and M. J. D. Low, *ibid.*, **73**, 327 (1969).
- (7) Details of such reactions will be given elsewhere.
- (8) M. J. D. Low and Y. Harano, *J. Res. Inst. Catal. Hokkaido Univ.*, **16**, 271 (1968).
- (9) (a) M. J. D. Low and N. Ramasubramanian, *J. Phys. Chem.*, **71**, 3077 (1967); (b) M. J. D. Low, N. Ramasubramanian, and V. V. Subba Rao, *ibid.*, **71**, 1726 (1967); (c) M. J. D. Low, N. Ramasubramanian, P. Ramamurthy, and A. V. Deo, *ibid.*, **72**, 2371 (1968); (d) M. J. D. Low and V. V. Subba Rao, *Can. J. Chem.*, **46**, 3255 (1968); **47**, 1281 (1969).
- (10) Aerosil 2491/380, Degussa, Inc., Kearny, N. J.
- (11) Bands observed with reactive silica are summarized in Table I of ref 5.
- (12) E. Borello, A. Zecchina, and C. Morterra, *J. Phys. Chem.*, **71**, 2938 (1967).
- (13) F. H. Hambleton, J. A. Hockey, and J. A. G. Taylor, *Trans. Faraday Soc.*, **62**, 801 (1966).

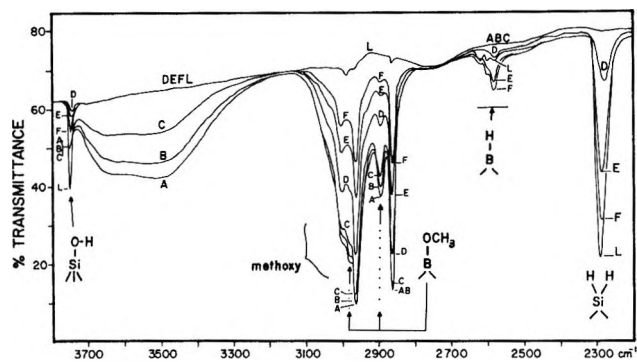


Figure 1. Spectra of methylated BIS. The sample was degassed sequentially at the following temperatures and times: A, 170°, 30 min; B, 250°, 30 min; C, 400°, 40 min. For D, E, F, L, see Figure 2. Other spectra of the complete sequence were omitted.

Table I:¹¹ Summary of Bands

Cm ⁻¹	Assignment
3703	B-OH
2973	=B-OCH ₃
2886	
2621	
2601	B-H
2580	
1957	B-D
1937	
1937	-C≡C-D
2123	Unknown
2051	

be very rapidly removed at temperatures of 200 to 250°. In contrast, the two broad bands of methylated BIS are only slowly diminished at roughly the same rates, even at 400° (spectra A-C, Figure 1).

Degassing at temperatures below 500° also removed a part of the B-OCH₃ groups, shown by the decline of the 2973- and 2886-cm⁻¹ bands. The decline of the B-OCH₃ groups was not accompanied by an increase in the Si-OCH₃ groups or the formation of the 3703-cm⁻¹ B-OH band,¹⁴ in contrast to the effects observed with porous glass.⁸ It is possible that the discrepancies in the effects observed with BIS and porous glass could have been brought about by the large differences in intensities of the Si-OCH₃ and B-OCH₃ bands of the BIS spectra. The intensity differences make quantitative measurements difficult. However, it seems more likely that the differences in behavior were caused by differences in the nature and character of the two adsorbents. It is difficult to determine from BIS spectra if outgassing at 500° could remove all of the B-OCH₃ groups. The broad absorptions in the 3700-3200 cm⁻¹ range were completely eliminated by degassing at 500° for 22 hr, but a small band at 2886 cm⁻¹ (the B-OCH₃ symmetric C-H stretching fundamental) could still be detected. No other changes were produced in the spectrum by such degassing.

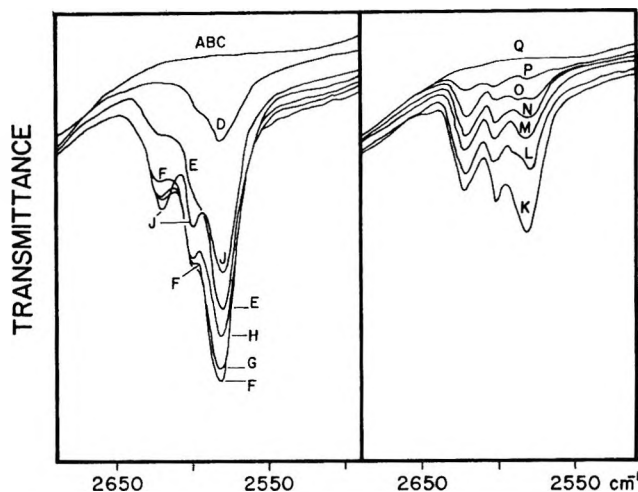


Figure 2. Formation and decomposition of surface boranes. The traces show the region near 2600 cm⁻¹, recorded using ordinate and abscissa expansion, of the spectra of the degassing sequence given in Figure 1. A, B, C: see Figure 1; D: 700°, 2 min; E: 700°, 5 min; F: 700°, 12 min; G: 700°, 25 min; H: 700°, 50 min; J: 700°, 105 min; K: 700°, 3 hr; L: 700°, 11 hr; M: 700°, 22 hr; N: 800°, 15 min; O: 800°, 1 hr; P: 800°, 2 hr; Q: 800°, 15 hr.

Large changes were observed if the degassing temperature was 550° or higher. At these higher temperatures, the elimination of the broad 3700-3200-cm⁻¹ absorption was complete in the first few minutes, the Si-OCH₃ bands decreased and the 2300-cm⁻¹ SiH₂ band^{5,6} grew as in the case of pure Aerosil, the B-OCH₃ bands declined more rapidly, and a new, complex absorption appeared in the 2650-2550-cm⁻¹ range. The complex absorption was always relatively weak, *e.g.*, Figure 1, and was therefore recorded with ordinate-scale expansion. Initially, only one band centered at 2580 cm⁻¹ (spectrum D, Figure 2) was detected. Two weak shoulders were then formed on the high-frequency side of the 2580-cm⁻¹ band and grew into distinct bands at 2621 and 2601 cm⁻¹. The latter became more evident on further degassing and were still increasing when the 2580-cm⁻¹ band had started to decline (spectra E-J, Figure 2). Finally, all three bands decreased, but at different rates (spectra K-Q, Figure 2), and were completely eliminated after about 2 hr at 800°. These effects occurred at a slower rate at lower temperatures, the elimination of the three bands requiring 70 hr at 700° and several days at 600°. The relative intensities of the three bands and their order of appearance were not affected by changes in the degassing temperature. The latter caused only marked changes in the desorption rate.

Nature of the Reactive Adsorbant. The results out-

(14) M. J. D. Low and N. Ramasubramanian, *Chem. Commun.*, 499 (1965); Preprints, Division of Petroleum Chemistry, 152nd National Meeting of the American Chemical Society, New York, N. Y., Sept 1966, p 133; *J. Phys. Chem.*, **70**, 2740 (1966).

lined above, as well as those of other experiments described later, showed the reactions of the activated adsorbent derived from BIS to be more complex than those of reactive silica prepared from pure Aerosil. However, inspection of all data showed the behavior of the BIS-derived samples to be due to a summation of two independent, although similar, sets of properties. The spectra showed that the surface structures related to the silica portion of the composite adsorbent, and their reactions, were entirely like those previously described^{5,6} for reactive silica prepared from pure Aerosil; a second set of structures and reactions was related to the boria portion. The adsorbent thus reacted as a composite, the silica, itself reactive, being a carrier for boria. Synergistic effects were not detected. Consequently, in the following description of the properties of the reactive BIS samples, attention is focused on the "reactive boria."

Surface Boranes. In close analogy to the activation of pure silica, the additional set of characteristics of the reactive BIS appears to be associated with the generation and destruction of surface hydrides; *i.e.*, the surface species absorbing near 2600 cm^{-1} . The three bands at 2621 , 2601 , and 2580 cm^{-1} fall in the range expected for B-H stretching vibrations¹⁵⁻¹⁷ and, in view of the results of experiments on isotopic substitution described later, there is little uncertainty in the assignment of these bands to surface borane groups. However, it is difficult to explain why three bands were formed. The assignment of two of the three bands to the asymmetric and symmetric stretching modes of $-\text{BH}_2$ groups, and that of the third band to the B-H stretch of a $=\text{B}-\text{H}$ group, must be rejected because (a) the two modes of $-\text{BH}_2$ usually are spaced about 100 cm^{-1} apart,¹⁵⁻¹⁷ and (b) the three bands were formed and destroyed independent of each other, as confirmed by the spectra of Figure 2. We must therefore conclude that each of the three bands is due to the B-H stretching mode of a particular surface $=\text{B}-\text{H}$ grouping.

The three types of $=\text{B}-\text{H}$ groups were distinguished by the obvious differences in the strength of the B-H bond, but the reasons for this are not known. Probably there were differences in the environment of the groups on the highly disorganized¹⁸ boria surface. This relation to surface topography is supported by the fact that the species absorbing at the higher wave numbers were formed during the later stages of reaction and were somewhat more tightly bonded, as their slower elimination bears out (Figure 2). However, the facts that (a) the band frequencies were constant while the bands formed and decayed, (b) the relative band intensities were constant, independent of the temperature of the initial degassing, and (c) the relative and absolute band intensities were reproduced when all the sample-preparation steps were reproduced, indicate that the three boranes were well defined energetically, much as if each

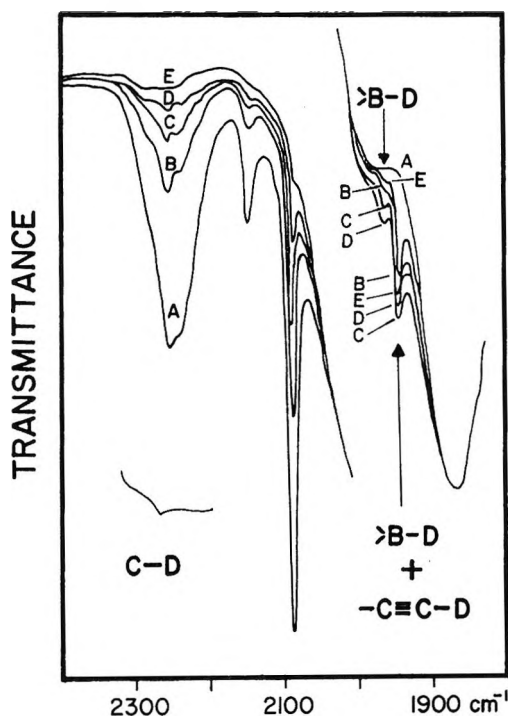


Figure 3. CD_3OD -treated BIS. The sample was methylated with CD_3OD , and then degassed at 250° for 15 min (A). The sample was then degassed at 800° for the following times in min: B, 1; C, 2; D, 5; E, 15.

of the $=\text{B}-\text{H}$ species were formed at a particular type of surface location. Conversely, if BIS is not taken as a mere dispersion of boria on silica, and $\text{Si}-\text{O}-\text{B}$ - and similar groupings are considered, the situation becomes somewhat more complex.

It is interesting to note that when diborane interacted with silica,¹⁹ the spectra always showed a strong band at 2580 cm^{-1} which Fripiat and Van Tongelen¹⁹ and Bavarez and Bastick²⁰ assigned to the stretching of a $=\text{B}-\text{H}$ group. Possibly a grouping like $\equiv\text{Si}-\text{O}-\text{BH}-\text{O}-\text{Si}\equiv$ was involved. Also, when other oxides were present in the silica, *e.g.*, alumina,¹⁹ the band shifted to 2585 cm^{-1} and new B-H bands at frequencies higher than 2600 cm^{-1} were found. A close comparison of past and present results and the assignment of each of the three bands to a specific surface location cannot be attempted because the wave number domain of the bands is too narrow to ascertain a precise distribution.¹⁹ However, the appearance of the three bands caused by three

(15) L. J. Bellamy, "Advances in Infrared Group Frequencies," Methuen & Co. Ltd., London, 1968, p 118.

(16) N. B. Colthup, L. H. Daly, and S. E. Wiberly, "Introduction to Infrared and Raman Spectroscopy," Academic Press, New York, N. Y., 1964, p 291 ff.

(17) R. M. Adams in "Boron, Metallo-Boron Compounds and Boranes," R. M. Adams, Ed., Interscience Publishers, New York, N. Y., 1964, p 507 ff.

(18) See the discussion on the structure of boria in ref 17, p 54 ff.

(19) J. J. Fripiat and M. Van Tongelen, *J. Catal.*, **5**, 158 (1966), and references therein.

(20) M. Bavarez and J. Bastick, *Bull. Soc. Chim. Fr.*, 3226 (1964).

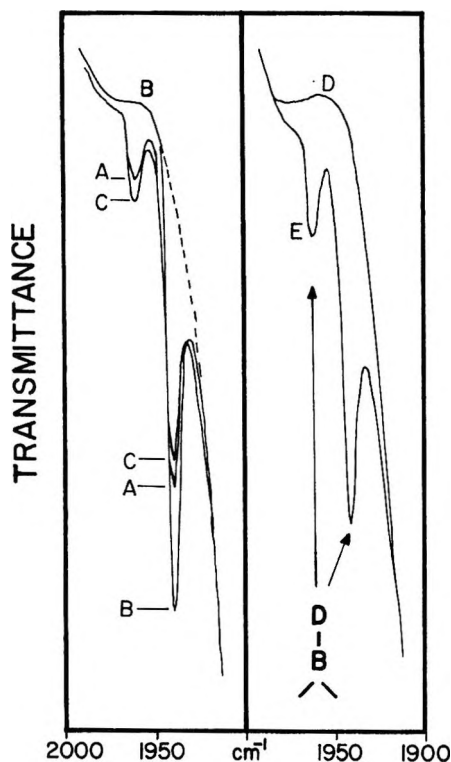


Figure 4. Isotope exchange. A BIS sample was methylated with CD_3OD and degassed for 15 min at 800° (A) and 15 hr at 800° (B). The sample was then exposed to 25 Torr D_2 at 700° for 2 hr (C), degassed and exposed to 35 Torr H_2 at 700° for 2 hr (D), and finally exposed to 30 Torr D_2 at 700° for 2 hr (E).

slightly varying $=\text{B}-\text{H}$ structures points to the importance of different local surface conditions, a familiar concept in heterogeneous catalysis.

Isotope Effects. When CD_3OD was used for methylation, the subsequent pyrolysis of surface $\text{CD}_3\text{O}-$ groups produced absorptions in the $200-1900\text{-cm}^{-1}$ range, as would be expected for $\text{B}-\text{D}$ stretching modes. However, as shown by the spectra of Figure 3, only two bands at 1957 and 1937 cm^{-1} were formed. The 1937-cm^{-1} band was the more intense and was superimposed on the band of the $\text{C}\equiv\text{C}$ mode of the surface deuterioacetylide⁵ formed during the pyrolysis. Consequently, additional experiments were carried out in order to resolve the spectra.

The pyrolyzed sample, which contained the $=\text{B}-\text{D}$ groups and a few $-\text{C}\equiv\text{C}-\text{D}$ groups (spectrum A, Figure 4), was degassed at 800° for 15 hr. The spectrum then showed only the 1937-cm^{-1} $\text{C}=\text{C}$ band (spectrum B, Figure 4). Deuterium was admitted and allowed to react at 700° for 2 hr, so that the acetylenic structure was destroyed⁵ and the surface $=\text{B}-\text{D}$ groups were partially re-formed (spectrum C, Figure 4). Hydrogen was then introduced and allowed to react for 2 hr at 700° , with the result (spectrum D) that the $=\text{B}-\text{D}$ groups were converted to $=\text{B}-\text{H}$ groups, the spectrum of the hydrogenated sample showing the usual three $=\text{B}-\text{H}$ bands. Finally, these $=\text{B}-\text{H}$ groups were

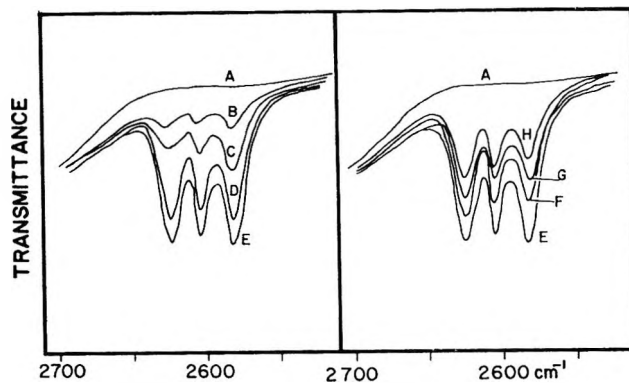


Figure 5. Reaction with H_2 . A BIS sample was methylated, pyrolyzed, and degassed for 30 hr at 800° , removing all boranes (A). The sample was then exposed to 40 Torr H_2 : B, 650° , 30 min; C, 650° , 2 hr; D, 700° , 1 hr; E, 700° , 3 hr. The sample was then degassed at 800° for 20 hr and exposed to 40 Torr H_2 at 700° for 15 hr (F). That cycle was repeated twice (G, H).

again converted to $=\text{B}-\text{D}$ groups with deuterium, the spectrum (E, Figure 4) showing bands at 1957 and 1937 cm^{-1} . The experiment showed that even if all three surface boranes were formed, only two bands could be resolved in the $\text{B}-\text{D}$ region. However, the second group of $=\text{B}-\text{H}$ bands, *i.e.*, those re-formed subsequent to the removal of the $=\text{B}-\text{D}$ groups formed during the initial pyrolysis, was of comparable intensity (like the bands shown in Figure 5), while the 1937-cm^{-1} $=\text{B}-\text{D}$ band was more intense than the 1957-cm^{-1} band even when the contribution of the $\text{C}\equiv\text{C}$ mode to the 1957-cm^{-1} band had been removed. These effects suggest that the 1937-cm^{-1} band resulted from the superimposition of two of the three $\text{B}-\text{D}$ modes, the third being resolved at 1957 cm^{-1} . The experiments also prove that the surface boranes could exchange completely in about 2 hr at 700° . The exchange reaction occurred at temperatures as low as 500° , but more slowly.

Reaction with Hydrogen. The elimination of the surface boranes by degassing leaves at least a part of the boron surface reactive to molecular hydrogen, but only at temperatures above 650° . When a pyrolyzed and degassed BIS sample was heated in hydrogen at temperatures below 500° , only the formation of $\text{Si}-\text{H}$ groups absorbing at 2227 cm^{-1} was observed;⁶ the normal⁶ formation of SiH_2 and $\text{Si}-\text{OH}$ groups occurred on heating at $500-650^\circ$. However, the three $=\text{B}-\text{H}$ species were formed on heating at temperatures higher than 650° . These three "secondary" $=\text{B}-\text{H}$ bands were centered at the same frequencies, but with different relative intensities, as the "primary" $=\text{B}-\text{H}$ bands produced by the initial pyrolysis (Figure 5). Over 10 hr was required to form the secondary bands at 650° . The reaction was faster at higher temperatures. However, in contrast to the primary generation of the boranes (Figure 2), the three secondary boranes were formed at more nearly the same rates (Figure 5). This

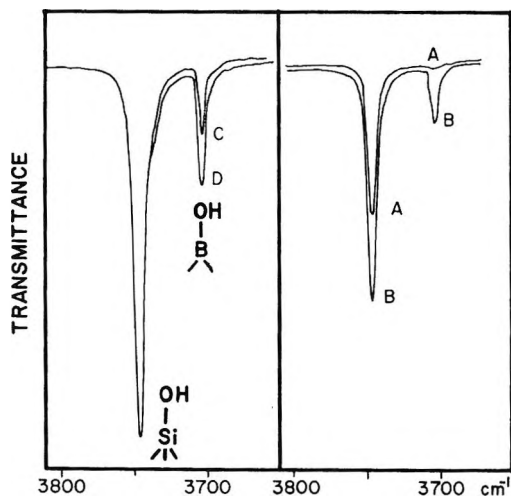


Figure 6. Formation of hydroxyls. Spectra A, B correspond to spectra A, E, respectively, of Figure 5. Spectra C, D were obtained with a BIS sample which had *not* been methylated but had been degassed at 800° for 35 hr (C), and then exposed to 40 Torr H₂ at 700° for 15 hr (D).

would mean that the differences in rates observed during the primary borane generation (Figure 2) reflect mainly differences in the rates of production of the sites at which the boranes could form. The intensity of the 2580-cm⁻¹ band was smaller (spectrum E, Figure 5) and comparable to the intensities of the other two bands, suggesting that the site responsible for the formation of the particular borane species had become partially "annealed" during the degassing step. Such annealing was general, and on repeating the degassing-rehydrogenation cycle several times (spectra E-H, Figure 5), some sites were made unreactive. The bands became progressively weaker, the intensity decline being faster for the species absorbing at the lower frequencies.

Surface B-OH groups were not formed during the pyrolysis (Figure 1), and it appears that the elimination of the boranes did not occur through a mechanism involving B-OH groups. On the other hand, the reaction of hydrogen with the reactive BIS led not only to the formation of the boranes but also to the formation of some free surface B-OH groups, shown by the appearance of a band at 3703 cm⁻¹ (spectra A, B, Figure 6). To clarify this situation, some additional experiments were carried out with BIS which had *not* been methylated. Such an untreated BIS sample was degassed for several hours at 800° and then exposed to hydrogen at temperatures ranging from 650 to 750°. In addition to the formation of silane and other effects described elsewhere,²¹ some B-OH groups were formed (spectra C, D, Figure 6). However, =B-H groups were not formed after this treatment nor after several successive degassing-hydrogenation cycles. The results indicate that the formation of some B-OH groups was independent of the formation of boranes, and was a general

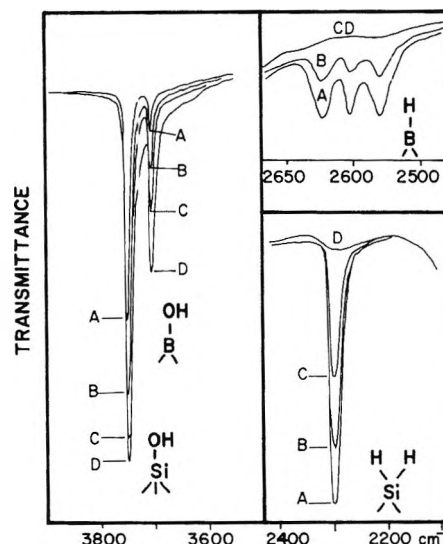


Figure 7. Reaction with O₂. A BIS sample was activated and exposed to H₂ so that the boranes were re-formed (A). The sample was then exposed to 100 Torr O₂: B, 450°, 3 hr; C: 450°, 16 hr; D: 650°, 1 hr.

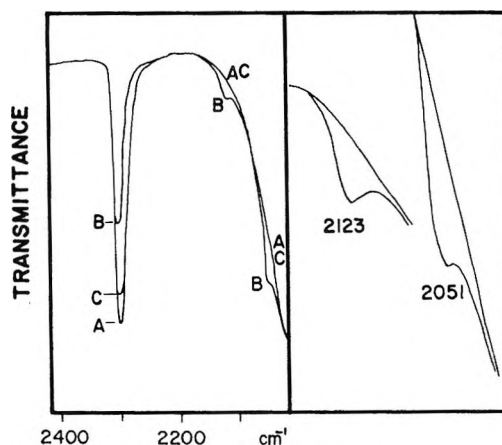


Figure 8. Weak bands. A: spectrum of BIS sample which had been activated and rehydrogenated with 30 Torr H₂ at 700° for 10 hr. B: after degassing for 22 hr at 800°. C: after exposure to 30 Torr H₂ at 700° for 19 hr. The right part of the figure shows the scale-expanded peaks at 2123 and 2051 cm⁻¹.

characteristic of borica-containing silica. This result is important from the mechanistic point of view, and could explain why the 3703-cm⁻¹ B-OH groups can be completely removed by prolonged outgassing at high temperature, while the Si-OH groups—which apparently cannot eliminate hydrogen but are destroyed through the elimination of H₂O—cannot be completely removed from silica surfaces. Also, the capacity for forming surface boranes was not a general characteristic of BIS, but was a property which was fully acquired only during the thermal collapse of the B-

(21) C. Morterra and M. J. D. Low. *Chem. Commun.*, 1491 (1968).

OCH₃ groups and which was slowly lost through some annealing process.

Reaction with Water. When activated BIS was exposed to water vapor at room temperature, the effects described for reactive silica were observed.⁶ Boranes present on the surface were immediately hydrolyzed, forming surface B-OH groups absorbing near 3700 cm⁻¹.

Reaction with Oxygen. The oxidation of the boranes with molecular oxygen began at 350°, a temperature somewhat higher than that necessary for the start of the oxidation of silanes.⁶ The borane oxidation was completed in 2 hr at 500° and in about 15 hr at 430°. The latter was not high enough to permit the complete oxidation of the silanes. A sharp band due to B-OH groups was formed at 3703 cm⁻¹ (Figure 7). The B-OH groups apparently were still formed after all boranes had been destroyed and while the remainder of the silanes were being oxidized (spectra C, D, Figure 7). This would suggest that some water was formed during the oxidation of silanes, the water then reacting with boria to produce B-OH groups. This apparently contradicts earlier results, which led to the conclusion that silane oxidation resulted in the formation of localized silanols.⁶ However, the B-OH band is overlapped by the tailing of the Si-OH band (spectra C, D, (Figure 7), so that the actual increase of the B-OH band was small.

2123- and 2051-Cm⁻¹ Bands. Two very weak absorptions were formed at 2051 and 2123 cm⁻¹ (Figure 8) when activated BIS was degassed for long periods near 800°. The bands were not formed near 700° during degassing periods up to 70 hr. The assignment of these bands is uncertain, even though it is known that (a) the formation of the bands was connected with the presence of boron, because they did not form at all on degassing pure silica; (b) they were somehow connected with the destruction of the surface boranes, because they were not observed with BIS samples which had not been subjected to the methylation-pyrolysis steps; they were not caused by a hydrogen-containing mode, because their position was unchanged with samples activated through reaction with CD₃OD. The two bands were eliminated by reaction with hydrogen above 400°, but the product is unknown. The frequency range and the above observations suggest that structures²² of the type -B=O, similar to those observed by Fripiat and Van Tongelen¹⁹ during the first stages of the reaction of diborane with silica-alumina, might be responsible for the bands, but the evidence for this assignment is weak.

Acknowledgment. Support by a grant from the National Center for Air Pollution Control is gratefully acknowledged.

(22) J. D. Mackenzie, *Trans. Faraday Soc.*, **52**, 1564 (1956); *J. Phys. Chem.*, **63**, 1875 (1959).

Thermodynamics of Globular Molecules. XVII. Heat Capacities and Transition Behavior of Bicyclo[2.2.2]octane and Bicyclo[2.2.2]octene¹

by Wen-Kuei Wong² and Edgar F. Westrum, Jr.³

Department of Chemistry, University of Michigan, Ann Arbor, Michigan 48104 (Received November 3, 1969)

The thermal properties of two globular molecules, bicyclo[2.2.2]octane and bicyclo[2.2.2]oct-2-ene, have been determined from 5°K into their liquid ranges (465°K and 411°K, respectively). The former undergoes a solid-solid phase transition at 164.25°K and melts at 447.48°K. The associated entropy increments, $\Delta S_t = 6.66$ cal/mol °K and $\Delta S_m = 4.48$ cal/mol °K, are positive evidence that the material is a plastic (or embefic) crystal. The octene undergoes solid-solid phase transitions at 110.50°K and at 176.47°K and melts at 389.75°K. The sum of the entropies of transition, 8.44 cal/mol °K, and the low entropy of fusion, 2.43 cal/mol °K, are evidence that this material is also an embefic crystal. Mechanistic considerations, consistent with the molecular geometries, that accord with the observed transitional entropies are presented. The standard molal value of heat capacities, entropies, and Gibbs energy functions for the crystalline octane and octene are 37.69, 37.46; 50.18, 50.30; and -25.68, -24.63 cal/mol °K, respectively, at 298.15°K. The standard Gibbs energies of formation are 18.21 kcal/mol of bicyclooctane and 38.48 kcal/mol of bicyclooctene, also at 298.15°K.

Introduction

Several of the previous papers in this series⁴ have reported the results of thermal studies on globular molecules whose geometry is related to that of bicyclo[2.2.2]octane. This family of open, cagelike structures is of particular interest because the thermodynamics describing the transition and fusion phenomena can be linked to subtle variations in the symmetry of the cage. The entropy values for transition and fusion of several of these compounds have been included in a recent review.⁵ This paper presents the results for the octane, bicyclo[2.2.2]octane, and the octene, bicyclo[2.2.2]oct-2-ene, and related substances and will cover the experimental data on which the review article was based and will discuss further mechanistic interpretations of the transitional entropy increments.

Of the several compounds in this family the octane can, with some logic, be considered the prototype and has been reported to possess either D_{3h} or C_3 symmetry.⁶ The latter formulation would provide a mechanism for strain relief. It has the most symmetrical cage structure and exhibits all the properties normally associated with embefic crystals.⁷ In the closely related octene, the threefold axis passing through the bridgehead carbons is lacking so that it is only an "almost" symmetrical-top type of molecule. The nature of the transitions in these materials has drawn the attention of several groups and three interpretations have been made.⁸⁻¹⁰

Experimental Section

A crude sample of the octane was obtained from the Hi Laboratory, Inc., and was subjected to multiple fractional sublimation followed by 20 passes of zone-melting refining. The elemental analysis results were 87.07% C and 12.75% H and are in satisfactory accord

with theoretical values of 87.19% and 12.81%. A sample (52.5856 g vacuum mass) of this material was sublimed into calorimeter W-42 for the cryogenic thermal measurements; and a sample (53.1178 g vacuum mass) into calorimeter W-22 for the intermediate temperature-range measurements covering the fusion region.

The octene was also obtained from the Hi Laboratory, Inc., and was treated in a similar manner. No impurities were detected by vapor-phase chromatography and the elemental analyses, 88.69% C and 11.05% H, accord well with the theoretical values, 88.82% and 11.18%. The cryogenic thermal measurements were conducted on a sample (22.5552 g vacuum mass) that had been sublimed into calorimeter W-37. A sample (36.2478 g vacuum mass) contained in calorimeter W-

(1) This work was supported in part by the Division of Research, United States Atomic Energy Commission.

(2) Abstracted in part from a dissertation submitted in partial fulfillment of the requirements for the Ph.D. degree from the Horace H. Rackham School of Graduate Studies at the University of Michigan.

(3) To whom correspondence concerning this paper should be addressed.

(4) S. S. Chang and E. F. Westrum, Jr., *J. Phys. Chem.*, **64**, 1551 (1960); C. M. Barber and E. F. Westrum, Jr., *ibid.*, **67**, 2373 (1963); J. C. Trowbridge and E. F. Westrum, Jr., *ibid.*, **67**, 2381 (1963); C. A. Wulff and E. F. Westrum, Jr., *ibid.*, **68**, 430 (1964).

(5) E. F. Westrum, Jr., "Thermochemistry and Thermodynamics" in "Annual Review of Physical Chemistry," Vol. 18, H. Eyring, Ed., Annual Reviews, Inc., Palo Alto, Calif., 1967, p 135.

(6) O. Ermer and J. D. Dunitz, *Chem. Commun.*, **10**, 567 (1968); A. F. Cameron, G. Ferguson, and D. G. Morris, *ibid.*, **6**, 316 (1968).

(7) C. A. Wulff, cited in ref 5 (p 137).

(8) I. Darmon and C. Brot, *Mol. Cryst.*, **2**, 301 (1967).

(9) L. M. Amzel and L. N. Becka, *J. Phys. Chem. Solids*, **30**, 521 (1969).

(10) J. A. Pople and F. E. Karasz, *ibid.*, **18**, 28 (1961).

Table I: Experimental Heat Capacity Determinations on Bicyclo[2.2.2]octane and Bicyclo[2.2.2]octene-2^a

\bar{T}	C_p	\bar{T}	C_p	\bar{T}	C_p	\bar{T}	C_p	\bar{T}	C_p	\bar{T}	C_p		
Bicyclo[2.2.2]octane						140.97	20.53	292.77	36.93	46.40	8.438		
Data Taken in Mark II Calorimetric Cryostat						147.49	21.34	302.10	37.99	51.16	9.173		
Series I		Series II		11.06	0.5577	155.12	22.44	311.48	39.12	56.41	9.889		
103.55	16.46	139.37	20.04	12.22	0.7561	164.34	24.54	320.80	40.21	62.14	10.62		
111.87	17.20	ΔH_f Run A		13.48	1.038	172.36	44.54	330.06	41.31	68.21	11.29		
120.67	18.06			14.82	1.376	175.87	464.9	339.27	42.45	75.12	12.02		
129.99	18.99			16.25	1.769	176.41	793.4	Series V		83.17	12.97		
139.37	20.07	Series III		17.88	2.262	177.04	393.4	151.76	21.95	91.91	14.45		
148.32	21.67	141.05	20.30	19.90	2.908	180.29	50.48	161.45	23.59	Series VIII			
156.47	27.96	145.88	21.04	22.12	3.639	Series II		$\Delta_2 H_f$ Run A		ΔH Run (I)			
162.16	62.40	150.52	22.38	24.46	4.412	115.43	20.13	184.44	28.70	86.52	13.43		
164.60	227.5	154.81	25.80	27.22	5.301	121.52	18.90	194.37	28.12	92.96	14.68		
165.50	291.3	158.45	34.65	30.45	6.275	128.82	19.24	204.23	28.70	97.46	16.49		
166.71	145.9	161.39	55.52	34.09	7.298	136.56	20.04	Series VI		102.04	18.30		
169.56	56.67	163.34	129.2	38.06	8.284	144.69	21.02	154.35	22.35	106.85	20.64		
175.17	29.32	164.16	423	42.28	9.196			162.73	24.09	111.46	21.98		
183.15	25.90	164.56	413	46.65	10.04			184.03	28.74	116.04	20.13		
192.17	26.35	165.08	255	51.52	10.87	Series III		$\Delta_2 H_f$ Run B		120.78	18.90		
201.57	27.10	165.80	204	56.78	11.64	103.65	19.20	184.03	28.74	125.55	18.97		
211.20	27.90	167.05	93.0	62.28	12.40	111.68	21.55	Series VII		130.23	19.37		
220.79	28.84	169.45	45.2	68.32	13.12	120.66	19.04	5.96	0.0533	145.67	21.17		
230.61	29.78	172.89	30.46	75.27	13.85	130.07	19.35	6.75	0.0835	155.42	22.55		
240.62	30.87	176.85	26.01	83.50	14.71	139.28	20.34	7.72	0.1416	$\Delta_2 H_f$ Run C			
250.32	31.88	181.04	25.81	92.63	15.57	148.34	21.51	8.68	0.2240	183.18	32.03		
259.83	32.96	185.23	25.83	102.25	16.38	157.46	22.89	9.64	0.3214	193.99	28.13		
269.12	34.00			ΔH Run		166.38	25.58	10.64	0.4389	204.31	28.71		
278.46	35.18	Series IV		138.35	19.96	173.06	58.68	11.69	0.5799	213.64	29.33		
287.72	36.41			Series V		175.73	496.6	13.00	0.7977	222.77	30.08		
296.88	37.57	5.24	0.0371	ΔH_f Run B		176.28	644.2	14.45	1.084	230.60	30.61		
306.21	38.71	6.25	0.0636	Series VI		177.18	278.0	15.90	1.405	Series IX			
315.60	40.00	7.07	0.1022	140.30	20.22	181.74	34.79	17.50	1.791	110.00	22.01		
324.73	41.25	7.96	0.1685	ΔH_f Run C		190.87	27.99	19.09	2.200	110.99	22.21		
333.66	42.25	8.95	0.2707			201.12	28.55	20.61	2.603	111.97	22.06		
342.38	43.51	9.99	0.4111			Series IV		22.29	3.057	$\Delta_{1,2} H_f$ Run D			
Data Taken in Mark IV Calorimetric Thermostat						231.49	30.83	24.22	3.591	Series X			
Series VII		446.82	1940	456.22	63.29	243.41	31.82	26.68	4.249	81.27	12.74		
309.31	39.13	446.95	2080	461.56	63.73	254.01	32.83	29.62	5.006	88.46	13.79		
319.73	40.58	447.05	3200	466.72	63.99	264.06	33.83	32.86	5.804	$\Delta_1 H_f$ Run A			
330.00	42.00	447.12	3700	471.87	64.73	Data Taken in Mark IV Calorimetric Thermostat							
340.14	43.30	448.64	188	477.00	65.64	Series XI		389.20	1001	ΔH_m Run A			
350.04	44.71	Series IX		482.14	66.14	294.59	36.50	389.81	309.4	Series XV			
359.79	45.96	ΔH Run 1		Series XII		302.49	37.60	392.47	53.17	ΔH_m Run B			
369.36	47.27	ΔH Run 2		ΔH Run 3		311.37	38.69	396.76	53.61	362.53	45.25		
378.94	48.53	426.95	55.18	413.20	53.28	320.34	39.72	402.69	54.49	371.09	46.53		
Series VIII		ΔH_f Run A		423.11	54.54	329.41	40.86	Series XIII		Series XVI			
ΔH Run 1		Series X		428.86	55.59	338.30	41.98	299.39	37.15	380.89	49.37		
382.36	49.03	418.57	53.89	433.96	56.40	347.01	43.18	307.94	38.40	384.29	63.56		
392.03	50.25	427.85	55.40	438.45	56.97	355.47	44.23	ΔH Run (I)		386.60	125.1		
401.64	51.62	ΔH_f Run B		442.80	61.30	363.66	45.41	370.70	46.52	387.87	249.8		
411.20	52.94			ΔH_f Run D		371.71	46.50	379.70	50.65	388.57	471.8		
420.65	54.25			450.65	62.47	379.60	48.13	385.52	81.67	388.97	799.1		
429.91	55.67	Series XI		454.89	62.84	385.35	78.95	387.33	177.7	389.21	1273		
438.97	57.21	430.93	55.83	459.12	63.54	387.85	255.6	388.21	334.0	389.41	1185		
445.00	200.0	ΔH_f Run C		463.33	63.86	388.81	621.8	388.72	586.1	391.04	55.52		
446.65	1210			Series XII						389.03	935.3	391.04	55.52
Bicyclo[2.2.2]octene						378.00	47.86	389.20	1911	394.68	53.52		
Data Taken in Mark III Calorimetric Cryostat						382.45	53.20	389.38	997.1	399.11	53.70		
Series I		273.76	34.87	36.64	6.642	385.97	92.46	Series XIV		403.72	54.77		
136.41	19.98	283.37	35.83	41.40	7.577	387.93	252.4	Series V		408.29	55.17		
						388.79	551.0	368.88	46.22				

^a Units: cal, mol, °K.

Table II: Thermodynamic Properties of Bicyclo[2.2.2]octane and Bicyclo[2.2.2]octene-2^a

\bar{T}	C_p	S°	$H^\circ - H^\circ_0$	$-(G^\circ - H^\circ_0)/\bar{T}$	\bar{T}	C_p	S°	$H^\circ - H^\circ_0$	$-(G^\circ - H^\circ_0)/\bar{T}$
Bicyclo[2.2.2]octane					460	63.49	75.50	17222	38.06
Crystal II Phase					470	64.69	76.88	17863	38.87
5	0.032	0.010	0.039	0.003	Bicyclo[2.2.2]octene-2				
10	0.400	0.108	0.847	0.024	Crystal II				
15	1.420	0.442	5.125	0.100	5	0.026	0.009	0.034	0.002
20	2.940	1.050	15.888	0.256	10	0.355	0.101	0.785	0.022
25	4.590	1.884	34.728	0.495	15	1.203	0.388	4.471	0.090
30	6.147	2.861	61.626	0.807	20	2.438	0.897	13.47	0.224
35	7.530	3.915	95.898	1.175	25	3.799	1.587	29.058	0.425
40	8.722	5.000	136.61	1.585	30	5.106	2.397	51.363	0.685
45	9.740	6.088	182.82	2.025	35	6.282	3.274	79.893	0.992
50	10.62	7.160	233.77	2.485	40	7.311	4.182	113.94	1.333
60	12.08	9.230	347.53	3.438	45	8.209	5.096	152.79	1.701
70	13.31	11.19	474.65	4.407	50	9.000	6.003	195.85	2.086
80	14.37	13.04	613.18	5.371	60	10.355	7.767	292.84	2.887
90	15.31	14.78	761.69	6.321	70	11.484	9.451	402.20	3.705
100	16.18	16.44	919.15	7.251	80	12.567	11.053	522.30	4.524
110	17.05	18.02	1085.2	8.159	Lower Transition Region				
120	17.98	19.55	1260.3	9.045	90	14.022	12.607	654.41	5.336
130	18.99	21.03	1445.1	9.910	100	17.120	14.230	808.71	6.143
Transition Region					110	22.170	16.094	1005	6.961
140	20.15	22.47	1641	10.76	110.50	22.450	16.196	1016	7.002
150	22.06	23.92	1850	11.59	120	19.042	17.888	1211	7.800
160	42.20	25.70	2130	12.41	130	19.347	19.415	1401	8.640
164.25	540	28.22	2540	12.78	140	20.433	20.887	1599	9.462
170	41.40	33.14	3350	13.42	150	21.709	22.340	1810	10.273
180	25.82	34.82	3650	14.56	160	23.445	23.791	2035	11.072
Crystal I Phase					Crystal I				
190	26.18	36.22	3905	16.66	170	31.65	25.343	2292	11.864
200	26.97	37.58	4171	16.72	176.47	(807)	27.798	2721	12.378
210	27.82	38.91	4445	17.74	180	59.20	29.791	3075	12.710
220	28.74	40.22	4728	18.73	Higher Transition Region				
230	29.73	41.52	5020	19.70	190	27.958	35.980	4178	13.988
240	30.78	42.81	5322	20.64	200	28.445	37.425	4460	15.124
250	31.77	44.09	5636	21.55	210	29.106	38.829	4748	16.220
260	32.99	45.36	5960	22.44	220	29.841	40.200	5043	17.279
270	34.15	46.63	6296	23.31	230	30.635	41.544	5345	18.305
273.15	34.53	47.02	6404	23.58	240	31.497	42.865	5656	19.300
280	35.36	47.89	6643	24.17	250	32.429	44.169	5975	20.269
290	36.63	49.16	7003	25.01	260	33.420	45.460	6304	21.213
298.15	37.69	50.18	7306	25.68	270	34.452	46.74	6643	22.135
300	37.93	50.42	7376	25.83	273.15	34.783	47.143	6753	22.421
310	39.26	51.68	7762	26.65	280	35.507	48.013	6993	23.037
320	40.60	52.95	8161	27.45	290	36.576	49.278	7354	23.920
330	41.93	54.22	8574	28.24	298.15	37.457	50.304	7656	24.627
340	43.26	55.49	8999	29.02	300	37.659	50.536	7725	24.786
350	44.59	56.76	9439	29.79	310	38.767	51.789	8107	25.637
360	45.95	58.04	9891	30.56	320	39.911	53.037	8500	26.473
370	47.33	59.32	10358	31.32	330	41.096	54.283	8905	27.297
380	48.71	60.60	10838	32.08	340	42.318	55.528	9322	28.109
390	50.07	61.88	11332	32.83	350	43.568	56.773	9752	28.910
400	51.40	63.17	11839	33.57	360	44.871	58.018	10194	29.702
410	52.72	64.45	12360	34.31	370	46.344	59.268	10650	30.484
420	54.15	65.74	12894	35.04	380	48.67	60.527	11120	31.258
430	55.72	67.03	13443	35.76	389.75	(48.97)	61.680	11565	32.016
440	(57.35)	68.32	14008	36.49	Liquid				
447.12	(58.38)	69.25	14419	37.00	389.75	(52.75)	65.123	12851	32.150
Liquid Phase					395	53.50	65.77	13159	32.46
447.12	(61.93)	73.73	16415	37.00	400	53.70	66.45	13428	32.88
450	62.29	74.12	16593	37.24	405	54.32	67.12	13698	33.30
					500	56.05	67.80	13974	33.71

^a Units: cal, mol, °K.

Table III: Enthalpy Increments of Transition and Melting for Bicyclo[2.2.2]octane and Bicyclo[2.2.2]octene-2^a

Source of data	Number of runs	T_1	T_2	$H_{T_2} - H_{T_1}$	$H_{190} - H_{135}$	Source of data	Number of runs	T_1	T_2	$H_{T_2} - H_{T_1}$	$H_{192} - H_{160}$
Bicyclo[2.2.2]octane Transition						Bicyclo[2.2.2]octene-2 Transition II					
Series I	10	134.80	187.55	2300	2362	Series I	6	159.55	177.38	1957	2199
Series II	2	134.62	188.67	2338	2365	Series III	7	162.10	185.69	2247	2199 ^b
Series III	17	138.61	187.33	2225	2366	Series V	3	156.74	189.39	2202	2200
Series V	2	133.69	189.19	2368	2364	Series VI	3	158.66	188.68	2135	2198
Series VI	2	135.70	189.39	2333	2363	Series VIII	3	160.18	199.61	2409	2200
Average value $H_{190} - H_{135} = 2364 \pm 1$						Average value $H_{192} - H_{160} = 2199 \pm 1$					
Graphical integration $H_{190} - H_{135} = 2364$						Graphical integration $H_{192} - H_{160} = 2200$					
Lattice contribution $H_{190} - H_{135} = 1268$						Lattice contribution $H_{192} - H_{160} = 849$					
$\Delta H_t = 1096$						$\Delta_{IT}H_t = 1350 \pm 1$					
$\Delta S_t = 6.66$						$\Delta_{IT}S_t = 7.66$					
$T_t = 164.25$						${}_{IT}T_t = 176.47$					
Source of data	Number of runs	T_1	T_2	$H_{T_2} - H_{T_1}$	$H_{395} - H_{375}$	Source of data	Number of runs	T_1	T_2	$H_{T_2} - H_{T_1}$	$H_{450} - H_{435}$
Bicyclo[2.2.2]octene-2 Melting						Bicyclo[2.2.2]octane Melting					
Series XII	8	375.68	394.63	2216	2276 ^b	Series VIII	8	434.47	450.13	2929	2872 ^b
Series XIV	1	373.13	391.79	2192	2276	Series IX	1	430.19	449.59	3116	2871
Series XV	1	375.33	393.55	2183	2276	Series X	1	432.44	451.94	3136	2870
Average value $H_{395} - H_{375} = 2276 \pm 0$						Average value $H_{450} - H_{435} = 2870 \pm 1$					
Graphical integration $H_{395} - H_{375} = 2275$						Graphical integration $H_{450} - H_{435} = 2870$					
Lattice contribution $H_{395} - H_{375} = 990$						Lattice contribution $H_{450} - H_{435} = 875$					
$\Delta H_m = 1286 \pm 0$						$\Delta H_m = 1995 \pm 1$					
$\Delta S_m = 2.43$						$\Delta S_m = 4.48$					
$T_m = 389.75$						$T_m = 447.48$					
Average value $H_{125} - H_{80} = 783 \pm 1$						Average value $H_{125} - H_{80} = 783 \pm 1$					
Graphical integration $H_{125} - H_{80} = 783$						Graphical integration $H_{125} - H_{80} = 783$					
Lattice contribution $H_{125} - H_{80} = 738$						Lattice contribution $H_{125} - H_{80} = 738$					
$\Delta_{IT}H_t = 45 \pm 1$						$\Delta_{IT}H_t = 45 \pm 1$					
$\Delta_{IT}S_t = 0.78$						$\Delta_{IT}S_t = 0.78$					
${}_{IT}T_t = 110.50$						${}_{IT}T_t = 110.50$					
Source of data	Number of runs	T_1	T_2	$H_{T_2} - H_{T_1}$	$H_{125} - H_{80}$	Source of data	Number of runs	T_1	T_2	$H_{T_2} - H_{T_1}$	$H_{125} - H_{80}$
Bicyclo[2.2.2]octene-2 Transition I						Bicyclo[2.2.2]octene-2 Transition I					
Series VIII	9	82.45	127.92	809	784	Series VIII	9	82.45	127.92	809	784
Series IX	3	76.64	123.99	806	783	Series IX	3	76.64	123.99	806	783

^a Units: cal, mol, °K. ^b A correction has been made for quasi-adiabatic conditions.

22 was utilized for the intermediate range thermal measurements extending through the fusion region.

The cryostats¹¹ (Mark II for the octane and Mark III for the octene) and the intermediate range thermostat¹² (Mark IV) have been described previously. The circuitry used to maintain adiabaticity as well as the calculational procedures have also been reported.¹¹

Results

The measured heat capacities are presented in Table I at the mean temperatures of each determination. The data are stated in terms of the defined thermochemical calorie equal to 4.1840 abs. J and an ice point of 273.15°K, and are presented in chronological sequence to facilitate estimation of temperature increments for measurements within a given series. Except in regions containing heat capacity anomalies, these have been corrected for curvature. Probable errors decrease from 5% at the lowest temperatures to 1% at 10°K and to 0.1%, or less, above 25°K. The data are depicted in Figures 1 and 2.

The molal values of the thermodynamic functions are presented in Table II. These were obtained from suitable integrations of computer-fitted polynomials through the data points with extrapolations below 5°K obtained from the Debye limiting T^3 relation. Increments through transition and fusion regions were integrated from large scale plots of the data. The probable errors in the derived functions are comparable to those in the heat capacities themselves.

The octane undergoes a solid-solid phase transition at 164.25°K. The process is apparently first order with heat capacities as high as 540 cal/mol °K and with characteristically slow thermal equilibration.

(11) E. F. Westrum, Jr., G. T. Furukawa, and J. P. McCullough, "Adiabatic Low-Temperature Calorimetry" in "Experimental Thermodynamics" J. P. McCullough and D. W. Scott, Ed., Butterworth and Co., Ltd., London, 1968.

(12) E. D. West and E. F. Westrum, Jr., "Adiabatic Calorimetry from 300 to 800°K" in "Experimental Thermodynamics," J. P. McCullough and D. W. Scott, Ed., Butterworth and Co., Ltd., London, 1968.

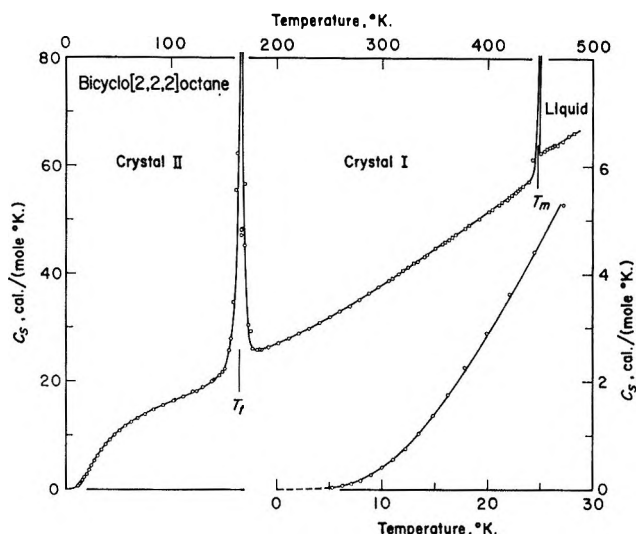


Figure 1. The heat capacity of bicyclo[2.2.2]octane.

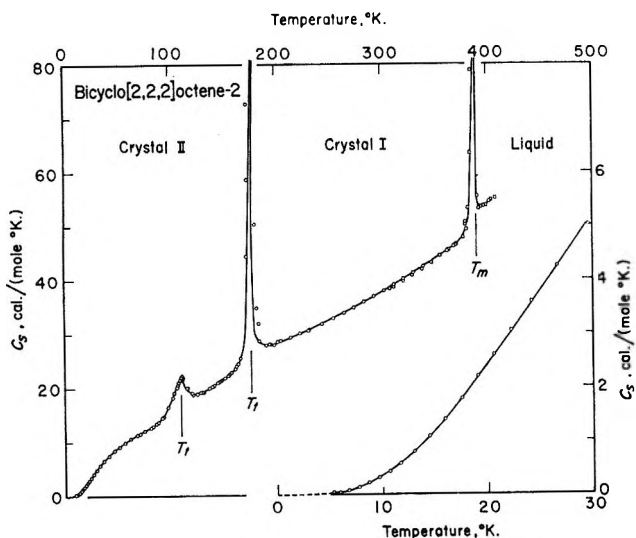


Figure 2. The heat capacity of bicyclo[2.2.2]octene-2.

Drifts extending from 10 to 14 hr were required for equilibrium. Six series of measurements through the transition region are listed in Table III. The crystal I phase melted at 447.48°K with ΔS_m equal to 4.48 cal/mol °K. Bartlett and Woods¹³ have reported 169–170°C as the melting temperatures. The ΔH_m value is based on five series of determinations also listed in Table III, while the melting temperature is derived from a fractional melting analysis presented in Table IV. Implicit in that analysis is the absence of solid-solid formation between octane and its 0.0014 mole fraction of total impurity.

The course of the solid-state heat capacities of the octene is marked by two thermal anomalies with apparent maxima at 110.50°K and 176.47°K. That the former is a higher than first-order transition is evidenced by the rapid attainment of equilibrium and hump-like shape. The rate of attainment of thermal

Table IV: Fractional Melting Data for Bicyclo[2.2.2]octane and Bicyclo[2.2.2]octene-2^a

T	C_s	ΔT	$\Sigma \Delta H$	T_{final}	$1/F$
Bicyclo[2.2.2]octane ^b					
446.65	1210	0.210	693	446.70	2.879
446.82	1940	0.132	948	446.89	2.104
446.95	2080	0.122	1203	447.01	1.658
447.05	3200	0.080	1459	447.09	1.368
447.12	3660	0.070	1715	447.16	1.163
Triple point of sample 447.190					
Triple point of pure compound 447.476					
Mole fraction impurity 0.0014					
Bicyclo[2.2.2]octene-2 ^c					
388.21	334	0.638	479	388.53	2.683
388.72	586	0.375	699	388.91	1.840
389.03	935	0.238	929	389.15	1.384
389.20	1911	0.118	1155	389.26	1.113
Triple point of sample 389.32					
Triple point of pure compound 389.75					
Mole fraction impurity 0.0018					

^a Units: cal, mol, °K. ^b Data from melting runs series VIII. ^c Data from melting runs series XII.

equilibrium between 85 and 120°K is the same as in the adjacent regions. The transition at 176.47°K is apparently first order with a sharp onset, slow equilibrium, and heat capacities in excess of 800 cal/mol °K. The results of several series of measurements through these transition regions and through fusion may also be found in Table III. Crystal I melts at 389.75°K with ΔS_m equal to 2.43 cal/mol °K. Table IV, which contains the fractional-fusion analysis, indicates a 99.82% purity on the assumption that the impurity is liquid-soluble, solid-insoluble.

Recent unpublished enthalpy of combustion data¹⁴ together with tabular values for the entropies of the elements¹⁵ can be combined with the third-law entropies of this study to provide standard enthalpies and Gibbs energies of formation. The results are $\Delta H_f^\circ = -35.15 \pm 0.10$ kcal/mol and $\Delta G_f^\circ = 18.21 \pm 0.11$ kcal/mol of octane and $\Delta H_f^\circ = -5.60 \pm 0.08$ kcal/mol and $\Delta G_f^\circ = 38.48 \pm 0.09$ kcal/mol of octene at 298.15°K.

Discussion

The low values of the entropies of fusion and the existence of highly energetic solid-solid transitions are clear evidence that both compounds fall into the embe-

(13) P. D. Bartlett and G. F. Woods, *J. Amer. Chem. Soc.*, **62**, 2933 (1940).

(14) S.-w. Wong and E. F. Westrum, Jr., unpublished data.

(15) D. D. Wagman, W. H. Evans, I. Halow, V. B. Parker, S. M. Bailey, and R. H. Schumm, U. S. National Bureau of Standards Technical Note 270-1, "Selected Values of Chemical Thermodynamic Properties," U. S. Government Printing Office, Washington, D. C. 20402, 1965.

fic crystal series. It is believed that the crystal I phases of such materials permit a considerable degree of orientational disorder for each molecule and that the low entropies of fusion reflect only the disappearance of long-range structure—the short range order having been dissipated at the solid–solid transition.

If one assumes D_{3h} symmetry for the octane, a mechanistic model of the solid–solid transition can be developed along the lines proposed by Guthrie and McCullough.¹⁶ The requirements of such a model are that the effective point symmetry of the molecule must be a subpoint group of the symmetry of the lattice site. The threefold molecular axis can be aligned with any of the four threefold axes of the cubic (O_h) lattice in two different ways that differ by a 60° rotation. The eight configurations arising in this manner can be augmented by twelve more arising from alignment of the molecular and lattice twofold axes and of the molecular mirror planes with the horizontal and diagonal mirror planes of the lattice. The twenty orientations considered possible correspond to a transitional entropy increment of $\Delta S_t = R \ln 20 = 5.95$ cal/mol $^\circ\text{K}$. (The implicit assumption that the crystal II phase is ordered is considered at greater length elsewhere.¹⁷) The difference between the observed ΔS_t and $R \ln 20$ or 0.7 cal/mol $^\circ\text{K}$ may well be due to increases in overall vibration of the molecules above the transition temperature.

The principal difference between the octene and the octane is the additional threefold asymmetry in the former caused by the double bond. While the crystal

structure of this material has not been determined, it is reasonable to assume that the molecules occupy O_h sites similar to those of the octane. If this is true, and the disordering process is mechanistically similar, one could expect 3×20 isoenergetic configurations for the molecules in the crystal I phase of the octene. The predicted entropy increment, $\Delta S_t = R \ln 60 = 8.14$ cal/mol $^\circ\text{K}$, is in fair accord with the sum of the two observed increments, $0.78 + 7.66 = 8.44$ cal/mol $^\circ\text{K}$. The magnitude of the difference is again that which might be expected for increases in overall vibration.

It is interesting to note that the threefold “rotational” asymmetry in the octene may also be reflected in the entropies of fusion. The difference in these quantities 4.48 (octane) $- 2.43$ (octene) $= 2.05$ cal/mol $^\circ\text{K}$ is tantalizingly close to $R \ln 3$.

Amzel and Becka⁹ have shown that these mechanisms are consistent with their extension of the melting theory of Pople and Karasz.¹⁰ They have included observations concerning the nmr interpretations of Darmon and Brot.⁸

Acknowledgment. The authors appreciate the support of the U. S. Atomic Energy Commission and the assistance of William G. Lyon in the experimental measurements.

(16) G. B. Guthrie and J. P. McCullough, *J. Phys. Chem. Solids*, **18**, 53 (1961).

(17) C. A. Wulff and E. F. Westrum, Jr., submitted to *J. Chem. Therm.*

Dimethyl Sulfoxide and Dimethyl Sulfone. Heat Capacities,

Enthalpies of Fusion, and Thermodynamic Properties¹

by H. Lawrence Clever and Edgar F. Westrum, Jr.²

Department of Chemistry, University of Michigan, Ann Arbor, Michigan 48104 (Received March 19, 1969)

Heat capacities of dimethyl sulfoxide (DMSO) from 5 to 350°K and of dimethyl sulfone (DMSO₂) from 5 to 420°K together with the enthalpy increments for melting [3434 cal/mol at 291.67°K for dimethyl sulfoxide 4374 cal/mol at 382.01°K for dimethyl sulfone] were determined by adiabatic calorimetry. Values at 298.15°K of C_p , S° , $(H^\circ - H^\circ_0)/T$, and $-(G^\circ - H^\circ_0)/T$ are 36.61, 45.12, 27.74, and -17.39 for DMSO(l) and 29.96, 34.77, 17.11, and -17.66 for DMSO₂(c). The potential energy barriers to methyl group rotation in both substances were estimated both by analysis solely of the low-temperature heat capacity of the solid and from a third-law entropy cycle involving the ideal gas evaluated from spectroscopic data and molecular parameters. The latter method gives a barrier 2.8 and 3.4 kcal/mol for each methyl group in DMSO and DMSO₂. Chemical thermodynamic properties of the ideal gases are evaluated to 1000°K. No corroborative evidence was found for the dielectric anomaly previously reported for DMSO.

Introduction

Chemical thermodynamic research on a substance with as dramatic a chemical and pharmaceutical nature as that of dimethyl sulfoxide, (CH₃)₂SO or DMSO, hardly needs further justification. Despite the systematic penetration of the skin, remarkable dipolar aprotic solvent characteristics, unique chemical reactivity, and association into molecular chains in the liquid phase, this compound, known for more than a century, has been extensively investigated only in recent years. Since relatively few thermochemical and thermal data exist on dimethyl sulfoxide and dimethyl sulfone, (CH₃)₂SO₂ or DMSO₂, this study provides precise cryogenic thermal properties of both compounds, answers to relevant structural questions, and resolution of the considerable discord among the few thermodynamic properties reported or estimated.

Thermal data on compounds containing methyl groups are interesting since they permit determination of potential barriers hindering internal rotation of these groups. Moreover, many methyl containing compounds have solid-solid transitions; e.g., methanol,^{3a} acetone,^{3b} methylamine,^{3c} methylamine hydrochloride,^{3d} methyl mercaptan,^{3e} methyl bromide,^{3f} and neopentane.^{3g} Two of these, methanol and neopentane, have entropies of melting less than the 5 cal/(mol °K) characteristic of a plastic crystal.⁴ Dimethyl sulfoxide, (CH₃)₂SO, and dimethyl sulfone, (CH₃)₂SO₂, show some properties suggestive of plastically crystalline behavior. The report of a small entropy of melting,⁵ ΔS_m , of only 5.4 cal/(mol °K) for dimethyl sulfoxide based upon cryoscopic depression suggested that this substance might also be a plastic crystal. However, subsequently reported determinations indicated values of 10.4⁶ and 11.1⁷ based upon cryoscopy and 11.4 ± 0.2 cal/(mol °K)⁸ based upon direct calorimetric determination.

The heat capacities (C_p) for the solid below the melting point [19.8 cal/(mol °K)] and for the liquid above the melting point (33.4) reported by the latter investigators⁸ are so at variance both with our determinations and with another calorimetrically determined value of 46 for the liquid near 305°K⁹ that reservations seemed appropriate. The trend of the dielectric loss factor *vs.* temperature¹⁰ for solid dimethyl sulfoxide has a maximum between 165 and 180°K. Dimethyl sulfone has a relatively high melting point (109°C) in comparison with the melting points of compounds such as SO₂Cl₂ and SO₂F₂, which are similar in structure and molecular weight. Mackle and O'Hare¹¹ made a statistical calculation of the ideal gas thermodynamic properties

(1) This work was supported in part by the Division of Research of the United States Atomic Energy Commission.

(2) To whom correspondence concerning this work should be addressed.

(3) (a) H. G. Carlson, U. S. Atomic Energy Commission Reports, TID-15153, 1962; (b) K. K. Kelley, *J. Amer. Chem. Soc.*, **51**, 1145 (1929); (c) J. G. Aston, C. W. Siller, and G. H. Messerly, *ibid.*, **59**, 1743 (1937); (d) J. G. Aston and C. W. Ziemer, *ibid.*, **68**, 1405 (1946); (e) H. R. Russell, Jr., D. W. Osborne, and D. M. Yost, *ibid.*, **64**, 165 (1942); (f) C. J. Egan and J. D. Kemp, *ibid.*, **60**, 2097 (1938); (g) J. G. Aston and G. H. Messerly, *ibid.*, **58**, 2354 (1936).

(4) J. Timmermans, *J. Phys. Chem. Solids*, **18**, 1 (1961).

(5) H. L. Schlafer and W. Schaffernicht, *Angew. Chem.*, **72**, 618 (1960); cf. H. Prückner, *Erdöl Kohle*, **16**, 188 (1963) and W. O. Ranky and D. C. Nelson in "Organic Sulfur Compounds," Vol. 1, N. Kharasch, Ed., Pergamon Press, London, 1961, p 170.

(6) J. J. Lindberg, J. Kenttamaa, and A. Nissema, *Suomen Kemistiilehti*, **34B**, 98 (1961).

(7) E. F. Weaver and W. Keim, *Proc. Indiana Acad. Sci.*, **70**, 123 (1960).

(8) T. Skerlak and B. Ninkov, *Glasnik Društva Hemizara Technol. S. R. Bosne Hercegovine*, **11**, 43 (1962); cf. *Chem. Abstr.*, **61**, 2496d (1964).

(9) Y. Murakami and T. Yamada, *Kagaku Kagaku*, **26**, 865 (1962).

(10) M. Freymann, *Compt. Rend.*, **253**, 2061 (1961).

(11) H. Mackle and P. A. G. O'Hare, *Trans. Faraday Soc.*, **58**, 1912 (1962).

of both dimethyl sulfoxide and dimethyl sulfone from spectral and molecular data then available. Sands¹² reported the dimethyl sulfone crystal structure. A review by Lindberg¹³ and two more recent reviews^{14,15} summarizing the structural and physicochemical properties of dimethyl sulfoxide have appeared.

Experimental Section

Samples. Both the dimethyl sulfoxide and dimethyl sulfone were supplied by the Crown Zellerbach Corporation, Camus, Wash. The dimethyl sulfoxide was specially purified by multistage contact with activated charcoal and subsequently distilled through a 20-plate glass-packed column, under 8 Torr pressure, a head temperature of 78°, and a reflux ratio of 4:1. Approximately 5% forerun and residue were discarded. Light transmission of the product was greater than 100% at 350 m μ compared to water. At 275 m μ the absorbance was 0.20, at 300 m μ 0.03, and 1.0 at 261 m μ . The freezing point was 18.51°. Maximum volatile impurities determined by gas chromatography were less than 0.04%. It was used as received after thorough degassing through several cycles of freezing, evacuating, and thawing. It was then poured through a closed glass-metal system under a low pressure of helium gas into a gold-plated copper calorimeter (laboratory designation W-24¹⁶). Helium gas was added as conduction medium and the calorimeter was sealed with a gold-gasketed demountable valve.

The dimethyl sulfone was purified by dissolution of 100 g of solute in 66 g of boiling water. Ammonium hydroxide was added to the hot solution until pH 9, and the solution was filtered. Crystallization was spontaneous on slight cooling and performed with continuous stirring to 3°. The filtered product was washed with water at 0° and air dried at 50°, and repeatedly sublimed under vacuum. The dimethyl sulfone melts at 108.85° and is neutral. No volatile impurities could be detected by gas phase chromatography. The sample was melted and poured into a silver calorimeter (laboratory designation W-22) in the nitrogen atmosphere of a drybox for the heat capacity measurements from 300 to 420°K. The gold-plated copper calorimeter (laboratory designation W-17A) was then filled in a similar manner for the low temperature heat capacity determinations. Sample mass (g, *in vacuo*), gram molecular weights (C-12 basis), and pressure (Torr) of conduction helium gas were respectively dimethyl sulfoxide (5–350°K) 86.517, 78.134, 219; dimethyl sulfone (300–420°K) 89.612, 94.133, 123; dimethyl sulfone (5–340°K) 72.007, 94.133, 269.

Cryogenic Apparatus. The Mark III cryostat¹⁷ with capsule-type platinum-resistance thermometer A-3 was used for the low temperature heat capacity determinations by the quasi-adiabatic technique.¹⁸ The intermediate temperature heat capacities were determined in the Mark IV¹⁹ thermostat with the

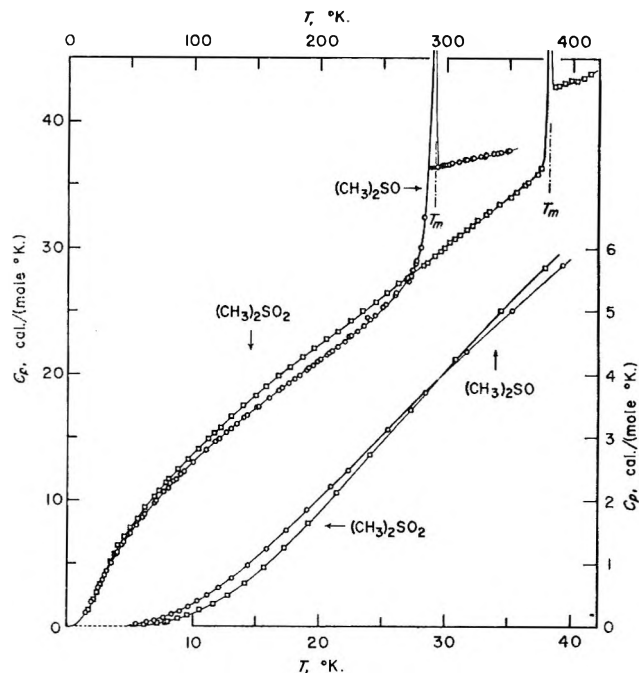


Figure 1. The heat capacity of dimethyl sulfoxide and dimethyl sulfone showing melting at T_m .

platinum-resistance thermometer A-7. The data were converted to thermodynamic functions by the computer program described earlier.²⁰

The heat capacity of the calorimeter-heater-thermometer assembly was determined by a separate series of measurements with small adjustments applied as needed for slight differences in the quantities of helium and thermal conductivity grease between determinations with and without sample. The sample heat capacity as a percentage of the sample-calorimeter-heater-thermometer total was: for dimethyl sulfoxide; a maximum of 93% at 10°K, minimum 68% at 100°K, 75% at 275°K, and 79% in the liquid region; for dimethyl sulfone (low temperature), 80% at 100°K, increasing to 86% at 340°K, and (intermediate temperature) greater than 78% above 300°K.

Manual shield control was used below 80°K; at higher temperatures three separate channels of record-

- (12) D. E. Sands, *Z. Krist.*, **119**, 245 (1963).
- (13) J. J. Lindberg, *Finska Kemistsamfundets Medd.*, **70**, 33 (1961).
- (14) D. Martin, A. Weise, and H. J. Niclas, *Angew. Chem., Int. Ed. Engl.*, **6**, 318 (1967).
- (15) W. S. MacGregor, *Ann. N. Y. Acad. Sci.*, **141**, 3 (1967); *cf. Chem. Abstr.*, **67**, 14797k.
- (16) E. T. Chang and E. F. Westrum, Jr., submitted to *J. Phys. Chem.*
- (17) E. F. Westrum, Jr., *J. Chem. Educ.*, **39**, 443 (1962).
- (18) E. D. West and E. F. Westrum, Jr., in "Experimental Thermodynamics," Vol. 1, J. P. McCullough and D. W. Scott, Ed., Butterworth and Co., Ltd., London, 1968, p. 333.
- (19) J. C. Trowbridge and E. F. Westrum, Jr., *J. Phys. Chem.*, **67**, 2381 (1963).
- (20) B. H. Justice, Appendix to Ph.D. Dissertation, University of Michigan; *cf. U. S. Atomic Energy Commission Report TID-12722*, 1961.

Table I: Heat Capacity of Dimethyl Sulfoxide and Dimethyl Sulfone^a

Dimethyl Sulfoxide						Dimethyl Sulfone ^a					
T	C _p	T	C _p	T	C _p	T	C _p	T	C _p	T	C _p
—Series I—						Low-Temperature Series					
270.50	27.33	205.80	21.54	61.88	8.920	Series I		6.99	0.052	78.24	11.333
275.42	28.74	214.11	22.15	70.18	9.881	Series II		7.82	0.079	Enthalpy Detn. A	
282.76	32.47	223.45	22.93	—Series VI—		116.40	15.35	8.71	0.121	148.50	18.28
288.69	73.3	ΔH _m Detns. A		61.79	8.913	Series III		9.58	0.189	157.58	19.05
291.15	308	298.11	36.49	69.19	9.774	73.20	10.75	10.51	0.269	166.94	19.82
291.41	960	301.38	36.61	77.70	10.72	80.61	11.63	11.59	0.358	176.37	20.57
291.52	3,420	—Series IV—		86.28	11.69	88.05	12.49	12.77	0.510	185.95	21.32
291.53	7,080	285.22	86.7	Enthalpy Detn. B		95.71	13.28	14.10	0.700	195.53	22.05
291.55	8,720	291.41	4,200	Enthalpy Detn. C		103.62	14.08	15.59	0.944	205.06	22.79
291.55	12,400	291.51	13,000	ΔH _m Detns. D		112.05	14.92	17.27	1.253	214.75	23.53
291.58	6,890	291.55	24,800	298.78	36.63	121.06	15.80	19.19	1.645	224.44	24.26
291.59	5,730	291.57	36,800	304.43	36.73	130.26	16.67	21.42	2.129	234.06	25.02
291.61	4,680	291.58	16,450	310.23	36.89	139.51	17.52	24.07	2.729	243.62	25.74
292.33	190.7	293.00	80.7	316.01	37.00	148.85	18.32	27.21	3.444	253.11	26.45
—Series II—						Series IV		30.79	4.241	262.76	27.20
226.06	23.10	—Series V—		321.75	37.15	Series III		34.38	5.004	272.45	27.96
235.10	23.87	5.50	0.037	327.48	37.30	6.33	0.036	37.89	5.704	281.91	28.70
243.90	24.66	6.28	0.062	—Series VII—		7.21	0.058	41.66	6.379	291.14	29.41
252.47	25.51	6.92	0.095	Enthalpy Detn. E		7.99	0.078	45.84	7.083	299.84	30.11
260.81	26.42	7.63	0.137	ΔH _m Detns. F		8.75	0.132	50.54	7.809	308.67	30.77
268.89	27.50	8.28	0.195	Enthalpy Detn. G		9.47	0.185	55.87	8.565	317.30	31.49
276.67	29.07	8.94	0.243	331.68	37.37	Series IV		62.16	9.411	325.77	32.24
—Series III—						337.55	37.50	69.07	10.259	334.08	32.92
76.88	10.63	10.33	0.410	343.38	37.59	6.01	0.028	76.52	11.130	342.24	33.51
84.47	11.49	11.12	0.498	348.02	37.68	Intermediate-Temperature Series					
92.20	12.28	12.03	0.611	—Series VIII—		Series I		381.99	295,200	Enthalpy Detn. A	
100.27	13.05	12.03	0.766	287.53	36.39	303.21	30.45	381.99	60,300	365.05	35.22
108.95	13.95	13.05	0.977	289.51	36.42	311.59	31.08	382.01	36,500	Enthalpy Detn. B	
117.68	14.67	14.33	1.237	292.48	36.44	321.53	31.81	382.99	220.1	394.22	43.08
125.98	15.40	15.79	1.526	295.77	36.55	331.88	32.71	386.07	42.89	398.93	43.35
134.09	16.08	17.36	1.853	299.05	36.65	342.01	33.45	Series III		Series V	
142.45	16.78	19.05	2.224	—Series IX—		351.97	34.04	362.68	35.09	Enthalpy Detn. C	
151.20	17.47	20.90	2.639	191.58	20.48	Series II		372.82	35.90	285.59	28.86
159.64	18.12	22.94	3.139	194.75	20.71	355.42	34.49	380.07	173.4	296.26	29.75
167.83	18.74	25.40	3.729	197.89	20.95	365.44	35.28	381.99	46,790	Enthalpy Detn. D	
175.79	19.32	28.36	4.371	200.99	21.18	375.57	36.41	381.99	96,800	Enthalpy Detn. C	
183.60	19.90	31.64	5.042	204.07	21.42	381.27	314.8	381.99	131,270	388.52	42.83
191.18	20.48	35.24	5.738	207.13	21.65	381.99	141,800	381.99	160,190	393.39	42.98
198.57	21.10	39.25	6.468			381.9	43,600	382.00	206,900	398.27	43.17
						381.99	142,900	385.49	90.66	403.27	43.30
						381.9	64,700	Series IV		408.49	43.54
						381.99	69,600	299.52	29.99	413.95	43.83

^a Units: cal, mol, °K.

ing electronic circuitry provided with proportional, rate, and reset control actions maintained the temperature of the adiabatic shield within approximately a milli-degree of the calorimeter temperature. Thus the energy exchange between calorimeter and surroundings was reduced so that it was negligible in comparison with other sources of error. All measurements of temperature, time, potential, resistance, and mass were referred to standardizations or calibrations of the National Bureau of Standards.

Results and Discussion

Heat Capacity. The experimentally measured heat capacities are shown in Figure 1 as a function of temperature and are presented in Table I in chronological order so that temperature increments across individual determinations in a series may be estimated from adjacent mean temperatures. The data are stated in terms of the defined thermochemical calorie exactly equal to 4.1840 J and an ice point of 273.15°K. The low-temperature and intermediate-temperature heat capacities

of dimethyl sulfone accord within 0.15% across the overlap region between 290 and 350°K. Two heat capacity measurements in the dimethyl sulfoxide under-cooled liquid range were obtained. No vaporization adjustment was made because the vapor pressure data on dimethyl sulfoxide of Douglas²¹ indicated the adjustment was less than 0.02%.

Long enthalpy-type determinations extending over relatively large ranges of temperature (Enthalpy Detns. B, C, E, and G for dimethyl sulfoxide, A and C for dimethyl sulfone; cf. Table I) required enthalpy increments which correlated well ($\pm 0.05\%$) with those evaluated by integration of the smooth curves over the same ranges. Such determinations also served to establish that no change in phase occurred, for example, during cooling for determinations in the helium region.

Melting. In the course of heat capacity measurements five sets of determinations were made through the dimethyl sulfoxide melting region and four through that of the dimethyl sulfone (cf. Table II). The en-

tion melted, $1/F$. The temperature corresponding to $1/F = 1$ is the triple point, T_1 , of the calorimetric sample. The temperature corresponding to $1/F = 0$ is the triple point, T_0 , of the pure sample. The mole fraction impurity, N_2 , is given by the expression $N_2 = \Delta H_m(T_0 - T_m)/RT_0^2$. Values of T_1 , T_0 , and N_2 , respectively, are for dimethyl sulfoxide 291.59, 291.67, 0.00159, and for dimethyl sulfone, 382.004, 382.01, and 0.00009.

Melting points of 18.55,⁵ 18.42,⁶ and 18.45°²² have been reported for the sulfoxide; the value 109°²³ for dimethyl sulfone is representative of the literature.

Thermodynamic Functions. The molal values of the heat capacity, entropy, enthalpy increment, and Gibbs energy function are listed in Table III at selected temperatures. The values of the derived thermal properties have been calculated with a high-speed digital computer by integration of a least-squares polynomial fitted through the data points.²⁰ Below 5°K the heat capacity data were extrapolated by means of the Debye T^3 limiting law. Nuclear spin and isotopic mixing contributions have not been included in the Gibbs energy functions and entropy. Estimated probable errors in the thermodynamic functions are less than 0.1% above 100°K.

Barriers to Internal Rotation

The magnitudes of the potential energy barriers which hinder internal rotation of the methyl groups in dimethyl sulfoxide and in dimethyl sulfone were estimated by two independent methods.

Wulff's Method. This approach²⁴ is based upon an analysis of the contributions to the experimental heat capacity (C_p), i.e., the lattice contribution (C_p^L), that of the internal vibrations (C_p^I), and internal rotation (C_p^R), and the difference ($C_p - C_v$). The lattice heat capacity is taken as a sum of Debye or Debye and Einstein functions fitted to the experimental C_p which has been corrected for C_p^I and ($C_p - C_v$) at relatively low temperatures. The internal vibrations are taken as $\Sigma g_i E(\theta_{E_i}/T)$ with the room temperature spectral assignments (assumed to be nearly temperature independent). The ($C_p - C_v$) difference is calculated from the quasi-thermodynamic equation of Lord,²⁵ ($C_p - C_v$) $\cong [aC_p^L + bC_p^I]^2 T$. An Einstein function is chosen to express the torsional oscillations of the methyl groups. After fitting C_p^L and C_p^I the contributions ($C_p - C_v$) and C_p^R are empirically adjusted to obtain the best agreement between the observed and calculated C_p . The barrier height can be calculated from the equation $V_0 = 0.04935I_r \times 10^{40}(\theta_E/n)^2$ cal/mol in which I_r is the

Table II: Enthalpy of Melting^a

Designation	Number of detns.	$H_{T_2} - H_{T_1}^b$	$\Delta H_m^{d,e}$
Dimethyl Sulfoxide			
Series I	14	3963.3 ^c	3431
Detns. A	2	3969.6	3438
Series IV	7	3968.7 ^c	3437
Detns. D	3	3967.4	3435
Detns. F	2	3960.8	3429
			3434 \pm 3
Dimethyl Sulfone			
Series II	12	4766.6 ^c	4384
Series III	8	4750.9 ^c	4368
Detn. B	1	4753.9	4371
Detn. D	1	4754.2	4371
			4374 \pm 5

^a Units: cal, mol, °K. ^b T_2 and T_1 are 300 and 280° for dimethyl sulfoxide, 385 and 375° for dimethyl sulfone. ^c Corrected for drift. ^d Lattice is 577 for dimethyl sulfoxide, 383 for dimethyl sulfone. ^e Additional 45 cal excess added for 220–280°K for the dimethyl sulfoxide.

thalpy of melting for dimethyl sulfoxide is $\Delta H_m = 3434 \pm 3$ cal/mol; that for dimethyl sulfone is $\Delta H_m = 4374 \pm 5$. The corresponding entropies of melting are $\Delta S_m = 11.78 \pm 0.01$ and $\Delta S_m = 11.45 \pm 0.01$ cal/(mol °K), respectively. These values indicate that neither compound is plastically crystalline.

The purity and melting point are defined by series I and IV for dimethyl sulfoxide and series II and III for dimethyl sulfone. The amount of liquid-soluble, solid-insoluble impurity can be estimated from a plot of the apparent melting temperature, T , against the frac-

(21) T. B. Douglas, *J. Amer. Chem. Soc.*, **70**, 2001 (1948).

(22) T. Smedslund, *Nord Kemistmötet (Helsingfors)*, **7**, 199 (1950).

(23) W. R. Fearheller, Jr., and J. E. Katon, *Spectrochim. Acta*, **20**, 1099 (1964).

(24) C. A. Wulff, *J. Chem. Phys.*, **39**, 1227 (1963).

(25) R. C. Lord, Jr., *ibid.*, **9**, 700 (1941).

Table III: Thermodynamic Functions of Dimethyl Sulfoxide and Dimethyl Sulfone^a

Dimethyl Sulfoxide					Dimethyl Sulfone				
T	C_p	S°	$H^\circ - H^\circ_0$	$-(G^\circ - H^\circ_0)/T$	T	C_p	S°	$H^\circ - H^\circ_0$	$-(G^\circ - H^\circ_0)/T$
		Crystal					Crystal		
5	0.027	0.009	0.03	0.002	5	0.016	0.005	0.02	0.001
10	0.358	0.100	0.78	0.022	10	0.210	0.056	0.44	0.012
15	1.092	0.374	4.28	0.088	15	0.843	0.246	2.89	0.054
20	2.047	0.816	12.08	0.212	20	1.817	0.616	9.44	0.144
25	3.060	1.381	24.84	0.388	25	2.940	1.141	21.31	0.289
30	4.051	2.072	42.63	0.606	30	4.070	1.778	38.85	0.483
35	4.994	2.723	65.28	0.858	35	5.128	2.486	61.89	0.718
40	5.860	3.448	92.44	1.137	40	6.087	3.234	89.97	0.985
45	6.651	4.184	123.8	1.434	45	6.949	4.002	122.6	1.278
50	7.376	4.923	158.8	1.746	50	7.730	4.775	159.3	1.589
60	8.682	6.386	239.3	2.398	60	9.120	6.130	243.7	2.248
70	9.870	7.814	332.1	3.070	70	10.37	7.811	341.3	2.936
80	10.989	9.206	436.4	3.751	80	11.54	9.274	450.9	3.637
90	12.05	10.562	551.7	4.432	90	12.66	10.698	571.9	4.343
100	13.05	11.884	677.3	5.112	100	13.71	12.087	703.8	5.048
110	14.00	13.174	812.6	5.786	110	14.73	13.442	846.1	5.750
120	14.89	14.430	957.1	6.454	120	15.70	14.765	998.2	6.446
130	15.74	15.656	1110.2	7.115	130	16.64	16.059	1160.0	7.136
140	16.56	16.852	1272	7.768	140	17.55	17.326	1331	7.819
150	17.36	18.022	1441	8.413	150	18.42	18.566	1511	8.494
160	18.15	19.168	1619	9.049	160	19.26	19.782	1699	9.162
170	18.91	20.291	1804	9.678	170	20.07	20.974	1896	9.822
180	19.66	21.394	1997	10.298	180	20.85	22.14	2100	10.47
190	20.38	22.476	2197	10.911	190	21.63	23.29	2313	11.12
200	21.10	23.54	2405	11.52	200	22.40	24.42	2533	11.76
210	21.83	24.59	2619	12.11	210	23.17	25.53	2761	12.39
220	22.61	25.62	2842	12.70	220	23.93	26.63	2996	13.01
230	23.45	26.64	3072	13.29	230	24.70	27.71	3239	13.62
240	24.33	27.66	3311	13.87	240	25.46	28.77	3490	14.23
250	25.26	28.67	3559	14.44	250	26.22	29.83	3749	14.84
260	26.29	29.68	3816	15.00	260	26.99	30.87	4015	15.43
270	27.67	30.70	4085	15.57	270	27.76	31.91	4288	16.02
273.15	28.27	31.02	4173	15.74	273.15	28.00	32.23	4376	16.21
280	30.07	31.74	4373	16.13	280	28.54	32.93	4570	16.61
291.67	...	32.56 ^b	4602 ^b	16.79 ^b	290	29.32	33.94	4859	17.19
		Liquid			298.15	29.96	34.77	5101	17.66
291.67	...	44.34 ^b	8036 ^b	16.79 ^b	300	30.10	34.95	5156	17.76
298.15	36.61	45.12	8270	17.39	350	34.07	39.89	6760	20.57
300	36.65	45.35	8339	17.56	382.01 ^b	...	42.97	7891	22.31
350	37.74	51.09	10198	21.95			Liquid		
					382.01 ^b	...	54.42	12265	22.31
					390	42.94	55.31	12606	22.99
					400	43.20	56.40	13036	23.81
					410	43.66	57.47	13470	24.62

^a Units: cal, mol, °K. ^b Assuming enthalpy of melting isothermal at T_m .

reduced moment of inertia of the methyl rotation, θ_E is the Einstein temperature obtained from the fitted C_p^R curve, and n is the number of maxima encountered in one complete revolution of the internal rotator.

The results of the heat capacity analysis are given in Table IV. For dimethyl sulfoxide the spectral assignments of Horrocks and Cotton²⁶ confirmed by Carter, Freeman, and Henshall²⁷ were used.

The lattice heat capacity of the flattened pyramidal dimethyl sulfoxide molecule²⁸⁻³¹ is well represented by

a combination of Debye and Einstein terms since it has a molecular weight large relative to its moment of

(26) W. D. Horrocks, Jr., and F. A. Cotton, *Spectrochim. Acta*, **17**, 134 (1961).

(27) J. H. Carter, J. M. Freeman, and T. Henshall, *J. Mol. Spectros.*, **20**, 402 (1966).

(28) O. Bastiansen and H. Viervoll, *Acta Chem. Scand.*, **2**, 7C2 (1948).

(29) H. Dreizler and G. Dendl, *Z. Naturforsch.*, **19a**, 512 (1964).

(30) R. Thomas, C. B. Shoemaker, and K. Eriks, *Acta Cryst.*, **21**, 12 (1966).

Table IV: Estimation of Magnitude of Barrier Heights by Wulff's Method

	Dimethyl sulfoxide	Dimethyl sulfone
C_v^L	$4D(130/T) + 2D(265/T)$	$3D(130/T) + 3D(197/T)$
C_v^R	$2E(385/T)$	$2E(380/T)$
a	0.0050	0.0064
b	0.0050	0.0016
n	3	3
Barrier height	4.1 kcal/mol	4.2 kcal/mol
Torsional libration	268 cm^{-1}	264 cm^{-1}

inertia; $C_v^L = 4D(130/T) + 2D(265/T)$ gives a methyl rotation barrier of 4.1 kcal/mol.

Analysis of the distorted tetrahedral dimethyl sulfone molecule¹² with the spectral assignment of Fearheller and Katon²³ and two Debye functions to represent the lattice contribution *i.e.*, $C_v^L = 3D(130/T) + 3D(197/T)$ corresponds to a methyl rotation barrier of 4.2 kcal/mol.

Third-Law Method. The height of the potential barrier was also obtained by comparison of the experimental and statistically calculated values of the vapor-phase third-law entropies for both compounds.

The third-law, ideal-gas entropy of dimethyl sulfoxide was calculated from the liquid entropy with an enthalpy of vaporization and a compression correction deduced from the vapor-pressure equation of Douglas:²¹ $\log P$ (Torr) = 26.49558 - 3538.32/ T - 6.0000 $\log T$ and $\Delta H_v = 16,196 - 11.922T$. The resulting third-law ideal-gas entropy of 73.32 cal/(mol °K) at 298.15°K was matched exactly by the spectroscopic entropy (*cf.* next section) provided assignment of a barrier of 2.8 kcal/mol (222 cm^{-1}) was made for each of the two methyl groups. The third-law, ideal-gas entropy of dimethyl sulfone was calculated from the liquid thermal entropy with the vapor pressure equation of Bushfield, Ivin, Mackle, and O'Hare:³² $\log P$ (Torr) = 7.624 - 2241/($t + 223.0$) and $\Delta H_v = (2.303)(2241)RT^2(t + 223.0)^{-2}$. The third-law entropy of 81.05 cal/(mol °K) at 385°K was matched by the statistical entropy (*cf.* next section) upon assignment of a methyl rotation potential barrier of 3.4 kcal/mol (237 cm^{-1}) for each methyl rotation.

Microwave spectroscopic evaluation for the internal rotation barrier in dimethyl sulfoxide yields a value of 3.07 kcal/mol.³³ For dimethyl sulfone a spectroscopic interpretation gives 3.74 kcal/mol.³⁴ Both of these spectral values accord better with thermal values derived by the third-law method than with those based solely on heat capacity data on the crystalline state.

The two unobserved torsional modes of dimethyl sulfoxide were assigned by Horrocks and Cotton²⁶ to 223 ± 20 and $197 \pm 20 \text{ cm}^{-1}$ by analogy with trimethylphosphine. Mackle and O'Hare¹¹ assumed that each

methyl group experiences an identical restriction to internal rotation and assigned an intermediate value of 210 cm^{-1} to the S-CH₃ torsional libration. This S-CH₃ corresponds to a barrier of 2.6 kcal mol⁻¹. The values from the present research with new molecular parameters and guidance from the third-law values to evaluate barrier heights (222 cm^{-1} , 2.8 kcal/mol) in conjunction with the tables of Pitzer and Gwinn³⁵ are in reasonable accord with these earlier estimates and direct spectroscopic determination.

For dimethyl sulfone, our rotational barrier and torsional modes (3.4 kcal and 237 cm^{-1}) are in good accord with the value determined of Fujimori, but are considerably higher than the admittedly tentative assignment of 106 cm^{-1} suggested by Fearheller and Katon.²³

Thermal Properties from Molecular Data. The ideal-gas, rigid-rotator, harmonic-oscillator, statistical-thermodynamic properties of dimethyl sulfoxide were calculated with the vibrational assignments of Horrocks and Cotton²⁶ and the structural parameters from an analysis of the microwave spectra by Dreizler and Dendl²⁹ given in Table V. The corresponding properties for dimethyl sulfone were calculated with the vibrational assignments of Fearheller and Katon²³ and the X-ray crystal structure parameters of Sands¹² also given in Table V. As usual, in both instances the effects of vibrational anharmonicity, rotation-vibration interaction, centrifugal stretching, etc., have been neglected. It has been assumed further that the barriers are of simple cosine shape, and that the Pitzer-Gwinn tables for internal rotation apply.

On the basis of the above vibrational assignments, moments, reduced moments of inertia, and potential barriers to internal rotation discussed in previous sections, values for the molal thermodynamic functions for both compounds were computed by standard procedures and are compiled in Table VI. Significant differences appear between these values and those devised earlier on less definitive data.¹¹ Comparison of the third-law and spectroscopic entropies is shown at three selected temperatures for both compounds in Table VII. The temperature dependence of the values is reasonable.

Gibbs Energies of Formation. Douglas³⁶ made a calorimetric study of the direct oxidation of dimethyl sulfide to dimethyl sulfoxide and of dimethyl sulfoxide to dimethyl sulfone at 291°K. For the reaction

(31) M. A. Viswamitra and K. K. Kannan, *Nature*, **209**, 1016 (1966).

(32) W. K. Bushfield, K. J. Ivin, H. Mackle, and P. A. G. O'Hare, *Trans. Faraday Soc.*, **57**, 1058 (1961).

(33) H. Dreizler and G. Dendl, *Z. Naturforsch.*, **20a**, 1431 (1965).

(34) K. Fujimori, *Bull. Chem. Soc. Jap.*, **32**, 1374 (1959).

(35) K. S. Pitzer and W. D. Gwinn, *J. Chem. Phys.*, **10**, 428 (1948).

(36) T. B. Douglas, *J. Amer. Chem. Soc.*, **68**, 1072 (1946).

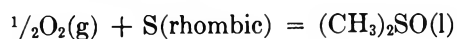
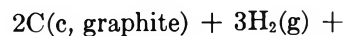
Table V: Fundamental Vibrations and Structural Parameters Used in the Calculation of Ideal Gas Statistical Thermodynamic Properties

Fundamental vibrations (in cm^{-1})	Dimethyl Sulfoxide		Dimethyl Sulfone	
	Reference 26		Reference 23	
	2973 (4), 2908 (2), 1455, 1440, 1419,		3008 (2), 2965 (2), 2922 (2), 1423 (2), 1407 (2),	
	1405, 1319, 1304, 1102, 1016, 1006,		1343, 1329, 1291, 1135, 1114, 1008, 995, 940,	
	929, 915, 689, 672, 382, 333, 308		756, 700, 502, 468, 383, 320, 292	
Structural parameters	Reference 29		Reference 12	
C—S	1.810 Å		1.778 Å	
S—O	1.477 Å		1.445 Å	
C—H	1.095 Å		1.095 Å	
\angle CSC	$96^\circ 23'$		$103^\circ 0'$	
\angle CSO	$106^\circ 43'$		$108^\circ 48'$	
\angle SCH	$107^\circ 31'$...	
\angle OSO	...		$117^\circ 54'$	
μ (int. rot.)	5.08×10^{-40}		5.26×10^{-40}	
$D = I_A I_B I_C$	2880.0×10^{-117}		7356.9×10^{-117}	

Table VI: Thermodynamic Properties of Dimethyl Sulfoxide and Dimethyl Sulfone in the Ideal Gas State

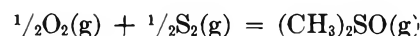
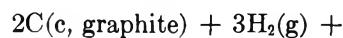
$^\circ\text{K}$	c_p°	s°	$\frac{-(G^\circ - H^\circ_0)}{T}$	$\frac{(H^\circ - H^\circ_0)}{T}$
Dimethyl Sulfoxide				
273.15	20.21	71.51	58.22	13.29
298.15	21.39	73.32	59.40	13.92
400	25.86	80.24	63.69	16.55
500	29.37	86.39	67.75	18.64
600	32.32	92.01	71.33	20.68
700	34.81	97.17	74.57	22.60
800	36.97	101.99	77.79	24.20
900	38.83	106.45	80.73	25.72
1000	40.46	110.63	83.52	27.11
Dimethyl Sulfone				
273.15	22.25	72.34	58.49	13.85
298.15	23.68	74.47	59.75	14.72
400	29.04	82.20	64.50	17.70
500	33.34	89.17	68.75	20.42
600	36.81	95.64	72.68	22.96
700	39.61	101.41	76.34	25.07
800	42.01	106.90	79.85	27.05
900	44.04	111.97	83.15	28.82
1000	45.84	116.70	86.27	30.43

$^\circ$ Units: cal, mol, $^\circ\text{K}$.



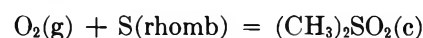
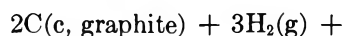
ΔH_f° at 298.15°K is (-48.86 ± 0.1) kcal/mol for liquid dimethyl sulfoxide after we updated the enthalpy increment of the hydrogen peroxide decomposition used by Douglas with recent critically evaluated data,³⁷ employed the recent ΔH_f° of dimethyl sulfide reported by McCullough, *et al.*,³⁸ and adjusted to 298.15°K . Use of the dimethyl sulfoxide entropy gives $\Delta S_f^\circ = -83.35$ cal/(mol $^\circ\text{K}$) and $\Delta G_f^\circ = -24.01$ kcal/mol for

liquid dimethyl sulfoxide at the same temperature. For formation of ideal gas as defined by the reaction



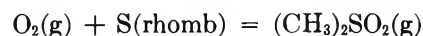
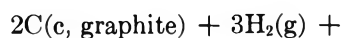
the ΔH_f° and ΔG_f° are (-51.56 ± 0.15) and (-33.49 ± 0.15) kcal/mol, respectively. These values involve Douglas'²¹ vapor pressure equation and the thermodynamics of the $2\text{S}(\text{rhomb}) = \text{S}_2(\text{g})$ sublimation.³⁷

A ΔH_f° of -107.31 kcal/mol at 298.15°K was obtained for the reaction



This value was obtained after revision of Douglas'²⁶ value for ΔH_f° of dimethyl sulfone by adjustment of the enthalpy increment for the hydrogen iodide oxidation,³⁷ use of the most recent ΔH_f° of dimethyl sulfide,³⁸ and adjustment of the temperature to 298.15°K . The result compares well with the (adjusted) value of ΔH_f° of (-107.45 ± 0.7) kcal/mol from heat of combustion studies of Busfield, *et al.*,³⁹ on dimethyl sulfone. The corresponding ΔS_f° and ΔG_f° values are -118.2 cal/(mol $^\circ\text{K}$) and -72.2 kcal/mol.

Busfield, *et al.*,³⁹ give an (adjusted) value of ΔH_f° for the ideal gas state



(37) D. D. Wagman, W. H. Evans, V. B. Parker, I. Halow, S. M. Bailey, and R. H. Schumm, "Technical Note 270-3," National Bureau of Standards, Washington, D. C. 20234.

(38) J. P. McCullough, W. N. Hubbard, F. R. Frow, I. A. Hosselopp, and G. Waddington, *J. Amer. Chem. Soc.*, **79**, 561 (1957).

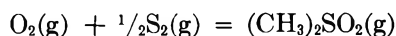
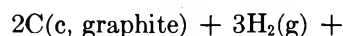
(39) W. K. Busfield, H. Mackle, and P. A. G. O'Hare, *Trans. Faraday Soc.*, **57**, 1054 (1961).

Table VII: The Third-Law and Spectroscopic Entropies of Dimethyl Sulfoxide and Dimethyl Sulfone at Several Temperatures^a

<i>T</i> or ΔT	Property	<i>S</i> or ΔS		
		at 298.15°K	at 320°K	at 350°K
Dimethyl Sulfoxide				
0-5°K	Debye T^3 extrapolation		0.01	
5° - T_m	Numerical quadrature of $\int C_p dT/T$, crystal		32.55	
291.67°K	$\Delta S_m^\circ = \Delta H_m^\circ/T_m$, melting		11.78	
$T_m - T$	Numerical quadrature of $\int C_p dT/T$, liquid	0.78	3.40	6.75
<i>T</i>	S° (liquid)	45.12	47.74	51.09
	$\Delta S_v = \Delta H_v/T$, vaporization	42.39	38.69	34.35
	$R \ln P$, compression to 1 atm	-14.19	-11.33	-8.06
	Ideal gas correction (assumed)	0.00	0.00	0.00
	S° (ideal gas) third law entropy	73.32	75.10	77.38
<i>T</i>	S° (ideal gas) spectroscopic entropy (cf. text)	73.32	74.82	76.92
Dimethyl Sulfone				
at 385°K at 400°K at 415°K				
0-5°K	Debye T^3 extrapolation		0.01	
5° - T_m	Numerical quadrature of $\int C_p dT/T$, crystal		42.96	
382.01	$\Delta S_m^\circ = \Delta H_m^\circ/T_m$, melting		11.45	
$T_m - T$	Numerical quadrature of $\int C_p dT/T$, liquid	0.33	1.98	3.58
<i>T</i>	S° (liquid)	54.75	56.40	58.00
	$\Delta S_v = \Delta H_v/T$, vaporization	35.22	33.53	31.98
	$R \ln P$, compression to 1 atm	-8.92	-7.61	-6.40
	Ideal gas correction (assumed)	0.00	0.00	0.00
	S° (ideal gas) third law entropy	81.05 ± 0.14	82.32 ± 0.18	83.58 ± 0.24
	S° (ideal gas) spectroscopic entropy (cf. text)	81.06	82.21	83.31

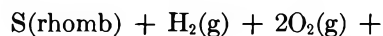
^a Units: cal (mol °K).

of (-89.1 ± 0.7) kcal/mol at 298.15°K. For the reaction



ΔH_f° and ΔG_f° are -104.4 and -75.1 kcal/mol, respectively, at 298.15°K if use is made of the recent enthalpy increment³⁷ for $2S(\text{rhomb}) = S_2(\text{g})$.

In calculating ΔH_f° from enthalpy of combustion data, the values were adjusted to the average value of two recent determinations of the enthalpy of formation of aqueous sulfuric acid.^{40,41} Their values of ΔH° at 298.15°K for the reaction



-212.17 and 212.24 kcal/mol are averaged as (-212.20 ± 0.04) kcal/mol.⁴²

The Dielectric Anomaly. No evidence for the dielectric anomaly observed by Freymann¹⁰ was noted in either the regular heat capacity determinations or in series IX heat capacity determinations with small temperature intervals.

Thermal Properties of the Liquid Phase. As pointed out by Lindberg¹³ the high polarity and pyramidal structure of the dimethyl sulfoxide molecule occasions organization in the liquid state which is reflected in the relatively high freezing and boiling points and high enthalpy of vaporization. As may be seen in Figure 1, the heat capacity of the liquid is about 9 cal/(mol °K) higher than that of the solid and appears to have a very

(40) W. D. Good, J. L. Lacina, and J. P. McCullough, *J. Amer. Chem. Soc.*, **82**, 5589 (1960).

(41) M. Månsson and S. Sunner, *Acta Chem. Scand.*, **17**, 723 (1963).

(42) D. W. Stull, E. F. Westrum, Jr., and G. C. Sinke, in "The Chemical Thermodynamics of Organic Compounds," John Wiley & Sons, Inc., New York, N. Y., 1969, p 560.

small temperature coefficient. From a study of the correlation factor and for other reasons Amey⁴³ concludes that intermolecular hydrogen bridges are unlikely in liquid dimethyl sulfoxide and that physical properties of dimethyl sulfoxide cited as evidence for association in the liquid (boiling point, entropy of vaporization, etc.)⁴⁴ are due primarily to its large molecular dipole moment (4.3 D) and to the presence in the liquid of strong (but non-specific) dipole-dipole forces.

Acknowledgment. The financial support of the U.

S. Atomic Energy Commission is recognized with gratitude. We thank Professor Claus A. Wulff for his interest and suggestions, Mr. E. M. Seidel and the Crown Zellerbach Corporation for the provision of purified samples, and also Dr. Geoffrey Pilcher for making his reevaluation of data on organic sulfur compounds available (for purposes of comparison) prior to actual publication.

(43) R. L. Amey, *J. Phys. Chem.*, **72**, 3358 (1968).

(44) D. Martin, A. Weise, and H. J. Niclas, *Angew. Chem., Int., Ed. Engl.*, **6**, 318 (1967).

Studies of Adsorbed Species. I. Electron Spin Resonance of Nitrogen Heterocyclics Adsorbed on Magnesium Oxide and Silica-Alumina

by K. S. Seshadri and L. Petrakis

Gulf Research & Development Company, Pittsburgh, Pennsylvania 15230 (Received May 20, 1969)

The esr spectra of radical ions of a series of nitrogen heterocyclics adsorbed on MgO and silica-alumina have been recorded. Most of these substances ordinarily either produce radical ions which are not well defined or they do not give any signal. However, the spectra of the radical ions of phenazine are well defined and, therefore, have been studied in considerable detail. The production of phenazine radical ions is a photochemical process. Spectral differences are noticed in the case of MgO and silica-alumina, and they are attributed to different charges on phenazine. Several possibilities for the mechanism by which the radical ions are generated on the surface are discussed. The spin densities on nitrogen atoms are calculated, and they suggest that there is no structural deformation due to adsorption. Temperature studies indicate that the radical ions have a certain degree of mobility on the surface at room temperature.

Introduction

The formation and stabilization of positive radical ions from polynuclear aromatic hydrocarbons on a surface such as silica-alumina and synthetic zeolite systems by electron-transfer processes are well known and extensively studied by several workers.¹⁻³ The radical ions have been used as probes of the properties of these catalytically active surfaces. A relatively limited amount of work, on the other hand, has been done on the formation and stabilization of negative ions⁴⁻⁶ which would permit the study of surfaces like alumina, magnesium oxide, barium oxide, and other similar surfaces. Simple inorganic molecules like O₂, CO₂, and CO react with electrons trapped at intrinsic centers in irradiated MgO⁷⁻⁹ to form the corresponding negative ions. These, as well as the surface defects themselves that are induced by irradiation on MgO,¹⁰ have been studied by esr spectroscopy. These studies have led to an improved understanding of electron-

transfer processes on these oxide surfaces. Nevertheless, there is little information about the mobility of adsorbed ions, structural changes due to adsorption, and interactions with the surface. In addition, most studies have been mainly confined to polyacene cations, and very little is known about corresponding molecules

(1) J. J. Rooney and R. C. Pink, *Trans. Faraday Soc.*, **58**, 1632 (1962).

(2) R. P. Porter and W. K. Hall, *J. Catal.*, **5**, 366 (1966).

(3) G. M. Muha, *J. Phys. Chem.*, **71**, 640 (1967).

(4) A. J. Tench and R. L. Nelson, *Trans. Faraday Soc.*, **63**, 2254 (1967).

(5) C. Naccache, Y. Kodratoff, R. C. Pink, and B. Imelik, *J. Chem. Phys.*, **63**, 341 (1966).

(6) D. Biji, H. Kainer, and A. C. Rose-Innes, *Nature*, **174**, 850 (1954).

(7) J. H. Lunsford and J. P. Jayne, *J. Phys. Chem.*, **69**, 2182 (1965).

(8) J. H. Lunsford and J. P. Jayne, *J. Chem. Phys.*, **44**, 1487 (1966).

(9) J. H. Lunsford and J. P. Jayne, *ibid.*, **44**, 1492 (1966).

(10) J. H. Lunsford, *J. Phys. Chem.*, **68**, 2312 (1964).

containing nitrogen, oxygen, and sulfur. The work reported here was undertaken to study the behavior of certain nitrogen-containing heteroaromatics when adsorbed on a variety of surfaces, and the bulk of the effort was directed to the detailed investigation of the spectra of phenazine radical ions.

Experimental Section

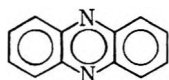
The magnesium oxide used in this investigation was prepared from reagent grade powder that was heated in boiling water for several hours, the supernatant liquid being decanted and replaced at intervals. The $Mg(OH)_2$ so formed was filtered, washed, and dried at 100° . Then it was sieved to 100 mesh and heated in air at 500° for 24 hr to dehydrate the hydroxide and to decontaminate the product of any organic impurities. Aerocat Triple A silica-alumina containing 25% Al_2O_3 by wt and heavy metal impurities ranging from 0.1 to 0.01% was heated in air for 24 hr at 500° and used. Phenazine and acridine were purified by recrystallization from hot ethanol and hot water, respectively. All other chemicals were purified by distillation.

All samples were prepared in air. A 0.5-g sample of the carrier material was placed in an appropriate container and activated by heating to 500° for 2 hr, and 2 ml of $10^{-2} M$ phenazine solution in THF was added to the carrier material as it was cooled. The excess solvent was pumped out and the residue was transferred to esr tubes under vacuum and then sealed.

A Varian epr-spectrometer operating at 9.5 GHz with 100-kHz field modulation and a 6-in. magnet was employed to obtain the esr spectra. The sample temperature was controlled with heated or cooled nitrogen gas flow into the cavity, and the temperature was measured with a Varian variable temperature accessory. Pitch in KCl was used for calibration purposes.

Results and Discussion

We have adsorbed several nitrogen-containing heterocyclics on MgO and silica-alumina and observed well-defined spectra only in the case of phenazine



A single-line spectrum was observed in the case of acridine having a peak-to-peak width of 24 G. This unusually large width for a radical ion even on solids suggests that the spectrum is an unresolved envelope of the triplet structure to be expected for acridine radical ions.

When phenazine is adsorbed on MgO, no coloration or resonance signal is observed even after keeping the sample for extended periods in the dark. However, after exposure to light from an incandescent lamp for about 10–12 hr, MgO turns pink in color and gives a five-line spin resonance spectrum which is centered at $g = 2.0032$. The five-line spectrum is unsymmetrical

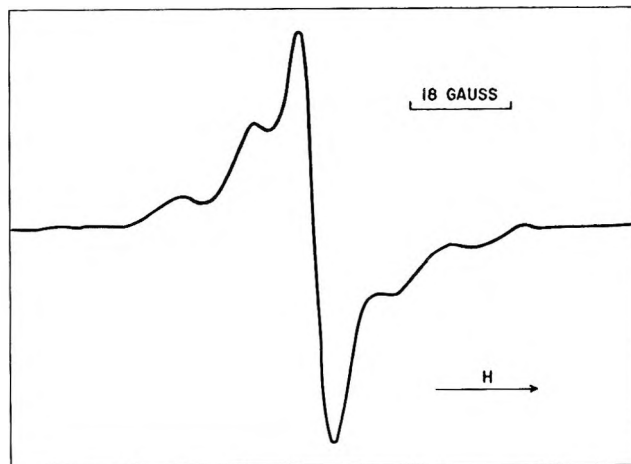


Figure 1. ESR spectrum of phenazine negative ion on MgO.

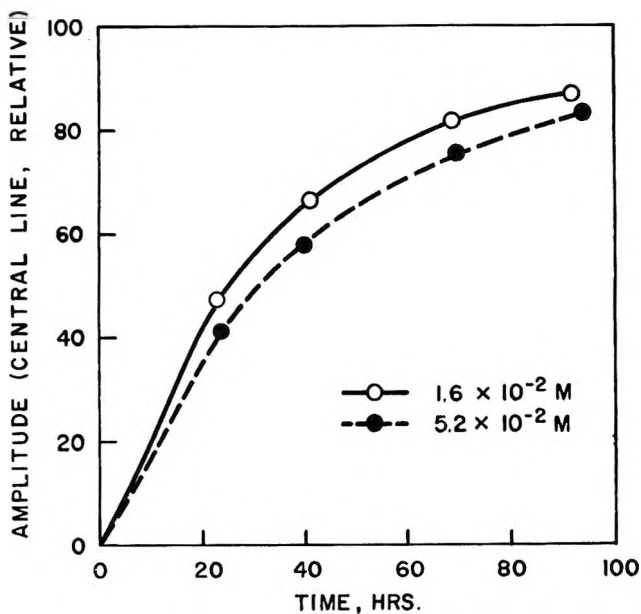


Figure 2. Amplitude of central line of phenazine esr signal as a function of exposure to light. (The spectra of the samples with different concentrations have been run at different instrument gains.)

with the high-field components being broader than the low-field ones (Figure 1). There is no evidence of any further structure superimposed on the five components. The intensity of the signal, as well as the shape of the line itself to a smaller extent, showed marked dependence on the length of exposure to light. Figure 2 shows the amplitude of the central line of the five-line pattern increasing rapidly with exposure to light. The intensity levels off after 200 hr of exposure.

In the case of phenazine adsorbed on silica-alumina, the sample turns green immediately on adsorption, and it is accompanied by a strong esr signal. Again, the intensity of the signal increases with exposure to light. Figures 3 and 4 show the marked changes that are observed as a function of the degree of exposure to light.

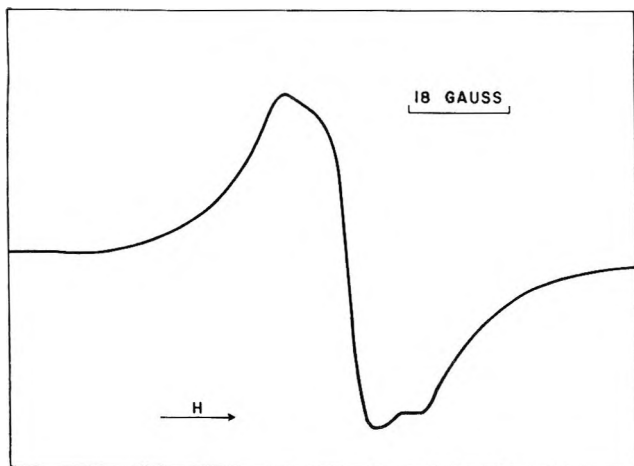


Figure 3. ESR spectrum of phenazine cation on silica-alumina immediately after preparation.

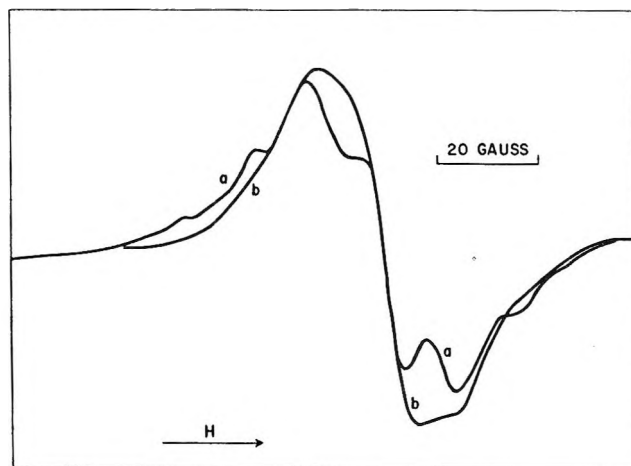


Figure 5. ESR spectrum of phenazine cation on silica-alumina at (a) room temperature and (b) -160° .

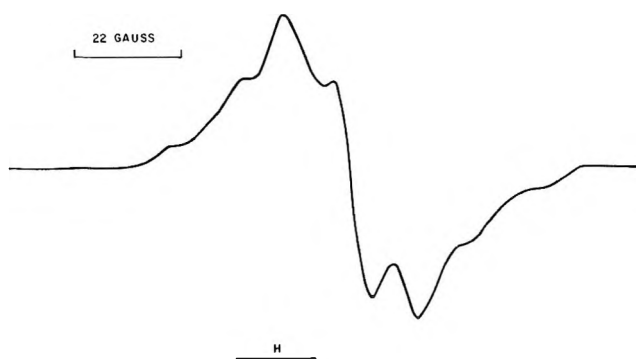


Figure 4. ESR spectrum of phenazine cation on silica-alumina after exposure to light.

Figure 3 is the spectrum observed immediately upon adsorption, while Figure 4 shows the same sample after several hours of exposure to light. Similarly, there is marked dependence of the signal on temperature. Figure 5 compares the spectrum at two temperatures, room and -160° , while Figure 6 shows the spectrum at 80 and 140° . There is a definite sharpening of the line with enhanced resolution at a high temperature, while at a low temperature the signal broadens and the five lines tend to coalesce into one broad envelope.

The mononegative radical ion of phenazine in tetrahydrofuran has been produced by reduction with alkali metal and has been studied in detail.¹¹ The resulting spectrum is isotropic with a large hyperfine splitting constant due to the nitrogen atoms ($A_{iso}^N = 5.14$ G) and smaller couplings due to the protons. The spectrum of phenazine radical ions on MgO shown here is highly asymmetric. The five-line pattern with the outside lines being broader than the central line and the high-field lines being broader than the corresponding low-field lines (Figure 1) suggests that it is due to a single radical ion with hyperfine and/or g anisotropy. Power dependence studies confirm the observation that we are dealing with a single radical species.

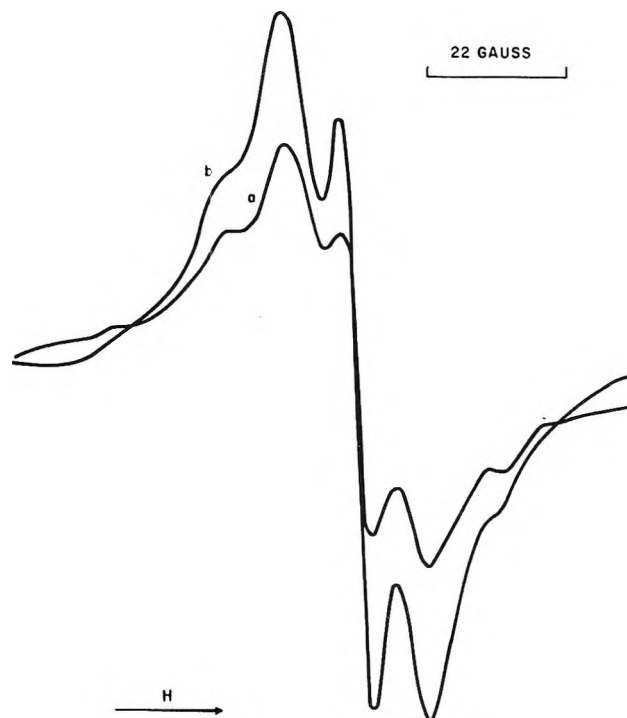


Figure 6. ESR spectrum of phenazine cation on silica-alumina at (a) 80° and (b) 140° .

We are interested at this stage in deriving the best set of spectral parameters from the observed spectra. The effective spin Hamiltonian that describes radicals of the type we are concerned with here is¹²⁻¹⁴

$$\mathcal{H} = \beta S \cdot g \cdot H + S \cdot T \cdot I \quad (1)$$

The first term is the energy of interaction of the electron

- (11) A. Carrington and J. dos Santos-Veiga, *Mol. Phys.*, **5**, 21 (1962).
- (12) S. M. Blinder, *J. Chem. Phys.*, **33**, 748 (1960).
- (13) J. R. Morton, *Chem. Rev.*, **64**, 453 (1964).
- (14) P. B. Ayscough, "Electron Spin Resonance in Chemistry," Methuen & Co., London, 1967.

spin S with the magnetic field H_0 , and the second term is the hyperfine interaction between the electron and the nuclear spin I . If the orbital angular momentum of the unpaired electron were not completely quenched, then the second rank tensor g would be anisotropic and have an average value different from the free-spin g . For systems such as the ones under consideration here, the deviation from the free-spin g value as well as the g anisotropy is small. Also, axial symmetry is often observed.

The hyperfine interaction between the electron and nuclear spin is represented by the second term of eq 1. The second rank tensor \mathbf{T} that describes this interaction can be resolved into isotropic and anisotropic components. The effective Hamiltonian for the hyperfine interaction is then given by

$$\mathcal{H}_{\text{hfs}} = AS \cdot I + S \cdot \mathbf{B} \cdot I \quad (2)$$

and the isotropic and anisotropic components of \mathbf{T} correlate with the first and second terms, respectively, of eq 2.

In eq 2 the first term is the Fermi or contact interaction and arises from the overlap of the nuclear and unpaired electron wave functions. This term was introduced by Fermi in the treatment of atomic hyperfine interaction, and he showed that the constant A is related to the value of the normalized wave function of the unpaired electron at the nucleus

$$A = (8\pi g\beta\gamma/3)|\psi(0)|^2 \quad (3)$$

where γ is the magnetogyric ratio of the nucleus and the other symbols have their usual significance. Clearly, isotropic hyperfine splitting will be nonzero only if $|\psi(0)|^2$ is nonzero; that is, the $|\psi(0)|^2$ screens out all contributions except for s orbitals since p , d , and f orbitals have nodes at the nucleus. The second term of eq 2 is the anisotropic hyperfine interaction. This classical interaction of the electron and nuclear dipoles can be observed only in rigid media and is given by

$$\mathcal{H}_{\text{anisohfs}} = -g\beta\gamma[(S \cdot I)r^{-3} - 3(S \cdot r)(I \cdot r)r^{-5}] \quad (4)$$

It is clearly a direction-dependent interaction since its magnitude depends on the angle α between the radius vector r from the nucleus to the electron and the direction of the magnetic field.

Because of the orbital motion of the electron, the spatial average of the orbital of the unpaired electron must be used for the orientation-dependent term of $\mathcal{H}_{\text{anisohfs}}$, as in

$$\mathcal{H}_{\text{anisohfs}} = BI \cdot S \quad (5)$$

where $B = g\beta\gamma \langle (1 - 3 \cos^2 \alpha)/r^3 \rangle_{\text{av}}$. For spherically symmetrical orbitals $\langle (1 - 3 \cos^2 \alpha)/r^3 \rangle_{\text{av}}$ vanishes; therefore, only non- s orbitals cause anisotropic interactions. The observed hyperfine splittings in rigid media can be contributed to by the isotropic hyperfine coupling A and the traceless anisotropic hyperfine interaction B . The interaction of an un-

paired electron in a $2p$ orbital with a magnetic nucleus is an axially symmetric tensor with observed hyperfine coupling $A + 2B$ parallel to the p -orbital direction (A_{\parallel}), and $A - B$ perpendicular to the p -orbital direction (A_{\perp}).¹²

In view of the above discussion, the observed spectrum of phenazine on MgO must arise from one of the following three possibilities. (1) The outer four lines are parallel hyperfine, and the central line is the remaining parallel feature on which all the perpendicular components are overlapping. (2) The outer four lines are perpendicular features, and the central line is formed by overlap of the remaining perpendicular features and all the five parallel components. (3) Each line is formed by the overlap of a parallel and perpendicular feature. The results satisfying these possibilities are, respectively, $A_{\parallel}^N = 13.95$, $A_{\perp}^N = 13.95$, and $A_{\parallel}^N = A_{\perp}^N = 13.95$ G. The third possibility requires that $A_{\text{iso}}^N = 13.95$ G, which is much larger than what has been observed for the phenazine negative ion in solution¹¹ and, therefore, can be readily rejected. To decide between the other two possibilities, we are assuming $A_{\text{iso}}^N = 5.14$ G.¹¹ This gives $A_{\parallel}^N = 13.95$ G and $A_{\perp}^N = 0.73$ G satisfying the first possibility and $|A_{\perp}^N| = 13.95$ G and $|A_{\parallel}^N| = 12.48$ G satisfying the second possibility. A large value for A_{\perp}^N is incompatible with the observed spectrum since the central line should show this splitting. Also, the B value that would be obtained from this assignment would lead to an unreasonable spin density value. Thus, we assign the first possibility as the correct one.

The transferability of the A_{iso}^N from the THF solution to the rigid medium might be questioned. In that case the line width of the central line could be used to give an independent measure of A_{\perp}^N . For the purpose of comparison, we have also calculated the A_{\perp}^N by this method, and all the results are shown in Table I. The g components are obtained from the center of gravity of the outer components (g_{\parallel}) and from the center of the central line (g_{\perp}). These values are also shown in Table I. Note that the g values show the expected behavior with small g anisotropy and g average slightly greater than the free-spin value. Also, as expected, g_{\perp} is greater than g_{\parallel} .

A phenazine radical ion on silica-alumina gives a markedly different spectrum from that on MgO. Saturation studies indicate that the spectrum is due to a single radical ion. The observed features can be explained if $g_{\perp} \sim g_{\parallel}$ and A_{\perp}^N is fairly large (3 G). In the previous case, g_{\perp} was slightly larger than g_{\parallel} and A_{\perp}^N was small. Because of these conditions, the central parallel component accommodated all the perpendicular features resulting in a five-line spectrum. If A_{\perp}^N is large, the central line may not accommodate all the perpendicular features, and one of them may appear resolved from the central line. The spectrum is analyzed by the procedure mentioned above, and an average value of $A_{\parallel} = 18.97$ G is obtained. Since one of the perpendic-

Table I: Hyperfine Splittings (in Gauss) and g Values of Phenazine Radical Ions

Support solvent	A_{\parallel}^N	A_{\perp}^N	g_{\parallel}	g_{\perp}	A	B	A_{iso}^N
MgO	13.95	0.73	2.0021	2.0038	5.14	4.30	...
MgO	13.95	<3.50 ^a	<3.98 ^a	>3.48 ^a	...
Silica-alumina	18.97	3.50	2.0019	2.0027	8.65	5.16	...
THF	5.14 ^b

^a Obtained by assuming that A_{\perp}^N is half of peak-to-peak width of the central line. ^b Reference 11.

ular features is resolved, by examining the central portion of the spectrum we have obtained an approximate value of 3.5 G for A_{\perp}^N .

Hyperfine structure due to protons has not been observed [proton splittings of 1.9 and 1.6 G have been reported in solution¹¹] and loss of structure may be due to several exchange processes and anisotropy of the coupling tensor for protons in positions 1 and 2. The hyperfine lines due to nitrogen broaden as the temperature is lowered and tend to coalesce, suggesting that the radical ion is mobile at room temperature, but the motion is not rapid enough to average the anisotropic tensor to allow the lines to be resolved or to give rise to isotropic spectrum. There is no direct evidence for chemical exchange, but this cannot be completely ruled out. Electron exchange could also contribute substantially to line broadening. We have studied, for example, spectra of the phenazine ion on MgO at two different concentrations, 1.6×10^{-2} and $5.2 \times 10^{-2} M$, and in the case of the more concentrated solution the outer lines are distinctly broader.

The spectral features of phenazine adsorbed on MgO and silica-alumina are significantly different, so that, when the differences in the properties of MgO and silica-alumina are also considered, it is reasonable to expect that phenazine negative radical ion is produced on MgO and the positive ion on silica-alumina. It is well established that Lewis acid sites on silica-alumina abstract electrons generating positive radical ions.¹ The phenazine radical ion on silica-alumina has a larger splitting. It has been observed in the solution spectra of polyacene ions that the positive ion splittings are generally larger than those of the corresponding negative ion.^{15,16} Also, dihydrophenazine cation has been shown to have $A^N = 6.14$ G.¹⁷ Colpa and Bolton¹⁶ have suggested an extension to the McConnell-Weissman^{18,19} equation to account for the charge effect. Though these equations may not be applicable to rigid systems, the charge effect may be responsible for the difference in spin densities between phenazine positive and negative ions.

The isotropic hyperfine interaction A and the anisotropic hyperfine interaction B give, by the nature of their origin, the s and p character of the orbital of the unpaired electron. The s character can be obtained from

$$A_N/A_0 = a_{2s}^2 \quad (6)$$

by comparing the observed isotropic hyperfine coupling with a parameter A_0 calculated from eq 3 as if the unpaired electron were entirely in the $2s$ orbital. Similarly, the p character of the orbital of the unpaired electron can be calculated from

$$B_N/B_0 = a_{2p}^2 \quad (7)$$

by comparing the observed anisotropic hyperfine splitting to the parameter B_0 calculated as if the unpaired electron were entirely in the $2p$ orbital. The spin populations in nitrogen $2s$ and $2p$ orbitals are given, respectively, by a_{2s}^2 and a_{2p}^2 . Values of $\psi^2(0)$ and $\langle r^{-3} \rangle_{2p}$ have been computed from suitable wave functions and the values $A_0 = 1540$ MHz and $B_0 = 48$ MHz¹³ have been used to get the spin densities given in Table II. For comparison, Table II also shows the corresponding values of several nitrobenzenes.

Table II: Spin Population of Nitrogen Atomic Orbitals

	a_{2s}^2	a_{2p}^2	a_{2p}^2/a_{2s}^2
Phenazine on MgO	0.009	0.257	28
Phenazine on MgO	0.012 ^a	0.202 ^a	17 ^a
Phenazine on silica-alumina	0.015	0.300	20
Nitrobenzene on MgO	0.020 ^b	0.491 ^b	25 ^b
<i>m</i> -Dinitrobenzene on MgO	0.022 ^b	0.483 ^b	22 ^b
<i>sym</i> -Trinitrobenzene on MgO	0.018 ^b	0.378 ^b	21 ^b

^a From the assumption that $A_{\perp}^N = 0.5 \Delta H_{pp}$. ^b Reference 4.

It should be pointed out that the spin densities are not as accurate as those obtained from the solution spectra, since we only have a rough estimate of A_{\perp}^N . The s character of the orbital of the unpaired electron is small, and its significance is somewhat uncertain because it is similar in magnitude to the spin polarization effect. It is reasonable to conclude that most ($\sim 60\%$)

(15) J. R. Bolton and G. K. Fraenkel, *J. Chem. Phys.*, **40**, 3307 (1964).

(16) J. P. Colpa and J. R. Bolton, *Mol. Phys.*, **6**, 273 (1963).

(17) B. L. Barton and G. K. Fraenkel, *J. Chem. Phys.*, **41**, 1455 (1964).

(18) H. M. McConnell, *ibid.*, **24**, 764 (1956).

(19) S. I. Weissman, *ibid.*, **25**, 890 (1956).

of the spin density is distributed between the two nitrogen atoms. This is somewhat larger than that calculated by molecular orbital theory.¹¹ If the rest of the spin density is distributed on carbons adjacent to nitrogens, the spin densities in positions 1 and 2 would be definitely less than what is expected from the solution spectra. This would lead to smaller proton splitting in the adsorbed species.

The value of a_{2s}^2 given for the phenazine negative radical ion could be slightly more than what is given in Table II, bringing a_{2p}^2/a_{2s}^2 for the radical anion and radical cation much closer. These are similar in magnitude to what has been observed in the case of nitrobenzene on MgO surface. No data from frozen solution are available to indicate whether any molecular distortion of phenazine is occurring as a result of adsorption, which in turn would have explained the larger value observed for the spin density on nitrogen than calculated by molecular orbital theory. Nevertheless, the value of a_{2p}^2 is closer to the spin density on nitrogen estimated from the solution spectra¹¹ and *m*-dinitrobenzene radical anion in frozen solution,²⁰ suggesting that there is no molecular distortion due to adsorption.

It is interesting to compare the spin densities in the corresponding positions of aromatic and nitrogen heteroaromatics to see the effect that a nitrogen atom has in altering the spin densities in other positions. Anthracene has been studied on silica-alumina by several authors,^{1,3} but no one has made an attempt to calculate the spin densities. But the coupling constants observed by Muha³ agree well with those observed in sulfuric acid solution. The spin densities in position 9 of the anthracene molecule using the excess charge relation of Colpa and Bolton are 0.224 and 0.215 for the positive and negative ions, respectively. Unfortunately, we do not have the complete electron distribution in the ring of the adsorbed molecule, and it is difficult to assess the effect of nitrogen on electron distribution.

The mechanism by which radical ions are formed on the surface of silica-alumina has been studied in detail. It is thought that positive radical ions are formed by electron transfer to Lewis acid sites. The surface of MgO has not been so extensively studied, and it has been postulated by Tench and Nelson⁴ that lattice O^{2-} ion on the surface is the source of electrons. We have observed that a rigorous dehydration of MgO surface is not required to generate nitrobenzene anion on its surface. Nitrobenzene radical anions have been detected

on MgO surface activated in air at 500°, brought into contact with a solution of nitrobenzene in a suitable solvent, which is then pumped off. Activation in air should be cleaning the surface to produce enough O^{2-} on the surface, which in all probability is the source of electrons. It has been estimated that any molecule having electron affinity less than 0.5 eV⁴ cannot acquire an electron by this mechanism. Nitrobenzenes having an electron affinity of 0.7 eV are in favorable positions. Some of the nitrogen heterocyclic molecules which we have studied in which no radical ion formation was observed have electron affinities probably less than 0.5 eV. Surface cleanliness may also be a problem. We have on certain occasions failed to produce phenazine anion on MgO which could be associated with the degree of surface cleanliness. We have also not been able to produce either nitrobenzene or phenazine radical anion on a CaO surface by activation in air. CaO is populated with more hydroxyl groups than MgO, and a more rigorous cleaning of its surface is perhaps required to produce an O^{2-} ion on the surface in sufficient quantity which is the supposed source of electrons. Work now in progress hopefully will allow us to draw some definite conclusions concerning the role of the basicity and degree of cleanliness of the surface.

Photochemistry of phenazine has been studied by several workers (references cited in ref 21). Recently Bailey and coworkers²¹ have studied the photoreduction of phenazine in acidic methanol. They have observed that in a weakly acidic medium, dihydrophenazine is formed, while in strongly acidic medium, phenazinium radical cations are formed. Phenazine is definitely photosensitive and MgO and silica-alumina surfaces seem to favor the formation of radical ions. Radical ions are not immediately formed on contact in the case of MgO. Different radical ionic species are produced on MgO and silica-alumina. All these point to the fact that both light and surface are required to generate the radical ions. Light facilitates the electron-transfer process on the surface.

Acknowledgment. We wish to acknowledge helpful discussions with Dr. W. K. Hall. Also, we thank Mr. Arthur V. Fareri for his diligent technical assistance.

(20) W. M. Fox, J. M. Gross, and M. C. R. Symons, *J. Chem. Soc., A*, 448 (1966).

(21) D. N. Bailey, D. K. Roe, and D. M. Hercules, *J. Amer. Chem. Soc.*, **90**, 6291 (1968).

Membrane Potentials of Fused Silica in Molten Salts. A Reevaluation

by Kurt H. Stern

Electrochemistry Branch, Naval Research Laboratory, Washington, D. C. 20390 (Received July 9, 1969)

A method for determining the parameters K' and n of the Eisenman equation from membrane potentials alone is presented. It is applied to data for alkali chloride-silver chloride mixtures. $n \cong 1$ for all the data, K' increases in the order $\text{Na} < \text{Li} < \text{K} < \text{Cs}$, but the difference arises largely from differences of the ion mobilities in the glass, rather than differences of the ion-exchange equilibrium constant.

It seems to be generally agreed¹⁻³ that the membrane potentials observed at glass-molten salt interfaces are best accounted for in terms of a theory proposed by Eisenman⁴ in which the glass is treated as a cation exchanger and the membrane potential, consisting of the sum of a phase boundary potential and a diffusion potential, is given by the equation

$$E_M = \frac{RT}{F} \ln [a^{1/n} + K'^{1/n} b^{1/n}]^n + \text{constant} \quad (1)$$

where a and b represent the activities in the melt of two cations exchanging on the glass, K' is the electrode selectivity constant which contains the ion-exchange equilibrium constant and the mobility ratio of the ions in the glass, and n is a constant characteristic of the particular ions and the glass.

Equation 1 or one of its modifications has been applied most frequently in molten salts with Ag^+ and Na^+ as the exchanging cations. Keenan, Notz, and Wilcox⁵ determined selectivity constants for several ions in nitrate melts for Pyrex, relative to sodium. Doremus³ determined K' for Ag^+ - Na^+ exchange on fused silica in the same melt. Both authors solved eq 1 for K' by taking $n = 1$. Doremus argued that the approximately constant value of K' obtained supported this assumption, on the basis of data obtained for a fairly narrow concentration range ($0.339 \leq X_{\text{AgNO}_3} \leq 0.836$).

However, Stern² calculated n values as high as 3.5 for various silver-alkali metal cation exchanges on fused silica in chloride melts from measurements in which the alkali halide concentration varied by a factor of more than 100. Also, Garfinkel⁶ has reported nonunity n values for various cation exchanges on a variety of glasses.

In view of the discrepancies in the above-mentioned works,^{2,3} the relevant equations and data have been reexamined. Additional data for fused silica in AgCl - NaCl melts have been obtained over as wide a concentration range as possible, *i.e.*, using solutions very dilute in sodium. In addition, the recent observation⁷ that above 800° the total ionic concentration of fused silica in AgCl - NaCl melts increases prompted us to make membrane potential measurements in this region.

Theory

For the concentration cell



the membrane potential $E_M = E_{\text{cell}} - E_{\text{electrode}}$ can be written for two exchanging ions as

$$E_M = \frac{RT}{F} \ln \left[\frac{a_1^{1/n} + K'^{1/n} b_1^{1/n}}{a_2^{1/n} + K'^{1/n} b_2^{1/n}} \right]^n \quad (2)$$

where the ionic activities are taken to be those of the melt components AX and MX , respectively. In the usual experimental arrangement one half-cell *e.g.*, I^- , is maintained at constant composition and eq 2 is then identical with eq 1. If this reference compartment is AgX without added NaX (a small, but not necessarily negligible, concentration of NaX is usually present as impurity) then $a_2 \cong 0$, $b_2 \cong 1$.

Doremus³ solved eq 2 by assuming $n = 1$. His result is equivalent to

$$K' = \frac{a_1}{\exp(E'_M) - b_1} \quad (3)$$

where we have written $E'_M = E_M/(RT/F)$ for convenience.

Stern² solved eq 1 from the initial condition that $E_M = 0$ when $a \cong 0$ which leads to

$$K' = \frac{a_1}{b_1 [\exp(E'_M/n) - 1]^n} \quad (4)$$

A comparison of eq 3 and 4 shows that even for $n = 1$, they are the same only if $b_1 = 1$, *i.e.*, in melts dilute in sodium. The difference arises because in transforming

(1) K. Notz and A. G. Keenan, *J. Phys. Chem.*, **70**, 662 (1966).

(2) K. H. Stern, *ibid.*, **72**, 1963 (1968).

(3) R. H. Doremus, *ibid.*, **72**, 2877 (1968).

(4) (a) G. Eisenman in "Advances in Analytical Chemistry and Instrumentation," Vol. 4, C. N. Reilly, Ed., John Wiley and Sons, New York, N. Y., p 305; (b) G. Eisenman in "Glass Electrodes for Hydrogen and Other Cations," G. Eisenman, Ed., Marcel Dekker, Inc., New York, N. Y., 1966, Chapter 5.

(5) A. G. Keenan, K. Notz, and F. L. Wilcox, *J. Phys. Chem.*, **72**, 1085 (1968).

(6) H. M. Garfinkel, *ibid.*, **72**, 4175 (1968).

(7) K. H. Stern, *ibid.*, **72**, 2256 (1968).

Table I: Membrane Parameters for Binary Alkali Chloride-Silver Chloride Melts at Various Constant Temperatures, 560-585°

M	G ^a				V ^b	
	<i>n</i>	<i>K'</i>	<i>u_M/u_{Ag}</i>	<i>K</i>	<i>n</i>	<i>K'</i>
Li	1.0	2.3 × 10 ⁻⁴	6	1.4 × 10 ⁻³	1.0	3.7 × 10 ⁻⁴
Na	...	6.9 × 10 ⁻⁵	4.8	3.3 × 10 ⁻⁴	...	1.2 × 10 ⁻⁴
	1.0 ^c	4.4 × 10 ⁻⁵		2.1 × 10 ⁻⁴		
	1.0 ^c	3.6 × 10 ⁻⁵ ^d		1.7 × 10 ⁻⁴		
K	1.2	4.9 × 10 ⁻³	0.06	1.7 × 10 ⁻⁴	1.1	4.9 × 10 ⁻³ (<i>a_M</i> < 1.5 × 10 ⁻³) 3.3 × 10 ⁻³ (<i>c_M</i> > 1.5 × 10 ⁻³)
	Cs	1.2		2.9 × 10 ⁻³ (<i>a_M</i> < 1.4 × 10 ⁻³)		...
	1.5	1.6 × 10 ⁻³ (<i>a_M</i> > 1.4 × 10 ⁻³)				

^a General Electric Type 204 fused silica. ^b Vycor. ^c From data of Figure 2. ^d 546°.

eq 1 into 4, *b* was not explicitly set equal to unity, which implicitly makes the constant in (1) contain a variable *b*. No significant errors were introduced into the numerical calculation of *K* by this error because all the melts used were in fact very dilute in sodium. However, a more serious error occurred in the calculation of *E'_M* from *E_M* because inadvertently the relation $E'_M = E_M (2.303RT/F)$ was used. As can be seen from eq 4 this leads to an error in the bracket which is particularly serious at low concentration. The data in Table I of ref 2 have therefore all been recalculated.

If the factor *n* is retained, eq 2 can be put into a linear form by substituting *a*₂ = 0, *b*₂ = 1. The result is

$$\exp(E'_M/n) - b_1^{1/n} = \frac{a_1^{1/n}}{K'^{1/n}} \quad (5)$$

The same result is obtained from eq 1 from the boundary condition that *E_M* = 0 when *a* = 0, *b* = 1, which leads to a value of $-(RT/F) \ln K'$ for the constant.

One might expect that a plot of the left side of eq 5 vs. *a*^{1/*n*} would give a straight line with slope *K'*^{1/*n*} only if the correct value of *n* is chosen. As can be seen from eq 1, however, this plot will be linear whenever *a*^{1/*n*} ≫ (*K'**b*)^{1/*n*} whether the correct value of *n* has been chosen or not. If *K'* is very small, as it is in the halide systems, eq 5 will produce a linear plot, *i.e.*, a constant *K'*, no matter what value of *n* is used. Therefore nonlinear behavior would only be observable in very dilute alkali halide solutions. Similarly, a plot of *E_M* vs. $\ln a$ will be linear with slope *RT/F*, no matter what the value of *n* is.

The problem of calculating *n* for systems in which (*K'**b*)^{1/*n*} ≪ *a*^{1/*n*} can also be seen when eq 5 is written in the form

$$Z_n = \log [\exp(E'_M/n) - b^{1/n}] = \frac{1}{n} \log a - \log K'^{1/n} \quad (6)$$

It might seem that this equation is well suited for the evaluation of *n* and *K'* from the same data. Thus, if *Z_n*, calculated for various values of *n*, is plotted against $\log a$ the plot having the correct value of *n* will be linear with slope 1/*n*, and *K'* is calculated from the limiting value of *Z_n* when *a* = 1. This form of the equation can then be used for successive approximations; *i.e.*, if the choice of *n* used for the calculation of *Z_n* disagrees with the slope, *n* is varied systematically until agreement is obtained. However, this procedure is sensitive to changes in *n* only if *K'* is sufficiently large.

The data of Doremus³ provide a good example where this condition is fulfilled. In Figure 1 are shown plots of *Z_n* vs. $\log a$ for *n* = 1 and *n* = 2. When *Z₁* is plotted against $\log a$, a slope corresponding to *n* = 0.93 is obtained. Extrapolation to *a* = 1 gives *K'* = 0.175, in good agreement with the method used by Doremus. A plot of *Z₂* vs. $\log a$ is also linear, but with a slope corresponding to *n* = 1.04, showing that the incorrect value of *n* had been selected. Evidently convergence of the equation is quite rapid.

In contrast to membrane potentials of fused silica in AgNO₃-NaNO₃ melts for which *K'* is fairly large, measurements for the same glass in AgCl-NaCl melts give very small *K'* values. Since previous data² were not obtained at sufficiently low NaCl concentrations, new measurements were made at very low concentrations. The rationalized membrane potential $E_M/(2.303RT/F)$ is plotted in Figure 2 as a function of $\log a$ for runs at two temperatures, 546 and 575°. Only for *a* ≲ 3 × 10⁻⁴ are deviations from linearity observed. Above that activity (for data used in the activity calculations, see below) the plots are linear with a slope of 0.93. The corresponding *Z* vs. $\log a$ plots are shown in Figure 3 for the 546° run. The *Z₁* plot is linear with a slope corresponding to *n* = 1.05, whereas the *Z₂* plot clearly deviates from linearity for *a* < 3 × 10⁻⁴, *i.e.*, in exactly the region where *E_M* itself deviates from linearity. For *a* < 3 × 10⁻⁴ the plot is linear with a slope corresponding

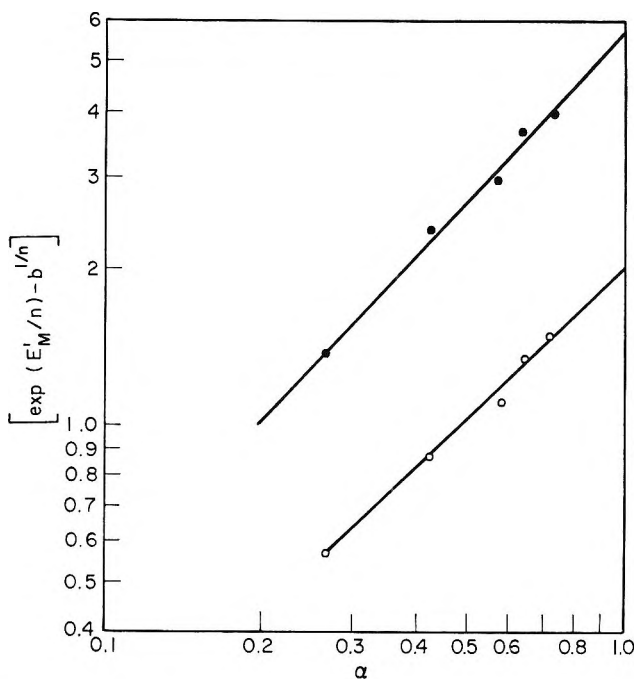


Figure 1. Plot of eq 6, data of ref 3: ●, $n = 1$; ○, $n = 2$.

to $n = 2.07$. Thus, had data only at the higher concentrations been available, they would have been consistent with either $n = 1$ or 2. K' can be determined either from the intercept of eq 6 or from the slope of eq 5. For dilute-solution data, which would involve a long extrapolation by using eq 6, eq 5 is preferable. However, both methods will be insensitive to n if $(K'b)^{1/n} \ll a^{1/n}$, i.e., both equations will be linear, and will yield nearly the same value of K' no matter what value of n is used. For example, from eq 5, using the linear portion of the 546° data in Figure 2, we get $K' = 3.75 \times 10^{-5}$ with $n = 1$ and $K' = 3.90 \times 10^{-5}$ with $n = 2$.

The results of the above analysis may be summarized as follows. (a) The membrane potential of cell A is given by eq 2. For the special case of $a_2 = 0$, $b_2 = 1$ this equation can be transformed into eq 5 and 6 which are linear for the correct choice of n . (b) If $(K'b)^{1/n} \ll a^{1/n}$ these equations are linear, independent of the choice of n . For this condition membrane potentials cannot be used to determine n . (c) If $(K'b)^{1/n}$ and $a^{1/n}$ are of the same order of magnitude, both K' and n can be determined from membrane potentials alone using eq 6 in a successive approximation method. (d) If only dilute solution (small a) data are available, eq 5 is preferable to eq 6 for the determination of K' . (e) For the condition described under (b) the value of K' is independent of the choice of n . It is therefore most easily calculated from eq 5 with $n = 1$.

Experimental Part

In order to obtain dilute solution data for cell A with $M = \text{Na}$, the previously described procedure² was modified by making the variable compartment of the cell from 22-mm o.d. tubing. With about one mole

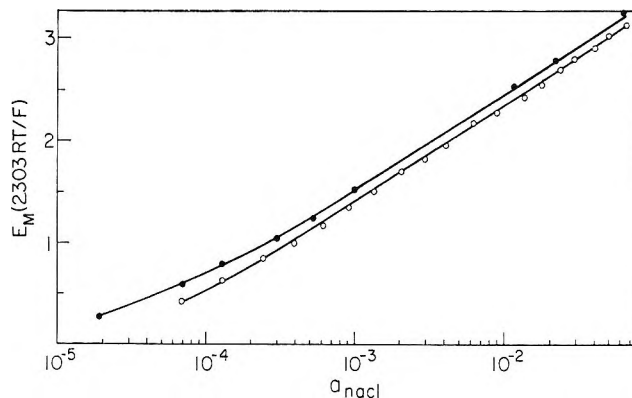


Figure 2. Plot of E'_M vs. a_{NaCl} : ●, 546°; ○, 575°.

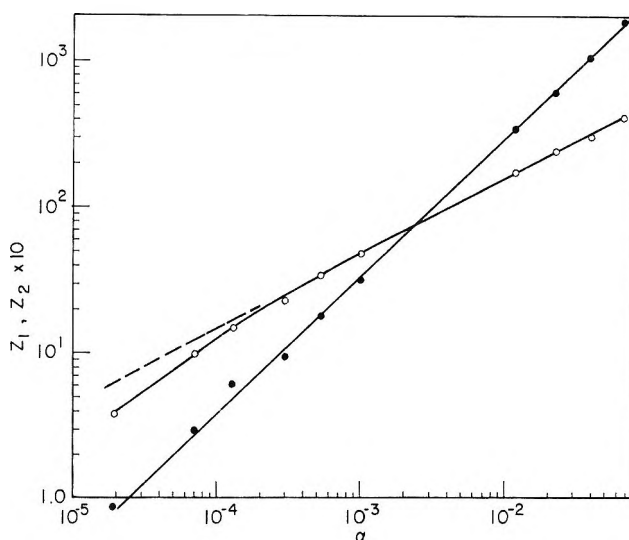


Figure 3. Plot of eq 6, 546° data of Figure 2. ●, $n = 1$; ○, $n = 2$.

of AgCl in this compartment, an NaCl concentration of 10^{-5} (10^{-3} mol %) corresponded to a weight of 0.6 mg, which could be weighed to ± 0.01 mg on a semimicro balance. Runs were made at 546 and 575° to supplement those reported previously² in this temperature range, and above 800° to see if the net ionic diffusior.⁷ into fused silica is reflected in the membrane potential behavior.

Since the NaCl impurity present in AgCl may constitute a significant fraction of the added NaCl for very dilute NaCl melts,² the batch of AgCl used was analyzed by flame photometry. No sodium could be detected, and the lower detection limit is estimated as 6×10^{-6} mol %. This impurity is therefore insignificant in even the most dilute melts employed. Similar measurements made at 823 and 865° differed from those at the lower temperatures in one significant respect. Whereas in the latter case steady emf's are obtained at even the lowest sodium concentration, this is not true above 800°. Up to concentrations near 3×10^{-4} the emf first increases (as expected) and then slowly decreases

after addition of NaCl, *i.e.*, it changes in the direction expected for a decrease of the Na⁺ concentration in the melt. This result is consistent with the observation⁷ that above 800° the total cationic concentration of fused silica immersed in molten salts increases. For concentrations above 3×10^{-4} fairly steady emf's are obtained and the dependence of E_M on the NaCl concentration is linear with an approximately Nernstian slope.

In order to separate the selectivity constant K' into its equilibrium and diffusion parts, mobility measurements of Ag⁺ and alkali metal cations in fused silica were also made. The procedure was similar to that used by Doremus,³ except that U-shaped cells, similar to those employed for the membrane potential measurements, were utilized. Since only AgCl melts below the temperature at which data were needed, the individual undried alkali halides were simply packed into the cell. Above 500° sintering of the salt was sufficient to give good contact with the membrane and the results were quite reproducible. The salts were successively tamped into the cell (which was cleaned between salts); a voltage of 200 V applied between Ag electrodes until the current became constant. The data for Li are somewhat uncertain since the electrolysis seemed to produce irreversible changes in the glass, as evidenced by the observation that currents for the other ions could not be reproduced after LiCl had been electrolyzed in the cell.

Results and Discussion

In this section we present the results of recalculating K' and K values for the data in ref 2, using procedures outlined in this paper.

Activity coefficients of the components were calculated using the regular solution equation and constants given by Lumsden.⁸ For the binary AgCl-alkali halide melts the activity coefficient of each component is given by

$$RT \ln \gamma_i = A(1 - X_i)^2 \quad (7)$$

The values of A are: Li, 2100; Na, 900; K, -2200; Cs, -4000. For AgCl melts dilute in two alkali halides the activity coefficient of each alkali halide was calculated by this equation, using the constant A appropriate for the cation being considered. In each case an attempt was made to calculate n from eq 6 by substituting successive values of n (usually $n = 1, 2, 3$) into the left side of the equation. If a plot of the left side *vs.* $\log a$ yielded a slope of $1/n$ no matter what n was, n was considered nondeterminable. K' was then determined from eq 5 with $n = 1$, but no n value is listed. If the same procedure gave a slope of $1/n$ for only one value of n , then that value of n is listed. In Table I are listed values of K' and n for all the melts in which only a single alkali halide (MCl) was added to AgCl. K' is defined by

$$K' = \frac{a_s b_g}{b_s a_g} \left(\frac{u_{Ag}}{u_M} \right)^n = K \left(\frac{u_{Ag}}{u_M} \right)^n \quad (8)$$

where a and b are the activities of the ions M⁺ and Ag⁺, and the subscripts s and g refer to the solution and glass phase, respectively. u_M and u_{Ag} are the ionic mobilities in the glass. The mobility ratios, determined by the procedure described in the preceding section and the ion-exchange equilibrium constant K , as defined by eq 8 and determined from the measured K' and mobility ratios, are also listed.

Only for Na was K' too small for n to be determined from the data in ref 2 and n was therefore determined from the data of Figure 2. This n value now agrees with that found by Doremus for the same glass in AgNO₃-NaNO₃ melts at 333°. However, the K' value in the chloride melt is smaller by four orders of magnitude. Because this effect is not likely to be due primarily to the difference in temperature, it would have to be accounted for in terms of the difference in anions. Since only cation and glass properties explicitly affect K' this may appear surprising. However, the effect of the anions can be made explicit by writing the standard Gibbs energy corresponding to the ion-exchange equilibrium constant K in the form

$$\Delta G^\circ = (\bar{G}_M^s - \bar{G}_{Ag}^s) + (\bar{G}_M^g - \bar{G}_{Ag}^g)$$

where \bar{G} is the chemical potential of the subscripted species and s and g refer to solution and glass, respectively. A change of solution anion will affect the first parenthesis, but not the second. More details of this "anion effect" will be reported in a subsequent paper.

In contrast to the Li and Na data which are well fitted over the entire concentration range with $n = 1.0$, the behavior of K and Cs is more complicated. For GE 204 glass the potassium data over the entire activity range ($2 \times 10^{-4} < a_K < 8.6 \times 10^{-3}$) are well fitted by $n = 1.2$, $K' = 4.9 \times 10^{-3}$, but for Vycor a single value of $n = 1.1$ produces two slightly different values of K' . The cesium data for GE 204 seem to be fitted best by two different values of n and corresponding K' 's. An examination of the original data (Figure 1 of ref 2) shows a kink in the K and Cs data (E'_M *vs.* X_{MCl}) of the kind that has been interpreted in terms of two kinds of ion-exchange sites.⁹ There is at present very little information concerning the possibility of two kinds of sites on these two glasses, though they cannot be ruled out. Alternatively, it is also possible that the results for K and Cs can be accounted for in terms of the method of calculation which assumes that only K⁺-Ag⁺ and Cs⁺-Ag⁺ exchange, respectively, are occurring. At very low concentrations of K⁺ and Cs⁺ the E_M values for these ions are very small and it is possible that the impurity Na⁺ in the AgCl is also involved in the exchange. This possibility can be examined

(8) J. Lumsden, "Thermodynamics of Molten Salt Mixtures," Academic Press, New York, N. Y., 1966.

(9) B. P. Nicolovsky, M. M. Shultz, and A. A. Belijustin, "Glass Electrodes for Hydrogen and Other Cations," G. Eisenman, Ed., Marcel Dekker, New York, N. Y., 1967, Chapter 6.

quantitatively by considering a system of several ions which may exchange between melt and glass. For N ions in a concentration cell¹⁰ of the type discussed

$$E'_M = \ln \frac{\sum_{i=1}^N \frac{u_i}{N} K_{1i} a_i}{\sum_{i=1}^N \frac{u_i}{N} K_{1i} a_i} \quad (9a)$$

or

$$E'_M = \ln \frac{\sum_{i=1}^N K'_{1i} a_i}{\sum_{i=1}^N K'_{1i} a_i} \quad (9b)$$

where the subscript 1 defines a "reference ion" and we have assumed the case $n = 1$, since this appears justified by the data in Table I. Equation 2 is obviously the two-ion form of eq 9 with $n = 1$. [Note that the first term of (9b) is $K'_{11}a_1 = a_1$.] The results in Table I were calculated by taking the alkali metal ion as the reference ion in each case, *i.e.*, for each ion K' is defined by eq 8 and may thus be notated K'_{MAg} .

For the case $M = Na$, only two terms in eq 9 are required for a satisfactory solution. Any impurity ion i would contribute a term $K'_{1i}a_i$ which is evidently negligible. This is also true if $M = Li$, but not for $M = K, Cs$. It is instructive to compare these two cases by assessing the relative importance of the impurity sodium in each case.

Using the subscripts 1, 2, 3 for the reference ion, Ag, and Na, respectively, gives

$$E'_M = \ln \frac{a_1 + K'_{12} a_2 + K'_{13} a_3}{K'_{12} a_2 + K'_{13} a_3} \quad (10)$$

From eq 8 it is evident that $K'_{13} = K'_{12}/K'_{32}$ when $1 = Li$, $K'_{LiNa} = K'_{LiAg}/K'_{NaAg} = (2.3 \times 10^{-4})/(6.9 \times 10^{-5}) = 3.3$. $a_3 \approx 10^{-5}$, $a_2 \approx 1$, $6 \times 10^{-3} \leq a_1 \leq 10^{-1}$. Hence $K'_{12}a_2 \approx 2 \times 10^{-4}$, $K'_{13}a_3 \approx 3 \times 10^{-5}$, which is small compared to $K'_{12}a_2$ and negligible compared to a_1 . Hence the effect of the sodium impurity is negligible. Moreover, since $K'_{12}a_2 \ll a_1$, a nearly Nernstian slope is observed for the dependence of E_M on a_{Li} .

When the reference ion is potassium $K'_{13} = K'_{KNa} = K'_{KAg}/K'_{NaAg}$. Assuming that the value of K'_{KAg} in Table I is approximately correct gives $K'_{KNa} \approx 5 \times 10^{-3}/7 \times 10^{-5} = 70$. Therefore $K'_{13}a_3 \approx 7 \times 10^{-4}$, $K'_{12}a_2 \approx 5 \times 10^{-3}$, compared to $2 \times 10^{-4} \leq a_1 \leq 9 \times 10^{-3}$. The relation between $K'_{13}a_3$ and $K'_{12}a_2$ is similar to the lithium case ($K'_{13}a_3 < K'_{12}a_2$) so that no large error resulted from the neglect of the former term. However, since $K'_{12}a_2$ is now comparable to a_1 the slope of E_M vs. $\ln a_1$ is now much less than RT/F . In view of the relatively small value of $K'_{13}a_3$ for fused silica it does not appear likely that the neglect of this term is the major reason for the slightly complicated behavior of

cesium for which K'_{12} is similar to the potassium value. In any case $K'_{13}a_3$ will be least important when a_1 is large, so that the K' value for potassium and cesium calculated for this condition are likely to be the best ones.

In view of the method that had to be used the mobility ratios are probably no better than $\pm 10\%$. It is clear, however, that the difference in K' values arises largely from this mobility term. For example, K' for sodium is 100 times as large as for potassium, but the ion-exchange equilibrium constant K is nearly the same for both ions. In all cases the glass greatly prefers the alkali metal ion to silver. Vycor and fused silica do not differ significantly.

The theory of the parameter n is not yet well developed. In purely thermodynamic terms $n = 1$ if the activity coefficient of the ions in the glass is independent of concentration. The parameter has also been discussed in terms of the interaction of ions in solution with the exchange sites of the glass.^{6,11} In fused silica these sites are probably $AlOSi^-$, in which Al^{3+} is surrounded tetrahedrally by four oxygens.¹² If the glass is a regular solution, n can be expressed as¹³

$$n = 1 - \frac{W_{AB}}{2RT} \quad (11)$$

where W_{AB} is the excess interaction energy of neighboring ions A and B. For $n > 1$, $W_{AB} < 0$, indicating repulsion between A and B. Using the known Al^{3+} concentration in fused silica, 65 ppm, and an Si-O distance of 1.8 Å gives an average distance of 2.8×10^4 Å between sites, a distance very large compared with ionic dimensions. At this distance even coulomb repulsion between point charges *in vacuo* is very small and this would be further reduced by the intervening medium. Therefore $W_{AB} \approx 0$ and $n \approx 1$, as is indeed found for fused silica. The "nonideality" observed for K^+ and Cs^+ may also arise if the glass (in this case the surface layer of the glass in equilibrium with the melt) is very dilute in one of the ions. In that case, even though the glass behaves as a regular solution, the activity coefficient may not be independent of composition¹⁴ and n calculated from eq 1 will exhibit a concentration dependence. A distinction between this explanation and the one discussed in terms of eq 10 above would require experimental data on ion exchange in fused silica. These are not yet available.

When more than one alkali metal chloride is present on each side of the membrane a total of three cations

(10) F. Conti and G. Eisenman, *Biophys. J.*, **5**, 247 (1965).

(11) N. Landquist, *Acta Chim. Scand.*, **9**, 595 (1955).

(12) G. Eisenman, *Biophys. J.*, **2**, 259 (1962).

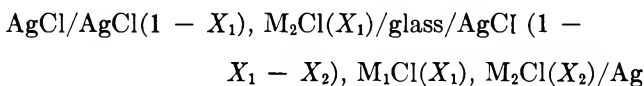
(13) R. M. Garrels and C. L. Christ, "Solutions, Minerals, and Equilibria," Harper and Row, New York, N. Y., 1965, pp 272-279.

(14) R. H. Doremus in "Ion Exchange," J. A. Marinsky, Ed., Marcel Dekker, Inc., New York, N. Y., Vol. II, p 19.

Table II: Ion Selectivity Constants $k = K'_{\text{NaAg}}/K'_{\text{MAg}}$ for Fused Silica, Vycor, and Pyrex⁶ from Data of Table I and Ref 5

M	Fused silica	Vycor	Pyrex (350°)
Na	1.00	1.00	1.00
Li	0.30	0.32	0.63
K	1.4×10^{-2}	2.4×10^{-2} ($a_M < 1.5 \times 10^{-3}$) 3.6×10^{-2} ($a_M > 1.5 \times 10^{-3}$)	0.070
Cs	2.4×10^{-2} ($a_M < 1.4 \times 10^{-3}$) 4.3×10^{-2} ($a_M > 1.4 \times 10^{-3}$)	4.8×10^{-2} ($a_M > 0.7 \times 10^{-3}$)	...
Ag	6.9×10^{-5}	1.2×10^{-4}	0.78

(plus impurities) may be involved in the exchange. Several measurements of the cell



with $M_1, M_2 = \text{Li}^+, \text{Na}^+, \text{K}^+$, and Cs^+ were reported in the original paper.² Since X_2 never exceeded a few mol %, X_1 remained virtually constant during a run and the change of E_M is accounted for by the change in X_2 on one side of the membrane. However, E_M also depends on X_1 . The situation can be illustrated for the case $M_1 = \text{Li}^+, M_2 = \text{Na}^+$. Emf data were determined for fused silica and three different values of X_2 : 0.00109, 0.00642, and 0.0411. In each case the dependence of $\exp E'_M$ on a_1 (the activity of LiCl) is linear, but the slope depends on X_2 . However, a plot of $\exp E'_M$ vs. $(a_1/a_2)(a_2$ is the activity of NaCl) gives a single straight line for the three different X_2 values. This observation can be expressed as

$$a_1/a_2 = K' \exp E'_M + \text{constant}$$

The constant is evaluated from the condition $E'_M = 0$ when $a_1 = 0$. A simple rearrangement then gives

$$\exp E'_M = \frac{a_1 + K'a_2}{K'a_2} \quad (12)$$

which is just eq 2 with $n = 1$ and the proper boundary conditions, *i.e.*, it is an equation derived for the exchange of two ions on glass. Since eq 10 must also apply to this cell ($1 = \text{Li}, 2 = \text{Na}, 3 = \text{Ag}$) it follows that $K'_{13a_3} = K'_{\text{LiAg}}a_{\text{Ag}}$ is much less than $K'_{12a_2} = K'_{\text{LiNa}}a_{\text{Na}}$. For the most dilute sodium solution the latter term is $(3.3)(1.09 \times 10^{-3}) = 3.6 \times 10^{-3}$, whereas $K'_{\text{LiAg}}a_{\text{Ag}} = 2.3 \times 10^{-4}$ so that for this system eq 10 reduces to eq 12. A further check on the identification of the K' in eq 12 with K'_{LiNa} can be made by solving eq 12 directly from the data. This is most easily done by putting it into the linear form

$$\exp E'_M - 1 = \left(\frac{a_1}{a_2}\right) \frac{1}{K'} \quad (13)$$

This gives $K' = 3.6$, which can be compared with the value of K'_{LiNa} calculated from Table I, *i.e.*, $K'_{\text{LiNa}} = K'_{\text{LiAg}}/K'_{\text{NaAg}} = 3.3$, in excellent agreement. Similarly,

for Vycor eq 13 gives 4.3 for K'_{LiNa} , whereas from the values in Table I we get 3.1, in good agreement. Further confirmation for these results comes from the set of data in which the roles of sodium and lithium are reversed, with sodium now the reference ion ($1 = \text{Na}, 2 = \text{Li}$). An analysis of these data by eq 13 now gives $K'_{\text{NaLi}} = 0.324$, corresponding to $K'_{\text{LiNa}} = 1/K'_{\text{NaLi}} = 3.1$.

The above procedure is also applicable to cells in which $M_1 = \text{Na}, M_2 = \text{K}$ ($X_2 = 0.0962, 0.0297$). Equation 13 gives $K'_{\text{NaK}} = 1.7 \times 10^{-2}$, whereas from Table I we get $K'_{\text{NaAg}}/K'_{\text{KAg}} = 1.4 \times 10^{-2}$. In terms of eq 10 this is because $K'_{13a_3} = K'_{\text{NaAg}}a_{\text{Ag}} \ll K'_{12a_2} = K'_{\text{NaK}}a_{\text{K}}$. Evidently, neglecting the slight nonunity of n for potassium has little effect on the results. The corresponding data for Vycor do not fit eq 13, although the K' values are nearly the same as for fused silica. We have no reasonable explanation for this result.

A direct comparison of the K' values in Table I with the ion selectivities k in ⁵ for Pyrex in nitrate melts can be made¹⁵ by dividing K'_{NaAg} by the respective K'_{MAg} . This yields ion selectivities relative to $k_{\text{Na}} = 1.00$. The results are shown in Table II. The selectivity sequence of all three glasses for the alkali metal ions is the same: $\text{Na} > \text{Li} > \text{K} \approx \text{Cs}$. This is to be expected in terms of the Eisenman theory¹² since for all three glasses the ratio of trivalent ions (Al^{3+} or B^{3+}) to monovalent ions is greater than unity. The much greater selectivity of Pyrex for silver suggests the possibility that in this glass there may be two kinds of exchange sites, one for the alkali metal cations and another for silver. Although this is very speculative it is consistent with the two-phase nature of this glass.¹⁶

Finally, it should be reemphasized that the electrode selectivity of the glass, as expressed either in terms of K' or the k values in Table II depends on *both* the ion exchange equilibrium constant K and the ionic mobilities in the glass. Any energetic arguments concerning ion-glass interactions depend on K alone. These K values decrease slightly in the sequence $\text{Li}^+ > \text{Na}^+ > \text{K}^+$, *i.e.*, the corresponding ΔG^0_{MAg} values

(15) I am indebted to Dr. H. M. Garfinkel, Corning Glass Works, for this suggestion.

(16) H. M. Garfinkel, *J. Phys. Chem.*, **73**, 1766 (1969).

become more positive, a trend also observed¹² for these ions exchanging on AlOSi^- sites in aqueous solution. This sequence is thus consistent with the view⁵ that in both aqueous solution and in molten salts it is the bare

ion which interacts with the exchange site on the glass.

Acknowledgements. I am greatly indebted to Dr. Hans Oser of the National Bureau of Standards for very helpful mathematical discussions.

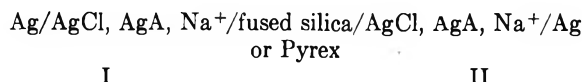
The Effect of Anions on Sodium-Determined Glass

Membrane Potentials in Molten Salts

by Kurt H. Stern

Electrochemistry Branch, Naval Research Laboratory, Washington, D. C. 20390 (Received July 28, 1969)

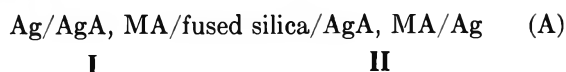
The effect of changing anion composition on the sodium-determined glass membrane potential was studied using the molten salt concentration cell



for low concentrations of Na^+ , and $\text{A} = \text{NO}_3^-, \text{SO}_4^{2-}, \text{CrO}_4^{2-}, \text{PO}_4^{3-}$. For all of these anions the ion-exchange selectivity constant increases in a regular manner with increasing oxyanion concentration. Since the cation mobility ratio in the glass is unaffected by changing melt composition, the ion-exchange equilibrium constant similarly increases. These results are accounted for in terms of Eisenman's selectivity theory and the double layer at the glass-melt interface.

Introduction

In a previous study¹ of the effect of added cations on the emf of concentration cells of the type



it was found that when $\text{M} = \text{Na}^+$ and $\text{A} = \text{Cl}^-$ or Br^- the membrane potential could be expressed as

$$E_M = -(RT/F) \ln [X_{\text{MA(II)}}/X_{\text{MA(I)}}] \quad (1)$$

for $X > 10^{-5}$, where X is the mole fraction. This is the result to be expected when the only potential-determining equilibrium at the salt-glass interface is $\text{Na}^+(\text{salt}) = \text{Na}^+(\text{glass})$, or more precisely, if the equilibrium $\text{Ag}^+(\text{salt}) + \text{Na}^+(\text{glass}) = \text{Ag}^+(\text{glass}) + \text{Na}^+(\text{salt})$ lies very far to the left. In the formulation of the cell emf there appears no parameter characteristic of the anions since both the Nernst emf for the electrode reaction and the interfacial potential involve cations only. When M is an ion other than sodium and ion-exchange processes at the glass-salt interface must be taken into account in the formulation of the cell emf, only cation exchange is considered to occur, in accord with direct studies of such processes.² When

the anion compositions on the two sides of the membrane are different, the anions appear explicitly, but only as part of the appropriate anion-cation pairs AgA' , AgA'' , MA' , and MA'' ; the electrode and phase boundary processes still only involve cations.^{1,3} This result may be described by saying that no specific anion-glass interaction need be postulated to account for the emf of cell (A) when Cl^- and Br^- are the anions.

It is now recognized that in general, the membrane potential of cell A is accounted for by the Eisenman equation⁴ which is of the form

$$E_M = RT/F \ln \left[\frac{a_1^{1/n} + K'^{1/n} b_1^{1/n}}{a_2^{1/n} + K'^{1/n} b_2^{1/n}} \right]^n \quad (2)$$

where the membrane potential $E_M = E_{\text{cell}} - E_{\text{Nernst}}$, a and b are the activities of the two cations M^+ and Ag^+ , respectively, K' is the ion-exchange selectivity

(1) K. H. Stern, *J. Phys. Chem.*, **72**, 1963 (1968).

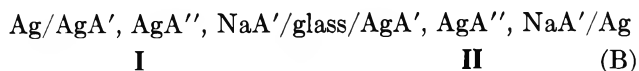
(2) K. H. Stern, *Chem. Rev.*, **66**, 355 (1966).

(3) K. H. Stern, *J. Electrochem. Soc.*, **114**, 1257 (1967).

(4) G. Eisenman, in "Glass Electrodes for Hydrogen and Other Cations," G. Eisenman, Ed, Marcel Dekker, Inc., New York, N. Y., 1966, Chapter 5.

constant, and n is a thermodynamic factor which is constant for a given pair of ions and a particular glass. If $K'b \ll a$, eq 2 reduces to eq 1. For fused silica in AgCl–NaCl mixtures, it was found⁵ that $n = 1$ and $K' = 4 \times 10^{-5}$ at 575°. However, Doremus⁶ found $n = 1$ and, $K' = 0.2$ for the same glass in AgNO₃–NaNO₃ melts at 333°.

Since K' values are expected to depend only on the cation, and it seemed questionable whether such a large difference in K' could be accounted for by a change in temperature alone, measurements of cell A have been repeated, but with a variety of anion mixtures. The methodology follows the earlier work¹ with fused silica membranes, except that mixed anion melts and only sodium salts were used. The cells can thus be described as



The factors limiting the choice of systems are (1) decomposition of the salts with increasing temperatures, and (2) increasing electrical resistance of fused silica with decreasing temperature. For example, at 350° the resistance of the membranes is in the 10¹¹–10¹² Ω range, which constitutes a practical upper limit for emf measurements with high-impedance pH meters. However, many silver salts decompose below this temperature and therefore are unsuitable. The following silver salts were used (mp in °C): AgNO₃ (212), Ag₂SO₄ (652), Ag₂CrO₄ (690), Ag₃PO₄ (849). The fused silica was the same as used previously,¹ General Electric Type 204; in some experiments Pyrex was used to determine the effect of glass composition on E_M .

Experimental Part

Construction of the cells and methods of measurements have been described previously.¹ Mixed silver anion melts AgA'–AgA'' were prepared by melting together weighed quantities of the two salts, pouring the mixture onto a tray, and grinding the quenched melt into powder. In any particular run the desired silver salt mixture AgA'–AgA'' was weighed into both cell compartments and the sodium salt added as either NaA' or NaA''. Since the concentration of sodium salt was kept low, generally $10^{-3} < X < 6 \times 10^{-2}$, the anion ratio was not greatly changed during the run. After additions of NaA had been made to one side of the cell, similar additions were made to the other side to provide a duplicate run. Reagent grade silver salts were used without purification. The various sodium salts were vacuum dried.

In order to see if the change in K' values depended on changes of cation mobilities in the glass, some conductance experiments were also carried out in U-shaped silica cells with a membrane in the middle of the U. This permitted changes in salt composition

to be made without changing the glass–melt interfacial area. Melts were electrolyzed between Ag electrodes at 200 V and the current measured on a Photovolt recorder.

Results

AgCl–Ag₂SO₄. The melting point of Ag₂SO₄ is 660° and decomposition is not appreciable below 750°. The solid–liquid equilibrium over the entire composition range was determined by Sokolov.⁸ Up to 75 mol % Ag₂SO₄ the system is liquid. Using the data for the liquidus line and the known heats of fusion and ΔC_p values, it can be shown⁹ that even at the eutectic temperature (304°, 30 mol % Ag₂SO₄) these solutions are nearly ideal ($\gamma_{\text{AgCl}} = 0.9$). Since solutions generally become more nearly ideal with rising temperature, the system can be regarded as approximately ideal at the temperature of the experiment (540–580°). Activity coefficients of NaCl in AgCl solutions are given by¹⁰ $RT \ln \gamma = 900X^2_{\text{AgCl}}$, corresponding to a dilute solution limit ($X_{\text{AgCl}} = 1$) of 1.7 at the temperature of the experiment. However, γ_{NaCl} remains essentially constant over the concentration range used. Thermodynamic data for Na₂SO₄–Ag₂SO₄ and for the ternary system Na⁺–Ag⁺–Cl–SO₄²⁻ are not available, and we therefore *provisionally* assume ideal behavior of Na⁺ in AgCl–Ag₂SO₄ melts. Cell B was run with AgCl–Ag₂SO₄ mixtures ranging from 10 to 58 mol % Ag₂SO₄ to determine how the effect of Na⁺ on the emf depends on the Cl⁻/SO₄²⁻ ratio. Figure 1 shows the results obtained for the addition of NaCl at various constant temperatures between 540 and 580°. In order to permit comparison of results at slightly different temperatures the membrane potential is plotted as $E_M/(2.303 \cdot RT/F) = E'_M$. E_M was calculated by subtracting the Nernst emf from the total cell emf. Up to 2 mol % NaCl this correction is only 1 mV. Open and closed symbols of the same shape represent duplicate runs and the Cl⁻/SO₄²⁻ ratio is shown next to the respective curves.

The addition of even 10 mol % Ag₂SO₄ to AgCl (Cl⁻/SO₄²⁻ = 9.0) notably inhibits the membrane response to additions of NaCl. For AgCl alone, plots are linear down to at least 10⁻⁴ with the theoretical slope of unity for E'_M vs. $\log X_{\text{Na}^+}$. In 10 mol % Ag₂SO₄ curvature begins to be noticeable just below 10⁻³. Moreover, although the plot is linear above that concentration, the absolute value of E'_M is mark-

(5) K. H. Stern, *J. Phys. Chem.*, **74**, 1323 (1970).

(6) R. H. Doremus, *ibid.*, **72**, 2877 (1968).

(7) K. H. Stern and E. L. Weise, "High-Temperature Properties and Decomposition of Inorganic Salts. Part I. Sulfates," NSRDS-NBS 7, 1966.

(8) S. I. Sokolov, *Zh. Fiz. Khim. Obshch.*, **62**, 2319 (1930).

(9) K. H. Stern and S. Caulder, in preparation.

(10) J. Lumsden, "Thermodynamics of Molten Salt Mixtures," Academic Press, New York, N. Y., 1966, p 94.

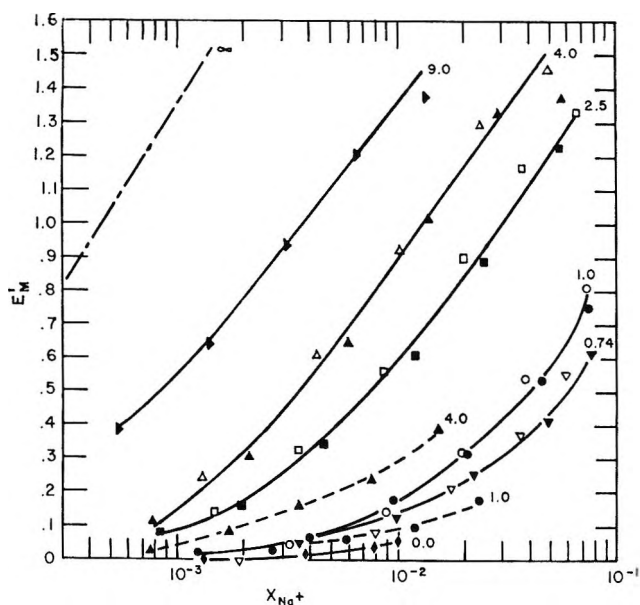


Figure 1. E'_M values vs. X_{Na^+} of cell B. $A' = Cl^-$, $A'' = SO_4^{2-}$. Numbers to the right of the respective curves are the molar ratios $X_{Cl^-}/X_{SO_4^{2-}}$. Open and closed symbols having the same shape are duplicate runs; ---, Pyrex.

edly depressed below that for pure AgCl so that for any X_{Na^+} , the membrane potential is less when Ag_2SO_4 is present. As the sulfate concentration increases, the nonlinear region shifts to progressively higher X_{Na^+} values so that E'_M for any constant X_{Na^+} decreases with increasing $X_{SO_4^{2-}}$. In all cases the slopes approach the theoretical value of unity at sufficiently high X_{Na^+} .

The data in Figure 1 could be accounted for if the sodium impurity content were as high as a few mole per cent, *i.e.*, if the added sodium were negligible compared to the sodium initially present. Although an impurity level of this magnitude in reagent Ag_2SO_4 appeared unlikely, the material was nevertheless analyzed for sodium by flame photometry. The upper limit for X_{Na^+} is 6×10^{-4} and therefore, the data of Figure 1 cannot be accounted for in this way. The critical importance of the sulfate ion in inhibiting the potential response of the glass to sodium is therefore clearly established.

To see if the effect depends on the glass composition as well as the anion, similar measurements were carried out with Pyrex cells using 20 and 50 mol % Ag_2SO_4 -AgCl melts. As can be seen from Figure 1 the Pyrex curves lie lower than the fused silica curves for the same melt composition; *i.e.*, the same SO_4^{2-} concentration is more effective in inhibiting the sodium response with Pyrex than with silica.

Although the above results may appear to be in disagreement with previous measurements¹¹ on Ag_2SO_4 - Na_2SO_4 concentration cells with Vycor membranes in which E'_M vs. $\log X_{Na^+}$ was linear with unit slope, the sodium concentration in that study always ex-

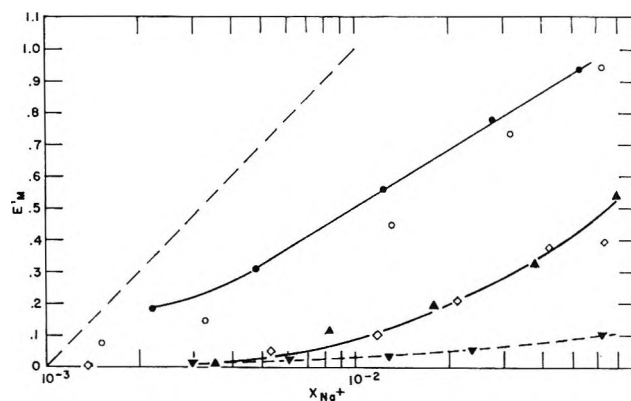


Figure 2. E'_M values vs. X_{Na^+} of cell B. $A' = Cl^-$, $A'' = NO_3^-$; ---, unit slope. ● $O_{X_{NO_3^-}} = 0.50$, Δ $X_{NO_3^-} = 0.76$, both GE204. ○, $X_{NO_3^-} = 0.50$, $X_{NO_3^-} = 0.80$ both Pyrex.

ceeded 90 mol %. Since the slopes of all the curves in Figure 1 increase with increasing X_{Na^+} and are close to unity even below 10 mol % Na^+ , they are expected to have the limiting value in high Na^+ melts because then $X_{Na} \gg K'X_{Ag}$.

$AgCl$ - $AgNO_3$. The respective melting points of AgCl and $AgNO_3$ are 455 and 212°; the system exhibits a eutectic at $X_{AgCl} = 0.185$ and 176°.¹² The working range of the solutions is limited by the thermal decomposition of $AgNO_3$ at higher temperatures and the high resistance of fused silica at the lower. The latter factor limits working temperatures to above 300° ($R < 10^{12} \Omega$) although Pyrex cells may be measured at lower temperatures. Above 350° gas evolution from the melt fixes the highest accessible AgCl composition at ~50 mol %.

$AgCl$ - $AgNO_3$ solutions are nearly ideal¹³ and the activity coefficient of $NaNO_3$ in $AgNO_3$ is given by¹⁴ $RT \ln \gamma = 760 X_{AgNO_3}^2$. As in the sulfate case, we provisionally use ion fractions instead of activities for the ternary melts dilute in sodium.

Plots of E'_M vs. $\log X_{Na^+}$ are shown in Figure 2 for two $AgCl$ - $AgNO_3$ concentrations with both fused silica and Pyrex membranes. As in the sulfate case E'_M is depressed considerably more on Pyrex for the same melt composition.

$AgCl$ - Ag_2CrO_4 . The phase diagram of this system has been determined by Lesnykh and Bergman.¹⁵ From 0 to ~80 mol % Ag_2CrO_4 the liquid is in equilibrium with β - Ag_2CrO_4 , with a eutectic at 40 mol % and 354°. At 437° α - and β - Ag_2CrO_4 are in equilib-

(11) K. H. Stern and S. E. Meador, *J. Res. Nat. Bur. Stand.*, **69A**, 553 (1965).

(12) M. A. Sacharatschenko and A. G. Bergman, *Samml. Aufsätze allgem. Chem. USSR*, **1**, 126 (1953).

(13) Reference 10, p 130.

(14) Reference 10, p 121.

(15) A. S. Lesnykh and A. G. Bergman, *Zh. Fiz. Khim.*, **30**, 1959 (1956).

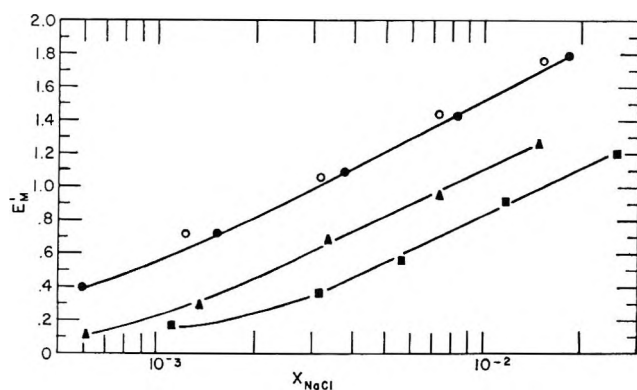


Figure 3. E_M' values vs. X_{Na^+} of cell B. $A' = Cl^-$, $A'' = CrO_4^{2-}$; ●, ○, $X_{CrO_4^{2-}} = 0.20$; ▲, $X_{CrO_4^{2-}} = 0.40$; ■, $X_{CrO_4^{2-}} = 0.60$.

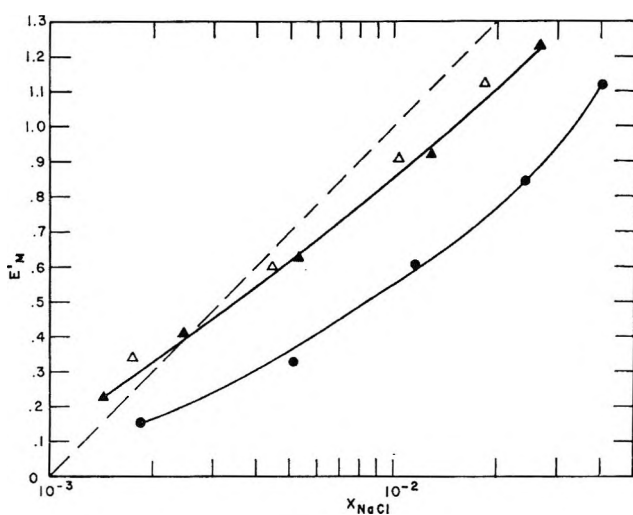


Figure 4. E_M' values vs. X_{Na^+} of cell B. $A' = PO_4^{3-}$; ▲, △, $X_{PO_4^{3-}} = 0.20$; ●, $X_{PO_4^{3-}} = 0.50$; ---, unit slope.

rium with the liquid. At higher temperatures, α - Ag_2CrO_4 is the stable solid phase. At 530° the liquid range extends from 0 to 85 mol % Ag_2CrO_4 . Results for three different Cl^-/CrO_4^{2-} ratios are shown in Figure 3. In contrast to the sulfate and nitrate systems all three plots of E_M' vs. $\log X_{NaCl}$ have nearly the expected slope of unity. Nevertheless, the actual values of E_M' for a given X_{NaCl} decrease with increasing CrO_4^{2-} concentration. This is likely to be the consequence of behavior similar to the sulfate and nitrate systems, but at concentrations lower than 10^{-3} . There appears to be some sign of increasing nonlinearity in the lower two curves to support this argument.

AgCl-Ag₃PO₄. Since no phase diagram of this system could be found in the literature, cooling curves were determined for several compositions and a phase diagram constructed. This is of the simple eutectic type with a eutectic at ~ 20 mol % Ag_3PO_4 at 415° . At 600° the liquid range extends from 0 to 60 mol % Ag_3PO_4 . E_M' vs. $\log X_{NaCl}$ curves are shown for two melt compositions in Figure 4. At $X_{Ag_3PO_4} = 0.20$

deviations from unit slope are noticeable and at $X_{Ag_3PO_4} = 0.50$ they are quite pronounced.

Discussion

The analysis of the data in Figures 1–4 was carried out using the procedure developed in a preceding paper.⁵ Briefly, the method consists of writing the equation for the membrane potential (the Eisenman equation) in the form

$$Z_n = \log [\exp(E_M'/n) - b^{1/n}] = \frac{1}{n} \log a - \log K'^{1/n} \quad (3)$$

where $E_M' = E_M/(RT/F)$, a and b are the Na^+ and Ag^+ activities in the melt, K' is a selectivity constant defined by

$$K' = \frac{a_s b_g (u_{Ag})^n}{b_s a_g (u_M)^n} = K \left(\frac{u_{Ag}}{u_M} \right)^n \quad (4)$$

where the subscripts s and g represent the solution and glass phases, respectively; n is a constant for a given pair of cations and glass and is a measure of ideal behavior ($n = 1$). n was determined from eq 3 by plotting Z_n vs. $\log X_{Na}$, the cation fraction of sodium in the melt. Since in the dilute solutions employed, the activity coefficient $\gamma = a/X$ presumably remains essentially constant, no error in the calculation of n arises from the assumption of dilute solution behavior. In nearly all cases, values of n very close to unity were obtained. K' was then calculated by putting eq 1 in the form

$$\exp(E_M'/n) - b^{1/n} = \frac{a^{1/n}}{K'^{1/n}} \quad (5)$$

and taking $n = 1$. (K' is insensitive to the choice of n .⁵) Since activity coefficients in the ternary melts are not known, ideal behavior was assumed. Thus the "true" K' differs from the calculated one by the factor γ .

The results of the calculations for all of the systems are listed in Table I. The n values listed are those obtained from a plot of eq 3 when $n = 1$ is substituted in the left side of that equation. The results are quite startling. In each Na^+-Ag^+ melt, an increase in the oxy-anion concentration produces an increase in K' . For example, in $Cl^-SO_4^{2-}$ mixtures an increase of X_{SO_4} from zero to 0.58 increases K' by three orders of magnitude. The effect is much too large to be accounted for by the slightly different temperatures at which runs for a particular anion pair were made. Although the melting points of the salts and their thermal stability necessitated a different temperature range for each such pair, the data for mixtures of SO_4^{2-} , CrO_4^{2-} , and PO_4^{3-} lie within a 60° range. A comparison of the effect of these ions on K' is thus meaningful. In addition, all the systems can be com-

Table I: Membrane Parameters for Cell B Obtained from Eq 3 and 5; for Explanation See Text

Oxyanion	Glass	X_A	t , °C	n	K'
SO_4^{2-}	G ^a	0.00	543	1.0	1.9×10^{-5}
		0.00	575	1.0 ^c	4.4×10^{-5d}
		0.10	560	1.0	4.2×10^{-4c}
		0.20	580	0.86	1.4×10^{-3}
	P ^b	0.28 ₆	560	0.95	3.2×10^{-3}
		0.50	546	0.89	1.9×10^{-2}
		0.58	553	0.98	2.8×10^{-2}
		1.00	737	1.5	6.5×10^{-1}
NO_3^-	G ^a	0.50	360	1.1	5.3×10^{-3}
	P ^b	0.50	322	0.8	3.1×10^{-2}
CrO_4^{2-}	G ^a	0.20	532	1.0	3.0×10^{-4}
		0.40	529	0.7	9.0×10^{-4}
		0.60	513	0.9	1.6×10^{-3}
PO_4^{3-}	G ^a	0.20	598	0.8	2.4×10^{-3}
		0.50	581	0.9	3.9×10^{-3}

^a General Electric Type 204 fused silica. ^b Pyrex. ^c Reference 5, AgCl-NaCl, calculated with activity correction. ^d From AgBr-NaBr, calculated with activity correction.

pared for their dependence of K' on the anion composition. As can be seen from a plot of K' vs. the oxyanion concentration for all the data in Table I (Figure 5), the following generalizations can be made. (a) The increase of oxyanion concentration X_A increases K' , but the increase is not quite linear, $\log K'$ increasing most rapidly at low X_A . (b) The slope $d \log K' / dX_A$ decreases in the sequence $\text{SO}_4^{2-} \approx \text{NO}_3^- > \text{CrO}_4^{2-} > \text{PO}_4^{3-}$. (c) K' depends on the glass as well as on the salt, being larger for Pyrex than for fused silica in both $\text{Cl}^- - \text{SO}_4^{2-}$ and $\text{Cl}^- - \text{NO}_3^-$ melts.

The selectivity constant K' defined by eq 4 is the product of a thermodynamic equilibrium constant K and a mobility ratio, $u_{\text{Ag}}/u_{\text{Na}}$. The question thus arises whether K' varies with the changing anion composition because the equilibrium constant K or the mobility term ($u_{\text{Ag}}/u_{\text{M}}$) varies. Although it seemed unlikely that a change in the anion composition of the melt would affect the cation mobilities in the glass, an experimental test nevertheless seemed desirable. For silver ion the conductance was measured in AgCl-Ag₂SO₄ melts at 630° from $X_{\text{Ag}_2\text{SO}_4} = 0$ to 0.30. No change in conductance was found and we therefore conclude that the silver mobility in the glass is independent of the anion composition of the melt. A similar experiment for sodium is more difficult. Sodium salts melt at higher temperatures than silver salts and it is therefore not possible to measure the conductance of liquid binary sodium salt melts at the

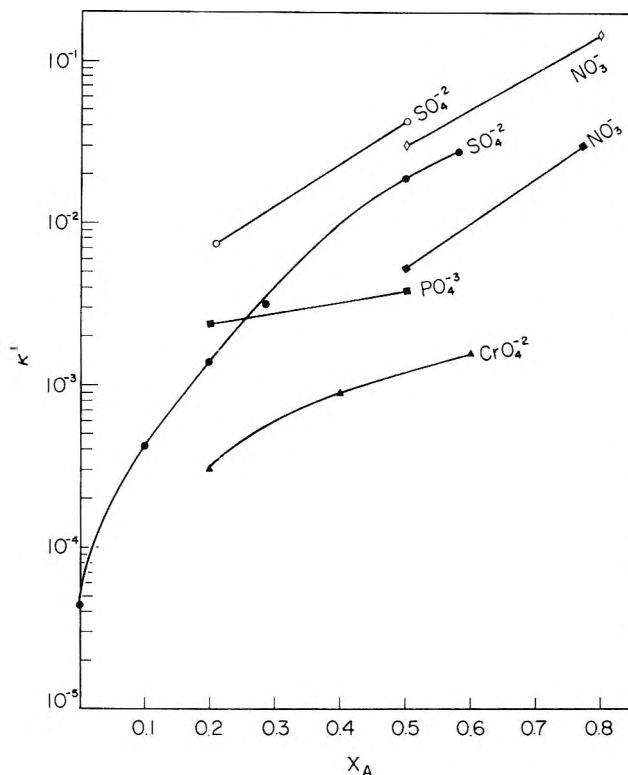


Figure 5. K' as a function of oxyanion concentration X_A . Closed symbols: GE204; open symbols: Pyrex.

same temperature at which the potential measurements were made. Nevertheless some measurements were made at temperatures below 800°, the melting point of NaCl. In NaCl-Na₂SO₄ melts at 722° for $X_{\text{Na}_2\text{SO}_4}$ between 0.23 and 0.35 and in NaCl-NaNO₃ melts at 616° for X_{NaNO_3} between 0.22 and 0.45 there was no change in the conductance of the glass with changing melt composition. Hence the sodium ion mobility in the glass is also independent of the anion composition of the melt. Therefore it seems reasonable to adopt the previously found value⁵ of 0.21 for $u_{\text{Ag}}/u_{\text{Na}}$.

The exchange equilibrium constant K contains cation activities in both the salt and the glass phase. The question then arises whether activities in either of these two phases are likely to vary with the anion composition of the melt. Since all of the anions for which the lowering of E_M at constant X_{Na} (hereafter called the "anion effect") had been observed were oxyanions which are larger than chloride, it seemed of interest to study the effect with a larger monatomic ion to see if size or structure influenced the effect. Therefore potential measurements, similar to those described, were carried out with AgBr-NaBr melts. At 543°, $K' = 1.9 \times 10^{-5}$ (the activities were calculated¹⁰ according to $RT \ln \gamma_{\text{NaBr}} = 1050 X_{\text{AgBr}}^2$), compared with 3.6×10^{-5} in AgCl-NaCl at the same temperature, a rather small difference. This small value of K' is also consistent with results¹ for the

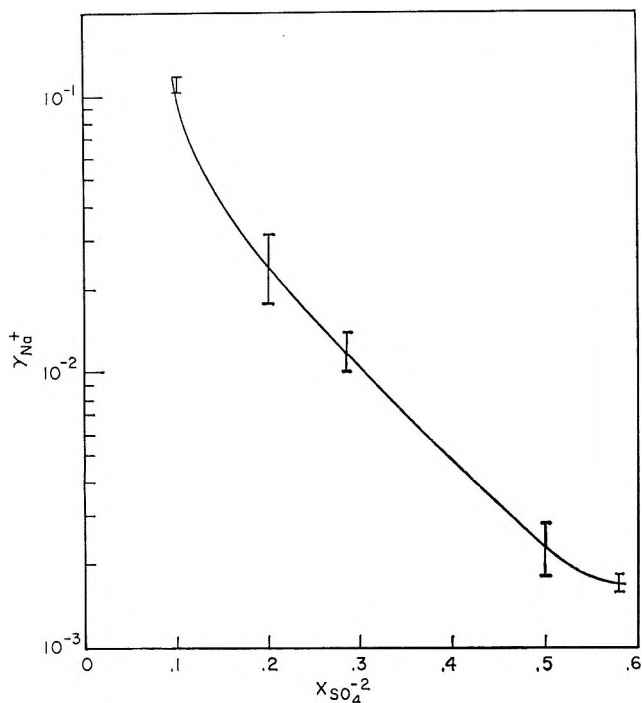


Figure 6. γ_{Na^+} as a function of $X_{SO_4^{2-}}$ in the ternary $Ag^+-Na^+-Cl^-SO_4^{2-}$ melt very dilute in sodium, calculated from eq 5 by assuming $K' = \text{constant}$. I indicates the variation of γ_{Na^+} at each anion composition. For further details see text.

cell $Ag/AgCl, NaCl/glass/AgBr, NaBr/Ag$. Therefore anionic size, *per se*, is not involved in the effect (but see below).

We next examine the thermodynamics of the melts. In terms of eq 5, the question is whether the substitution of the sodium cation fraction for the thermodynamic activity leads to a spurious value of K' . Thus, if K' had the same value in all the melts that it has in $AgCl-NaCl$ we could calculate a . The result for the $Cl^-SO_4^{2-}$ melts is shown in Figure 6. For each anion composition $\gamma_{Na^+} = a_{Na^+}/X_{Na^+}$ is approximately independent of X_{Na^+} as expected for these dilute sodium melts but decreases by two orders of magnitude as X_{Cl^-} increases from 0.1 to 0.58. The question is then whether such small activity coefficients are reasonable. The Cl^- oxyanion melts are all ternary and these are ideal only if ΔG° for the exchange reaction $NaCl + AgX = NaX + AgCl$ is zero.¹⁶ This is usually not the case. However, K' values for the binary $Na_2SO_4-Ag_2SO_4$ melts at 737° (Table I) and $NaNO_3-AgNO_3$ melts at 333° are both much larger than for the pure halide melts, and these melts are reasonably close to ideal. Thus there is at least strong circumstantial evidence that the "anion effect" is not primarily due to neglect of the solution thermodynamics.

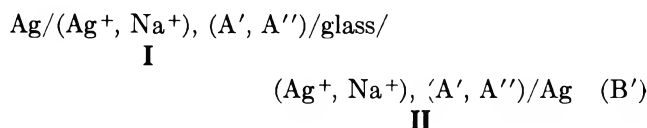
It would of course be desirable to know more precisely how large an error is made by assuming ideal behavior in the ternary melts. Unfortunately, there are no thermodynamic data available for the ternary melts

used in this work.¹⁷ Although ternary melts are rarely ideal they are frequently regular, or nearly so, *i.e.*, ΔS° for the exchange reaction is zero. We compare below ΔS° for the three reactions for which thermodynamic data are available. S°_{298} values are taken

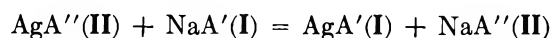
	ΔS°_{600} (cal deg ⁻¹)
$AgCl + NaBr = AgBr + NaCl$	1.13
$AgCl + NaNO_3 = AgNO_3 + NaCl$	-0.40
$2AgCl + Na_2SO_4 = Ag_2SO_4 + 2NaCl$	-1.16

from NBS Circular 500 or its revision (NBS Technical Note 270), $S_T - S^\circ_{298}$ values from U. S. Bur. Mines Bull. 584. For salts that are not liquid at 600°K, ΔS°_{fus} was added to give S°_{600} for a hypothetical liquid. ΔS°_{600} therefore is for the reaction in the liquid state. The departures from regular solution behavior are evidently the same for all three solutions. So far, the emf of concentration cells with membranes and reciprocal regular solutions has been derived only for the case when K' is very small.¹⁸

If cell B is written



then the cell reaction is



and the emf of cell B' is

$$E = [(X_{A'(\text{II})} - X_{A'(\text{I})})(-E^\circ_{A'Ag} + \\ E^\circ_{NaA'} - E^\circ_{NaA''} + E^\circ_{AgA''})] + \\ RT/F \ln \left[\left(\frac{X_{Na(\text{II})}}{X_{Na(\text{I})}} \right) \left(\frac{X_{Ag(\text{I})}}{X_{Ag(\text{II})}} \right) \right] \quad (6)$$

where the X are the cation or anion fractions of the named ions. For the $Ag^+-Na^+-Br^-Cl^-$ system experimental results are in good agreement for Ag^+ -rich melts.¹⁹ Evidently K' values in this system, of the order 10^{-5} , are sufficiently small. For the cells used in this study the first term of eq 6 is zero since the anion composition of the two half cells is the same. Therefore E depends only on the cation composition of the melt. For solutions dilute in sodium ($X_{Ag} \approx 1$) E is then a linear function of $\ln X_{Na}$ with slope RT/F . This is the same behavior expected in ideal solutions with small K' . In terms of eq 2 this condition is more precisely

(16) *E.g.*, M. Blander, in "Molten Salt Chemistry," Interscience, New York, N. Y., 1964, p 197 ff.

(17) Data for $Ag^+-Na^+-Cl^-NO_3^-$ by M. Blander and J. Braunstein, *Ann. N. Y. Acad. Sci.*, **79**, 838 (1960), are only for very dilute solutions of Ag^+ .

(18) K. Grjotheim, K. H. Stern, and L. Thulin, submitted to *Electrochim. Acta*.

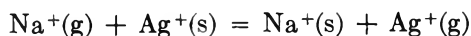
(19) K. H. Stern, submitted to *J. Electrochem. Soc.*

expressed as $K'b \ll a$. For the Cl^- - SO_4^{2-} melts in Figure 1 the plots are fairly linear with a slope of $\sim RT/F$ when $K'X_{\text{Ag}} \leq 3X_{\text{Na}}$. If a similar plot is constructed for hypothetical values of a , b , and various values of K' it is apparent that approximately linear plots are obtained whenever $K'b \leq 3a$. In particular, this relationship would apply if $a = a_{\text{Na}}$. From the similarity of the hypothetical and the real plot it seems likely that γ_{Na} cannot be a strong function of the anion composition as it would have to be (Figure 6) if the variation of K' were to be accounted for by the thermodynamics of the melts. It follows that, even if the neglect of nonideality has produced incorrect K' values in Table I, the change of K' with anion composition is not an artifact of the method of calculation.

We therefore examine next the ways in which anions in the melt may affect cations in the glass. In terms of eq 4, the ion-exchange equilibrium constant

$$K = \frac{(\text{Na}^+)_{\text{s}}(\text{Ag}^+)_{\text{g}}}{(\text{Na}^+)_{\text{g}}(\text{Ag}^+)_{\text{s}}}$$

where the parentheses represent activities. Since we have just shown that the ratio $(\text{Na}^+)_{\text{s}}/(\text{Ag}^+)_{\text{s}}$ is unlikely to be much affected by changes in the anion composition of the melt, it would seem to follow that, if the anion effect is determined only by the thermodynamic properties of the bulk phases, then (for a fixed value of the melt ratio) the ratio $(\text{Ag}^+)_{\text{g}}/(\text{Na}^+)_{\text{g}}$ must be anion dependent. In particular, an increase in the oxyanion concentration increases $(\text{Ag}^+)_{\text{g}}/(\text{Na}^+)_{\text{g}}$. In terms of the exchange reaction



for which

$$\Delta G^\circ = (\mu^\circ_{\text{Na}} - \mu^\circ_{\text{Ag}})_{\text{s}} + (\mu^\circ_{\text{Ag}} - \mu^\circ_{\text{Na}})_{\text{g}} \quad (7)$$

and the difference in the second parenthesis must decrease with increasing oxyanion concentration.

In view of the anionic nature of the glass network and its exchange sites, there is no obvious way in which anions in the melt can affect cation exchange at these sites. From aqueous solutions halide ions have been observed²⁰ to migrate into glass from their respective acids, the order of adsorption being $\text{HCl} \gg \text{HBr} > \text{HI}$, but this migration was into the hydrated layer of the glass. In this layer the water activity was changed and consequently the potential of glass electrodes exhibits an "acid error." This effect is absent for fused silica in molten salts. However, some diffusion of chloride ions into fused silica at 900° has been observed.²¹ No such data are available at lower temperatures. The diffusion rate of silver into glass has, however, been observed²² to vary with the melt anion although no reasonable explanation for this phenomenon has been offered. The situation can be summed up by saying that there is virtually no information bearing on glass-anion interactions.

In view of this situation and the likelihood that melt anions do not interact directly with the exchange sites, we assume such interactions to be absent or insignificant for cation exchange. Consequently, the second parenthesis in eq 7 is not dependent on the melt anion.

We have therefore proved that ΔG° is independent of the anionic composition of the bulk melt; yet ΔG° does change with the anion composition of the melt.

In view of this dilemma we *postulate* that the subscripts s and g do not refer to the bulk phases but only to those parts of the phases which constitute the interface. This hypothesis is certainly justified on the glass side of the interface since no silver ions are present in the glass initially and steady emf's are established so quickly that these ions cannot have penetrated very deeply into the glass interior during this time. We therefore examine a model in which the composition of the interface on the melt side also differs from that of the bulk melt.

At metal-solution interfaces such a model is referred to as a double layer. It is also well known for semiconductor-solution interfaces. According to the Eisenman theory²² of selectivity, cations exchange on anionic sites on the glass. These sites are of two types, AlOSi^- and SiO^- , whose ratio is determined by the $\text{M}^+/\text{Al}^{3+}$ ratio in the glass. In fused silica this ratio is approximately 0.1 (for a listing of ionic impurities in fused silica and Vycor see ref 1) and so most of the sites are AlOSi^- . In terms of this model these sites in or near the surface will have cations exchanging on them. In effect there will then exist a kind of double layer structure with the plane of exchange sites furthest into the glass, a layer of cations adsorbed on the sites and a layer of solution anions on the melt side of the interface. In terms of this simple model the anionic adsorption sites and the melt anions "compete" for the cations.

If this competition is purely electrostatic, a simple Coulomb's law calculation of ΔG° is possible. In this calculation the conceptual difficulties inherent in attributing thermodynamic meaning to a phenomenon occurring on sites at least 100 \AA apart are ignored and chemical potentials are identified with Coulomb interaction energies, *i.e.*, $\mu^\circ_+ = Ne^2/(r_+ + r_-)$. For cations in the melt r_- represents the radius of the melt anion; in the glass r_- is the "equivalent anionic radius"²³ of the AlOSi^- anion. In Table II are listed the ionic radii used, mostly Pauling radii, and the corresponding values of μ°_+ .

Although the individual values of μ°_+ in Table II are quite dependent on the particular values of the ionic radii, it is clear that ΔG° calculated from eq 7 will

(20) K. Schwabe, H. Dahms, Q. Nyuyen, and G. Hoffman, *Z. Elektrochem.*, **66**, 304 (1962).

(21) K. H. Stern, *J. Phys. Chem.*, **72**, 2256 (1968).

(22) M. Richter, *Glastechn. Ber.*, **11**, 123 (1933).

(23) G. Eisenman, *Biophys. J.*, **2**, Part 2, 259 (1962).

Table II: Ionic Radii and μ_i° for Various Cation-Anion Pairs

Ion	r_i , Å	Ion pair	$-\mu_i^\circ$, kcal mol ⁻¹
Ag ⁺	1.25	Ag ⁺ -Cl ⁻	107
Na ⁺	0.95	Ag ⁺ -Br ⁻	103
Cl ⁻	1.81	Ag ⁺ -NO ₃ ⁻	92
Br ⁻	1.95	Ag ⁺ -SO ₄ ²⁻	95
NO ₃ ⁻	2.3	Ag ⁺ -CrO ₄ ²⁻	89
SO ₄ ²⁻	2.2	Ag ⁺ -PO ₄ ³⁻	89
CrO ₄ ²⁻	2.4 ^a	Ag ⁺ -AlOSi ⁻	103
PO ₄ ³⁻	2.4 ^a	Na ⁺ -Cl ⁻	119
AlOSi ⁻	1.95	Na ⁺ -Br ⁻	113
		Na ⁺ -NO ₃ ⁻	101
		Na ⁺ -SO ₄ ²⁻	104
		Na ⁺ -CrO ₄ ²⁻	98
		Na ⁺ -PO ₄ ³⁻	98
		Na ⁺ -AlOSi ⁻	113

^a A. F. Kapustinskii and K. B. Yatsimirskii, *J. Gen. Chem. USSR*, 19, 219 (1949).

be virtually independent of the anionic radii selected and will depend primarily on the cationic radii. The equation also contains no temperature dependence and no simple way of including anion mixtures. In choosing the experimental values of ΔG° for comparison with the calculated ones, only those for single-anion melts are considered. For Cl⁻, Br⁻, and SO₄²⁻ melts experimental data are available from this work, although not at the same temperature. For CrO₄²⁻ and PO₄³⁻ melts the data in Figure 5 have been extrapolated linearly to $X_A = 1$. For NO₃⁻ melts this procedure gives $K' = 0.15$, compared with 0.18 obtained by Doremus⁶ from measurements in AgNO₃-NaNO₃ melts. However, the mobility ratio u_{Na}/u_{Ag} given by Doremus is 13.7, whereas we have measured 5; it is this discrepancy that accounts for the difference in ΔG° .

In Table III are listed ΔG° values calculated by eq 7 and the experimental values for various anions.

Although the experimental values of ΔG° are afflicted with some uncertainties—correct value of the mobility ratio, temperature—it is clear that the agreement be-

Table III: ΔG° for the Exchange Reaction Na⁺(g) + Ag⁺(s) = Na⁺(s) + Ag⁺(g) in Various Melts

Melt anion	ΔG° , kcal, eq 7	ΔG° , kcal, exptl
NO ₃ ⁻	1	1, ^a 0
SO ₄ ²⁻	1	2.3, ^b 0 ^c
CrO ₄ ²⁻	1	-6.3, ^d -4.7 ^e
PO ₄ ³⁻	1	-5.3
Cl ⁻	-2	-14.1
Br ⁻	0	-15.0

^a Reference 6. ^b 737°. ^c 550°, extrapolated from Figure 5. ^d (u_{Na}/u_{Ag}) = 5. ^e (u_{Na}/u_{Ag}) = 13.7.

tween the electrostatic model and the experimental ΔG° is quite good for SO₄²⁻ and NO₃⁻, fair for PO₄³⁻ and CrO₄²⁻, but very poor for Cl⁻ and Br⁻.

This same lack of agreement between the model and the experimental values is also evident for Li⁺-Ag⁺ and K⁺-Ag⁺ exchange on fused silica in the chloride melts⁶ in Table IV.

Table IV

	r_i , Å	$\Delta G^\circ_{\text{calcd}}$, kcal	$\Delta G^\circ_{\text{exptl}}$, kcal	$\Delta G^\circ_{\text{calcd}} - \Delta G^\circ_{\text{exptl}}$
Li ⁺	0.60	-4	-10.6	7
Na ⁺	0.95	-2	-14.1	12
K ⁺	1.33	0	-14.0	14

It thus appears likely that a nonelectrostatic factor which is operative in halide, but not in oxyanion melts, has been neglected in the calculation of ΔG° . Since the glass surface is presumably not changed by changing the anion composition of the melt, this additional factor must affect the first term of eq 7. This term would have to be more negative by ~ 12 kcal in order to agree with experiment. One factor which has obviously been neglected in the calculation is the known tendency of silver to form halide complexes, but the alkali metal cation dependence of ($\Delta G^\circ_{\text{calcd}} - \Delta G^\circ_{\text{exptl}}$) shows that these ions may also interact more specifically with Cl⁻, at least near the glass surface. The fact that the smallest difference is observed for the cation with the highest polarizing power (somewhat akin to complex formation) lends some support to this idea. Not enough is known about CrO₄²⁻ and PO₄³⁻ in these melts to warrant speculation about the moderate discrepancy between calculation and experiment for these ions.

As can be seen from Figure 5, values of K' for fused silica and Pyrex are not the same, but the slope $d \ln K'/dX_A$ is approximately the same for the two glasses and a particular anion. In terms of eq 7 this is because only the second term is glass dependent, *i.e.*, [$\Delta G^\circ(\text{glass 1}) - \Delta G^\circ(\text{glass 2})$] is a constant for a given melt composition. In the Eisenman theory the difference [$(\mu_i - \mu_i)_{\text{glass 1}} - (\mu_i - \mu_i)_{\text{glass 2}}$] is accounted for by the different ratios of exchange sites in the various glasses. The variation of $\ln K'$ with X_A is anion-specific. The initial slope, (at low X_A) is anion-concentration dependent, but at higher values of X_A a constant slope, independent of X_A but varying with the nature of the anion, is reached. This phenomenon is probably related to the complicated ionic interactions, but there seems to be no simple way to account for it quantitatively.

The model presented here is quite speculative and difficult to test experimentally. Measurements of the

double-layer capacitance at the glass-molten salt interface might be used to explore this region and the effect of changing melt composition on it. Thermodynamic measurements of the melt in the presence of very finely divided glass, so that most of the melt is close to the glass surface, could be used to see if the properties of the melt near the surface differ from those in the bulk.

Regardless of the validity of the explanation presented here, the experimental results show clearly that although glass is a cation exchanger, the melt anions exert a large influence on the energetics of the exchange.

Acknowledgment. Part of the experimental work was done at the National Bureau of Standards.

Determination and Comparison of Hittorf and Cell Transference

Numbers for Aqueous Silver Nitrate Solutions at 25°¹

by Michael J. Pikal and Donald G. Miller

Lawrence Radiation Laboratory, University of California, Livermore, California 94550 (Received September 17, 1969)

Precise emf's for aqueous silver nitrate concentration cells at 25° were measured from 0.05 to 14 *m*. These and activity coefficient data were used to calculate cell transference numbers for Ag⁺ in aqueous silver nitrate. Hittorf transference numbers for the above system were also determined and are in excellent agreement with the cell values. These experimental data are suitable for testing the validity of the Onsager reciprocal relations for isothermal electrical and matter transport.

I. Introduction

Historically, the Hittorf transference number t_i^h and the concentration cell transference number t_i^c of the *i*th ion have been generally accepted as identical since Helmholtz.² Onsager pointed out in 1931³⁻⁵ that this identity

$$t_i^h = t_i^c \quad (1)$$

is equivalent to an Onsager reciprocal relation (ORR)

$$l_{12} = l_{21} \quad (2)$$

for a single binary electrolyte in a neutral solvent like water, where the l_{ij} are the ionic transport coefficients of irreversible thermodynamics.⁶ The l_{ii}/N can be viewed as "intrinsic" mobilities and the l_{ij}/N as interaction mobilities.

An examination of the experimental evidence for the ORR⁷ showed the validity of eq 1 for a number of salts within the experimental errors of existing measurements. However, it can be shown from eq 22 and 26 of ref 6 that

$$\frac{t_1^h}{t_1^c} = \frac{z_1 l_{11} + z_2 l_{12}}{z_1 l_{11} + z_2 l_{21}} = \frac{z_1(l_{11}/N) + z_2(l_{12}/N)}{z_1(l_{11}/N) + z_2(l_{21}/N)} \quad (3)$$

where N is the normality in equivalents per liter and z_1 and z_2 are the signed valences of the cation and anion, respectively. Electrolyte theory⁸ shows that l_{ii}/N

is finite, whereas l_{12}/N is zero at infinite dilution. Further, experimental data⁶ show that l_{11}/N is not very concentration dependent, whereas l_{12}/N rises rapidly with concentration, occasionally reaching a maximum at higher concentrations.

Because l_{11}/N is a common, additive, and larger term than l_{12}/N and l_{21}/N , it becomes clear from eq 3 that a good percentage test of eq 1 does not imply a good percentage test of eq 2. Therefore, a test of eq 2 will be better, the larger l_{12} and l_{21} are relative to l_{11} .

Because there existed no experiments expressly designed to test the ORR for electrical and matter transport in aqueous solutions, it seemed useful to provide some on a suitable salt. Transference experiments are difficult, and the necessary calculations magnify the

(1) This work was performed under the auspices of the U. S. Atomic Energy Commission.

(2) H. von Helmholtz, *Ann. Phys.*, **3**, 201 (1878).

(3) L. Onsager, *Phys. Rev.*, **37**, 405 (1931).

(4) E. H. Wiebenga, *Rec. Trav. Chim.*, **65**, 273 (1946).

(5) D. G. Miller, *Amer. J. Phys.*, **24**, 595 (1956).

(6) D. G. Miller, *J. Phys. Chem.*, **70**, 2639 (1966).

(7) D. G. Miller, *Chem. Rev.*, **60**, 15 (1960).

(8) L. Onsager and R. M. Fuoss, *J. Phys. Chem.*, **36**, 2689 (1932). Theoretical expressions for the l_{ij} may be derived from their explicit equation for the dissipation function. Note also the remarks on p 2761.

experimental errors. Therefore, if a direct test of the ORR is desired, exceptional care is required.

Aqueous AgNO_3 appeared to be a good choice because it (1) is soluble to high concentration (14 *m*), where (l_{12}/N) and (l_{21}/N) are larger; (2) is partially associated in concentrated solutions^{9,10} so should have a larger interaction coefficient; (3) has electrochemical properties suitable for the measurements; and (4) has data for the diffusion coefficient *D*, conductance Λ , and activity coefficients γ necessary to calculate l_{11} .⁶

Our original intent was to measure cell emf's to high concentration and calculate t_1^c using available activity data, to compare with existing Hittorf (H) data¹¹ to 10.5 *m* and moving boundary (MB) data¹² to 2 *m*, where *m* is the molality in moles per kilogram of solvent. These H and MB results, however, were not consistent with one another above 0.5 *m*. Transference numbers calculated from both our preliminary concentration cell measurements and those of Pelzer and Haase¹³ were more consistent with Campbell and Singh¹¹ at lower concentrations. However, at higher concentrations our cell results were substantially higher than the Hittorf. Because of the possibility of systematic error introduced by approximations in the theory of the MB experiment¹⁴ and of the known difficulties of the Hittorf method, it seemed desirable both to repeat the latter and to extend the Emf measurements of Pelzer¹³ to saturation.

The details of our transference measurements are reported below. Our Hittorf results confirm the earlier Hittorf measurements¹¹ rather than moving boundary¹² from 0.5 to 2 *m*, but the earlier Hittorf results are increasingly lower at concentrations above 4 *m*.

We find good agreement between our t_1^h and t_1^c . In a subsequent paper, these data will be combined with existing data for *D*, Λ , and γ to compute all the l_{ij} and to test the ORR for isothermal electrical and matter transport in aqueous AgNO_3 solution.

II. Experimental Section

A. Concentration Cells. Materials. The silver nitrate solutions studied were prepared by one of two methods.

Method 1. Reagent grade silver nitrate was recrystallized from distilled water and a stock solution of about 13 *m* was prepared by adding distilled water to the wet silver nitrate crystals. The exact concentration of the stock solution was determined by the conventional gravimetric silver chloride precipitation. Solutions of desired concentrations were then prepared by diluting weighed quantities of the stock solution with weighed quantities of distilled water. The accuracy of the concentrations is estimated to be within about $\pm 0.1\%$.

Method 2. Distilled water was saturated with reagent grade silver nitrate at about 90°, and concentrated nitric acid was added to precipitate silver nitrate. Water and nitric acid were removed by heating about

400 g of the wet crystals in a vacuum fusion cell through which a stream of dry nitrogen passed. A water-cooled condenser and a liquid nitrogen cold trap were placed between the fusion cell and the vacuum pump. The furnace temperature was gradually raised to the fusion point of silver nitrate (209°). The temperature was maintained at 209° until all droplets of liquid in the condenser tube had vanished. The silver nitrate was then removed from the fusion cell, ground, and placed in a desiccator. Complete removal of nitric acid was verified by checking the pH of a solution prepared from a sample of the silver nitrate. Using this procedure, the silver nitrate did not actually fuse. In fact, if the heating was continued until the silver nitrate became a melt, it was found that the crystals obtained were "off-white" in color, presumably due to the formation of Ag_2O .¹⁵

Solutions of the desired concentrations were then prepared by adding weighed amounts of distilled water to weighed quantities of the silver nitrate. The solution concentrations are estimated to be accurate to within about $\pm 0.03\%$. Solutions prepared by this method were used to determine the emf's of cells 1B, 13B, 14-23 (Table I).

Electrodes. Silver electrodes were prepared using the thermal decomposition of Ag_2O , as described by Ives and Janz.¹⁶ Briefly, a spiral of platinum wire was covered with a wet paste of silver oxide and then heated slowly until the silver oxide decomposed to pure silver.¹⁷ Normally, electrodes were prepared in sets of twelve. However, two electrodes from a given set were often found to differ by as much as 0.2 mV when placed in the same solution. This bias potential often changed significantly with time.

The following electrode treatment was found to decrease bias potentials to less than 0.02 mV in nearly

(9) H. Lee and J. K. Wilmshurst, *Aust. J. Chem.*, **17**, 943 (1964).

(10) R. E. Hester and R. A. Plane, *Inorg. Chem.*, **3**, 769 (1964).

(11) A. N. Campbell and K. P. Singh, *Can. J. Chem.*, **37**, 1959 (1959).

(12) R. Haase, G. Lehnert, and H. J. Jansen, *Z. Phys. Chem. (Frankfurt am Main)*, **42**, 32 (1964).

(13) H. Pelzer, Diplomarbeit, Technische Hochschule, Aachen, 1961.

(14) R. Haase, *Z. Phys. Chem. (Frankfurt am Main)*, **39**, 27 (1963).

(15) G. J. Janz, D. W. James, and J. Goodkin, *J. Phys. Chem.*, **64**, 937 (1960).

(16) D. J. Ives and G. J. Janz, "Reference Electrodes," Academic Press, Inc., New York, N. Y., 1961, pp 198-210.

(17) We note some further details of our procedure. The Pt spirals were given a final cleaning by dipping in concentrated HNO_3 , heating to whiteness, and repeating several times. The Ag_2O , after 30 washings, was dried and ground in a mortar. It was then reground wet, washed another 15 times, and stored in distilled water. The preliminary drying time in a 100° oven was only a few minutes to avoid crumbling of the Ag_2O paste. After heating at 450-500° in a furnace, the electrodes were allowed to cool in 1 atm of flowing N_2 . At least four coats of Ag_2O were applied to fill holes and cracks and to obtain as smooth a ball of Ag as possible. The first coat was thick and the others thin, as suggested in ref 16, but the final ball was about 4-6 mm in diameter. The electrodes are porous, as just after removal from the oven they will visibly soak up water from the next application of Ag_2O paste.

all cases. It consists of passing a low current (0.5 mA) through a dilute perchloric acid solution (0.02 *M*) with a platinum wire as cathode and the electrode to be treated as anode. A set of electrodes were "anodized" in series under these conditions for about 2–3 hr. After an "equilibration" time of about 12 hr in a silver nitrate solution, a set of electrodes prepared in this way showed very low bias potentials, and it was not difficult to select groups of four electrodes such that the maximum bias potential between any two electrodes of the group was less than 0.01 mV. Low bias potentials remained when these electrodes were put in a solution of different concentration.

A group of four electrodes was selected according to the above criterion for use in a given concentration cell. The bias potentials were found to remain below 0.01 mV until the electrodes had been used in concentration cells three or four times. A repetition of the anodizing treatment would normally restore the electrodes such that the bias potentials would again be less than 0.01 mV. This anodizing was found to be slightly superior to an alternate method in which freshly prepared electrodes were "cathodized" under similar conditions.¹⁸

Apparatus. The concentration cell and electrode designs are illustrated in Figure 1.

The electrode (E) consists of a platinum wire sealed through the closed off portion of a 14/35 male Pyrex ground joint. This section in turn is sealed to a 14/20 female Pyrex ground joint. The silver is shown at the end of the platinum wire. Apiezon W wax was placed in the interior of the electrode at its base to ensure a liquid tight seal. The potentiometer lead ends in a copper plug ground to 14/20 taper with a Pt wire soldered into the bottom. Mercury was used to establish electrical contact between the Pt wire of the potentiometer lead and the electrode Pt wire.

The cell, with electrodes in place, was loaded with silver nitrate solutions of lower and higher concentrations through stopcocks A and B, respectively. The liquid-liquid junction was formed by opening the large 120° three-way stopcock C. The cell, if necessary, can be flushed with an inert gas and filled in the absence of air. The ball joint and small stopcock are to connect to a vacuum pump or to allow elimination of bubbles. All ground joints are 14/20, and all ground surfaces were lightly greased with Dow-Corning silicone vacuum grease.

Either a Leeds and Northrup K-3 potentiometer or a Vidar integrating voltmeter was used to measure the cell potentials. The temperature was maintained at $25.00 \pm 0.01^\circ$ in a large water thermostat.

Procedure. Prior to assembling a concentration cell, each electrode was allowed to soak, for about 12 hr, in a silver nitrate solution of the same concentration as the solution the electrode would be in contact with during the emf measurement. The concentration cell was then assembled as described above and placed in the thermo-

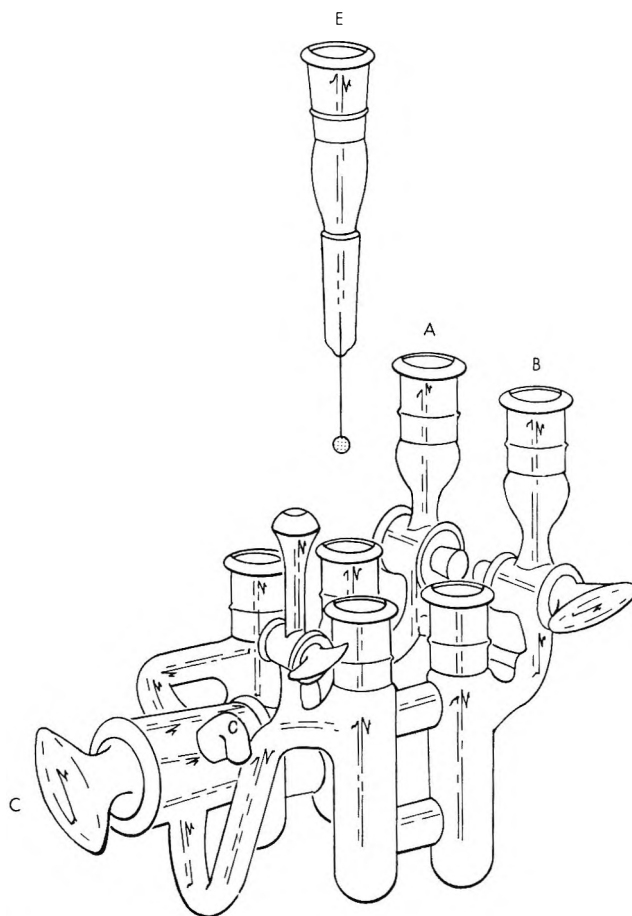


Figure 1. Design of concentration cell and electrode.

stat. After thermal equilibrium had been established, the emf's were measured for several hours and were found to remain constant for at least 24 hr. Stopcock C was closed after each measurement. To minimize errors in emf due to heat of mixing at the liquid-liquid junction,¹⁹ the difference in silver nitrate concentration between the two half-cells was kept less than 3 *m*.²⁰ Since each half-cell contained two electrodes, each cell provided four voltage measurements for each concentration pair. In general three cells were used for each concentration pair.

Errors in Emf Values. From a consideration of standard deviations given in Table I, of reproducibility of independent measurements (*i.e.*, cells 1 and 1B, cells 13 and 13B), and of consistency within 0.02 mV of combinations of cells from Table I, the probable error in a given emf value is estimated to be less than ± 0.015 mV. The emf of a concentration cell was found to be insensitive to dissolved oxygen in the silver nitrate solution.

(18) F. H. MacDougall and S. Peterson, *J. Phys. Chem.*, **51**, 1346 (1947).

(19) W. J. Hamer, *J. Amer. Chem. Soc.*, **57**, 662 (1935).

(20) Crude calorimetric measurements showed that 3 *m* is the maximum concentration difference consistent with Hamer's criterion¹⁹ that the heat of dilution between the two concentrations be less than 800 cal/mol.

Table I: The Potentials of Silver Nitrate Concentration Cells at 25°

Cell no.	m_1	m_2	Emf, mV	σ , mV
1	1.0000	0.05000	64.760	± 0.008
1B	1.0000	0.05000	64.772	± 0.023
2	1.0000	0.06999	56.567	± 0.008
3	1.0000	0.10000	48.004	± 0.005
3B	1.0000	0.14560	39.224	± 0.005
4	1.0000	0.19997	31.976	± 0.024
5	1.0000	0.29996	23.089	± 0.015
6	1.0000	0.4000	17.091	± 0.008
7	1.0000	0.4999	12.595	± 0.014
8	1.0000	0.6999	6.207	± 0.007
9	1.4996	1.0000	6.173	± 0.005
10	2.0001	1.0000	9.929	± 0.008
11	2.4998	1.0000	12.477	± 0.005
12	3.0000	1.0000	14.329	± 0.008
13	3.0000	0.05000	79.101	± 0.014
13B	3.0000	0.05000	79.115	± 0.009
14	0.4999	0.05000	52.172	± 0.005
15	3.000 ₀	0.4999	26.939	± 0.005
16	5.000	3.000 ₀	4.269	± 0.019
16B	4.999	3.000 ₀	4.242	± 0.005
17	5.000	3.500	2.800	± 0.007
18	5.000	4.000	1.675	± 0.004
19	5.000	4.500	0.784	± 0.008
20	6.000	5.000	1.225	± 0.009
21	7.000	5.000	2.196	± 0.007
22	6.000	3.000 ₀	5.465	± 0.008
23	4.000	3.000 ₀	2.527	± 0.010
24	7.000	6.000	0.952	± 0.008
25	8.999	7.000	1.462	± 0.006
26	8.999	7.999	0.659	± 0.005
27	10.000	8.999	0.590	± 0.006
28	11.000	8.999	1.095	± 0.005
29	11.998	11.000	0.467	± 0.006
30	12.994	11.998	0.428	± 0.006
31	13.998	11.998	0.832	± 0.005
32	8.999	6.000	2.405	± 0.005
33	11.998	8.999	1.568	± 0.005

Preliminary experiments also showed the emf's were unaffected by several weeks' exposure to laboratory light. However, as an added precaution, the experiments were carried out under conditions of partial darkness.

B. Hittorf Experiments. Preparation of Solutions. The silver nitrate solutions were prepared according to method 2 above.

Description of Apparatus. The Hittorf cells used were of the design employed by MacInnes and Dole.²¹ Two different cells, both constructed from 10-mm Pyrex tubing, were used in the measurements. In the larger cell, the volumes of the electrode compartments were about 25 ml, and in the smaller cell, these volumes were about 12 ml. Platinum was used for the cathodes, and short lengths of silver rod (99.95% pure) were used as anodes. A P.A.R. Model TC-100. 2BR voltage/current reference source was used to supply a constant current to the cell. Standard resistors were used at

each end to detect possible current leaks into the thermostat. The thermostat temperature was maintained at $25.00 \pm 0.01^\circ$.

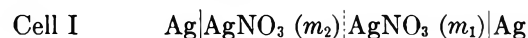
Procedure. The electrolysis conditions were chosen to ensure at least a 10% change in concentration in the electrode compartments, without introducing excessive electrical Joule heating and thereby convective mixing. The maximum current used in these experiments was 50 mA. Our criterion, based on an analysis of MacInnes and Dole's successful results,²¹ was that the current I in amperes be less than about $0.1\lambda^{1/2}$ for a 1-cm diameter tube or smaller, where λ is the specific conductance of the solution.

After electrolysis, the weights of solution in the anode and cathode compartments were determined, and homogeneous samples of the solutions in the electrode compartments were analyzed. To verify that mixing between the electrode compartment and the middle compartment had not occurred, samples of the solutions in the anode middle and cathode middle compartments were also analyzed. In no case was there evidence that mixing had occurred.

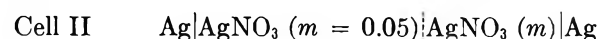
A controlled potential coulometric method (relative precision about $\pm 0.06\%$) was used to determine the composition in weight % of silver nitrate. However, when silver nitrate solutions of known composition were analyzed by this method, it was found that the compositions, in weight %, were subject to a systematic relative error of about 0.14%, giving erroneously high values for the composition. Fortunately, this *systematic error* in the composition has a negligibly small effect on the calculated transference number.

III. Emf Results

Experimental emf values in millivolts for concentration cells of the form



are given in Table I. Nearly every value represents the mean of at least 12 individual voltage measurements. The last column lists the standard deviation from the mean, σ , in millivolts, corresponding to each mean emf. To calculate emf transference numbers, emf values for concentration cells of the form



are needed. By suitably combining the emf's of the experimentally measured concentration cells from Table I, values for cells symbolized by II were calculated²² and are given in Table II.

As a check on the accuracy of our data, values for the

(21) D. A. MacInnes and M. Dole, *J. Amer. Chem. Soc.*, **53**, 1357 (1931).

(22) When necessary, a small correction was applied to the data in Table I to obtain emf's at round values of the molality. Whenever there was more than one way to combine the emf's, all possible combinations were averaged.

Table II: Potentials of the Concentration Cells
Ag|AgNO₃ (*m* = 0.05)||AgNO₃ (*m*)|Ag

<i>m</i>	Emf, mV	<i>m</i>	Emf, mV
0.07	8.214	3.5	80.544
0.10	16.762	4.0	81.669
0.14560	25.542	4.5	82.560
0.20	32.794	5.0	83.344
0.30	41.680	6.0	84.569
0.40	47.675	7.0	85.530
0.50	52.172	8.0	86.325
0.70	58.563	9.0	86.985
1.0	64.768	10.0	87.573
1.5	70.943	11.0	88.078
2.0	74.695	12.0	88.545
2.5	77.245	13.0	88.976
3.0	79.105	14.0	89.377

Table III: Comparison of Potentials of Some Silver Nitrate Concentration Cells at 25°

<i>m</i> ₁	<i>m</i> ₂	Emf, mV		
		This research	H.P. ^a	M. B. ^{b,c}
0.1000	0.05000	16.762	16.75	16.74
1.000	0.05000	64.768	64.73	
1.000	0.2000	31.974	31.97	
1.000	0.5000	12.596	12.60	
1.000	0.7000	6.207	6.19	

^a Reference 13. ^b Reference 27. ^c Data adjusted to round values of molality.

potentials of several concentration cells are compared with available literature data in Table III. Excellent agreement is obtained between our results and those of Haase and Pelzer,¹³ the average difference being only 0.015 mV, which is well within the combined estimated experimental errors.

The cell transference number of the nitrate ion, *t*₂^c, may be calculated from emf data for cells like II and activity coefficient data using the relation⁶

$$t_2^c = \frac{\mathfrak{F}}{2\hat{R}T} \frac{d\mathcal{E}(m)}{d \ln(m\gamma/K)} \quad (4)$$

$$K = (m\gamma)_{m=0.05} \quad (5)$$

where $\mathcal{E}(m)$ is the emf of the cell II at molality *m*, and γ is the mean molal activity coefficient of silver nitrate. The symbols \mathfrak{F} , \hat{R} , and *T* are the Faraday constant, gas constant, and absolute temperature, respectively.

Numerical values of the quantity, $\ln(m\gamma/K)$, were obtained by numerical integration of smoothed ϕ data for silver nitrate, where ϕ is the osmotic coefficient.²³

A computer-executed four-point Lagrangian integration technique was used. The osmotic coefficient data were obtained from three sources. (1) A set of isopiestic osmotic coefficients were recalculated using the

original isopiestic molalities of aqueous potassium chloride and aqueous silver nitrate reported by Robinson and Tait²⁴ together with the newer osmotic coefficients of aqueous potassium chloride tabulated by Robinson and Stokes.²⁵ (2) Unsmoothed vapor pressure data for six concentrated aqueous silver nitrate solutions²⁶ were used to calculate another set of osmotic coefficients. (3) Activity coefficient data for dilute solutions given by MacInnes and Brown²⁷ were least squared by a Debye-Hückel type equation, which was then transformed²³ to yield a third set. The three sets of data were then graphically smoothed. These smoothed ϕ 's and the calculated values of $\ln(m\gamma/K)$ appear in Table IV. These ϕ 's are believed to be more

Table IV: Osmotic Coefficients and Cell Transference Numbers of Aqueous AgNO₃ Solutions at 25°

<i>m</i>	ϕ^a	$\ln(m\gamma/K)$	<i>t</i> ₂ ^c
0.05	0.9266	0	0.468 ± 0.002
0.07	0.9172	0.3009	0.468 ± 0.002
0.1	0.9050	0.6137	0.468 ± 0.002
0.2	0.8748	1.2008	0.470 ± 0.002
0.3	0.8512	1.5273	0.471 ± 0.002
0.4	0.8311	1.7492	0.473 ± 0.002
0.5	0.8129	1.9146	0.475 ± 0.002
0.7	0.7808	2.1501	0.479 ± 0.002
1.0	0.7413	2.3823	0.486 ± 0.002
1.5	0.6889	2.6201	0.497 ± 0.003
2.0	0.6465	2.7699	0.508 ± 0.003
2.5	0.6102	2.8739	0.518 ± 0.003
3.0	0.5786	2.9506	0.527 ± 0.004
3.5	0.5495	3.0086	0.535 ± 0.004
4.0	0.5244	3.0551	0.542 ± 0.004
4.5	0.5024	3.0936	0.548 ± 0.005
5.0	0.4833	3.1265	0.554 ± 0.005
6.0	0.4523	3.1782	0.564 ± 0.006
7.0	0.4280	3.2218	0.574 ± 0.007
8.0	0.4086	3.2581	0.582 ± 0.008
9.0	0.3930	3.2898	0.590 ± 0.009
10.0	0.3805	3.3181	0.598 ± 0.010
11.0	0.3702	3.3435	0.605 ± 0.012
12.0	0.3623	3.3675	0.613 ± 0.014
13.0	0.3563	3.3902	0.620 ± 0.016
14.0	0.3515	3.4084	0.626 ± 0.020

^a More figures are reported than are significant. The uncertainty is believed to be less than ±0.002.

(23) The mathematical relationship between $\ln \gamma$ and ϕ may be found in most thermodynamics texts. See, for example, G. N. Lewis and M. Randall, "Thermodynamics," 2nd ed, McGraw-Hill Book Co., Inc., New York, N. Y., 1961.

(24) R. A. Robinson and D. A. Tait, *Trans. Faraday Soc.*, **37**, 569 (1941).

(25) R. A. Robinson and R. H. Stokes, "Electrolyte Solutions," 2nd ed, Academic Press, Inc., New York, N. Y., 1959.

(26) W. Kangro, private communication, 1966. At 25° these data, quoted with permission, are 3.643, 0.0686; 4.974, 0.0833; 7.100, 0.1037; 11.252, 0.1395; 13.527, 0.1586; 15.12 (saturated), 0.1723; for *m* and $\Delta p/p^\circ$, respectively, where *p*[°] is the vapor pressure of pure water and *p* is the vapor pressure of water above the solution. Smoothed data are given in W. Kangro and A. Groeneveld, *Z. Phys. Chem.* (Frankfurt am Main), **32**, 110 (1962).

(27) D. A. MacInnes and A. S. Brown, *Chem. Rev.*, **18**, 335 (1936).

accurate than the values tabulated by Robinson and Stokes.²⁵

Although values of the cell transference number may be obtained by the direct differentiation indicated by eq 4, it was found desirable to proceed somewhat differently. If we define an "integral transference number" \bar{T} , by

$$\bar{T} = \frac{\mathfrak{F}}{2\hat{R}T} \frac{\mathcal{E}(m)}{\ln(m\gamma/K)} \quad (6)$$

where K is defined in eq 5, then eq 4 may be written in the form

$$t_2^c = \bar{T} + (m\gamma/K) \ln(m\gamma/K) \frac{d\bar{T}}{d(m\gamma/K)} \quad (7)$$

The main advantage in using eq 7 instead of eq 4 to compute values for the cell transference number is that the defined function, \bar{T} , is a simple and slowly varying function of $(m\gamma/K)$. "Experimental" values of \bar{T} were calculated from the data in Tables II and IV, and the empirical equation

$$\begin{aligned} \bar{T} = & 0.5319 - 1.126 \times 10^{-4}(m\gamma/K) - \\ & 2.004 \times 10^{-5}(m\gamma/K)^2 \quad (8) \\ \sigma = & \pm 0.0004 \end{aligned}$$

was found to represent the \bar{T} data over the entire concentration range studied. The standard deviation, σ , is well within the estimated experimental error in \bar{T} . Combination of eq 7 and 8 and the $\ln(m\gamma/K)$ data in Table IV, allowed cell transference numbers of the nitrate ion, t_2^c , to be calculated at selected molalities. The corresponding cell transference numbers of the silver ion, t_1^c , are given in Table IV.

In an attempt to obtain an estimate of the uncertainty in the cell transference numbers, values of $\ln(m\gamma/K)$ and t_1^c were computed using a variety of methods for treating the experimental data.²⁸ It was observed that a number of methods were compatible with the experimental data, and yet the calculated values of $\ln(m\gamma/K)$ and t_1^c differed somewhat from the corresponding values in Table IV, the latter values being intermediate between the extremes. These differences were taken as a rough estimate of the uncertainties in $\ln(m\gamma/K)$ and t_1^c . From the above considerations it is estimated that the probable error in $\ln(m\gamma/K)$, as reported in Table IV, is about 0.3%, and the estimated probable error in the reported value of t_1^c is about ± 0.002 below 1 m , ± 0.005 around 5 m , ± 0.009 at 9 m , and ± 0.020 at 14 m . The uncertainty of about 0.015 mV in the emf values has little effect on the calculated transference numbers. The uncertainty in t_1^c is largely a reflection of uncertainty in osmotic coefficient data. Future more accurate ϕ data could be combined with the present emf data to yield better t_1^c .

IV. Hittorf Results

The Hittorf transference numbers were calculated from the raw data by the usual procedure,²⁹ which may be summarized by the equations

$$1 - t_1^h = t_2^h = \frac{\mathfrak{F}}{I\tau} \frac{W_0}{10^3} |(m_F - m_I)| \quad (9)$$

$$W_0 = \frac{W}{1 + 10^{-3}m_F M_s} \quad (10)$$

where t_1^h is the Hittorf transference number of the silver ion, \mathfrak{F} is 96,496 C (equiv)⁻¹, W_0 and W are the weights of water and solution in the electrode compartment after electrolysis, respectively, I is the electric current in amperes, τ is the time of electrolysis in seconds, m_I and m_F are the molalities of the solutions in the electrode compartment before and after electrolysis, respectively, and M_s is the molecular weight of the solute, AgNO₃. Although not completely obvious from the conventional discussion,²⁹ it can be shown^{4,5} that t_1 defined as the fraction of current carried by ion 1 referred to a fixed quantity of solvent and t_1 defined by eq 9 are identical.

The experimental data concerning our Hittorf measurements are summarized in Table V. Here, m_s is the molality of the stock solution and m_a , m_{am} , m_c , and m_{cm} are molalities of the anode, anode-middle, cathode, and cathode-middle compartments, respectively, after electrolysis. The quantity q represents the number of Faradays of electricity passed through the cell. Hittorf transference numbers of Ag⁺, calculated from the compartments, are given in columns 7 and 8. In the last column are listed maximum errors in the "cathode" transference numbers. These error limits were estimated from the uncertainty in the molalities³⁰ and represent approximately 90% confidence limits. The initial molality of the solution in the electrode compartment, m_I , was calculated by computing the weighted mean of m_s , m_{am} , and m_{cm} , assigning a weight of four to m_s and weights of unity to m_{am} and m_{cm} . It should be noted that the molalities of the middle compartments agree with the stock molality well within the estimated

(28) For example, one method involved smoothing the ϕ data by means of a five-parameter polynomial in $m^{1/2}$, whose coefficients were determined by the method of least squares. Values of $\ln(m\gamma/K)$ were then obtained from the polynomial equation by integration. The values of $\ln(m\gamma/K)$ obtained were slightly different than the results given in Table IV. The calculation of t_1^c was then carried out as described earlier, using eq 7 and an equation of the same form as eq 8.

(29) M. Spiro, "Determination of Transference Numbers," in "Physical Methods of Organic Chemistry, Part IV," A. Weissberger, Ed., 3rd ed, Interscience Publishers, Inc., New York, N. Y., 1960, pp 3049-3111.

(30) The major source of error in Hittorf measurements is in the precision with which the final molalities, m_F , can be determined. The limit of precision (90% confidence) in the weight % is estimated at $\pm 0.15\%$ of the value of the weight %. This error limit corresponds to a relative uncertainty in the molality of $\pm 0.15\%$ at 0.1 m , $\pm 0.2\%$ at 2 m , and $\pm 0.4\%$ at 11 m . The values of m_a , m_c , m_{am} , and m_{cm} given in Table V are all subject to the above uncertainties.

Table V: Hittorf Transference Numbers of Ag^+ in Aqueous Silver Nitrate at 25°

m_s	m_{am}	m_{cm}	m_a	m_c	10% q	t_1^h		Error limit
						Anode	Cathode	
0.10772	0.10780	0.10760	0.12483	0.08982	0.7185	0.465	0.465	± 0.005
0.10772	0.10770	0.10790	0.12484	0.08978	0.7208	0.467	0.464	± 0.005
0.5825		0.5823		0.4814	4.252	0.484	0.483	± 0.005
0.5825	0.5824	0.5828	0.6759	0.4876	4.009	0.484	0.478	± 0.005
1.5753	1.5737	1.576	1.8364	1.3005	11.305	0.505	0.503	± 0.006
1.5753	1.5767	1.5761	1.8404	1.3341	6.071	0.501	0.501	± 0.007
2.1215	2.1216	2.1226	2.4164	1.8120	12.813	0.515	0.509	± 0.006
2.1215	2.1233	2.1192	2.3594	1.8678	10.148	0.514	0.512	± 0.008
4.0432	4.0422	4.0435	4.6061	3.4198	24.880	0.548	0.544	± 0.008
5.958	5.956		6.8522	4.983	39.49	0.569	0.568	± 0.007
7.371	7.366	7.388	8.479	6.267	46.43	0.584	0.579	± 0.010
7.372	7.366	7.372	8.407	6.223	44.78	0.591	0.580	± 0.010
9.174	9.168		10.415	7.903	50.30	0.597	0.592	± 0.010
10.937	10.952	10.955	12.124	9.825	26.27	0.611	0.600	± 0.018
10.937	10.932	10.955	12.310	9.732	30.71	0.607	0.611	± 0.014

error limits in m_{am} and m_{cm} ,³⁰ thus verifying the assumption that mixing between compartments was negligible.

After electrolysis was complete, it was noticed that the solution in the anode compartment contained a significant quantity of finely divided silver, which had separated from the anode during electrolysis. Thus the anode results may be subject to a small systematic error, and cathode results are considered to be more accurate.

V. Discussion

In Figure 2, Hittorf transference numbers determined in this research are compared with the data of Campbell and Singh,¹¹ who used the Hittorf method, and with the data of Haase and coworkers,¹² who used the moving boundary technique. The vertical lines represent the estimated error limit (90% confidence) for our transference numbers.³¹ Although all three sets of data are in agreement below about 0.5 m (and also in agreement with MacInnes and Brown²⁷), systematic differences are obvious at higher concentrations. In the region around 2 m , the two sets of Hittorf measurements are in good agreement, but are consistently lower than the moving boundary results.

It should be noted that the usual calculation of a Hittorf transference number from moving boundary data is exact only if it is assumed that the partial molal volumes of the electrolytes involved are independent of composition.^{14,32} The failure of this assumption leads to a systematic error in the calculated transference number. This error is expected to increase as the concentration increases. Using a less restrictive assumption (the partial molal volumes of the following electrolyte are constant between the electrode and the boundary), Milios and Newman³³ developed a more accurate equation for calculating a Hittorf transference number from the MB experiment. When the data of Haase, *et al.*,¹² at 0.2 m were reevaluated in terms of this more

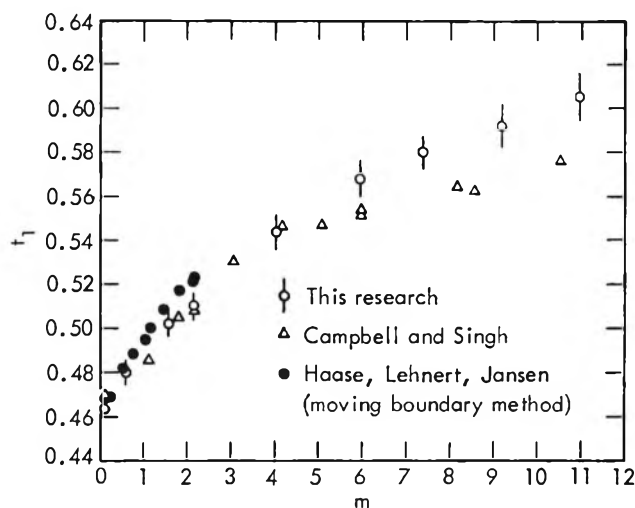


Figure 2. Comparison of Hittorf transference numbers, t_1^h , for AgNO_3 at 25°.

accurate equation,³³ the corresponding transference number was found to be 0.4693, compared to the value of 0.4708 as originally reported. In view of this result, we feel confident that the serious lack of agreement in the silver nitrate data around 2 m is the result of the above systematic error in the moving boundary results. In any case, the theoretical analysis of Milios and Newman³³ and the results of this research do indicate that moving boundary results for concentrated solutions, even though smooth and reproducible, should be treated with caution.³⁴

(31) In cases where a plotted point represents the mean of two values, the error limit for the mean transference number was taken to be the mean error limit divided by $\sqrt{2}$.

(32) R. J. Bearman, *J. Chem. Phys.*, **36**, 2432 (1962).

(33) D. Milios and J. Newman, *J. Phys. Chem.*, **73**, 298 (1969).

(34) NOTE ADDED IN PROOF. We have subsequently been informed by Professor Newman (private communication) that the correction at 0.2 m is actually an order of magnitude smaller than was reported. Nevertheless we believe our conclusion remains correct.

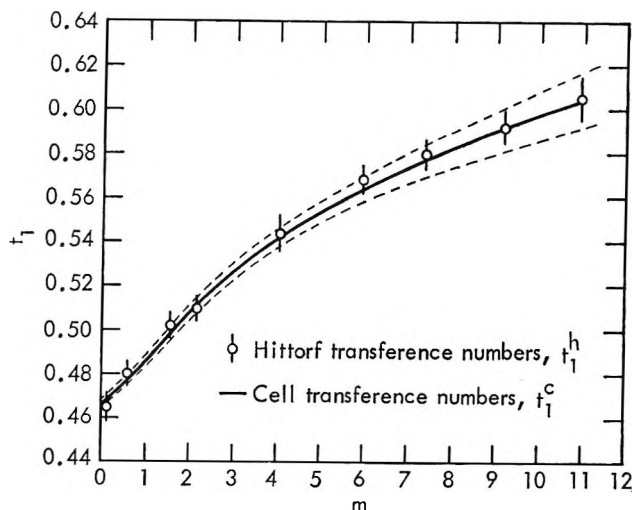


Figure 3. Comparison of t_i^c and t_i^h of this research for AgNO_3 at 25° . The dotted lines represent the uncertainties given in Table IV for the cell transference numbers.

The two sets of data obtained with the Hittorf method are in excellent agreement up to about 4 m . At higher concentrations, however, the data of Campbell and Singh¹¹ are consistently lower than ours. Assuming their transference numbers were correctly calculated (they give no details), the large differences at very high concentrations are difficult to understand. In the absence of measurements from a third labora-

tory, we will assume our Hittorf transference numbers are correct.

The main purpose of this research, as stated earlier, was to compare the cell transference numbers with the Hittorf transference numbers, thereby providing data for an experimental test of the Onsager reciprocal relations. Hittorf transference numbers from Table V and cell transference numbers from Table IV are graphically compared in Figure 3. The agreement between the two sets of data is excellent throughout the entire concentration range. In fact, in view of the rather large uncertainty in the cell transference numbers at high concentrations, the near perfect agreement above 7 or 8 m could be regarded as somewhat fortuitous. It may be concluded that our experimental transference number data are completely in accord with the Onsager reciprocal relations as represented by eq 1.

A more direct test of the Onsager reciprocal relations may be made by comparing numerical values of l_{12} and l_{21} . This will be done in a forthcoming paper.³⁵

Acknowledgments. We wish to thank Dr. Jack Harrar for his aid in analyses and Professors R. Haase, W. Kangro, and B. Steele for their unpublished or raw data on AgNO_3 solutions.

(35) NOTE ADDED IN PROOF. We have used $\hat{R} = 8.3144$ J/mol deg; molecular weight of AgNO_3 , $M_s = 169.87$; and $25^\circ\text{C} = 298.15^\circ\text{K}$.

A Kinetic Study of the Dehydration and Dehydrobromination of *trans*-Dibromobis(ethylenediamine)cobalt(III) Diaquoxygen

Bromide, *trans*-[Co(en)₂Br₂](H₅O₂)Br₂

by H. Eugene LeMay, Jr.

Department of Chemistry, University of Nevada, Reno, Nevada 89507 (Received September 2, 1969)

The kinetics of dehydration and dehydrobromination of *trans*-[Co(en)₂Br₂](H₅O₂)Br₂ were studied *in vacuo*. The reaction is deceleratory nearly throughout and appears to occur in a single step. At higher temperatures the reaction obeys the contracting-parallelepiped rate law with more rapid propagation of the reaction-product interface parallel to the (100) planes than perpendicular to them. At lower temperatures and with smaller particles this rate law gives a much poorer fit of kinetic data except where the particles are nucleated over their entire surfaces prior to kinetic study. The Arrhenius activation energy for the growth stage of the dehydration-dehydrobromination reaction is 37 ± 2 kcal mol⁻¹. The results are interpreted in terms of the known crystal structure of *trans*-[Co(en)₂Br₂](H₅O₂)Br₂ and are compared with results of previous studies of the dehydration-dehydrohalogenations of halide salts containing the H₅O₂⁺ ion.

Introduction

The diaquoxygen ion, H₅O₂⁺, was first postulated in 1936¹ as a component of acid solutions. Since 1952, this ion has been found in a number of solids. Evidence for this species in solids has been obtained by X-ray diffraction,²⁻⁸ neutron diffraction,^{9,10} and infrared spectral studies.^{11,12}

When halide salts containing the diaquoxygen ion are heated in the solid phase, they undergo dehydration and dehydrohalogenation. The overall reaction is



Among the compounds which contain the H₅O₂⁺ ion is a family of the general type *trans*-[M(AA)₂X₂](H₅O₂)X₂ where M is cobalt, chromium, or rhodium, (AA) is a bidentate amine, and X is chloride or bromide.^{11,12} During dehydration and dehydrohalogenation of compounds of this sort, the *trans*-[M(AA)₂X₂]⁺ ion generally maintains its geometric configuration. However, in the cases of *trans*-[Co(pn)₂Cl₂](H₅O₂)Cl₂¹³ and *trans*-[Co(pn)₂Br₂](H₅O₂)Br₂,¹⁴ the complex cation undergoes a *trans*-to-*cis* isomerization during loss of water and hydrogen halide from the crystal lattice.

We have recently undertaken a study intended to elucidate the mechanism of the *trans*-to-*cis* isomerization of [Co(pn)₂Cl₂](H₅O₂)Cl₂. Comparison of the crystal structures of *trans*-[Co(pn)₂Cl₂](H₅O₂)Cl₂⁵ and *trans*-[Co(en)₂Cl₂](H₅O₂)Cl₂² does not suggest to us any reason why the first compound should isomerize while the second compound does not. Moreover, comparison of the dehydration and dehydrohalogenation reactions of these two compounds¹⁵ reveals them to be very similar, although the *trans*-[Co(pn)₂Cl₂](H₅O₂)Cl₂

seems to exhibit a greater resistance to loss of HCl and H₂O from the (100) planes than does the ethylenediamine complex. The present study of *trans*-[Co(en)₂Br₂](H₅O₂)Br₂ was undertaken to ascertain whether such restricted loss of HX and H₂O is of importance in explaining the *trans*-to-*cis* isomerization and to gain further insight into such dehydration-dehydrohalogenation reactions.

Experimental Section

The *trans*-[Co(en)₂Br₂](H₅O₂)Br₂ was prepared from *trans*-[Co(en)₂Cl₂]Cl: 1.2 g of *trans*-[Co(en)₂Cl₂]Cl was added to 15 ml of water containing 1 ml of 6 N NH₃. The resulting mixture was warmed to obtain a red-violet solution of [Co(en)₂(H₂O)₂]³⁺. Twenty-three ml of concd HBr was then added, and the solution was concentrated by blowing air over its surface until the green *trans*-[Co(en)₂Br₂](H₅O₂)Br₂ precipitated. The

- (1) M. L. Huggins, *J. Phys. Chem.*, **40**, 723 (1936).
- (2) A. Nakahara, Y. Saito, and H. Kuroya, *Bull. Chem. Soc. Jap.*, **25**, 331 (1952).
- (3) S. Ooi, Y. Komiyama, Y. Saito, and H. Kuroya, *ibid.*, **32**, 263 (1959).
- (4) S. Ooi, Y. Komiyama, and H. Kuroya, *ibid.*, **33**, 354 (1960).
- (5) Y. Saito and H. Iwasaki, *ibid.*, **35**, 1131 (1962).
- (6) J.-O. Lundgren and I. Olovsson, *Acta Cryst.*, **23**, 966 (1967).
- (7) J.-O. Lundgren and I. Olovsson, *ibid.*, **23**, 971 (1967).
- (8) I. Olovsson, *J. Chem. Phys.*, **49**, 1063 (1968).
- (9) J. M. Williams, *Inorg. Nucl. Chem. Lett.*, **3**, 297 (1967).
- (10) J. M. Williams, *J. Amer. Chem. Soc.*, **91**, 776 (1969).
- (11) R. D. Gillard and G. Wilkinson, *J. Chem. Soc.*, 1640 (1964).
- (12) D. Dollimore, R. D. Gillard, and E. D. McKenzie, *J. Chem. Soc.*, 4479 (1965).
- (13) A. Werner and A. Frohlich, *Chem. Ber.*, **40**, 2228 (1907).
- (14) H. E. LeMay, Jr., unpublished results.

product was recrystallized from water by the addition of concd HBr. *Anal.* Calcd for $[\text{Co}(\text{en})_2\text{Br}_2](\text{H}_5\text{O}_2)\text{Br}_2$: Br, 59.62; HBr + H_2O , 21.82. Found: Br, 59.3; HBr + H_2O , 21.52.

Samples of differing particle sizes were obtained by controlling the rate of recrystallization from concd HBr solutions, and these samples were then further sized with sieves. Microscopic observations indicated a large proportion of the sample which passed 200 mesh to be comprised of particles $2\text{--}8 \times 10^{-2}$ mm in length, while the two batches of 60–100 mesh crystals were mainly in the 1.5 to 0.30-mm range. The particles were of approximately equal length and width, but their height (perpendicular to the prominent (100) faces) was generally less than one-half their length.

The samples were stored wet; prior to study occluded H_2O and HCl were removed by pumping at about 0.10 Torr until constant weight was obtained for a period of 1 hr at room temperature. Mass-loss studies were conducted at 0.05–0.15 Torr using 15–20-mg samples spread over a flat glass holder of about 1.5 cm diameter. All equipment employed has been described elsewhere.¹⁵

The X-ray powder pattern of $\text{trans-}[\text{Co}(\text{en})_2\text{Br}_2](\text{H}_5\text{O}_2)\text{Br}_2$ was obtained using Cu $K\alpha$ radiation and is in agreement with reflections calculated from the unit cell dimensions reported³ for this compound. The most prominent d spacings are 10.10 (s), 5.96 (m), 4.49 (s), 4.08 (m), 3.43 (m), 3.35 (s), 2.93 (m) and 2.09 Å (m). The prominent d spacings of $\text{trans-}[\text{Co}(\text{en})_2\text{Br}_2]\text{Br}$ (obtained by heating $\text{trans-}[\text{Co}(\text{en})_2\text{Br}_2](\text{H}_5\text{O}_2)\text{Br}_2$) are 7.56 (m), 7.25 (s), 6.07 (m), 4.87 (m), 4.26 (s), 3.81 (m), 3.60 (s), 3.51 (m), 3.46 (m), 3.02 (s), and 2.93 Å (m).¹⁶ This compound does not appear to be isomorphous with $\text{trans-}[\text{Co}(\text{en})_2\text{Cl}_2]\text{Cl}$.

Results and Discussion

The tga and dta results are very similar to those obtained previously with $\text{trans-}[\text{Co}(\text{en})_2\text{Cl}_2](\text{H}_5\text{O}_2)\text{Cl}_2$ and $\text{trans-}[\text{Co}(\text{pn})_2\text{Cl}_2](\text{H}_5\text{O}_2)\text{Cl}_2$ ¹⁵ and suggest that $\text{trans-}[\text{Co}(\text{en})_2\text{Br}_2](\text{H}_5\text{O}_2)\text{Br}_2$ loses HBr and H_2O in a single step. Dollimore and coworkers have proposed that such dehydration–dehydrohalogenation reactions occur stepwise with the initial loss of water.^{12,17} Only in the case of $\text{trans-}[\text{Co}(2,3,2\text{-tet})\text{Cl}_2](\text{H}_5\text{O}_2)\text{Cl}_2$ do their mass-loss data indicate loss of HCl and H_2O in separate stages.¹⁷ In other cases, the occurrence of two endothermic dta peaks in the temperature range corresponding to dehydration and dehydrohalogenation was cited as evidence for stepwise dehydration and dehydrohalogenation. Tga studies of $[\text{As}(\text{C}_6\text{H}_5)_4](\text{H}_5\text{O}_2)\text{Cl}_2$ and $[\text{As}(\text{C}_6\text{H}_5)_4](\text{H}_5\text{O}_2)\text{Br}_2$ have also indicated that dehydration precedes dehydrohalogenation.¹⁸ However, it is still not clear whether such a two-step loss of H_2O and HX is general for halide salts containing the diaquohydrogen ion. The dta results, in particular, are inconclusive. At any rate, there is no indication of stepwise dehydration and dehydrobromination in the

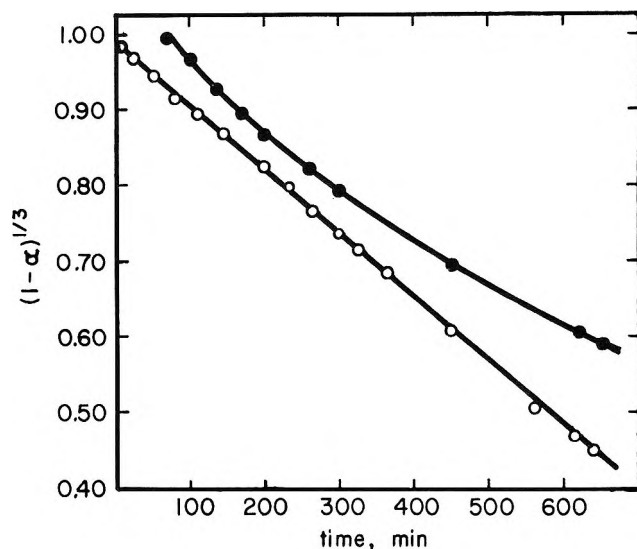


Figure 1. Rate plots for the dehydration–dehydrobromination of $\text{trans-}[\text{Co}(\text{en})_2\text{Br}_2](\text{H}_5\text{O}_2)\text{Br}_2$: O, thermally nucleated sample at 58.4°; ●, nonnucleated sample at 59.0°.

present study, and the kinetic data are readily interpreted in terms of either simultaneous or nearly simultaneous loss of H_2O and HBr.

Visual examinations of the crystals were made as they were heated on a micro hot stage and revealed two extremes of behavior depending on particle size and temperature. Under conditions in which the reaction was largely complete within about an hour the reaction proceeded in the same fashion as previously reported for $\text{trans-}[\text{Co}(\text{pn})_2\text{Cl}_2](\text{H}_5\text{O}_2)\text{Cl}_2$.¹⁵ When viewed perpendicular to the (100) faces, the reaction appeared to proceed like a contracting square because of greater rate of reaction parallel to the (100) faces than perpendicular to them. At room temperature, on the other hand, nuclei are seen to form and grow on all faces in a more random fashion, and a uniform reactant–product interface never develops over the entire crystal surface.

Results of isothermal mass-loss studies conducted *in vacuo* are consistent with these visual observations. The rate law was found to depend on temperature, particle size, and whether the surface was thermally nucleated. When the particles were large and the temperature was high (when total reaction time was short), the mass loss was found to fit the contracting-cube rate law, $(1 - \alpha)^{1/3} = 1 - kt$, for α (fraction of dehydration–dehydrobromination) from about 0.1 to 0.9. This rate expression also fits the results obtained with small particles at low temperatures (long reaction times) when the particles were thermally nucleated. Thus, for

(15) H. E. LeMay, Jr., *Inorg. Chem.*, **7**, 2531 (1968).

(16) Only the strong (s) and medium (m) intensity reflections are given.

(17) D. Dollimore, R. D. Gillard, E. D. McKenzie, and R. Ugo, *J. Inorg. Nucl. Chem.*, **30**, 2755 (1968).

(18) H. E. LeMay, Jr., *Inorg. Nucl. Chem. Lett.*, **5**, 941 (1969).

example, when a sample of 60–100 mesh size was heated to 90–95° and then rapidly quenched to 20° (about 4% mass loss occurred during this treatment), subsequent kinetic studies at 58.4° fit the contracting-cube rate law. On the other hand, samples which were not preheated in this manner did not fit this rate expression except over a very short range of α . This is illustrated in Figure 1 which compares the results of a thermally nucleated sample at 58.4° and a nonnucleated sample at 59.0°. Presumably, the preheating allows rapid surface nucleation and formation of a relatively uniform reactant–product interface over all the surfaces of the particles which is not otherwise possible at lower temperatures.

As the temperature at which mass loss is being studied is lowered or as particles of smaller size are used at a given temperature, the range of α over which the contracting-cube law fits the data decreases. At 55.8°, the 200 mesh sample fit the contracting-cube expression from $\alpha = 0.05$ – 0.37 while at 50.0°, the 60–100 mesh sample fit from $\alpha = 0.01$ – 0.25 . At the low-temperature particle-size limit studied in this investigation, the rate law $-\log(1 - \alpha) = kt^{1/2} + c$ was found to fit the data from about $\alpha = 0.15$ to 0.90 . The physical significance of this equation is not completely understood, but attempts to fit the data to more standard rate laws were unsuccessful. Perhaps at still lower temperatures or smaller particle sizes a more meaningful kinetic relation could be found.

Nonetheless, these results are qualitatively those predicted by Mampel,¹⁹ whose equations reduce to the contracting-cube law for small values of the reaction time to particle radius ratio and to the random nucleation or "first-order" rate law, $-\log(1 - \alpha) = kt + c$, for large values of this ratio. Apparently, in the first case there is time for the surface to become completely nucleated before any appreciable penetration has occurred, while in the second case the rate is controlled by the process of nucleation.

Since more than one nucleus can be seen to form at room temperature on each particle of *trans*-[Co(en)₂Br₂](H₃O₂)Br₂, and these nuclei grow at a relatively slow rate, it is not surprising that the random-nucleation law does not fit the data at low temperatures. However, there is an intermediate range of temperatures (and/or particle sizes) where the random-nucleation law does give a good data fit, probably as a result of some fortuitous combination of factors. We previously reported that the contracting-cube rate law described the dehydration–dehydrochlorination of *trans*-[Co(en)₂Cl₂](H₃O₂)Cl₂ in static air but that the random-nucleation law gave a better fit *in vacuo*.¹⁵ It is likely that this difference was due to the different temperature ranges employed; the static air studies were conducted at the higher temperatures.

The kinetic results for the dehydration–dehydrobromination of *trans*-[Co(en)₂Br₂](H₃O₂)Br₂ are sum-

Table I: Rate Constants for the Dehydration–Dehydrobromination of *trans*-[Co(en)₂Br₂](H₃O₂)Br Calculated Using the Contracting-Cube Rate Law

Sample mesh size	Temp, °C	k , sec ⁻¹	
200	55.8	4.00×10^{-6a}	
	60.2	8.89×10^{-5a}	
	61.2	1.00×10^{-4a}	
	65.2	2.07×10^{-4a}	
	65.8	2.34×10^{-4a}	
	68.0	2.67×10^{-4a}	
	73.4	4.04×10^{-4}	
	77.5	5.67×10^{-4}	
	83.0	8.00×10^{-4}	
	60–100 (I)	72.6	$9.50 \times 10^{-5a,b}$
		72.9	9.00×10^{-5a}
77.2		1.67×10^{-4a}	
80.1		$2.70 \times 10^{-4a,b}$	
85.2		5.13×10^{-4a}	
85.4		5.66×10^{-4a}	
89.6		$1.00 \times 10^{-3a,b}$	
89.6		1.00×10^{-3a}	
97.1		1.65×10^{-3a}	
60–100 (II)		50.0	3.31×10^{-6a}
	53.3	6.60×10^{-6a}	
	58.4	$1.41 \times 10^{-5a,b}$	
	59.0	1.83×10^{-5a}	
	65.6	5.74×10^{-4a}	
	67.0	$7.08 \times 10^{-5a,b}$	
	69.3	9.92×10^{-5a}	
	70.6	1.07×10^{-4a}	
	78.0	4.16×10^{-4a}	
	80.6	5.25×10^{-4}	
	82.8	6.74×10^{-4}	
	83.2	8.20×10^{-4b}	
	88.4	1.35×10^{-3}	
95.0	1.87×10^{-3}		

^a Rate constants used in least-squares analysis for the determination of E_a . ^b Thermally nucleated samples.

marized in Table I in terms of the rate constants for the contracting-cube rate law. Even at the lower temperatures where this rate law fits the data for a short range, the rate constants agree with those for thermally nucleated samples. This can be seen in Figure 2, an Arrhenius activation energy plot for one of the 60–100 mesh samples in which open circles are nonnucleated samples and shaded circles are the thermally nucleated samples. This agreement is also in keeping with Mampel's equations since during the initial portion of each reaction, the reaction time to particle size ratio is low. As we have noted, under this condition Mampel's equations reduce to the contracting-cube rate law.

The deviation from a straight line which is evident at high temperatures in Figure 2 can be attributed to self-cooling of the sample which can be expected for an

(19) K. L. Mampel, *Z. Phys. Chem.*, **A 187**, 43 (1940); K. L. Mampel, *ibid.*, **A 187**, 235 (1940); see D. A. Young, "Decomposition of Solids," Pergamon Press, New York, N. Y., 1966, pp 28–33.

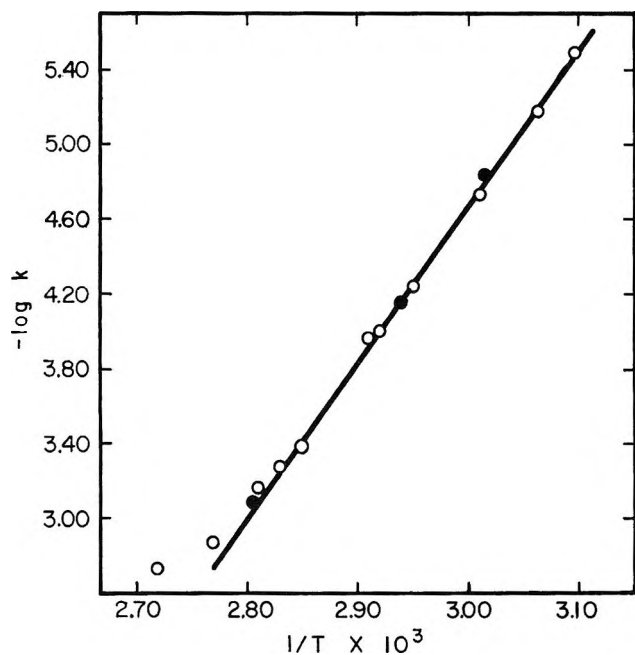


Figure 2. Arrhenius plot for a 60–100 mesh sample of $\text{trans-[Co(en)}_2\text{Br}_2\text{]}\cdot\text{(H}_5\text{O}_2\text{)Br}_2$. O, nonnucleated samples; ●, thermally nucleated samples.

endothermic reaction studied under reduced pressure. Least-squares analysis of the straight-line portions of this curve and similar ones for the other samples gave Arrhenius activation energies of $38.8 \pm 0.6 \text{ kcal mol}^{-1}$ (200 mesh), $34.7 \pm 1.0 \text{ kcal mol}^{-1}$ (60–100 mesh, batch I), and $37.3 \pm 1.8 \text{ kcal mol}^{-1}$ (60–100 mesh, batch II) where the uncertainties are standard deviations calculated assuming error only in the rate constants. The activation energy appears to be independent of particle size at least over a limited range of sizes.

Comparisons of the activation energies exhibited by $\text{trans-[Co(en)}_2\text{Br}_2\text{]}\cdot\text{(H}_5\text{O}_2\text{)Br}_2$ and the two chloro complexes which we previously studied are possibly not warranted. The $16 \pm 1 \text{ kcal mol}^{-1}$ activation energy reported for dehydration and dehydrochlorination of $\text{trans-[Co(pn)}_2\text{Cl}_2\text{]}\cdot\text{(H}_5\text{O}_2\text{)Cl}$ and $\text{trans-[Co(en)}_2\text{Cl}_2\text{]}\cdot\text{(H}_5\text{O}_2\text{)Cl}_2$ may be low due to sample self-cooling. It seems certain, however, that the activation energy for such dehydration–dehydrohalogenation reactions is not simply related to the vibration of the H_5O_2^+ ion as we previously suggested.¹⁵

Kinetic studies were also conducted using three very well formed single crystals. The rate data were found to fit a slightly simplified form of the contracting parallelepiped rate law

$$\alpha = \frac{abc - (a - 2k_a\tau)(b - 2k_b\tau)(c - 2k_c\tau)}{abc}$$

where a , b , and c are the edge lengths of the parallelepiped-shaped crystal; k_a , k_b , and k_c are the rates of reaction propagation in the a , b , and c directions, respectively; and τ is time corrected for the reaction induction

period. This equation was simplified somewhat by assuming the rate of propagation parallel to the (100) planes to be the same in all directions ($k_a = k_b = k_{\parallel}$) while propagation perpendicular to the (100) planes was assumed to be different ($k_c = k_{\perp}$). These are reasonable assumptions in terms of the crystal structure³ since the a and b directions are similar (though not identical) and the c direction is definitely unique. This assumption is also in keeping with visual observations made on this compound and results previously reported¹⁵ for $\text{trans-[Co(pn)}_2\text{Cl}_2\text{]}\cdot\text{(H}_5\text{O}_2\text{)Cl}_2$ and $\text{trans-[Co(en)}_2\text{Cl}_2\text{]}\cdot\text{(H}_5\text{O}_2\text{)Cl}_2$ which have crystal structures similar to their bromine analogs. The contracting-cube rate law found for smaller particles can be obtained from the contracting-parallelepiped expression where $a - 2k_a\tau = b - 2k_b\tau = c - 2k_c\tau$. The contracting-parallel epiped rate law reduces to the contracting-square rate law when $a = b$, $k_a = k_b = k/2$, and $k_c = 0$.

Values of k_{\parallel} and k_{\perp} for the single crystals were obtained by simultaneous solution of equations obtained from the contracting-parallelepiped rate law by substitution of experimental values of a , b , c , α , and τ (the induction period was estimated from a plot of α vs. time). This yields the solutions at each temperature which are given in Table II. At 102.6° both solutions indicate more rapid reaction parallel to the (100) planes than perpendicular to them. At 97.8° and 90.3° , solutions were obtained not only for $k_{\parallel} > k_{\perp}$ but also for $k_{\parallel} \approx k_{\perp}$. Since the crystals have different surface areas, they may experience different degrees of self-cooling. Because of this possibility and because there are two solutions for both k_{\parallel} and k_{\perp} at each temperature, determination of activation energies from these data is highly speculative.

The extent of data fitting possible for single crystals using the contracting-parallelepiped rate law is illustrated in Figure 3. The solid lines represent the

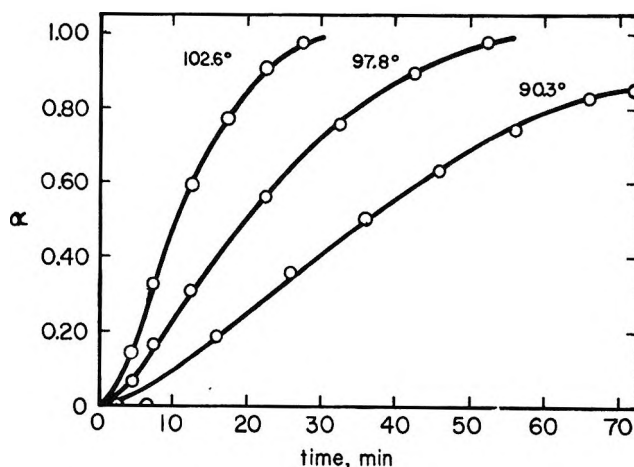


Figure 3. Comparison of calculated (open circles) and experimental (solid lines) extent of reaction, α , for single crystals of $\text{trans-[Co(en)}_2\text{Br}_2\text{]}\cdot\text{(H}_5\text{O}_2\text{)Br}_2$. Calculated values were obtained from the contracting parallelepiped rate law.

Table II: Rate Constants for Dehydration and Dehydrobromination of Single Crystals of *trans*-[Co(en)₂Br₂](H₅O₂)Br₂ Calculated Using the Contracting-Parallelepiped Rate Law

Temp, °C	Crystal dimensions, mm	$k_{ }$, mm sec ⁻¹	k_{\perp} , mm sec ⁻¹
90.3	4.0 × 3.0 × 1.2	2.75 × 10 ⁻⁶	8.3 × 10 ⁻⁶
		1.05 × 10 ⁻⁶	1.27 × 10 ⁻⁴
97.8	3.8 × 3.3 × 1.0	4.75 × 10 ⁻⁶	1.7 × 10 ⁻⁵
		1.93 × 10 ⁻⁶	1.77 × 10 ⁻⁴
102.6	5.5 × 4.0 × 1.0	1.21 × 10 ⁻⁵	1.0 × 10 ⁻⁵
		7.06 × 10 ⁻⁶	3.20 × 10 ⁻⁴

experimental fraction of dehydration-dehydrobromination as a function of time. The open circles are values of α calculated using the contracting-parallelepiped rate law together with the values of $k_{||}$ and k_{\perp} found in Table II.

That the dehydration-dehydrobromination of *trans*-[Co(en)₂Br₂](H₅O₂)Br₂ can propagate more rapidly parallel to the (100) planes than perpendicular to them is consistent with this compound's crystal structure³ and with the behavior previously reported for *trans*-[Co(pn)₂Cl₂](H₅O₂)Cl₂.¹⁵ It appears probable that this behavior is general for those *trans*-[M(AA)₂X₂](H₅O₂)-X₂-type compounds which have a layer-type lattice. Slight differences may arise from different packings in or between the (100) planes or from differences in the evolved hydrogen halide.

Although *trans*-[Co(en)₂Br₂](H₅O₂)Br₂ and *trans*-

[Co(pn)₂Cl₂](H₅O₂)Cl₂ both resist loss of H₂O and HX from the (100) planes, only the *trans*-[Co(pn)₂Cl₂](H₅O₂)Cl₂ isomerizes during this process. This strongly suggests that this isomerization is not due simply to stereospecific attack of the complex cation by the evolved water or hydrogen halide. Radiochloride exchange experiments have been conducted recently which suggest an alternate explanation for such isomerization. A preliminary report of this work appears elsewhere.^{20,21}

(20) H. E. LeMay, Jr. in "Coordination Chemistry," S. Kirschner, Ed., Plenum Press, New York, N. Y., 1969, p 303.

(21) NOTE ADDED IN PROOF. Manganese(II) formate dihydrate whose crystal lattice like that of *trans*-[Co(en)₂Br₂](H₅O₂)Br₂ belongs to monoclinic space group P2₁/c has been reported to dehydrate in a manner very similar to that reported here for *trans*-[Co(en)₂Br₂](H₅O₂)Br₂: R. C. Eckhardt and T. B. Flanagan, *Trans. Faraday Soc.*, **60**, 1239 (1964); see also T. A. Clarke and J. M. Thomas, *J. Chem. Soc., A*, 227 (1969).

The Thermal Decomposition of Orthorhombic

Ammonium Perchlorate Single Crystals

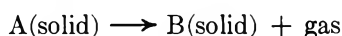
by K. J. Kraeutle

Naval Weapons Center, China Lake, California 93555 (Received January 31, 1969)

The isothermal decomposition of ammonium perchlorate (AP) single crystals has been studied from 211° to 231° under vacuum, at 1 atm of air, and at 35 atm of nitrogen. The development and course of the decomposition were examined microscopically. The kinetics of the decomposition is not affected by the pressure and nature of the surrounding atmosphere and is independent of the amount of AP which is decomposed. The velocity of the interface decomposition is time independent and has activation energies between 19.8 and 21.1 kcal/mol.

Introduction

Of the two temperature regions which can be distinguished in the thermal decomposition of AP, the low-temperature region extends from about 200 to 350° and is characterized by an incomplete decomposition of the type



Numerous studies of the low-temperature decomposition of AP have been made.¹⁻⁴ The first comprehensive work was done by Bircumshaw and Newman¹ who observed decomposing AP crystals with the optical microscope and reported the partial decomposition in the low-temperature range (30% weight loss). Galwey and Jacobs³ used AP in the form of powder, whole crystals, and pressed pellets in their work. Davies, Jacobs, and Russell-Jones⁴ investigated the decomposition of AP pellets over a wide temperature range and in different atmospheres. Most studies were concerned with the decomposition rate of AP. Methods frequently used to determine the rates were the observation of pressure changes,²⁻⁴ the measurement of weight losses,⁴ or the measurement of ion currents⁵ (mass spectrometry). In view of the variety of results it was desirable to use a direct method of rate measurement.

Raevskii and Manelis⁶ made the first direct measurement of the decomposition rate between 215 and 272°. They determined the growth rate of decomposition centers on rhombic crystal faces (c-faces) and on rectangular faces (m-faces). From the data they could calculate the kinetic constants of the surface reaction. After the coalescence of nucleation centers the AP decomposition occurs at an interface.² In this paper it is shown that the direct observation of the interfacial advance of the decomposition allows the determination of the kinetic parameters. The method was applied earlier with great success in the investigation of the dehydration of crystalline hydrates.^{7,8} Purely geometrical equations can be derived for the interface decomposition if large crystals of known shape are available.

Experimental Section

The single crystals used in the decomposition experiments were grown in-house from aqueous solutions by a carefully controlled temperature-lowering technique. The mother liquor was prepared with ultrahigh-purity AP of the American Potash and Chemical Corp. An analysis is shown in Table I.

Table I: Analysis of AP Used for Growing Single Crystals

NH ₄ ClO ₄	99.8%
NH ₄ Cl	0.02%
NaClO ₃	Trace
Moisture (surface)	0.008%
Sulfated ash	Trace
(NH ₄) ₂ SO ₄	Trace
NaBrO ₃	Trace
Insoluble	0.002%
Metal oxide (nonalkali)	0.001%
pH	5.0%
Moisture (total)	0.079
Na	5 ppm
K	4 ppm
Ca	N.D. (1 ppm max)

The material was superior to reagent grade AP from other sources. Recrystallization during crystal growth probably did not much change the impurity concentrations listed in Table I. The large crystals were cleaved

(1) L. L. Bircumshaw and B. H. Newman, *Proc. Roy. Soc. (London)*, **A227**, 115 (1954).

(2) L. L. Bircumshaw and B. H. Newman, *ibid.*, **A227**, 228 (1955).

(3) A. K. Galwey and P. W. M. Jacobs, *ibid.*, **A254**, 455 (1960).

(4) J. V. Davies, P. W. M. Jacobs, and A. Russell-Jones, *Trans. Faraday Soc.*, **63**, 1737 (1967).

(5) V. R. Pai Verneker and J. N. Maycock, *J. Chem. Phys.*, **47**, 3618 (1967).

(6) A. V. Raevskii and G. B. Manelis, *Dokl. Akad. Nauk SSSR*, **151**, 886 (1963).

(7) J. Hume and J. Colvin, *Proc. Roy. Soc. (London)*, **A125**, 635 (1929).

(8) J. Hume and J. Colvin, *ibid.*, **A132**, 548 (1931).

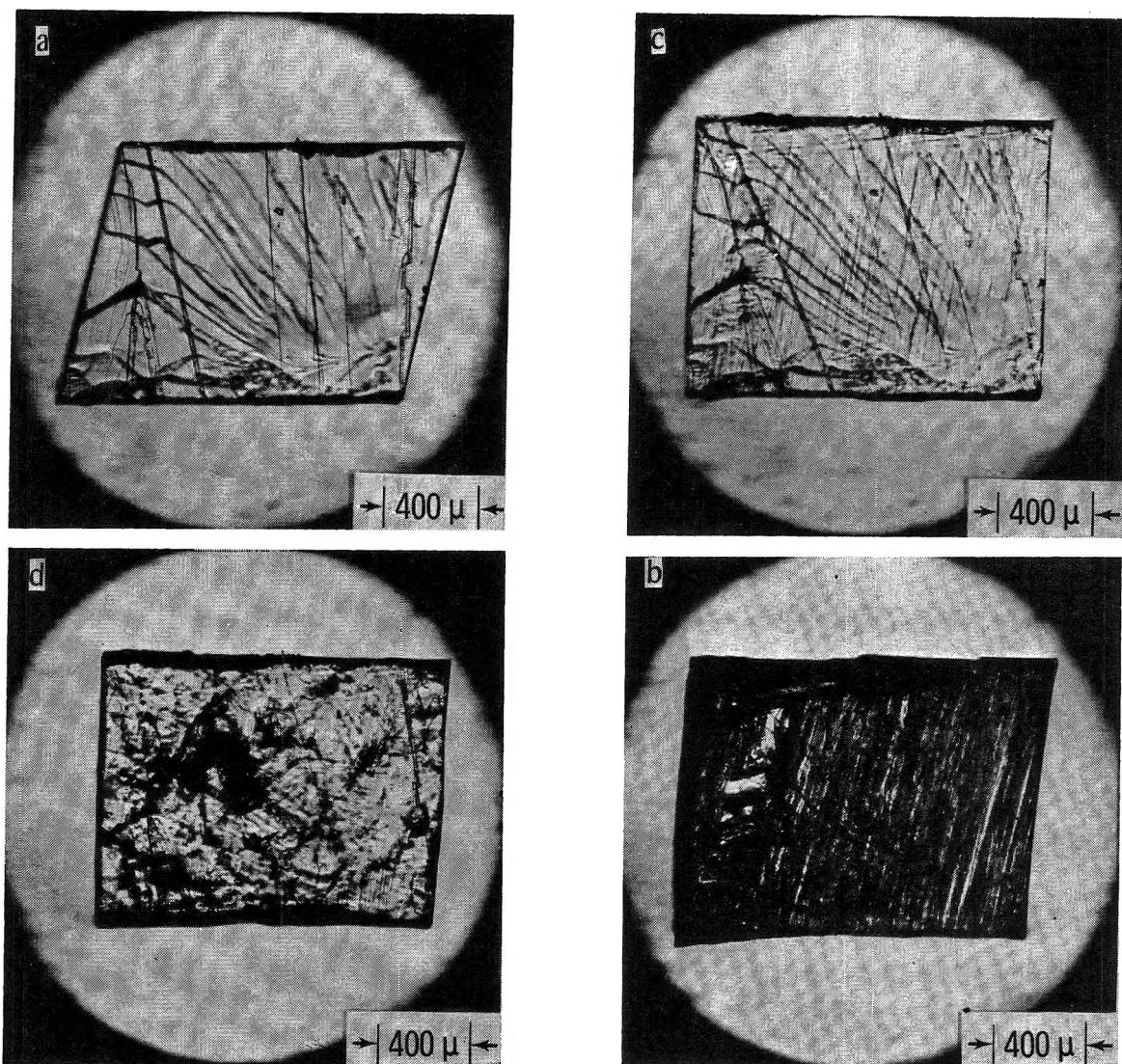


Figure 1. (a) The *c*-face of AP single crystal at room temperature, (b) during the transition orthorhombic \rightarrow cubic at about 240° , (c) in the cubic phase at 250° , and (d) after the transition cubic \rightarrow orthorhombic.

to the required size of approximately $2 \times 3 \times 4$ mm. Cleaving also allowed the removal of crystal sections containing visible imperfections. The crystals could be cleaved easiest parallel the (210) and (001) planes resulting in smaller crystals with four rectangular *m*-faces and two rhombohedral *c*-faces.

Decompositions under vacuum and at atmospheric pressure were carried out in a 24 cm long quartz tube furnace. Decompositions at a pressure of 35 atm were made in a small ceramic furnace which could be placed in a high-pressure bomb. The bomb was pressurized with dry nitrogen.

A typical decomposition experiment consisted of a heat-up period of about 5 min, an isothermal decomposition for a certain time at a programmed temperature ($\pm 0.25^\circ$), and cooling to room temperature. Cooling had to be done very carefully to prevent the porous residue layer from splitting off the undecomposed crystal core. After cleaving of the partially decomposed crys-

tal, the thickness of the porous residue layer or of the undecomposed crystal was measured microscopically. Both values can be used to determine the decomposition rate.

AP is orthorhombic below 240° and cubic above 240° . The *c*-face of a crystal is shown in the orthorhombic phase at room temperature (Figure 1a), during the transition orthorhombic \rightarrow cubic at about 240° (Figure 1b), in the cubic phase at 250° (Figure 1c), and at room temperature after the transition cubic \rightarrow orthorhombic (Figure 1d). Crystals in a state as shown in Figure 1d could not be cleaved because the phase change caused severe cracking throughout the crystal. Therefore, all experiments were made with orthorhombic AP between 221 and 231° to allow rate measurements as described above. At temperatures below approximately 220° the decomposition rates were too small to make the necessary number of rate determinations.

A new crystal was used for each decomposition experi-

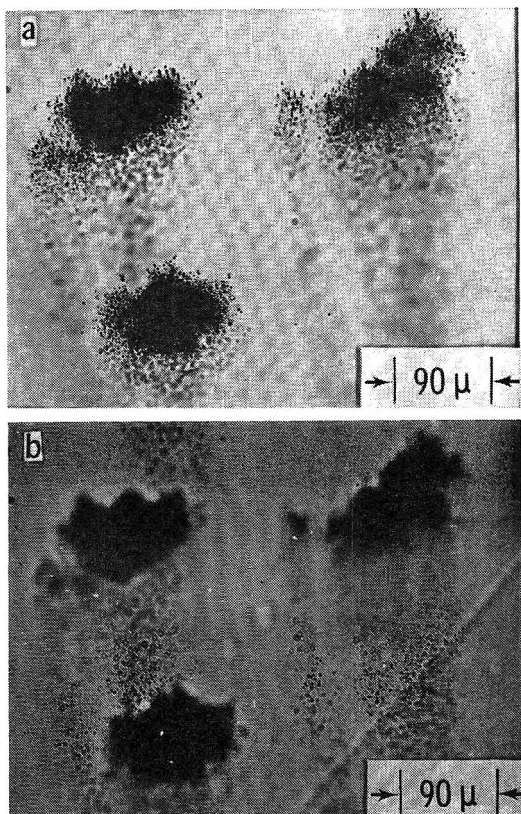


Figure 2. Decomposition sites on m-face of AP single crystal; focus is on surface in picture a and approximately $200\ \mu\text{m}$ below the surface in picture b.

ment. The course of the decomposition was examined with the optical and scanning electron microscopes. The scanning electron microscope (SEM) is an especially useful tool to study surface features of solids because it combines high magnification with an almost unlimited depth of focus. The optical microscope, in contrast, allowed the study of the interior of transparent solids like AP and the observation of the samples during decomposition.

Samples decomposed at 221 and 231° under atmospheric pressure were weighed before and after the decomposition. The results were compared with data calculated from a contracting-sphere equation.

Results and Discussion

The observation of AP single crystals with a hot stage microscope showed that the three major decomposition steps are nucleation, nuclei growth, and interface decomposition. This agrees with the results reported in a number of papers.^{2,6,9}

The generation of a decomposition site on the m-face of an AP crystal was first noticed by a slight, barely visible darkening of a very small surface area. A few minutes later distinct dark spots appeared suddenly within this area. Their number increased with time and eventually the decomposition site became opaque in transmitted illumination. Figure 2a shows three

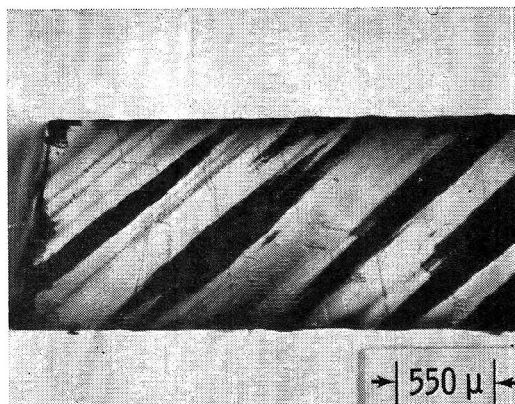


Figure 3. Decomposition sites on c-face of AP single crystal; focus is on surface.

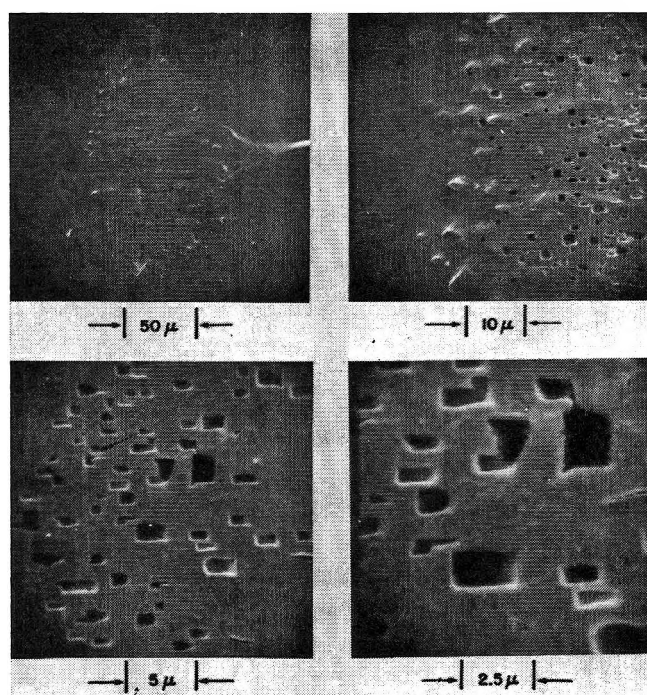


Figure 4. SEM photograph of decomposition site on m-face of AP single crystal.

sites on the surface (m-face) in an advanced state of decomposition. The dark spots whose size is in the range of $1\ \mu\text{m}$ can be seen around the big opaque sites. There the decomposition proceeded into the single crystal accompanied by sudden appearance or rearrangement of small dark spots. A motion as reported by Raevskii and Manelis⁶ was not observed although the sudden appearance of a microspot may simulate its movement from a place nearby. Figure 2b shows the sample approximately $200\ \mu\text{m}$ below the surface. A streak of small decomposition nuclei can be seen originating at the dense opaque centers on the surface and extending into the crystal. These streaks are parallel

(9) V. V. Boldyrev, Yu. P. Savintsev, and V. F. Komarov, *Kinet. Katal.*, **6**, 732 (1965).

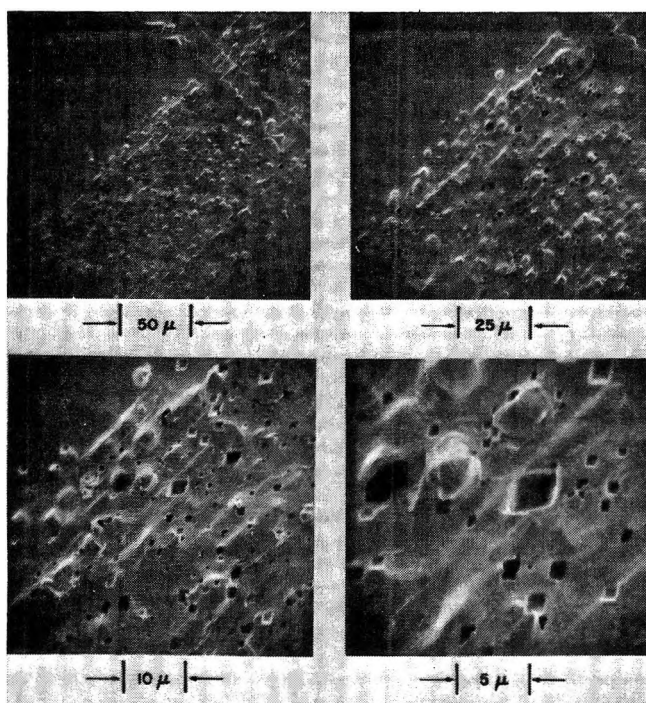


Figure 5. SEM photograph of decomposition site on c-face of AP single crystal.

to the crystallographic b axis. They remained thin in the bulk of the undecomposed crystal throughout the decomposition. On the surface they developed to dense streaks as shown on the photomicrograph of a c-face in Figure 3.

Examination with the scanning electron microscope revealed the microstructure of the decomposition sites. Figure 4 shows the m-face and Figure 5 shows the c-face of a crystal which decomposed for about 2 hr at 226° and atmospheric pressure. It can be seen in Figure 4 that the decomposition centers which appeared as small dark spots in Figure 2a are holes which reflect the crystal habit of the m-face. Similarly, the fine structure of a streak on the c-face (Figure 3) is composed of rhombohedral holes (Figure 5). Some of the holes on the m-face as well as the c-face seem to be covered with a lid of AP, especially in the transition area between decomposition site and undecomposed crystal. Debris found in the environment of the sites indicated that some of the lids popped off during the reaction. This would explain the sudden appearance of dark spots as described above. The dark spots point out a subsurface reaction before the decomposition centers become visible.

The disk-shaped centers on m-faces and streaklike centers on c-faces grew, overlapped, and eventually formed a continuous layer of porous AP. Figure 6 shows two centers in an early stage of overlapping. The single crystal was cleaved perpendicular to the c-face and photographed with incident illumination. The centers are asymmetrical if the crystal is cleaved parallel to the c-face and viewed in direction of the c axis (Figure 7). The decomposition was faster parallel to the b axis

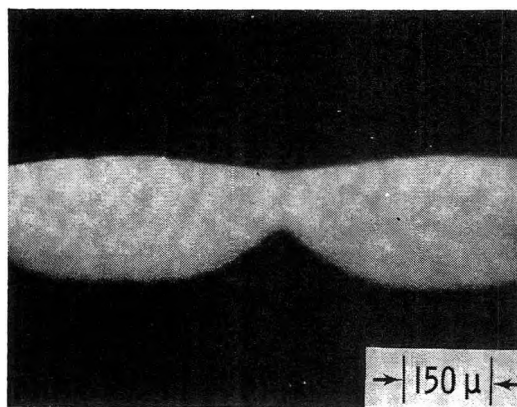


Figure 6. Cross-section through two decomposition sites on m-face of AP single crystal after overlapping.

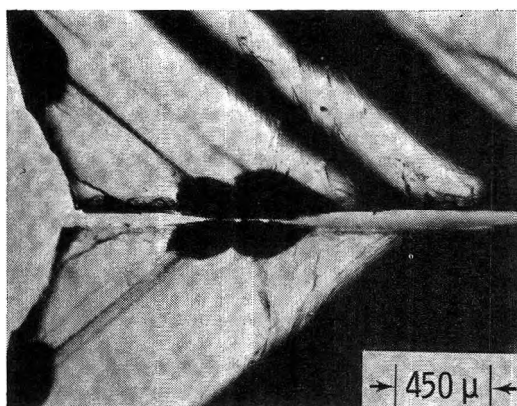


Figure 7. AP single crystal cleaved at an early stage of decomposition. View is on corresponding c-faces; dark bands are decomposition streaks at the surface (out of focus).

(direction of streaks) than parallel to the a axis (in picture plane perpendicular to the streaks). However, the difference is not as pronounced as in the case of streaks which grew on the surface of a crystal (Figure 3). This anisotropy of the growth of the interface could be observed during the early stage of decomposition (acceleratory phase) as long as the individual reaction sites were not completely overlapping.

After a continuous layer of porous residue was established, the reaction proceeded at the interface between layer and undecomposed crystal. A cleavage plane parallel to the c-face (001 plane) of a crystal which was decomposed for 6 hr at 226° and atmospheric pressure is shown in Figure 8. The layer appears dark in transmitted illumination. Only very limited bulk decomposition in the single crystal along the b axis is indicated by the photomicrograph. The dark spots are debris and an artifact of cleaving. At this stage of decomposition the advance of the interface seems to be isotropical (Figure 8). One cannot separate decomposition parallel to b axis (direction of streaks) and a axis any more. Consequently, cleaving parallel to the (001) plane, which was done throughout this work, did not show anisotropic advance of the interface.

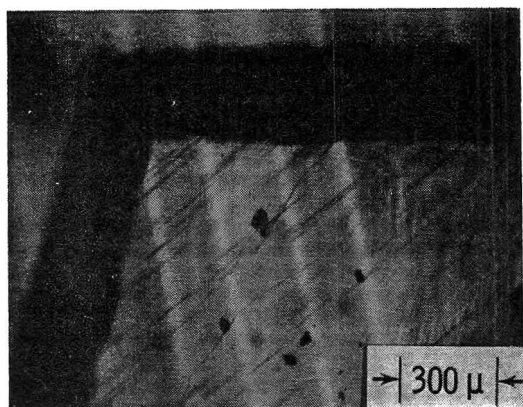


Figure 8. Cross-section through partially decomposed AP single crystal after cleaving; view on *c*-face.

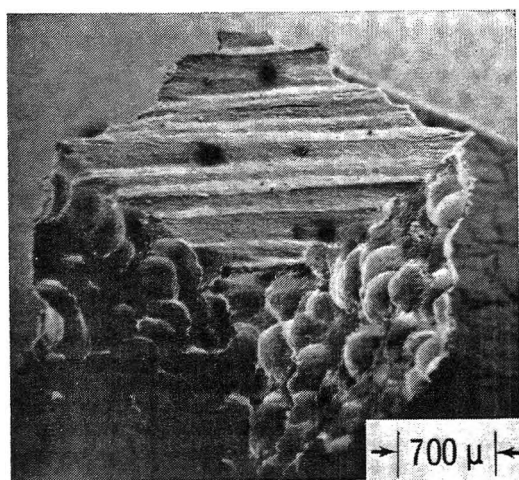


Figure 9. AP single crystal in advanced state of decomposition under a vacuum of 50×10^{-3} mm; view on *c*-face (line structure) and two *m*-faces.

The thickness of the porous layer was measured as a function of decomposition time and temperature for decompositions made at atmospheric pressure and at 35 atm of nitrogen. During vacuum decomposition most of the porous residue sublimed. Figure 9 shows a side view of a crystal in an advanced state of decomposition in a vacuum of 50×10^{-3} mm. The top *c*-face is characterized by the streak structure. The two visible *m*-faces show shallow concave dips imaging the disklike nucleation centers at the beginning of a decomposition. Only approximately $100 \mu\text{m}$ of the residue layer was left, and the advance of the interface had to be determined from the difference between the dimensions of the single crystal before and after decomposition.

Plots of the interface penetration d vs. time yielded straight lines for constant temperature. This holds true for decompositions under a vacuum of 50×10^{-3} mm (Figure 10), at atmospheric pressure (Figure 11), and at 35 atm of nitrogen (Figure 12). The decomposition velocities k were calculated from the slopes of the straight lines (least-squares fits) under the assumption

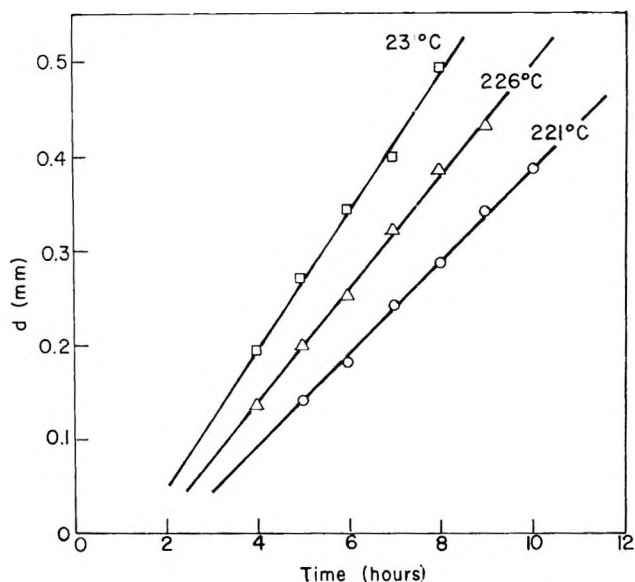


Figure 10. Penetration d of the decomposition interface into an AP single crystal as a function of time; decomposition under a vacuum of 50×10^{-3} mm.

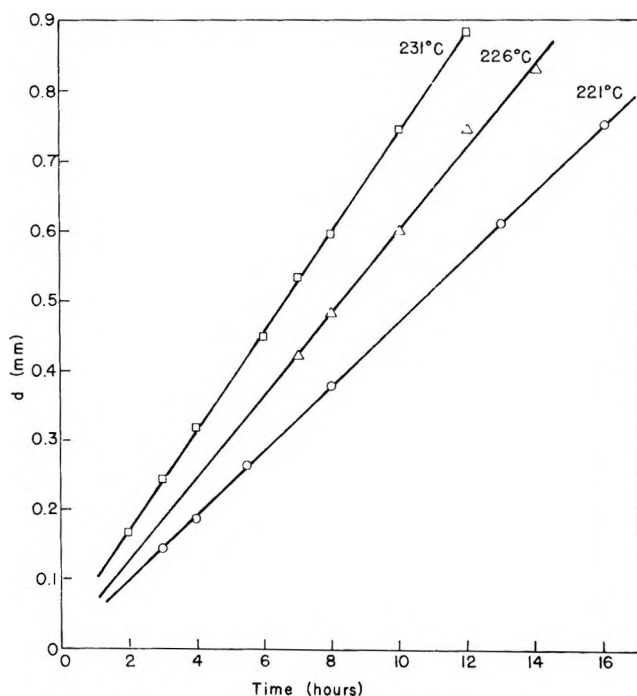


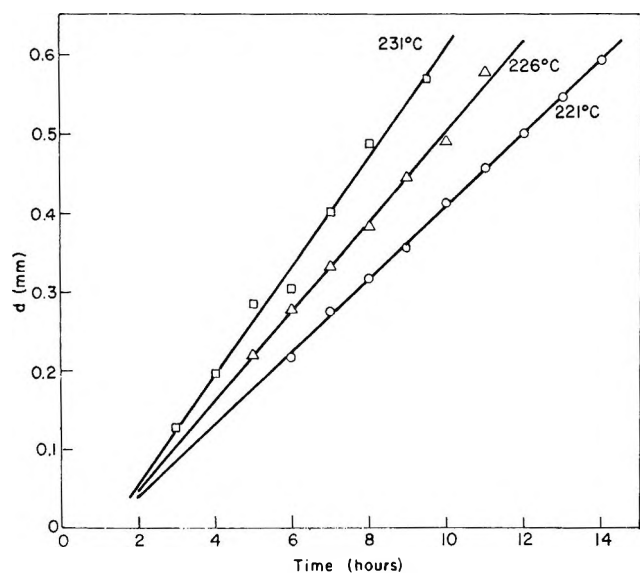
Figure 11. Penetration d of the decomposition interface into an AP single crystal as a function of time; decomposition at atmospheric pressure.

that each individual observation had equal weight. The values of k are put together in Table II.

The velocities k were found to be isotropic in the (001) plane. However, there seems to be a decrease of the interface velocities parallel to the *c* axis. A few decompositions made with large single crystals which were cleaved parallel the (210) plane only indicated the rates parallel to the *c* axis to be about 0.9 times the rates in directions perpendicular to the *c* axis. The

Table II: Decomposition Velocities As a Function of Temperature and Pressure

Pressure, atm	Temp, °C	Decomp. velocity k , (cm/sec) $\times 10^6$
7×10^{-5}	221	1.36 ± 0.04
7×10^{-5}	226	1.67 ± 0.07
7×10^{-5}	231	2.03 ± 0.10
1.0	221	1.30 ± 0.01
1.0	226	1.66 ± 0.07
1.0	231	1.99 ± 0.02
35.0	221	1.28 ± 0.02
35.0	226	1.59 ± 0.05
35.0	231	1.93 ± 0.09

**Figure 12.** Penetration d of the decomposition interface into an AP single crystal as a function of time; decomposition at 35 atm of nitrogen.

crystals used in this work were not large enough to make simultaneous determinations of the velocities parallel to m - and c -faces. The velocities k are independent of time, amount of residue AP, and amount of undecomposed AP. With a constant linear decomposition rate, the interface decomposition should obey a contracting-volume¹⁰ equation

$$\alpha_t = \frac{V_d}{V_0} = \frac{V_0 - V_t}{V_0} \quad (1)$$

where α_t is the fractional decomposition, V_d the volume of partially decomposed AP, and V_t the volume of undecomposed AP, respectively, at the time t . V_0 is the volume of undecomposed AP at the beginning of an experiment ($t = 0$).

Equation 1 was checked directly by measuring the relative weight loss ΔW_t as a function of time at atmospheric pressure and comparing it with the relative weight loss ΔW which, according to eq 1 is

$$\Delta W = K\alpha = K \frac{V_0 - V_t}{V_0} \quad (2)$$

K is the maximum relative weight loss after a complete partial decomposition, that is when the interface is collapsed in the center of a single crystal. V_t can be calculated using the rates of Table II. Figure 13 shows the experimental and calculated weight loss data plotted vs. time. The agreement between the values is good. This can be considered as a direct proof of the contracting volume model because all necessary information was obtained by direct observation.

In Figure 14 the decomposition velocities k are plotted vs. the reciprocal temperature. The activation energies were calculated assuming that the values of $1/T$ were well known and that the individual measurements from which the rates k were computed, but not the rates k and their logarithms, had equal precision. The first assumption is justified because small variations of the temperature (random) became averaged in the calculation of the velocities k (Figures 10, 11, and 12) from experimental values of equal weight. The rate constants k have been used with different weights according to a method described by McBride and Villars.¹¹ The values of E and their errors are listed in Table III. The preexponential factors (750–2900 cm/sec) do not have much significance considering the uncertainty ΔE of the activation energy.

Table III: Activation Energies E for the Decomposition of Orthorhombic AP at Different Pressures

Pressure, atm	E , kcal/mol
7×10^{-5}	19.8 ± 2.8
1.0	21.1 ± 0.5
35.0	20.4 ± 1.9

The nature and the concentration of decomposition products at the interface seem to be without influence on the decomposition rates. No pressure dependence of the low-temperature decomposition can be derived from the rate values and the kinetic parameters. Thus the rate-limiting step appears to be a condensed phase reaction. It is not clear yet if the reaction occurs at the surface of the undecomposed single crystal or a short distance below the surface leading to the porous residue. The pressure independence of the low-temperature decomposition agrees with the observations of Strunin and Manelis,¹² and Davies, Jacobs, and Russell-Jones.⁴

(10) D. A. Young, "Decomposition of Solids," Pergamon Press, Oxford, 1966, p 37.

(11) W. R. McBride and D. S. Villars, *Anal. Chem.*, **26**, 901 (1954).

(12) V. A. Strunin and G. B. Manelis, *Bull. Acad. Sci., USSR, Div. Chem. Sci. (English Transl.)*, 2127 (1964).

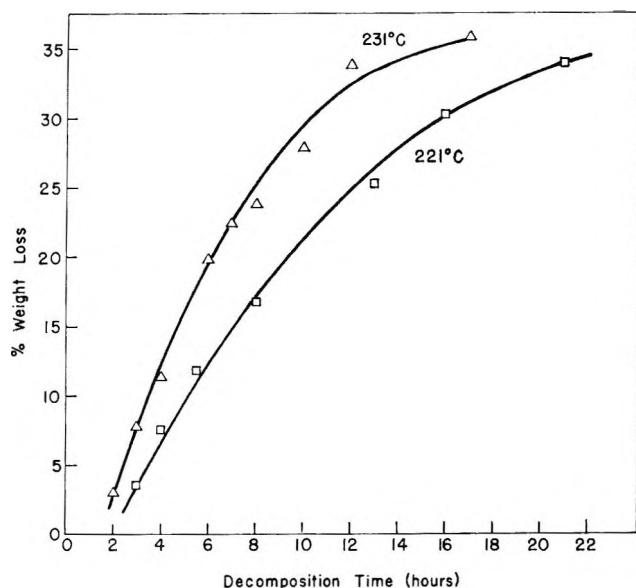


Figure 13. Relative weight loss of orthorhombic AP single crystals as a function of time; decomposition at atmospheric pressure; solid lines represent calculated values.

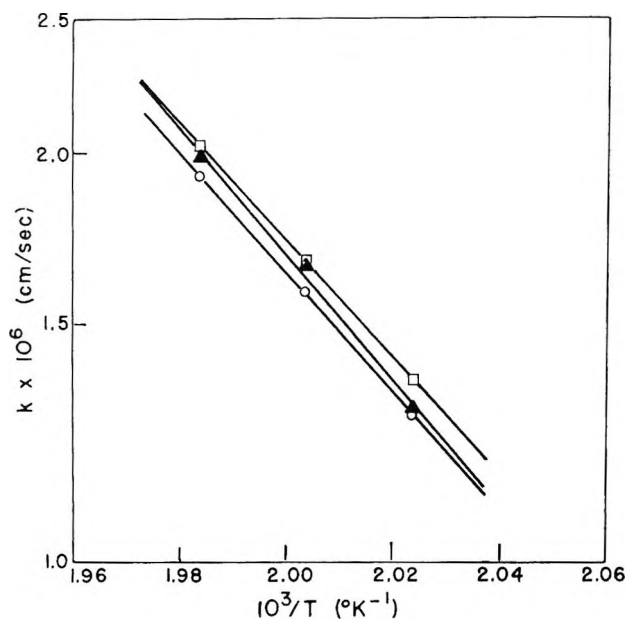


Figure 14. Arrhenius diagram of AP decomposition rates vs. $1/T$; decomposition at 50×10^{-3} mm (\square), at atmospheric pressure (\blacktriangle), and at 35 atm of nitrogen (\circ).

The activation energies of Table III are at the lower end of the range of values (17–40 kcal/mol) found in the literature for the decomposition of orthorhombic AP. However, the data seem to concentrate at about 30 kcal/mol. The activation energies of Table III

disagree with this value as well as with the activation energy measured for sublimation^{4,13} (28 kcal/mol). The discrepancy suggests a decomposition mechanism with a rate-limiting step different from proton transfer. Other mechanisms have been proposed.^{2,3,14} It is difficult to decide in favor of one of the mechanisms or to establish a new one, solely on the basis of the activation energy and morphology of the decomposition, without knowing more about such important details as secondary reactions, the nucleation and nuclei growth, the role (catalytic) of reaction products, and the cessation of the decomposition after 30–35% loss of weight.

The large variation in values of E reported in the literature may be due not only to different experimental methods and analyses, but also to AP different in quality and shape. For example, to study interface decomposition the crystals must be large enough for an interface to be established, and the period of interface decomposition (usually called decay period) has to be long compared with the period of nucleation and nuclei growth. This condition may not be reached for small size granular AP. With activation energies of 31–33 kcal/mol for nuclei growth⁶ and about 20 kcal/mol for the interface decomposition (Table III), one would indeed expect kinetic constants to be a function of particle size and number of nuclei developing on the sample surface. Results which indicate this have been published.³ However, a clear-cut correlation between particle size and kinetic data is not available to date. Secondary reactions of primary (interface) reaction products on the surface of the pores are another factor which may contribute to the scattering of reported kinetic parameters. These reactions would, among other factors, depend on the surface and shape of the porous residue and, hence, also on particle size. The difficulties associated with crystal purity, crystal structure, and contribution of transient nucleation processes are minimized in the present technique for determination of rates and activation energy, while the microscopic studies of the crystal condition reveal details of the decomposition that may ultimately prove more significant than the activation energy.

Acknowledgments. The author is indebted to Dr. W. R. McBride for growing the excellent single crystals, to E. W. Price for many fruitful discussions concerning the decomposition of AP, and to the Naval Ordnance Systems Command for support of this work.

(13) K. J. Kraeutle, Preprint No. 69-20, Spring Meeting, Western States Section, The Combustion Institute, China Lake, Calif., 1969.

(14) J. N. Maycock and V. R. Pai Verneker, *Proc. Roy. Soc. (London)*, **A307**, 303 (1968).

On the Gas-Phase Thermal Reaction between Perfluoroacetone and Propene

by Alvin S. Gordon

Research Department, Chemistry Division, Naval Weapons Center,
China Lake, California 93555 (Received September 2, 1969)

The gas-phase thermal reaction between perfluoroacetone and propene has been studied in a quartz vessel in the temperature range 448–687°K. It is shown to be a homogeneous reaction, forming a product, $\text{CH}_2=\text{CHCH}_2\text{C}(\text{CF}_3)_2\text{OH}$, whose rate of formation equals $k [(\text{CF}_3)_2\text{CO}][\text{C}_3\text{H}_6]$, where

$$k = T^{1/2}(10^{4.90 \pm 0.10})10^{-(19,000 \pm 200)/4.67} M^{-1} \text{ sec}^{-1}$$

where the limits are for one standard deviation. The Arrhenius parameters indicate that the reaction must be a cooperative process, since the E_a is much too low for a stepwise reaction path. The preexponential factor is some 10^5 lower than the collision rate, also consistent with the large steric demand of a cooperative reaction.

Introduction

In a recent paper, Urry, *et al.*,¹ have made an extensive study of the reaction between perfluoroacetone and olefins in the liquid phase, a type of reaction first reported by England.² Terminal olefins were found to be more reactive than nonterminal olefins. Adelman³ in another study in the liquid phase noted that electron-donating groups on the carbon atom of the olefin linkage increased the reactivity. He postulated that the reaction occurred *via* a zwitterion intermediate. He supported his thesis by showing that ion-catalyzed polymerization occurred in the presence of the reacting system. It has also been postulated that a six-member cyclic intermediate is involved.⁴

The studies in the liquid phase were not designed to permit an elucidation of kinetic factors. If conditions for a homogeneous reaction could be established, a gas-phase kinetics study would permit an evaluation of the kinetic factors, as well as order of the reaction with respect to each of the reactants. Since the dielectric constant in the gas phase is so low, the mechanism would be restricted to nonionic paths. For all these reasons, a study of the gas-phase reaction was undertaken.

Apparatus and Procedure

The pyrolyses were carried out in a quartz cylindrical vessel of 45.7 cm³ capacity with a surface:volume ratio (s/v) of 1.6 cm⁻¹. To determine the effect of surface, a similar vessel was packed with shell quartz tubing whose axes were parallel to the axis of the vessel, increasing the s/v to 7.6 cm⁻¹. The pyrolyzed mixture (less than 2% reacted) was transferred to a gas chromatography apparatus and analyzed. The product was trapped, followed by mass spectrometer analysis. It was identified as $\text{CH}_2=\text{CHCH}_2\text{C}(\text{CF}_3)_2\text{OH}$ by its mass spectrum and its appearance time in the gas chroma-

tographic analysis. An authentic sample was used for comparison.⁵ The sample was also used to calibrate the gc peak areas as moles.

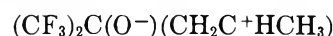
In separate experiments it was shown that perfluoroacetone did not react with ethylene in the temperature and pressure range of this research. In another experiment, it was shown that the concentration of $\text{CH}_2=\text{CHCH}_2\text{C}(\text{CF}_3)_2\text{OH}$ formed in the reaction did not appreciably react with perfluoroacetone under the experimental conditions of this work. In order to generate the minimal sufficient product for accurate measurement of the gas chromatography peak, the reaction was run at variable times, from 1 hr at the lowest temperature to 3 min at the highest temperature.

Results and Discussion

The only product found in the gc analysis is $(\text{CH}_3)_2\text{C}(\text{OH})\text{CH}_2\text{CH}=\text{CH}_2$. Data for the Arrhenius plot are shown in Table I, and the Arrhenius plot with the statistical best straight line placed through the points is shown in Figure 1. The tabulated results show clearly that the rate of reaction is homogeneous and first order with respect to concentration of both the reactants.

The specific rate constant calculated from the best straight line as seen in Figure 1 equals $T^{1/2}(10^{4.90 \pm 0.10}) \times 10^{-(19,000 \pm 200)/4.67}$.

The zwitterion structure of the intermediate proposed by Adelman



(1) W. H. Urry, J. H. Y. Niu, and L. G. Lunsted, *J. Org. Chem.*, **33**, 2302 (1968).

(2) D. E. England, *J. Amer. Chem. Soc.*, **83**, 2205 (1961).

(3) R. L. Adelman, *J. Org. Chem.*, **33**, 1400 (1968).

(4) (a) H. R. Davis, Abstracts, 140th National Meeting of the American Chemical Society, Chicago, Ill., Sept 1961; (b) I. L. Krunyants and B. L. Dyatin, *Bull. Acad. Sci. USSR, Div. Chem. Sci.*, 329 (1966).

(5) Kindly furnished by Dr. J. H. Y. Niu.

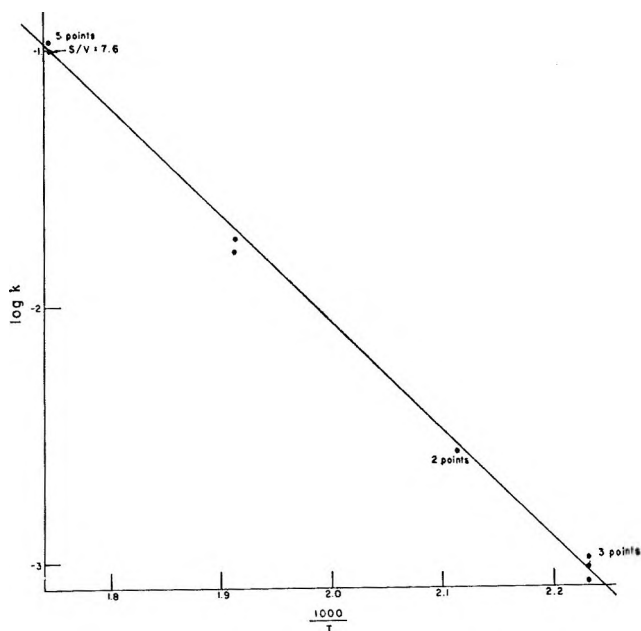
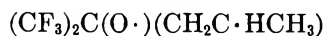


Figure 1. Arrhenius plot for the reaction between propene and perfluoroacetone.

would require many electron volts for charge separation in the gas phase. Also, such an intermediate would have a very strong drive to form an oxetane contrary to the experimental results.

A stepwise mechanism involving a biradical intermediate



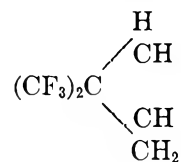
would be endothermic by at least 50 kcal/mol. The experimental E_a of just over 19 kcal/mol rules out both

Table I: Rate Data for Thermal Reaction of Perfluoropropene with Perfluoroacetone. (Surface/Volume of Reaction Vessel = 1.6 Except As Noted)

$T, ^\circ\text{K}$	C_3H_6	$\text{Mol/l.} \times 10^3$ CF_3COCF_3	Rate of formation of $\text{CH}_2 = \text{CHCH}_2-$ $\text{C}(\text{CF}_3)_2\text{OH mol/l.}$ $\text{sec} \times 10^6$	$\text{Log } k, \text{l. mol}^{-1}$ sec^{-1}
448	3.58	3.58	1.21	-3.023
448	3.58	3.58	1.07	-3.077
448	3.58	3.58	1.21	-3.023
448	3.58	3.58	1.30	-2.995
448	3.58	3.58	1.30	-2.994
473	1.69	1.69	0.79	-2.559
473	3.39	3.39	3.13	-2.564
523	1.53	1.53	3.90	-1.78
523	3.07	3.07	17.20	-1.74
573	1.40	1.40	19.90	-0.993
573	2.79	1.40	42.90	-0.959
573	1.05	1.05	11.60	-0.978
573	2.10	2.10	47.10	-0.973
573 ^a	1.40	1.40	19.50	-1.005

^a $S/V = 7.6$.

the above intermediates and suggests a cooperative mechanism with a six-membered cyclic intermediate



as consistent with the experimental order of the reaction and the E_a , as well as the unusually low preexponential factor reflecting the high steric demands of such a reaction path.

Paramagnetic Resonance of Sulfur Radicals in Synthetic Sodalites

by S. D. McLaughlan and D. J. Marshall

Royal Radar Establishment, Malvern, Worcester, England (Received September 19, 1969)

The paramagnetic resonance spectra of sulfur-doped synthetic sodalites, produced by the hydrothermal process, have been examined after various heat treatments. The blue-colored variety of sodalite, known as ultramarine, has been shown to arise from the presence of S_3^- radicals while the radicals responsible for green ultramarine have been identified with reasonable certainty. Results suggest that the sulfur is quite mobile in the sodalite and that the effect of heat treatment under vacuum is to make the sulfur aggregate to form radicals like S_3^- . Some comments are made on the effects of varying the Al:Si ratio of the framework.

1. Introduction

This investigation is part of a general study being made on sulfur-doped sodalites in connection with their photochromic properties. No correlation between photochromic behavior and the sulfur radicals reported here was established. However, some indication of the behavior of sulfur in sodalites was obtained and this may well be important for complete understanding of all the processes involved.

The chemical composition of sodalite is $6NaAlSiO_4 \cdot 2NaCl$. It has an open aluminosilicate framework with a group of four Na^+ ions arranged tetrahedrally around one Cl^- ion in each cavity of the framework.¹ The Cl^- ions can be replaced by OH^- , Br^- , I^- , or sulfur in some form. At high sulfur levels, blue powders are generally produced which are normally referred to as ultramarines (natural species, lazurite). Ultramarine is a generic name used for a wide range of compounds derived from sodalite and can be obtained in various colors, e.g., blue, green, red, and violet. An early review of the constitution and structure of ultramarine is given by Jaeger² but no firm conclusions as to the source of the color were given. Since that time various paramagnetic resonance studies have been made on natural and synthetic ultramarines^{3,4} and it has been generally agreed that the coloration arises from sulfur radicals. However, the actual radicals responsible have not been identified. Hofmann, *et al.*,⁵ have by a pyrolytic process prepared ultramarines which were blue, green, violet, and red. On the basis of chemical analysis and spin concentration measurements, they concluded that the optical absorption bands at 590, 520, and 380 nm were due to S_2^- and/or S_3^- , S_2O and S_2^{2-} radicals, respectively. More recently, Hodgson, *et al.*,⁶ observed two of the radicals reported here during an investigation of photochromic sodalites. They attributed one to an unspecified sulfur-containing species and the other to a defect on oxygen and neither affected the photochromic properties of the sodalite. Here these radicals are tentatively identified as specific sulfur radicals and the conditions under which they are produced are described.

The sulfur radical responsible for blue ultramarine is identified with reasonable certainty, while green ultramarine is produced when another sulfur radical is present in addition to that responsible for blue ultramarine.

2. Experimental Section

The sodalites were synthesized by the hydrothermal process in welded platinum capsules of 0.25–1.5 ml capacity. Grade 1 alumina (Johnson Matthey, Ltd.) was thoroughly mixed with finely crushed "Spectrosil" silica (Thermal Syndicate, Ltd.) in the ratio $Al_2O_3:2SiO_2$ and the required quantity was weighed into the capsule together with sulfur in the form of $Na_2S \cdot 9H_2O$ or Na_2S_4 , and in some cases sodium chloride or bromide was also added. Sodium hydroxide solution was then added and the capsule sealed. The capsules were heated in commercially available apparatus using Tuttle-type autoclaves. The temperature was maintained at 410–420° and 550–600 bars pressure for 3–6 days. The autoclaves were then allowed to cool, the capsules opened, and the product thoroughly washed and dried at 110°.

The sodalites crystallized as euhedral rhombic dodecahedra which could be from 5 to 500 μm in size but were usually in the range 15–25 μm . Each product was identified by X-ray diffraction using Debye-Scherrer cameras with filtered Cu radiation. Unit cell parameters were determined from carefully measured films using the Straumanis technique and the Nelson-Riley extrapolation method.⁷ Selected powders were ana-

(1) L. Pauling, *Natl. Acad. Sci.*, **16**, 453 (1930); *Z. Krist.*, **74**, 213 (1930).

(2) F. M. Jaeger, *Trans. Faraday Soc.*, **25**, 320 (1929).

(3) D. M. Gardner and G. K. Fraenkel, *J. Amer. Chem. Soc.*, **77**, 6399 (1955).

(4) Y. Matsunaga, *Can. J. Chem.*, **38**, 309 (1960).

(5) U. Hofmann, E. Herzenstiel, E. Schönemann, and K. H. Schwarz, *Z. Anorg. Allg. Chem.*, **367**, 119 (1969).

(6) W. G. Hodgson, J. S. Brinen, and E. F. Williams, *J. Chem. Phys.*, **47**, 3719 (1967).

(7) J. B. Nelson and D. P. Riley, *Proc. Phys. Soc.*, **57**, 160 (1945).

lyzed for halide and sulfur content by mass spectrometry before and after heat treatments.

The paramagnetic resonance spectra of the powders were examined using a 9-GHz superheterodyne spectrometer, capable of working between room temperature and 1.4°K. The powder was contained in a thin polyethylene bag which covered the bottom of the H_{011} rectangular cavity. A small block of ruby having the c axis vertical (so that the Cr^{3+} resonance lines were independent of magnetic field orientation) was placed in a corner of the cavity and the Cr^{3+} lines used to compare the spectral intensities of the radicals in the powders.

3. Results

Samples containing hydroxyl or halide ions and having high sulfur doping levels were generally blue and were usually examined without treatment. The lightly doped powders (up to 0.5 at. % S) were colorless as grown. If these were heated to 900° in an evacuated nickel tube they changed color from white to yellow, then green and sometimes blue. The time taken to cover the whole color sequence seemed to depend on the composition of the powder. It was also found that this behavior was generally characteristic of powders doped with Na_2S_4 rather than Na_2S . Colorless or pale blue sodalites doped at higher levels (1.5–2.0 at. % S) with Na_2S_4 became deep blue after a few minutes at 800–900° in air.

Because the crystal size was so small we were obliged to work with powders, usually about 50 mg for each investigation. Hence the angular dependence of the epr spectra relative to the crystal axes could not be studied. Similarly, any attempt at isotopic enrichment was unlikely to provide any information due to the complexity of overlapping spectra. However, the spectroscopic g values can be readily deduced from the observed spectra.⁸ These can then be compared with those from sulfur radicals in other lattices as they do not seem to be sensitive to their environment.

Powders which had a fairly high sulfur content (~2.0 at. %) consisted of mixed blue and colorless crystals. X-ray powder diffraction studies showed the colorless crystals to be hydroxysodalite and the blue, ultramarine. As the sulfur concentration was increased further, only blue crystals were obtained. The ultramarine was found to have the sodalite structure but with a unit cell edge of 9.03–9.06 Å. The diffraction pattern, however, contained a first-order line of variable intensity arising from the (100) planes, which is not present in other sodalites.

These blue powders showed the most unambiguous sulfur radical spectrum at 1.4° (see Figure 1). This can be interpreted as a rhombic spectrum having g values $g_1 = 2.005$, $g_2 = 2.036$ and $g_3 = 2.046$. The line width is estimated to be about 10 G, similar to that observed for the F-center in sodalite.⁶ Above 77°K the

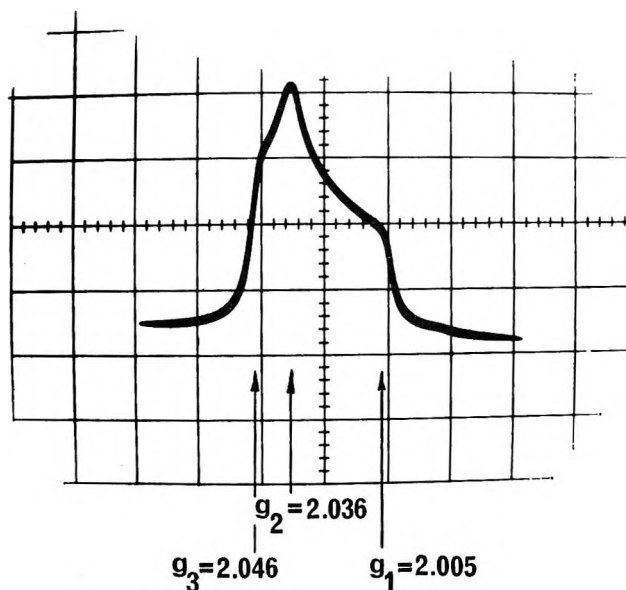


Figure 1. Paramagnetic resonance spectrum of the S_3^- radical in sodalite powder (blue ultramarine) at 1.4°K.

radical begins to rotate and at room temperature an almost symmetrical line at $g = 2.027 \pm 0.001$ is observed (in good agreement with $g_1 + g_2 + g_3/3 = 2.028$). We will refer to this radical as C. For comparison with previous work on ultramarine, in particular that of Gardner and Fraenkel,³ we decided to examine one of the commercially available ultramarines—"Reckitt's blue." From this powder we observed an isotropic line $g = 2.029$ as reported by Gardner and Fraenkel and this remained isotropic even at 1.4°K. Some boroultramarine, produced by fusing borax, boric acid, and sodium sulfide to form a deep blue glass, was also examined and in this case a rhombic spectrum $g_1 = 2.008 \pm 0.002$, $g_2 = 2.035 \pm 0.001$, and $g_3 = 2.046 \pm 0.002$ was observed at room temperature, similar to that observed by Matsunaga.⁴ We believe that all these resonances arise from the same sulfur radical in different environments.

Some lightly doped sodalites having ~0.2 at. % S, *i.e.*, those used for photochromic purposes, were also examined before and after treatment in an evacuated nickel tube at 900°. Before treatment, no sulfur resonances could be observed probably because the spectra were highly anisotropic or because they were nonparamagnetic. Powders doped with Na_2S were largely unchanged after heat treatment while those having the sulfur added as Na_2S_4 altered radically, the rate of change increasing with the sulfur content. After a short time (~0.5 hr, depending on the composition of the powder) and quenching to room temperature, the powders were found to be still white in color. The epr spectra observed from these powders consisted mainly of a single line $g = 2.005$ arising from a radical which

(8) F. K. Kneubühl, *J. Chem. Phys.*, **33**, 1074 (1960).

Table I: Comparison of Sulfur Radicals Previously Observed with Those in Sodalite

Radical	Host	g_1	g_2	g_3	g_{rot}	Method of identification and origin of results
SO_3^-	$\text{Na}_2\text{S}_2\text{O}_6 \cdot 2\text{H}_2\text{O}$	2.004	2.004	2.004	...	$^{33}\text{SO}_3^-$ spectrum observed ref 9
S_2O_2^-	$\text{Na}_2\text{S}_2\text{O}_3 \cdot 5\text{H}_2\text{O}$	2.0030 ± 0.0002	2.0050 ± 0.0002	2.0083 ± 0.0002	...	Isotopic enrichment, ref 16
A	Sodalite	2.005 ± 0.001	2.005 ± 0.001	2.005 ± 0.001	...	This paper and Hodgson, <i>et al.</i> , ref 6
SSO ⁻	$\text{Na}_2\text{S}_2\text{O}_3 \cdot 5\text{H}_2\text{O}$	2.0035	2.0106	2.0287	...	Ref 17
B	Sodalite	2.001^a	2.011 ± 0.002	2.029 ± 0.002	2.015 ± 0.001	This paper and Hodgson, <i>et al.</i> , ref 6
S_3^-	NaCl	2.0014 ± 0.0003	2.0308 ± 0.0003	2.0465 ± 0.0003	...	Isotopic enrichment ENDOR, ref 18, 19
C	Sodalite	2.005 ± 0.001	2.036 ± 0.001	2.046 ± 0.001	2.028 ± 0.001	This paper

^a Measurement made by W. Hodgson, *et al.*

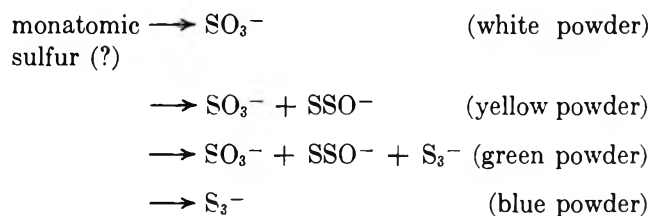
we will label A. Further heating (total treatment time ~ 1 hr) resulted in the powder turning yellow in color and in the formation of a further radical B in addition to A. This had g values $g_1 = 2.002$ (difficult to determine due to overlap with A), $g_2 = 2.011$, and $g_3 = 2.029$. Above 77°K this radical began to rotate and at room temperature its spectrum consisted of an isotropic line at $g = 2.015$ (again in good agreement with $g_1 + g_2 + g_3/3 = 2.014$). When the heat treatment time was extended still further (~ 2 hr, but dependent on the actual sulfur concentration) the powder turned green. The epr spectrum then consisted of radicals A, B, and C in roughly equal proportions. Further heating generally resulted in a blue powder which showed only radical C in the epr spectrum. It was found that the epr spectra of radicals A, B, and C were most readily separated out in the green powders at room temperature as here all these radicals give more or less isotropic resonance lines with the minimum of overlap (see Figure 2).

4. Identification of Sulfur Radicals

Since only powders were available it was not possible to relate the axes of the g tensor to the crystallographic axes of sodalite. However, one can determine whether the crystalline field acting on the radicals is cubic, axial, or rhombic, and the principal values of the g tensor. For sulfur radicals, with the exception of S_2^- , the g values tend to be rather insensitive to the environment so that the radicals can be determined with a fair degree of certainty by comparing values obtained from other host lattices. Radical C is a particularly good example. In Table I, the g values obtained for the S_3^- radical in NaCl are compared with those of radical C and one can see that there is good agreement. Similarly, radical B would appear to be SSO^- beyond reasonable doubt. One cannot be so certain in the case of radical A as there are two possibilities, either SO_3^- or S_2O_2^- . This difficulty arises because of the similarity of sulfur and oxy-

gen so that these radicals give similar spin resonance spectra. However, the spectrum of S_2O_2^- previously observed was slightly rhombic. This was not observed but may have been concealed by the resonance line width and also by radical B which was generally present at a lower level. We feel that the SO_3^- radical is more likely.

Thus it would appear that initially the sulfur is in some form whose epr spectrum could not be detected, probably monatomic, and this is first converted to SO_3^- , the progression with increasing time of heating being



The visible optical absorption spectrum of these powders was studied. The fact that a colorless powder was obtained when only SO_3^- was present agrees with the results of Chantry, *et al.*,⁹ who found that the main absorption bands occurred at 270 and 240 nm. The yellow coloration which arises from a band at 390 nm might be associated with the SSO^- radical. However, the possibility that it arises from some radical which is either nonparamagnetic or has a highly anisotropic g tensor cannot be ruled out (*e.g.*, S^{2-} or S_2^-). The blue powder shows a single absorption band at 610 nm due to the S_3^- radical. This conclusion is supported by Morton,¹⁰ who performed a combined optical esr experiment on blue-green $\text{KI}:\text{S}_3^-$ and $\text{RbI}:\text{S}_3^-$ crystals. He showed that the coloration is due to the

(9) G. W. Chantry, A. Horsfield, J. R. Morton, J. R. Rowlands, and D. H. Whiffen, *Mol. Phys.*, **5**, 233 (1962).

(10) J. R. Morton, Colloque Ampère XV, North-Holland (Amsterdam), 1969, p 299.

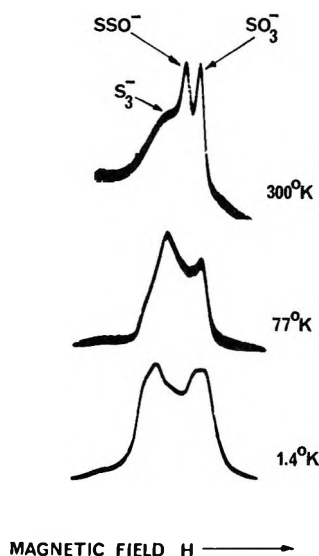


Figure 2. Temperature dependence of the radical spectrum observed from "green ultramarine." The three types of radical present are readily separated at 300°K due to rotational averaging.

${}^2B_1 \rightarrow {}^2A_1$ allowed transition of the S_3^- radical, and suggested that this might also account for the color of ultramarine. Green powders are produced by the simultaneous presence of the S_3^- and SSO^- radicals. In the samples examined the intensity of the SO_3^- spectrum could be increased by X-irradiating the powders but not that of SSO^- and S_3^- spectra. Further evidence for the presence of S_3^- in blue ultramarine is given by Holzer, *et al.*,¹¹ who compared the Raman vibrational spectra of RbI and KI known to contain S_3^- with that of ultramarine, and observed an identical vibrational frequency of 545 cm^{-1} from each.

5. Discussion

Chloro- or bromosodalites which showed the color change white-yellow-green-blue were analyzed and found to contain slightly less sulfur after treatment. Thus on heating the powders under vacuum, only a small amount of sulfur volatilizes, most atoms eventually aggregating to form S_3^- radicals. This blue-colored sodalite is quite stable when heated in air but can be bleached by heating to 900° in a stream of flowing hydrogen and is then photochromic. Thus it would appear that this treatment redisperses the sulfur throughout the lattice in some monatomic form. If the sulfur is replaced by Se or Te the color of the ultramarine changes from blue to blood red-yellow (see ref 2). This lends additional support to connecting the blue coloration with some sulfur radical. The progression of the absorption band to shorter wavelengths is probably due to the greater spin-orbit coupling of the heavier atoms.

The absolute sulfur content seems to have little bearing on the final coloration. However, those having a high sulfur content are blue initially and can only be

bleached by heat treating in hydrogen. The higher the sulfur concentration in the uncolored powders, the quicker they go through the color cycle during heat treatment. Powders grown with the sulfur added in the form of Na_2S_4 show this color cycle more readily than those doped with $Na_2S \cdot 9H_2O$. It seems to be immaterial whether the sodalite contains a halide or hydroxide. The structure of S_8 is known, the sulfur atom spacings being 2.12 \AA and bond angle 105° .¹² Thus it would appear to be difficult to get the S_3^- radical into the cage with the four sodium ions which are normally tetrahedrally coordinated round the central anion at a distance of $\sim 2.8\text{ \AA}$. Furthermore there is no indication of any ${}^{23}Na$ ($I = 3/2, 100\%$) hyperfine interaction on any of these radicals, but this may be due to a very small overlap on to the sodium nuclei. It is possible that the sodium ions are not present and that the S_3^- radical occupies the whole cage, free to rotate. This can be the case if one assumes that the Al:Si ratio is not 1:1. Indeed Jaeger points out that ultramarines having an Al:Si ratio of 1:1.5 have a deeper color. Barth¹³ suggests that the composition of the framework is not necessarily $[Al_6Si_6O_{24}]^{6-}$ but is more generally $[(Al, Si)_{12}O_{24}]^{n-}$ where the number of negative valences n is fixed by the Al:Si ratio. Hence if one had an Si-rich cage there would be no need to have four Na^+ ions present for charge balance. The cage might then contain only the sulfur radical and this may explain its ability to rotate. The above remarks are also applicable to the SSO^- and SO_3^- radicals.

Hoffman¹⁴ gives the "theoretical" composition of the various colored forms of sodalites. The transition from white to green to blue, he states, is connected with a reduction in the number of sodium atoms present. The more recent work of Barrer and Cole¹⁵ also suggests that the sodium content of sodalites can be varied over wide limits. (See Table I for citation of ref 16-19.)

6. Conclusions

Under certain conditions the sulfur atoms seem to be extremely mobile in sodalites and this fact may well have far reaching effects on the photochromic properties. The reasons for the different behavior of $Na_2S \cdot 9H_2O$ and Na_2S_4 -doped sodalites are not known but it would appear to be advantageous to add the sulfur as $Na_2S \cdot 9H_2O$ to obtain photochromic sodalite as it seems

(11) W. Holzer, W. F. Murphy, and H. Bernstein, to be published; see ref 10.

(12) B. E. Warren and J. T. Burwell, *J. Chem. Phys.*, **3**, 6 (1935).

(13) T. F. W. Barth, *Z. Krist.*, **83**, 405 (1932).

(14) R. Hoffman in "Das Ultramarin," Braunschweig, 1902, p 87.

(15) R. M. Barrer and J. F. Cole, *J. Phys. Chem. Solids*, **29**, 1755 (1968).

(16) J. R. Morton, *Can. J. Chem.*, **43**, 1948 (1965).

(17) J. R. Morton, *J. Phys. Chem.*, **71**, 89 (1967).

(18) J. Schneider, B. Dischler, and A. Rauber, *Phys. Stat. Sol.*, **13**, 141 (1966).

(19) J. Suwalski and H. Seidel, *ibid.*, **13**, 159 (1966).

to be less prone to aggregate when introduced in this form. The S_3^- and SSO^- radicals are free to rotate above 77°K and do not show any apparent line broadening due to interaction with the four sodium nuclei which ought to be in the cage. These facts, coupled with Jaeger's observations that silicon rich ultramarines have a deeper color, suggest that the Al:Si ratio may have considerable bearing on the types of radicals formed. If the cage can be devoid of sodium atoms, then it might be possible to obtain an F center which would not show the usual 13-line epr spectrum due to the four adjacent sodium nuclei. Indeed the presence of atomic hydrogen, apparently in a sodalite cage not

containing sodium, will be reported in a related publication.

Further work is planned using samples of known Al:Si ratio and single crystals as soon as they become available.

Acknowledgments. We would like to thank H. W. Evans for heat treating the samples and for assisting in the epr investigations. Thanks are also due to P. A. Forrester and M. J. Taylor for interesting discussions and R. J. Heritage for analyzing the samples. This paper is published with the permission of the Controller Her Majesty's Stationery Office.

The Molecular Structure of Perfluoroborodisilane, Si_2BF_7 , as Determined by Electron Diffraction

by C. H. Chang, R. F. Porter, and S. H. Bauer

Department of Chemistry, Cornell University, Ithaca, New York 14850 (Received August 15, 1969)

An electron diffraction structure analysis of Si_2BF_7 in the gas phase shows that the connectivity in the molecule is $\text{F}_3\text{Si}-\text{SiF}_2-\text{BF}_2$, confirming conclusions derived from nmr spectra. Bond lengths are $(\text{Si}-\text{B}) = 2.008 \pm 0.017 \text{ \AA}$, $(\text{Si}-\text{Si}) = 2.361 \pm 0.012 \text{ \AA}$, $(\text{B}-\text{F}) = 1.309 \pm 0.009 \text{ \AA}$, and $(\text{Si}-\text{F})_{\text{ave}} = 1.575 \pm 0.002 \text{ \AA}$. The bond angles are $\angle\text{SiSiB} = 125.0 \pm 2.9^\circ$, $\angle\text{SiBF} = 120.6 \pm 1.3^\circ$, $\angle\text{BSiF} = 109.1 \pm 2.4^\circ$, $\angle\text{SiSiF}(\text{center}) = 102.9^\circ \pm 1.7^\circ$, and $\angle\text{SiSiF}(\text{terminal}) = 109.5 \pm 1.0^\circ$. The most populous conformations are those in which the terminal $-\text{SiF}_3$ and $-\text{BF}_2$ are staggered with respect to the central $-\text{SiF}_2$. By assuming a potential function of the form $V = \frac{1}{2}V_0(1 - \cos 3\theta)$, a barrier height of 2.35 kcal/mol for rotation about the Si-Si bond was estimated, using Karle's method.

Introduction

Aside from the high-temperature silicon borides,^{1,2} only a few compounds containing silicon-boron bonds have been reported and for the latter no structural data are available. A series of compounds $\text{BSi}_n\text{F}_{2n+3}$ with n ranging from 2 to 13, were prepared by Timms, *et al.*,³ by low temperature acid-base reactions between SiF_2 and BF_3 .⁴ From nmr, ir, and mass spectral data, they concluded that these compounds should be classified as a homologous series $\text{SiF}_3-(\text{SiF}_2)_{n-1}-\text{BF}_2$. Although SiBF_5 was later synthesized by Timms⁵ in the reaction between BF and SiF_4 , the yield was very poor. The simplest member of this series available in sufficient quantity is Si_2BF_7 . This report is on the molecular structure of Si_2BF_7 as determined by electron diffraction in the gas phase.

Experimental Section

Samples of Si_2BF_7 which contained small amounts of

silicon oxyfluoride, (Si_2OF_6 bp = -23.3°) as detected from mass spectra, were provided by Thompson and Margrave.⁶ These were purified by distilling off the impurity at -18° . An ampoule containing the liquid sample Si_2BF_7 was connected directly to the nozzle lead tube of the electron diffraction apparatus. The amount of vapor injected into the apparatus was controlled with a Teflon needle valve. Where needed Kel-F grease was used on glass joints and stopcocks in the inlet system. Sector electron diffraction photographs were taken with the sample at room temperature. The chamber

(1) C. F. Cline, *J. Electrochem. Soc.*, **106**, 322 (1959).

(2) V. I. Matkovich, *Acta Cryst.*, **13**, 679 (1960).

(3) P. L. Timms, *et al.*, *J. Amer. Chem. Soc.*, **87**, 3819 (1965).

(4) P. L. Timms, R. A. Kent, T. C. Ehlert, and J. L. Margrave, *ibid.*, **87**, 2824 (1965).

(5) P. L. Timms, *Chem. Eng. News*, **44**, (39), 50 (1966).

(6) J. C. Thompson and J. L. Margrave, private communication.

pressure when exposures were made remained at 6×10^{-6} Torr. The beam was 3.1×10^{-8} A, and accelerating voltage 65 kV; exposure times were 90 sec for the long nozzle-to-plate distance (25.6 cm) and 150 sec for plates at the short distance (12.4 cm).

A thin layer of a light yellowish deposit was found on the plates after they were developed. This was probably due to an attack of the emulsion surface by the Si_2BF_7 , which degassed from the cryopump before the apparatus was vented. The plates were cleaned with a dilute HCl solution (about 0.5 N). The methods for measuring plates and reducing data have been adequately described.⁷⁻⁹

Analysis of the Diffraction Data

The experimental intensities are listed in Table I. They are sketched in Figure 1 along with background curves for two ranges of diffraction angles spanning $q = 7$ to 120 \AA^{-1} ; $q \equiv (40/\lambda) \sin \theta/2$. The refined experimental radial distribution (RDR) curve, shown in Figure 2, was calculated with a damping factor of $\gamma = 0.00162$. Also shown in this figure is the difference curve between the experimental and theoretical RDR curves for two models. Four bonded distances may be distinctly resolved in the RDR curve: B-F at 1.309, $(\text{SiF})_{\text{av}}$ at 1.575, Si-B at 2.008, and Si-Si at 2.361 Å. Three neighboring F...F distances appear in the next peak: $\text{F}^6 \cdots \text{F}^7 = 2.253$, $\text{F}^4 \cdots \text{F}^5 = 2.520$, and $\text{F}^8 \cdots \text{F}^9 = 2.572$ Å. The peak centered at 3.22 \AA can be resolved into $\text{Si}^3 \cdots \text{F}^4 = 3.117 \text{ \AA}$ and $\text{Si}^1 \cdots \text{F}^8 = 3.246 \text{ \AA}$. The inside shoulder at 2.94 consists of $\text{Si}^1 \cdots \text{F}^6 = 2.902$ and $\text{B}^2 \cdots \text{F}^4 = 2.930 \text{ \AA}$. Longer nonbonded distances are also indicated. Refer to Figure 3 for atom designation.

Twelve geometrical parameters were introduced to specify the structure of the molecule. They are five bonded distances and seven angles (see Figure 3); the latter are $\angle \text{Si-Si-B}$, $\angle \text{Si-B-F}$, $\angle \text{Si-Si-F}^8$, $\angle \text{Si-Si-F}^4$, $\angle \text{B-Si-F}^4$, and the two torsional angles for the terminal -BF⁶ and -SiF⁸ relative to the middle SiF⁴, α and β , respectively.

The final structure was obtained by a least-squares analysis of the $qM(q)$ curve. In these least-squares calculations, all the geometrical parameters were varied, but only bonded and the shorter nonbonded atom

Table I: Intensity Data

HVL		HVS		HVS	
Q	Intensity	Q	Intensity	Q	Intensity
7	0.6419	36	0.2264	83	0.2704
8	0.5043	37	0.2269	84	0.2708
9	0.3955	38	0.2298	85	0.2716
10	0.3361	39	0.2354	86	0.2728
11	0.3277	40	0.2385	87	0.2757
12	0.3430	41	0.2402	88	0.2791
13	0.3936	42	0.2397	89	0.2837
14	0.4362	43	0.2378	90	0.2872
15	0.4762	44	0.2325	91	0.2905
16	0.4943	45	0.2287	92	0.2932
17	0.5101	46	0.2244	93	0.2958
18	0.5224	47	0.2212	94	0.2969
19	0.5288	48	0.2213	95	0.2972
20	0.5231	49	0.2250	96	0.2975
21	0.5035	50	0.2311	97	0.2994
22	0.4908	51	0.2393	98	0.3005
23	0.4958	52	0.2437	99	0.3023
24	0.5325	53	0.2464	100	0.3054
25	0.5960	54	0.2465	101	0.3088
26	0.6633	55	0.2458	102	0.3134
27	0.7083	56	0.2434	103	0.3168
28	0.7257	57	0.2394	104	0.3208
29	0.7233	58	0.2348	105	0.3242
30	0.7214	59	0.2314	106	0.3272
31	0.7207	60	0.2320	107	0.3292
32	0.7246	61	0.2358	108	0.3309
33	0.7232	62	0.2406	109	0.3325
34	0.7176	63	0.2470	110	0.3356
35	0.7121	64	0.2521	111	0.3383
36	0.7191	65	0.2546	112	0.3411
37	0.7420	66	0.2556	113	0.3459
38	0.7704	67	0.2552	114	0.3503
39	0.7992	68	0.2553	115	0.3553
40	0.8242	69	0.2548	116	0.3580
41	0.8399	70	0.2538	117	0.3620
42	0.8486	71	0.2520	118	0.3645
43	0.8453	72	0.2511	119	0.3664
44	0.8321	73	0.2515	120	0.3708
45	0.8178	74	0.2530		
46	0.8020	75	0.2560	HVL	25.6 cm
47	0.7964	76	0.2593	HVS	12.4 cm
48	0.8023	77	0.2641		
49	0.8281	78	0.2679	Sample-to-plate	
50	0.8552	79	0.2704	distance	
51	0.8739	80	0.2713		
52	0.8904	81	0.2706		
53	0.9058	82	0.2708		

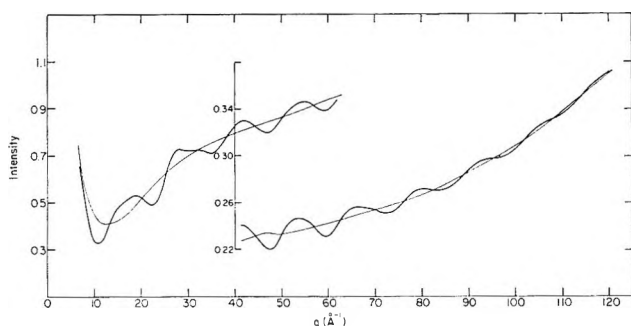


Figure 1. The experimental intensity and background curves.

pair l_{ij} (root-mean-square amplitudes of vibration) were allowed to vary. As is well known, the intensity patterns are relatively insensitive to the l_{ij} for the longer nonbonded atom pairs.⁸ The mean amplitudes for nonbonded distances larger than 4.20 \AA were either estimated from the RDR curve or averaged from preliminary runs and constrained in the final analysis.

(7) J. L. Hencher and S. H. Bauer, *J. Amer. Chem. Soc.*, **89**, 5527 (1967).

(8) R. L. Hilderbrandt and S. H. Bauer, *J. Mol. Struct.*, **3**, 325 (1969).

(9) W. Harshbarger, *et al.*, *Inorg. Chem.*, **8**, 1683 (1969).

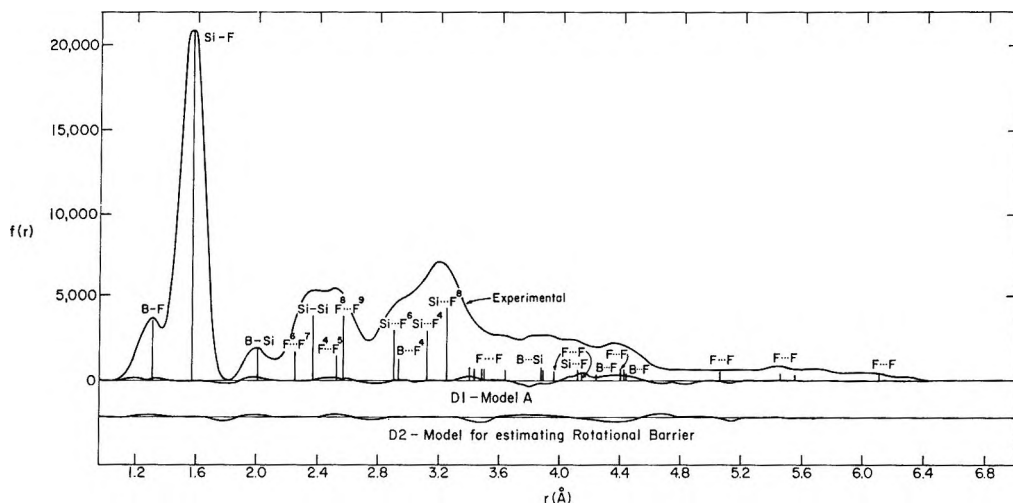


Figure 2. The refined experimental radial distribution curve and difference curve between the experimental and theoretical values for two models.

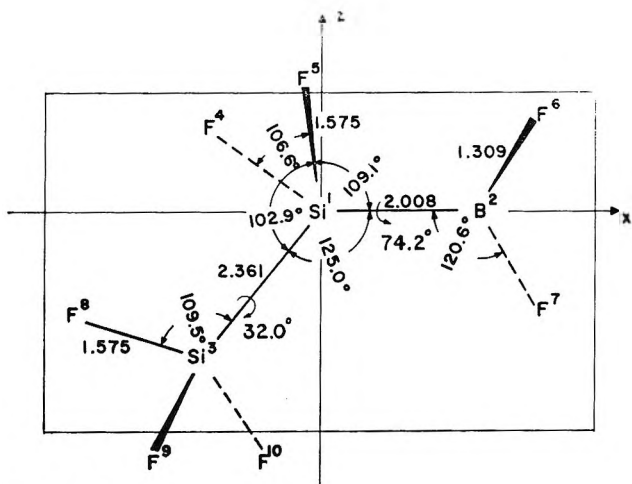


Figure 3. Structure of Si₂BF₇.

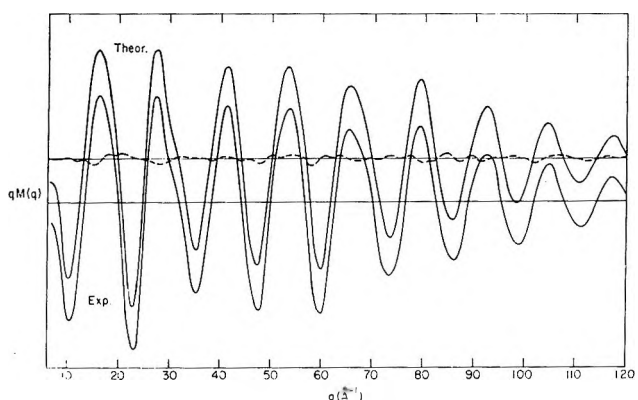


Figure 4. The reduced experimental molecular scattering curve and that calculated for the best least-squares model. The dotted line is the difference curve.

Converged geometrical parameters and l_{ij} are listed in Table II. The correlation matrix indicates that for the listed parameters which were varied the correlations are small. Figure 4 shows the reduced experimental molecular scattering curve for Si₂BF₇, and that cal-

culated for the best least-squares model is shown below it.

The estimation of error limits for bond distances and angles as derived from electron diffraction data has been discussed in the previous publications.^{8,9} To allow for possible but not probable distortion in plate dimensions and intensity which were not fully compensated by the calibration steps, due to washing of the plates in dilute HCl solution, the estimated error limits were set

Table II: Geometrical and Thermal Parameters (Standard Deviations)^a

	A (Si-F ⁴ =Si-F ⁸)	B
Si-B	2.008 (0.0042)	2.007 (0.0044)
Si-Si	2.361 (0.0029)	2.362 (0.0030)
B-F	1.309 (0.0022)	1.309 (0.0022)
Si-F ⁴	1.575 (0.0005)	1.581 (0.0171)
Si-F ⁸	1.575 (0.0005)	1.570 (0.0119)
∠SiSiB	125.0 (0.72)	125.2 (0.74)
∠SiBF	120.6 (0.32)	120.6 (0.33)
∠SiSiF ⁶	109.5 (0.26)	109.6 (0.46)
∠BSiF	109.1 (0.60)	109.0 (0.85)
∠SiSiF ⁴	102.9 (0.42)	102.6 (0.75)
α	51.9 (8.53)	52.5 (8.11)
β	43.6 (1.81)	43.3 (1.78)
⟨l ² ⟩ _{ij} ^{1/2} B-F	0.055 (0.0019)	0.055 (0.0020)
Si-F	0.048 (0.0003)	0.048 (0.0024)
Si-B	0.053 (0.0041)	0.053 (0.0042)
Si-Si	0.065 (0.0014)	0.065 (0.0013)
[F ⁴ ...F ⁶		
F ⁶ ...F ⁷	0.083 (0.0027)	0.087 (0.0022)
F ⁸ ...F ⁹		
[Si...F ^{6,7}		
B...F ^{4,6}	0.103 (0.0022)	0.103 (0.0022)
[Si...F ^{4,5}		
Si...F ^{8,9,0}	0.097 (0.0026)	0.096
[F ⁴ ...F ^{8,9,0}		
F ⁴ ...F ^{6,7}	0.171 (0.0060)	0.165 (0.0060)

^a Distances in Å; angles in degrees.

at four times the standard deviations calculated by the least-squares analysis.

Karle's method¹⁰ for separating the effect of torsional motion from the skeletal vibrations was used to estimate the rotational barrier height for the terminal $-\text{SiF}_3$ group. In applying the method, the l_{ij} for the fluorine atom pairs, $\text{F}^4 \cdots \text{F}^8$, $\text{F}^4 \cdots \text{F}^9$, and $\text{F}^4 \cdots \text{F}^{10}$, should be determined as accurately as possible. Since the complete least-square analysis is relatively insensitive to these variables, a follow-up analysis was run in which all the parameters listed in Table II (Model A) except those which depend on the two rotational angles were constrained to the magnitudes listed in the table. The result is given in Table III (equilib-

Table III: Equilibrium Distances, Angles, and Root-Mean-Square Amplitudes^a

	r , Å	θ_e , Å	$\langle l^2 \rangle^{1/2}$, Å
Si-F	1.575		0.099 ± 0.0017
$\text{F}^7 \cdots \text{F}^9$	4.759		0.129 ± 0.018
$\text{F}^4 \cdots \text{F}^9$	4.367	132.0	0.105 ± 0.006
$\text{F}^4 \cdots \text{F}^8$	3.859	-88.0	0.178 ± 0.020
$\text{F}^4 \cdots \text{F}^6$	3.344	32.0	0.129 ± 0.018
$\text{F}^4 \cdots \text{F}^5$	3.570	-74.2	0.137 ± 0.061
$\text{F}^4 \cdots \text{F}^7$	3.817	105.8	0.201 ± 0.077
$\text{B}^2 \cdots \text{F}^9$	4.544		0.143 ± 0.039

^a $\alpha = -74.2 \pm 6.5^\circ$; $\beta = 32.0 \pm 3.6^\circ$.

rium angles and distances). In terms of Karle's notation, we set $\rho = (C_1 - C_2 \cos \theta)^{1/2}$ [rather than $(C_1 + C_2 \cos \theta)^{1/2}$]; $C_1 = 15.048 \text{ Å}$, $C_2 = 4.559 \text{ Å}$, $T = 298^\circ \text{K}$, $A = 1.0$, $B = 0.0$, $n = 3$, $a = \pi/3$, $\varphi_e = 132.0^\circ$, -88.0° , 32.0° . For solution of the simultaneous equations, refer to Figure 5, which indicates that $V_0 = 2.35 \text{ kcal/mol}$.

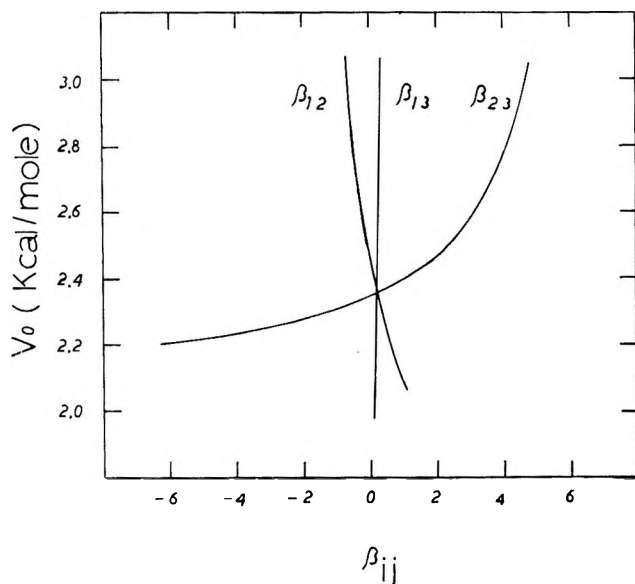


Figure 5. Graphical solution of the rotational barrier height for the terminal SiF_3 group.

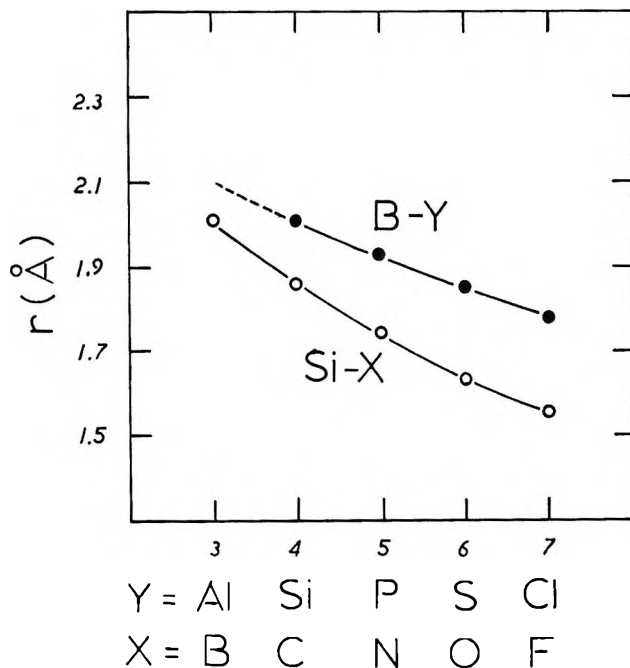


Figure 6. Bond distances of Si-X ($X = \text{B, C, N, O, and F}$) and B-Y ($Y = \text{Si, P, S, and Cl}$), atomic pairs.

Discussion

The structure deduced in this electron diffraction study confirms the conclusions based on nmr data¹ that Si_2BF_7 has the molecular framework $\text{F}_3\text{Si}-\text{SiF}_2-\text{BF}_2$. The Si-B bond length of $2.008 \pm 0.016 \text{ Å}$ is close to the 1.96 Å predicted from the Pauling-Schomaker-Stevenson empirical equation¹¹

$$R(A - B) = r_a + r_b - C|\chi_a - \chi_b|$$

with $r_{\text{Si}} = 1.17$, $r_{\text{B}} = 0.81 \text{ Å}$, $\chi_{\text{Si}} = 1.8$, $\chi_{\text{B}} = 2.0$, and $C = 0.08 \text{ Å}$. As shown in Figure 6, the bond distances Si-X ($X = \text{B, C, N, O, and F}$) and B-Y ($Y = \text{Si, P, S, and Cl}$) correlate well with the atomic numbers of X and Y. From the figure one may predict the previously unreported bond length for B-Al as 2.11 Å . The Si-Si bond length of $2.361 \pm 0.012 \text{ Å}$ is comparable to published values derived from X-ray diffraction studies: Si-Si = 2.352 Å in metallic Si,¹² 2.36 Å in $(\text{CH}_3)_3\text{Si}_3\text{O}_8$,¹³ $2.34 \pm 0.10 \text{ Å}$ in $(\text{CH}_3)_3\text{Si}-\text{Si}(\text{CH}_3)_3$,¹⁴ and 2.35 Å in $[(\text{CH}_3)_4\text{Si}_2\text{O}]_2$.¹⁵ It is longer than the magnitudes reported for $\text{H}_3\text{Si}-\text{SiH}_3$,¹⁶ $2.32 \pm 0.03 \text{ Å}$, and $2.294 \pm 0.05 \text{ Å}$ in

(10) (a) R. E. Knudsen, C. F. George, and J. Karle, *J. Chem. Phys.*, **44**, 2334 (1966); (b) J. Karle, *ibid.*, **45**, 4149 (1966).

(11) L. Pauling, "The Nature of the Chemical Bond," 3rd ed, Cornell University Press, Ithaca, N. Y., 1960, p 229.

(12) M. E. Straumanis and E. Z. Aka, *J. Appl. Phys.*, **23**, 330 (1952).

(13) T. Higuchi and A. Shimada, *Bull. Chem. Soc. Jap.*, **39**, 1316 (1966).

(14) H. Murata and K. Shimizu, *J. Chem. Phys.*, **23**, 1968 (1955).

(15) T. Takano, N. Kasai, and M. Kakudo, *Bull. Chem. Soc. Jap.*, **36**, 585 (1963).

(16) L. O. Brockway and J. Y. Beach, *J. Amer. Chem. Soc.*, **60**, 1836 (1938).

Cl₃Si-SiCl₃¹⁷ based on electron diffraction measurements; the differences are within the range of experimental errors.

The B-F bond distances in BF₃ has been carefully determined by Kuchitsu, Konaka, and their coworkers.^{18,19} The length 1.309 ± 0.009 Å in Si₂BF₇ is in excellent agreement with their result, 1.3119 ± 0.0008 Å in BF₃. A brief list of various Si-F bond distances is tabulated in Table IV. It is interesting to note that the Si-F

distance 1.581 ± 0.08 Å in the -SiF₂ group is indeed longer than the 1.570 ± 0.04 Å in the -SiF group, the high correlation and magnitude of uncertainties force the conclusion that these Si-F bond lengths are too close to distinguish with the present data. An average value of 1.575 ± 0.002 Å obtained by setting the two values equal in the analyses, is more meaningful. It agrees well with 1.572 ± 0.006 Å in CH₃SiF₃ and 1.577 ± 0.001 Å in SiH₂F₂.

As stated earlier, the *l_i* are insensitive parameters in electron diffraction determinations. For that reason, we did not attempt to estimate the rotational barrier for the terminal -BF₂ group, particularly since Karle's method is strongly dependent on the assumed form for the potential function. The least-squares refinement showed that the equilibrium position of F⁶ and F⁷ are -74° and 106° away from BSiF⁴ plane, respectively. One may question the accuracy of the estimated rotational barrier for the F₃Si-SiF₂ bond. There are two values in the literature for rotational barriers about Si-Si bonds; in Cl₃Si-SiCl₃, 1.0 kcal/mol,¹⁷ in H₃Si-SiH₂F, 1.05 kcal/mol.²⁰ The value for Si₂BF₇ appears to be too large by about a factor of 2, and this may be a consequence of the difficulty in obtaining accurate amplitudes in Si₂BF₇.

Acknowledgments. We wish to thank J. C. Thompson and J. L. Margrave for providing the sample. This work was supported by the Material Science Center, Cornell University (MSC ARPA SD-68) and the Army Research Office, Durham.

Table IV: Si-F Bond Distances

Compd	Si-F bond distance, Å
SiF ₄	1.55 ± 0.02 ^a
SiHF ₃	1.565 ± 0.005 ^b
SiH ₂ F ₂	1.577 ± 0.001 ^c
SiH ₃ F	1.592 ± 0.002 ^d
CH ₃ SiF ₃	1.572 ± 0.006 ^e
CH ₃ SiHF ₂	1.583 ± 0.002 ^f
CH ₃ SiH ₂ F	1.600 ± 0.005 ^g

^a H. Braune and P. Pinnow, *Z. Phys. Chem.*, **B35**, 239 (1937).
^b J. Sheridan and W. Gordy, *J. Chem. Phys.*, **19**, 965 (1951). ^c V. W. Laurie, *ibid.*, **26**, 1359 (1957). ^d B. Bak, J. Bruhn, and J. Rastrop-Anderson, *ibid.*, **21**, 752 (1953). ^e R. H. Schwendeman, *Dissertation Abs.*, **18**, 1645 (1958). ^f J. D. Swalen and B. P. Stoicheff, *J. Chem. Phys.*, **28**, 671 (1958). ^g L. Pierce, *ibid.*, **29**, 383 (1958).

bond length is somewhat longer in those compounds with the larger number of H atoms attached to the Si atom, parallel to the case for the analogous carbon series. We investigated the possibility that there may be a significant difference between the Si-F bond distances in terminal SiF₃ and the center SiF₂. The result of a least-squares analysis in which the two Si-F bond lengths were varied independently is shown in Table II (B). Although there are indications that the Si-F

- (17) Y. Morino and E. Hirota, *J. Chem. Phys.*, **28**, 185 (1958).
 (18) S. Konaka, Y. Murata, K. Kuchitsu, and Y. Morino, *Bull. Chem. Soc. Jap.*, **39**, 1134 (1966).
 (19) K. Kuchitsu and S. Konaka, *J. Chem. Phys.*, **45**, 4342 (1966).
 (20) R. Varma and A. P. Cox in a personal communication from E. B. Wilson, Jr., to R. G. Parr, quoted in J. P. Lowe and R. G. Parr, *J. Chem. Phys.*, **44**, 3001 (1966).

Effect of Membranes and Other Porous Networks on the Equilibrium and Rate Constants of Macromolecular Reactions

by J. Calvin Giddings

Department of Chemistry, University of Utah, Salt Lake City, Utah 84112 (Received September 22, 1969)

Porous networks reduce the number of possible configurations of macromolecules in solution to a degree which depends on molecular size. The thermodynamic properties of such molecules in porous media are therefore altered in a size-dependent manner. If reactions occur which involve a net size change, equilibrium is shifted with respect to its bulk-solution value. In a like manner reaction rates are shifted if the activated complex involves a size change. The rules governing these equilibrium and rate shifts are presented with examples. Several applications are noted.

Porous networks are increasingly important as an environment for macromolecular systems. This environment has a role in certain biological membrane processes and in the many fractionation systems employing gels and other porous media. Examples of the latter include diverse forms of exclusion chromatography (gel filtration and permeation chromatography, with rigid and nonrigid networks), gel electrophoresis, dialysis, and ultrafiltration. Also gel filtration chromatography has been used as a tool for the study of protein association reactions and the monomer molecular weight.¹ The theoretical basis for this has been treated especially by Ackers.²

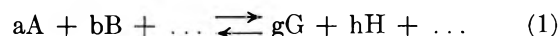
It is the object of the present work to determine the magnitude and direction of the shifts in macromolecular equilibrium and rate parameters caused by porous networks.

Theory

A porous network imposes certain geometrical restrictions on the position, orientation, and conformation of molecules, since any configuration involving overlap with the network is forbidden.³ With fewer permissible statistical states, entropy is decreased and free energy or chemical potential is increased with respect to bulk solutions of the same species. The resulting shift in physical equilibrium (distribution coefficient) has been studied for both rigid³ and flexible chain⁴ molecules in order to arrive at fundamental expressions for elution volume in exclusion chromatography.

Since the thermodynamic state of a macromolecule is altered by a small-pore environment, and the degree of alteration is a function of molecular size, the equilibrium and rate constants for any reaction involving a size change will likewise be shifted by the porous environment. Here we formulate the rules governing this shift.

Equilibrium Shifts. Consider the general reaction



for which the bulk phase equilibrium constant is, assuming ideal solutions

$$K_0 = \frac{(G)_0^g (H)_0^h \dots}{(A)_0^a (B)_0^b \dots} \quad (2)$$

In the porous-network phase (considering it to be in complete physical and chemical equilibrium with the bulk phase), each concentration in eq 2 is altered by a factor equal to the distribution coefficient, K , of that species. Thus

$$\frac{\kappa}{K_0} = \frac{K_G^g K_H^h \dots}{K_A^a K_B^b \dots} \quad (3)$$

This equation, relating chemical κ and physical K equilibrium constants, is general for any reacting system with components distributed between phases, as can be verified by simple thermodynamic arguments. Whether or not it can yield a useful result depends upon the availability of experimental or theoretical distribution coefficients for each species. Much information is available on the latter from studies in gel filtration⁵

(1) D. Winzor and H. A. Scheraga, *J. Phys. Chem.*, **68**, 338 (1964); P. Andrews, *Biochem. J.*, **91**, 222 (1964); K. Kakiuchi, S. Kato, A. Imanishi, and T. Isemura, *J. Biochem.*, (Tokyo), **55**, 102 (1964); G. K. Ackers and T. E. Thompson, *Proc. Nat. Acad. Sci., U. S.*, **53**, 342 (1965); H. Fritz, I. Trantschold, and E. Werle, *Z. Physiol. Chem.*, **342**, 253 (1965); S. W. Henn and G. K. Ackers, *J. Biol. Chem.*, **244**, 405 (1969).

(2) G. K. Ackers, *J. Biol. Chem.*, **243**, 2056 (1968).

(3) J. C. Giddings, E. Kucera, C. P. Russell, and M. N. Myers, *J. Phys. Chem.*, **72**, 4397 (1968).

(4) E. F. Casassa, *Polym. Lett.*, **5**, 773 (1967); E. F. Casassa and Y. Tagami, *Macromolecules*, **2**, 14 (1969).

(5) H. Determann, "Gel Chromatography," Springer-Verlag, New York, N. Y., 1968, Chapter 4.

and permeation⁶ chromatography. The theoretical basis is discussed below.

Distribution coefficient K for a species in an inert network is (3)

$$K = \frac{c(\text{network})}{c(\text{bulk})} = \frac{\Omega}{\Omega_0} \quad (4)$$

which is the ratio of microscopic configurations available in the porous network to those in the bulk phase. This quantity has been evaluated for various models. For rigid molecules the most generally valid theoretical expression is³

$$K = \exp(-s\bar{L}/2) \quad (5)$$

where s is the pore surface area per unit free volume (reciprocal hydraulic radius) and \bar{L} is the mean external length of the molecule averaged over all orientations. Substitution of eq 5 into 3 yields

$$\kappa/\kappa_0 = \exp[-(s/2)(\Sigma\bar{L}_p - \Sigma\bar{L}_r)] \quad (6)$$

where $\Sigma\bar{L}_p$ is the sum of mean external lengths for all product fragments, *i.e.*, $g\bar{L}_G + h\bar{L}_H + \dots$, and similarly for the reactant term, $\Sigma\bar{L}_r$. Equation 6 shows that the direction and degree of shift in chemical equilibrium hinges on the amount of contraction or expansion in total molecular dimensions.

By way of example, if the reactant is rod shaped and the reaction consists of lateral ruptures to form several shorter rods of equal total length, then $\Sigma\bar{L}_p = \Sigma\bar{L}_r$ and $(\kappa/\kappa_0) = 1$, *i.e.*, there is no equilibrium shift. (We use here the fact that for any thin rod of length L_1 , $\bar{L} = L_1/2$.)³

If the rod is ruptured axially to form two rods, each with the original length, L_1 , then $\Sigma\bar{L}_p - \Sigma\bar{L}_r = L_1/2$ and $(\kappa/\kappa_0) = \exp(-sL_1/4)$, *i.e.*, equilibrium is shifted toward the associated side.

Intuitively one might expect porous networks to cause increased dissociation—a shift in equilibrium toward smaller fragments. However, the smaller fragments are more numerous, and with each contributing an increment to the free energy, the equilibrium may actually shift in the opposite direction, as just seen.

In the case of a helix-coil or other unimolecular transformation, eq 6 yields $\kappa/\kappa_0 = \exp(-s(\bar{L}_p - \bar{L}_r)/2)$, a ratio which may be greater or less than unity depending on whether the mean external length of the reactant molecule, \bar{L}_r , is larger or smaller than that of the product molecule, \bar{L}_p .

In all the above cases the shift depends on the mean pore size as reflected in parameter s ; its magnitude is typically like K^{-1} values, in the range 1–10, but can be much larger. Also if there are chemical or adsorptive interactions in the network, the two effects must be superimposed.

The following empirical function, instead of eq 5, is often used to relate K to molecular dimensions,⁵ in this

case in the form of molecular weight, M

$$K = Q - P \log M \quad (7)$$

where Q and P are constants for the gel and the molecular type. Substitution into eq 3 yields

$$\frac{\kappa}{\kappa_0} = \frac{(Q - P \log M)_G^a (Q - P \log M)_H^b \dots}{(Q - P \log M)_A^a (Q - P \log M)_B^b \dots} \quad (8)$$

where, of course, $\Sigma M_p = \Sigma M_r$, due to conservation of mass in the reaction.

Although eq 7 works well over a limited range, it fails to approach the proper limiting behavior for both very high and low molecular weights (for which K should approach zero and unity, respectively). In addition, eq 8 is a relatively awkward form for obtaining general rules about equilibrium shifts.

A "calibration" by Ackers⁷ shows to good approximation the correct limiting behavior in terms of the following error function complement

$$K = \text{erfc} \left[\frac{a - a_0}{b_0} \right] \quad (9)$$

where a is molecular radius and a_0 and b_0 are the constants of a Gaussian pore size distribution. This expression can similarly be substituted into eq 3 to determine equilibrium shifts.

Reaction Rates. The rate of macromolecular transformations will also be affected by the geometrical constraints of porous networks. This is best seen by writing the bulk-phase constant, k_0' , in terms of absolute reaction rate theory⁸

$$k_0' = (kT/h)\kappa_0^\ddagger \quad (10)$$

where κ_0^\ddagger is the "equilibrium constant" for activated complexes, k is Boltzmann's constant, T is temperature, and h is Planck's constant. The term κ_0^\ddagger is shifted in the same manner as chemical equilibrium constants, eq 3. Thus

$$\frac{k'}{k_0'} = \frac{K^\ddagger}{K_A^a K_B^b \dots} \quad (11)$$

is obtained where K^\ddagger is the (hypothetical) partition coefficient for the activated complex. By analogy with eq 6 this can be approximated by

$$k'/k_0' = \exp[-s/2)(\bar{L}^\ddagger - \Sigma\bar{L}_r)] \quad (12)$$

in which \bar{L}^\ddagger is the mean external length of the activated complex.

For a simple dissociation in which a single bond is ruptured, k'/k_0' is approximately unity. This is be-

(6) K. Altgelt in "Advances in Chromatography," Vol. 7, J. C. Giddings and R. A. Keller, Ed., Marcel Dekker, Inc., New York, N. Y., 1968.

(7) G. K. Ackers, *J. Biol. Chem.*, **242**, 3237 (1967).

(8) S. Glasstone, K. J. Laidler, and H. Eyring, "The Theory of Rate Processes," McGraw-Hill, New York, N. Y., 1941, p 190.

cause the activated complex is only slightly larger (by one "stretched" bond) than the reactant. For association, on the other hand, rates will usually be enhanced since $\bar{L}^\ddagger < \Sigma\bar{L}_r$. An exception would be found, as in the equilibrium discussion, for the end-to-end association of rod-shaped molecules.

If the total reaction process involves many steps, the above formulation will apply one step at a time, but not necessarily to the overall process. The "critical" step for example, may itself become altered by the network.

Some Applications

Below we discuss three phenomena whose characteristics depend on the above considerations. This list is by no means inclusive.

Chromatographic Migration. Migration properties, primarily equilibrium dependent, vary in nature among the multifold forms of chromatography. One important distinction for all nonlinear systems is between species velocity and pulse velocity. The theory for such systems has been given.^{2,9,10} We note only that, in general, the details of partitioning equilibrium must be known for any migration rate calculation.

Each chromatographic species approaches its own unique partitioning equilibrium as well as general chemical equilibrium, the latter being different for each phase. Chemical equilibrium, however, may be complicated by unequal partition coefficients, *e.g.*, for $A \rightleftharpoons B + C$, the undue partitioning of B will give the non-stoichiometric condition, $(C)_0 > (B)_0$, in the mobile phase. However, in some experiments involving steady plateaus, stoichiometry is forced upon the mobile phase but will not exist in the stationary network.

The calculation of the concentration of each species in each phase proceeds by using, first, the usual relationships, *i.e.*, equilibrium in the bulk (mobile) phase, conservation of total mass, etc. The additional constraints needed can be obtained from the species partition coefficients, *e.g.*, $K_A = (A)/(A)_0$.

At a given point the center of mass of a reacting solute system migrates with the effective partition coefficient

$$K' = \frac{\Sigma K_i(i)_0 M_i}{\Sigma(i)_0 M_i} \quad (13)$$

where M_i is the molecular weight of species i . This is simply a weight average partition coefficient, confirming Acker's method.² However, as noted above, care may be needed in specifying the equilibrium concentration terms, $(i)_0$, for the bulk phase.

Chromatographic Boundary Spreading. Boundary

and peak shapes, and thus chromatographic resolution, are affected by both equilibrium and rate factors. If interconversion rates are slow, undue spreading occurs. This case has been treated for isomerization in linear chromatography.¹¹ The final result is influenced by the rate constant in the stationary as well as in the mobile phase, thus requiring the use of eq 11 and 12 for a full characterization.

Membrane Permeation. Whereas chromatographic migration velocities are ordinarily fixed by the state of equilibrium, membrane permeation rates depend on both equilibrium parameters and diffusivities. Thus the rate of permeation of a single species through an ideal membrane is $(A)_0 K_A D_A / h$, where D_A is the diffusion coefficient of the species and h is the membrane thickness.

If chemical equilibrium is attained slowly compared to the mean residence time in the membrane, the effective permeation flux (relative to species with the mass of A) is simply the sum of individual values

$$J = \frac{1}{h} \Sigma(i)_0 K_i D_i M_i / M_A \quad (14)$$

Selective uptake, however, will lead to regeneration by reaction of the depleted species in solution, *i.e.*, it will increase the $(i)_0$ term for highly permeable species. Thus the total mass flux will be greater than the independently summed components as a result of reaction.

If, at the other limit, chemical equilibration is instantaneous, the species permeate cooperatively with the overall effective but not necessarily constant diffusivity, $D' = \Sigma(i) D_i M_i / M_A$. Local concentrations, (i) , and perhaps their ratio, will vary with distance according to mass transport and chemical equilibrium requirements. A full treatment of this and the intermediate cases are beyond the scope of the present treatment. We note, however, that both rate and equilibrium factors within the membrane enter the final result. We note also the possibility that a completely nonpermeating species can leak through a membrane in some transformed but minor equilibrium state.

Acknowledgment. This work was supported by Public Health Service Research Grant GM 10851-12 from the National Institutes of Health.

(9) F. Helfferich and D. L. Peterson, *Science*, **142**, 661 (1963); D. L. Peterson and F. Helfferich, *J. Phys. Chem.*, **69**, 1283 (1965).

(10) G. A. Gilbert, *Nature*, **210**, 299 (1966).

(11) J. C. Giddings, "Dynamics of Chromatography. Part 1. Principles and Theory," Marcel Dekker, Inc., New York, N. Y., 1965; R. A. Keller and J. C. Giddings, *J. Chromatogr.*, **3**, 239 (1960).

Intercombination Bands in the Spectra of Some Quadrate

Chromium(III) Complexes¹

by Robert K. Lowry, Jr.,² and Jayarama R. Perumareddi

Department of Chemistry, Florida Atlantic University, Boca Raton, Florida 33432

The diffuse reflectance spectra of a number of mono- and disubstituted octahedral complexes of chromium(III) have been measured. The low-intensity spin-forbidden transitions in the region of $15,000\text{ cm}^{-1}$ have been observed in all the systems studied and resolved well in most of the systems. These bands along with the spin-allowed transitions have been assigned and fitted exactly with the theoretical energy equations of d^3 configuration in quadrate fields including configuration interaction. The parameters of the ligand field, which include cubic and axial, and of the electron correlations have been evaluated. The electron correlation parameters seem to follow similar trends as in the cubic complexes. The Dt axial parameter in some of these quadrate compounds has been evaluated previously and found to agree well with the calculated value from the crystal field model. The same agreement has been found to be true in the remaining complexes also.

Introduction

Recently the theory of cubic ligand fields has been extended to include noncubic ligand fields for d^3 electronic configuration.³ However, the application of the extended theory, particularly the theory of quadrate fields, to actual experimental situations has been limited to only a few complexes^{4,5} because of the lack of precise data. It is well-known that each of the predicted spin-allowed and spin-forbidden transitions to the excited orbital doublet or triplet states of octahedral complexes splits into two components on substitution resulting in quadrate symmetry. In many of the substituted octahedral complexes which can be treated under quadrate fields the spectra do not show the expected splittings of the spin-allowed quartet-quartet transitions, either because of the predicted splittings being small and hence nonobservable in solution absorption spectra or because of the larger widths of the bands or a combination of both. The spin-forbidden quartet-doublet transitions are seldom observed because of their low intensity and if observed seldom resolved into the expected number of components. In order to extend the application of the theory successfully, attention should be directed at finding systems in which the ligand arrangement is such that the expected splitting of the quartet transitions can be resolved and the doublet transitions can be uncovered easily and resolved into their components. The resolution of the split component structure of all the spin-allowed bands allows a definitive evaluation of the axial ligand field parameters Dt and Ds and of the electron correlation parameter B . The other electron correlation parameter C can only be evaluated by fitting the spin-forbidden bands. A knowledge of the axial ligand field parameters is necessary in the study of the perturbation of the excited electronic states of the central

metal ion and that of the electron correlation parameters in understanding the bonding nature of the ligands such as the covalency. Examination of the trends in the electron correlation parameters of these complexes relative to the parent complexes of octahedral point group should be of particular interest.

A beginning had been made earlier^{4,5} in the evaluation of the axial ligand field parameters in complexes where a definitive resolution of the splitting of the quartet transitions has been observed. However, in most of these systems and others the low-intensity doublet transitions have not been uncovered, thus precluding the exact evaluation of the second interelectronic repulsion parameter C . During our systematic studies on the spectra of a variety of substituted octahedral complexes of chromium(III), we uncovered the intraconfigurational doublets in the low-energy region of the spectra of a number of complexes and were successful in obtaining the resolution of these doublets.⁶ The present report details these observations along with the assignments of the observed transitions on the basis of quadrate fields and evalua-

(1) Presented, in part, at the Southeastern Regional Meeting of the American Chemical Society held at Tallahassee, Fla., Dec 4-7, 1968.

(2) Taken from the M.S. Thesis of R. K. Lowry, Jr.

(3) J. R. Perumareddi, *J. Phys. Chem.*, **71**, 3144 (1967), and references therein.

(4) J. R. Perumareddi, *ibid.*, **71**, 3155 (1967).

(5) R. Krishnamurthy, W. B. Schaap, and J. R. Perumareddi, *Inorg. Chem.*, **6**, 1338 (1967).

(6) In addition to the importance of the doublets as noted above, they find application in other studies such as in the mechanism of the photoreactions [(a) H. L. Schläfer, *Z. Phys. Chem.* (Frankfurt am Main), **11**, 65 (1957); (b) R. A. Plane and J. P. Hunt, *J. Amer. Chem. Soc.*, **79**, 3343 (1957); (c) A. W. Adamson, *J. Inorg. Nucl. Chem.*, **13**, 275 (1960)] and in understanding luminescent behavior of complexes [(d) H. L. Schläfer, H. Gausmann, and H. Witzke, *J. Chem. Phys.*, **46**, 1423 (1967)].

tion of the various parameters. A few compounds in which the quartet transitions have been found to be split, but not fitted with the theoretical energy equations earlier, have also been included.

Experimental Section

Preparations of the complexes and their analyses were carried out as reported in the literature.⁷⁻¹⁰ All products were recrystallized several times before the spectra were taken. The only exception was the iodopentaammine complex which is photosensitive. Its spectra were measured on freshly prepared samples. A reliable solution spectrum could not be obtained since the complex quickly decomposed even in iodine-containing solutions.

The diffuse reflectance spectra were measured at room temperature on a Carl Zeiss PMQ II spectrophotometer with RA2 reflectance attachment. Optical grade lithium fluoride was used as a white standard. The reflectance spectra were plotted with the Kubelka-Munk function as the ordinate. The Kubelka-Munk function, $f(R)$, given by $f(R) = (1 - R)^2/2R$, where R is the fractional reflectance, is roughly proportional to the extinction coefficient. Absorption spectra on solutions were also measured and found to agree closely with the published data.¹¹

Results and Discussion

The observed spectra are shown in Figures 1 and 2. These include spectra for the acidopentaammines and *cis*- and *trans*-diacidotetraammines or bis(ethylenediamines). Various other monosubstituted and *cis*- and *trans*-disubstituted octahedral complexes were made, and their spectra were measured. However, because of inability to uncover the spin-forbidden bands definitively, these systems have not been included.

Two of the lower energy, spin-allowed bands in the spectrum of the fluoropentaammine complex have been reported in its solution spectrum previously.⁸ Our study reveals a third band in the ultraviolet region and provides resolution of the doublet bands. The reflectance spectrum of iodopentaammine has not been reported before, and the solution spectrum does not reveal any doublet transition.¹² Splitting of the lowest energy quartet band has been reported in solution,¹² but better resolution has been achieved in our study. Only the maxima of the quartets, but not the complete spectra, have been reported in the solution spectra of the *trans*-difluoro- and aquofluorobis(ethylenediamine) complexes.¹⁰ Our figures show complete spectra of these systems including the low-intensity doublets. The spectrum of the *cis*-chloroaquotetraammine complex has not been reported before. Since the spectra in the quartet region of the aquo- and bromopentaammine and oxalatotetraammine complexes do not show any new features from those already published, only the doublet region of the spectra is displayed for these

in Figure 2. Excellent resolution of the four-component structure of the doublets was obtained in the aquo- and bromopentaammines. Only one doublet for the aquo¹³ and two for the bromo⁴ complexes have been reported previously.

Both diffuse reflectance and absorption data are summarized in Table I. The table also includes the data on the chloropentaammine complex, since exact fitting of the doublets in its spectrum¹⁴ was not made earlier. The nature of the band in the vicinity of 33,000 cm^{-1} in the aquo- and fluoropentaammine complexes and of that at 37,000 cm^{-1} in the oxalato-tetraammine complex is puzzling.¹⁵ It is a broad band and the intensity is of the same order or less than that of the other two spin-allowed bands, except in the oxalato where it is considerably more intense. However, it appears at too low an energy to be the third cubic quartet transition, ${}^4T_{1g}$, or to be one of its quadratic components, which are predicted to be positioned at several thousand wave numbers higher in energy.¹⁶ Yet it occurs at too high an energy to be a split component of the second spin-allowed band.

Difficulties in fitting the third quartet band have been encountered in a spectral study of crystals containing Cr^{3+} ions.^{17,18} Although it could be due to forbidden charge-transfer absorption, the question remains why it appears only in a few compounds but not in all. Thus, the nature of this transition remains unsolved. Note, however, that the above-mentioned difficulty arises only when the B value derived by

(7) *Inorg. Syn.*, **5**, 132 (1957).

(8) E. Kyuno, N. Kamada, and N. Tanaka, *Bull. Chem. Soc. Jap.*, **40**, 1848 (1967).

(9) G. G. Schlessinger, "Inorganic Laboratory Preparations," Chemical Publishing Co., New York, N. Y., 1962.

(10) J. W. Vaughn, O. J. Stvan, and V. E. Magnuson, *Inorg. Chem.*, **7**, 736 (1968).

(11) The extinction coefficients of the spin-allowed bands for the aquopentaammine complex reported in ref 8 are in error. Ours agree with those published by several other authors. See for instance, C. E. Schäfer, *J. Inorg. Nucl. Chem.*, **8**, 149 (1958).

(12) M. Linhard and M. Weigel, *Z. Anorg. Allgem. Chem.*, **266**, 49 (1951).

(13) M. R. Edelson and R. A. Plane, *J. Phys. Chem.*, **63**, 327 (1959).

(14) Our studies of this spectrum confirm the earlier results⁴ showing two doublets. We use these values in fitting procedure, although a recent spectrum by H. F. Wasgestian and H. L. Schäfer, *Z. Phys. Chem. (Frankfurt am Main)*, **62**, 127 (1968), shows the low-energy doublet to be split into two components. The actual band maxima are not given in this paper.

(15) The band in the aquo and the oxalato complexes has been noted in ref 8. (See also ref 11.) Although the spectrum of the aquo complex has been reported by several other authors (see for references, J. R. Perumareddi, *Coord. Chem. Rev.*, **4**, 73 (1969)), none of them makes any mention of this band. We have found it not only in the samples prepared according to ref 8, but in the other preparations also.

(16) For the parameters shown in Table II the calculated maxima of the third band components, 4A_2 and 4E , are as follows: aquo: 44,589 and 44,850 cm^{-1} ; fluoro: 43,984 and 44,319 cm^{-1} ; oxalato: 43,515 and 43,255 cm^{-1} .

(17) W. Low, *Phys. Rev.*, **105**, 801 (1957).

(18) D. S. McClure, "Electronic Spectra of Molecules and Ions in Crystals," Academic Press, New York, N. Y., 1959.

Table I: Spectral Data of Mono- and Disubstituted Chromium(III) Complexes^a

Complex	Spin-forbidden bands		Spin-allowed bands		
	1	2	1	2	3
$[\text{Cr}(\text{NH}_3)_5(\text{H}_2\text{O})]^{2+}$	15,450; 15,700 15,250(0.25)	16,150; 16,350	21,000 20,700(36.0)	28,000 27,900(29.5)	33,050 33,000(30.7)
$[\text{Cr}(\text{NH}_3)_5\text{F}]^{2+}$	15,300; 15,400	15,700	20,000 20,050(46.9)	27,300 27,100(45.0)	33,000 33,200(46.3)
$[\text{Cr}(\text{NH}_3)_5\text{Cl}]^{2+}$	14,800	15,500	19,400 19,200(36.0)	26,700 26,500(36.6)	
$[\text{Cr}(\text{NH}_3)_5\text{Br}]^{2+}$	15,000; 15,200	15,475; 15,650	19,000; 21,500 19,150(36.0); 21,400(27.4)	26,500 26,400(44.0)	
$[\text{Cr}(\text{NH}_3)_5\text{I}]^{2+}$	14,500	14,900	18,400; 21,000		
<i>cis</i> - $[\text{Cr}(\text{NH}_3)_4(\text{C}_2\text{O}_4)]^+$	15,100 15,100(0.9)	15,800 15,900(1.4)	20,200 20,200(56.9)	26,900 27,000(70.7)	37,250 38,400(351)
<i>cis</i> - $[\text{Cr}(\text{NH}_3)_4(\text{H}_2\text{O})\text{Cl}]^{2+}$	15,050; 15,250	15,500; 15,700	19,600 19,700(37.5)	26,500 26,600(34.6)	
<i>trans</i> - $[\text{Cr}(\text{en})_2\text{F}_2]^+$	15,200	15,800	19,300; 21,600 19,250(21.0); 21,600(25.0)	25,100; 28,700 25,000(19.0); 28,400(21.0)	
<i>trans</i> - $[\text{Cr}(\text{en})_2(\text{H}_2\text{O})\text{F}]^{2+}$	15,200; 15,350	15,900	19,300; 22,100 19,150(31.6); 21,650(26.0)	26,900 26,750(24.2)	

^a The band positions (cm^{-1}) from diffuse reflectance measurements are given in the first row, and the band positions (cm^{-1}) followed by extinction coefficients ($\text{cm}^{-1} \text{mol}^{-1}$) in parentheses from solution absorption measurements are given in the second row.

fitting the second band is used in calculating the position of this band. Agreement can be obtained if it is assumed that the B values are different for these

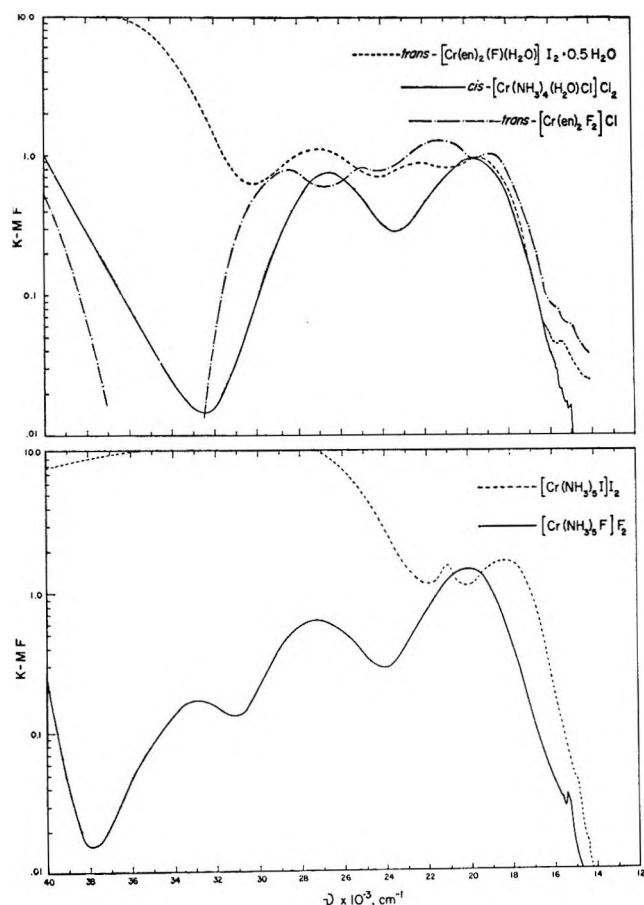


Figure 1. Diffuse reflectance spectra of some mono- and disubstituted octahedral chromium(III) complexes.

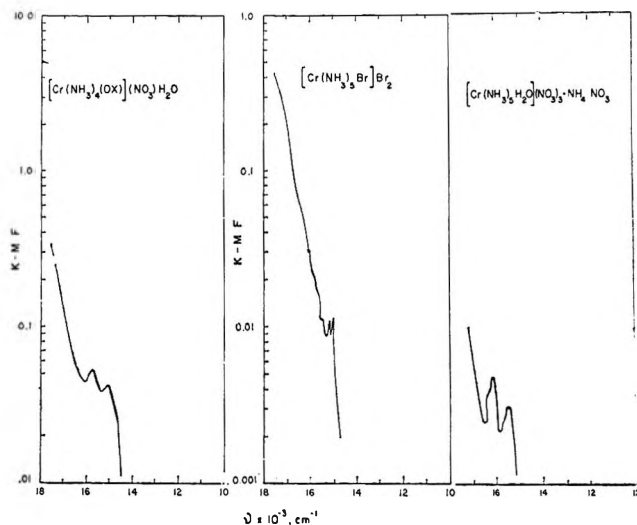


Figure 2. Spectra of $[\text{Cr}(\text{NH}_3)_5\text{Br}]\text{Br}_2$, $[\text{Cr}(\text{NH}_3)_5(\text{H}_2\text{O})](\text{NO}_3)_3 \cdot \text{NH}_4\text{NO}_3$, and $[\text{Cr}(\text{NH}_3)_4(\text{C}_2\text{O}_4)](\text{NO}_3)_3 \cdot \text{H}_2\text{O}$, showing only the doublet portions.

different transitions, the excited states of which arise from different electronic configurations.

The fitting of the remaining bands with the theoretical energy equations³ has been carried out as follows. The Dq parameter was taken from the parent octahedral complex. It had been shown earlier³ that the ${}^4\text{B}_1 \rightarrow {}^4\text{B}_2$ quadrate transition is expected at this energy. Taking account of configuration interaction, the Dt value can be calculated exactly by fitting¹⁹ the second component of the first cubic transition, namely, ${}^4\text{B}_1 \rightarrow$

(19) By an exact fitting we mean within $200\text{--}300 \text{ cm}^{-1}$ for the spin-allowed bands, since their maxima are usually spread over several hundred wave numbers and within 100 cm^{-1} for the spin-forbidden bands, which are sharp.

Table II: Observed (Diffuse Reflectance) and Calculated Spectral Data for Spin-Allowed Bands of Chromium(III) Complexes^a

Complex	⁴ E(⁴ T _{2g})	⁴ B ₁ (⁴ T _{2g})	⁴ A ₂ (⁴ T _{1g})	⁴ E(⁴ T _{1g})	D _q	D _t	B
[Cr(NH ₃) ₆ (H ₂ O)] ³⁺	21,000		28,000				
	20,473	21,550	27,546	28,123	2155	-120	675
[Cr(NH ₃) ₅ F] ²⁺	20,000		27,300				
	20,148	21,550	27,006	27,763	2155	-155	650
[Cr(NH ₃) ₅ Cl] ²⁺	19,400		26,700				
	19,482	21,550	25,918	27,054	2155	-225	600
[Cr(NH ₃) ₅ Br] ²⁺	19,000	21,500	26,500				
	19,000	21,550	25,458	26,866	2155	-275	600
[Cr(NH ₃) ₅ I] ²⁺	18,400	21,000					
	18,513	21,550	24,998	26,685	2155	-325	600
<i>trans</i> -[Cr(en) ₂ F ₂] ⁺	19,300	21,600	25,100	28,700			
	18,939	21,850	25,410	28,660	2185	-300	710
<i>trans</i> -[Cr(en) ₂ (H ₂ O)F] ²⁺	19,300	22,100	26,900				
	19,168	21,850	26,293	27,759	2185	-290	675
<i>cis</i> -[Cr(NH ₃) ₄ (C ₂ O ₄)] ⁺	20,200		26,900				
	20,517	19,500	27,375	26,858	1950	120	650
<i>cis</i> -[Cr(NH ₃) ₄ (H ₂ O)Cl] ²⁺	19,600		26,500				
	19,994	18,500	26,654	25,909	1850	180	625

^a The observed band positions (cm⁻¹) are given in the first row and the calculated band positions (cm⁻¹) are given in the second row for the parameters (cm⁻¹) shown. The κ value in all cases is +1 except for *trans*-[Cr(en)₂F₂]⁺ where it is +2. For the other parameters see Table III.

⁴E. A reasonable variation of the other parameters does not affect the exact value of *Dt*, so that the *Dq* and *Dt* values of a complex are reasonably accurate. In addition, the *Dt* value can also be calculated from the parent octahedral *Dq* values of the substituted and substituting ligands.²⁰ These calculated *Dt* values agree fairly well with the values evaluated by an exact fitting, when the two-component structures can be resolved.^{4,5} Among the complexes listed in Table I the *Dt* values for the chloro-, bromo-, and iodopentaamines have been previously evaluated by fitting⁴ and have been compared with the calculated values. In the remaining complexes only the *trans*-difluoro- and -fluoro-aquo complexes show the resolution of the first quartet, and once again the *Dt* values evaluated by fitting agree with the calculated values. For the remaining complexes the calculated *Dt* values have been used to predict the position of the two components. In all of these cases the predicted splittings are small, on the order of 1000–1500 cm⁻¹, and, thus, resolution was not achieved. An additional note is needed here on the complexes in which the two substituting ligands are not the same. In such heterodisubstituted systems the same principle of averaging the fields of the *trans* ligand pairs employed in justifying the treatment of *cis* complexes under tetragonal fields^{6,20} is used. Thus, the complex *trans*-[Cr(en)₂F(H₂O)]²⁺ is approximated to [Cr(en)₂X₂], where $Dq_X = \frac{1}{2}(Dq_F + Dq_{H_2O})$.

The value of κ , which is the ratio of *Ds* and *Dt* parameters, determines the splitting of the second cubic quartet transition. Except in the case of the *trans*-difluoro complex none of the complexes showed resolution of the second quartet band, implying that the

value of κ is small in these cases.^{4,20} A value of unity was chosen to arrive at a theoretically predicted small amount of splitting. An exact fitting of the splitting in the case of the *trans*-difluoro requires a value of 2 for κ .⁴ The actual placement of the components of the second band is determined by the value of the electron correlation parameter *B*. Thus the value of *B* was derived either by the fitting of the two observed components in the case of the *trans*-difluoro complex or in the case of other complexes by varying *B* until the observed band falls within the predicted region of the two-component structure of the second band. Since in most of these systems the predicted splitting is small, such a procedure necessarily puts a restraint on the limit of variation of the *B* value. The assignments of the quartets along with the parameters *Dq*, *Dt*, κ , and *B* for all the complexes appear in Table II.

Having fixed the values of the parameters *Dq*, *Dt*, κ , and *B*, these are in turn used while varying the value of *C* until a fairly reasonable fitting¹⁹ of the observed spin-forbidden bands is obtained in each case. This fitting along with the *C* values evaluated are shown in Table III. It should be noted that the calculated splittings of the doublets are on the order of a few tens of wave numbers although the observed splittings where complete resolution was achieved are always around 200 cm⁻¹. The reasons for this discrepancy, we believe, are as follows. The estimated maxima of these low intense transitions from the experimental spectra are usually within ± 50 cm⁻¹. In addition, spin-orbit perturbation resolves the ²E^Q into two states Γ_6^Q and

(20) J. R. Perumareddi, *Coord. Chem. Rev.*, **4**, 73 (1969).

Table III: Observed (Diffuse Reflectance) and Calculated Spectral Data for Spin-Forbidden Bands of Chromium(III) Complexes^a

Complex	¹ A ₁ (² E _g)	³ B ₁ (² E _g)	³ E(² T _{1g})	² A ₂ (⁴ T _{1g})	<i>B</i>	<i>C</i>
[Cr(NH ₃) ₆ (H ₂ O)] ²⁺	15,450	15,700	16,150	16,350		
[Cr(NH ₃) ₅ F] ²⁺	15,605	15,615	16,147	16,159	675	3500
[Cr(NH ₃) ₅ Cl] ²⁺	15,300	15,400		15,700		
	15,356	15,369	15,865	15,884	650	3475
[Cr(NH ₃) ₅ I] ²⁺		14,800		15,500		
	14,882	14,899	15,321	15,357	600	3433
[Cr(NH ₃) ₅ Br] ²⁺	15,000	15,200	15,475	15,650		
	15,077	15,098	15,503	15,554	600	3500
[Cr(NH ₃) ₄ (C ₂ O ₄)] ⁺		14,500		14,900		
	14,476	14,502	14,894	14,966	600	3305
<i>trans</i> -[Cr(en) ₂ F ₂] ⁺		15,200		15,800		
	15,171	15,249	15,806	15,820	710	3300
<i>trans</i> -[Cr(en) ₂ (H ₂ O)F] ²⁺	15,200	15,350		15,900		
	15,275	15,302	15,792	15,852	675	3400
<i>cis</i> -[Cr(NH ₃) ₄ (C ₂ O ₄)] ⁺		15,100		15,800		
	15,130	15,120	15,642	15,645	650	3400
<i>cis</i> -[Cr(NH ₃) ₄ (H ₂ O)Cl] ²⁺	15,050	15,250	15,500	15,700		
	15,163	15,149	15,635	15,646	625	3470

^a The observed band positions (cm⁻¹) are given in the first row and the calculated band positions (cm⁻¹) are given in the second row for the parameters (cm⁻¹) shown. For the other parameters see Table II.

Γ_7^Q resulting in a five-component structure with considerable configuration interaction. Thus, the inclusion of spin-orbit coupling may give rise to a better fitting than is presented here.

Resultant electron correlation parameters for each complex are summarized in Table IV and are compared with the corresponding values of the free ion.²¹ Species like H₂O and F⁻ which are known to form compounds of least covalency would be expected to have higher *B* values, *i.e.*, closer to the free-ion value. Likewise, species such as the Cl⁻, Br⁻, and I⁻ ligands which exhibit greater covalency would be expected to have relatively lower *B* values. These general trends are evident for the complexes in this study. Due to the rather limited number of complexes, the varied nature of the ligands, and the different modes of substitution involved, no attempt is made at this time to attach quantitative significance to the *B* values. The expected trends, however, do appear similar to the purely octahedral complexes.

Table IV: Values of Electron Repulsion Parameters for Quadrate Chromium(III) Complexes [Free-Ion Values: *B*₀ = 920 cm⁻¹, *C*₀ = 3680 cm⁻¹]

Complex	<i>B</i> , cm ⁻¹	<i>B</i> / <i>B</i> ₀	<i>C</i> , cm ⁻¹	<i>C</i> / <i>C</i> ₀
[Cr(NH ₃) ₆ (H ₂ O)] ²⁺	675	0.73	3500	0.95
[Cr(NH ₃) ₅ F] ²⁺	650	0.71	3475	0.94
[Cr(NH ₃) ₅ Cl] ²⁺	600	0.65	3433	0.93
[Cr(NH ₃) ₅ Br] ²⁺	600	0.65	3500	0.95
[Cr(NH ₃) ₅ I] ²⁺	600	0.65	3500	0.95
<i>trans</i> -[Cr(en) ₂ F ₂] ⁺	710	0.77	3300	0.90
<i>trans</i> -[Cr(en) ₂ (H ₂ O)F] ²⁺	675	0.73	3400	0.92
<i>cis</i> -[Cr(NH ₃) ₄ (C ₂ O ₄)] ⁺	650	0.71	3400	0.92
<i>cis</i> -[Cr(NH ₃) ₄ (H ₂ O)Cl] ²⁺	625	0.68	3470	0.94

One reason in initiating this work has been to study the variation of *C* in complexes. Throughout the entire series of complexes, *C* remains remarkably constant and not much reduced from the free-ion value. Whereas *B* is considerably reduced and varies from 65 to 77% of the free-ion *B* value, *C* varies only from 90 to 95% of the free-ion *C* value. Similar effects have been noted previously for a series of crystal lattices containing Cr³⁺ ion.²² The reason why *B* varies and *C* remains constant in different complexes is apparently due to the ways in which these parameters are evaluated. Evaluation of *B* is based on the quartet transitions which involve a change in electron configuration ($t_{2g}^3 e_g \rightarrow t_{2g}^2 e_g$, etc.). Parameter *C*, however, is evaluated on the basis of the doublet transitions whose electron configuration is the same as that of the quartet ground state. Thus, the *B* value is an average of many different electron repulsion integrals, whereas the *C* value is an average of but a few electron repulsion integrals.³ If *C* is to be useful in bonding descriptions, it probably has to be evaluated on the basis of higher energy spin-forbidden transitions in which there is a change in the electron configuration from the ground state. Difficulties are immediately obvious, however, since such transitions are usually buried under the more intense spin-allowed or charge-transfer bands.

Conclusions

By the exercise of care in the preparation of complexes and in the measurement of their electronic spectra we

(21) A. D. Liehr, *J. Phys. Chem.*, **67**, 1314 (1963).

(22) D. L. Wood, J. Ferguson, K. Knox, and J. F. Dillon, Jr., *J. Chem. Phys.*, **39**, 890 (1963).

have discovered the low-intensity intercombination bands in a number of substituted chromium(III) octahedral complexes. These bands, along with the spin-allowed quartets in the complexes studied, have been assigned on the basis of quadrature fields and the electron correlation parameters have been evaluated. Although these parameters are subject to minor variation because of the uncertainty in the ligand field parameters, the general trend in the variation of these parameters with varying complexes seems to follow a pattern similar to that noted in cubic complexes. In order to refine further the evaluation of the parameters and confirm the noted trends, studies have to be made on an extended number of complexes. Such studies

should include uncovering the low-intensity doublets, better resolution of the spin-allowed quartets, and, finally, confirmation of the band assignments by polarized spectral measurements on single crystals. Investigations along these lines are currently in progress.

Acknowledgments. We wish to thank Mr. Bruce Alper of the Florida Atlantic University Computer Center for programming and Professor S. F. Clark for making many helpful suggestions in the writing of the manuscript. Acknowledgment is made to the donors of the Petroleum Research Fund, administered by the American Chemical Society, for partial support of this research.

Nuclear Magnetic Resonance Techniques for the Study of Preferential Solvation and the Thermodynamics of Preferential Solvation

by Lawrence S. Frankel,¹ Cooper H. Langford,² and Thomas R. Stengle³

Departments of Chemistry, Amherst College, and the University of Massachusetts, Amherst, Massachusetts 01002 (Received September 4, 1969)

Two methods for investigating the degree of preferential solvation in mixed solvents have been developed. One depends on the effect of solvent on the nmr chemical shift of sensitive nuclei in the solute. The other utilizes the effect of paramagnetic solutes on the transverse relaxation times of solvent nuclei. The solvation of tris-acetylacetonate complexes of Co(III) and Cr(III) in several solvent mixtures has been studied. A thermodynamic model of preferential solvation has been devised to interpret these results.

Introduction

When a solute is dissolved in a mixed solvent, the solvation shell of the solute need not have the same composition as the bulk solvent, but it may preferentially contain one component of the solvent mixture. Such a case is shown in Figure 1 which illustrates preferential solvation by chloroform in a $\text{CCl}_3\text{H}-\text{CCl}_4$ mixture. This phenomenon has long been considered important, and it has been tentatively explored by thermodynamic methods which unfortunately often focus on the properties of the bulk solvent rather than on the solvation shell itself.

Recently nmr spectroscopy has been applied to this problem with encouraging results.⁴ Two techniques capable of observing preferential solvation were developed. One depends on the effect of the solvent on the nmr chemical shift of the solute, while the other utilizes the effect of a paramagnetic solute on the transverse relaxation time (T_2) of the solvent nuclei. The interactions responsible for both of these effects are

short ranged,^{5,6} and they should isolate contact solvation.

Experimental Section

Materials. The solutes, tris(acetylacetonate)cobalt(III) and tris(acetylacetonate)chromium(III)⁷ were prepared by previously described methods.⁸ The solvents

(1) Research Laboratory, Rohm and Haas Co., Philadelphia, Pa.

(2) Department of Chemistry, Carleton University, Ottawa 1, Canada.

(3) University of Massachusetts; author to whom correspondence should be addressed.

(4) L. S. Frankel, T. R. Stengle, and C. H. Langford, *Chem. Commun.*, 393 (1965).

(5) J. S. Griffith and L. E. Orgel, *Trans. Faraday Soc.*, **53**, 601 (1957); J. S. Griffith and L. E. Orgel, *ibid.*, **60**, 1803 (1964).

(6) N. Bloembergen and L. O. Morgan, *J. Chem. Phys.*, **34**, 842 (1961).

(7) Hereafter referred to as $\text{Co}(\text{acac})_3$ and $\text{Cr}(\text{acac})_3$.

(8) W. C. Fernelius and J. E. Blanch, *Inorg. Syn.*, **5**, 130 (1957); B. E. Bryant and W. C. Fernelius, *ibid.*, **5**, 188 (1957).

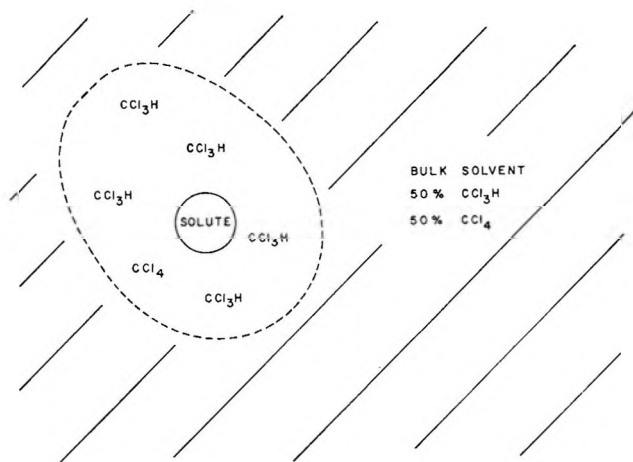


Figure 1. Preferential solvation by chloroform from a chloroform-carbon tetrachloride mixture.

either were of reagent grade quality or were purified by distillation at reduced pressure.

Nmr Measurements. Proton relaxation times were measured from absorption mode spectra taken on a Varian A-60 or a DP-56.4 spectrometer. Values of T_2 were determined from the line width at half-height. The maximum error was 5%, although a lower value was achieved in favorable cases. Chemical shifts for ^{59}Co were measured on the Varian DP instrument operating at 8.1 MHz. The spectra were recorded as derivative curves of the absorption mode. A set of coaxial sample tubes was used to measure the chemical shift of the solute in a mixed solvent relative to the solution in a pure solvent as an external standard. An error of 2 ppm, or 1%, was usually observed in this procedure.

Results

Two methods for the nmr study of preferential solvation were developed. In the first method one observes the effect of solvent composition on the chemical shift of a nucleus in the solute. For this experiment we have chosen a diamagnetic, neutral solute which contains a nucleus which is especially sensitive to its environment. The complex $\text{Co}(\text{acac})_3$, which contains the sensitive ^{59}Co nucleus, served as the paradigm for this work. The second method depends on the effect of a paramagnetic solute on the transverse relaxation time (T_2) of nuclei in the solvent molecules. We have chosen $\text{Cr}(\text{acac})_3$ as the paramagnetic solute because one expects the solvation properties of $\text{Co}(\text{acac})_3$ and $\text{Cr}(\text{acac})_3$ to be quite similar. Thus the two methods can be used to check one another.

Chemical Shift Method. The chemical shift of the ^{59}Co nucleus in $\text{Co}(\text{acac})_3$ is very sensitive to solvent.⁹ In a mixed solvent the composition of the solvation shell will fluctuate about some average value. If the fluctuations are fast compared with the reciprocals of the chemical shifts (in cycles per second), the observed shift will reflect the average solvation shell composition.

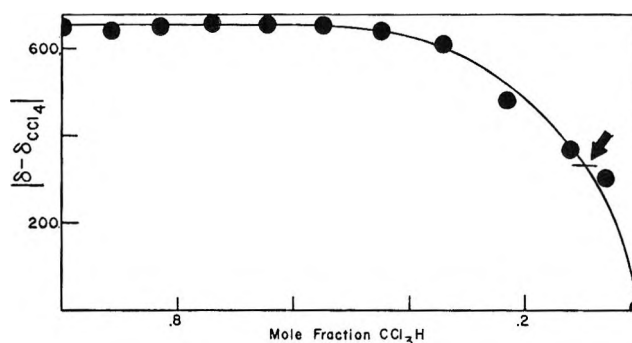


Figure 2. Solvation of $\text{Co}(\text{acac})_3$ in chloroform-carbon tetrachloride mixtures; ^{59}Co chemical shift method. The equisolvation point is indicated by the arrow.

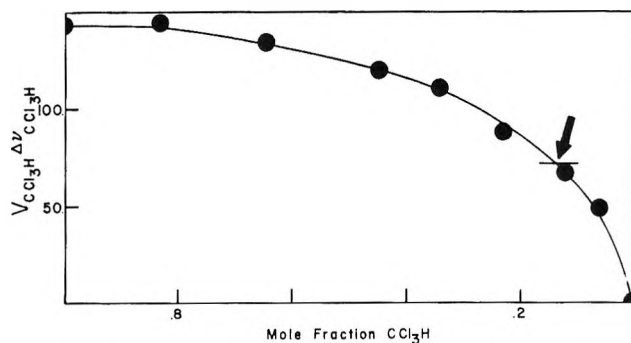


Figure 3. Solvation of $\text{Cr}(\text{acac})_3$ in chloroform-carbon tetrachloride mixtures; solvent relaxation time method. The equisolvation point is indicated by the arrow.

In the absence of strong chemical bonds, the residence time of solvent molecules in the solvation shell is quite short, and the fast exchange condition is fulfilled. When no preferential solvation occurs, a plot of ^{59}Co chemical shift vs. bulk solvent composition will yield a straight line. The results of such an experiment for the $\text{CCl}_3\text{H}-\text{CCl}_4$ solvent system are given in Table I, and shown in Figure 2. The pronounced deviation from a straight line indicates strong preferential solvation, with CCl_3H predominating in the solvation shell. A convenient measure of the degree of preference is the bulk solvent composition at which both solvents participate equally in the contact solvation shell. This is the composition at which the chemical shift lies midway between the values for the pure solvents. We have called this the equisolvation point; it is indicated by an arrow in Figures 2 and 3.

The chemical shift method can be used only when the solute contains a nucleus which is particularly solvent sensitive. In this sense, the ^{59}Co nucleus is a good probe since the low-lying excited electronic states cause the chemical shift to be exceedingly sensitive to the surroundings.⁵

Relaxation Time Method. In the vicinity of a paramagnetic solute there are strong fluctuating magnetic

(9) R. Freeman, G. R. Murray, and R. E. Richards, *Proc. Rcy. Soc.*, A242, 455 (1957).

fields which cause nearby nuclei to have very short relaxation times. If solvent molecules exchange rapidly between a diamagnetic (bulk solvent) environment and a paramagnetic (solvation shell) environment, the observed relaxation time will be the average of the values in the two environments weighted for the fraction of solvent present in the two environments. That is, the experimental relaxation time (determined from the width of the absorption line at half-height by $T_2^{-1} = \pi\Delta\nu$) is given by¹⁰

$$\frac{1}{T_2} = \frac{p_A}{T_{2A}} + \frac{p_B}{T_{2B}} \quad (1)$$

where p_A is the probability of finding a solvent molecule in the diamagnetic environment, T_{2A} is the relaxation time in that environment, and p_B and T_{2B} are the corresponding quantities for the paramagnetic environment. In solutions relatively dilute in paramagnetic solute, p_A is near unity, and T_{2A} can be estimated from relaxation times in the absence of paramagnetic solute. Thus for a solution the experimental line width minus a small correction for T_{2A} is proportional to p_B/T_{2B} . One cannot readily determine T_{2B} , but under the assumption that it is a constant, information concerning values of p_B for different solvent compositions can be obtained. For a given component of a mixed solvent (e.g., CCl_3H in a $\text{CCl}_3\text{H}-\text{CCl}_4$ mixture) the product of p_B/T_{2B} with the bulk concentration of that component is proportional to the number of moles of that component in environment B. In the absence of preferential solvation the fraction of CCl_3H in the solvation shell will be directly proportional to the bulk concentration of CCl_3H . The effect of preferential solvation is to cause a deviation from linearity in a plot of the solvation shell composition *vs.* bulk solvent composition. The appropriate plot is shown in Figure 3 using data from Table I. Here the product of the line width (corrected for T_{2A}) of CCl_3H and the volume fraction of CCl_3H in the solvent mixture is plotted *vs.* the mole fraction of CCl_3H in the bulk solvent. The shape of the curve shows preferential solvation by CCl_3H ; it is almost identical with Figure 2. The equisolvation point occurs at a chloroform mole fraction of 0.075. This compares well with the value of 0.090 obtained by the chemical shift method for $\text{Co}(\text{acac})_3$. The line width experiment was performed on two sets of solutions one of which contained twice the $\text{Cr}(\text{acac})_3$ concentration of the other. The line widths of the concentrated solutions were double those of the dilute solutions, and the same solvation shell compositions resulted. The data reported here are the averages of both runs with the line width normalized to the lower concentration of $\text{Cr}(\text{acac})_3$.

There is an important assumption inherent in this approach. This is, the magnetic coupling between the central metal atom and a given molecule in the solvation

Table I: Preferential Solvation of Cobalt(III) and Chromium(III) Acetylacetonates in $\text{CCl}_3\text{H}-\text{CCl}_4$ Mixtures

Mole fraction CCl_3H	Volume fraction CCl_3H	Line width CCl_3H	^{59}Co chemical shift, ^a Hz
1.000	1.000	38.4	647
0.916	0.900	42.9	640
0.829	0.800	46.1	652
0.738	0.700	51.6	656
0.645	0.600	61.3	649
0.548	0.500	73.5	652
0.447	0.400	86.4	635
0.342	0.300	115	607
0.232	0.200	149	550
0.119	0.100	256	434
0.060	0.050		303
0.000	0.000		000

^a Reported as the shift between the given solution and the pure CCl_4 solution.

sphere is independent of the overall composition of the solvation sphere. For example, we assume that the replacement of some CCl_3H molecules by CCl_4 will not affect the coupling between the metal atom and each of the remaining CCl_3H molecules. Although this assumption seems quite valid for the systems studied here, it will not necessarily hold for every system. It should be carefully checked when applying these techniques to other systems, particularly for systems involving strong or unusual types of solvent-solute interaction.

The assumptions involved were tested by determining solvation curves for a number of solvent systems. The consistency of the results obtained by the chemical shift method, used for $\text{Co}(\text{acac})_3$, and the relaxation time method, used for $\text{Cr}(\text{acac})_3$, is shown by the equisolvation data in Table II. The nature of the magnetic coupling leading to paramagnetic relaxation is quite different from that which produces the ^{59}Co chemical shifts. Since the two methods give similar results, the assumption of a lack of dependence of the magnetic coupling on the solvation sphere composition is amply confirmed. Furthermore, the expectation that solvation will be similar for such similar solutes is fulfilled. The most preferred solvents in the list are CCl_3H and CH_3OH , the only ones capable of forming hydrogen bonds. Recent work has shown that these two solvents do indeed form weak hydrogen bonds with acetylacetonate complexes.¹¹

Discussion

In many respects preferential solvation resembles preferential adsorption from a liquid mixture onto a surface-active solid. Indeed, the thermodynamics of both processes can be described in similar terms. In

(10) H. M. McConnell, *J. Chem. Phys.*, **28**, 430 (1958).

(11) T. S. Davis and J. P. Fackler, Jr., *Inorg. Chem.*, **5**, 242 (1966).

Table II: Equisolvation Points for Various Solvent Systems

Solvent system	Equisolvation point mole fraction chloroform	
	Line width method ^a	⁶⁰ Co chemical shift method
CCl ₃ H-CCl ₄ (25°)	0.075	0.090
CCl ₃ H-CCl ₄ (48°)	0.135	
CCl ₃ H-acetone	0.265	0.245
CCl ₃ H- <i>p</i> -dioxane	0.235 ^b	0.220
CCl ₃ H-C ₆ H ₆ (5°)	^c	0.135
CCl ₃ H-C ₆ H ₆ (22°)	^c	0.160
CCl ₃ H-C ₆ H ₆ (36°)	^c	0.190
CCl ₃ H-CH ₃ OH	0.55 ^d	0.70
CCl ₃ H-dimethylformamide	^c	0.435

^a The line width of the chloroform was used to determine the solvation. ^b The width of the dioxane line gives the equisolvation point as 0.32. ^c The line width method could not be applied because the two solvent signals overlap. ^d The hydroxyl line width of the CH₃OH gives the equisolvation point as 0.72.

preferential solvation we consider the solvent to be distributed between two phases, the bulk solvent and the solvation shell of the solute. We assume that the solvation shell is made up of independent sites which are always occupied. For simplicity we will take the solvation number to be the same for both solvents and assume that there is a one-to-one replacement of solvent molecules. Thus if J is the solvation number, and we take a quantity of solution containing $1/J$ moles of solute, the solvation shell phase will contain exactly 1 mol of solvent regardless of its composition.

If one starts with N moles of a mixed solvent containing x_A mole fraction of A and x_B of B and adds to it $1/J$ moles of pure solid solute, the solution process which takes place causes n_A moles of solvent A and n_B moles of B to be removed from the bulk and transferred to the solvation shell phase. The size of the system is such that $n_A + n_B = 1$. After the solution has been formed, the bulk phase consists of $x_A N - n_A$ moles of A and $x_B N - n_B$ moles of B. The change in free energy for the process can be represented as

$$\Delta G = \Delta G' - T\Delta S_{(\text{configuration})} \quad (2)$$

$$\Delta G' = n_A \Delta H_A + n_B \Delta H_B -$$

$$n_A T \Delta S_{A(\text{thermal})} - n_B T \Delta S_{B(\text{thermal})} \quad (3)$$

Where ΔH_A is the molar enthalpy change associated with the transfer of solvent A from the bulk phase to the solvation shell, and $\Delta S_{A(\text{thermal})}$ includes all entropy changes for A molecules other than those due to the composition of the two phases. Similar definitions hold for solvent B. If we define

$$\Delta G'_A = \Delta H_A - T \Delta S_{A(\text{thermal})} \quad (4)$$

and make a similar definition for solvent B, we have

$$\Delta G = n_A \Delta G'_A + n_B \Delta G'_B - T \Delta S_{(\text{configuration})} \quad (5)$$

The configuration entropy can be calculated on the assumption that both the bulk solvent and the solvation shell obey the laws of regular solutions. Then we can use the relationship

$$S_{(\text{configuration})} = -R \sum_i x_i \ln x_i \quad (6)$$

to calculate $S_{(\text{configuration})}$ for the three phases of interest: (1) the bulk solvent before the solution process, *i.e.*, N moles of liquid composed of $x_A N$ moles of A and $x_B N$ moles of B, (2) the bulk solvent in the final state, *i.e.*, $N - 1$ moles of liquid composed of $x_A N - n_A$ moles of A and $x_B N - n_B$ moles of B, and (3) the solvation shell in the final state, 1 mol of mixture composed of n_A moles of A and n_B moles of B. We obtain the result

$$\Delta S_{(\text{configuration})} = S_4 + S_3 + S_2 - S_1 \quad (7)$$

The additional term, S_4 , is the entropy of mixing the $1/J$ moles of solute into the $N - 1$ moles of bulk solvent. It is a constant in reasonably dilute solutions; that is, it depends only on solute concentration, and not on n_A and n_B . Rewriting eq 7 in more detail, we have

$$\begin{aligned} \Delta S_{(\text{configuration})} = & -R \{ [n_A \ln (n_A) + n_B \ln (n_B)] + \\ & (x_A N - n_A) \ln [(x_A N - n_A)/(N - 1)] + \\ & (x_B N - n_B) \ln [(x_B N - n_B)/(N - 1)] - \\ & N [x_A \ln (x_A) + x_B \ln (x_B)] \} + S_4 \quad (8) \end{aligned}$$

The condition for equilibrium is that the ΔG of eq 2 be a minimum with respect to composition of the solvation shell. Differentiating with respect to n_A while holding the total quantities of all phases constant (*e.g.*, use $n_A + n_B = 1$), as well as temperature and pressure, and then equating the result to zero gives

$$\begin{aligned} \frac{\partial \Delta G}{\partial n_A} = & (\Delta G'_A - \Delta G'_B) + \\ & RT \ln [n_A(x_B N - n_B)/n_B(x_A N - n_A)] \quad (9) \end{aligned}$$

and

$$-\Delta G^0/RT = \ln [n_A(x_B N - n_B)/n_B(x_A N - n_A)] \quad (10)$$

where

$$\Delta G^0 = \Delta G'_A - \Delta G'_B \quad (11)$$

The expression for ΔG^0 can be cast into a familiar form if we note that the argument of the logarithm is simply a ratio of mole fractions. That is

$$\Delta G^0 = -RT \ln K \quad (12)$$

with the definition

$$K = y_A Y_B / y_B Y_A \quad (13)$$

where y_A and y_B refer to the mole fractions of A and B in the solvation shell, and Y_A and Y_B refer to the bulk solvent.

This treatment of preferential solvation predicts a simple relationship between the composition of the bulk solvent and the solvation shell along an isotherm, *i.e.*, $y_A/y_B = K(Y_A/Y_B)$. A plot of the proper ratios should give a straight line of slope K . For this purpose it is awkward to use systems that have a very large (or very small) value of K . Here the solvation shell is made up almost entirely of one component, and a small experimental error in the mole fraction in the predominant component will lead to a large error in the mole fraction of the minor component. This will be particularly true when the relaxation time method cannot be used to study the minor component directly. For this reason the $\text{CCl}_3\text{H}-\text{CCl}_4$ system will not be discussed in this context. A value of K can be estimated from the data taken in solutions quite rich in CCl_4 ; the result is $K \approx 14$.

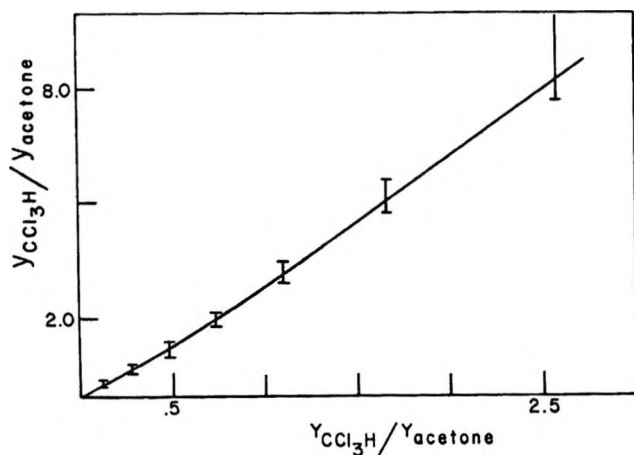


Figure 4. Solvation isotherm of $\text{Co}(\text{acac})_3$ in chloroform-acetone mixtures; ^{59}Co chemical shift method.

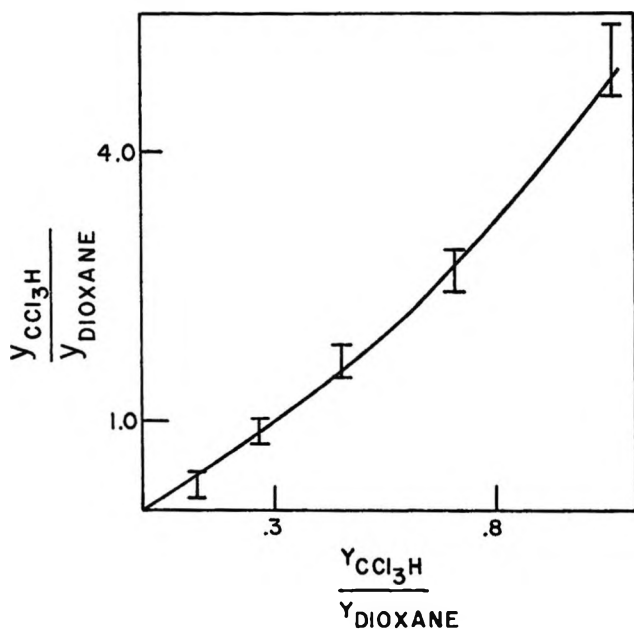


Figure 5. Solvation isotherm of $\text{Co}(\text{acac})_3$ in chloroform-*p*-dioxane mixtures; ^{59}Co chemical shift method.

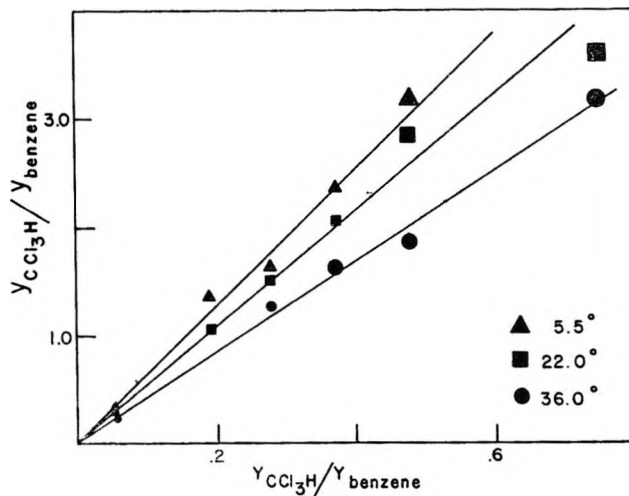


Figure 6. Temperature dependence of the solvation isotherm of $\text{Co}(\text{acac})_3$ in chloroform-benzene mixtures; ^{59}Co chemical shift method.

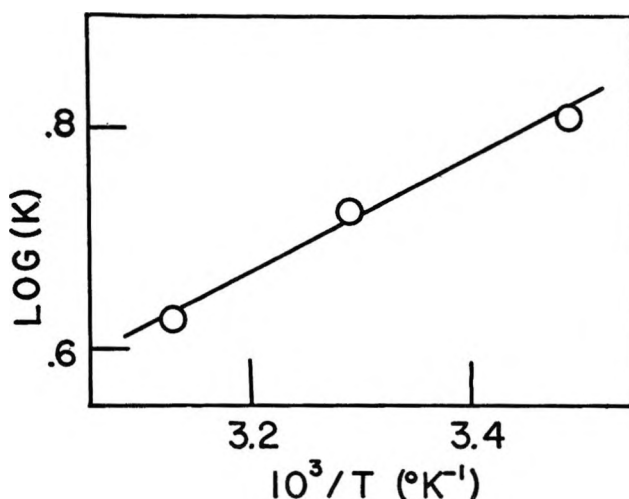


Figure 7. van't Hoff plot for the solvation of $\text{Co}(\text{acac})_3$ in chloroform-benzene mixtures.

The appropriate plots for solvent mixtures containing chloroform with acetone, with *p*-dioxane, and with benzene are presented in Figures 4, 5, and 6. Both the acetone and *p*-dioxane systems show some curvature just outside the limit of experimental error. This is most probably due to a weak interaction with the chloroform causing the bulk phase to be a nonregular solution. However it could also be due to a breakdown of the assumption of equal solvation numbers.

Since the $\text{CCl}_3\text{H}-\text{C}_6\text{H}_6$ system seemed to be especially well behaved, it was studied at several temperatures. Due to overlap of the proton signals, the relaxation time method could not be used, and all the data are derived from ^{59}Co chemical shift measurements. As one would expect, the solvation becomes less preferential at higher temperatures. Figure 6 shows the equilibrium plot for three different temperatures and the resulting values of K . Applying the van't Hoff equation to these data gives the plot shown in Figure 7.

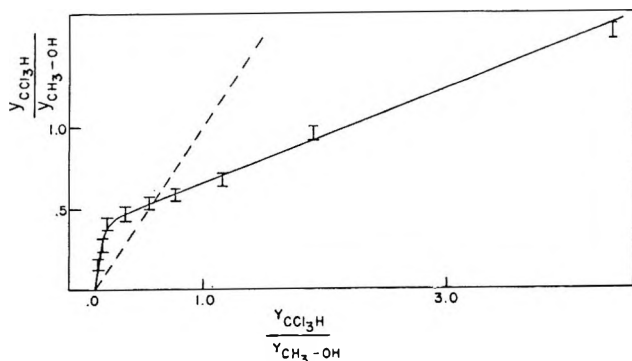


Figure 8. Solvation isotherm of $\text{Co}(\text{acac})_3$ in chloroform-methanol mixtures; ^{59}Co chemical shift method.

From this we obtain the values $\Delta H^0 = -2.3$ kcal and $\Delta S^0 = -4.7$ eu. In this treatment the ΔH^0 obtained is the quantity $\Delta H_A - \Delta H_B$ and ΔS^0 is $\Delta S_{A(\text{thermal})} - \Delta S_{B(\text{thermal})}$, evaluated at 298°K .

Not all solvent mixtures show the isotherm predicted by eq 12 and 13. A deviant system is illustrated by Figure 8 which is the isotherm plot for chloroform-methanol solvation. The results for this system are somewhat less precise than usual because the solvent shift of the ^{59}Co resonance is small, and when using the line width technique, difficulty is encountered because the signals from the two solvents often overlap. The ^{59}Co data give the equisolvation point as 0.70 mol fraction CCl_3H , while the line width of the hydroxyl group yielded 0.70 and of the CCl_3H gave 0.55. In Figure 8 the dashed line is the isotherm that would be followed in the case of random solvation, *i.e.*, for $K = 1$. The

experimental curve divides itself into two distinct regions. At low CCl_3H concentration, CCl_3H is preferred in the solvation shell; at high CCl_3H concentration, CH_3OH is the solvent of preference. This result can be understood in terms of the structure of liquid methanol and the effect produced by diluting it with a second solvent. In the pure liquid state, methanol exists as a mixture of various polymeric hydrogen-bonded species.^{12,13} The addition of a small amount of CCl_3H will not affect this structure significantly. In mixtures which are dilute in CCl_3H it is seen that CCl_3H is the preferred solvent, and that the preference for methanol is to remain in the polymeric bulk solvent state rather than enter the solvation shell. At high CCl_3H concentration, however, the polymeric methanol structure is broken up, and in the main, the methanol exists as free CH_3OH molecules. In these circumstances, methanol is the preferred solvent. In short, the deviation shown by the $\text{CCl}_3\text{H}-\text{CH}_3\text{OH}$ system is simply due to the fact that the bulk solvent phase is not a regular solution. This is consistent with the results of Moelwyn-Hughes and Missen,¹⁴ who observed that this system exhibited large excess entropies of mixing and is thus far from regular.

Acknowledgment. This investigation was supported by the Directorate of Chemical Science, Air Force Office of Scientific Research under Grants AFOSR 212-65 and 68-1384.

(12) M. Falk and E. Whalley, *J. Chem. Phys.*, **34**, 1554 (1961).

(13) E. D. Becker, *ibid.*, **31**, 269 (1959).

(14) E. A. Moelwyn-Hughes and R. W. Missen, *J. Phys. Chem.*, **61**, 518 (1957).

Kinetic Studies of the Reaction of Triphenylmethane Dyes in Acid and Alkaline Media. I. Ethyl Violet in Alkaline Medium

by Sudhir K. Sinha and Sarvagya S. Katiyar¹

Department of Chemistry, Indian Institute of Technology, Kanpur, India (Received July 14, 1969)

The reaction of ethyl violet in alkaline medium has been investigated spectrophotometrically at varying parameters like ionic strength, temperature, hydroxyl ion concentration, dielectric constant, etc. The reaction was found to be bimolecular in nature. Increasing concentrations of neutral electrolytes decreased the rate in accordance with the Brønsted-Christiansen-Scatchard equation. Salt effect data in aqueous and solvent-water mixtures indicate increased solvation of the dye cation in the presence of organic solvents. The rate varied in an anomalous manner with change in the dielectric constant of the medium. The data at different temperatures have been utilized for the calculation of thermodynamic quantities. Entropy of activation ΔS^\ddagger corresponded to $-19.48 \text{ cal deg}^{-1} \text{ mol}^{-1}$ in aqueous medium. The suggested mechanism is in agreement with the experimental data.

Introduction

Ethyl violet (EV), (C.I. Basic violet 4), a triphenylmethane dye, chemically known as [4[bis[*p*-(diethylamino)phenyl]methylene]-2,5-cyclohexadiene-1-ylidene] diethylammonium chloride, has found numerous chemical,^{2,3} biological,^{4,5} and medicinal⁶ uses. It has been reported that it possesses a good tumor-inhibitory activity.⁷ In recent years it has also been used as an analytical reagent⁸⁻¹⁰ for the detection and determination of Au, Re, Ta, Ga, Sb, etc. The dye decolorizes with time in acid and alkaline media. In view of its biological uses in the pH range 7 and analytical applications, the nature and mechanism of the reaction merits investigation. The present paper reports a systematic study of the reaction of ethyl violet in alkaline medium at varying parameters, *viz.*, ionic strength, hydroxyl ion concentration, temperature, dielectric constant, etc. The data have further been utilized for the evaluation of thermodynamic quantities of activation on which no data exist in the literature.

Experimental Section

Materials. Ethyl violet used was supplied by National Aniline Division, Allied Chemical Corp. Sodium hydroxide employed was a B.D.H. AnalaR sample. Potassium chloride used for varying ionic strength was an E. Merck Guaranteed Reagent. Acetone, dioxane, and methanol employed were of B.D.H. AnalaR grade reagents and were further purified by usual methods.¹¹ Carbonate free sodium hydroxide solutions were standardized against potassium acid phthalate.

Method. The reaction was studied spectrophotometrically using a Beckman DU spectrophotometer. The cell compartment was kept at the desired constant temperature by circulating water in the thermostat set from an external thermostat maintained at $\pm 0.1^\circ$.

To avoid the adsorption of the dye at the glass surface during the kinetic run, the experimental vessels were coated inside by a thin layer of purified paraffin wax, which satisfactorily checks the adsorption for sufficiently long durations. The 10-mm rectangular quartz cells used for measuring the absorption were rinsed after every kinetic run with ethanol to remove any adsorbed dye. The computation of a_i , fitting of data to straight line by the least-square method, and calculations of standard deviations were done with the help of an I.B.M. 7044 digital computer.

Results and Discussion

EV showed the absorption maximum in water and 0.8 *M* KCl solutions at 598 $m\mu$, which was shifted to 599 $m\mu$ in (40% v/v) dioxane-water and acetone-water and to 596 $m\mu$ in (20% v/v) methanol-water mixtures. In all the spectra, there appears a secondary maximum whose existence was explained by Lewis,¹² *et al.* Nonapplicability of Beer's law to the triphenyl methane dyes

(1) To whom all the correspondence should be addressed.

(2) L. M. Kul'berg and N. I. Davydova, *Dokl. Akad. Nauk SSSR*, **95**, 551 (1954).

(3) J. N. Brazier and W. I. Stephen, *Anal. Chem. Acta*, **33** (6), 625 (1965).

(4) W. Litsky, W. L. Mallomann, and C. W. Fifield, *Stain Technol.*, **27**, 229 (1962).

(5) F. Yanagisawa, T. Takeuchi, G. Yamasaki, and A. Miyabayshi, *Tagku to Seibutsugaku Med. Biol.*, **33**, 225 (1954).

(6) S. Nagai, *Science*, **130**, 1188 (1959).

(7) M. R. Lewis and P. P. Goland, *Cancer Res.*, **13**, 130 (1953).

(8) H. K. Lin and J. C. Yu, *Hua Hsueh Tung Pao*, **4**, 244 (1965).

(9) J. C. Yu and H. N. Shu, *Hua Hsueh Hsueh Pao*, **34** (4), 338 (1965).

(10) S. C. Hsu and L. C. Lo, *K'o Hsueh T'ung Pao*, **17** (2), 82 (1966).

(11) A. I. Vogel, "A Text Book of Practical Organic Chemistry," 3rd ed, Longmans Green and Co., London, 1957, pp 169, 171, 177.

(12) G. N. Lewis, T. T. Magel, and D. Liplin, *J. Amer. Chem. Soc.*, **64**, 1774 (1942).

has been reported in literature.^{13,14} EV was found to obey Beer's law up to a concentration of $1 \times 10^{-5} M$, with a molar extinction coefficient $\epsilon 9 \times 10^4$. The reaction was, therefore, investigated at concentrations of the dye being lower than $10^{-5} M$ and was followed by observing the change in absorbance with time at the respective λ_{max} in aqueous as well as in solvent-water media.

The reaction responsible for the fading of color of EV in alkaline medium is reversible in nature. In the presence of a small amount of NaOH, therefore, the fading reaction did not proceed to completion even after a lapse of considerable interval of time. In order to minimize the backward reaction which may occur simultaneously with the forward reaction, a very large excess of sodium hydroxide was taken, which shifted the equilibrium to the side of products. The kinetic data were recorded in the first few minutes of the reaction when the backward reaction was negligible. The rate constants were found to be reproducible within the experimental error range of $\pm 0.2 \times 10^{-3} \text{ l. mol}^{-1} \text{ sec}^{-1}$. The error in measurement of activation energy was estimated to be $\pm 150 \text{ cal mol}^{-1}$.

Effect of Hydroxyl Ion Concentration on the Rate. Studies were made by taking a fixed EV concentration ($8 \times 10^{-6} M$) and varying the hydroxyl ion concentration in the range 5.1×10^{-2} to $0.102 M$. The logarithmic variation of absorbance with time gave straight line plots indicating the first-order nature of the reaction in all the runs. The values of apparent rate constant k obtained from the slopes of these plots were found to increase with the increasing concentration of alkali (Table I). Graphical analysis shows the linear

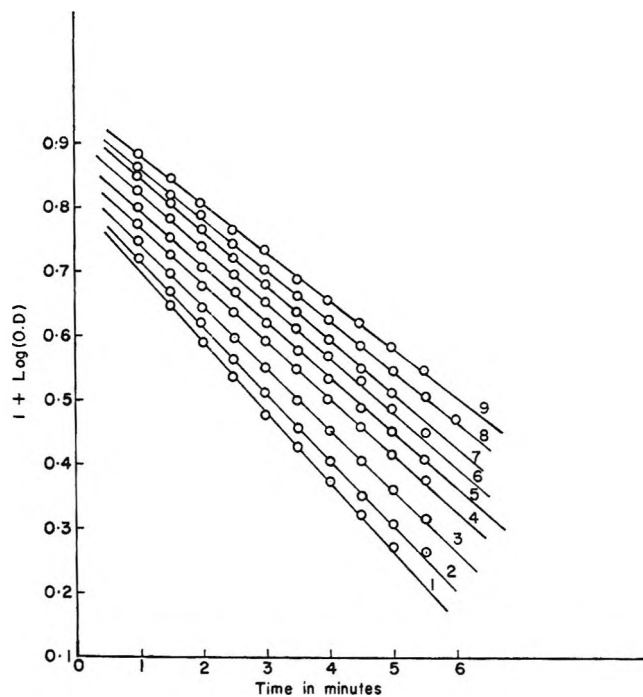


Figure 1. Kinetic runs at varying ionic strength in aqueous medium. Ionic strengths: 1, 0.146; 2, 0.196; 3, 0.246; 4, 0.296; 5, 0.346; 6, 0.446; 7, 0.496; 8, 0.546; 9, 0.596.

by recording the kinetic runs with varying concentrations of EV (1×10^{-5} to $5 \times 10^{-6} M$) and fixed amount of sodium hydroxide ($0.0612 M$). Analysis of these data by graphical method yielded linear plots with almost the same slope. It is interesting to note that the values of k given in Table I are independent of the initial concentration of EV. This indicates that the reaction under investigation is bimolecular.

Effect of Ionic Strength in Aqueous Medium. The dependence of reaction rate on ionic strength was investigated by taking fixed concentrations of EV ($8 \times 10^{-6} M$) and sodium hydroxide ($0.096 M$) and varying concentrations of KCl. Ionic strength was varied in the range 0.096 – 0.896 . Figure 1 gives a typical set of kinetic data obtained at varying ionic strength. It is instructive to note that an increase in ionic strength of the system decreases the rate of reaction. Analysis of the data by the Brønsted equation¹⁵

$$\log k' = \log k_0' + 2AZ_A Z_B \sqrt{\mu} \quad (2)$$

yielded qualitative and inconclusive results. In this equation, A is the Debye-Hückel constant, $Z_A Z_B$ are the charges on the reacting species, and k_0' is the bimolecular rate constant at zero ionic strength. The variation of $\log k'$ with $\sqrt{\mu}$ is shown in plot 1 of Figure 2. If this equation were valid in the investigated range of ionic strength the plot of $\log k'$ vs. $\sqrt{\mu}$ should have been a straight line, but in the present case, the points are

(13) S. E. Sheppard and A. L. Gedds, *J. Amer. Chem. Soc.*, **66**, 1995 (1944).

(14) L. Michaelis and S. Granich, *ibid.*, **67**, 1212 (1945).

(15) E. S. Amis, "Solvent Effects on Reactions Rates and Mechanism," Academic Press, New York, N. Y., 1966, p 24.

Table I^a

EV = $8 \times 10^{-6} M$		NaOH = $0.0612 M$	
NaOH concn, mol/l.	k , sec ⁻¹ $\times 10^3$	EV concn, mol/l. $\times 10^6$	k , sec ⁻¹ $\times 10^3$
0.0510	2.59	10.0	3.09
0.0612	3.02	8.0	3.02
0.0714	3.49	7.2	3.07
0.0816	3.84	6.0	3.04
0.0918	4.15	5.0	3.11
0.1020	4.49

^a Temperature = 25°.

variation of k with OH^- ion concentration. Since the concentration of OH^- is much higher than the concentration of EV, the real velocity constant k' was obtained

$$k' = \frac{k}{\text{OH}^-} = \frac{2.303(\Delta \log C_{\text{EV}})}{(\Delta t)(C_{\text{OH}^-})} \text{ l. mol}^{-1} \text{ sec}^{-1} \quad (1)$$

Effect of EV Concentration on the Rate. The dependence of the rate on the concentration of EV was studied

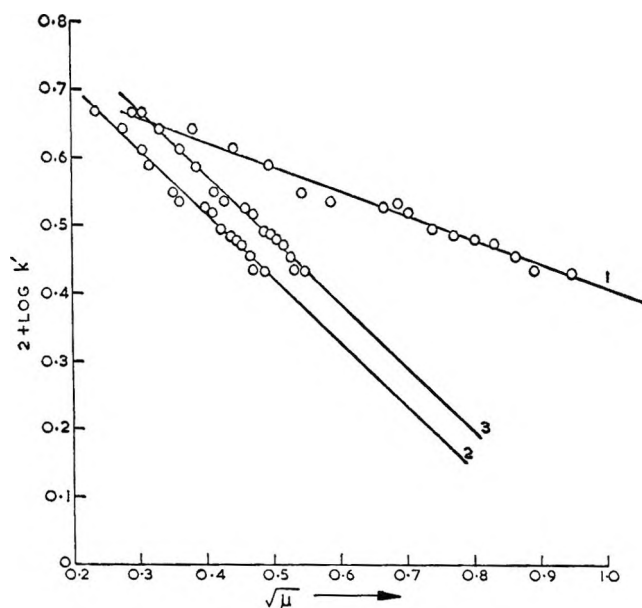


Figure 2. Variation of $\log k'$ as a function of ionic strength in aqueous medium: 1, $\sqrt{\mu}$; 2, $\sqrt{\mu}/(1 + \sqrt{\mu})$; 3, $2A\sqrt{\mu}/(1 + \beta a_i\sqrt{\mu})$. Scale of plot 3 is shifted by 1 cm on $\sqrt{\mu}$ axis.

scattered and deviate appreciably from the linear behavior. This shows the nonapplicability of Brønsted's equation. However, if an attempt is made to draw a straight line, then its slope gives a value of -0.35 for $Z_A Z_B$. This is a very low value for $Z_A Z_B$ and it does not give conclusive evidence regarding the magnitude of charge of the reacting species but it indicates that the reacting species are oppositely charged.

The nonapplicability of the above equation is expected in view of the limited applicability of the Debye-Hückel limiting law. Use of the eq 3 given below, which is an approximation of the modified Debye-Hückel equation (4) and is obtained by taking βa_i equal to unity, produces better results.

$$\log k' = \log k_0' + \frac{1.02Z_A Z_B \lambda \sqrt{\mu}}{1 + \sqrt{\mu}} \quad (3)$$

The variation of $\log k'$ vs. $\frac{\sqrt{\mu}}{1 + \sqrt{\mu}}$ shown in plot 2 of Figure 2 is linear over a wider range of μ ; the slope of this plot gave a value of -0.93 for $Z_A Z_B$, which is closer to unity. The standard deviations, obtained by fitting the data to a straight line, also suggest that the data as treated and plotted according to eq 3 represent a better straight line than they do when treated according to eq 2. The standard deviations for plot 1 and plot 2 of Figure 2 are 0.01 and 0.009, respectively.

Modification of the Debye-Hückel equation by introducing a factor for the size of the ions was done by Scatchard, and using this modification in the Brønsted-Christiansen equation, one obtains¹⁵

$$\log k' = \log k_0' + \frac{2AZ_A Z_B \sqrt{\mu}}{1 + \beta a_i \sqrt{\mu}} \quad (4)$$

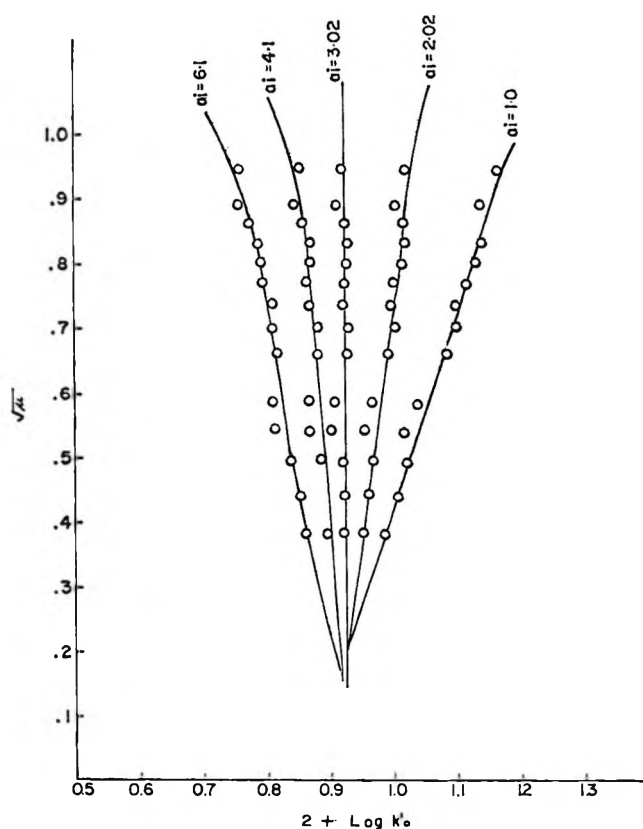


Figure 3. Variation of $\log k_0'$ with $\sqrt{\mu}$ in aqueous medium.

where β and A are Debye-Hückel constants and a_i is the ionic interaction parameter. The value of a_i was computed by a successive trial method by putting different values of a_i in eq 4 and observing its influence on the $\log k_0'$ vs. $\sqrt{\mu}$ plots. According to eq 4 the plot of $\log k_0'$ vs. $\sqrt{\mu}$ should be linear and parallel to the $\sqrt{\mu}$ axis, provided a correct value of a_i is used. Figure 3 gives some typical plots of $\log k_0'$ vs. $\sqrt{\mu}$ at different values of a_i . In these calculations the values of $2A$ and β taken were 1.018 and 0.3286×10^8 , respectively, in aqueous medium.

It is interesting to note that all the plots except the one for $a_i = 3.02 \text{ \AA}$ are not parallel to the $\sqrt{\mu}$ axis, but are divergent lines. This suggests that the value of a_i for EV in aqueous medium is 3.02 \AA . Taking this value for a_i the variation of $\log k'$ vs. $\frac{2A\sqrt{\mu}}{1 + \beta a_i \sqrt{\mu}}$ was

studied. Plot 3 of Figure 2 represents the best average slope obtained by least-square method. The standard deviation of the points from the straight line corresponded to 0.008, which is less than that of plots 1 and 2 of Figure 2. The plot 3 gave a value of -0.97 for $Z_A Z_B$. This value suggests that the reaction is occurring between oppositely charged species of unit charges.

Effect of Ionic Strength. Organic Solvent-Water Mixtures. As seen above, the salt effect leads to an indirect determination of the ionic interaction parameter, a_i , which is dependent on the size of the solvated ion. The salt effect studies were, therefore, carried out

Table II: Variation of k' with Ionic Strength in Solvent-Water Mixtures at 25°

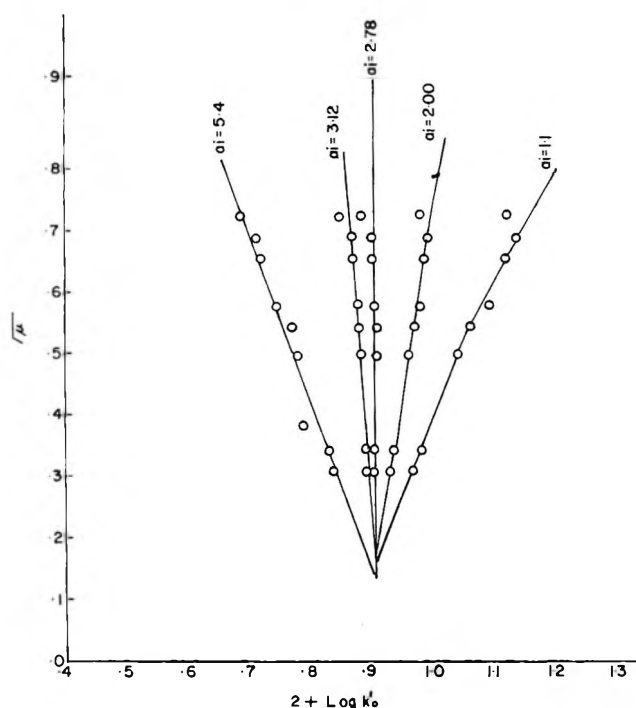
40% Acetone-water		40% Dioxane-water		20% Methanol-water	
Ionic strength	$k \times 10^{-3}$ l. mol ⁻¹ sec ⁻¹	Ionic strength	$k' \times 10^{-3}$ l. mol ⁻¹ sec ⁻¹	Ionic strength	$k' \times 10^{-3}$ l. mol ⁻¹ sec ⁻¹
0.096	3.46	0.096	4.84	0.0192	6.53
0.118	3.28	0.146	4.43	0.0392	5.44
0.146	2.83	0.196	4.05	0.1192	4.48
0.246	2.50	0.246	3.83	0.1692	4.23
0.296	2.35	0.296	3.55	0.2192	4.14
0.396	2.08	0.396	3.24	0.3192	3.56
0.496	1.87		3.09	0.5192	3.36
0.546	1.79		2.81	0.6192	3.30
0.596	1.66		2.56	1.0192	3.07

in mixed media, *viz.* acetone-water (40% v/v), dioxane-water (40% v/v), and the data have been used for calculating a_i in these media. The kinetic runs were recorded at constant concentrations of EV and sodium hydroxide which were $8 \times 10^{-6} M$ and $0.096 M$, respectively, at different KCl concentrations. In these runs the reaction was found to obey a first-order rate law. However, in the case of methanol-water it was observed that at compositions of methanol higher than 20%, the reaction became very fast and did not follow the first-order rate law. This presumably was due to the reaction of dye base with the solvent.¹⁶ Kinetic data were, therefore, recorded at lower concentration of sodium hydroxide ($0.0192 M$) in order to study the reaction in methanol-water under present experimental conditions. The values of bimolecular rate constants k' listed in Table II follow the same trend as was observed in the aqueous medium. Analysis of the data by eq 2 and 3 yielded results similar to those obtained in aqueous medium. The values of $Z_A Z_B$ computed from these data are given in Table III.

Table III: Values of $Z_A Z_B$ by Different Plots in Different Media

Medium	$a_i, \text{Å}$	$\log k'$ vs. $\sqrt{\mu}$	$\log k'$ vs. $\sqrt{\mu}/(1 + \sqrt{\mu})$	$\log k'$ vs., $\frac{2A\sqrt{\mu}}{\beta a_i \sqrt{\mu}} / (1 + \frac{2A\sqrt{\mu}}{\beta a_i \sqrt{\mu}})$
Water	3.02	-0.35	-0.93	-0.97
40% Acetone-water mixture	2.78	-0.41	-0.96	-1.00
40% Dioxane-water mixture	5.20	-0.21	-0.47	-0.95
20% Methanol-water mixture	4.18	-0.29	-0.51	-0.95

The values of a_i in mixed media were calculated. For these calculations A and β in different solvents were obtained by relations available in literature.¹⁷ The effect of varying a_i on the consistency of eq 4 in 40%

Figure 4. Variation of $\log k'_0$ with $\sqrt{\mu}$ in 40% acetone-water mixture.

acetone-water is shown in Figure 4. It may be noted from this figure that plot of $\log k'_0$ vs. $\sqrt{\mu}$ becomes parallel to the $\sqrt{\mu}$ axis for a value of 2.78 Å for a_i , suggesting it to be the correct value of a_i . For dioxane-water and methanol-water also, plots similar to Figure 4 were obtained, which gave a_i values as 5.2 and 4.18 Å , respectively. Feeding back the values of the ionic interaction parameter a_i , obtained in different mixed solvents, into eq 4, the corresponding values of $Z_A Z_B$ were determined from the slopes of plots of $\log k'$ vs. $\frac{2A\sqrt{\mu}}{\beta a_i \sqrt{\mu}} / (1 + \frac{2A\sqrt{\mu}}{\beta a_i \sqrt{\mu}})$. These are reported in the last column of Table III. It is instructive to note that $Z_A Z_B$ is almost equal to -1 when obtained from eq 4 whereas eq 2 and 3 yielded fractional values for $Z_A Z_B$

(16) S. K. De and S. R. Palit, *J. Ind. Chem. Soc.*, **43** (11), 679 (1966).

(17) J. C. Turgeon and V. K. LaMer, *J. Amer. Chem. Soc.*, **74**, 5988 (1952).

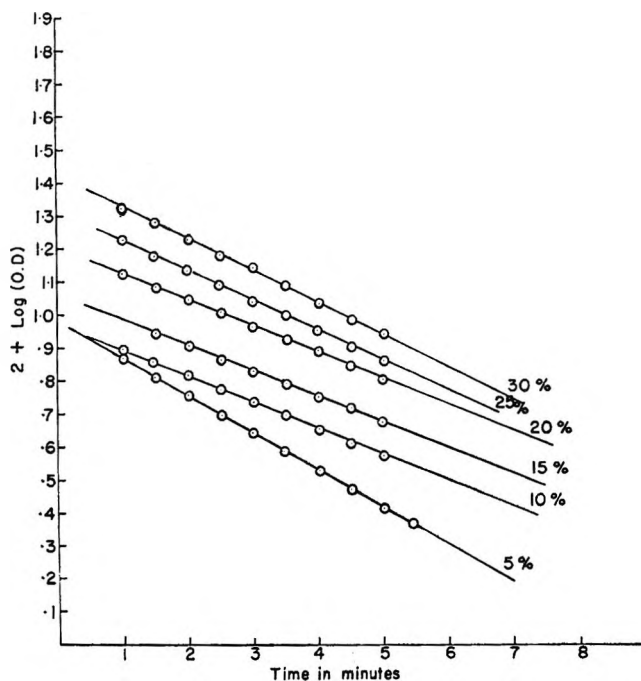


Figure 5. Kinetic runs in varying dioxane-water compositions. Scale is shifted by 1 cm progressively on log (O.D.) axis.

leading to inconclusive results about the nature of the reacting species. Hence, the species involved in the rate-determining step of the reaction in solvent-water mixtures are of opposite and unit charge. Looking at the values of a_i in water and solvent-water mixtures given in Table III one can see that ionic interaction parameter has a comparatively larger values in 40% dioxane-water and 20% methanol-water mixtures than in water. The physical meaning of ionic interaction parameter a_i is not well defined and one can only suggest from the results that the EV ion is presumably more solvated in dioxane-water and methanol-water mixtures than in water. A slightly lower value of a_i (2.78 Å) in acetone-water than in water alone (3.02 Å) is rather puzzling. Evidence of increased solvation of dye cation in presence of organic solvents from salt effect data has also been reported¹⁷⁻¹⁹ by earlier workers.

Effect of Dielectric Constant. The experiments were carried out in presence of different organic solvent-water isocomposition mixtures, keeping the dye and sodium hydroxide concentrations constant, *viz.*, $8 \times 10^{-6} M$ and $0.096 M$, respectively, so that change in dielectric constant is the only rate affecting factor. Figure 5 gives the variation of logarithm of absorbance with time in dioxane-water medium. Similar kinetic data were obtained in acetone-water medium. The linearity of the plots indicates the first-order nature of the reaction. In the case of methanol-water medium, the reaction became quite fast so that concentration of sodium hydroxide was kept at $0.024 M$. Dielectric constant values were obtained from the data of Akerlof.^{20,21}

Analysis of the data was done by the Brönsted-Christiansen-Scatchard²² equation

$$\ln k_0' = \ln k_{0'}' - \frac{\epsilon^2 Z_A Z_B}{kDT r} \quad (5)$$

where $k_{0'}'$ is the molar rate constant in a medium of dielectric constant, $D = \infty$, r is the radius of the intermediate complex, ϵ is the electronic charge, k is the Boltzmann constant, T is the absolute temperature, and the other symbols have the meaning as specified earlier. According to this equation, the addition of low dielectric constant solvents such as acetone, dioxane, or methanol to the solvent should result in an increase in the rate of reaction provided the reaction is occurring between oppositely charged species. It is of interest to note that in case of dioxane-water and acetone-water media the rate first decreases as the dielectric constant decreases and then increases. However, in methanol-water the reaction becomes very fast and does not remain first order in nature at methanol concentrations higher than 25%. The decrease in value of k' instead of increase as expected on the basis of salt effect data may be attributed to the specific solvent effects in these media. It has been observed in certain reactions²³ that small specific solvent effects observed as a result of lowering the dielectric constant of the medium disappeared when normalized mole fraction rate constants²⁴ k_N' were substituted for the volume molar rate constants. However, in the present reaction, the initial decrease in rate constant with decrease in dielectric constant is not due to the use of volume molar rate constants instead of k_N' . Figure 6 gives the plot of $\log k_0'$ vs. $1/D$. It is instructive to note from the figure that plots 1 and 2 which are for dioxane-water and acetone-water, respectively, show minima. Deviation from the expected behavior is presumably due to the fact that at lower percentage of the organic solvent, *i.e.*, when the decrease in dielectric constant is less, specific solvent effect predominates and decreases the rate but at higher concentration of the organic solvent; *i.e.*, when the decrease in dielectric constant is more, the effect due to change in dielectric constant surpasses the specific solvent effect and, thereafter, the rate goes on increasing with decreasing dielectric constant. But the third plot of Figure 6 obtained for methanol-water medium shows an increase in rate even at low concentrations of methanol. These data could not be used for quantitative anal-

(18) S. S. Katiyar, *Bull. Chem. Soc. Jap.*, **35**, 1772 (1962).

(19) S. S. Katiyar, *Z. Phys. Chem. (Frankfurt am Main)*, **34**, 346 (1962).

(20) G. Akerlof, *J. Amer. Chem. Soc.*, **54**, 4125 (1932).

(21) G. Akerlof and O. A. Short, *ibid.*, **58**, 1241 (1936).

(22) E. S. Amis, "Kinetics of Chemical Change in Solution," The Macmillan Co., New York, N. Y., 1949, p 77.

(23) H. G. Davies and V. K. LaMer, *J. Chem. Phys.*, **10**, 585 (1942).

(24) G. Scatchard, *ibid.*, **7**, 657 (1939); *Ann. New York Acad. Sci.*, **39**, 341 (1940).

Table IV: The Thermodynamic Quantities of Activation at 25°

Medium	E^\ddagger , kcal mol ⁻¹	A , l. mol ⁻¹ sec ⁻¹	ΔS^\ddagger , cal deg ⁻¹ mol ⁻¹	ΔF^\ddagger , kcal deg ⁻¹ mol ⁻¹	ΔH^\ddagger , kcal mol ⁻¹
Aqueous	14.03	9.38×10^8	-19.48	19.24	13.44
5% Dioxane	14.05	7.09×10^8	-20.03	19.43	13.46
10% Dioxane	14.60	1.58×10^9	-18.43	19.50	14.01
15% Dioxane	14.97	2.82×10^9	-17.29	19.53	14.38
5% Acetone	14.72	2.45×10^9	-17.57	19.36	14.12
10% Acetone	14.90	2.73×10^9	-17.35	19.48	14.31
15% Acetone	15.32	4.95×10^9	-16.16	19.54	14.73

ysis since methanol has been reported¹⁶ to react with the dye base of EV. It appears, therefore, that the increase in rate is not only due to dielectric constant change but has a contribution due to simultaneous reaction of methanol with the product. These studies were not extended to media where $D < 50$ because the computation of k_0' in such media has been found unjustifiable. Further, the presence of the specific solvent effect sets a limitation for the investigations in isodielectric mixtures.

Effect of Temperature. The studies on the reaction of EV with alkali in aqueous medium were carried out in the temperature range 293–313°K at the dye concentration of $8 \times 10^{-6} M$ and alkali concentration of 0.0612 M . The graph of $\log k'$ vs. $1/T$ gave a straight line as expected from the Arrhenius equation. The slope of this plot yielded a value of 14.03 kcal for E^\ddagger , the average energy of activation. This value of E^\ddagger along with the

values of k' at different temperatures was utilized for the calculation of frequency factor A , and other quantities such as average free energy (ΔF^\ddagger), entropy (ΔS^\ddagger), and heat (ΔH^\ddagger) of activation with the help of the equations²⁵

$$\Delta F^\ddagger = 2.303RT \left(\log \frac{TR}{Nh} - \log k' \right) \quad (6)$$

$$\Delta S^\ddagger = 2.303R \left(\log A - \log e \frac{RT^\ddagger}{Nh} \right) \quad (7)$$

The value of thermodynamic quantities are tabulated in Table IV.

Similar types of kinetic data were obtained in 5, 10, and 15% (v/v) dioxane–water and acetone–water mixtures at a $8 \times 10^{-6} M$ concentration of EV. The concentration of sodium hydroxide was 0.137 M and 0.096 M in dioxane and acetone–water, respectively. It is seen from Table IV that the value of k' decreases with the increasing percentage of organic solvent at a particular temperature in agreement with the previous findings. Arrhenius plots obtained in dioxane–water and acetone–water mixtures were sensibly linear. Figure 7 represents a set of typical plots obtained in acetone–water media. The average value of E^\ddagger at different compositions of the solvent obtained from the slopes, along with other thermodynamic quantities are given in Table IV. The values of ΔS^\ddagger are negative which indicates that the reaction is taking place between ionic species. Further, the value of ΔS^\ddagger becomes less negative as the solvent percentage increases. This is due to the solvated nature of the activated complex and reactants. The increase in entropy of activation with solvent percentage is because the reacting ions are of positive and negative charges. The activated complex therefore bears less charge, exerting thereby less "electrorestrictions" to the neighboring solvent molecules, and hence causing an increase in entropy. The initial decrease in case of 5% dioxane–water mixture is due to change in ionic strength of the medium. The increase in value of energy of activation in solvent–water mixtures is consistent with the specific solvent effect

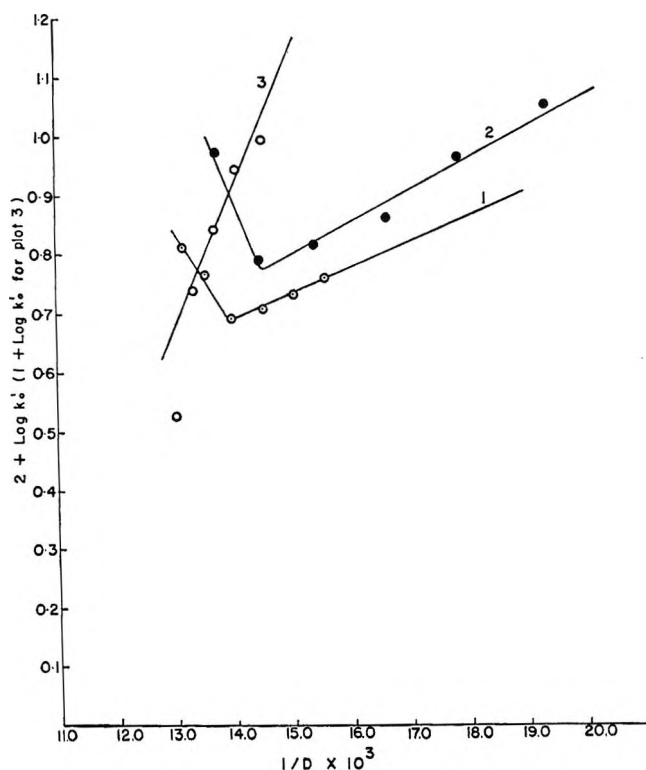


Figure 6. Variation of $\log k_0'$ with $1/D$ in different media: 1, dioxane–water; 2, acetone–water; 3, methanol–water.

(25) S. Glasstone, K. J. Laidler, and H. Eyring, "The Theory of Rate Processes," McGraw-Hill Book Co., Inc., New York, N. Y., 1941, pp 195, 417.

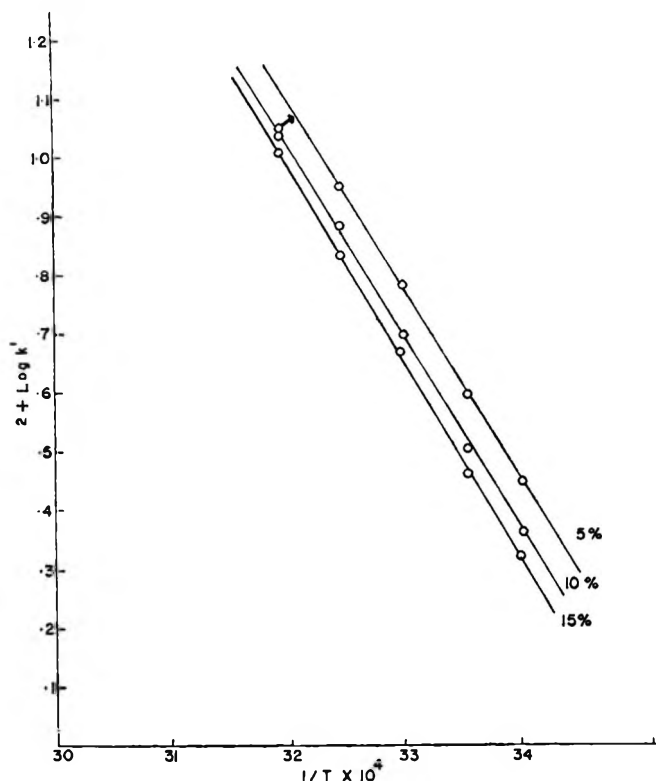
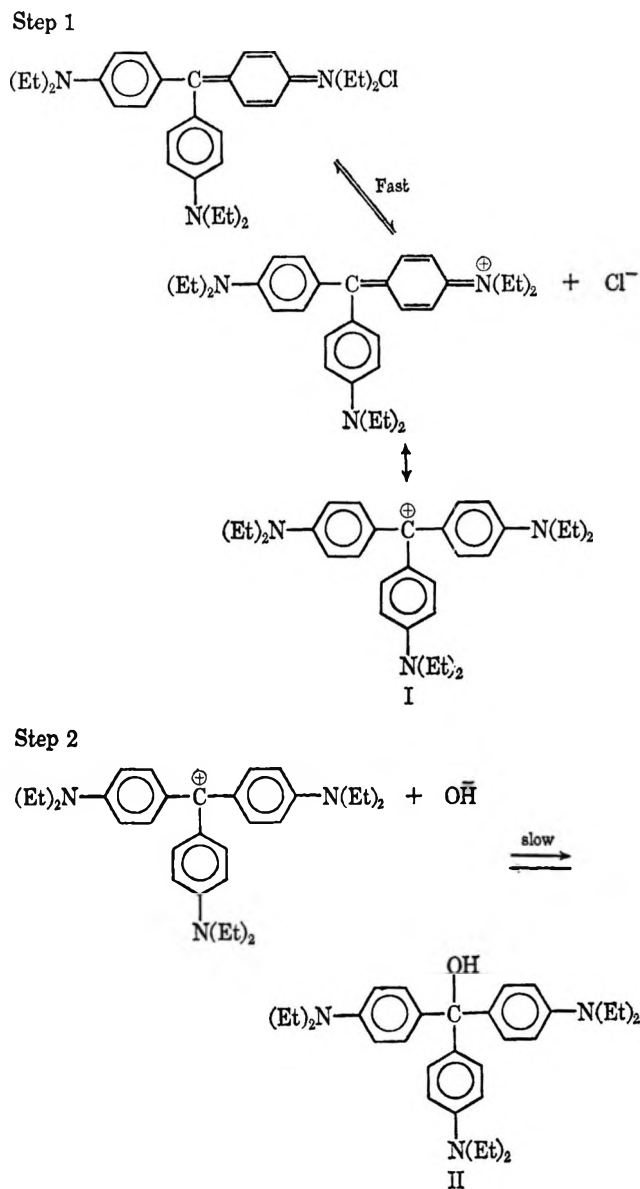


Figure 7. Variation of $\log k'$ with $1/T$ in acetone-water.

resulting from the preferential solvation of the EV ion by an organic substance rather than water. The values of ΔH^\ddagger as expected are comparable with the average activation energies. The existence of specific solvent effect renders the determination of $\Delta F^\ddagger_{\text{isodiel.}}$ and $\Delta S^\ddagger_{\text{isodiel.}}$ impossible.

Nature of the Product and Reaction Mechanism. It was established by De and Palit¹⁶ that when EV reacts with alkali the corresponding carbinol (II) is formed. They isolated the product and established its structure. The stoichiometry arrived at from our observations is in agreement with the structural determination. Based on the above observations the following mechanism can be suggested. In the first step, the dye cation with unit positive charge is produced and it does not contribute to the rate process studied kinetically. The positive charge on the dye cation resonates on all nitrogen atoms and the central carbon atom. The dye cation then reacts with the hydroxyl ion present in the system to form the carbinol (II). The experimental



observations strongly suggest the rate-determining nature of the second step described above involving the reaction between unit and oppositely charged species. Thus, the kinetic investigations indicate that the reaction under consideration is bimolecular in nature with a solvated carbonium ion intermediate.

Acknowledgments. Thanks are due to Mr. R. M. Prasad and Dr. P. B. Rao for helping in computation.

NOTES

S-H...S Type Hydrogen-Bonding Interaction

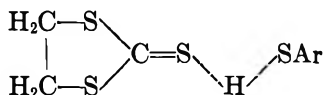
by Samaresh Mukherjee, Santi R. Palit,¹*Department of Physical Chemistry, Indian Association for the Cultivation of Science, Jadavpur, Calcutta-32, India*

and Sadhan K. De

Chemistry Department, Indian Institute of Technology, Kharagpur, West Bengal, India (Received May 26, 1969)

Although there is evidence of the formation of S-H...O, O-H...S, and S-H...N type hydrogen bonds,¹⁻⁴ earlier workers considered hydrogen bonding of the type S-H...S to be unlikely.^{2a,b} However, recent evidence on the formation of S-H...S hydrogen bonds in thiophenols at concentrations exceeding *ca.* 1.0 *M* in carbon tetrachloride has been observed.⁵⁻⁹

So far no quantitative studies have been done on the S-H...S type hydrogen bonding. We report herein some results of our studies on such hydrogen-bonding interaction where the S atom in ethylene trithiocarbonate (ETTC) acts as proton acceptor and S-H in thiophenols acts as proton donor. In our studies we have utilized Nagakura and Baba's suggestion¹⁰ that



transition of organic molecules with suitable chromophores undergoes a blue shift in proton donor solvents due to solute-solvent hydrogen bonding interaction and also quantitative estimation of such interaction can be made by spectral measurements at the shifted peak.^{10,11}

Experimental Section

ETTC and *p*-bromothiophenol were kindly provided by Evans Chemetics, Inc., while *p*-thiocresol and thiophenol were obtained as gift samples from Fallek Chemical Corp. The nonhydrogen-bonding solvent used was Merck's carbon tetrachloride, purified by standard method.¹² The solutions were made gravimetrically and all the spectral measurements were taken on freshly prepared solutions in a Hilger uv spectrophotometer. Optical density measurements were taken at 35° (a temperature constant within ±0.5° being maintained by circulating water through the cell holder).

Results and Discussion

The $n-\pi^*$ transition of ETTC in CCl₄ at 458 $m\mu$

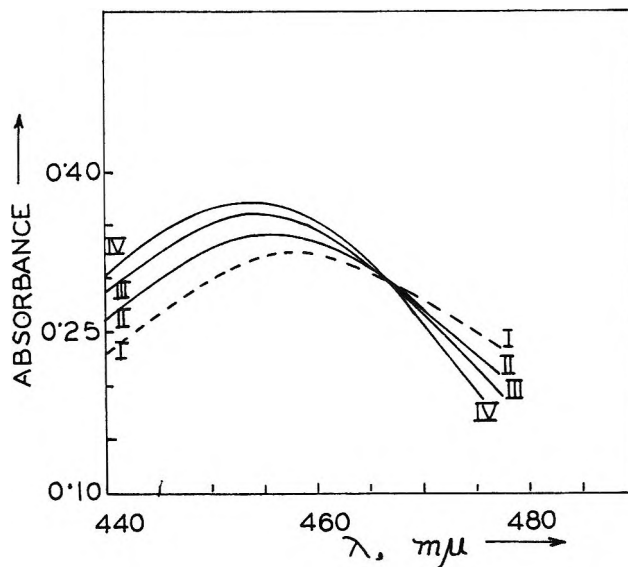


Figure 1 Absorption spectra of ETTC in 0, (I); 1.90, (II); 2.72, (III); and 4.25 (IV) *M* thiophenol in carbon tetrachloride. Concentration of ETTC was 4.53×10^{-3} *M* for all absorption curves.

undergoes a blue shift in thiophenols. Figure 1 shows how the $n-\pi^*$ band in CCl₄ undergoes progressive blue shift with increasing concentration of proton donor and it was found that at 454 $m\mu$ the ETTC exists completely in the hydrogen-bonded state.

Optical density measurements were made on mixtures of ETTC and thiophenols at various concentrations of proton donors at the shifted peak (454 $m\mu$) and the equilibrium constant *K* was calculated by using eq 1.¹¹ When [A] ≫ [B] and the base B forms a 1:1

- (1) To whom all correspondence should be addressed.
- (2) (a) M. J. Copley, C. S. Marvel, and E. H. Ginsberg, *J. Amer. Chem. Soc.*, **61**, 316 (1939); (b) W. Gordy and S. C. Standford, *ibid.*, **62**, 497 (1940).
- (3) S. K. De and S. R. Palit, *J. Phys. Chem.*, **71**, 444 (1967).
- (4) B. Ellis and P. J. F. Griffiths, *Spectrochim. Acta*, **22**, 2005 (1966).
- (5) M. L. Josien, C. Castinel, and P. Saumagne, *Bull. Soc. Chim. Fr.*, 648 (1957).
- (6) R. A. Spurr and H. F. Byers, *J. Phys. Chem.*, **62**, 425 (1958).
- (7) J. G. David and H. E. Hallam, *Trans. Faraday Soc.*, **60**, 2013 (1964).
- (8) J. G. David and H. E. Hallam, *Spectrochim. Acta*, **21**, 841 (1965).
- (9) S. H. Marcus and S. I. Miller, *J. Amer. Chem. Soc.*, **88**, 3719 (1966).
- (10) S. Nagakura and H. Baba, *ibid.*, **74**, 5693 (1952).
- (11) A. K. Chandra and S. Basu, *Trans. Faraday Soc.*, **56**, 632 (1960).
- (12) "Techniques of Organic Chemistry," A. Weissberger, Ed., Vol. VII, Interscience Publishers, Inc., New York, N. Y., 1955.

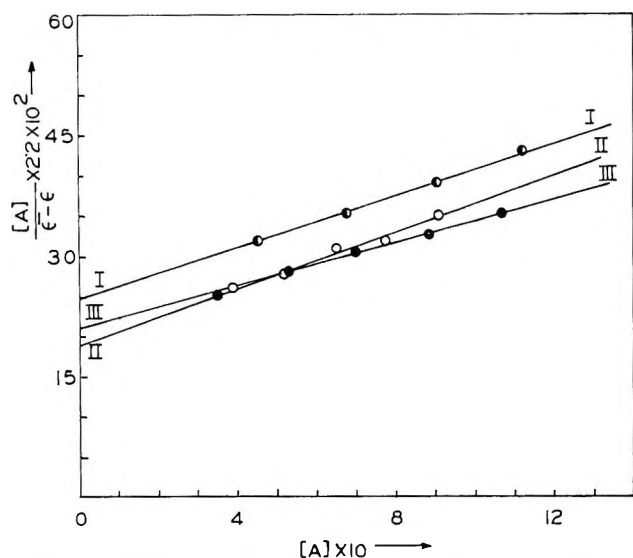


Figure 2 Plot of $[A]/(\bar{\epsilon} - \epsilon_0)$ vs. $[A]$ for I, thiophenol; II *p*-bromothiophenol; and III, *p*-thiocresol. ETTC concentration in all cases was $4.53 \times 10^{-3} M$. Spectral measurements were made at $454 m\mu$.

complex with a proton donor A, then

$$\frac{[A]}{\bar{\epsilon} - \epsilon_0} = \frac{1}{K(\epsilon_1 - \epsilon_0)} + \frac{[A]}{(\epsilon_1 - \epsilon_0)} \quad (1)$$

where $[A]$ is the concentration of proton donor, $[B]$ is that of the solute (*i.e.*, ETTC), ϵ_0 and ϵ_1 are the extinction coefficients of the solute and complex, respectively, and $\bar{\epsilon}$ is the formal extinction coefficient given by $\bar{\epsilon} = D/[B]_0 l$, where D is the measured optical density of the solution containing an initial concentration of $[B]_0$ mol/l. and l is the path length in cm.

The plots of $[A]/\bar{\epsilon} - \epsilon_0$ vs. $[A]$ were found to be linear in all cases (Figure 2). In order to study any effect due to solute concentration, the ETTC-thiophenol system was studied at two different concentrations of ETTC and no significant variation in the equilibrium constant was observed. The results are summarized in Table I. It is evident that thiophenols

Table I: Equilibrium Constants of H-Bonded Complexes between ETTC and Thiophenols at 35°

Thiophenols	Equilibrium constant, M^{-1}
Thiophenol	0.64 ± 0.08
Thiophenol ^a	0.65 ± 0.10
<i>p</i> -Thiocresol	0.75 ± 0.12
<i>p</i> -Bromothiophenol	0.87 ± 0.10

^a [ETTC] was $7.77 \times 10^{-3} M$. In all other cases [ETTC] was $4.53 \times 10^{-3} M$.

form weak 1:1 hydrogen-bonded complexes with ETTC and the stability constants follow the order, *p*-bromothiophenol > *p*-thiocresol > thiophenol. Such order is not in parallel with the expected acidity of proton donors in water.

The Circular Dichroism of Some Aliphatic Amino Acid Derivatives. A Reexamination

by Claudio Toniolo

Institute of Organic Chemistry, University of Padua, Padua, Italy
(Received June 2, 1969)

In 1964, Closson and Haug¹ identified the low-intensity ultraviolet (uv) absorption band near $210 m\mu$ in the spectra of saturated carboxy derivatives as an $n \rightarrow \pi^*$ transition of the chromophore.

A number of papers concerning circular dichroism (CD) studies of saturated carboxylic acids and esters have recently appeared in the literature.²⁻⁶

It was found that *S*-lactic acid and its derivatives exhibit, in addition to the 210 – 220 - $m\mu$ CD Cotton effect,^{3,5-7} a weak CD band of opposite sign centered in the 240 – 250 - $m\mu$ region.^{5,6} Djerassi and coworkers⁶ interpreted their results assuming that both dichroic bands are associated with the $n \rightarrow \pi^*$ transition of the carboxy-chromophore and possibly related to different rotamers, in conflict with Anand and Hargreaves,⁵ who attributed the lower-energy Cotton effect to an $n \rightarrow \pi^*$ transition and the stronger Cotton effect at about $210 m\mu$ to a $\pi \rightarrow \pi^*$ transition.

In view of the importance of the $n \rightarrow \pi^*$ band in the assignment of configuration and in the application of octant and related rules in carboxylic acid derivatives, it was of interest to us to reexamine² the optical rotatory properties of the configurationally related amino acids.

To obtain further information on the transitions involved in the carboxy chromophore, we have also examined the CD spectra (by a Roussel-Jouan Dichrographe-185 CD model) of *R*-lactic acid in solvents of different polarity and at different pH's in the 200 – 260 - $m\mu$ region.

Both the positive band nearest the visible and the negative band at about $210 m\mu$ blueshift and decrease in intensity on changing the solvent from cyclohexane-dioxane to trifluoroethanol (Table I and Figure 1), possibly indicating a common origin, *i.e.*, the $n \rightarrow \pi^*$ transition of the carboxy chromophore (for the OH group the expected region of absorption is below $180 m\mu$ ⁸).

(1) W. D. Closson and P. Haug, *J. Amer. Chem. Soc.*, **86**, 2384 (1964).

(2) M. Legrand and R. Viennet, *Bull. Chem. Soc. Fr.*, 679 (1965).

(3) S. Uyeo, J. Okada, and S. Matsunaga, *Tetrahedron*, **24**, 2859 (1968).

(4) J. D. Renwick and P. M. Scopes, *J. Chem. Soc., C*, 2574 (1968).

(5) R. D. Anand and M. K. Hargreaves, *Chem. Commun.*, 421 (1967).

(6) G. Barth, W. Voelter, E. Bunnenberg, and C. Djerassi, *ibid.*, 355 (1968).

(7) C. Toniolo, V. Perciaccante, J. Falcetta, R. Rupp, and M. Goodman, *J. Org. Chem.*, in press.

(8) D. W. Turner in "Determination of Organic Structures by Physical Methods," F. C. Nachod and W. D. Phillips, Ed., Academic Press, New York, N. Y., 1962, p 339.

Table I: Circular Dichroism of R(-)Lactic Acid at 22°

Solvent ^a	Band 1		Band 2 ^b	
	λ_{\max} m μ	$\Delta\epsilon_{\max}$	λ_{\max} m μ	$\Delta\epsilon_{\max} \times 10^3$
TFE	208	-0.75	242.5	+3.5
Water	210	-0.8	243.5	+4.6
Ethanol	211.5	-0.85	246.5	+5.6
C.E./Diox.	212.5	-1.1	247	+13.6
1 N NaOH	212.5	-0.2

^a TFE, trifluoroethanol; C.E./Diox., cyclohexane/dioxane 1:1. ^b In order to examine band 2, 1% solutions have been used with an optical path length of 10 mm.

The investigation of the optical rotatory properties of the α -hydroxy acid at different pH's confirms this assignment. In fact, the ionization of the carboxyl group appears to cause a marked decrease in ellipticity of the strong negative $n \rightarrow \pi^*$ band and the disappearance of the weak positive $n \rightarrow \pi^*$ band (Table I and Figure 1), as expected² on the basis of the greater symmetry of the carboxylate ion.

The interpretation of CD spectra of amino acids in the 230–250 m μ region is complicated by the contribution of an optically active transition involving the nitrogen nonbonding electrons of the amino group.⁹ In fact, S-alaninol exhibits a weak positive Cotton effect at 235 m μ which disappears on protonation (Table II).

We have measured the circular dichroism of some aliphatic amino acids at pH 1 (0.1 N HCl), pH 7 (phos-

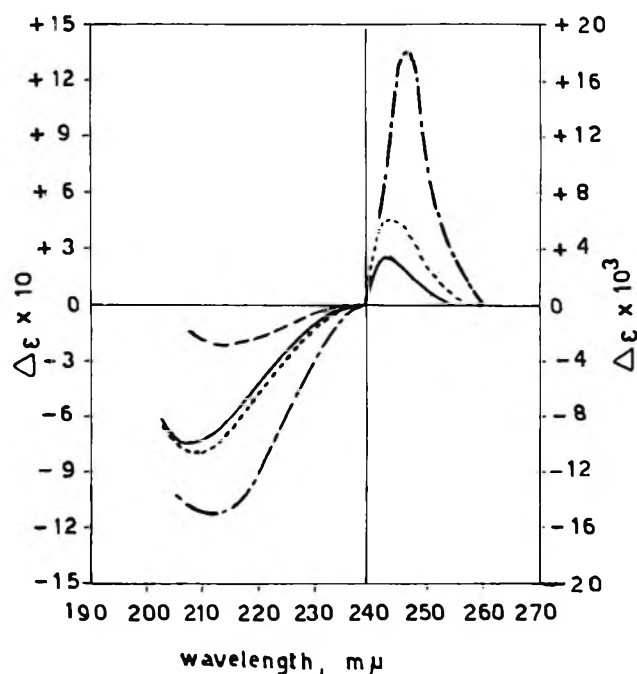


Figure 1. CD spectra of R-lactic acid in trifluoroethanol (—), water (···), cyclohexane-dioxane (— · —), and 1 N NaOH (---).

phate buffer), and pH 13 (0.1 N NaOH), where their protonated, zwitterionic, and anionic species, respectively, prevail. Moreover, this study has been extended to their ester hydrochlorides in water and in 0.1 N NaOH.

The amino acids at pH 1 and their ester hydrochlorides in water exhibit two Cotton effects of opposite signs centered at 206–209 m μ (band 1) and at 244–252 m μ (band 2), respectively (ref 2 and Tables II and III). This behavior parallels that of lactic acid in

Table II: Circular Dichroism Data at 22° in the 230–270-m μ Region

Compound ^a	Solvent ^b	λ_{\max} m μ	$\Delta\epsilon_{\max} \times 10^3$
S-Alaninol	1 N HCl
	0.1 N NaOH	235	+0.8
S-Ala	0.1 N HCl	250	-0.1
	—pH 7—
S-Abu	0.1 N NaOH	240	-3.1
	0.1 N HCl	251	-0.5
S-Nval	—pH 7—
	0.1 N NaOH
S-Val	0.1 N HCl	250.5	-0.7
	—pH 7—
S-Ileu	0.1 N NaOH
	0.1 N HCl	250.5	-1.3
S-Leu	—pH 7—
	0.1 N NaOH
S-Pro	0.1 N HCl	249.5	-1.0
	—pH 7—
S-Pro	0.1 N NaOH
	0.1 N HCl	251.5	-1.0
S-Pro	—pH 7—
	0.1 N NaOH
S-Pro	0.1 N HCl	250.5	-0.7
	—pH 7—
S-Pro	0.1 N NaOH
	0.1 N NaOH	236.5	-16

^a For abbreviations of amino acids, see E. Schroder and K. Lubke, "The Peptides," Vol. I, Academic Press, London, 1965. ^b pH 7, phosphate buffer.

water, in these three cases the carboxyl group representing the only chromophore optically active in this region of the spectrum. Recently, Legrand and Vienne² demonstrated that the intensity of band 1, which is three orders of magnitude higher than band 2, increases with increasing side-chain length. A similar trend, although not so evident, is apparent for band 2.

In addition, our results (Table II) on the amino acids in their zwitterionic forms (at pH 7) confirm previous reports that protonated amino groups⁹ and carboxylate anions^{5,6} do not show any Cotton effect in the 230–270-m μ region.

In Table II it is noteworthy that the intensity of the negative Cotton effect of S-proline and S-alanine at

(9) J. Parello and F. Picot, *Tetrahedron Lett.*, 5083 (1968).

Table III: Circular Dichroism Data at 22°

Compound	Solvent	Band 1		Band 2	
		λ_{\max} , m μ	$\Delta\epsilon_{\max}$	λ_{\max} , m μ	$\Delta\epsilon_{\max} \times 10^3$
S-Ala-OMe-HCl	Water	207	+0.92	248	-0.1
S-Ala-O <i>t</i> Bu-HCl ^a	0.1 N NaOH	211	+0.90	238	-139
S-Val-OMe-HCl	Water	206	+1.82	244	-1.9
S-Val-O <i>t</i> Bu-HCl	0.1 N NaOH	215	+1.70	253	-0.7
S-Leu-OMe-HCl	Water	207	+1.98	246	-1.3
S-Leu-O <i>t</i> Bu-HCl	0.1 N NaOH	214	+1.54	249.5	-6.1

^a Because of the instability of methyl esters in 0.1 N NaOH, *t*-butyl esters have been measured in these experimental conditions.

pH 13 is 25–30 greater than that at pH 1; unexpectedly, this Cotton effect is not apparent in alkaline aqueous solutions of S- α -amino butyric acid, S-norvaline, S-valine, S-isoleucine, and S-leucine. Some screening of the nitrogen nonbonding electrons involved in the optically active transition in 0.1 N NaOH, brought about by the hydrogen atoms of β or γ methyl groups, could account for the observed phenomenon. The different behaviors of alanine and lactic acid in NaOH confirm that the above noted effect is associated with the amino group.

Furthermore, the data reported in ref 2 and in Table II show that for the amino acids, under the conditions (pH 1 \rightarrow pH 13) where band 1 shifts red, band 2 shifts blue. This is not inconsistent with previous assignments, since we believe that the CD band near 250 m μ at pH 1 is related to an $n \rightarrow \pi^*$ transition of the carboxy chromophore and at pH 13 to an $n \rightarrow \sigma^*$ transition of the amino chromophore.

At last, in the case of amino esters (Table III) it must be noted that S-alanine alkyl ester hydrochlorides band 2 shifts blue whereas S-valine and S-leucine alkyl ester hydrochlorides band 2 shifts red. The possible contribution of both carboxy and amino chromophores in the 230–270-m μ region in the alkaline aqueous solutions of these esters and the above observed influence of the structural properties of aliphatic side chains, which is also apparent in Table III (compare $\Delta\epsilon_{\max}$ values for band 2 of S-alanine-*t*-butyl ester hydrochloride and of S-valine- and S-leucine-*t*-butyl ester hydrochlorides in 0.1 N NaOH), could be responsible of this apparently inconsistent behavior.

Thus, our results extend to amino acid derivatives the description of the occurrence of two Cotton effects in the 207–255-m μ region, which have already been shown in the lactams,¹⁰ oligopeptides,¹¹ diketopiperazines,¹² hydroxyacid derivatives,^{5,6} polyesters,^{13,14} and random-coiled poly- α -amino acids.^{15,16}

In view of these findings, we suggest that care is to be taken before any correlation between sign and magnitude of Cotton effects, and absolute configuration and molecular conformation of carboxy derivatives could be made.

In addition, a theoretical reinvestigation of the opti-

cal rotatory properties of the carboxy chromophore in this spectral range appears to be necessary.

Acknowledgment. The author wishes to thank Professor E. Scoffone and Dr. E. Peggion for reading the manuscript and helpful suggestions.

(10) M. Goodman, C. Toniolo, and J. Falcetta. *J. Amer. Chem. Soc.*, **91**, 1816 (1969), and references therein.

(11) (a) M. Goodman, A. S. Verdini, C. Toniolo, W. D. Phillips, and F. A. Bovey, *Proc. Natl. Acad. Sci. U. S.*, **64**, 444 (1969); (b) M. Goodman, C. Toniolo, and A. S. Verdini, paper presented to the Tenth European Peptide Symposium, Abano Terme (Padua), Italy, 1969.

(12) M. D'Alagni, B. Pispisa, and F. Quadrioglio, *Ricerca Sci. Ital.*, **38**, 910 (1968).

(13) R. C. Schulz and A. Guthmann, *J. Polym. Sci., B*, **5**, 1099 (1967).

(14) M. Goodman, personal communication to R. C. Schulz, ref 13.

(15) S. N. Timasheff, H. Susi, R. Townend, L. Stevens, M. J. Gorbunoff, and T. F. Kumosinski, in "Conformation of Biopolymers," G. N. Ramachandran, Ed., Academic Press, New York, N. Y., 1967, p 173.

(16) M. L. Tiffany and S. Krimm, *Biopolymers*, **6**, 1379 (1968).

The Effect of Visible and Ultraviolet Light on the Palladium-Catalyzed Oxidation of Carbon Monoxide

by Raymond F. Baddour and Michael Modell

Department of Chemical Engineering, Massachusetts Institute of Technology, Cambridge, Massachusetts 02139
(Received September 18, 1969)

While many studies of the effect of light on chemisorption and catalysis by semiconductors have been reported,¹ very few results are available for metal adsorbents and catalysts, and most of these are rather qualitative observations. Photodesorption of carbon monoxide from nickel powder,^{2–4} nickel ribbon,⁵ and

(1) See, e.g., T. Freund and W. P. Gomes, *Catal. Rev.*, **3**, 1 (1969).

(2) A. N. Terenin, *Probl. Kinet. Katal. Akad. Nauk, SSSR*, **8**, 17 (1955).

(3) A. N. Terenin and Y. P. Solonitzin, *Discussions Faraday Soc.*, **28**, 28 (1959).

(4) P. E. Valnev, *Zh. Fiz. Khim.*, **30**, 1308 (1956).

(5) W. J. Lange and H. Riemersma, *Trans. Nat. Vacuum Symp.*, **8**, 167 (1961).

tungsten ribbon⁶ is effected by radiation in the 2400 to 3500-Å region, and water adsorbed on cadmium and zinc^{3,4} is photodesorbed by ultraviolet light. Benzaldehyde adsorbed on powdered copper² is photodissociated with liberation of carbon monoxide by light below 3300 Å, and acetone on nickel⁷ is photodissociated by 2400-Å radiation. In the only previous report of a nondissociative photocatalyzed metal surface reaction, a gas condensable at liquid air temperature (believed to be CO₂) was formed when a mixture of carbon monoxide and oxygen adsorbed on vapor-deposited bismuth was exposed to light.²

In these previous studies, no background reaction was measured in the absence of light. The present study was undertaken to determine quantitatively the effect of light on the rate of a reaction which also proceeds in the absence of radiation. The system chosen, carbon monoxide oxidation over palladium, has been studied in the absence of light by many investigators.⁸

Experimental Section

Approximately 40 cm of an 0.008-in. diameter palladium wire (Engelhard Industries, 99.9%) was coiled into a cylindrical helix of 7-mm diameter and sealed through feed-throughs in the ends of a 13-mm o.d. quartz tube (see Figure 1). The superficial surface area was 8.5 cm². The wire temperature was monitored by measuring the resistance on a Wheatstone bridge. The reactor and 1000-W water-cooled high-pressure mercury arc lamp (G.E., Type AH-6) equipped with a quartz water-cooling jacket (G.W. Gates & Co.) were housed in a 12-in. diameter reflector cavity lined with specular reflecting aluminum sheet (see Figure 1). Cut-off filters of No. 9730 Pyrex and No. 7900 Vycor tubes were fitted over the quartz water jacket.

A recirculating loop was used to maintain differential reaction conditions and to minimize the wire temperature rise due to absorption of light. Within the recirculation loop, a miniature vaneaxial blower (Globe Industries, Model SC-19A-652) with dry Teflon bearings (Barden Corp., Bartemp SR-2-BSSX) was totally enclosed in a brass, water-cooled housing. The recirculation rate was *ca.* 60 l./min, the recirculation-to-feed ratio was of the order of 1000:1, and the volume of the loop was *ca.* 700 cm³. The gases were heated before and cooled after passing through the reactor; the remainder of the loop was maintained at room temperature.

Reaction mixtures contained typically 1% CO (Matheson C.P., 99.5% minimum purity) and 1% O₂ (99.5% minimum purity) in He (99.99% minimum purity). The helium diluent was used to maintain rapid heat transfer from wire to gas. Pressure in the reactor was typically a few inches above atmospheric. Product mixtures were analyzed in an on-line gas chromatograph. Conversion to CO₂ was maintained below 4%. Wire temperature ranged from 130 to 250°.

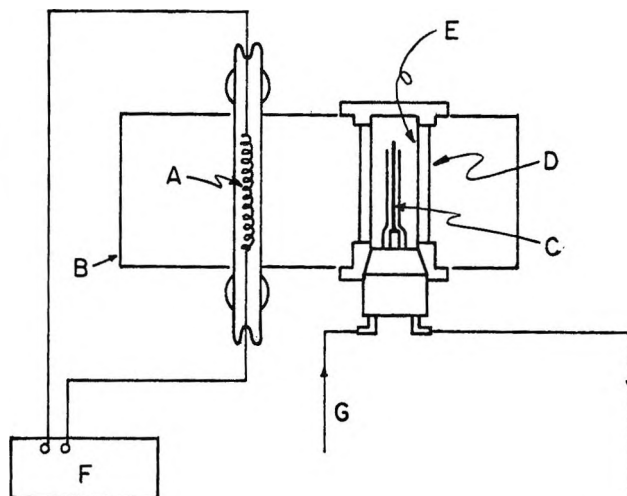


Figure 1. Reactor and irradiation chamber: A, coiled wire catalyst; B, aluminum reflector cavity; C, mercury arc lamp; D, glass cut-off filter; E, quartz water jacket; F, resistance bridge; G, cooling water.

The reaction rates reported below were obtained under steady-state conditions.

Results

Dark reaction rates were measured with and without catalyst. In the latter case, a small background conversion was observed. The catalyzed dark reaction rate, corrected for the background rate, was first order in oxygen partial pressure in the range investigated (1 to 10 Torr O₂). Carbon dioxide partial pressure was varied between 0.8 and 7 Torr; the rate was inverse first order above 2 Torr of CO and fell close to zero order at the lowest pressures studied. For the region above 2 Torr of CO, the reaction rate, *R*, in mol CO₂/min cm² superficial area was

$$R = 4.7 \times 10^{12} \left[\exp \left(\frac{21,400}{T} \right) \right] \frac{P_{O_2}}{P_{CO}}$$

The activity was relatively constant for a 2-day period under reaction conditions, but some variation in activity was observed after that time. It was found that the activity could be maintained relatively constant ($\pm 10\%$) over at least a 6-day period by degassing each night at 300° (using ohmic heating) and 10⁻⁶ Torr.

A blank run was made by irradiating the quartz reactor without the palladium catalyst. No reaction above the dark background rate was observed.

The irradiated reaction rate was measured using unfiltered light at constant oxygen and carbon monoxide partial pressures of 14.7 and 6.1 Torr, respectively, at

(6) W. J. Lange, *J. Vacuum Sci. Technol.*, **2**, 74 (1965).

(7) A. N. Terenin, *J. Chim. Phys.*, **54**, 114 (1957).

(8) See, e.g., R. F. Baddour, M. Modell, and U. K. Heusser, *J. Phys. Chem.*, **72**, 3621 (1968).

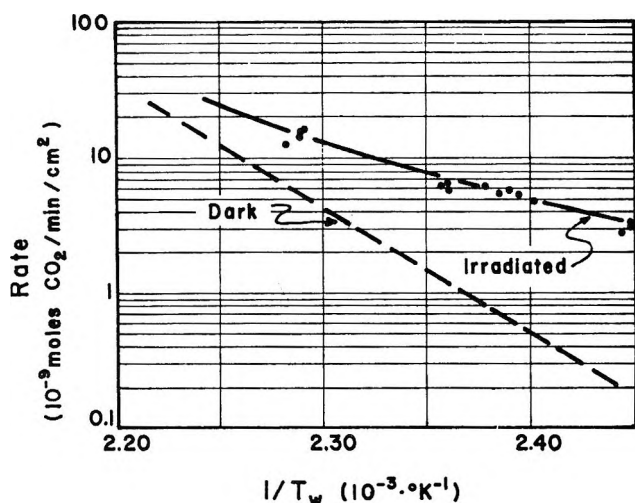


Figure 2. Effect of irradiation on reaction rate (14.7 Torr of O_2 , 6.1 Torr of CO , remainder He).

temperatures varying between 130 and 170°. The results are shown in Figure 2, wherein the temperature is that of the wire measured under experimental conditions (*i.e.*, during irradiation). The reaction rate increased by 1000% at 135° and 300% at 165° due to irradiation. The decreasing photoeffect with increasing temperature was confirmed in subsequent experiments. At 230 to 250° (not shown in Figure 2), no enhancement of the dark rate was observed under irradiation with unfiltered light.

The irradiated reaction rate using the Vycor cut-off filter was the same order of magnitude as that observed with unfiltered light. However, with the Pyrex cut-off filter, the irradiated reaction rate was indistinguishable from that of the palladium-catalyzed dark reaction.

Discussion

The palladium-catalyzed dark reaction results are in agreement with results reported previously.^{8,9} The apparent activation energy of 42.5 kcal/mol is indicative of a fresh palladium catalyst which has not undergone break-in. The overnight degassing procedure is apparently effective in delaying the break-in process.

The observed effect of irradiation is clearly not a thermal effect. Since metals have a high extinction for visible and ultraviolet light, the refracted light is absorbed within a small distance of the surface. However, under steady-state conditions, the bulk wire temperature must be equal to or greater than the surface temperature because the only significant heat leak is from wire to gas (end effects were negligible with the long length of wire used here). Thus, the bulk wire temperature obtained by resistance measurement is no less than the wire surface temperature (a maximum 0.5° rise from surface to bulk was calculated).

A second factor for discounting a thermal effect is the frequency dependence of the effect of radiation. The photon energies responsible for the effect lie between

those transmitted by Vycor and absorbed by Pyrex. Vycor 7900 has a broad cut-off between 2400 and 3300 Å with 50% transmission at 2900 Å,¹⁰ whereas the corresponding range for Pyrex 9730 is 2800 to 3600 Å with 50% transmission at about 3200 Å.¹¹ However, the total photon energy passed by Pyrex is not appreciably less than that passed by Vycor. Since the reflectivity of palladium does not vary appreciably in the near-ultraviolet-visible region, there is no reason to expect a radical change in a thermal effect between Vycor and Pyrex.

The region of active radiation for the photoeffect has been estimated conservatively as 2700 to 3200 Å. This relatively narrow range is indicative of a photochemical excitation of a surface species. Under the conditions studied here, adsorbed carbon monoxide is the dominant surface species and oxygen coverage is believed to be very small.^{8,9} Thus, the photoeffect is probably due to excitation of an adsorbed carbon monoxide species by absorption of a photon. The excited species can desorb, react, or become deactivated (by a variety of processes). Of course, if deactivation to the ground state is rapid relative to desorption or reaction, the steady-state concentration of excited species will be small and a photoeffect would be non-existent.

For CO oxidation over palladium, the rate-limiting step for the dark reaction is thought to be either molecular oxygen adsorption or surface reaction.⁹ Carbon monoxide inhibits the rate by reducing either the rate or the extent of oxygen adsorption. Thus, either desorption or reaction of electronically excited CO surface species could lead to an enhanced reaction rate during irradiation.

The observed temperature dependence of the photocatalyzed reaction is considerably less than that of the dark catalyzed reaction. Electronic excitation could result in either a more or less stable surface species (depending on whether the transition is from bonding to antibonding orbital or vice versa) and, thus, a higher or lower activation energy. It should be noted that in some cases the photocatalytic technique may be more sensitive than the photodesorption method used by previous workers: excitation to a more strongly bound or more reactive surface species would not necessarily be detected by photodesorption but would be clearly observable under conditions of irradiation with steady-state reaction.

Acknowledgments. This work was supported in part by an American Oil Company Preceptorship.

(9) R. F. Baddour, M. Modell, and R. L. Goldsmith, *J. Phys. Chem.*, in press.

(10) L. R. Koller, "Ultraviolet Radiation," John Wiley & Sons, New York, N. Y., 1952, p 149.

(11) Data sheet for Pyrex Brand Glass No. 9730, Corning Glass Works, Electrical Products Div., Corning, N. Y.

Gas-Phase Photolysis at 1470 Å of Mixtures of Cyclohexane with Benzene and with Nitrous Oxide at 750 Torr

by Robert R. Hentz and D. B. Peterson

Department of Chemistry and the Radiation Laboratory,¹
University of Notre Dame, Notre Dame, Indiana 46556
(Received September 25, 1969)

Holroyd and coworkers² have observed that both benzene and N₂O as solutes reduce $\phi(\text{H}_2)$ from photolysis of liquid cyclohexane at 1470 Å and have attributed this reduction to energy transfer from excited cyclohexane to the solute. Hentz and Knight³ studied hydrogen quantum yields in the 1470-Å photolysis of *c*-C₆H₁₂-C₆H₆ and *c*-C₆H₁₂-N₂O mixtures in the gas phase at total pressures of 1 and 70 Torr. They concluded that the results show no evidence of energy transfer from that state of cyclohexane initially excited. Consequently, an upper limit of 0.2 nsec was estimated for the lifetime, τ , of that state of cyclohexane initially excited at 1470 Å in the gas phase. It was noted³ that for $\tau < 0.2$ nsec, the results of Holroyd, *et al.*,² require specific rates of transfer from *c*-C₆H₁₂* in the liquid to benzene and N₂O of $k > 1.6 \times 10^{10} \text{ M}^{-1} \text{ sec}^{-1}$ and $k > 3.4 \times 10^{10} \text{ M}^{-1} \text{ sec}^{-1}$, respectively. Thus, results of the gas-phase photolyses at 70 Torr do not permit an unambiguous decision as to whether or not H₂ formation occurs from the same excited state of cyclohexane in both the gas and liquid phases. Consequently, a closer estimate of the gas-phase τ was sought in the present work by extension of the previous study of $\phi(\text{H}_2)$ in the 1470-Å photolysis of *c*-C₆H₁₂-C₆H₆ and *c*-C₆H₁₂-N₂O mixtures to a total pressure of 750 Torr at 95°.

Sources and methods of purification of cyclohexane, benzene, and N₂O have been described.^{3,4} As in previous work^{3,4} the light source was a microwave-powered Xe resonance lamp but with a sapphire window. The only significant emission below 2500 Å was at 1470 Å. The lamp was sealed into a 600-ml Pyrex reaction cell in such a way that the window extended well into the interior of the cell. The cell contained a magnetically driven stirrer to provide efficient mixing of gases near the window. Gases were introduced or collected through a stainless steel valve which connected the cell to a vacuum manifold. The cell and adjoining valve were enclosed in a small oven with which the system was maintained at 95° during photolysis. Collection and measurement of gas non-condensable at 77°K^{3,4} and gas chromatographic analysis of such gas for H₂⁵ have been described.

Pure N₂O at 20 Torr and room temperature was used as an actinometer with $\phi(\text{N}_2 + \text{O}_2) = 1.6$.⁶

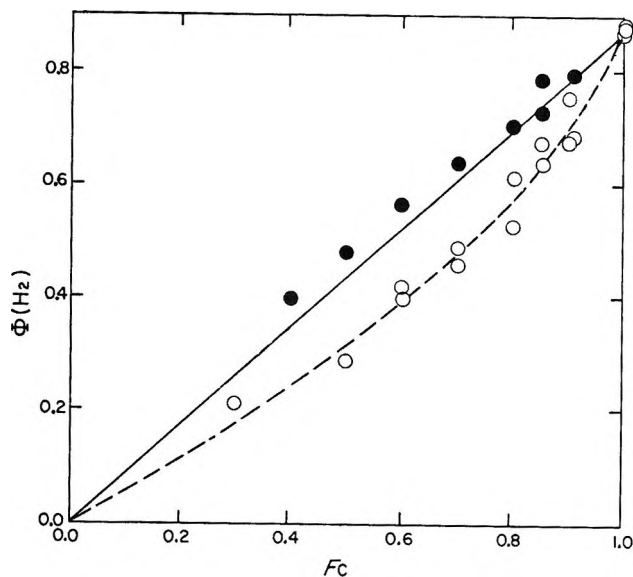


Figure 1. $\phi(\text{H}_2)$ in 1470-Å photolysis of cyclohexane mixtures at 750 Torr and 95° vs. F_C , the fraction of light absorbed by cyclohexane: O, *c*-C₆H₁₂-C₆H₆; ●, *c*-C₆H₁₂-N₂O. The broken curve is calculated as described in the text.

Intensities varied somewhat throughout the course of the work but were usually about 5×10^{14} quanta sec^{-1} . Actinometry immediately preceded each photolysis. There was no significant decrease in intensity during any one photolysis. A slight intensity decrease did occur after a number of photolyses owing to buildup on the lamp window of polymer which was removed periodically by photolysis of oxygen in the cell.⁴ Reduced polymer deposition on the window in this work may be a result of stirring (absent in the earlier work^{3,4}) or the higher temperature. The maximum conversion in pure cyclohexane was $\sim 10^{-3}\%$. Conversions in all experiments were such that less than 10% of the H atoms produced would be scavenged by unsaturated products.

Values of $\phi(\text{H}_2)$ were calculated without correction for an estimated decrease of $\sim 6\%$ in transmission of the sapphire window at 95°. Such values of $\phi(\text{H}_2)$ are presented in Figure 1 as a function of the fraction of light F_C absorbed by cyclohexane in the mixtures with benzene or N₂O at 95° and a total pressure of 750 Torr. As in the previous study,³ values of F_C were calculated

(1) The Radiation Laboratory of the University of Notre Dame is operated under contract with the U. S. Atomic Energy Commission. This is AEC Document No. COO-38-695.

(2) R. A. Holroyd, *J. Phys. Chem.*, **72**, 759 (1968); J. Y. Yang, F. M. Servedio, and R. A. Holroyd, *J. Chem. Phys.*, **48**, 1331 (1968).

(3) R. R. Hentz and R. J. Knight, *J. Phys. Chem.*, **72**, 4684 (1968).

(4) R. R. Hentz and S. J. Rząd, *ibid.*, **71**, 4096 (1967).

(5) R. R. Hentz and R. J. Knight, *ibid.*, **72**, 1783 (1968).

(6) J. Y. Yang and F. M. Servedio, *J. Chem. Phys.*, **47**, 4817 (1967).

(7) A. H. Laufer, J. A. Pirog, and J. R. McNesby, *J. Opt. Soc. Am.*, **55**, 64 (1965).

using 408,⁸ 159,⁸ and 110⁹ atm⁻¹ cm⁻¹ as decadic extinction coefficients (measured at 25°) for cyclohexane, benzene, and N₂O, respectively. The solid line in Figure 1 indicates the behavior expected of $\phi(\text{H}_2)$ in the absence of any kind of interaction between the mixture components.

Values of $\phi(\text{H}_2)$ for *c*-C₆H₁₂-C₆H₆ mixtures fall below the straight line expected for no interaction between the components. The broken curve in Figure 1 is based on the assumption that energy transfer from *c*-C₆H₁₂* to C₆H₆ is solely responsible for the deviation from linearity. The curve was calculated by use of $\tau = 4.7 \times 10^{-11}$ sec in eq 1

$$\phi = \phi^0 F_C / (1 + Z\tau) \quad (1)$$

in which ϕ^0 represents the quantum yield for pure cyclohexane ($F_C = 1$) and Z the frequency of collision of *c*-C₆H₁₂* with the energy acceptor,¹⁰ in this case C₆H₆. The value $\tau = 4.7 \times 10^{-11}$ sec is necessarily an upper limit because (1) the collision diameters are probably a lower limit for excitation-transfer diameters¹¹ and (2) H-atom scavenging by C₆H₆, in competition with abstraction from *c*-C₆H₁₂, is expected to contribute to deviation of $\phi(\text{H}_2)$ from linearity.³ Indeed, with the assumption that H atoms contribute ~20% to $\phi^0(\text{H}_2)$ ¹² and with a reasonable estimate of the specific rate of scavenging relative to that of abstraction at 95°, a curve can be calculated (for no energy transfer) that fits the data about as well as the broken curve in Figure 1.

As noted in the earlier work,³ complications associated with H-atom reactions should be absent in the *c*-C₆H₁₂-N₂O mixtures because all H are expected to react with *c*-C₆H₁₂ over the range of mixture compositions used. The results presented in Figure 1 for such mixtures at 750 Torr and 95° show no evidence of energy transfer from *c*-C₆H₁₂* to the potential acceptor N₂O.² An upper limit for τ can be estimated with the reasonable assumption that a deviation from linearity corresponding to $\phi/\phi^0 F_C < 0.9$ at $F_C = 0.4$ should have been manifest (*i.e.*, not obscured by experimental errors) in a plot such as that of Figure 1. Thus, from eq 1 with $\phi/\phi^0 F_C > 0.9$ and $Z = 5.1 \times 10^9$ sec⁻¹ at $F_C = 0.4$, $\tau \approx 2 \times 10^{-11}$ sec is obtained as an upper limit.

We conclude from the results shown in Figure 1 that absorption of a 1470-Å photon by cyclohexane in the gas phase produces an excited state with a lifetime that is certainly less than 4.7×10^{-11} sec and probably less than 2×10^{-11} sec. It is clear from present results that H₂ formation cannot occur from the same excited state of cyclohexane in both the gas and liquid photolyses at 1470 Å. For example, if the results in Figure 1 are attributable to energy transfer alone, then the excited state involved must transfer energy more efficiently to benzene than to N₂O; however, such behavior is contrary to that observed in the liquid phase.² Furthermore, even for $\tau = 4.7 \times 10^{-11}$ sec,

the results of Holroyd and coworkers² require specific rates of transfer from *c*-C₆H₁₂* in the liquid to C₆H₆ and N₂O of 6.8×10^{10} M⁻¹ sec⁻¹ and 14.5×10^{10} M⁻¹ sec⁻¹, respectively.

The simplest interpretation of present results is that (1) H₂ formation in the gas phase occurs from that state of cyclohexane produced by absorption of a 1470-Å photon and (2) H₂ formation in the liquid phase occurs from a lower, longer-lived state of excitation. Such an interpretation is consistent with recent conclusions of Hirayama and Lipsky¹³ from their observations on the fluorescence of saturated hydrocarbons. Fluorescence was observed from alkanes, including cyclohexane, when excited as neat liquids at wavelengths in the range 1470–1720 Å. With excitation in the liquid at 1470 Å, sensitization of benzene fluorescence was shown to accompany quenching of cyclohexane fluorescence. However, no fluorescence was observed on excitation of alkane vapors at 1470 Å. Excitation of the vapor at wavelengths longer than ~1600 Å produced an emission which, except for a slight blue shift, was identical with the liquid fluorescence. The authors conclude that both liquid and vapor emissions are of molecular origin with the upper state being strongly predissociated in the vapor above ~7.7 eV.

(8) Values for cyclohexane and benzene were obtained by S. Lipsky with a high-pressure Ar lamp at 1467 Å and were privately communicated.

(9) M. Zelikoff, K. Watanabe, and E. C. Y. Inn, *J. Chem. Phys.*, **21**, 1643 (1953).

(10) Collision frequencies were calculated using 6.1, 5.3, and 3.9 Å as the collision diameters of *c*-C₆H₁₂, C₆H₆, and N₂O, respectively; *cf.*, J. O. Hirschfelder, C. F. Curtiss, and R. B. Bird, "Molecular Theory of Gases and Liquids," John Wiley & Sons, Inc., New York, N. Y., 1954, p 1111.

(11) T. Watanabe, *Advances in Chemistry Series No. 82*, American Chemical Society, Washington, D. C., 1968, p 176.

(12) Hentz and Rzd (ref 4) have made a rough estimate of ~10% for the H-atom contribution.

(13) F. Hirayama and S. Lipsky, *J. Chem. Phys.*, **51**, 3616 (1969).

Nuclear Magnetic Resonance Study of Solvent Effects on Hydrogen Bonding in Methanol¹

by William B. Dixon²

Chemistry Division, Argonne National Laboratory, Argonne, Illinois 60439 (Received October 25, 1969)

For the past decade or more, nmr techniques have been very fruitfully applied to the study of hydrogen-bonded systems in solution.^{3,4} This success is due to

(1) Based on work performed under the auspices of the U. S. Atomic Energy Commission.

(2) Resident Research Associate from Wheaton College, Wheaton, Ill. Department of Chemistry, State University College, Oneonta, N. Y. 13820.

the large chemical shifts experienced by protons when they become involved in hydrogen bonds and to the accuracy with which these shifts may be measured. The method has been applied to the determination of such thermodynamic quantities as equilibrium constants for hydrogen bond formation and hydrogen bond energies as well as to the investigation of the structures of hydrogen-bonded species. In much of this work solvent effects have been largely ignored, and more recently it has become evident that some of the so-called inert solvents may interact appreciably with the systems under investigation,⁴ thus casting doubt on some of the quantitative conclusions that have been reached. Also, it is quite probable that infrared studies of hydrogen bonding in solution have been similarly influenced. The present work is a study of the effects that several different solvents have on the extent of self-association in methanol through hydrogen bonding.

Experimental Section

Spectra were recorded with a Varian HA-60 60-Mc spectrometer and frequency measurements made by the side-band technique. For some of the weaker lines signal-to-noise ratios were improved by accumulating repeated scans using a Varian C-1024 time averaging computer. All spectra were recorded at $25 \pm 0.5^\circ$.

Reagent grade solvents were dried over Linde molecular sieve pellets and used without further purification. All solutions were prepared volumetrically and in most cases contained 0.5% by volume cyclopentane as an internal reference. The hydroxyl proton peak of methanol was often split into a quartet through spin-spin interaction with the methyl group, and it was sometimes convenient to collapse and sharpen this peak by adding 0.5% by volume concentrated hydrochloric acid solution or dry HCl gas to the otherwise pure methanol used in preparing the solutions. Observations in a number of instances both with and without the added HCl showed no significant difference in the chemical shift.

Results and Discussion

The chemical shifts of the hydroxyl proton of methanol at 25° as a function of concentration in cyclohexane, cyclopentane, benzene, carbon tetrachloride, and acetonitrile are shown in Figure 1. In all cases the shifts are given relative to cyclopentane, which was used as the internal reference. However, in the cyclohexane solution the solvent itself was used as the internal reference and a correction of +3.5 cps made in the measured shifts to account for the shift between cyclohexane and cyclopentane. The use of an internal reference eliminates the influence of solvent bulk susceptibility on the observed shifts and, in principle, virtually cancels out other nonspecific solvent effects,⁵ in particular, that due to the van der Waals interaction between the solute and solvent and that due to the anisotropy of the magnetic susceptibility of the solvent molecules.

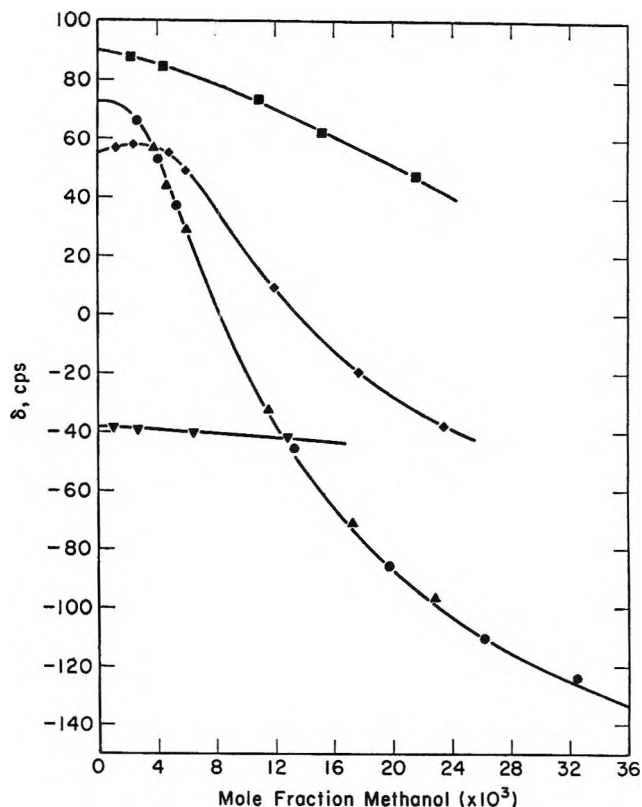


Figure 1. Chemical shift of the methanol hydroxyl proton (relative to cyclopentane as internal reference) as a function of concentration at 25° . Solvents: ●, cyclohexane; ▲, cyclopentane; ■, benzene; ◆, carbon tetrachloride; ▼, acetonitrile. The curve drawn through the cyclohexane points is a calculated one while the others are experimental curves.

For the nonpolar solvents, cyclohexane, cyclopentane, benzene, and carbon tetrachloride, the reaction field effects, too, should be small and not contribute significantly to the shift. Thus, in these four solvents at least, differences in the hydroxyl shift should be due almost entirely to specific interactions of the solute-solvent or solute-solute type or both.

For the four nonpolar solvents the dilution curves show the expected downfield shift of the hydroxyl proton resonance with increasing concentration, as more of the protons become involved in hydrogen bonds between solute molecules. This tendency toward self-association would depend mainly on the dielectric constant of the solvent if other factors were the same, since hydrogen bonding is largely an electrostatic effect. However, the marked variation in the slopes of the dilution curves, in spite of the similarity in solvent dielectric constants, indicates an inhibiting effect by

(3) G. C. Pimentel and A. L. McClellan, "The Hydrogen Bond," W. H. Freeman and Co., San Francisco, Calif., 1960.

(4) P. Laszlo in "Progress in Nuclear Magnetic Resonance Spectroscopy," Vol. 3, J. W. Emsley, J. Feeney, and L. H. Sutcliffe, Ed., Pergamon Press, Oxford, 1967, pp 279-310.

(5) A. D. Buckingham, T. Schaefer, and W. G. Schneider, *J. Chem. Phys.*, **32**, 1227 (1960).

benzene and carbon tetrachloride on self-association of the solute. These two solvents are evidently involved in solute-solvent interactions which are serious enough to discourage their use in any quantitative study of self-association by hydrogen-bonding solutes.

The behavior of methanol in the two relatively inert solvents, cyclohexane, and cyclopentane, deserves particular attention. The only previously reported nmr investigation⁶ of an alcohol in an aliphatic hydrocarbon solvent did not include dilute solutions, and only fairly recently have any such infrared studies been made.^{7,8} Because of the rapid exchange that takes place between the monomer and the various possible dimeric and polymeric species of methanol in solution, the hydroxyl protons show only a single resonance whose shift is the weighted average of the shifts attributed to the individual species. The same observation is true of the methyl proton resonance as well. Infrared spectra of alcohols, on the other hand, show the presence of individual species but their interpretation is not completely straightforward, and the estimation of concentrations from band intensities is hazardous. Therefore, in the present work, no special restrictions from this source were placed on the choice of a model for the structure of methanol in solution.

Of the various simple models, monomer-dimer, monomer-trimer, and monomer-tetramer, normally considered for the structure of hydroxylic compounds in solution, the monomer-tetramer model gave by far the best fit to the hydroxyl proton shift data for methanol in cyclohexane. The excellent agreement is shown in Figure 1, where the *calculated* curve for this model is drawn through the experimental points for methanol in cyclohexane. The experimental points for the solvent cyclopentane lie very close to the same theoretical curve.

In carrying out the calculations from which this curve was derived, the observed shift was assumed to be given by

$$\delta_{\text{obsd}} = (n_{\text{M}}/n_0)\delta_{\text{M}} + 4(n_{\text{T}}/n_0)\delta_{\text{T}}$$

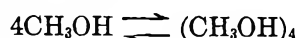
where n_0 is the total number of moles of methanol added to the solution and n_{M} and n_{T} are the number of moles of monomer and tetramer, respectively, present at equilibrium; δ_{M} and δ_{T} are the shifts attributed to the monomer and tetramer alone. Substituting

$$n_{\text{M}} = n_0 - 4n_{\text{T}} \quad (1)$$

into the above equation yields

$$\delta_{\text{obsd}} = \delta_{\text{M}} + 4(n_{\text{T}}/n_0)(\delta_{\text{T}} - \delta_{\text{M}}) = \delta_{\text{M}} + 4(n_{\text{T}}/n_0)\Delta_{\text{T}} \quad (2)$$

where Δ_{T} is the hydrogen bond shift between monomer and tetramer alone. The chemical equilibrium is expressed by the equation



and the corresponding equilibrium constant is given by

$$K_4 = X_{\text{T}}/X_{\text{M}}^4 \quad (3)$$

where X_{M} and X_{T} are the mole fractions of monomer and tetramer in the solution. This can be further expressed in terms of n_0 , n_{T} , and n_{S} , the number of moles of solvent, as

$$K_4 = (n_{\text{T}}/n_0)[(n_{\text{S}}/n_0) + 1 - 3(n_{\text{T}}/n_0)]^3/[1 - 4(n_{\text{T}}/n_0)]^4$$

For any assumed value of K_4 , n_{T}/n_0 may be calculated for each solution from its known n_{S}/n_0 value. This computation was readily accomplished by an iterative procedure using a Wang 360 programmable desk calculator. After elimination of δ_{M} from eq 2, yielding

$$\delta_{\text{obsd}2} - \delta_{\text{obsd}1} = 4[(n_{\text{T}}/n_0)_2 - (n_{\text{T}}/n_0)_1]\Delta_{\text{T}}$$

pairs of n_{T}/n_0 values together with the corresponding values of δ_{obsd} were used to calculate Δ_{T} . The best value of K_4 was the one which resulted in the most nearly equal values of Δ_{T} obtained in this way for various pairs of experimental points. The value of K_4 so obtained at 25° and the corresponding values of the other parameters are

$$K_4 = 3.1(\pm 0.2) \times 10^5 \text{ (mole fraction units)}$$

$$\Delta_{\text{T}} = -305 \pm 3 \text{ cps}$$

$$\delta_{\text{M}} = 73 \text{ cps}$$

The hydrogen bond shift for the tetramer, Δ_{T} , is seen to lie in the vicinity of the hydroxyl proton shift, -277 cps, for pure methanol relative to that of the monomer. The latter value was found by subtracting δ_{M} from the hydroxyl shift, -203.5 cps, of pure methanol relative to cyclopentane as internal reference, which was measured in this work. The rough agreement tends to support the monomer-tetramer model as opposed to the monomer-dimer and monomer-trimer models, for which unrealistically large hydrogen bond shifts were calculated. The "best" value for the hydrogen bond shift as calculated from the monomer-dimer model, for example, was in the neighborhood of -1000 cps.

The present value of K_4 may be compared with that of Saunders and Hyne,⁹ who obtained a result of 3.1×10^4 (after conversion from units of liter³ per mol³ to mole fraction) based on a monomer-tetramer model for methanol in carbon tetrachloride. The tenfold difference between the two values may be attributed to the inhibiting effect of the solute-solvent interaction upon hydrogen bonding between methanol molecules in carbon tetrachloride.

(6) A. B. Littlewood and F. W. Willmot, *Trans. Faraday Soc.*, **62**, 3287 (1966).

(7) H. C. Van Ness, J. Van Winkle, H. H. Richtol, and H. B. Hollinger, *J. Phys. Chem.*, **71**, 1483 (1967).

(8) A. N. Fletcher and C. A. Heller, *ibid.*, **71**, 3742 (1967).

(9) M. Saunders and J. B. Hyne, *J. Chem. Phys.*, **29**, 1319 (1958).

It should be emphasized that even though the simple monomer-tetramer model provides an excellent fit to the experimental data, the existence of significant though smaller concentrations of dimer or trimer is by no means ruled out. It is possible, for example, to include a small amount of dimer contribution in a predominantly monomer-tetramer model by making appropriate choices for the monomer-dimer equilibrium constant and the dimer hydrogen bond shift and still obtain a reasonably good fit to the data. Such a modification of the model is in fact necessary in order to secure consistency with infrared results, which provide strong evidence for the presence of dimers as well as polymers in dilute solutions of methanol and other aliphatic alcohols.^{3,7,8} Because of the presence of dimers, moreover, the dilution curve for methanol would not be expected to have a slope of zero at infinite dilution like that of the theoretical curve in Figure 1. It should have a more negative slope at the very lowest concentrations, which were not accessible for study, and intersect the δ axis at a point somewhat farther upfield. Thus, the value of δ_M , the monomer shift for

methanol, might be more correctly estimated as 80 ± 5 cps.

It is interesting to note the large percentage of methanol molecules present as tetramer, even at the low concentrations studied. At a methanol mole fraction of 0.02, for example, the model indicates that 52% of the methanol exists as tetramer.

As seen from Figure 1, the infinite dilution shift for methanol in carbon tetrachloride lies downfield from the shift in cyclohexane. This observation is consistent with a hydrogen bonding type of interaction between methanol and carbon tetrachloride. The upfield infinite dilution shift for methanol in benzene may be interpreted in terms of the type of model proposed by Schneider,¹⁰ involving a directed solute-solvent interaction and the magnetic anisotropy of the benzene ring.

Acknowledgment. The author expresses his appreciation to Dr. J. C. Hindman for his interest and suggestions during the course of this work.

(10) W. G. Schneider, *J. Phys. Chem.*, **66**, 2653 (1962).

COMMUNICATIONS TO THE EDITOR

Multiple Equilibria in Donor-Acceptor Complexing Studied by Ultracentrifugation

Sir: There are serious difficulties in attempting to measure unambiguously the formation and properties of donor-acceptor (D-A) complexes in solution.¹⁻⁴ The influence of solvation^{2,3} and component activities¹ has been discussed. Recently the possible presence of significant contributions from 2:1 and 1:2 D plus A complexes, in addition to the commonly assumed 1:1 stoichiometry, has been considered as a potential source of error in spectral and nmr determinations.⁴⁻⁶ However, no direct evidence for such higher aggregates has been offered as yet.

In order to examine states of aggregation in D-A solutions we have employed equilibrium ultracentrifugation⁷ with the optical absorption scanner.⁸ Charge-transfer (CT) absorption can be measured as a function of radius in the spinning sample (36,000 to 56,000 rpm) to obtain information on D plus A aggregates by equilibrium sedimentation analyses. The effective reduced

molecular weight σ_w for a single ideal species at equilibrium at the radius r is given by⁷

$$\sigma_w(r) = \frac{d(\ln C)}{d(r^2/2)} = \frac{M(1 - \bar{V}\rho)\omega^2}{RT} \quad (1)$$

where C = concentration of the solute species at radius r , M = molecular weight (g/mol) of the solute, \bar{V} = partial specific volume (cm/g) of the solute, ρ = solution density (g/cm³), ω = angular velocity (radians/sec), R = gas constant, T = abs temperature (°K).

(1) R. L. Scott, *Rec. Trav. Chim. Pays-Bas*, **71**, 1104 (1952); **75**, 787 (1956).

(2) P. J. Trotter and M. W. Hanna, *J. Amer. Chem. Soc.*, **88**, 3724 (1966), and references therein.

(3) S. Carter, *J. Chem. Soc., A*, 404 (1968).

(4) D. A. Deranleau, *J. Amer. Chem. Soc.*, **91**, 4050 (1969).

(5) S. D. Ross and M. M. Labes, *ibid.*, **79**, 76 (1957).

(6) G. D. Johnson and R. E. Bowen, *ibid.*, **87**, 1655 (1965).

(7) (a) J. W. Williams, K. E. Van Holde, R. L. Baldwin, and H. Fujita, *Chem. Rev.*, **58**, 715 (1958); (b) K. E. Van Holde and R. L. Baldwin, *J. Phys. Chem.*, **62**, 734 (1958); (c) D. A. Yphantis, *Biochemistry*, **3**, 297 (1964).

(8) H. K. Schachman and S. J. Edelstein, *ibid.*, **5**, 2681 (1966).

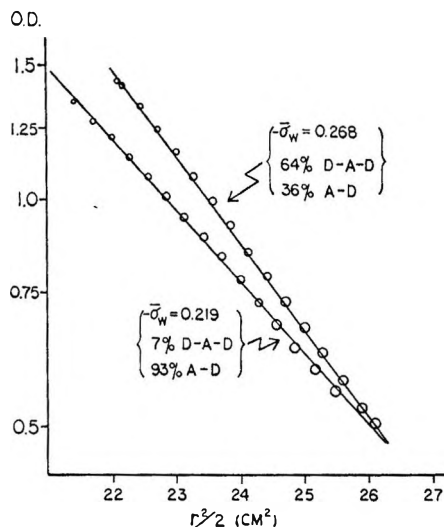


Figure 1. Experimental data for sedimentation (actually flotation) equilibrium for two TCNE-HMB solutions. The optical density is presented on a logarithmic scale as a function of $r^2/2$. The mean slopes are the indicated values of $\bar{\sigma}_w$. Conditions: 28° ; 36,000 rpm; $2.5 \times 10^{-4} M$ TCNE in CH_2Br_2 . Lower curve, $0.014 M$ HMB; upper curve, $0.53 M$ HMB donor concentration. The percentages of DAD were calculated using eq 5.

Use of optical density (OD) to determine concentration distributions in a system with more than one solute species in solution leads to an optical weight average of the $\sigma_w(r)$ which is given by

$$\bar{\sigma}_w(r) = \frac{d(\ln \text{OD})}{d(r^2/2)} = \frac{\sum_{i=1}^n (\text{OD}_i) \sigma_i}{\sum_{i=1}^n \text{OD}_i} = \frac{\omega^2 \sum_{i=1}^n (\text{OD}_i) M_i (1 - \bar{V}_i \rho)}{RT \sum_{i=1}^n \text{OD}_i} \quad (2)$$

where σ_i is the $\sigma_w(r)$ of the species i , and where the sums are taken over all absorbing species. Equations 1 and 2 assume the solutions to be ideal; this assumption appears justified here in view of the low solute concentrations and in view of the observations that the apparent molecular weights of the individual components are independent of concentration over the ranges used for observation of the CT complexes. For the low molecular weight systems examined here the values of $\bar{\sigma}_w(r)$ were found to be essentially constant across the cell for each solution so that we may use the mean value $\bar{\sigma}_w$ to characterize a particular solution.

The hexamethylbenzene (HMB) plus tetracyanoethylene (TCNE) D-A system in CH_2Br_2 as solvent was examined, under conditions where $(D) \gg (A)$, for the presence of DAD 2:1 complexes. Since the solvent is more dense than the solutes there is flotation of the complexes at equilibrium. Experiments utilizing measurements at the charge-transfer absorption maximum show an increasing absolute value of the

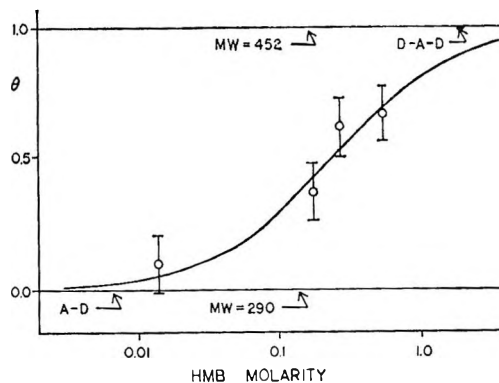


Figure 2. Optical fraction, θ , of D-A-D vs. donor concentration in the TCNE-HMB system. The solid curve was calculated from the stoichiometric mode of eq 3 and 4 using the value found for $K_2 \epsilon_2 / \epsilon_1$. The experimental points correspond to the $\bar{\sigma}_w$ observed at $\lambda = 546 m\mu$ and 36,000 rpm.

slope of $\ln \text{OD}$ vs. $r^2/2$ with increasing donor concentration. This slope approaches a $\bar{\sigma}_w$ corresponding to 70% DAD complexes at $(D) = 0.5 M$ (molar), near the solubility limit under our conditions. Typical experimental data are shown in Figure 1 for two conditions: 7% D-A-D at $(D) = 0.014 M$, and 64% D-A-D at $(D) = 0.53 M$.

Separate experiments with pure donor or pure acceptor in the same CH_2Br_2 solvent, utilizing OD at appropriate wavelengths, showed these to exist as unassociated monomers over the concentration spans used for studies of complex formation. (Acceptor concentrations were about $3.0 \times 10^{-4} M$ so we could approximate the final (D) concentration in the complexing solution by (D_0) the total donor concentration.)

These results imply the following equations



where $K_1 = (AD)/(A)(D)$, ϵ_1 = molar CT extinction coefficient of AD, σ_1 = effective reduced molecular weight of AD, $K_2 = (DAD)/(D)(AD)$, ϵ_2 = molar CT extinction coefficient of DAD, σ_2 = effective reduced molecular weight of DAD, and where D-A-D is written as a sandwich structure because no D-D bonding was observed in this system. Assuming Beer's law (*i.e.*, ϵ_1 and ϵ_2 constant) eq 2 gives θ , the optical fraction of DAD contributing to the CT absorption, as

$$\theta = \frac{\epsilon_2(\text{DAD})}{\epsilon_1(\text{AD}) + \epsilon_2(\text{DAD})} = \frac{\bar{\sigma}_w - \sigma_1}{\sigma_2 - \sigma_1} \quad (5)$$

Figure 2 presents θ as a function of (D) concentration for the system HMB plus TCNE. Note that the corresponding average molecular weights (values of \bar{V} used to estimate molecular weights were obtained from density data in the literature or estimated from ultracentrifuge experiments at concentrations low enough

so that the observed values of $\bar{\sigma}_w$ were independent of component concentrations) increase from that of AD (290) toward that of DAD (452). Combining eq 5, the equilibrium condition (DAD) = $K_2(D)(AD)$, and (D) = (D₀), we obtain

$$\frac{\sigma_2 - \sigma_1}{\sigma_2 - \bar{\sigma}_w} = \frac{K_2 \epsilon_2}{\epsilon_1} (D_0) + 1 \quad (6)$$

The graph according to eq 6 was linear within experimental error and give $K_2 \epsilon_2 / \epsilon_1 = 3.2 M \pm 0.5 l. mol^{-1}$. This relation may be used with a spectral formulation such Deranleau's⁴ to solve for K_1 , ϵ_1 , and K_2 , ϵ_2 , (see Deranleau's eq 14).⁴ For HMB-TCNE we analyze the spectral and ultracentrifugal data to obtain (in molar units): $K_1 = 24 \pm 3$, $\epsilon_1 = 3900 \pm 600$ and $K_2 = 3 \pm 1$, $\epsilon_2 = 4800 \pm 200$ at 28°. Using the Scott modification¹ of the usual Benesi-Hildebrand⁹ graphical procedures on our spectral data we obtain apparent⁴ constants for this system of $K_{app} = 21 \pm 2$ and $\epsilon_{app} = 4700 \pm 900$. In view of these large contributions from DAD complexes we must question experimental determinations and theoretical predictions based on the usual assumption of only 1:1 stoichiometry.¹⁰

The HMB plus chloranil D-A system was also examined as a further example of π - π complexing in both CH_2Br_2 and *n*-hexane as solvents. In these experiments we found behavior similar to that of HMB-TCNE with large contributions from DAD complexes.

Pyridine plus iodine in hexane provides an example of an *n*- σ bonding system in which the DAD complex is significant for (D) > 0.2 *M* pyridine. This system is being analyzed further.

The D and A components in all of the above experiments were monomeric over the concentration ranges studied. However, there is a possibility that D or A may self-associate in some systems.¹¹ We have tested this and we found that pure trinitrobenzene in CH_2Br_2 forms significant amounts of higher aggregates as shown by 30-40% increase in $\bar{\sigma}_w$ at 2.5 mol % concentration compared to infinite dilution.

Pressures of about 100 atm are generated near the bases of the solution columns at the speeds used here. Such pressures can affect the results in two ways: first through the volume changes on reaction, and second through differential compressibility of solvent and solute components. We have estimated the magnitude of such pressure effects utilizing data from high-pressure studies¹² of CT complexing and find, at most, only small corrections (about 3-4% in $\bar{\sigma}_w$).

Further ultracentrifugal and spectral analyses on these systems are being completed and we intend to publish a more detailed report. Thus far we have shown that higher order D plus A complexes are important in analyzing charge transfer systems, and that

the ultracentrifuge provides a powerful tool for analyzing the stoichiometries of such low molecular weight complexes.

Acknowledgment. Supported in part by NSF Grants GB-8164 and GB-13790, and by PHS training Grant GM-00265 to the Marine Biological Laboratory. Computer costs were defrayed through NSF Grant GJ-9 to the University of Connecticut computing center.

(9) H. A. Benesi and J. H. Hildebrand, *J. Amer. Chem. Soc.*, **71**, 2703 (1949).

(10) L. J. Andrews and R. M. Keefer, "Molecular Complexes in Organic Chemistry," Holden-Day Inc., San Francisco, Calif., 1964.

(11) D. W. Tanner and T. C. Bruice, *J. Phys. Chem.*, **70**, 3816 (1966).

(12) A. H. Ewald, *Trans. Faraday Soc.*, **64**, 733 (1968).

PHYSICAL CHEMISTRY SECTION PHILIP J. TROTTER
NEW ENGLAND INSTITUTE
RIDGEFIELD, CONNECTICUT 06877

BIOCHEMISTRY AND BIOPHYSICS SECTION DAVID A. YPHANTIS
BIOLOGICAL SCIENCES GROUP AND
INSTITUTE OF MATERIAL SCIENCE
UNIVERSITY OF CONNECTICUT
STORRS, CONNECTICUT 06268

RECEIVED NOVEMBER 7, 1969

Holography and Holographic Interferometry for Thermal Diffusion Studies in Solutions

Sir: Thermal diffusion in binary liquid systems can be studied *in situ* by various optical methods such as image displacement methods,¹⁻⁴ Gouy diffractometry,^{5,6} Rayleigh interferometry,⁷ and wave-front-shearing interferometry.⁸ In this paper we wish to report the application of a holographic interferometer.

Holographic interferometry—in particular real-time holography—was introduced by Brooks, Heflinger, *et al.*,^{9,10} in 1965. Finite-fringe holographic interferometry was used for electrochemical studies by

(1) C. C. Tanner, *Trans. Faraday Soc.*, **49**, 611 (1953).

(2) J. A. Bierlein, C. R. Finch, and H. Bowers, *J. Chim. Phys. Physicochim. Biol.*, **59**, 872 (1957).

(3) J. Chanu and J. Leroble, *ibid.*, **53**, 309 (1956); **55**, 743 (1958).

(4) H. J. V. Tyrrell, J. G. Firth, and M. Kennedy, *J. Chem. Soc.*, 3432 (1961).

(5) J. A. Bierlein, *J. Chem. Phys.*, **36**, 2793 (1962).

(6) J. G. Becsey and J. A. Bierlein, *ibid.*, **41**, 1853 (1964).

(7) L. G. Longworth, "The Structure of Electrolytic Solutions," W. J. Hamer, Ed., John Wiley and Sons, New York, N. Y., 1959.

(8) S. E. Gustafsson, J. G. Becsey, and J. A. Bierlein, *J. Phys. Chem.*, **69**, 1016 (1965).

(9) R. E. Brooks, L. O. Heflinger, and R. F. Wuerker, *Appl. Phys. Lett.*, **7**, 248 (1965).

(10) L. O. Heflinger, R. F. Wuerker, and R. E. Brooks, *J. Appl. Phys.*, **37**, 642 (1965).

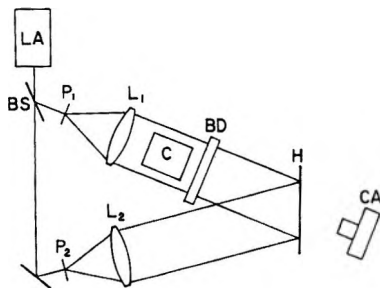


Figure 1. Schematic diagram of holographic interferometer.

Knox, *et al.*¹¹ Our interferometer in principle is similar to theirs, but instead of tilting the base hologram to introduce a finite basic fringe pattern, we use a variable prism system as a beam deflector placed in the object beam path between the cell and the hologram. The schematic diagram of our interferometer is shown in Figure 1. The laser (LA) was a Spectra Physics Model 125. Because of the relatively short coherence length (about 15 cm) of this laser, the difference in optical path lengths was maintained within this limit. Two 20- μ pinholes (P_1 , P_2) served as spatial filters. The beam splitter (BS) was of the variable-ratio type; an object-reference beam ratio of 2.5 was used. The focal length of both collimator lenses (L_1 , L_2) was about 70 cm. The beam deflector (BD) consisted of two identical precision wedges (about 1° wedge angle), mounted in counterrotating holders. The focal length of the recording camera (CA) was 24 cm, and it was focused on the exit window of the cell (C) with the aid of extension rings. In order to obtain a small depth of field (otherwise the pinhole of the object beam may have been partially focused), the largest aperture was used. For the holograms (H) we used Kodak 649F plates developed with D-19 (5 min at 68°F). The spacing and inclination of the basic finite fringe pattern can be adjusted conveniently (but not independently) with the beam deflector. Since the interferogram is superimposed on the image of the diffusion cell, the coordinate system is defined unambiguously.

Our experiments were run as isothermal relaxations from the thermodiffusional steady state, obtained by prolonged unmixing under the influence of a fixed temperature gradient. To interpret an interferogram, we need to know the optical path difference ΔP between conjugate rays of light traversing the diffusion cell at equal distances above and below the midplane. Straightforward application of phenomenological and optical principles described elsewhere^{8,12} yields the required theoretical relation

$$\Delta P_{th} = \frac{8}{\pi^2} \sigma \tau K_1 L \sum_{k=1}^{\infty} \frac{1}{k^2} \sin \frac{k\pi}{2} \sin \frac{k\pi v}{a} \exp(-k^2 t / \theta) \quad (1)$$

Here σ is the Soret coefficient; τ is the applied temperature difference; $K_1 = n_0(-n_0) \partial \mu / \partial n$, where n_0 is the overall composition expressed in mole fraction

	time, min.	$[\Delta P / \lambda]_{obs.}$	$[\Delta P / \lambda]_{calc.}$
	11.5	13.14	13.06
	21.0	11.96	12.14
	63.0	9.53	9.44
	134.5	6.48	6.48
	186.4	4.97	4.87
	256.1	3.11	3.18
	320.4	1.97	1.99
	471.7	0.03	0.14
	594.1	-0.64	-0.73

$$v = 0.365 \text{ cm}, \quad Q = 0.792 \text{ cm}, \quad L = 7.948 \text{ cm}$$

$$K_1 = 1.253 \times 10^{-2}, \quad \tau = 2.104^\circ \text{C}, \quad \lambda = 632.8 \text{ nm}$$

$$B_{calc.} = -2.11$$

Figure 2. Fringe patterns obtained during thermal diffusion in 0.5 *m* CdSO₄ solution.

and n and μ are, respectively, the local instantaneous composition and refractive index; L is the geometric length of the diffusion cell; a is the height of the cell and v is the vertical coordinate measured from the midplane; t is the elapsed time; and $\theta = a^2 / \pi^2 D$, where D is the isothermal diffusivity.

On the interferogram, the distance between adjacent fringes at conjugate coordinates $\pm z$ corresponds to a path difference of one wavelength λ . Hence, from a series of measurements of $(\Delta P / \lambda)_i$ at different times t_i , σ and D can be evaluated by least-squares minimization of the expression

$$\sum_{\text{all } i} [(\Delta P_{obsd} / \lambda)_i - (\Delta P_{th} / \lambda)_i - B] \quad (2)$$

where ΔP_{th} is given by eq 1. The constant B is an additional adjustable parameter which is peculiar to each experiment but has no physical content of general interest. It lumps together two effects: the weak prismatic character of any real diffusion cell which arises from lack of perfect parallelism of its windows, and the inherent inclination of the basic linear fringe pattern which has to be accepted along with the particular finite spacing that is selected in the initial setting of the beam deflector.

A grid-search type nonlinear least-squares method¹³ was applied in the data reduction process. The infinite series was truncated to eight significant figures. The interferograms obtained in 0.5 *m* CdSO₄ solutions are shown in Figure 2. The Soret coefficient calcu-

(11) C. Knox, R. R. Sayano, E. T. Seo, and H. P. Silverman, *J. Phys. Chem.*, **71**, 3102 (1967).

(12) J. A. Bierlein, *J. Chem. Phys.*, **23**, 10 (1955).

(13) J. G. Becey, L. Berke, and J. R. Callan, *J. Chem. Educ.*, **45**, 728 (1968).

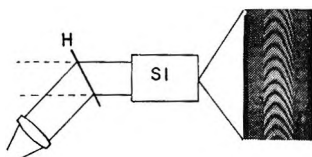


Figure 3. Wave-front reconstruction and analysis. The fringes were formed by recalling the wave form stored in the hologram and then passing it through a wave-front-shearing interferometer of the kind described in ref 8.

lated from our results is $(5.50 \pm 0.05)10^{-3} \text{ deg}^{-1}$ and the isothermal diffusivity is $4.21 \times 10^{-6} \text{ cm}^2/\text{sec}$, both at 28.2° mean temperature; these values are in reasonable agreement with other determinations.⁵⁻⁸ These results are considered only preliminary; improvements in optics and temperature control are in progress. The advantages of the method compared with classical Rayleigh interferometry is the simplicity of the optical system.

It is also possible to record the entire refractive index field in the cell by taking holograms during the thermal diffusion process. If these holograms are illuminated by a collimated laser beam incident from the same angle as the original reference beam, the recalled real object beam can be studied by different optical methods. Figure 3 shows an interferogram obtained from the hologram (H) with a wave-front-shearing interferometer (SI). This capability is of great value, since the refractive index fields can be stored and evaluated at leisure by means of any read-out procedure the experimenter wishes to employ.

(14) Aerospace Research Laboratories.

(15) Air Force Flight Dynamics Laboratory.

AEROSPACE RESEARCH LABORATORIES JULIUS G. BECSEY¹⁴
AND AIR FORCE FLIGHT DYNAMICS GENE E. MADDUX¹⁵
LABORATORY NATHANIEL R. JACKSON¹⁴
WRIGHT-PATTERSON AIR FORCE BASE JAMES A. BIERLEIN¹⁴
OHIO 45433

RECEIVED JANUARY 26, 1970

A Comment on the Infrared Spectrum of Carbon Monoxide Adsorbed on Silica-Supported Platinum

Sir: In a recent paper, Clarke, Farren, and Rubalcava¹ reported that the adsorption of CO on Pt dispersed on silica (Cab-O-sil) gave rise to a weak absorption band near 476 cm^{-1} . This was assigned to the Pt-C stretching vibration of linearly adsorbed CO molecules. Despite the low transmission of their silica, they suggested that this observation was possible because the background transmission of the Pt-SiO₂ disk increased

with temperature from 5% at room temperature to 40% at 250° . Ogilvie² criticized this interpretation and pointed out that this apparent increase in transmission could be an artifact resulting from the increased emission of the sample. In reply, Clarke, *et al.*,³ rejected this criticism as unjustified. However, we have shown elsewhere⁴ that for sufficiently hot and opaque samples, emission errors of the type discussed by Ogilvie can easily arise even at frequencies as high as 3500 cm^{-1} . These can be avoided by chopping the source radiation before the sample and not between sample and detector. The spectrometer used by Clarke, *et al.*,¹ (a Grubb-Parsons Spectromaster) has the latter type of chopping and it is the purpose of the present note to show that their results may well be an artifact, as suggested by Ogilvie.

The Pt-SiO₂ catalyst used in our work was prepared in a manner similar to that described by Clarke, *et al.*⁵ Silica aerosil (Cab-O-sil HS5, surface area $330 \text{ m}^2/\text{g}$) was impregnated ten times with an aqueous solution of $\text{Pt}(\text{NO}_2)_2(\text{NH}_2)_2$ (Engelhard Industries) of strength such that the final material contained 10% Pt. Hydrogen chemisorption on the reduced catalyst in a manner similar to that described by Dorling, Burlace, and Moss⁶ indicated a monolayer coverage equivalent to 1.47 cm^3 (STP)/g of catalyst, from which the mean crystalline size was estimated to about 30 \AA . The final catalyst was dried at 100° , ground in a Wig-L-Bug and pressed into platelets weighing about 10 mg cm^{-2} , the same thickness employed by Clarke, *et al.*¹

The platelets were placed in an infrared cell which was connected to a vacuum line and suspended in the sample compartment of a Beckman IR-12 spectrometer. This instrument has provision for chopping either before or after the sample, thus enabling the measurement of transmission plus emission or true transmission spectra. The infrared cell was similar to that described by Eberly⁷ and for this work it was fitted with CsI windows. The pretreatment, which was carried out in the cell, consisted of circulating H₂ (which had been diffused through a hot palladium thimble) over the platelet at 320° for 2 hr followed by evacuation for 1 hr at 320° to a pressure of less than 10^{-5} Torr. H₂O was removed by a -195° trap in the circulating system.

(1) J. K. A. Clarke, G. M. Farren, and H. E. Rubalcava, *J. Phys. Chem.*, **72**, 327 (1968).

(2) J. F. Ogilvie, *ibid.*, **72**, 2688 (1968).

(3) J. K. A. Clarke, G. M. Farren, and H. E. Rubalcava, *ibid.*, **72**, 2688 (1968).

(4) N. W. Cant and W. K. Hall, *Trans. Faraday Soc.*, **64**, 1093 (1968).

(5) J. K. A. Clarke, G. Farren, and H. E. Rubalcava, *J. Phys. Chem.*, **72**, 2376 (1968).

(6) T. A. Dorling, C. J. Burlace, and R. L. Moss, *J. Catal.*, **12**, 207 (1968).

(7) P. E. Eberly, *J. Phys. Chem.*, **71**, 1717 (1967).

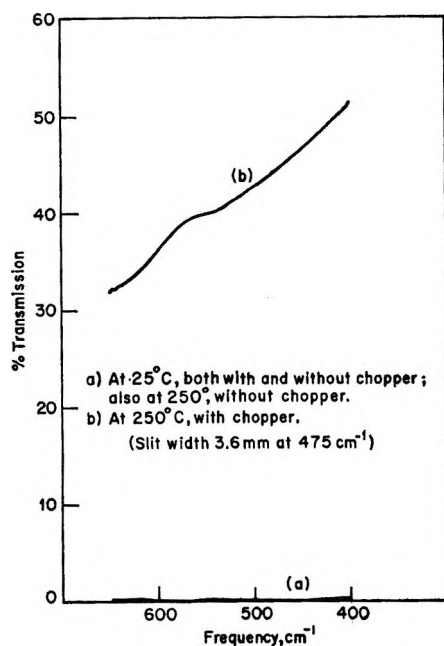


Figure 1. Infrared spectra from 10% Pt on silica catalyst.

Following pretreatment, the Pt-SiO₂ sample was cooled to room temperature *in vacuo* and the instrument settings adjusted to provide sufficient energy for normal operations. The spectrum shown was (a) in Figure 1 was then obtained regardless of whether the chopper between sample and detector was in operation or not, *i.e.*, the transmission of the platelet was much less than 1% between 400 and 650 cm⁻¹. The temperature was then raised to 250°. A spectrum measured at this stage with the monochromator chopper disconnected (*i.e.*, sample emission not chopped or recorded) was identical with (a), *i.e.*, no change in transmission had occurred. However, when this chopper was reconnected, the spectrum changed to that given by (b) in Figure 1, with an *apparent* transmission of 43% at 475 cm⁻¹. This value is quite close to that reported by Clarke, *et al.*,¹ but the agreement must be

regarded as fortuitous since, as expected for emission, it changed in proportion to the square of the slit width, and was therefore dependent upon the exact value chosen for this instrumental parameter. We have made similar measurements with disks of Cab-O-sil alone.

These results leave no doubt that the transmission of Pt-SiO₂ platelets of this type and thickness is close to zero between 400 cm⁻¹ and 650 cm⁻¹, regardless of temperature, and that the apparent increase in transmission with temperature, as reported by Clarke, *et al.*,¹ is *solely* due to sample emission. Hence, the measurement of meaningful transmission spectra of CO adsorbed on Pt-SiO₂ would appear to be impossible in this spectral range.

In our work, we were unable to observe any change in either spectrum (a) or (b) when CO was admitted to the cell to a pressure of 10 Torr or was subsequently removed by evacuation. These negative findings were certainly not due to the absence of CO adsorbed on Pt since concurrent measurements near 2100 cm⁻¹ showed the usual single absorption band due to linearly adsorbed carbon monoxide.⁸ (Following evacuation for 1 hr at 250°, this band had the following characteristics: at 25°, $\nu = 2069$ cm⁻¹, $\Delta\nu_{1/2} = 30$ cm⁻¹, and optical density 0.68; at 250°, $\nu = 2048$ cm⁻¹, $\Delta\nu_{1/2} = 42$ cm⁻¹, and optical density 0.28.)

In agreement with Ogilvie,² we therefore conclude that the band observed by Clarke, *et al.*,¹ at 476 cm⁻¹ should not be attributed to CO adsorbed on Pt.

Acknowledgment. This work was sponsored by the Gulf Research and Development Co. as part of its research program on the Fellowship on Petroleum.

(8) R. P. Eischens, S. A. Francis, and W. A. Pliskin, *J. Phys. Chem.*, **60**, 194 (1956).

MELLON INSTITUTE
CARNEGIE-MELLON UNIVERSITY
PITTSBURGH, PENNSYLVANIA 15213

NOEL W. CANT
W. KEITH HALL

RECEIVED NOVEMBER 4, 1969